ASME
SETTING THE STANDARD

Journal of Engineering for Gas Turbines and Power

Published Quarterly by ASME

VOLUME 128 • NUMBER 3 • JULY 2006

Transactions of the ASME, Journal of Engineering for Gas Turbines and Power (ISSN 0742-4795) is published quarterly (Jan., April, July, Oct.) by The American Society of Mechanical Engineers, Three Park Avenue, New York, NY 10016. Periodicals postage paid at New York, NY and additional mailing offices. POSTMASTER: Send address changes to Transactions of the ASME, Journal of Engineering for Gas Turbines and Power, c/o THE AMERICAN SOCIETY OF MECHANICAL ENGINEERS, 22 Law Drive, Box 2300, Fairfield, NJ 07007-2300.
CHANGES OF ADDRESS must be received at Society headquarters seven weeks before they are to be effective. Please send old label and new address.
STATEMENT from By-Laws. The Society shall not be responsible for statements or opinions advanced in papers or ... printed in its publications (B7.1, par. 3).

TECHNICAL PAPERS

(Contents continued on inside back cover)

This journal is printed on acid-free paper, which exceeds the ANSI Z39.48-1992 specification for permanence of paper and library materials. ♾™
♻ 85% recycled content, including 10% post-consumer fibers.

(Contents continued)

Journal of Engineering for Gas Turbines and Power JULY 2006

Volume 128, Number 3

(Contents continued on facing page)

Journal of Engineering for Gas Turbines and Power **JULY 2006**

Volume 128, Number 3

Thermodynamic Properties

The ASME Journal of Engineering for Gas Turbines and Power is abstracted and indexed in the following:

AESIS (Australia's Geoscience, Minerals, & Petroleum Database), Applied Science & Technology Index, Aquatic Sciences and Fisheries Abstracts, Civil Engineering Abstracts, Compendex (The electronic equivalent of Engineering Index), Computer & Information Systems Abstracts, Corrosion Abstracts, Current Contents, Engineered Materials Abstracts, Engineering Index, Enviroline (The electronic equivalent of Environment Abstracts), Environment Abstracts, Environmental Science and Pollution Management, Fluidex, INSPEC, Mechanical & Transportation Engineering Abstracts, Mechanical Engineering Abstracts, METADEX (The electronic equivalent of Metals Abstracts and Alloys Index), Pollution Abstracts, Referativnyi Zhurnal, Science Citation Index, SciSearch (The electronic equivalent of Science Citation Index), Shock and Vibration Digest

A Numerical Simulation Capability for Analysis of Aircraft Inlet-Engine Compatibility[1]

Alan Hale

Milt Davis

Jim Sirbaugh

Aerospace Testing Alliance (ATA),
Arnold Engineering Development Center,
Arnold AFB, TN 37389-9013

Two primary aircraft propulsion subsystems are the inlet and the engine. Traditionally these subsystems have been designed, analyzed, and tested as isolated systems. The interaction between the subsystems is modeled primarily through evaluating inlet distortion in an inlet test and then simulating this distortion in engine tests via screens or similar devices. Recently, it has been recognized that significant improvements in both performance and operability can be realized when both the inlet and the engine are designed with full knowledge of the other. In this paper, a computational tool called Turbine Engine Analysis Compressor Code is used to evaluate the effect of inlet distortion on a three-stage military fan. This three-stage military fan is further connected to an F-16 inlet and forebody operating at an angle of attack and sideslip to demonstrate the effect of inlet distortion generated by flight maneuvers. The computational approach of simulating an integrated inlet-engine system is expected to provide additional insight over evaluating the components separately. [DOI: 10.1115/1.1925649]

1 Introduction

Integration of a weapon system airframe and its propulsion system encompasses a number of issues ranging from aircraft stability and control to inlet-engine compatibility. To address these issues, the test and evaluation process requires the application of a variety of test resources as well as a wide range of analytical and computational tools. Testing for airframe-propulsion integration, and in particular inlet-engine compatibility, generally requires the coupling of component tests conducted in both wind tunnels and engine altitude facilities.

The advent of technologies allowing for controlled flight at extremely high angles of attack and sideslip has enabled weapon system developers to consider supermaneuver and poststall maneuver capabilities as combat tactics. As a result, future fighter aircraft may be required to execute maneuvers containing drastic changes in flight conditions at the high power settings demanded by combat. Such maneuvers bring forth the question of what role the distortion time history might play in the inlet-engine integration task. Large and transient changes in angle of attack can produce hysteresis and, therefore, deviations from the steady-state condition.

The inlet-engine integration test methodology currently involves two separate processes that are loosely coupled [1]. Subscale inlet tests are conducted in a wind tunnel to determine the conditions that must be simulated at the face of a full-scale engine. These conditions, although a function of angle of attack, sideslip, and flight condition, are characterized by a distortion indexing methodology that may lessen the influences of each individual flight variable. Similarly, the engine test methodology measures the effect of a series of distortion patterns based upon distortion screens on engine operability and performance. Keeping with one of the fundamental precepts of the recommended practice set forth in the ARP-1420 [2] and in its companion document, AIR-1419 [3] (namely, that engine stability can be defined by tests using equivalent levels of steady-state distortion), aircraft manufacturers, engine manufacturers, and testing organizations have implemented testing procedures which reflect that premise.

The inlet-engine integration test methodology currently is based on engine tests that show that the engine experiences distortion patterns that last for a time of the order of one engine RPM as if they were steady-state conditions. [Note that this methodology does not address aerostructural effects on the engine (e.g., high cycle fatigue).] Thus, subscale inlet tests in a wind tunnel are used to select the conditions that must be simulated at the face of a full-scale engine. These conditions, although a function of angle of attack, sideslip, and flight condition, are characterized by a distortion-indexing methodology. The accuracy of this distortion-indexing methodology is dependent upon the thoroughness of dedicated engine tests with classic distortion patterns and realistic distortion patterns for the particular application. ′Discussion of the accuracy of this process is a subject beyond the scope of this paper.

In the absence of the inlet and airframe, the direct-connect test methodology for propulsion (see Refs. [1,4] for a full description of the methodology) must rely on additional techniques to simulate the distortion produced by the inlet. A number of methods have been applied to simulate steady-state inlet distortion as well as various aspects of time-variant distortion. The two most widely used inlet distortion simulators are the distortion screen and the air-jet distortion generator. Although efforts are proceeding to improve the inlet simulation devices placed in front of an engine, the current devices neglect time history, flow angularity (swirl), and certain interactions such as the effect of the compressor face on the inlet characteristics. The current status for airframe-engine integration was best summarized by R. E. Smith, Jr. in the AIAA 1995 Wright Brothers Lectureship in Aeronautics [5]:

"*In spite of all the improvements cited in this assessment, significant portions of the current state of the art for the airframe-engine integration process are still dependent on empiricism and scaling rules. Such dependencies always contain exposure to risks that the next configuration and/or next mission requirement will lie outside the bounds of applicability of the empiricism and/or scaling rules. These risks portend the possibility of a major negative surprise. The airframe-engine integration process has produced many such surprises in its history.*"

[1]The research reported herein was performed by the Arnold Engineering Development Center (AEDC), Air Force Material Command (AFMC). Work and analysis for this research were done by personnel of Aerospace Testing Alliance (ATA), technical services contractor for AEDC. Further reproduction is authorized to satisfy the needs of the U. S. Government.

Contributed by the International Gas Turbine Institute (IGTI) of ASME for publication in the JOURNAL OF ENGINEERING FOR GAS TURBINES AND POWER. Manuscript received October 1, 2003; final manuscript received March 1, 2004. IGTI Review Chair: A. J. Strazisar. Paper presented at the International Gas Turbine and Aeroengine Congress and Exhibition, Vienna, Austria, June 13–17, 2004, Paper No. 2004-GT-53473.

Clearly the volume of issues facing future integrations of inlet and engine into viable aircraft systems (such as the F/A-22, Joint Strike Fighter, F/A-18, and UAV's) demands improved test techniques coupled with dynamic numerical simulations.

2 Inlet Numerical Simulation Capability

The computational simulation of inlets, especially for advanced fighter aircraft, requires modeling of complex geometries and physical phenomena. The inlets can be highly curved to hide observables such as hot engine parts and radar-reflective material. This leads to the inlet's having become an essential part of the aircraft fuselage and its thus being forced to have a wide range of cross-sectional shapes, introducing issues such as nonuniform flow, significant cross-flow velocities, and flow separations prior to the engine face.

Simulating these complex geometries and the associated complex physical phenomena of engine inlets requires simulation tools capable of capturing unsteady, three-dimensional (3D), turbulent flow fields. Because of the highly 3D nature of the flow and the potential for significant flow separation, full Reynolds-averaged, Navier–Stokes equations with sophisticated turbulence models must be solved.

The Navier–Stokes solver needs to have the capability to model unsteady phenomena such as the time history of fluctuating pressures at the compressor face, inlet unstart, and inlet buzz. Also, the simulation tool needs to have the capability to solve for or model the effects of the presence of the engine, in particular the first stages of the compressor, on the inlet flow field. Current computational fluid dynamics (CFD) capabilities do not include resolution of the total pressure fluctuations of the flow; only the "steady-state" total pressures are obtained. In the case of time-accurate solutions, this limitation also applies. In spite of these limitations, CFD solutions of inlet duct flows have been useful in understanding inlet/engine integration problems.

Navier–Stokes codes in use today have the capability to model a majority of the flow phenomena needed to adequately simulate the inlet flow field. The most challenging requirements are turbulence modeling; fast, time-accurate simulation; and the modeling of the effects of inlet distortion on rotating turbomachinery, and vice versa. Two such codes, NXAIR [6] and WIND [7], are capable of meeting some of these challenges. Each code has advantages and disadvantages, depending on the application. These codes have been used for calculation of aircraft inlet flow fields and are suitable for marriage with other codes for application to the engine-inlet configuration. The F-16 system has been chosen to illustrate the computational capability of the current state-of-the-art CFD inlet simulations. Of particular interest are the effects of the aircraft forebody on the flow field at the aerodynamic interface plane (AIP) as presented in Fig. 1. The total pressure recovery using the CFD results was compared to experimental results by interpolating the CFD solution to the same points in space where the total pressure probes exist in the experimental results. This allows for a one-to-one comparison with the experimental results since the experimental results were area-averaged to derive the total pressure recovery as shown in the bottom of Fig. 1

Shown at the top of Fig. 1 are total pressure contours around the nose of the fuselage and at the beginning of the inlet. Of particular interest was the vortex shedding produced by the two small antennas near the nose of the fuselage during a 6-deg sideslip condition. The effect of the vortex shedding on the flow field is apparent at the AIP, as illustrated in the figure. The vortex shedding also has an effect on the total pressure recovery near the low end of the flow regime. This particular case was an extreme 6-deg angle of sideslip (AOS) at supersonic Mach number. The antenna vortex interacted with the inlet boundary-layer diverter flow and inlet shock to create a larger than desired, shock-induced flow separation. The separated flow was ingested into the inlet. This scenario was unique to testing and is not an operational concern.

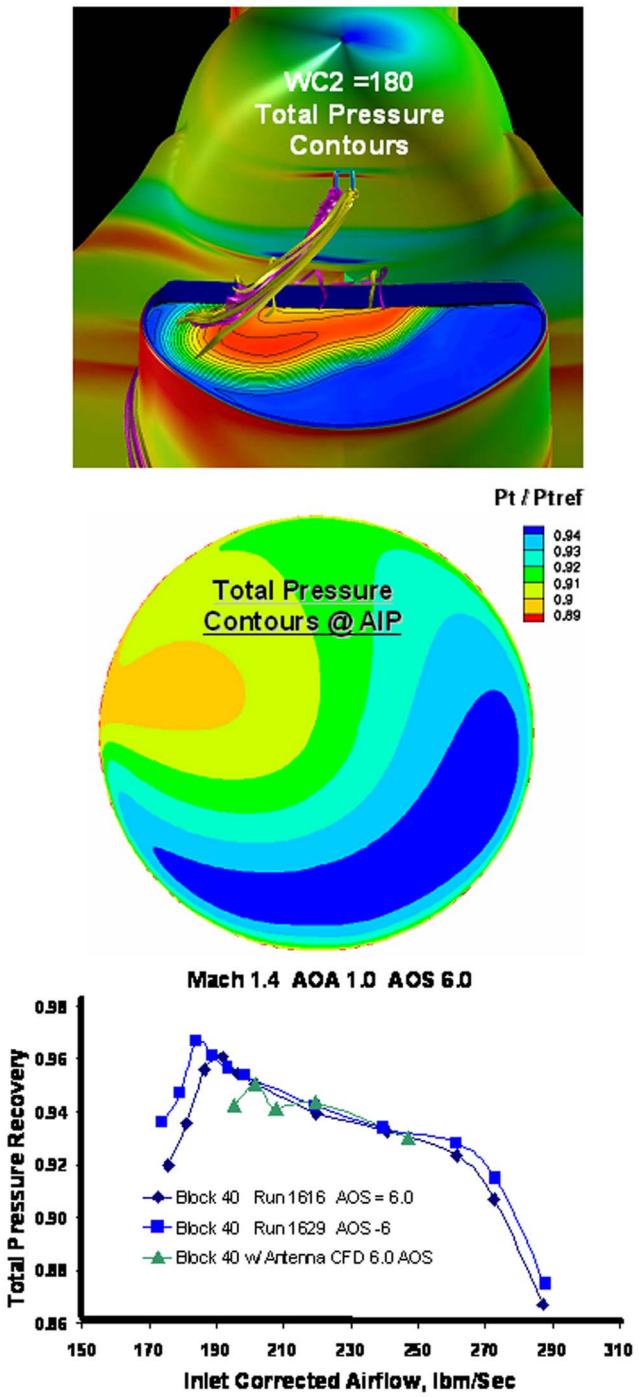

Fig. 1 CFD flow field and inlet computations of the F-16 inlet and AIP

Inlet calculations can characterize the flow field at the AIP that the propulsion system must be able to accept. However, characterizing the distorted flow field with a distortion index such as that described in SAE ARP-1420 [2] does not necessarily provide enough information to determine the effect on the gas turbine engine compression system. Engine testing with inlet distortion is usually prescribed. To augment testing, numerical simulations capable of calculating compression system and eventually engine performance and/or operability are required.

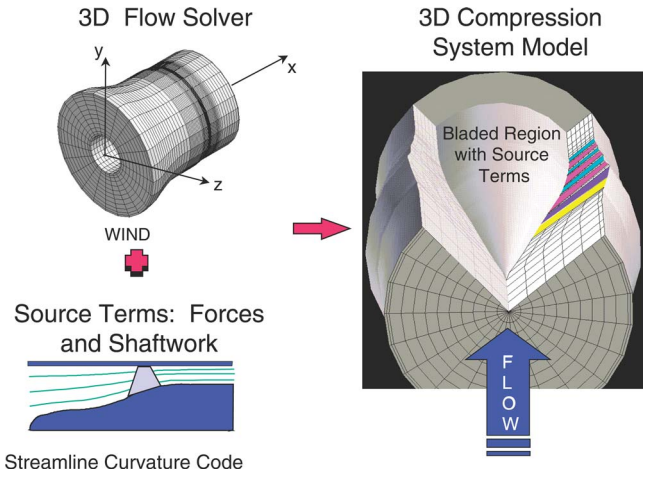

Fig. 2 TEACC technical approach

3 Compression System Numerical Simulation Capability

To compute time-dependent, complex inlet distortion effects on the compressor flow field and vice versa in a timely manner, one must accept more empiricism in the modeling approach. The approach discussed in this paper is the development of a 3D compression system model that uses source terms to represent turbomachinery components instead of the traditional turbomachinery CFD approach. A general purpose 3D flow simulation computer code, the WIND code, has been modified to accept turbomachinery source terms using semiactuator disk theory. These turbomachinery source terms are calculated using a streamline curvature code, HTO300 [8]. This approach for developing a 3D compression system simulation, known as Turbine Engine Analysis Compressor Code (TEACC), [9,10] is conceptually presented in Fig. 2.

3.1 Governing Equations. The governing equations used in TEACC are developed by applying the conservation of mass, momentum, and energy principles. In turbomachinery flows, the viscous effects predominate mostly along the wall, making an accurate simulation of the flow field away from the wall possible by using the Euler equations with turbomachinery source terms. These source terms represent the effects of the blades and the walls on the fluid, thus allowing a less intense grid but a more empirically based calculation. The equations of fluid motion using the thermally and calorically perfect ideal gas assumption with turbomachinery source terms are as follows:

$$\frac{\partial \mathbf{Q}}{\partial t} + \frac{\partial \mathbf{E}}{\partial x} + \frac{\partial \mathbf{F}}{\partial y} + \frac{\partial \mathbf{G}}{\partial z} = \mathbf{S}$$

where

$$\boldsymbol{Q} = \begin{bmatrix} \rho \\ \rho u \\ \rho v \\ \rho w \\ \rho e_t \end{bmatrix} \quad \boldsymbol{E} = \begin{bmatrix} \rho u \\ \rho u^2 + P \\ \rho uv \\ \rho uw \\ (\rho e_t + P)u \end{bmatrix} \quad \boldsymbol{F} = \begin{bmatrix} \rho v \\ \rho vu \\ \rho v^2 + P \\ \rho vw \\ (\rho e_t + P)v \end{bmatrix}$$

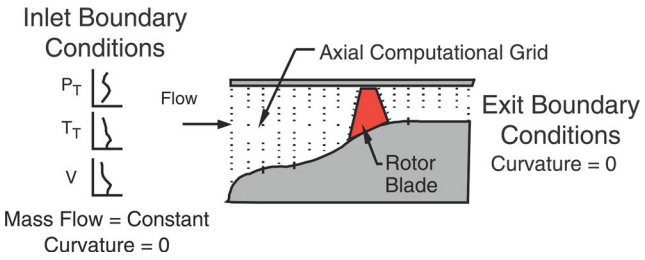

Fig. 3 Streamline curvature code geometry and far-field boundary condition

$$\boldsymbol{G} = \begin{bmatrix} \rho w \\ \rho wu \\ \rho wv \\ \rho w^2 + P \\ (\rho e_t + P)w \end{bmatrix} \quad \mathbf{S} = \begin{bmatrix} S_{\dot{m}} \\ S_{Fx} \\ S_{Fy} \\ S_{Fz} \\ S_{\dot{W}} + (S)_{\text{Bleed}} \end{bmatrix}$$

The volumetric turbomachinery source terms are: (1) bleed per volume (2) forces per volume in the x, y, and z directions, and (3) rate of shaft work per volume.

3.2 Solution Technique. Three-dimensional blade force and rate of shaft work terms are supplied by streamline curvature code (SLCC). The SLCC is based on a radial redistribution of blade forces and shaft work, producing an "axisymmetric flow with swirl" in the form of streamlines. Necessary inputs include overall geometry, blade geometry, and loss and deviation correlations. A typical SLCC grid is illustrated in Fig. 3.

The streamline curvature code delivers a velocity flow field in the form of streamlines. The SLCC has been further modified to calculate turbomachinery source terms at the blades within each stream tube. A single SLCC control volume with multiple forces acting upon the control surfaces as well as the control volume is illustrated in Fig. 4. The inlets and exists of the control volume represent the leading and trailing edges of a blade. The top and bottom of the control volume define streamlines from a converged solution of the SLCC. For steady-state conditions, blade forces are equal to the pressure forces plus momentum forces. The pressure forces are accounted for on all surfaces, but momentum forces are not included across the streamline surface since, by definition, flow is not allowed to cross a streamline. The blade forces represented in Fig. 4 are a portion of the turbomachinery sources, which are implemented into the 3D CFD algorithm. The other turbomachinery source terms are the shaft work and bleed flows. Shaft work is obtained by applying the same control volume analysis to the energy equation, and the user specifies the bleed flows. For dynamic behavior, it is necessary that the streamline curvature code calculate turbomachinery source terms across individual blades. Boundary conditions illustrated in Fig. 5 are obtained from the latest time step of the three-dimensional integrator. SLCC inlet boundary conditions are curvature, total pressure, total temperature, and swirl angle as a function of radius, along with integrated mass flow. The only exit boundary condition specified is curvature as a function of radius. Curvature is calculated directly from the transient velocity field and its gradients.

The SLCC and the 3D integrator use the same axial stations in front of and behind the bladed region. However, there is a different radial distribution within the 3D control volumes. The three-dimensional integrator uses a fixed grid. The streamlines produced by the streamline curvature code are a function of flow conditions and are used to construct a grid to calculate turbomachinery source terms. Interpolation procedures have been constructed [9] for passing information between the streamline curvature code and the three-dimensional integrator.

TEACC is a time-dependent, numerical algorithm requiring a

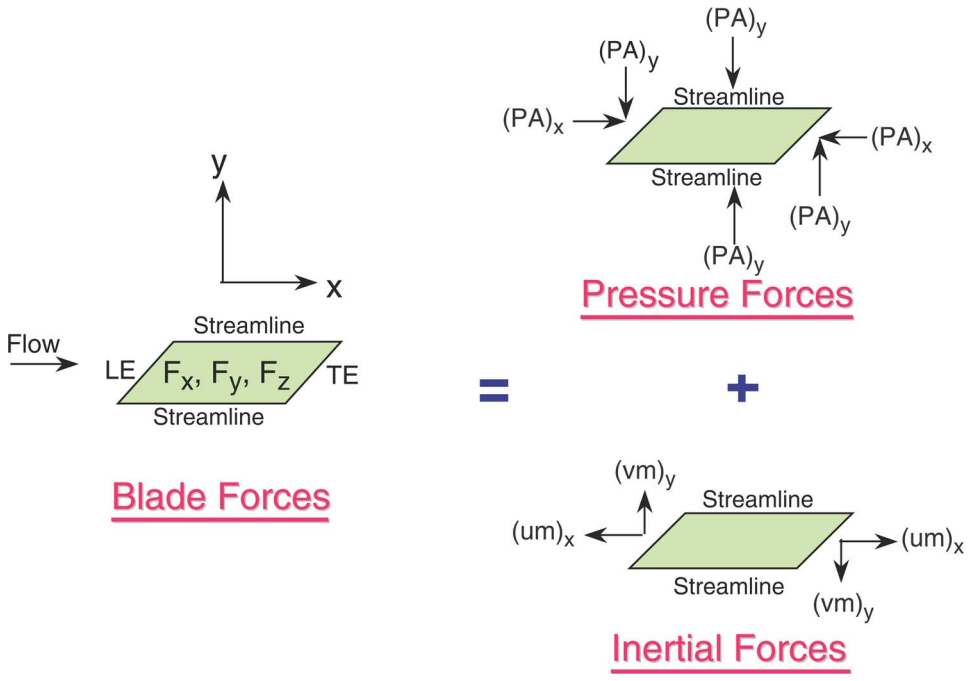

Fig. 4 Steady-state methodology for calculating turbomachinery source terms

set of initial conditions. A set of *initial conditions* is obtained from a converged solution of the SLCC for the full geometry (i.e., inlet duct, compressor, and exit duct). An axisymmetric segment of the 3D grid is used as the geometry of the SLCC. A complete set of conditions (ρ, ρu, ρv, ρw, ρe, and turbomachinery source terms) is provided for all control volumes within TEACC by the SLCC for undistorted, steady flow. Proper specification of *boundary conditions* is necessary for establishing steady-state convergence and uniqueness. Four types of boundaries are modeled in TEACC: wall, rotationally periodic, inflow, and outflow. The wall boundary conditions are assumed to be slip-wall; the normal velocity components are set equal to zero at the solid walls. A rotationally periodic (overlap) boundary condition is used in the circumferential direction, where three circumferential segments overlap the seam of the grid. The inflow boundary condition is based on reference plane characteristics, and the total pressure and total temperature at the inlet are specified. Inlet flow directions are assumed to be normal to the boundary. The exit boundary condition is either the specification of a variable static pressure capable of supporting the exit profile of strong swirl, or the specification of exit mass flow rate.

4 Three-stage Military Fan Application

The three-stage fan modeled in this effort represents a modern, high-performance military fan. It consists of a structural strut, a variable inlet guide vane (IGV) attached to the back of the strut, and three rotor/stator pairs. For this fan, only overall experimental performance data were available for comparison; no blade-row-by-blade-row or radial distribution of flow quantities was available. As a result, only overall performance is compared with data. An axial-radial representation of the grid used for the three-stage fan is shown in Fig. 6. The three-dimensional grid on which the flow-field solution was obtained was uniformly spaced in the circumferential direction at 15-deg intervals.

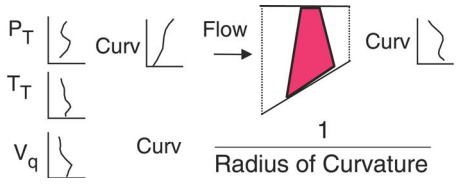

Fig. 5 Modifications to SLCC for calculating dynamic source terms over a single blade row

5 Undistorted Inlet

Illustrated in Fig. 7 is a 3D view of the total pressure distribution for the three-stage military fan, normalized by the inlet total pressure, with clean inlet flow at standard-day conditions and 101% of corrected design speed. Below the 3D figure is the total-pressure map for corrected speeds of 80%, 90%, and 101%. These three speeds were selected because experimental data were available. TEACC solutions were obtained at a high flow point for each speedline. To obtain the rest of the speedline, the exit static pressure was ramped at a rate to ensure quasi-steady performance

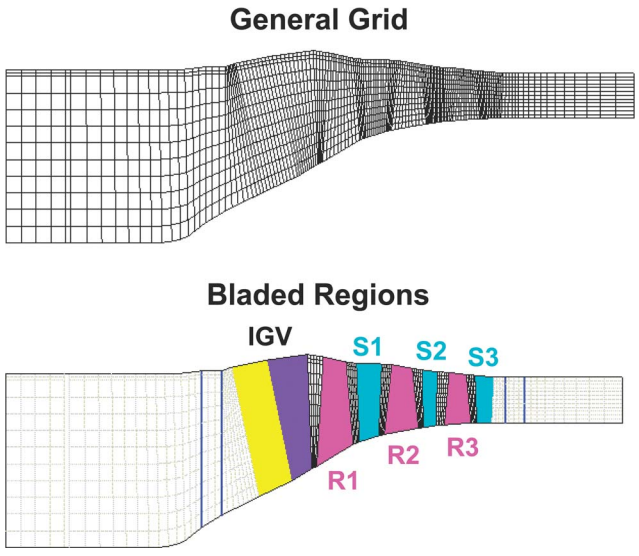

Fig. 6 Grid layout for three-stage fan

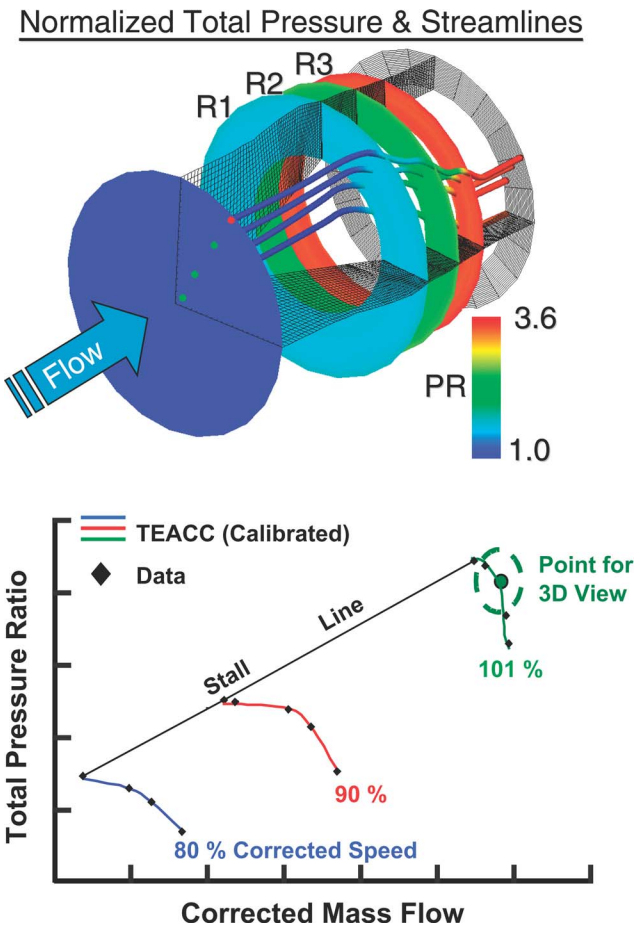

Fig. 7 Three-stage military fan performance for clean inlet flow

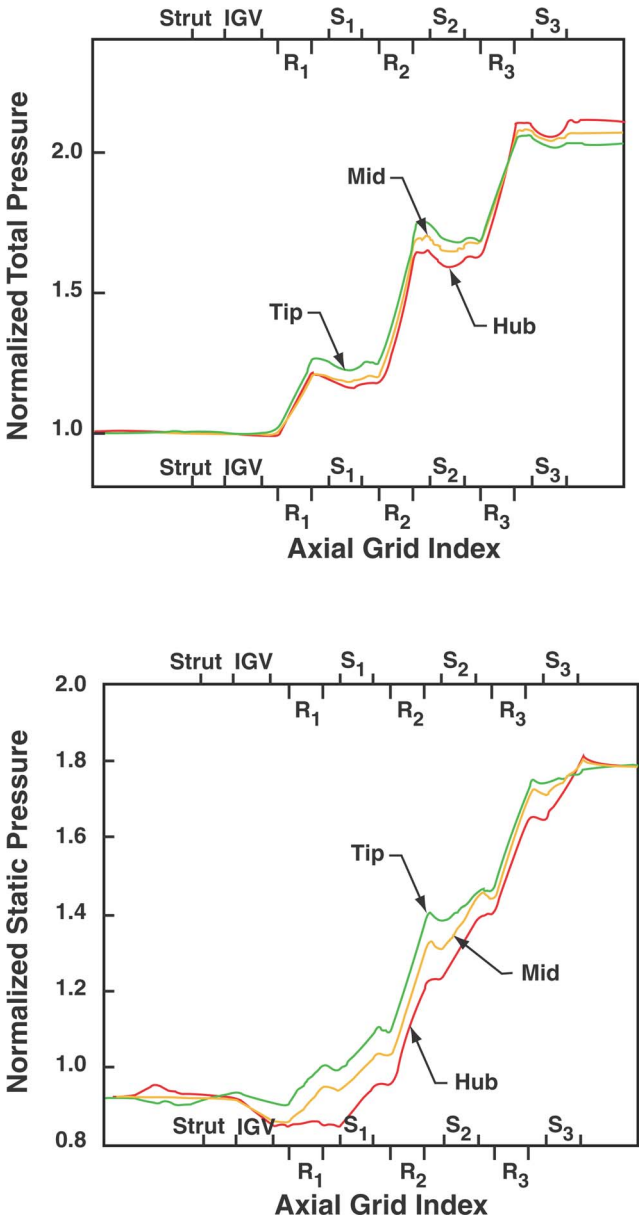

Fig. 8 Total and static pressure for three-stage fan at 80% corrected speed

up to the indicated instability limit. As can be seen on the pressure map, the TEACC simulation of this three-stage fan produced clean inlet performance within 0.5% of the overall experimental results. Indicated on the map is the flow point (101% speed) that was chosen to illustrate the pressure distribution in the 3D flow field. Shown in the 3D figure is total pressure at the exit of each rotor as labeled R1, R2, and R3. Since the flow is undistorted, each rotor exit plane indicates a uniform total pressure distribution. Also shown are representative streamlines that indicate flow turning after each rotor and flow straightening to near axial after each stator.

Figure 8 illustrates in much more detail the character of total and static pressure. Presented in the upper portion of Fig. 8 is the normalized total pressure as a function of axial station and radial location. This figure is presented with the axial grid points equally spaced for ready comparison of the hub, mean, and tip performance. In actuality, the axial stations are not equally spaced. The relative spacing of the axial grid points can be seen in Fig. 6. As expected, there is an increase in total pressure across each of the rotors, and a small decrease in total pressure across each of the stators. The total pressure is highest at the tip and lowest at the hub through most of the fan. The normalized static pressure is illustrated in the lower portion of Fig. 8. Again, the value of static pressure is typically highest at the tip and lowest at the hub. It can also be seen, by the continual increase in static pressure, that the flow is being diffused in both the rotors and the stators. The rise in static pressure across the stators occurs because stators not only turn the flow to direct it to the next rotor, but also act as diffusers. TEACC was tailored to simulate the three-stage military fan performance for undistorted airflow by calibrating the SLCC used to calculate the turbomachinery source terms. The calibration was done by specifying a radial distribution of loss and exit relative flow angle in addition to that generated by the SLCC to match overall pressure and temperature experimental data. Annular blockage was also specified when necessary to get a better match with experimental results. This calibration was left alone once inlet distortion was applied. No further adjustments of the loss and deviation correlations were conducted for the distorted inflow cases.

6 Distorted Inlet

During testing in ground test environments for effects of inlet distortion on compression system performance and operability, a screen is used to simulate total-pressure inlet distortion that represents what might be seen at the AIP. As such, a screen boundary condition for the numerical simulation was chosen to simulate the effect of total-pressure inlet distortion. A porous wall boundary condition was used to model the distortion screen. This boundary condition is semiempirical (i.e., the loss in total pressure as a

function of Mach number, porosity, and Reynolds number was established by taking experimental data across a variety of screens). The value of total pressure at the exit of the screen is calculated from the continuity and energy equations (total enthalpy equal to a constant) and an empirical pressure loss coefficient. A single screen with a 90-deg, one-per-revolution pattern was used in the analysis of the three-stage military fan. An arbitrary value of inlet distortion produced by a 15% porosity screen was chosen. At the 90% speed, the screen produced a total pressure loss of 5% in the quadrant, and at 80% the simulated screen produced 3% degradation in total pressure in that same quadrant.

An overall total pressure ratio performance map for the three-stage military fan is presented in Fig. 9 for two corrected speeds of 80% and 90%. The clean speedlines are presented to give a proper orientation of the distorted data, with stall depicted for each speedline at its lowest corrected mass flow rate. A conservative, but simple, stalling criterion was imposed on the TEACC simulation. When any one of the circumferential segments acquired a corrected mass flow that exceeded stall for the clean inlet, the compressor was considered stalled (i.e., according to parallel compressor theory). Likewise, the TEACC simulation was halted when any one of the circumferential segments exceeded the clean inlet data on the choked end of the speedlines. These two restrictions define the distortion calculation limits presented for each speed in Fig. 9.

In addition to total-pressure distortion, the TEACC code can model the effects of inlet temperature distortion as might be experienced because of weapons fire or hot gas re-ingestion during short take-off and vertical landing (STOVL) operation. Illustrated in Fig. 10 are the results of a temperature transient of approximately 8000 R/s applied uniformly to one quarter of the inflow boundary. This temperature transient rate is consistent with that experienced with hot gas ingestion caused by rocket or gun gas weapons firing [11,12]. Two phenomena (temperature ramp and temperature distortion) are being simulated by the single act of ramping the inlet total temperature in one quadrant. These combinations of temperature distortion and temperature ramp rate have a combined effect on system stability. To understand these combined effects, let us first analyze each effect separately.

First, for a temperature ramp, the effect on the engine is as if the operating line is shifting toward the stability limit. In some cases, when the ramp rate is quick enough, the transient will go beyond the steady-state stability limit as it is defined on a compressor map. This transition beyond the stability limit occurs because the corrected mass flow and corrected speed are functions of the inlet temperature and reflect the driving factor (i.e., the temperature ramp) and not the effect on compression system stability. In fact, because temperature is convected at fluid speed and not acoustic speed as is the case for a pressure wave, the temperature increase to the critical stage lags behind pressure as it progresses axially down the compressor. If the critical stage (the stage where stall initiates) is further downstream, the compression system inlet temperature increase will be higher than if the critical stage causing stall were nearer the front of the machine.

Second, for circumferential temperature distortion, the stability limit is lowered as for pressure distortion, but much more severely than for the same percentage level [13]. Thus, the stall point during the distorted temperature transient is different than it would be for quarter-quadrant steady temperature distortion alone. The blade loading is also important. As shown in the upper figure, the pressure ratio at the exit of stage 3 is decreased in the same circumferential region as is the imposed total-temperature distortion. The circumferential region of the compressor, with the imposed total-temperature distortion, operates with a lower corrected speed and a lower corrected mass flow than the other circumferential regions of the compressor. Therefore, this circumferential region of the compressor, with inflow distortion, produces a reduction in total pressure and operates closer to stall. Because of the near stall operation the distorted region of the compressor experiences an increase in blade work, which results in an increase in total temperature. Thus, both a temperature distortion (increase in total temperature) and a pressure distortion (decrease in total pressure) are presented to the core compressor as a result of the imposed temperature distortion at the inflow boundary condition.

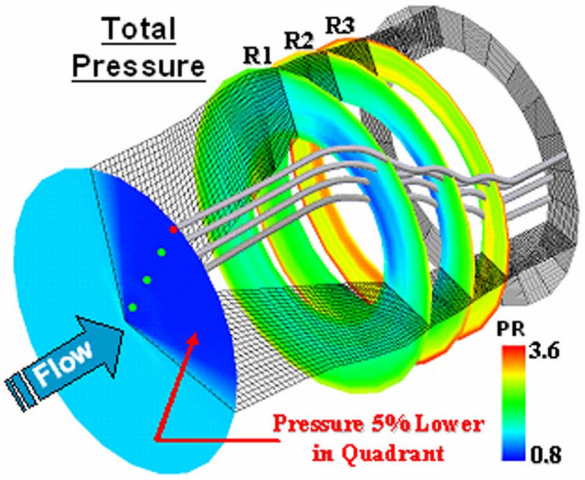

9a. Stage Pressure Distribution at Stall

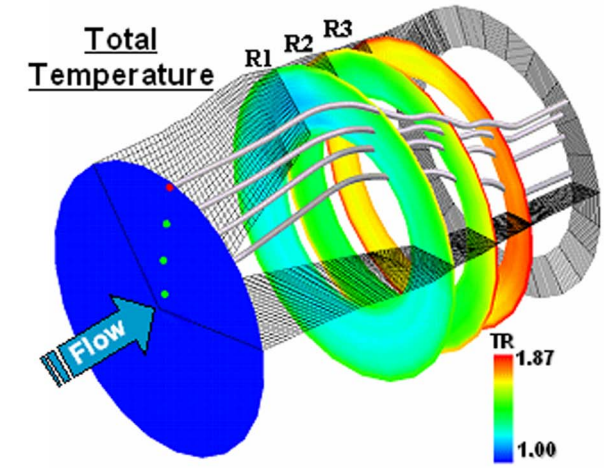

9b. Stage Temperature Distribution at Stall

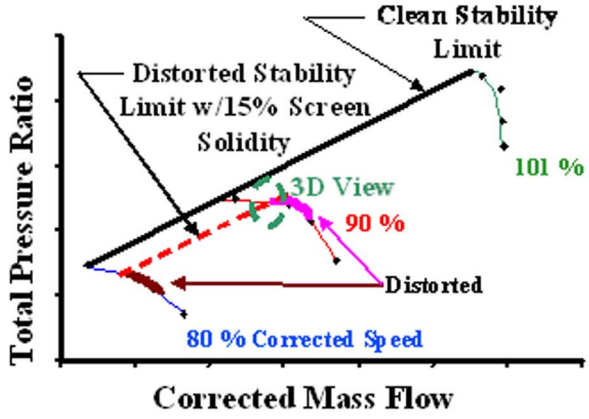

9c. Pressure Transient Portrayed on Map

Fig. 9 Three-stage military fan at 90% speed with total pressure distortion in one quadrant

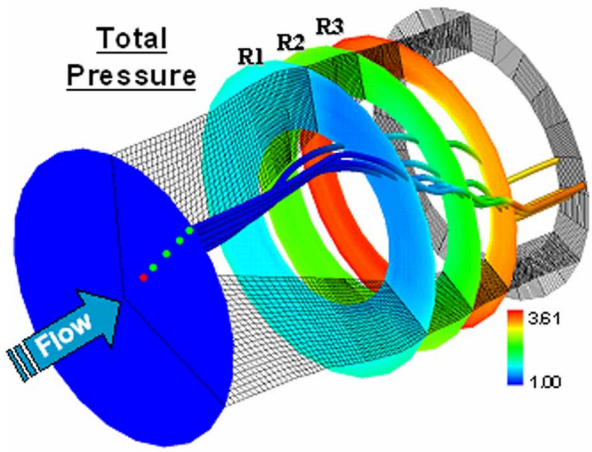

10a. Stage Pressure Distribution at Stall

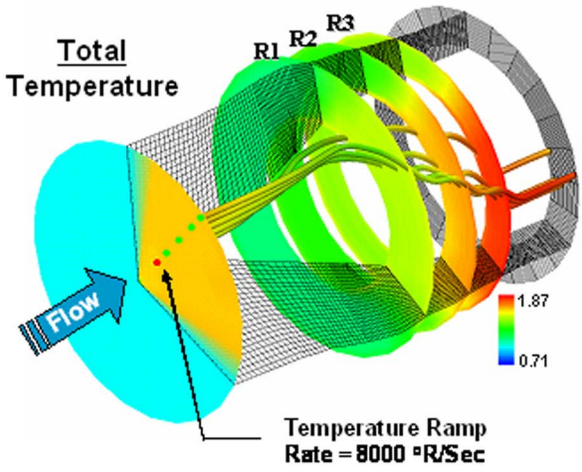

10b. Stage Temperature Distribution at Stall

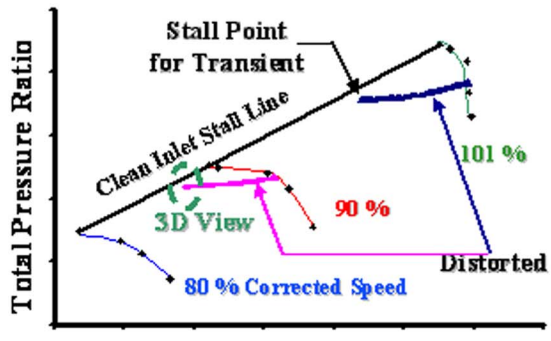

10c. Temperature Transient Portrayed on Map

Fig. 10 Three-stage military fan at 90% speed with total-temperature distortion in one quadrant

For cases when weapons fire occurs during an aircraft maneuver, it is desirable to be able to analyze the effects of both temperature and pressure distortion together. In this case, there are basically two worst-case scenarios one must consider: a case when the pressure and temperature distortion happen concurrently (i.e., both in the same area of the AIP), and second, a case when they oppose each other (i.e., each occurs in a different area of the

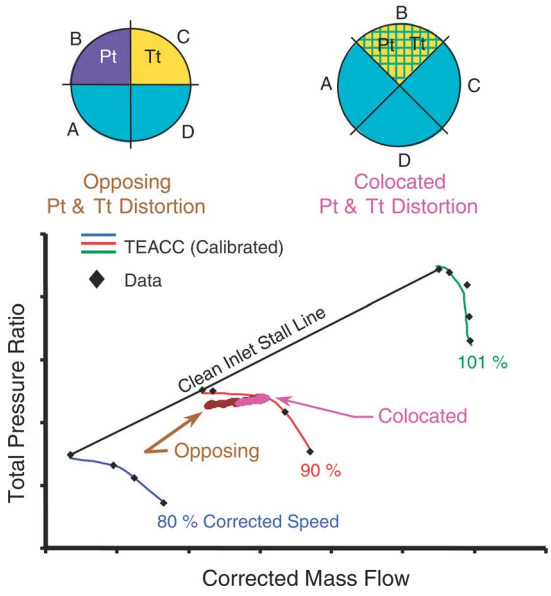

Fig. 11 Fan transient with both pressure and temperature distortion present—collocated and opposing

AIP). A demonstration was conducted with the three-stage military fan that illustrates the combined pressure and temperature distortion capability of the TEACC code. Presented in Fig. 11 is the fan map associated with combined temperature and pressure distortion transients.

In these cases, the total pressure distortion of 5% (based on 15% screen porosity) was first imposed on a 90-deg circumferential segment and the solution allowed to come to steady state. Then, based on whether the temperature distortion would be concurrent or opposing, a temperature ramp of 5000 R/s was imposed upon the appropriate 90-deg segment until the stall was indicated. As presented in Fig. 11, the collocated case was the most detrimental to compression system operability. Although no cases are presented in this paper, the TEACC code can deal with swirl distortion and dynamic distortion [14]. These effects will become more important as realistic distortion patterns such as the one generated by the F-16 with the external antennas are accounted for in the analysis.

7 Combined Inlet-compression System Capability

A more physically realistic approach to modeling the effects of the engine on the inlet flow field or vice versa is to model the flow as it passes through the compressor stages and the inlet simultaneously. This can be accomplished at various levels of empiricism. The most rigorous technique for simulating the effects of the rotating turbomachinery on the inlet flow is to simulate the engine hardware itself. This can be done by modeling the unsteady flow through the rotating blades for each row simultaneously by using turbomachinery CFD. Integrating a three-dimensional Navier–Stokes CFD inlet model with a corresponding complex 3D CFD engine model for the study of inlet distortion is often not feasible for the required turnaround with the current computational hardware even with parallelization taken into account. Therefore, in order to compute time-dependent complex inlet distortion effects on the compressor flow field and vice versa, one must accept more empiricism in the modeling approach. As discussed in this paper, one such approach would be to use the TEACC compression system simulation in combination with a CFD inlet code. In this case we recognize that the CFD inlet code gives only the "steady-state" or "time-averaged" distortion rather than the "dynamic" distortion. However, the implications of the presence of the fan on the

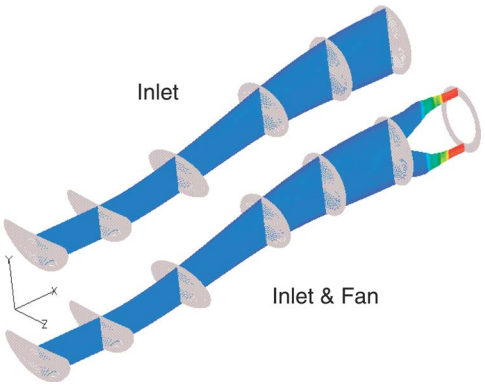

Fig. 12 Inlet computational setup with and without the three-stage military fan

inlet flow field at the AIP can be seen. The combination of the TEACC simulation and the inlet CFD code is illustrated in Fig. 12.

Presented in Fig. 13 are total- and static-pressure profiles with and without the three-stage military fan hooked up to the inlet associated with a very benign flight condition (zero angle of attack and zero sideslip). As can be seen, the total pressure at the AIP is nearly identical with and without the three-stage military fan connected. However, the contours of static pressure are different. Some of the difference can be explained by the presence of the bulletnose, but some of it may be effect of the fan on the flow prior to the flow's entering the fan compressor. In either case, current simulation boundary condition philosophy may require modifications.

To demonstrate a more realistic situation, the same computational setup was subjected to a high angle-of-attack condition of 26 deg and sideslip of 10 deg as illustrated in Fig. 14. This condition produced the total pressure distortion shown in the middle of the figure. Again it must be recognized that the inlet CFD code gives only the "steady-state" distortion. This condition produced the steady-state distortion as shown in the middle of the figure. Total-pressure distortion levels ranged from approximately 5% to 13% over much of a 180-deg segment. This distortion pattern reduced the performance of the three-stage military fan by approximately 6% in pressure ratio at a constant corrected airflow (lower part of the figure). Although the simulation was not run at near compression system instability, the performance loss is an

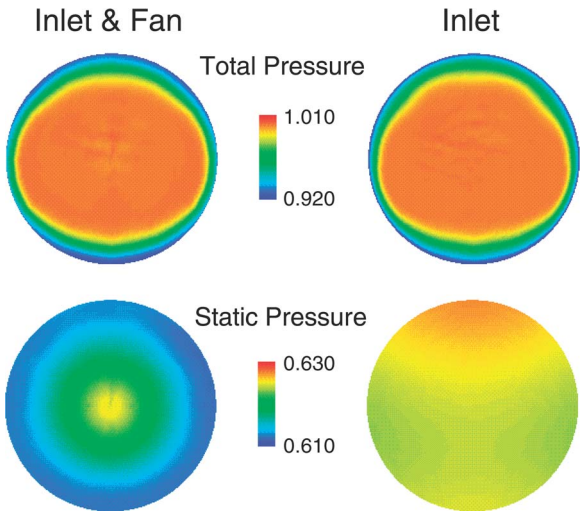

Fig. 13 Total and static pressure profiles at the AIP with and without the three-stage military fan connected to the inlet

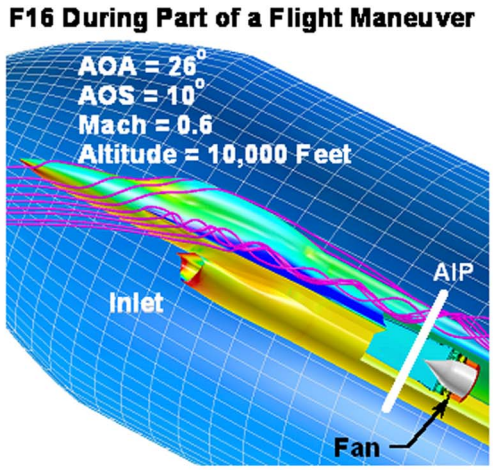

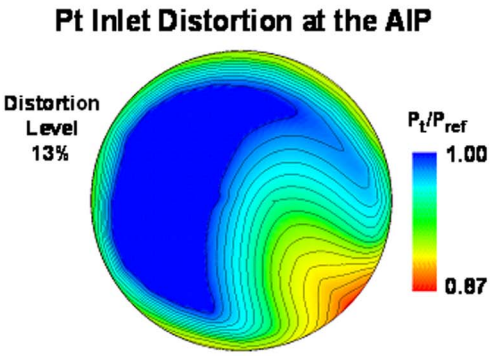

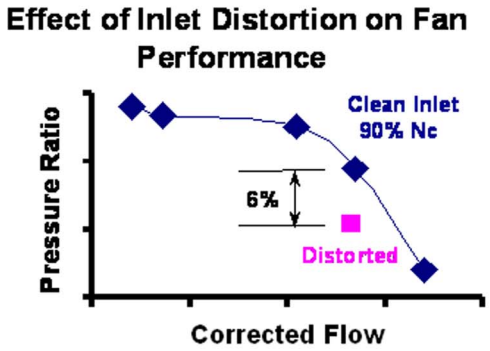

Fig. 14 Simulation of F-16 inlet-fan combination while at high angles of attack and sideslip

indication of the potential for loss in stall margin due to inlet distortion. In addition, if the corresponding "dynamic" distortion pattern were used, the inferred loss in stall margin could even be larger. Although there were no data to verify this prediction, it is of the order seen with other systems with similar levels of distortion.

8 Summary

This paper presents an initial analysis capability for inlet and engine aerodynamic compatability. Inlet CFD calculations have been prevalent for at least the last decade. Computations of inlet distortion on compression system performance and/or operability, whether characterized by total pressure or by some other parameter such as swirl angle, have not been readily available because of the complexity associated with turbomachinery. With the advent of the TEACC 3D code, inlet distortion can now be analyzed for both circumferential and radial effects. Now that this analysis

capability has been demonstrated, application to inlet-engine systems such as the Joint Strike Fighter (F-35) can be studied to provide insight into the effects of flow dynamics such as swirl on system performance and operability.

Acknowledgment

The authors wish to acknowledge the support of fellow colleague Jason Klepper for his contributions in applying the TEACC code to the three-stage military fan. The Air Force Office of Scientific Research (AFOSR) and AEDC (in-house) provided funding for this work during FY00-FY03.

Nomenclature

A = cross-sectional area
AIP = aerodynamic interface plane
AOA = angle of attack
AOS = angle of sideslip
e = internal energy and kinetic energy per mass
$\boldsymbol{E},\boldsymbol{F},\boldsymbol{G}$ = flux vectors
$\mathbf{F}$ = force
F = component of force
$\dot{m}$ = rate of mass flow
Nc = corrected speed
P = pressure
$\mathbf{Q}$ = conservation variables
r = radial direction
$\mathbf{S}$ = source vector
S = component of source vector
$\dot{\mathrm{SW}}$ = rate of shaft work
T = temperature
u = velocity in the x direction
$\mathbf{V}$ = velocity vector
V = component of velocity
v = velocity in the y direction
WC2 = mass or airflow rate corrected to engine inlet
w = velocity in the z direction
x,y,z = Cartesian right-handed coordinate directions
ρ = density

Subscripts

b = bleed
ref = reference condition
T or t = total
θ = circumferential direction

References

[1] Davis, Jr., M. W., et al., 2002, "A Proposal for Integration of Wind Tunnel and Engine Test Programs for the Evaluation of Airframe-Propulsion Compatibility Using Numerical Simulations," J. Eng. Gas Turbines Power, **124**, pp. 447–458.
[2] SAE Aerospace Recommended Practice ARP-1420, 1978, "Gas Turbine Engine Inlet Flow Distortion Guidelines."
[3] SAE Aerospace Information Report, 1983, "Inlet Total-Pressure Distortion Considerations for Gas Turbine Engines," No. AIR-1419.
[4] Davis, M., and Montgomery, P., 2002, "A Flight Simulation Vision for Aeropropulsion Altitude Ground Test Facilities," ASME Paper No. 2002-GT-30003.
[5] Smith, R. E., 1995, "Marrying Airframes and Engines in Ground Test Facilities—An Evolutionary Revolution," Paper No. AIAA-95-0950.
[6] Nichols, R. H., 1991, "Calculation of the Flow in an Circular S-Duct Inlet," Paper No. AIAA-91-0174.
[7] Bush, R. H., Power, G. D., and Towne, C. E., 1998, "WIND: The Production Flow Solver of the NPARC Alliance," Paper No. AIAA-98-0935.
[8] Hearsey, R. M., 1970, "HTO300—A Computer Program for the Design and Analysis of Axial Turbomachinery."
[9] Hale, A. A., and O'Brien, W. F., 1998, "A Three-Dimensional Turbine Engine Analysis Compressor Code (TEACC) for Steady-State Inlet Distortion," J. Turbomach., **120**, pp. 422–430.
[10] Hale, A., et al., 1999, "Turbine Engine Analysis Compressor Code: TEACC—Part II: Multi-Stage Compressors and Inlet Distortion," Paper No. AIAA-99-3214.
[11] Wallner, L. E., Useller, J. W., and Saari, M. J., 1957, "A Study of Temperature Transients at the Inlet of a Turbojet Engine," NACA RM E57C22.
[12] Childs, H. H., et al., 1955, "Stall and Flame-Out Resulting from Firing of Armament," NACA RM E55E25.
[13] Davis, Jr., M. W., 1991, "Parametric Investigation into the Combined Effects of Pressure and Temperature Distortion on Compression System Stability," Paper No. AIAA-91-1895.
[14] Davis, M., Hale, A., and Beale, D., 2002, "An Argument for Enhancement of the Current Inlet Distortion Ground Test Practice for Aircraft Gas Turbine Engines," J. Turbomach., **124**, pp. 235–241.

A High-Pressure Droplet Model for Spray Simulations

Changlin Yan

Suresh K. Aggarwal[1]
e-mail: ska@uic.edu

Department of Mechanical Engineering,
University of Illinois at Chicago,
842 West Taylor Street, MC 251,
Chicago, IL 60607-7022

Droplet vaporization models that are currently employed in simulating sprays are based on a quasisteady, low-pressure formulation. These models do not adequately represent many high-pressure effects, such as nonideal gas behavior, solubility of gases into liquid, pressure dependence of gas- and liquid-phase thermophysical properties, and transient liquid transport in the droplet interior. In the present study, a high-pressure quasisteady droplet vaporization model is developed for use in comprehensive spray simulations for which more rigorous vaporization models, such as those based on unsteady formulations, are beyond the present computational capabilities. Except for the gas-phase quasisteady assumption that is retained in the model, the model incorporates all high-pressure effects. The applicability of the model for predicting droplet vaporization in diesel and gas turbine combustion environments is evaluated by comparing its predictions with the available experimental data and with those from a more comprehensive transient model. Results indicate a fairly good agreement between the quasisteady (QS) and transient (TS) models for a wide range of pressures at low ambient temperatures, and for pressure up to the fuel critical pressure at high ambient temperatures. The QS model generally underpredicts the vaporization rate during the earlier part of droplet lifetime and overpredicts during the later part of lifetime compared to those using the TS model, and the difference becomes increasingly more significant at higher ambient pressure and temperature. The differences can be attributed to the quasisteady gas-phase average temperature and composition assumption for the QS model that reduces and increases the gas-phase heat and mass fluxes at the droplet surface during the earlier and later part of lifetime, respectively. The applicability of the QS model is quantified in terms of the maximum pressure as a function of ambient temperature. [DOI: 10.1115/1.1915390]

Introduction

The gasification behavior of a liquid fuel droplet has been a subject of extensive research. This research has been motivated by two major considerations. First, the droplet gasification model provides a fundamental input for the simulation of reacting two-phase flows that typically occur in gas turbine, liquid rocket, and diesel engine combustors. Second, the droplet gasification phenomenon is scientifically challenging as it involves the coupled processes of fluid flow, heat and mass transport, phase change, and interphase coupling. For a combusting droplet, it also involves radiation and chemical reactions.

The basic droplet gasification model was formulated in the 1950s by Godsave [1] and Spalding [2] for an isolated pure fuel droplet in a stagnant environment. This model was termed the d^2-law model as it predicted that the square of the droplet diameter decreases linearly with time. Since then this model has been studied extensively both experimentally and theoretically. Reviews of these studies have been provided by Williams [3], Law [4], Sirignano [5], and Peng and Aggarwal [6]. The key assumptions in the basic model are that the gas-phase processes are quasisteady, the droplet and gas flow are in dynamic equilibrium (zero slip velocity), the droplet surface temperature is constant (droplet heating time is negligible compared to its lifetime), and the thermophysical properties of the gas film surrounding the droplet are invariant. The effects of relaxing these restrictions have been investigated by Law [4], Sirignano [7], Aggarwal et al. [8], and Abramzon and Sirignano [9]. In particular, they have considered the effect of transient liquid-phase heating on the droplet vaporization rate, and proposed four different models with varying degree of complexity to include this effect in the d^2-law model. The four models have been termed, respectively, as the infinite-conductivity or rapid-mixing model, the conduction-limit model, the effective conductivity model, and the vortex model. In addition, the effects of relative gas velocity or forced convection [6,10], multicomponent fuel [4,7,11,12], and variable transport properties [9,12] have been included in the modified d^2-law model.

Except for some variations, the state-of-the-art droplet gasification model that is currently employed in multidimensional spray computations in diesel and gas turbine combustors has the following general features:

1. The assumptions of gas-phase processes being quasi-steady and spherically-symmetric are retained. The effect of transient liquid heating is included by using an infinite conductivity model, whereby the liquid temperature is considered temporally varying but spatially uniform.
2. The effect of relative gas velocity is included by using a semiempirical correlation representing the effects of droplet Reynolds number and Prandtl (or Schmidt) number on the interphase heat and mass transport.
3. The phase equilibrium at the droplet surface is represented by the Clausius-Clapeyron or an equivalent expression.
4. The effects of variable thermophysical properties are incorporated in an ad hoc manner. For example, the effect of temperature on the gas-phase properties, such as specific heat, thermal conductivity, viscosity, and mass diffusivity are included. However, the effect of composition is generally neglected, and the variation of liquid transport properties is not considered.
5. A pure or single-component fuel is considered, although most practical fuels are multicomponent in nature.
6. Many important high-pressure effects are not considered. These include the gas-phase nonidealities, liquid-phase solubility of gases, and variation of gas- and liquid-phase properties with pressure.

[1]To whom correspondence should be addressed.

Contributed by the Combustion and Fuels Division of ASME for publication in the JOURNAL OF ENGINEERING FOR GAS TURBINES AND POWER. Manuscript received August 4, 2003; final manuscript received May 5, 2004. Assoc. Editor: P. C. Malte.

Motivation and Objective

Clearly, a spray code based on the droplet gasification model described above would be inadequate for simulating two-phase flows in high pressure combustors, where the gas temperature and pressure typically exceed the critical temperature and pressure of the fuel. Under such conditions, aspects dealing with the high-pressure and transcritical phenomena become extremely important. In particular, the gas-phase nonidealities and the liquid-phase solubility of gases become essential considerations as pressure approaches the fuel critical value. As a consequence, interphase processes at the droplet surface and liquid-phase processes inside the droplet become significantly more complex. The phase equilibrium at the droplet surface can no longer be represented by Clausius–Clapeyron-type equation. The solubility of gases into liquid implies that a single component fuel behaves like a multicomponent fuel. In addition, the liquid- and gas-phase thermophysical properties become pressure dependent. Since the liquid boiling temperature increases with pressure, the droplet heat-up time becomes a significant part of droplet lifetime, and an infinite-conductivity model may be inadequate to represent the liquid-phase transport inside the droplet. As the droplet surface reaches the critical state, the latent heat of vaporization reduces to zero, and the gas and liquid densities become equal at the droplet surface. Then, transient effects in the gas phase become as important as those in the liquid phase, since the characteristic times for transport processes in the two phases become comparable. These high-pressure effects are not adequately represented in the low-pressure droplet models used in spray codes that are deployed for multidimensional simulations of two-phase flows in diesel engines and gas-turbine combustors.

Motivated by these considerations, the present study aims to develop a high-pressure droplet gasification model, which can replace the low-pressure droplet models that are currently used in high-pressure spray simulations. The new model incorporates the high-pressure effects described above, which are generally not considered in the low-pressure QS models. These include the gas-phase nonidealities, liquid-phase solubility of gases at the droplet surface, pressure dependency of the gas- and liquid-phase thermophysical properties, high-pressure gas- and liquid-phase equilibrium at the droplet surface, and transient transport in the droplet interior. The applicability of the quasisteady model is examined by comparing its predictions with those using a transient droplet model, and with experimental data. Using this comparison, the validity of the quasisteady assumption is quantified for a wide range of ambient pressures and temperatures.

It is important to note that modeling capabilities are currently available to incorporate high-pressure effects described above in a comprehensive, transient droplet gasification model. Issues pertaining to the inclusion of these effects and the various forms of the high-pressure transient models have been studied by several investigators [13–23,26]. However, such transient models, although they are extremely useful to examine the subcritical/supercritical vaporization behavior of a single droplet, cannot be incorporated in practical spray codes, at least in the foreseeable future. Zhu et al. [36] employed a detailed quasisteady model to quantify the gas-phase unsteadiness as a function of ambient pressure and temperature. However, this model is still too complex to be useful for simulating sprays in practical systems. Thus there is a clear need to develop a high-pressure droplet model for the simulation of high-pressure, two-phase flows that are encountered in various propulsion applications. The model should provide a realistic representation of the important high-pressure effects, and still be sufficiently simplified so that it can easily be incorporated into comprehensive spray codes. This provided another motivation for the present study.

In the following, we first present the quasisteady high-pressure droplet model, and its validation using results from experiments and a comprehensive transient droplet model. This is followed by detailed results dealing with the range of applicability of the QS model, the sensitivity of vaporization rate to thermotransport properties, the effect of pressure on these properties, and the quantification of the quasisteady assumption in terms of ambient pressure and temperature. Finally, the conclusions are presented.

The Theoretical Model

Quasi-Steady Gas Phase Model. An isolated fuel droplet evaporating in a high-temperature, high-pressure environment is analyzed. The droplet size, ambient temperature and pressure are considered in a range that corresponds to a wide range of power requirements for diesel and gas turbine combustion. The gas-phase processes are assumed to be quasi-steady, which implies that the characteristic gas-phase time is much shorter compared to the liquid-phase transient time as well as the time associated with the surface regression rate. Other assumptions include spherical symmetry, phase-equilibrium at the droplet surface, and negligible secondary diffusion and radiation. With these assumptions, the energy and fuel-vapor species conservation equations can be simplified to a steady, one-dimensional form, and their solution respectively yields the droplet gasification rate as:

$$\frac{\dot{m}}{4\pi\rho_g D_g Le_g}[1/r_s - 1/r_\infty] = \ln\left[1 + \frac{C_{pg}(T_\infty - T_s)}{H}\right] \tag{1}$$

$$\frac{\dot{m}}{4\pi\rho_g D_g}[1/r_s - 1/r_\infty] = \ln\left[\frac{1 - Y_{f\infty}}{1 - Y_{fs}}\right] \tag{2}$$

Details can be found in Refs. [24,25]. Here r_s and r_∞ represent, respectively, the radial locations at droplet surface and ambient (assumed to be at infinity), Le_g the gas-phase Lewis number, Y_f the fuel vapor mass fraction, and H the energy supplied to the droplet per unit mass of fuel vaporized used for droplet heating and vaporization. Equation (2) can also be written as

$$\frac{\dot{m}}{4\pi\rho_g D_g}[1/r_s - 1/r_\infty] = \ln(1 + B) \tag{3}$$

where B is the transfer number [7] given by

$$B = \frac{Y_{fs} - Y_{f\infty}}{1 - Y_{fs}} \tag{4}$$

Equating Eqs. (1) and (3) yields an expression for H

$$H = \frac{C_{p_g}(T_\infty - T_s)}{(1 + B)^{1/Le_g} - 1} \tag{5}$$

The droplet size history is computed by using the equation

$$\frac{dr_s^2}{dt} = -\frac{\dot{m}}{2\pi r_s \rho_l} \tag{6}$$

Liquid Phase: Diffusion-Limit Model. For this model, which has been extensively discussed in previous studies [4,8,24], the heat and mass transport in the droplet interior are assumed to be governed by the transient heat and mass diffusion equations. Since, these equations involve a moving boundary problem, a transformation is used to cast the moving boundary (droplet surface) into a fixed one. The transformed equations are:

$$\frac{\partial \bar{T}_l}{\partial \bar{t}} = \frac{1}{\bar{r}^2}\frac{\partial}{\partial \bar{r}}\left(\bar{r}^2 \frac{\partial \bar{T}_l}{\partial \bar{r}}\right) - \bar{r}\bar{m}\frac{\rho_g D_g}{\rho_l \alpha_l}\frac{\partial \bar{T}_l}{\partial \bar{r}} \tag{7}$$

with the initial and boundary conditions as

$$\bar{T}_l = 0 \quad \text{at} \quad \bar{t} = 0$$

$$\frac{d\bar{T}_l}{d\bar{r}} = 0 \quad \text{at} \quad \bar{r} = 0$$

$$\frac{\partial \bar{T}_l}{\partial \bar{r}} = \bar{m}\frac{\rho_g D_g}{k_l(T_b - T_0)}(H - L) \quad \text{at} \quad \bar{r} = 1 \tag{8}$$

where, $\bar{T}_l(\bar{r},\bar{t})$, $\bar{r}$, and $\bar{t}$ are the normalized liquid temperature, radial location, and temporal variable respectively. These are given by

$$\bar{T}_l = \frac{(T_l - T_o)}{(T_b - T_o)}$$

$$\bar{r} = r/r_s$$

$$\bar{t} = \alpha_l \int_0^t \frac{dt}{r_s^2}$$

$$\bar{m} = \frac{\dot{m}}{4\pi\rho_g D_g r_s} \tag{9}$$

where T_o is the initial droplet temperature, T_b is a reference boiling temperature, r_s the instantaneous droplet radius, α_l the liquid thermal diffusivity, and $\bar{m}$ is the normalized vaporization rate. A Crank–Nicolson implicit scheme with a variable grid is employed to solve these equations.

Vapor–Liquid Equilibrium at Droplet Surface. For low-pressure models, the phase equilibrium at the droplet surface is represented by the Clausius–Clapeyron or an equivalent expression, relating fuel vapor mass fraction and temperature at the droplet surface. This representation, however, assumes ideal gas behavior and neglects solubility of gases into liquid. In order to include the nonideal gas behavior and gas solubility, which become important at high pressures, various approaches have been suggested [23,26]. Our previous investigation [26] has established that the Peng–Robinson (P–R) equation of state (EOS) provides an accurate representation of the nonideal gas behavior and the vapor-liquid equilibrium at droplet surface. It can be written as

$$P = \frac{RT}{V - b} - \frac{a}{V^2 + 2bV - b^2} \tag{10}$$

where a and b are functions of species properties and mole fractions.

When the droplet surface is in mechanical and thermodynamic equilibrium, the temperature, pressure, and fugacity of each species in the gas phase is equal to the corresponding property of the same species in the liquid phase. The equality of fugacity of species i is expressed as

$$\phi_i^v y_i = \phi_i^l x_i \tag{11}$$

where the superscripts v and l refer to the vapor and liquid phase, respectively. ϕ_i is the fugacity coefficient of ith species, and is a function of pressure, temperature, and composition. It is given in terms of the volumetric properties of the mixture by the following thermodynamic relation:

$$RT\ln(\phi_i) = \int_v^\infty \left[\left(\frac{\partial P}{\partial n_i}\right)_{T,V,n_j} - \frac{RT}{V}\right] dV - RT\ln Z \tag{12}$$

where Z is the compressibility factor, and n_j is the mole number of jth species. By substituting the equation of state into Eq. (12), the fugacity of the ith species in the liquid and gas phase mixture is given by [27]:

$$\ln\phi_i = \frac{bi}{b}(Z - 1) - \ln(Z - B^*) + \frac{A^*}{2B^*\sqrt{2}}\left(\frac{b_i}{b} - \delta_i\right)\ln\frac{Z + B^*(1 + \sqrt{2})}{Z + B^*(1 - \sqrt{2})} \tag{13}$$

where

$$A^* = \frac{aP}{R^2T^2}$$

and

$$B^* = \frac{bP}{RT}$$

$$\frac{b_i}{b} = \frac{T_{ci}/P_{ci}}{\sum_j y_j T_{cj}/P_{cj}} \quad \text{and} \quad \delta_i = \frac{2\sqrt{a_i}}{a}\sum x_j\sqrt{a_j}(1 - k_{ij}) \tag{14}$$

The binary interaction coefficient k_{ij} in the above equation is taken from Knapp et al. [28]. It is 0.1441 for P–R EOS for n-heptane–nitrogen system. Equations (10)–(14) provide the basic relations for vapor–liquid equilibrium calculation.

For a multicomponent mixture, the latent heat of vaporization of each species is defined as the difference between the partial molar enthalpy of that species in the vapor and liquid phases. The following thermodynamic relation then gives the partial molar enthalpy of the kth species:

$$\bar{H}_i - \bar{H}_i^0 = -RT^2\frac{\partial}{\partial T}(\ln\phi_i) \tag{15}$$

where the superscript 0 denotes the quantity in an ideal state. Equation (15) is solved iteratively along with Eqs. (10)–(14).

Thermophysical and Transport Properties. The gas- and liquid-phase thermodynamic and transport properties are considered functions of temperature, pressure and composition. The densities of both gas- and liquid-phase are calculated directly from the P–R EOS. The heat capacity of both phases is calculated by a fourth-order polynomial of temperature, and is then extended to mixtures using the mixing rule of Filippov [29]. The thermal conductivity of pure liquid component is estimated by the Baroncini et al. method [30] followed by the Baroncini et al. correction [27] for the effect of pressure, and is then extended to mixtures using the mixing rule of Filippov [29]. The thermal conductivity of pure gas component is calculated by the method of Chung [31,32], while the method of Mason and Saxena [27] is used for gas mixtures, and the Stiel and Thodos modification [27] is used to consider the effect of pressure. The method of Wilke and Lee [27] is used to estimate the gas binary-diffusion coefficient between n-heptane and nitrogen, and the Takahashi correction [33] is employed to predict its value at high pressure.

All the gas-phase mixture properties are computed at the weighted-averaged temperature and species mass fractions, obtained from the temperature and composition at the droplet surface and those in the gas phase at infinity, as

$$\Phi_{\text{avg}} = \Phi_s + \beta(\Phi_\infty - \Phi_s) \tag{16}$$

where Φ is a generic quantity representing either temperature or mass fraction, and the averaging factor β is selected to be as 1/3. It is important to note that the gas-film thickness changes with time during droplet evaporation, and also varies with ambient properties. Consequently, the averaging factor β should be adjusted accordingly. This aspect is examined using results of the transient droplet model.

The Solution Procedure. The theoretical model described above is applicable to a single isolated fuel droplet. A general procedure involves calculating phase equilibrium at droplet surface by using T_s at the old time step. Then, the average gas temperature and species mass fractions are obtained from Eq. (16), and the thermotransport properties of the gaseous mixture are calculated by using the equations described above. Similarly, the liquid fuel properties, such as specific heat, thermal conductivity, and density, are computed. Note that liquid temperature and species mass fractions used for calculating these properties are the average values obtained using values at the droplet surface and

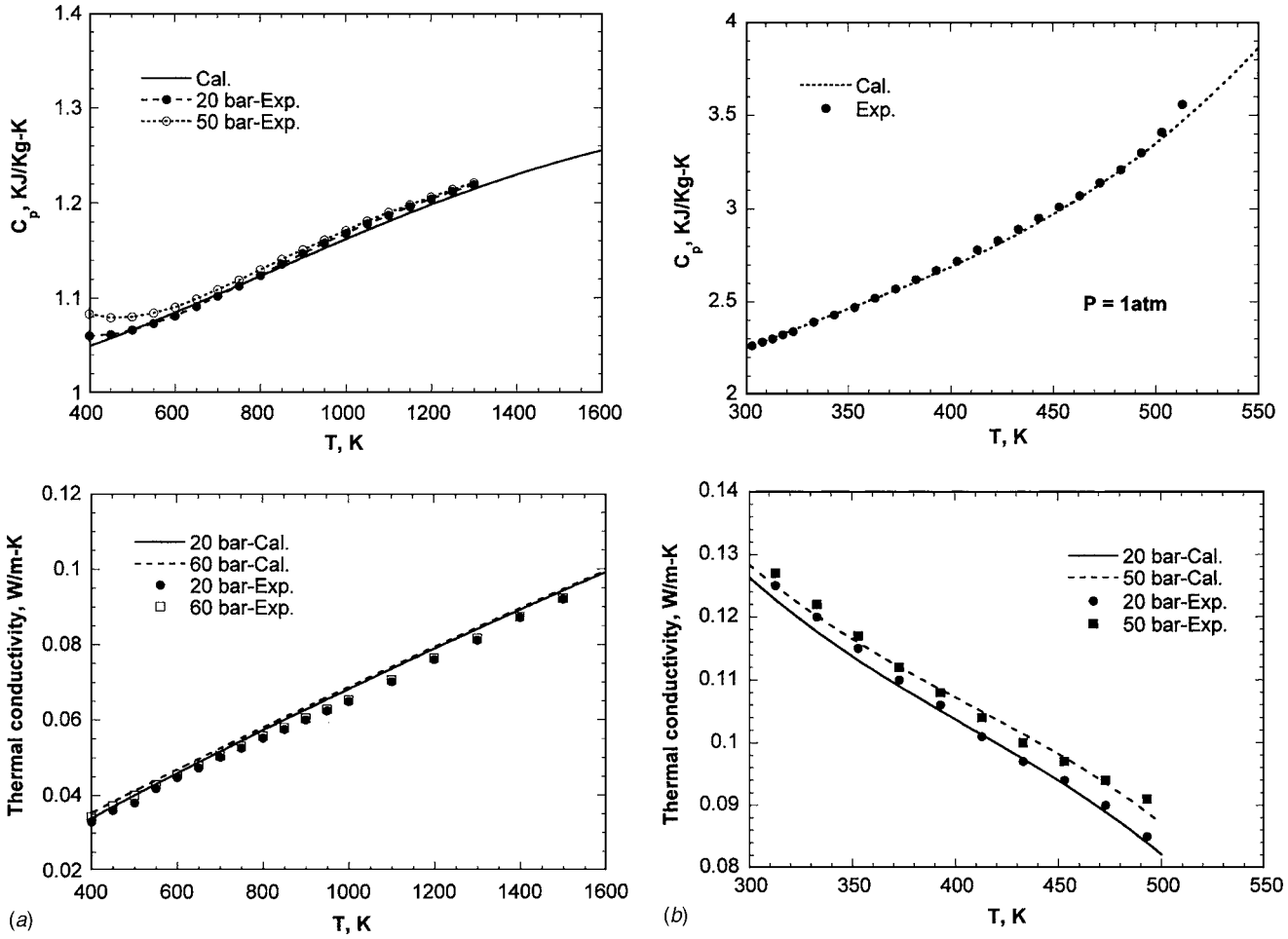

Fig. 1 Comparison of predicted thermophysical and transport properties with measured data; (*a*) gas (nitrogen) properties and (*b*) liquid (*n*-heptane) properties

center. The new T_s is then computed using the diffusion-limit model. Finally, the droplet radius is calculated from Eq. (6).

Results and Discussions

The simulations consider an *n*-heptane droplet evaporating in a nitrogen environment. The environment temperature and pressure are treated as parameters. Results are first presented to validate the methodology used to calculate the thermophysical and transport properties, and the liquid–vapor phase equilibrium. This is followed by the validation of the quasisteady (QS) model by comparing its predictions with the available experimental data and with a detailed transient (TS) model. Detailed results of the QS model and comparisons between the predictions of the QS and TS models are then presented, and the range of applicability of the QS model is quantified.

Model Validation. The gas and liquid-phase thermophysical properties were calculated as functions of temperature and pressure, and compared with the available experimental data [34]. The properties include the density, thermal conductivity, mass diffusivity and specific heat of both the gas and liquid species. Figure 1 shows a comparison of the predicted and measured specific heat and thermal conductivity of nitrogen as well as the specific heat and thermal conductivity of liquid *n*-heptane. The predicted values are in good agreement with the experimental data.

The predicted phase equilibrium using the P–R EOS for a *n*-heptane-nitrogen system as a function of pressure and temperature were compared with the available experimental data [28]. The phase equilibrium in terms of the variation of nitrogen mole fraction with pressure for two different temperatures is presented in Fig. 2. An excellent agreement is indicated between the predicted and experimental results. This also indicates that the densities of both the gas- and liquid-phase can be predicted accurately using P–R EOS. Additional validation of the P–R EOS is provided in Ref. [26].

In Fig. 3, we compare the predictions of quasisteady (QS) and

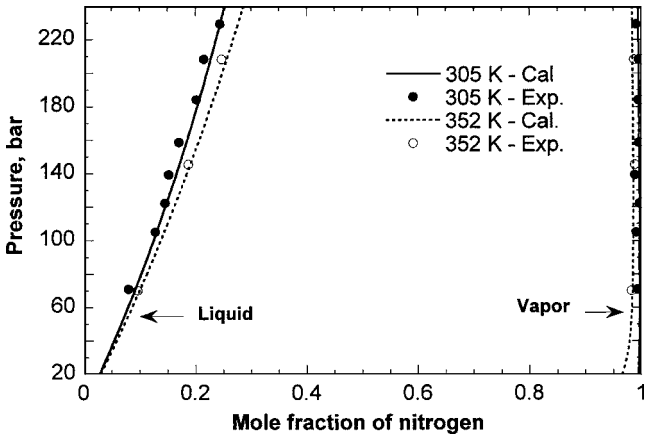

Fig. 2 Comparison of predicted mole fraction of nitrogen with measured data at two different temperatures for an *n*-heptane-nitrogen binary system

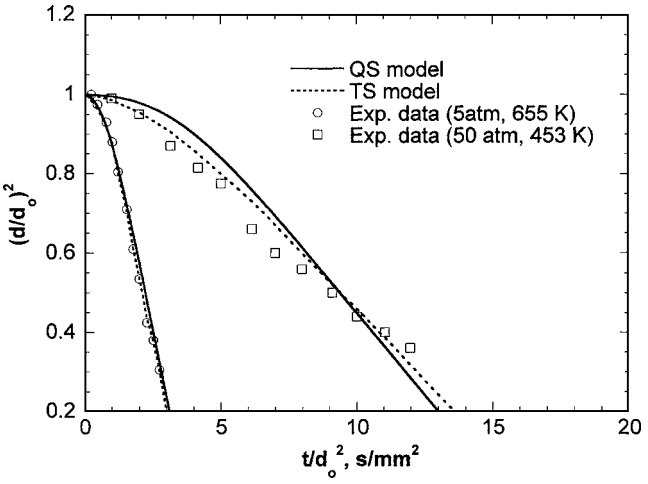

Fig. 3 Temporal variation of nondimensional surface area for two different ambient conditions; comparison of predictions using the transient (TS) and quasisteady (QS) models with experimental data from Ref. [35]

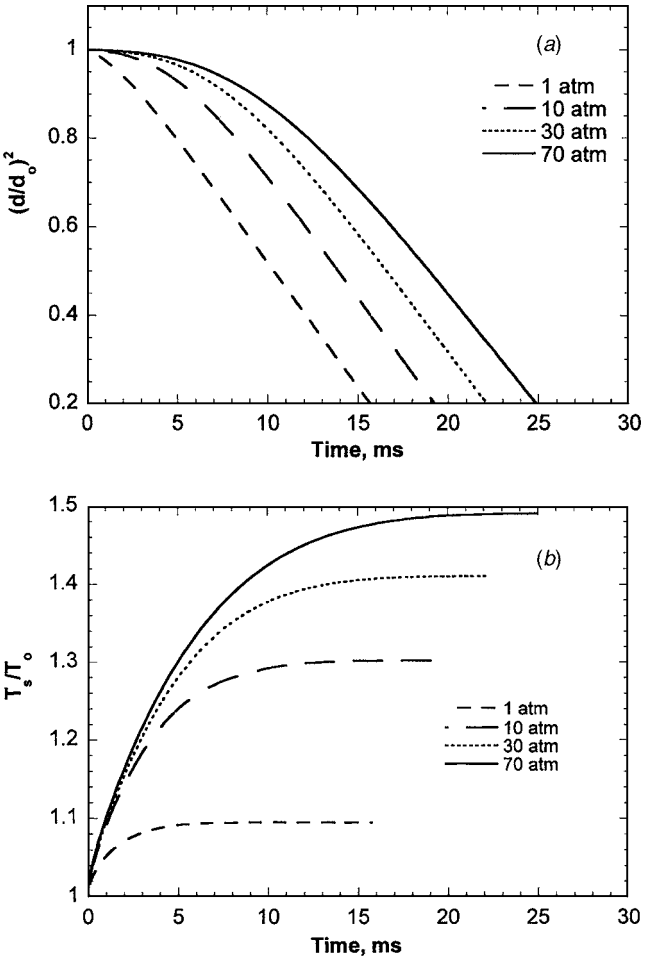

Fig. 4 Temporal histories of nondimensional surface area and temperature predicted using the QS models at different ambient pressures for T_a=500 K; (*a*) surface area and (*b*) surface temperature. The initial droplet diameter (d_0) is 0.05 mm and temperature (T_0) is 300 K.

transient (TS) models with the experimental data taken from Ref. [35]. The details of the TS model are to be found in our previous papers [26,36]. Results are presented in terms of the temporal variation of nondimensional surface area for two different ambient conditions. For the QS model, when pressure is low, i.e., 5 atm, the results agree reasonably well with the results of both the TS model and measurements. However, at high pressure, i.e., 50 atm, the predictions of both QS and TS models exhibit some differences from the measurements. The QS model underpredicts the surface regression rate during the early part of droplet lifetime and overpredicts it during the later part of the lifetime, as discussed in the next section. Apart from this difference, the predictions of both the QS and TS models as well as the measurements indicate that after the transient heating period, the surface regression rate nearly follows the d^2-law behavior. The results also show that as the pressure increases, the droplet heatup time becomes a more significant part of droplet lifetime, since the liquid boiling temperature increases with pressure.

Results of QS Model. In order to assess the applicability of the high-pressure QS model, several results are now presented using the QS model. The initial droplet temperature is 300 K. The ambient temperature and pressure range between 500–1500 K and l–70 atm, respectively. The initial droplet diameter is 0.05 mm. These ranges cover the environmental states of *n*-heptane fuel droplet and include the conditions in which practical droplets and sprays evaporate.

Figure 4(*a*) shows the temporal variation of nondimensional surface area obtained using the QS model for four different ambient pressures at 500 K. The droplet lifetime increases as the ambient pressure is increased. This can be directly attributed to the increase in droplet heat-up time with pressure, since the fuel boiling temperature increases with pressure. As indicated in Fig. 4(*b*), the heat-up time increases as ambient pressure is increased, and becomes a more significant part of droplet lifetime at high pressures. These results agree qualitatively with those of previous studies [17,26]. It is also interesting to note that following the transient heatup period, during which the droplet surface reaches the wet-bulb temperature, the surface regression nearly follows the d^2-law behavior, and the evaporation rate constant is nearly independent of pressure. At low ambient temperature, the transient effect is caused mainly by the liquid-phase heating. Consequently, as the pressure is increased, it increases the droplet heat-up time, and, thereby, the droplet lifetime.

Results concerning the effect of pressure on droplet vaporization at higher ambient temperature are presented in Figs. 5 and 6. The comparison of Fig. 4 with Figs. 5 and 6 indicates that the effect of pressure on vaporization is markedly different at low and high ambient temperatures. The global effect of pressure on droplet vaporization is presented in Fig. 7, which shows the variation of droplet lifetime with pressure at different ambient temperatures. As pressure is increased, the droplet lifetime increases at low T_a, but decreases at high T_a. At low T_a, the effect on pressure is predominantly due to its effect on the boiling temperature. Since the boiling temperature increases with pressure, the droplet heatup time increases, which in turn increases the droplet lifetime as indicated in Fig. 4. In contrast, at high T_a, the effect of pressure appears mainly through the heat of vaporization that decreases with pressure, and, consequently, the lifetime decreases. This is clearly indicated in Figs. 5 and 6.

Another important effect of pressure at higher ambient temperature pertains to the attainment of critical mixing state at the droplet surface. The critical mixing state, which is defined when the droplet surface temperature (T_s) attains the critical mixing temperature (T_{cm}) for a given ambient pressure, distinguishes between the subcritical and supercritical vaporization. For subcritical vaporization, $T_s < T_{cm}$, there is a distinct liquid-gas interface, and the vaporization is characterized by the regression of this interface. However, for $T_s \geq T_{cm}$, the distinction between the two phases disappears, and then the vaporization is generally characterized by the inward movement of the critical mixing surface. While the

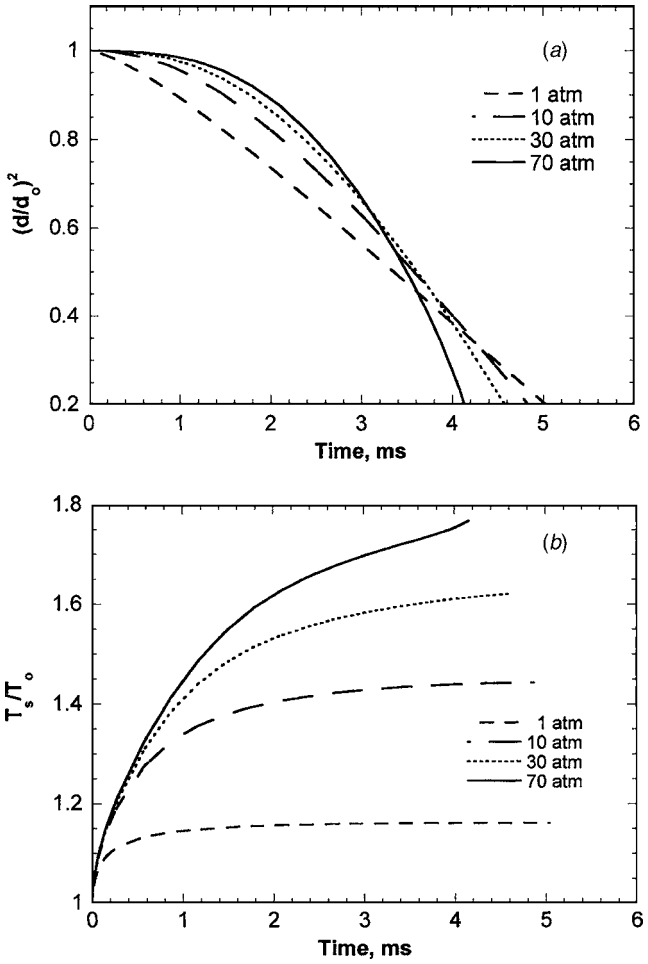

Fig. 5 Temporal histories of nondimensional surface area and temperature predicted using the QS models at different ambient pressures for T_a=1000 K; (*a*) surface area and (*b*) surface temperature

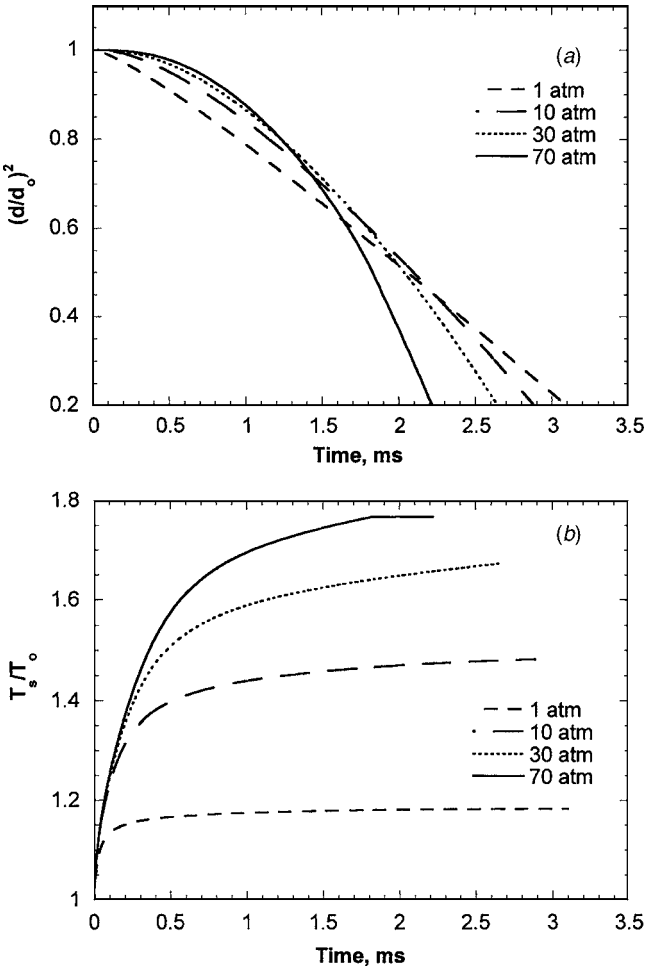

Fig. 6 Temporal histories of nondimensional surface area and temperature predicted using the QS models at different ambient pressures for T_a=1500 K; (*a*) surface area and (*b*) surface temperature

attainment of the critical mixing state has been discussed in the context of transient vaporization models [26,36], it has not been observed or discussed within the framework of quasisteady models. In Fig. 8 we present the final droplet surface temperature as a function of ambient pressure and temperature. In order to discuss the critical mixing state, the boiling line and the critical mixing line are also shown in the figure. At low T_a, as pressure is increased, the final surface temperature, which may be termed as the wet-bulb temperature, increases but does not reach the critical mixing value during the lifetime. However, at higher ambient temperature, the final surface temperature reaches the critical mixing state at some ambient pressure. The higher the ambient temperature, the lower is the value of pressure at which the droplet surface reaches the critical mixing state. The QS model is highly questionable for such conditions.

Comparison of Quasisteady (QS) and Transient (TS) Models. In Figs. 9 and 10, we compare the predictions of the QS and TS models for different ambient temperatures and pressures. The comparison is presented in terms of the temporal histories of nondimensional surface area and temperature obtained using the two models. In general, the differences between the predictions of the two models are relatively small at low to moderate pressures, but become noticeable at high pressures. The QS model underpredicts and overpredicts the droplet surface temperature and evaporation rate during the earlier and later part of droplet lifetime, respectively, compared to the TS model. The QS model also un-

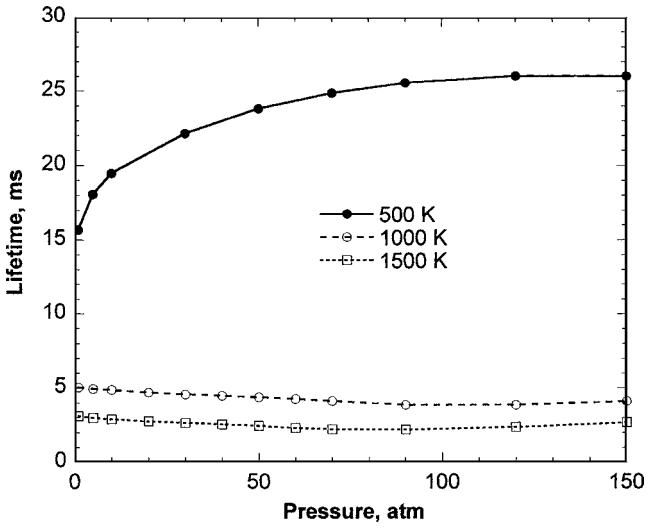

Fig. 7 Droplet lifetime versus pressure at different ambient temperatures

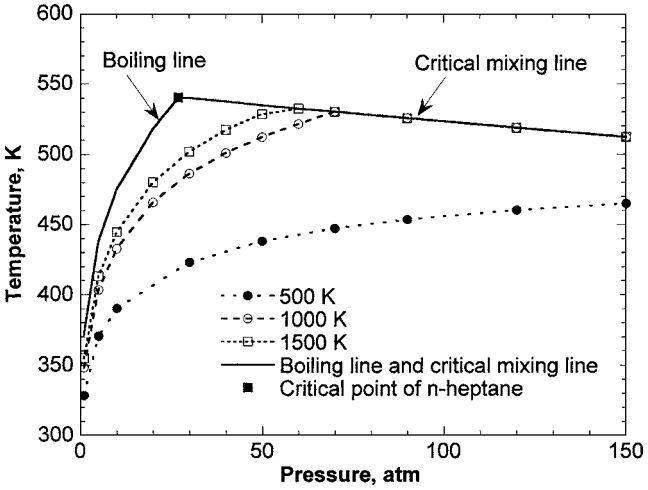

Fig. 8 Final droplet surface temperature plotted as a function of pressure for different ambient temperatures. The boiling line and critical mixing line are shown in the figure.

derpredicts the droplet lifetime compared to the TS model. As discussed in the following, these differences can be attributed to the quasisteady assumption in the QS model, since both the models employ the same algorithm for calculating the transport and

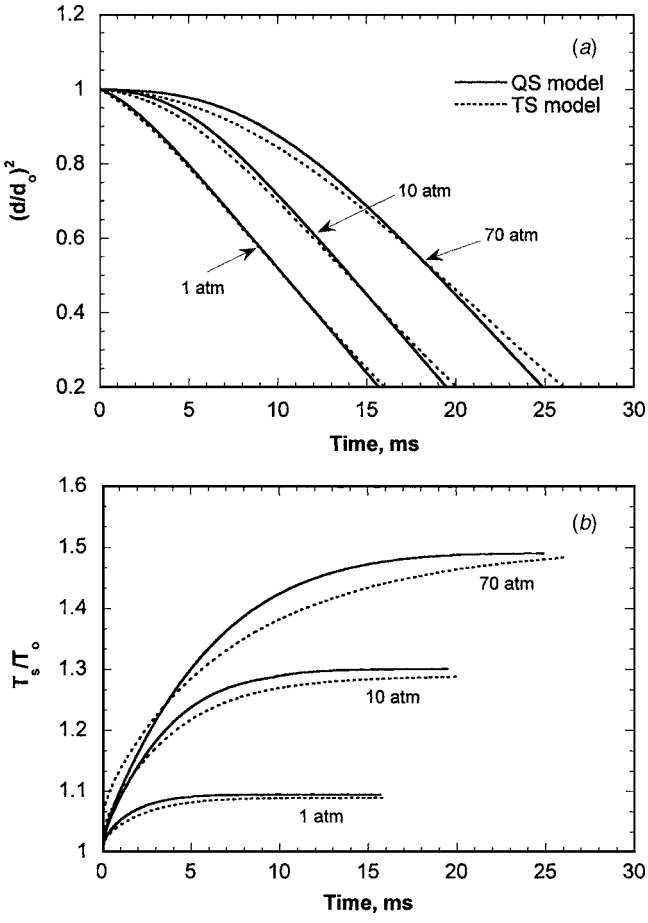

Fig. 9 Comparison of temporal histories of nondimensional surface area and temperature predicted using the QS and TS models at three different ambient pressures. (*a*) Surface area and (*b*) surface temperature. T_a=500 K. The initial droplet diameter (d_0) is 0.05 mm and temperature (T_0) is 300 K.

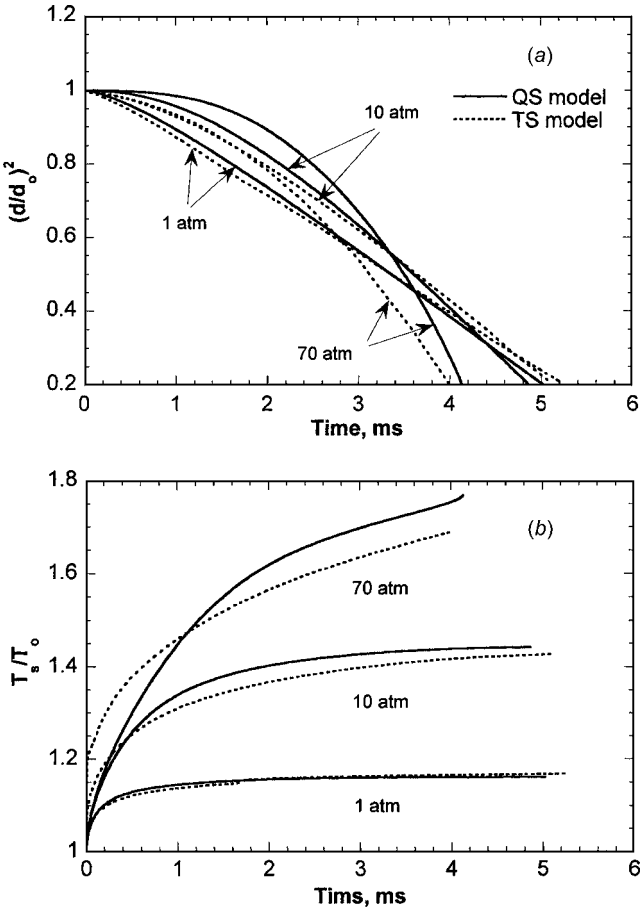

Fig. 10 Comparison of temporal histories of nondimensional surface area and temperature predicted using the QS and TS models at three different ambient pressures. (*a*) Surface area and (*b*) surface temperature. T_a=1000 K. The initial droplet diameter (d_0) is 0.05 mm and temperature (T_0) is 300 K.

thermodynamic properties.

Initially at $t=0$, as the droplet is introduced into the hot ambient, the gas film thickness, i.e., the gas layer between the droplet surface and gas ambient, is zero. Consequently, for the TS model, there is a large temperature gradient between high-temperature ambient gas and droplet surface, which results in high heat flux from the gas phase to the droplet surface. Since this effect is captured in the TS model, but not in the QS model that computes the heat flux using a suitable average of the droplet surface and ambient temperatures, it leads to higher droplet surface temperature for the TS model compared to the QS model, as indicated in Figs. 9(*b*) and 10(*b*). Consequently, the QS model underpredicts the evaporation rate during the early part of droplet lifetime compared to the TS model, as indicated in Figs. 9(*a*) and 10(*a*). Also note that for the QS model, the gas thermal conductivity is computed by using an average gas temperature and composition; see Eq. (16). The averaging procedure, which employs the one-third rule, implicitly assumes a gas-film thickness that is significantly larger than the actual value during the early part of drop lifetime. This leads to lower average gas temperature and higher fuel vapor mass fraction. While the lower gas temperature results in lower gas thermal conductivity and the higher fuel vapor mass fraction results in higher gas thermal conductivity, the net effect is the lower gas thermal conductivity, which leads to lower surface temperature for the QS model initially.

As the vaporization proceeds, the thickness of gas film for the TS model increases with time, which results in a smaller heat flux to the droplet surface. In contrast, for the QS model, the average

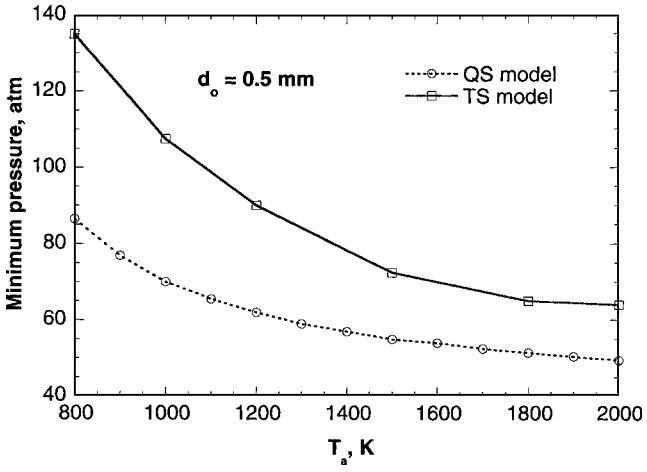

Fig. 11 Minimum pressure required for an *n*-heptane fuel droplet to attain the critical mixing state, plotted as a function of ambient temperature

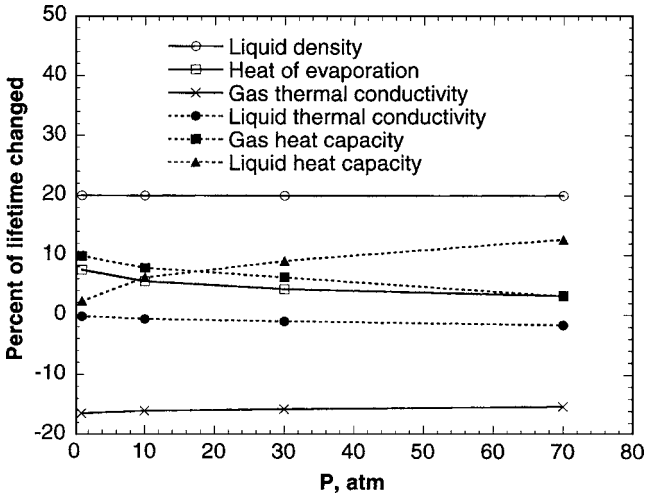

Fig. 12 Variation of droplet lifetime, resulting from an increase of a given property by 20%, plotted versus pressure for T_a = 1000 K

gas–film temperature increases as the droplet surface temperature increases with time. This leads to an overprediction of heat flux from the ambient gas to the droplet surface. As a consequence, during the later part of droplet lifetime, the surface temperature for the QS model is higher than that for the TS model. This also results in a higher fuel vapor mass fraction, and, consequently, higher gas thermal conductivity and higher evaporation rate during the later part of drop lifetime for the QS model. Additional results were obtained for both the QS and TS models by changing the initial droplet diameter. The differences between the predictions of the two models were found to be essentially independent of the initial droplet size.

An important aspect of high pressure vaporization is that the droplet surface may reach the critical mixing state during its lifetime, depending upon the ambient temperature and pressure. The transcritical vaporization behavior and the attainment of the critical mixing state in the context of transient model have been examined by several investigators [14–23]. Zhu and Aggarwal [26] quantified this behavior by plotting the minimum pressure required for the droplet surface to attain the critical mixing state as a function of ambient temperature. Figure 11 presents similar plots for both the QS and TS models. In order to obtain the minimum pressure value at a fixed ambient temperature, simulations were performed with increasingly higher pressures until the critical mixing state was observed at the droplet surface near the end of the droplet lifetime. As seen from the figure, the QS model predicts a vaporization process that reaches the critical mixing state at a significantly lower ambient pressure compared to that for the TS model. This is attributable to the fact that the QS model predicts higher surface temperature compared to the TS model during the later part of droplet lifetime.

The Effect of Thermotransport Properties on Vaporization Rate. Due to the importance of the gas- and liquid-phase properties to predict accurately the process of vaporization, we performed a sensitivity analysis to quantify as to which thermotransport property has the most influence on the predictions of the QS model. The sensitivity analysis is performed by increasing the value of a given property by 20%, and then examining its effect on droplet lifetime. Figure 12 shows the variations of droplet lifetime, resulting from an increase of a given property by 20%, plotted as a function of pressure at an ambient temperature of 1000 K. The droplet lifetime is most sensitive to liquid density and gas thermal conductivity. Increasing the liquid density by 20% increases the lifetime by 20%, since more energy is needed for liquid heating and vaporization. In contrast, increasing the gas thermal conductivity by 20% decreases the droplet lifetime by 16%, since higher gas thermal conductivity results in higher heat flux to the droplet, and thus a shorter lifetime. Other important properties are gas- and liquid-phase heat capacity and heat of vaporization. The droplet lifetime increases with increasing either of the heat capacities, since it lowers the liquid temperature. Increasing the heat of evaporation increases the lifetime, since more energy is needed for evaporation. In addition, the sensitivity of droplet lifetime to these three properties increases at higher pressures. The liquid thermal conductivity affects the droplet surface temperature through its influence on temperature distribution inside the droplet. However, the droplet lifetime is not affected noticeably by a 20% change in liquid thermal conductivity. Finally, it should be noted that the gas density and mass diffusivity change significantly with pressure.

High-Pressure Effects on Thermo-Transport Properties. An important issue in the context of developing a high-pressure vaporization model deals with the high-pressure effects on thermotransport properties. The high-pressure effects considered in the present study include gas-phase nonidealities, solubility of gases into liquid, high-pressure phase equilibrium at the droplet surface, transient liquid-phase heating, and high-pressure effects on thermotransport properties. The first four effects are clearly important, and have been modeled fairly accurately in the present study. Regarding the last effect, it is important to quantify as to which thermotransport property is most sensitive to the high-pressure effect. Our results indicate that the effect of pressure and temperature on the heat of vaporization should be represented accurately. The high-pressure effects on gas-phase thermal conductivity and specific heat become important for gas temperatures near the critical mixing point, but are negligible for higher temperatures.

The Effects of the Averaging Rule for Gas Temperature and Composition. The QS model generally uses the one-third rule to obtain the average gas temperature and composition, which are then used for calculating the thermotransport properties. As discussed in preceding sections, this leads to an underprediction of droplet surface temperature and, hence, of vaporization rate during the early part of drop lifetime, and their overprediction during the later part of lifetime for the QS model compared to that for the TS model. The underprediction and overprediction become more significant at higher ambient pressure and temperature. In order to reduce this error, a variable averaging factor should be used. During the early part of drop lifetime, a larger value should be used, while during the later part, a smaller value should be used. In

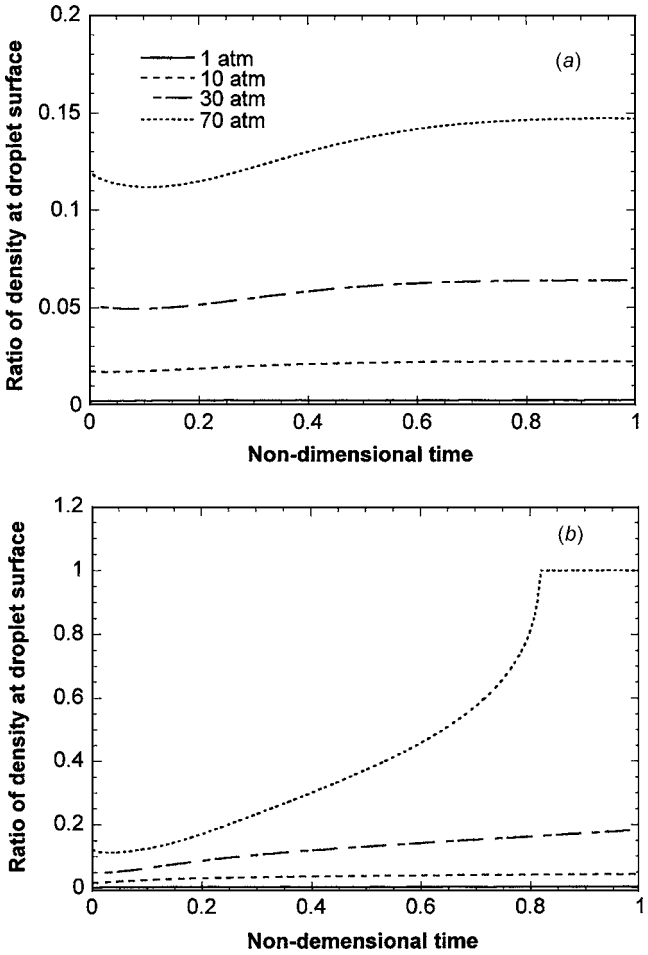

Fig. 13 Temporal variation of the ratio of gas density (at the droplet surface) to liquid density plotted versus pressure. (*a*) T_a=500 K, (*b*) T_a=1500 K.

addition, the higher the pressure and/or temperature, the larger the amount by which the averaging factor should be changed during the droplet lifetime.

The Range of Applicability of the QS Model. The justification for using the quasisteady model is based on the consideration that the gas density is much smaller than the liquid density [4]. In Fig. 13, the ratio of gas density to liquid density at the droplet surface is plotted versus the time, normalized by the corresponding lifetime, at different pressures. In accordance with the results presented earlier, the ratio is small at lower pressures, but becomes increasingly more significant at higher pressures. In addition, this ratio depends strongly on ambient temperature, and the effect becomes more significant at higher pressures.

In Fig. 14, we plot the final ratio (the final value corresponds to the time at which the droplet nondimensional surface area is 0.2) of gas density to liquid density as a function of pressure at three different ambient temperatures. At low ambient temperature, the final ratio linearly increases with pressure, but has a relatively small value even at very high pressures. In contrast, at high ambient temperature, the final ratio increases rapidly as the pressure exceeds the fuel critical pressure, and approaches unity as the critical mixing state is reached. This indicates that the quasisteady assumption becomes increasingly questionable as the ambient pressure exceeds the fuel critical pressure at high ambient temperature.

To obtain the range of applicability for the QS model, we plot in Fig. 15 the maximum pressure for which the final ratio of gas density to liquid density is smaller than 0.2 as a function of ambient temperature. The maximum pressure decreases as ambient temperature is increased, and approaches a constant value near the critical pressure. This indicates that the QS model can be used for a wide range of pressures at low ambient temperature, and for pressure up to the fuel critical pressure at high ambient temperature. The effect of droplet size is also shown in the figure, which indicates that the maximum pressure for the applicability of the QS model is independent of the initial droplet size.

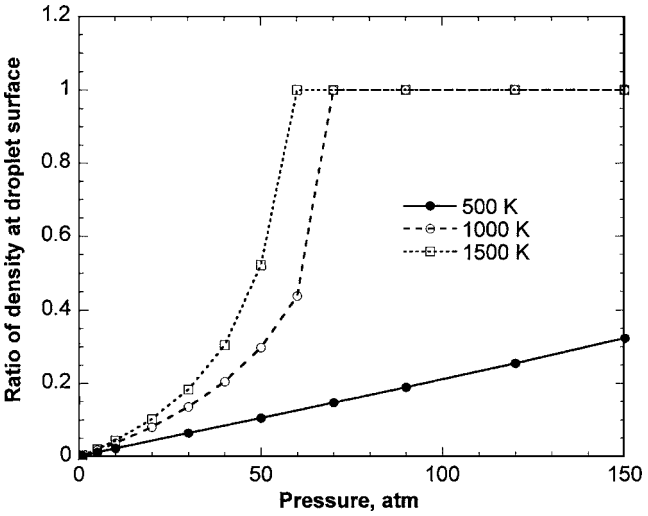

Fig. 14 The final ratio of gas density (at the droplet surface) to liquid density plotted versus pressure at different ambient temperatures

Conclusions

A quasisteady, high-pressure droplet gasification model has been developed and evaluated under conditions pertinent to high-pressure conditions in diesel and gas turbine combustors. The model includes a realistic representation of the high-pressure effects, and still is sufficiently simplified so that it can easily be incorporated into comprehensive spray codes. While the model retains the quasisteady gas-phase assumption, it considers the transient liquid-phase, transport inside the droplet. In addition, all the high-pressure effects are incorporated into the model. These include gas-phase nonidealities, solubility of gases into liquid, high-pressure phase equilibrium at the droplet surface, and depen-

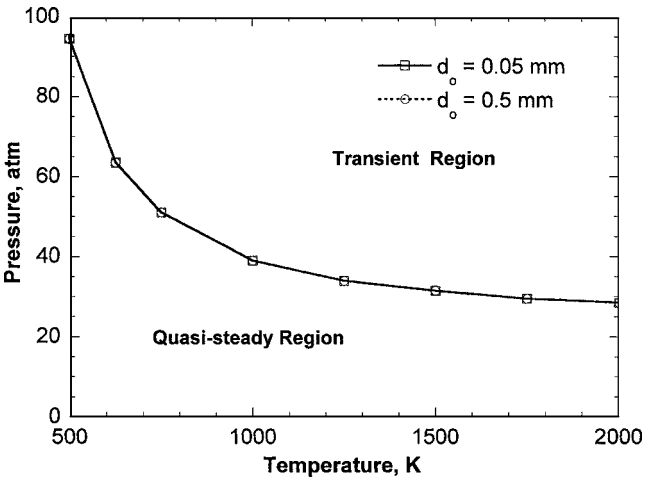

Fig. 15 The range of applicability of the QS model in terms of the limiting pressure plotted as a function of ambient temperature

dency of the gas- and liquid-phase properties on pressure. The validity of the quasisteady model is examined by comparing its predictions with those using a more comprehensive transient droplet model, as well as with the available experimental data. Based on these comparisons, the applicability of the quasisteady assumption is quantified in terms of ambient pressures and temperatures. Important conclusions are as follows:

1. There is a fairly good agreement between the QS and TS models for a wide range of pressures at low ambient temperatures, and for pressures up to the fuel critical pressure at high ambient temperature. Thus, the QS model developed in the present study can be used reliably for a relatively wide range of pressures at low ambient temperature, and for pressure up to the fuel critical pressure at high ambient temperature.
2. Compared to the TS model, the QS model predicts a lower evaporation rate initially and a higher rate during the later period of drop lifetime. This is mainly due to the assumption of gas-phase quasisteadiness and the averaging rule used in the QS model, which lead to smaller and larger gas-phase heat flux at the droplet surface, and thus lower and higher droplet surface temperature during the early and later periods of lifetime, respectively. The differences between the predicted evaporation rates using the two models become more significant at higher ambient temperatures and pressures. In addition, the vaporization process predicted using the QS model reaches the critical mixing state earlier, i.e., at lower ambient temperature and/or pressure than that predicted with the TS model. This is due to the higher droplet surface temperature predicted during the later part of drop lifetime for the QS model.
3. The droplet lifetime is very sensitive to the gas thermal conductivity and liquid density. Increasing the gas thermal conductivity or decreasing the liquid density decreases the lifetime. Other important properties are gas- and liquid-phase heat capacity. The lifetime increases with increasing either heat capacity.
4. Since the gas–film thickness changes during droplet lifetime, the QS model can be further refined by using a variable averaging factor for calculating the average gas temperature and composition used to compute the gas-phase thermotransport properties. During the early part of droplet lifetime, a larger value should be used, while during the later part, a smaller value should be used. In addition, the higher the ambient pressure and/or temperature, the larger the amount by which the averaging factor should be changed during droplet lifetime [37].

Acknowledgment

This research was partially funded by the GE Aircraft Engines. The code for the unsteady droplet model was provided by G. S. Zhu of Detroit Diesel Corporation. Many fruitful discussions with G. S. Zhu are also appreciated.

Nomenclature

a,b,A^*,B^* = dimensionless parameters for Peng–Robinson equation of state
B = transfer number
C_p = specific heat at constant pressure (kJ/kg K)
d = droplet diameter (mm)
D = mass diffusivity (m^2/s)
H = energy supplied to the droplet per unit mass of fuel vaporized (kJ/kg)
$\bar{H}$ = enthalpy of vaporization (kJ/kmol)
k = thermal conductivity (W/m K)
k_{ij} = binary interaction coefficient for Peng–Robinson equation of state
L = latent heat of vaporization (kJ/kg)
Le = Lewis number
$\dot{m}$ = evaporation rate (kg/s)
$\bar{m}$ = normalized evaporation rate
n = mole number
P = pressure (atm)
r = radial coordinate
$\bar{r}$ = normalized radial coordinate
R = gas constant (kJ/kg K)
t = time (s)
$\bar{t}$ = normalized temporal variable
T = temperature (K)
$\bar{T}$ = normalized temperature
V = molar volume (m^3/mol)
x = liquid mole fraction
y = vapor mole fraction
Y = vapor mass fraction
Z = compressibility factor

Greek Symbols

ρ = density (kg/m^3)
α = thermal diffusivity (m^2/s)
ϕ = fugacity coefficient
Φ = averaging gas temperature or mass fraction
β = averaging factor

Superscript

0 = ideal state
v = vapor
l = liquid

Subscript

a = ambient
avg = average
b = boiling point
c = critical point
f = fuel
g = gas
i, j = species i or j
l = liquid
s = droplet surface
o = initiate state
∞ = infinity or ambient

References

[1] Godsave, G. A. E., 1953, "Studies of the Combustion of Drops in a Fuel Spray—The Burning of Single Drops of Fuel," Fourth Symposium (International) on Combustion, Williams and Wilkins, Baltimore, pp. 818–830.
[2] Spalding, D. B., 1953, "The Combustion of Liquid Fuels," Fourth Symposium (International) on Combustion, Williams and Wilkins, Baltimore, pp. 847–864.
[3] Williams, A., 1973, "Combustion of Droplet of Liquid Fuels: A Review," Combust. Flame, **21**, pp. 1–31.
[4] Law, C. K., 1982, "Recent Advances in Droplet Vaporization and Combustion," Prog. Energy Combust. Sci., **8**, pp. 171–201.
[5] Sirignano, W. A., 1983, "Fuel Droplet Vaporization and Spray Combustion," Prog. Energy Combust. Sci., **9**, pp. 291–322.
[6] Peng, F. and Aggarwal, S. K., 1995, "A Review of Droplet Dynamics and Vaporization Modeling for Engineering Calculations," ASME J. Eng. Gas Turbines Power, **117**, pp. 453–461.
[7] Sirignano, W. A., 1979, "Theory of Multicomponent Fuel Droplet Vaporization," Archives of Thermodynamics and Combustion, **9**, pp. 231–251.
[8] Aggarwal, S. K., Tong, A., and Sirignano, W. A., 1984, "A Comparison of Vaporization Models in Spray Calculations," AIAA J., **22**, pp. 1448–1457.
[9] Abramzon, B. and Sirignano, W. A., 1989, "Droplet Vaporization Model for Spray Combustion Calculations," Int. J. Heat Mass Transfer, **32**, pp. 1605–1618.
[10] Faeth, G. M., 1983, "Evaporation and Combustion of Sprays," Prog. Energy Combust. Sci., **9**, pp. 1–76.
[11] Aggarwal, S. K., 1987, "Modeling of Multicomponent Fuel Spray Vaporization," Int. J. Heat Mass Transfer, **30**, pp. 1949–1961.
[12] Aggarwal, S. K., Shu, Z., Mongia H. and Hura, H. S., 1998, "Multicomponent Fuel Effects on the Vaporization of a Surrogate Single-Component Fuel Droplet," ASME Paper No. 98-0157.
[13] Matlosz, R. L., Leipziger, S., and Torda, T. P., 1972, "Investigation of Liquid

Drop Evaporation in a High Temperature and High Pressure Environment," Int. J. Heat Mass Transfer, **15**, pp. 831–852.
[14] Hsieh, K. C., Shuen, J. S., and Yang, V., 1991, "Droplet Vaporization in High-Pressure Environment, I: Near-Critical Conditions," Combust. Sci. Technol., **76**, pp. 111–132.
[15] Curtis, E. W. and Farrell, P. V., 1992, "A Numerical Study of High-Pressure Droplet Vaporization," Combust. Flame, **90**, pp. 85–102.
[16] Shuen, J. S., Yang, V., and Hsiao, C. C., 1992, "Combustion of Liquid-Fuel Droplets in Supercritical Conditions," Combust. Flame, **89**, pp. 299–319.
[17] Jia, H. and Gogos, G., 1993, "High Pressure Droplet Vaporization; Effects of Liquid-Phase Gas Solubility," Int. J. Heat Mass Transfer, **36**, pp. 4419–4431.
[18] Yang, V., Lin, N. N., and Shuen, J. S., 1994, "Vaporization of Liquid Oxygen (LOX) Droplets in Supercritical Hydrogen Environments," Combust. Sci. Technol., **97**, pp. 247–270.
[19] Givler, S. D. and Abraham, J., 1996, "Supercritical Droplet Vaporization and Combustion Studies," Prog. Energy Combust. Sci., **22**, pp. 1–28.
[20] Curtis, E. W., Ulodogan, A. and Reitz, R. D., 1995, "A New High Pressure Droplet Vaporization Model for Diesel Engine Modeling," SAE Paper No. 952431.
[21] Abraham, J. and Givler, S. D., 1999, "Conditions in Which Fuel Drops Reach a Critical State in a Diesel Engine," SAE Paper No. 1999-01-0511.
[22] Sirignano, W. A. and Delplanque, J.-P., 1999, "Transcritical Vaporization of Liquid Fuels and Propellants," AIAA J., **15**, pp. 896–902.
[23] Yang, V., 2000, "Modeling of Supercritical Vaporization, Mixing, and Combustion Processes in Liquid-Fueled Propulsion System," Proc. of the Combustion Institute, Vol. 28, pp. 925–942.
[24] Sirignano, W. A., 1999, *Fluid Dynamics and Transport of Droplets and Sprays*, Cambridge University Press, Cambridge, UK.
[25] Aggarwal, S. K., and Mongia, H., 2002, "Multicomponent and High-Pressure Effects on Droplet Vaporization," ASME J. Eng. Gas Turbines Power, **124**, pp. 248–257.
[26] Zhu, G. and Aggarwal, S. K., 2000, "Transient Supercritical Droplet Evaporation with Emphasis on the Effects of Equation of State," Int. J. Heat Mass Transfer **43**, pp. 1157–1171.
[27] Reid, R. C., Prausnitz, J. M., and Poling, B. E., 1987, *The Properties of Gases and Liquids*, McGraw-Hill, New York.
[28] Knapp, H., Doring, R., Oellrich, L., Plocker, U. and Prausnitz, J. M., 1982, *Vapor-Liquid Equilibria for Mixture of Low Boiling Substances, Chemical Engineering Data Series*, Vol. VI, Dechema, Frankfurt.
[29] Filippov, L. P., 1955,"Thermal Conduction of Solutions in Associated Liquids: Thermal Conduction of 50 Organic Liquids," Chem. Abstr. **49**, Col. 15430–15431; Chem. Abstr. 1956, **50**, Col. 8276.
[30] Baroncini, C., Di Filippo, P., and Latini, G., 1983, "Comparison Between Predicted and Experimental Thermal Conductivity Values for the Liquid Substances and the Liquid Mixtures at Different Temperatures and Pressures," paper presented at the Workshop on Thermal Conductivity Measurement, IMEKO, Budapest.
[31] Chung, T. H., Ajlan, M., Lee, L. L., and Starling, K. E., 1988, "Generalized Multiparameter Correlation for Nonpolar and Polar Fluid Transport Properties," Ind. Eng. Chem. Res. **27**, pp. 671–679.
[32] Chung, T. H., Lee, L. L., and Starling, K. E., 1984, "Applications of Kinetic Gas Theories and Multiparameter Correlation for Prediction of Dilute Gas Viscosity and Thermal Conductivity," Ind. Eng. Chem. Fundam., **23**, pp. 8–13.
[33] Takahashi, S., 1974, "Preparation of a Generalized Chart for the Diffusion Coefficients of Gases at High Pressures," J. Chem. Eng. Jpn., **6**, pp. 417–420.
[34] Vargaftik, N. B., 1983, *Handbook of Physical Properties of Liquids and Gases, Pure Substances and Mixtures*, 2nd ed., Hemisphere, New York.
[35] Nomura, H., Ujiie, Y., Rath, H. J., Sato, J., and Kono, M., 1996, "Experimental Study of High-Pressure Droplet Evaporation Using Microgravity Conditions," Twenty-Sixth Symposium (International) on Combustion, The Combustion Institute, pp. 1267–1273.
[36] Zhu, G. S., Reitz, R. D., and Aggarwal, S. K., 2001, "Gas-phase Unsteadiness and Its Influence on Droplet Vaporization in Sub- and Super-critical Environments," Int. J. Heat Mass Transfer, **44**, pp. 3081–3093.
[37] Zhu, G.-S., and Reitz, R. D., 2001, "Engine Fuel Droplet High-Pressure Vaporization Modeling," ASME J. Eng. Gas Turbines Power, **123**(2), pp. 412–418.

Study on Biomass Pyrolysis Kinetics

Xiaodong Zhang
Min Xu
Rongfeng Sun
Li Sun

Energy Research Institute of
Shandong Academy of Sciences,
No. 19 Keyuan Road,
Jinan 250014, China

Pyrolysis is the most fundamental process in thermal chemical conversion of biomass, and pyrolysis kinetic analysis is valuable for the in-depth exploration of process mechanisms. On the basis of thermal gravity analysis of different kinds of biomass feedstock, thermal kinetics analysis was performed to analyze the pyrolysis behavior of biomass. With the apparent kinetic parameters derived, a kinetic model was proposed for the main reaction section of biomass pyrolysis process. The pyrolysis characteristics of three kinds of biomass material were compared in view of corresponding biochemical constitution. Through model simulation of different pyrolysis processes, the diversity in pyrolysis behavior of different kinds of biomass feedstock was analyzed and pyrolysis mechanism discussed. The results derived are useful for the development and optimization of biomass thermal chemical conversion technology. [DOI: 10.1115/1.2135816]

Introduction

With much more concern paid to global resources and environment, the utilization of fossil fuels has been greatly limited. As one kind of renewable energy, biomass can achieve zero emission of CO_2 and also can help sustainable development [1]. Thermal chemical conversion was believed to be the most prominent way for biomass high-efficiency conversion, converting biomass feedstock into gaseous, liquid, and solid energy products under thermal conditions. Several types of technology have been developed, including pyrolysis, gasification, combustion, etc., with controlling the process parameters. Pyrolysis is the most basic process in thermal chemical conversion of biomass, and it is also the original and accompanying reaction in gasification and combustion [2,3]. The analysis of pyrolysis of biomass is helpful for the control and optimization of an efficient biomass thermal chemical conversion process.

Pyrolysis kinetics analysis is one important tool for the description of the effect of process parameters on the feedstock conversion process [3]. With kinetic analysis, the reaction system and mechanism during pyrolysis can be discussed, and some fundamental data of thermal chemical conversion can be provided. However, the investigation on the pyrolysis kinetics of biomass material is relatively scarce. Although the research on cellulose pyrolysis kinetics has prevailed for the past century, the kinetics research on whole biomass pyrolysis has its own characteristics that baffle the progress in this field [4–6]. As the complicated polymer of cellulose, hemicellulose, lignin, and some extracts, biomass behaves differently from cellulose during the pyrolysis process. And also, the pyrolysis behavior of different kinds of biomass varies with biochemical composition [4,5]. Because of the different analysis apparatus and mathematics tools being applied, the result achieved from researchers around the world varies greatly and is even disputed sometimes, which weakens the foundation of the fundamental theory system of biomass thermal chemical conversion. With the rise of biomass as one kind of renewable resource, some comprehensive review on the pyrolysis kinetics of biomass is expected.

Experimental

Thermal gravity (TG) analysis of biomass was performed to study the pyrolysis kinetics with one set of Seiko TG-DTA6200, with N_2 as the load gas. Several heating rates were adopted, such as 5, 10, 20, 30, 50, and 100 K/min. Several kinds of biomass feedstock with different physical and chemical characteristics were analyzed, and the proximate analysis of part of the feedstock is shown in Table 1. Before TG analysis, all feedstock should be grinded into 200～500 μm and well mixed.

The biochemical composition is important for the analysis of biomass pyrolysis processes. In pyrolysis, cellulose, hemicellulose, and lignin behave differently, and also some extent of interaction may occur, which increases the complexity of the overall process. The biochemical constitution of selected biomass feedstock was compared in Table 2. According to the biochemical constitution, biomass feedstock selected is classified into three types in this paper. Straw and stalk materials are those with relatively high cellulose content, such as corn stalk, cotton stalk, wheat straw, and tree skin. Wood chip, peanut shell, and seed shell are classified as woody materials whose lignin content is relatively high. And cotton and filter paper are classified as cellulosic materials, which are mainly composed of pure cellulose.

Results and Analysis

Kinetic Processing of Biomass TG Analysis Data. From TG analysis, the weight-loss curve of biomass materials under different pyrolysis circumstances can be achieved. A typical biomass TG and DTG profile is illustrated in Fig. 1, with corn stalk as the feedstock. For different feedstock, the curves are similar in shape, with some difference in the start, end, and the peak point of the reaction; weight loss velocity; and the pyrolysis residue ratio.

From the TG and DTG curve, the pyrolysis of biomass can be divided into three stages. The first stage is the process of removal of surface water, continued to 400 K, during which period some depolymerization and vitrification conversion occurred [3,7]. The second stage is the main reaction stage of pyrolysis, where 80–90% of weight loss occurred, extending from 400 K to 570–670 K, and the weight-loss velocity reaches the maximum at the curve peak. During the third stage, the pyrolysis residue slowly decomposed, with the weight-loss velocity becoming smaller and smaller and the residue ratio tends to be constant at the end. Usually, the kinetic analysis focuses on the most severe stage of pyrolysis, that is, the main reaction period. For different biomass feedstock, the main reaction stage has a different range and behavior.

During the TG-DTG analysis, the biomass sample with original mass m_0 decomposed under program-controlled heating. As time goes on, the mass of the sample changes to m at time t, so the decomposition velocity of biomass can be written as

Contributed by the International Gas Turbine Institute (IGTI) of ASME for publication in the JOURNAL OF ENGINEERING FOR GAS TURBINES AND POWER. Manuscript received October 1, 2003; final manuscript received March 1, 2004. IGTI Review Chair: A. J. Strazisar. Paper presented at the ASME Turbo Expo: Power for Land, Sea and Air, Reno–Tahoe, Nevada, June 6–9, 2005, Paper No. GT2005-68350.

Table 1 Proximate analysis of selected biomass (dry base)

	Volatile (%)	Fixed carbon (%)	Ash (%)
Wheat straw	74.9	17.9	7.2
Corn stalk	80.9	14	5.1
Cotton stalk	72.9	19.9	7.2
Rice straw	74.9	11.6	13.5
Peanut shell	76.5	9.6	13.9
Bean stalk	81.0	12.4	6.6
Wood chip	84.1	11.1	4.8
Rice husk	69.3	14.9	15.8

$$\frac{dx}{dt} = kf(x) \tag{1}$$

The conversion ratio x is defined as $x=(m_0-m)/(m_0-m_\infty)$, in which m_∞ is the residue mass of the pyrolysis process at the end of pyrolysis process. According to the Arrhenius correlation, the velocity constant of the reaction can be written as $k=A\exp(-E/RT)$, in which E is the activation energy, A the frequency factor, R the gas constant, and T the reaction temperature.

$f(x)$ represents the function related with conversion ratio x, whose format depends on the reaction mechanism of pyrolysis. For simple reactions, we can use the following function format, $f(x)=(1-x)^n$, with n as the reaction order. That is, $f(x)$ is assumed to be only related with conversion ratio x. Thus, we can get

$$\frac{dx}{dt} = A\exp\left(-\frac{E}{RT}\right)(1-x)^n \tag{2}$$

At the same time, the heating rate of TG analysis is $\beta=dT/dt$; thus,

$$\frac{dx}{dT} = \frac{A}{\beta}\exp\left(-\frac{E}{RT}\right)(1-x)^n \tag{3}$$

Equation (3) can be converted into logarithm format

$$\ln\left(\frac{dx}{dT}\right) - n\ln(1-x) = \ln\left(\frac{A}{\beta}\right) - \frac{E}{RT} \tag{4}$$

It can be seen that on the left-hand side of Eq. (4) $\ln(dx/dT) - n\ln(1-x)$ has a linear relation with $1/T$; that is, the relation can be written as $Y=aX+b$, with $(-(E/R))$ as the slope and $\ln(A/\beta)$ as the intercept. The determination of reaction order n can be achieved from programing calculation or trial calculation. In this work, many values were trailed for n in Eq. (4) with TG-DTG data calculation. From the comparison of calculation results, the determination of n for particular biomass pyrolysis process should correspond to the calculation result with the best linearity. From the results of several kinds of biomass feedstock, the value of n was determined to be mostly close to 1. That is, the pyrolysis of biomass can be approximately looked as a one-order reaction. This conclusion is consistent with the results of most other researcheres [4,7]. Thus, $n=1$ was used in our work, with satisfying correctness revealed from the comparison of experiment and calculation results.

Derivation of Biomass Pyrolysis Kinetic Parameters. In order to get the kinetic parameters of pyrolysis, TG-DTG data from different biomass feedstock and different pyrolysis conditions were processed with Eq. (4). Table 3 lists the results of corn stalk got from different heating rates.

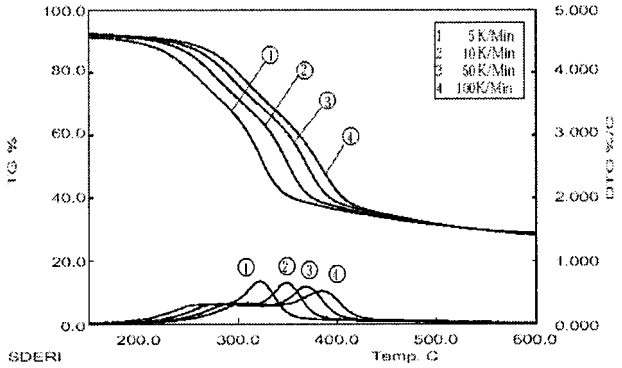

Fig. 1 Typical TG and DTG curve of biomass

It can be seen that the kinetic parameters vary with heating rate, and, generally, the activation energy increases with frequency factor. The pyrolysis process of biomass is closely related to the reaction condition, so that the shape of the TG curve can be correlated with heating rates. For this, the corresponding kinetics compensation effect should be considered. According to some related research, the effect that A varies with E can be partly compensated with the following equation: $\ln A=aE+b$ [3].

The kinetic parameters of corn stalks were listed in the $\ln A \sim E$ coordinate, and linear fitting was performed, as shown in Fig. 2. The following kinetic compensation expression can be gotten

$$\ln(A) = 0.0324E + 5.9049 \tag{5}$$

Then kinetic parameters can be achieved and apparent kinetic expression erected as

$$\frac{dx}{dT} = \frac{3165.55}{\beta}\exp\left(-\frac{66518}{8.314\times T}\right)(1-x) \tag{6}$$

The parameters achieved after compensation will lessly be influenced by experimental conditions, and the description of the pyrolysis process with these kinetic parameters will be more stable. From the simulation results with Eq. (6), there is satisfying fitting between model calculation and experimental data.

Effect of Heating Rates on Biomass Pyrolysis. The influence of heating rate on pyrolysis process can be realized from the simulation of the pyrolysis process under different heating rates. Figure 3 shows the results of simulation of corn-stalk pyrolysis under heating rates 5, 10, 20, 30, and 50 K/min. Compared to the experimental results shown in Fig. 1, the accuracy of the simulation results with kinetic parameters is satisfactory. There lies obvious influence of heating rate on the start and end point and the duration of the main pyrolysis stage. However, heating rate has little effect on the ending state of pyrolysis process, just as resulting in similar residue ratio.

With the increase of heating rate, the start and end temperature of biomass pyrolysis increased, and also the weight loss climax point in DTG curve. This may be due to the thermal lag effect in biomass pyrolysis. With relatively small heat conductivity coeffi-

Table 2 Biochemical constitution of selected biomass feedstock (dry base)

	Wheat straw (wt. %)	Corn stalk (wt. %)	Peanut shell (wt. %)	Tree skin (wt. %)	Cotton (wt. %)
Cellulose	33.2	41.7	35.7	48.6	99.4
Hemicellulose	24.6	27.2	18.7	25.5	
Lignin	15.1	20.3	30.2	19.3	

Table 3 Kinetic parameters of corn-stalk pyrolysis

Heating rate (K/min)	Activation energy E (kJ/mol)	Frequency factor A (s^{-1})
5	63.95	2812.8
10	65.26	3086.9
20	65.84	3179.5
30	67.57	3352.1
50	69.97	3463

cient, the increase of temperature from the outside to the inside in a biomass particle is slow. When the temperature inside the particle reaches the level pyrolysis reaction needs, the temperature outside the particle will become higher. Under higher heating rates, the temperature gradient inside the biomass particle increases, resulting in a higher temperature level for the pyrolysis reaction to proceed. From the general trend, the weight-loss curves under different heating rates are basically parallel, which reveals that there lies a consistent or similar reaction mechanism. So, the pyrolysis reaction is mainly influenced by reaction temperature. The pyrolysis process can be quickly accomplished as long as the relatively high-level reaction temperature can be reached.

Pyrolysis Kinetic Parameters of Different Biomass Feedstock. With similar method mentioned above, kinetic parameters of pyrolysis for many kinds of biomass feedstock can be derived, as shown in Table 4. There is big difference for different kinds of biomass feedstock.

The activation energy are at the level of 60–80 KJ/mol for straw and stalk materials (such as wheat straw and corn stalk), 80–100 KJ/mol for woody materials (such as wood chip and peanut shell), and above 200 KJ/mol for cellulosic materials (such as

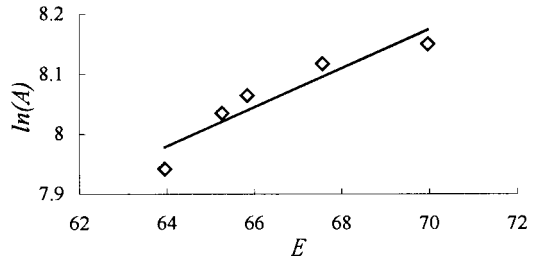

Fig. 2 Compensation of kinetic parameters under different heating rates

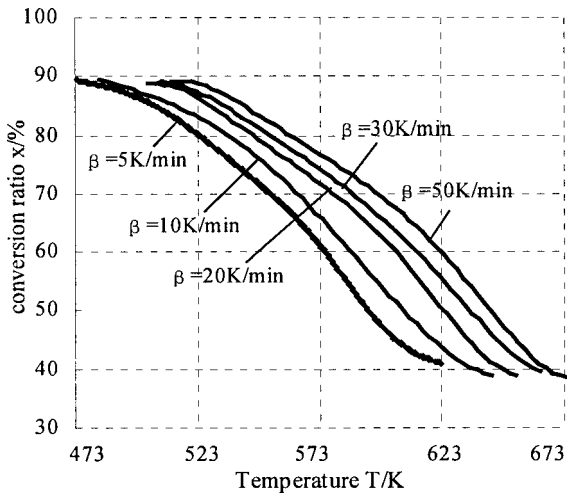

Fig. 3 Effect of heating rate on biomass pyrolysis process

Table 4 Pyrolysis kinetic parameters of biomass feedstock

Biomass feedstock	Activation energy E (KJ/mol)	Frequency factor A (s^{-1})
Corn stalk	66.518	3.16×10^{3}
Wheat straw	70.516	1.96×10^{6}
Cotton stalk	71.055	9.15×10^{5}
Tree skin	77.316	2.62×10^{5}
Wood chip	85.393	1.42×10^{6}
Peanut shell	84.47	1.47×10^{6}
Seed shell	91.462	4.55×10^{6}
Cotton	200.9	2.93×10^{14}
Filter paper	227.296	3.43×10^{16}

cotton and filter paper. The reason can be traced to the difference of the biochemical composition of feedstock. Generally, biomass is mainly composed of cellulose, hemicellulose, lignin, and a small quantity of extracts, which behave differently under heating conditions [4,7,8]. The main decomposition zone of cellulose is about 523–773 K with a high pyrolysis rate, resulting in little carbon. The pyrolysis of lignin starts relatively early and last almost the overall pyrolysis process, resulting in relatively large quantity of carbon. Hemicelluse is the most unsteady component in biomass, quickly decomposed between 500–600 K. With the programing increase of temperature, the decomposition of three components starts at different temperatures and with different reaction duration, resulting in different pyrolysis residue. The difference of biomass composition, combined with the complicated heat transfer and mass transfer condition in the pyrolysis process, results in the diversity of pyrolysis behavior of different kinds of biomass.

The extent of difficultness of the pyrolysis process of different biomass feedstock can be compared from kinetic parameters. The larger the activation energy, the slower the pyrolysis process of that biomass feedstock under the same temperature level will be, and the more difficult the pyrolysis process is.

Comparison of Pyrolysis Kinetic Behavior of Different Biomass Feedstock. There is little difference in the activation energy for the same kind of biomass feedstock, resulting in great similarity in pyrolysis behavior. The simulation results under the same heating rate for several kinds of straw and stalk material are shown in Fig. 4. Great similarity is revealed, except for some difference in the start and end points and the ultimate residue ratio, which is mainly due to the difference in biomass feedstock

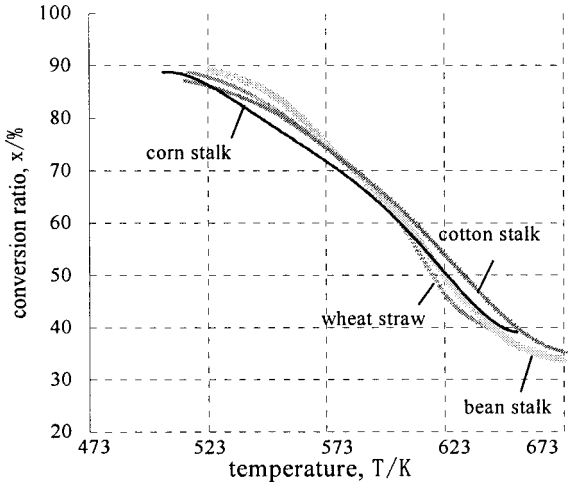

Fig. 4 Comparison of pyrolysis behavior of similar kind of biomass feedstocks (heating rate β=20 K/min)

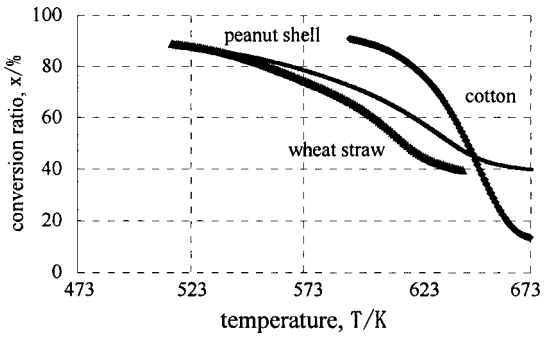

Fig. 5 Comparison of pyrolysis behavior of different kind of biomass feedstocks (heating rate β=20 K/min)

composition and ash content. According to some research, ash content in biomass has some effect on the pyrolysis behavior, which is not discussed in the present paper [4,9].

There lies big difference in the activation energy of pyrolysis among different kinds of biomass feedstock, resulting in different pyrolysis behavior. The simulation results of pyrolysis of three different kinds of biomass feedstock (wheat straw, peanut shell, and cotton) are compared in Fig. 5. Cellulosic biomass material quickly decomposed in a very limited temperature range of 590–670 K, with a larger decomposition rate than the other two kinds of material. However, the duration of the pyrolysis process of woody material (such as peanut shell) is the longest, with smallest reaction rate. That is, woody materials are the most difficult for pyrolysis. The pyrolysis of straw materials (such as wheat straw) starts earlier than the other two kinds of material, with a medium reaction rate. Therefore, primary theoretical analysis of the biomass pyrolysis process can be performed through kinetic simulation, and this is most valuable for the design and optimization of pyrolysis reactor and technology.

Conclusion

The different constitution of cellulose, hemicellulose, and lignin in biomass feedstock, combined with the different decomposition behavior of each component, results in the diversity in pyrolysis behavior of different kinds of biomass feedstock. Cellulosic biomass materials quickly decomposed in a very limited temperature range of 590–670 K, with larger decomposition rate. Woody materials are the most difficult for pyrolysis, with the longest duration. The pyrolysis of straw materials starts earlier than the other two kinds of material, with a medium reaction rate. From kinetic analysis of the pyrolysis process, kinetic parameters were achieved for a large variety of biomass feedstock, which can provide valuable fundamental data for the development of efficient biomass thermal chemical conversion technology.

Acknowledgment

The work cited in this paper is funded by the National Basic Research Program of China (Grant No. 2004CB719700). The authors also extend thanks for the financial support of the project "study on the biomass characteristics in thermal chemical conversion" from the Natural Science Fund of Shandong Province (Grant No. Z2000F03) and Doctor Fund of Shandong Academy of Sciences project "Efficient hydrogen production from biomass." In addition, the contributions of our colleagues, Xiaolu Yi, Dongyan Guo, and Guihuan Yan, in the experimental work and data processing are greatly appreciated.

Nomenclature

A = frequency factor
a = constant
b = constant
DTG = differential thermal gravity analysis
E = activation energy
$f(x)$ = function related with x
k = velocity constant of the reaction
m = mass of sample
m_0 = original mass of sample
m_∞ = final mass of sample
n = reaction order
R = gas constant
T = temperature
t = time
TG = thermal gravity analysis
x = conversion ratio
β = heating rate of TG analysis

References

[1] Wu, C., and Ma, L., 2003, *Modern Utilization Technology of Biomass Energy*, Chemistry Industry Press, Beijing, pp. 1–11.
[2] Sun, L., 1998, "The Properties of Biomass Materials Relation to Pyrolysis and Gasification in a Solid Bed Gasifier," Shandong Sci., **11**, pp. 1–7.
[3] Cai, Z., 1993, *Thermal Analysis*, Higher Education Press, Beijing, pp. 54–66.
[4] Michael, J. A., 1995, "Cellulose Pyrolysis Kinetics: The Current States of Knowledge," Ind. Eng. Chem. Res., **34**, pp. 703–717.
[5] Sharma, T., and Rajeswara Rao, T., 1999, "Kinetics of Pyrolysis of Rice Husk," Bioresour. Technol., **67**, pp. 53–59.
[6] Brigewater, A. V., 1992, "Innovative Technologies for Conversion of Biomass," Energy Fuels, **6**, pp. 113–120.
[7] Siddhartha, G. and Thomas, B. R., 1995, "An Atlas of Thermal Data for Biomass and Other Fuels, Tech. Report TP-433-7965, NREL, Golden, CO, pp. 3–20
[8] Sun, L., Xu, M., and Sun, R. F., 2003, "Secondary Decomposition of Pyrolysis Gas for Hydrogen-Rich Gas Production," *Pyrolysis and Gasification of Biomass and Waste*, CPL Press, UK, pp. 283–288.
[9] Blackadder, W. H., 1994, "High-Yield Hydrogen Production by Catalytic Gasification of Coal or Biomass," Int. J. Hydrogen Energy, **19**, pp. 413–419.

Reduction of Nitric Oxides and Soot by Premixed Fuel in Partial HCCI Engine

Dae Sik Kim
Mechanical Engineering
and Technology Research Institute,
Hanyang University,
17 Haengdang-Dong,
Sungdong-Gu, Seoul 133-791, Korea

Myung Yoon Kim
Graduate School of Hanyang University,
Hanyang University,
17 Haengdang-Dong,
Sungdong-Gu, Seoul 133-791, Korea

Chang Sik Lee[1]
Department of Mechanical Engineering,
Hanyang University,
17 Haengdang-Dong,
Sungdong-Gu, Seoul 133-791, Korea
e-mail: cslee@hanyang.ac.kr

In order to obtain the reduction effect of NO_x *and soot emission in a partial homogeneous charge compression ignition engine, premixed fuel was supplied with direct injection diesel fuel. Several additional systems such as a premixed fuel injection system, exhaust gas recirculation (EGR) system, supercharger, and air heating system were equipped in the intake manifold of conventional diesel engine. Premixed fuel with air was compressed and ignited by the directly injected diesel fuel in the combustion chamber at the end of compression stroke. The effect of premixed fuel on combustion and emission characteristics of HCCI diesel engine was investigated experimentally under various conditions of intake air temperature, pressure, and EGR rate. The results showed that in case of the use of gasoline as a premixed fuel, single stage ignition is found, but premixing the diesel fuel accompanies the cool flame prior to the combustion of the directly injected diesel fuel. For the gasoline premixed fuel, both* NO_x *and soot can be reduced by the increase of premixed ratio simultaneously. However, for the diesel premixed fuel, the increase of premixed ratio does not have a significant effect in reducing the soot emission.* [DOI: 10.1115/1.2132382]

1 Introduction

A homogeneous charge compression ignition (HCCI) engine can be considered as a hybrid between the spark ignition (SI) and compression ignition (CI) engine. As in SI engines the homogeneous mixture is created prior to the compression stroke using a low pressure injection system or by direct injection with very early injection timing. This charge is then compressed by a piston motion and auto-ignited as in CI engines. HCCI engines have substantially lower emissions of nitrogen oxides (NO_x) and particulate matters (PM) due to the ultra-lean and diluted combustion. The lean operation keeps the peak temperature low so that little NO_x is formed and the dilute fuel in air does not form soot [1,2]. Another advantage of HCCI engine is its high efficiency, which approaches the performance of a CI engine.

Despite many advantageous features of HCCI combustion, use of HCCI engines is not widespread because these engines still have some yet unsolved problems. The most difficult hurdle facing HCCI engines may be the control of the ignition. The ignition in HCCI engine is determined by the charge mixture composition and its temperature history [3–5]. Accordingly, over a wide range of speeds and loads it is rather difficult to keep the timing of the start of combustion near top dead center (TDC) in commercial engines. Several control methods have been proposed for providing the compensation required for changes in speed and load. One of the most promising methods for controlling the ignition timing is varying the amount of exhaust gas recirculation (EGR) [6,7]. Other proposed methods are variable compression ratio (VCR) [8] and variable valve actuation (VVA) [9,10]. However none of these methods are satisfactory over a wide range of engine speeds and loads.

Many studies have focused on the application of partial HCCI engine as a control mechanism for HCCI combustion and a solution for technical obstacles to implementing HCCI such as the ignition control and limited operating range. Partial HCCI combustion is at once the combination of HCCI and diesel combustion for the reduction of the harmful exhaust gas from diesel engines.

A partial HCCI engine has a fuel injector in the combustion chamber for ignition control like a direct injection (DI) diesel engine. However, the amount of fuel injected directly at the end of the compression stroke is much lower compared to the DI diesel engine and most of combustion is achieved by the premixed charge formed in advance in the cylinder like the HCCI engine. Accordingly, a partial homogeneous charge combustion engine can provide the HCCI engine with control of ignition and combustion even though there is some non-premixing combustion. In addition, the amount of NO_x and PM emissions from DI diesel engines has been reduced [11–18].

Yokota et al. [11] and Hasegawa et al. [12] realized the partial HCCI concept by early injecting the fuel directly into the cylinder at the early compression stroke. Then DI fuel is injected at the late compression stroke or early expansion stroke for controlling the combustion. This concept is regarded as the simplest partial HCCI engine since it does not need any additional injection system for the premixed fuel. Reductions in NO_x and PM emissions could be achieved in narrow operation conditions because the fuel was injected at low ambient pressure.

Suzuki et al. [13,14], Simescu et al. [15], and Lee et al. [16] used port fuel injectors in the intake manifold of a DI diesel engine to form a premixed air-fuel charge. Partial HCCI engines in this category guarantee more effective premixing of the fuel because more time is provided for the evaporation of premixed fuel by this method than by in-cylinder direct injection and this has been reported to have an excellent effect on NO_x and soot reduction.

Osses et al. [17] and Zaidi et al. [18] introduced a partial fumigation system and showed the influence of partial premixing fumigation of the intake air with diesel fuel on the exhaust emissions and the engine performance parameters in a DI diesel engine.

Despite these many experimental and numerical studies on the partial HCCI concept, the correlation between combustion characteristics and emissions of the partial HCCI engine are not still understood.

This research focuses on analyzing the effect of premixed fuel on the combustion and emission characteristics of diesel engine

[1]To whom correspondence should be addressed.

Contributed by the Internal Combustion Engine Division of ASME for publication in the JOURNAL OF ENGINEERING FOR GAS TURBINES AND POWER. Manuscript received December 20, 2004; final manuscript received September 26, 2005. Review conducted by D. Assanis.

Table 1 Engine specifications

Injection system	Direct injection
Number of cylinder	1
Compression ratio	19
Displacement	673 cc
Bore × stroke	95 mm × 95 mm
Combustion chamber	Toroidal
Injection nozzle (directly injected)	0.28 mm × 4 holes

Table 2 Test conditions

Engine speed		1200–1800 rpm
Engine load		0–30 Nm
Intake air temperature		20–80°C
EGR rate		0–20%
Boost pressure		0, 0.2 bar
Fuel	Premixed	Gasoline and diesel
	Directly injected	Diesel
Injection pressure	Premixed	55 bar
	Directly injected	220 bar
Injection timing	Premixed	TDC at compression stroke
	Directly injected	−22–0 deg ATDC
Premixed ratio		0—maximum operating regime

over wide range of equivalence ratio and premixed fuel ratio, and at various experimental conditions such as boost pressure, intake air temperature, and EGR rate. Also, a direct comparison of combustion and emission characteristics according to the kind of premixed fuel has not been reported in the previous studies. In this work, the gasoline and diesel fuels were used as the premixed fuel to analyze the effect of each premixed fuel on the combustion.

2 Experimental Apparatus and Procedure

2.1 Experimental Apparatus. The research engine was based on a single cylinder, direct-injection, and four-stroke cycle diesel engine with 673cc of piston displacement. This engine has the toroidal type combustion chamber with a cavity diameter of 50 mm. The fuel was directly injected through a nozzle with four 0.28-mm-diam holes. The specifications and dimensions of the test engine are listed in Table 1.

The experimental apparatus is composed of the combustion analyzer, the exhaust gas analyzer system, the electronic air-temperature control system, EGR system, and the premixed fuel injection system. Figure 1 shows the schematic diagram of the intake and exhaust system. A premixture chamber with a volume of 9,000 cm^3 and 20 cm diameter is installed in upstream of the intake port for more effective premixing of air and fuel. The boost pressure is generated by a supercharger controlled by a separate external power. And the cooled EGR system is applied in this work as it has been reported to be superior to the hot EGR in its emission characteristics and operational range [19].

2.2 Experimental Procedure. Injection system for premixed fuel is composed of the injector for direct injection spark ignition (DISI), separate fuel tank for gasoline and diesel premixed fuels, and the injection controller. The injection of premixed fuel with a high-pressure DISI injector is considered to be more useful for atomization of premixed fuel compared to a low-pressure port fuel injector [20].

The premixed ratio r_p is defined as the ratio of energy of premixed fuel Q_p to total energy Q_t. The premixed ratio can be obtained from

$$r_p = \frac{Q_p}{Q_t} = \frac{m_p h_{up}}{m_p h_{up} + m_d h_{ud}} \tag{1}$$

where, m_p is the mass of premixed fuel, m_d is the mass of directly injected fuel, h_u is the lower heating value, and subscripts p and d denote premixed and directly injected fuel, respectively.

The tests covered a wide range of engine load and various engine speeds and the intake air temperature was heated up to 80°C and the exhaust gas was recirculated up to 20% of volumetric intake air flow rate. The experimental conditions in this work are summarized in Table 2.

3 Results and Discussion

3.1 Premixed Gasoline Fuel. Figure 2 shows the effect of the premixed ratio of gasoline fuel on the combustion pressure and rate of heat release at an engine load of 20 Nm and intake air temperature of 20°C. As shown in this figure, the increase of premixed ratio prevents the sharp increase of heat release in the premixed combustion region of conventional diesel combustion of $r_p=0$. Also, a higher premixed ratio increased the second peak for

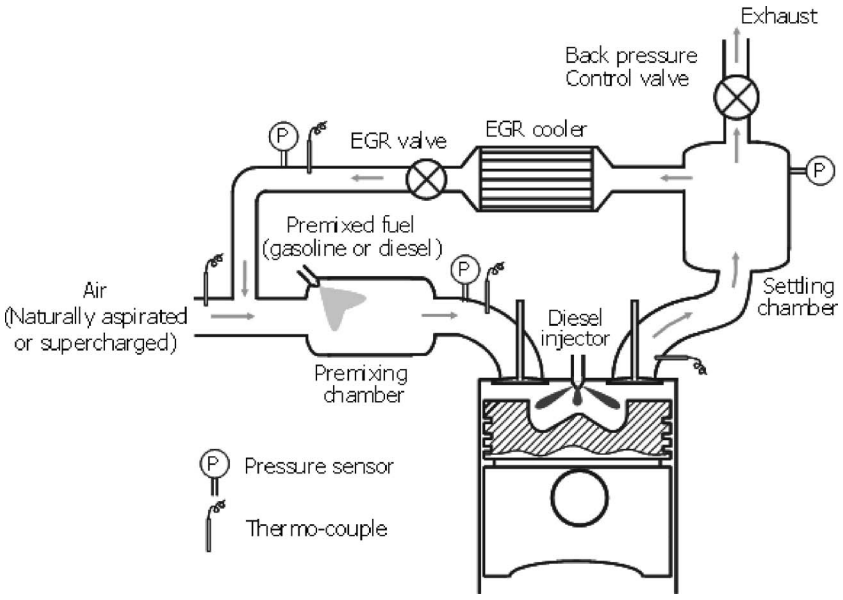

Fig. 1 Schematic diagram of experimental apparatus

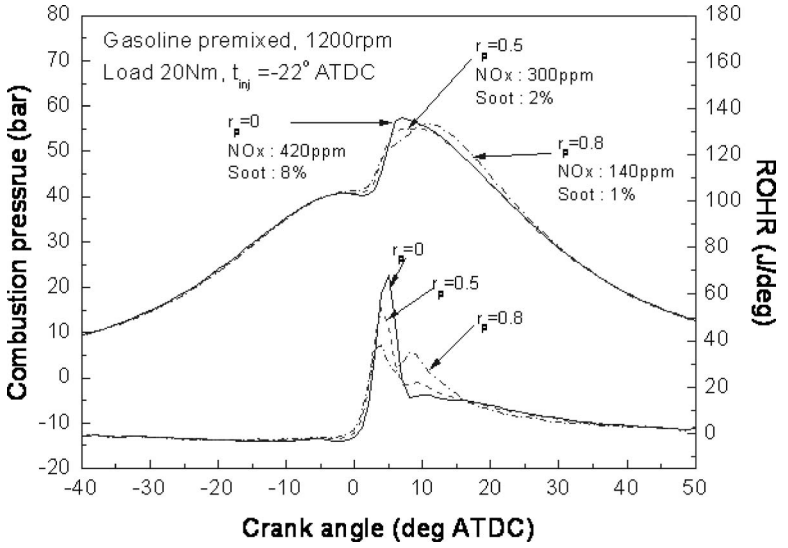

Fig. 2 Effect of premixed ratio (Gasoline premixed, 20 Nm load, 1200 rpm)

the rate of heat release that corresponds to the diffusive combustion region of direct injection only and the late combustion phase of the conventional diesel engine became somewhat reduced.

Also, the effects of the premixed ratio on the NO_x and soot emission for gasoline premixing are shown in this figure. For gasoline premixed fuel, the NO_x concentration of the 0.8 premixed ratio is reduced to one-third of conventional diesel combustion (r_p=0). In this work, the soot emissions are measured as the unit of % in the gray level. It is found that soot concentration decreased with increases in the premixed ratio owing to the air-fuel charge by homogeneous mixing of the premixed fuel and increase of the burned fraction by gasoline fuel which is a low-soot fuel.

Figure 3 presents the additional reduction of NO_x in partial HCCI engine by EGR. Like other emission data in relation with EGR [19], the increase of EGR rate reduced the NO_x concentration, but on the other hand, deteriorated soot emission. For EGR, the effect of premixed ratio on the NO_x and soot emissions has a different trend compared to Fig. 2 in which a linear reduction of NO_x and soot can be obtained with the increase of premixed ratio. Both NO_x and soot were decreased until a 0.25 premixed ratio and then remained almost constant regardless of the premixed ratio. These results might be due to the introduction of exhaust gas reducing the air flowrate which has an adverse effect on premixing the gasoline fuel with air. Hence EGR diminished the effect of NO_x and soot reduction by the premixed fuel.

In Fig. 4, injection timing of DI diesel fuel is shown to affect the combustion and emission characteristics of the partial HCCI engine. At each injection timing, the premixed ratio of gasoline fuel was controlled to 0.6 approximately. As shown in this figure, a dramatic reduction in NO_x was obtained by retarding the injection timing of direct injection diesel fuel. Simescu et al. [15]

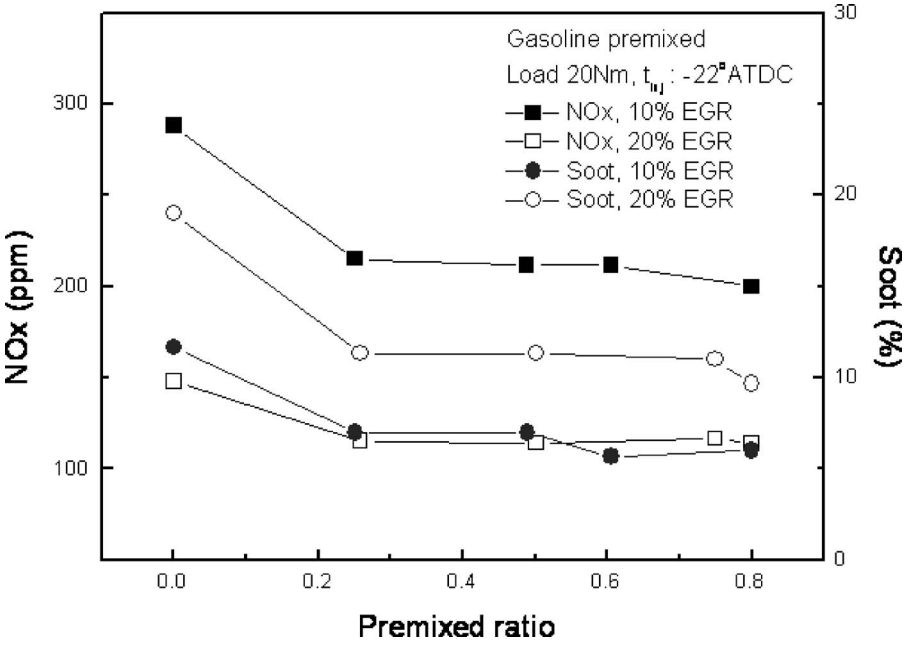

Fig. 3 Effect of EGR on NO_x and soot emissions (gasoline premixed, 20 Nm load, 1200 rpm)

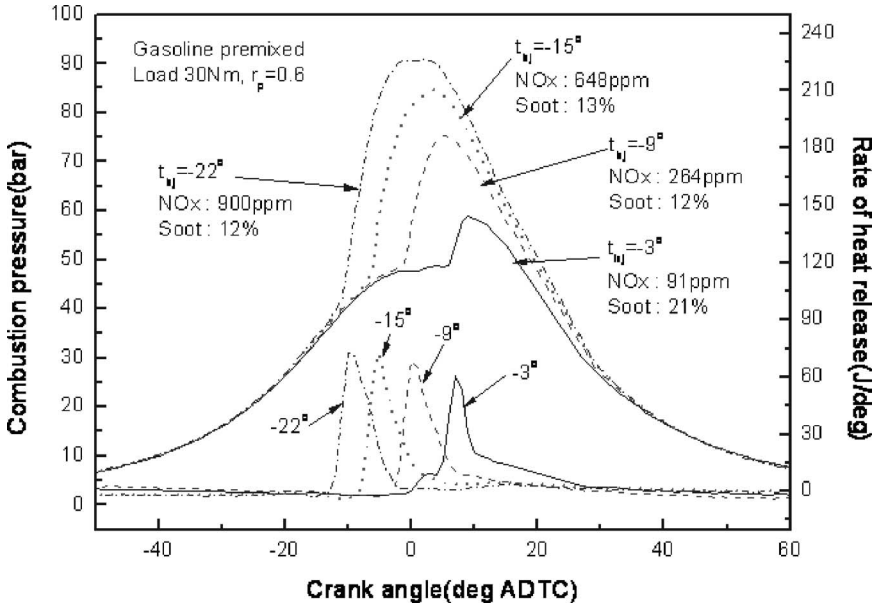

Fig. 4 Effect of main injection timing (gasoline premixed, 30 Nm load, 1500 rpm)

showed through their PCCI-DI (premixed charge compression ignition-direct injection) diesel combustion system with premixed diesel fuel that retarding the injection timing of DI diesel fuel was restricted by the increase of soot emission and specific fuel consumption although retarding the injection timing have a significant effect on NO_x reduction. In this work, the soot was found to be emitted almost constantly until an injection timing of BTDC 9 degree (t_{inj}=−9 deg). However in the case of t_{inj}=−3 deg, soot emission was greatly increased to 21%. The cause of this sudden increase can be inferred from the rate of heat release of this condition. Combustion for t_{inj}=−3 deg has been shifted toward the expansion stroke where the in-cylinder temperature is low enough to freeze the soot oxidation and thus to result in higher soot emissions.

Previous studies [11–18] have pointed out that the emissions of hydrocarbon (HC) and carbon monoxide (CO) are problems of partial HCCI systems. Figure 5 shows the unburned HC and CO emissions relative to the premixed ratio. In this study, the increased amount of the premixed fuel increases emissions of HC and CO as it did in pervious papers. Also, at a high premixed ratio, the maximum temperature of bulk gas in the combustion chamber becomes lower than that of low premixed ratio illustrated in the study by Zaidi et al. [18]. Accordingly, in order to increase bulk gas temperature, heating the intake air is effective in the reduction of HC emissions as shown in this figure.

Figure 6 shows the effect of boost pressure on the emission characteristics. This figure shows that both NO_x and soot emissions can be reduced over 20% by 0.2 bar of charged pressure although the increased charge pressure has often lead to an increase of NO_x in another study [14]. At comparatively high premixed ratio, the air-fuel ratio around the DI fuel jet became leaner than the stoichiometric value because the amount of DI fuel was

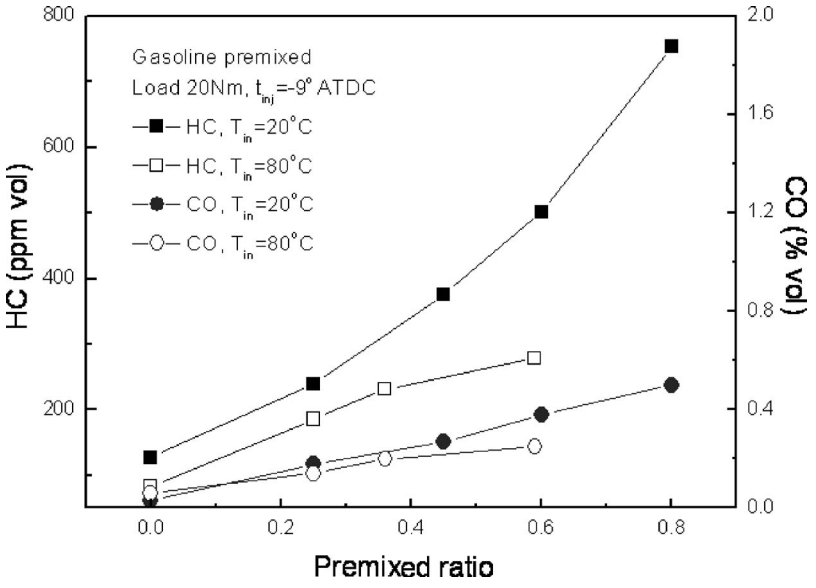

Fig. 5 Effect of intake air temperature on HC and CO emission (gasoline premixed, 20 Nm load, 1200 rpm)

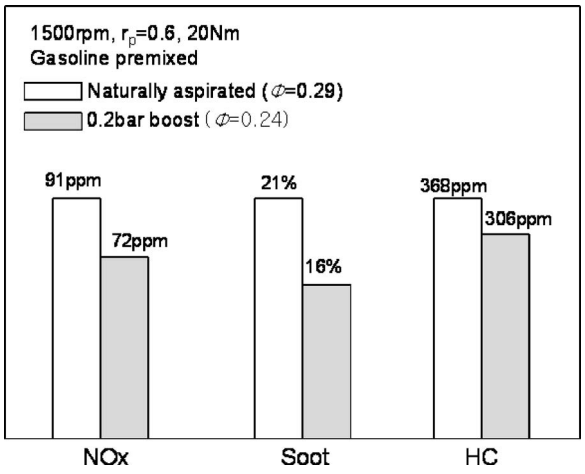

Fig. 6 Effect of boost pressure on emissions (gasoline premixed, T_{in}=20°C, 20 Nm load, r_p=0.6)

very small and at the same time the amount of air was increased by supercharging. This leaner air-fuel ratio results in the NO_x reduction for the boosted charge.

3.2 Premixed Diesel Fuel. Figure 7 shows the effect of the premixed diesel fuel ratio on the combustion pressure and the rate of heat release under the conditions of a 30 Nm load, 1200 rpm, and an intake air temperature of 20°C. For the diesel premixed fuel, a small peak of heat released by low temperature reactions is found at approximately BTDC 25 deg, unlike the case of gasoline premixed fuel in Fig. 2. The phenomenon of a cool flame appears at almost constant timing regardless of the premixed ratio. Simescu et al. [15] presented that the timing of cool flame in their systems depended on the in-cylinder temperature and engine load, not on the air-fuel ratio of premixed fuel as was found in the current study. According to the elevated cylinder gas temperature, this cool flame advanced the start of combustion of the premixed fuel and shortened the ignition delay of directly injected fuel. Thus the HCCI combustion of the premixed fuel and the premixed combustion of the directly injected fuel coincided with each other. Therefore, the start of main combustion for diesel premixing is influenced by the premixed ratio than is the start of combustion for gasoline premixing.

As mentioned in Fig. 5, heating the inlet charge is useful for reducing HC and CO emissions. Air-charge temperature is regarded as more influential factor in the combustion of partial HCCI for diesel premixed fuel than in gasoline premixed charge. Gray et al. [21] suggested that the heating temperature of intake air should be over 130°C for injection pressure of 4 bar with the gasoline port fuel injector used in their experiment. But, in this work, the injection pressure of premixed fuel was set to 55 bar higher than the injection pressure they used. This increased injection pressure would be more effective in atomization of premixed fuel droplets.

Lee et al. [16] and Simescu et al. [15] showed that the improved atomization characteristics of premixed fuel was very helpful for the homogeneous mixing of air and premixed fuel. Accordingly, even with an intake charge temperature lower than 130°C, heating is expected to affect the premixed fuel in this experiment.

The effect of the intake air temperature on combustion characteristics of diesel premixed fuel around the premixed ratio of 0.5 is shown in Fig. 8. In-cylinder temperature seems to considerably affect the timing of the cool flame as well as the main combustion as mentioned in the preceding paragraph. At T_{in}=80°C, the cool flame was advanced to BTDC 30 deg before the direct injection timing (BTDC 22 deg) and the HCCI combustion of the premixed fuel was also more advanced. The combustion pressure and temperature are increased by the advanced start of combustion. Further heating of intake charge is limited because the excessively advanced start of combustion leads to an increase of specific fuel consumption and NO_x emissions.

Figure 9 shows the effect of premixed ratio on the NO_x emission for diesel premixed fuel. This reduction trend of NO_x by the induction of premixed fuel in DI diesel engine is still maintained without heating like the gasoline premixed fuel. For T_{in}=80°C, the NO_x emission was reduced up to a certain critical value of the premixed ratio. Then the NO_x emission increases almost linearly with increases in the premixed ratio. This is caused by the elevated combustion temperature due to the excessively advanced start of combustion as shown in Fig. 8.

Figure 10 illustrates the relationship between the soot, HC, and

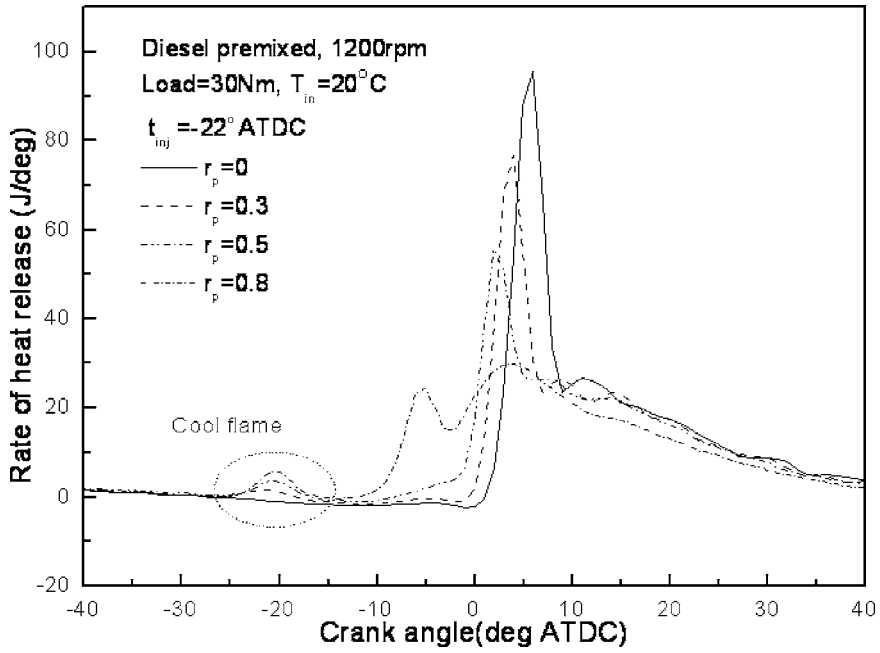

Fig. 7 Effect of premixed ratio (diesel premixed, 30 Nm load, 1200 rpm)

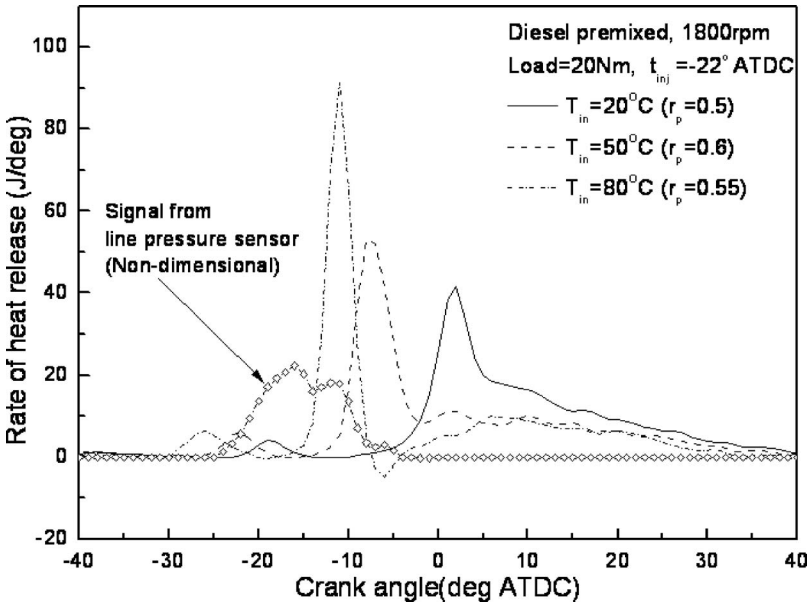

Fig. 8 Effect of intake air temperature on combustion (diesel premixed, 20 Nm load, 1800 rpm)

CO emissions and the premixed ratio for the diesel premixed fuel under various engine speeds. Contrary to NO_x emission, the increase of premixed ratio is not found to be effective in reducing the soot emission. Many previous works on the diesel fueled HCCI or partial HCCI systems revealed that achieving acceptable HCCI combustion with diesel fuel can be difficult because diesel fuel is not readily vaporized at low ambient temperatures, which can cause difficulties in creating a uniform mixture. Accordingly, in the fuel rich area, the possibility of soot formation becomes higher.

As a similar study, Christensen et al. [8] and Grey et al. [21] investigated diesel fueled HCCI with port fuel injection (PFI), similar to the method used in this work and presented that the increased soot emission was due to poor vaporization of the diesel fuel which creates an inhomogeneous mixture. Accordingly, the constant soot emissions for diesel premixing were thought to be due to combustion occurring in scattered diffusion flames around large droplets by poor vaporization.

As the view of a little different analysis, Simescu et al. [15] explained using their diesel fueled partial HCCI engines that the occurrence of HCCI combustion by the premixed fuels changes the in-cylinder temperature at the start of diffusion combustion by DI diesel fuel and may offset the trade-off between soot formation and soot oxidation during diffusion combustion. Finally, as the premixed ratio was increased, the amount of DI fuel was reduced and so was the in-cylinder turbulent kinetic energy production associated with the diesel spray, possible resulting in deteriorated mixing of the DI fuel.

Based on these previous analyses and the results of current work, it is believed that the soot emissions in this work may be

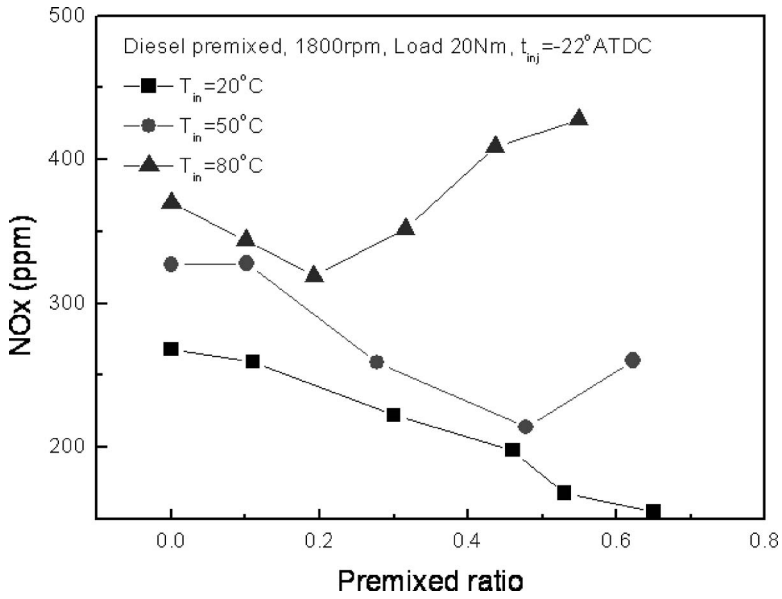

Fig. 9 Effect of premixed ratio and intake air temperature on NO_x emission (diesel premixed, 20 Nm load, 1800 rpm)

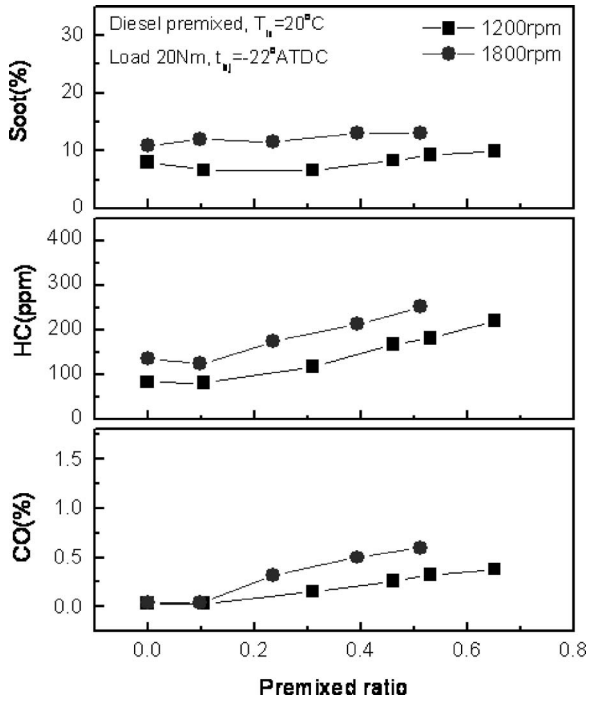

Fig. 10 Effect of premixed ratio and engine speed on soot, HC, and CO emissions (diesel premixed, 20 Nm load, T_{in}=20°C)

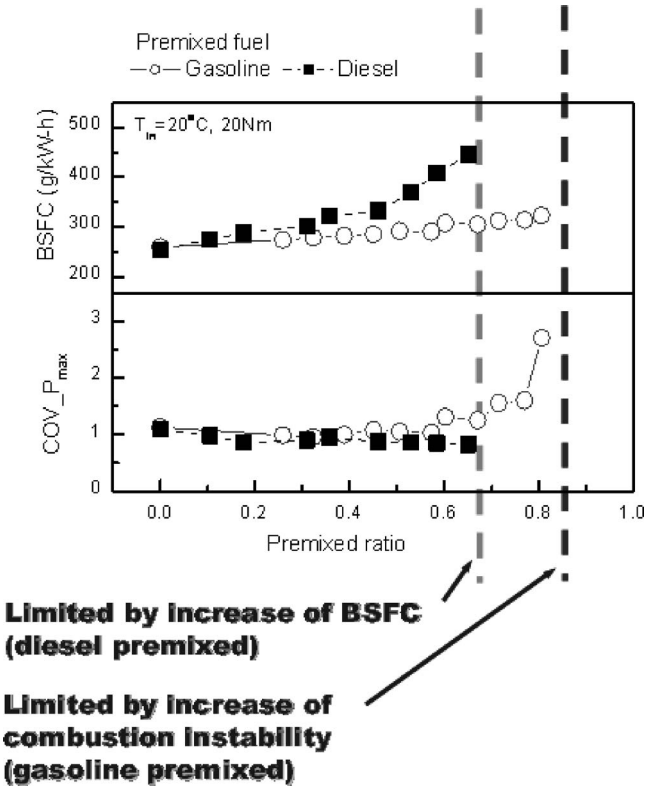

Fig. 12 Operational range for gasoline and diesel premixed fuels

caused by the compound influences of factors mentioned above.

Figure 11 shows the effect of premixed ratio and intake air temperature on the soot emissions at 1800 rpm. Heating the intake charge causes the increase of soot emission owing to the reduction of air flow rate. At higher inlet temperature (T_{in}=20°C), soot is shown to be minutely reduced up to a premixed ratio of 0.2. However, in the premixed ratio larger than 0.2, soot rises with the increase of premixed ratio again.

3.3 Comparison between Gasoline and Diesel Premixed Fuel. Figure 12 shows the limitation of operational region for each premixed fuel at 20 Nm engine load and 20°C intake air temperature. In case of diesel premixing, the brake specific fuel consumption (BSFC) is deteriorated by the increase of premixed ratio without heating, comparing to the gasoline premixed fuel. One of major reasons seems to be the wall wetting of diesel premixed fuel on intake port or cylinder because of its poor vaporization and premixing characteristics. For gasoline premixing, the operational range could be extended because it was found that the increase of BSFC was not as serious as in diesel premixing. How-

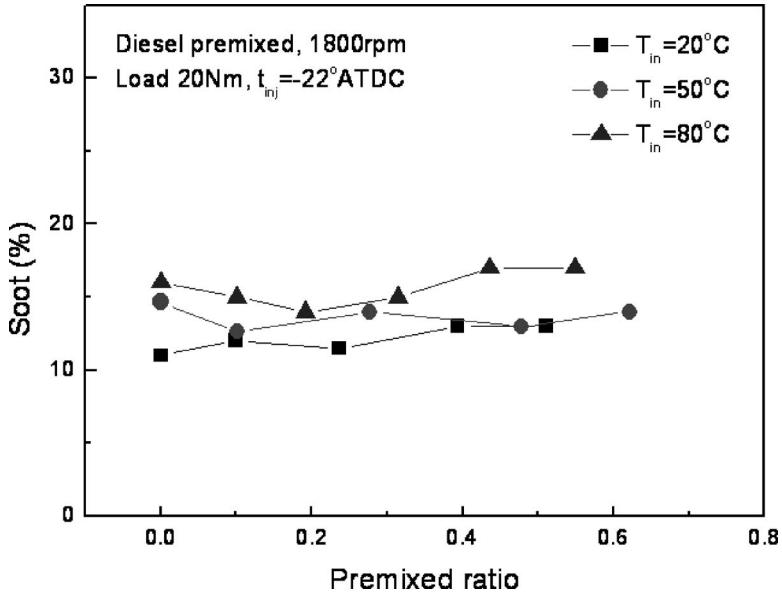

Fig. 11 Effect of premixed ratio and intake air temperature on soot emission (diesel premixed, 20 Nm load, 1800 rpm)

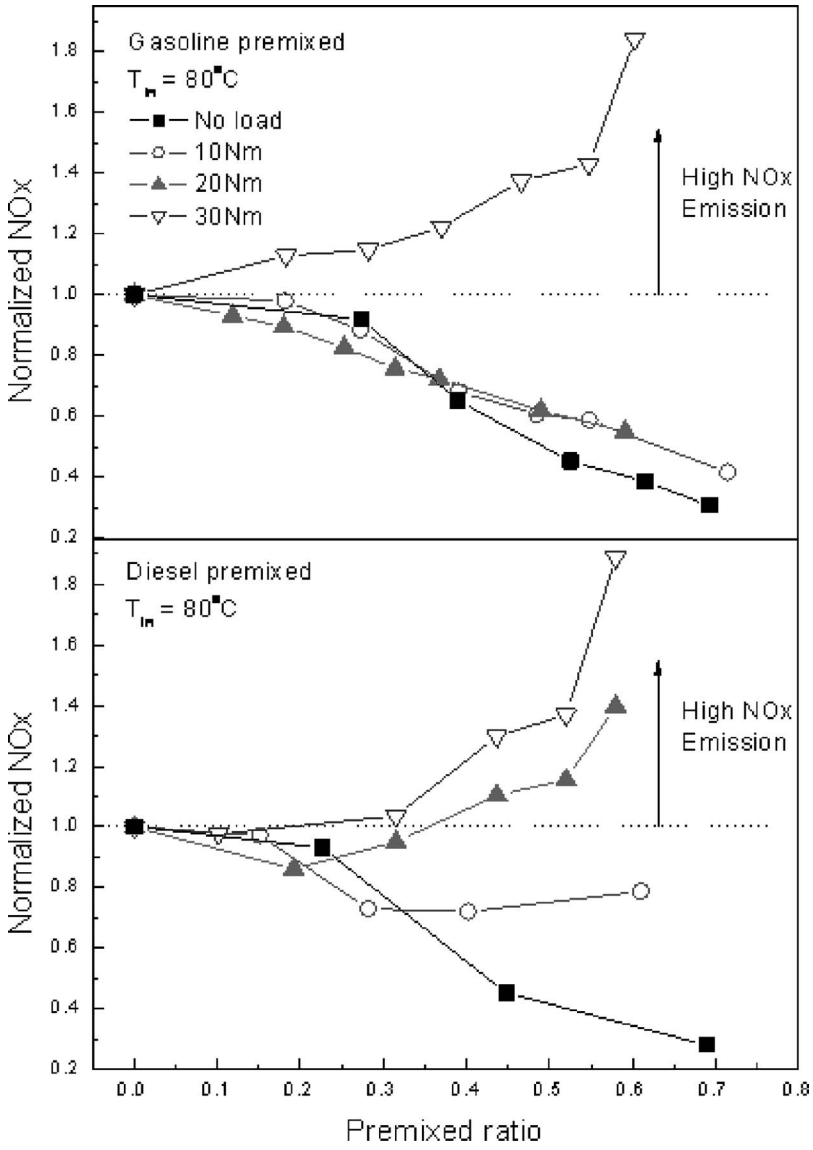

Fig. 13 Limitation of NO_x reduction for gasoline and diesel premixed fuels

ever, further increasing the amount of premixed fuel was limited by the extreme combustion instability. In this paper, cycle by cycle variation was estimated by the coefficient of variation (COV) of the peak combustion pressure for each cycle. As shown in lower part of Fig. 12, a considerable increase of COV is detected over 0.7 premixed ratio of gasoline fuel. At this condition, the injection amount of DI fuel is remarkably reduced to less than 30% of diesel injection only (r_p=0) with same engine load. This may be due to unstable ignition timing and variable combustion pressure as shown in this figure.

In Fig. 5, heating the intake charge was shown to be effective in reducing the HC and CO emissions at a high premixed ratio. However, the increase of NO_x emission at high intake air temperature worked as another factor to limit the operation region of this partial HCCI system. Figure 13 shows the NO_x emissions under various engine loads with each premixed fuel. For easier comparison of various conditions, normalized NO_x was introduced. This means the ratio of NO_x concentration in each premixed ratio to NO_x concentration emitted from conventional diesel engine. In both cases, NO_x emissions have increased at higher intake temperature (80°C) and higher engine load. This trend was found easier in case of diesel premixed fuel. Heating the intake air causes an increase of combustion temperature and results in a higher chemical reaction rate. Also, higher intake air temperature facilitates the vaporization of premixed fuels and can be more efficient in forming the homogeneous charge before ignition than lower temperature. Hence the fast combustion can be obtained in spite of a small amount of diesel fuel at high premixed ratio and cause the severe knocking in some cases. This knocking combustion results in the rise of combustion temperature and NO_x emission.

From these results, it can be concluded that the increase of premixed ratio is limited by the cycle variation and fuel consumption at lower intake air temperature while at higher intake air temperature a major limitation factor is the increase of NO_x.

4 Conclusions

The effects of the premixed ratio, initial air temperature, and EGR on the combustion of partial HCCI engine were investigated using gasoline and diesel premixed fuel. On the basis of the results obtained, the following conclusions can be drawn:

1. For the gasoline premixed fuel, both NO_x and soot can be reduced more than 70% of concentrations from the conven-

tional diesel engine except the high initial temperature condition. Also, introduction of EGR results in the additional reduction of NO_x in partial HCCI system.

2. Retardation in injection timing of DI fuel decreases NO_x emissions. However, the soot emission highly increases when the gasoline premixed fuel is ignited before the injection of DI fuel because of the excessive retardation of DI fuel injection.
3. For diesel premixing, the low temperature reactions called "cool flame" are accompanied before main combustion and its timing is dependent upon the cylinder temperature, not the premixed ratio. The start of main combustion is shown to be more influenced by the premixed ratio than the case of gasoline premixed fuel.
4. Effect of NO_x reduction under most conditions can be obtained by diesel premixed fuel. However, the increase of premixed ratio does not have a significant effect in reducing the soot emission.
5. Excessive increase of COV and BSFC are major limiting factors in operational range of partial HCCI combustion. Also, operational range with gasoline premixed fuel is found to be wider than in case of diesel premixed fuel.
6. Heating of intake air temperature is an effective method for preventing the increase of HC and CO emissions. However, initial charge temperature in high engine load is limited by the increase of NO_x emission caused by the increase of combustion temperature.

Acknowledgment

This study was supported by the CEFV (Center for Environmentally Friendly Vehicle) of Eco-STAR project from MOE (Ministry of Environment, Republic of Korea) and BK21 Program of Korea Research Foundation.

Nomenclature

Symbols

h_u = lower heating value (J/g)
P = pressure (MPa)
ppm = part per million by volume
Q = supplied heat (J)
r_p = premixed ratio
t = timing (deg)
T = temperature (K)
φ = equivalence ratio

Subscripts

in = inlet
inj = injection
p = premixed

Acronyms and Abbreviations

ATDC = after top dead center
BSFC = brake specific fuel consumption
BTDC = before top dead center
CI = compression ignition
CO = carbon monoxide
COV = coefficient of variation
DI = direct injection
EGR = exhaust gas recirculation
GDI = gasoline direct injection
HC = unburned hydrocarbons
HCCI = homogeneous charge compression ignition
NO_x = nitrogen oxides
PCCI-DI = premixed charge compression ignition-direct injection
PM = particulate matters
ROHR = rate of heat release
ROPR = rate of pressure rise
SI = spark ignition
TDC = top dead center
VCR = variable compression ratio
VVA = variable valve actuation

References

[1] Christensen, M., and Johansson, B., 1998, "Influence of Mixture Quality on Homogeneous Charge Compression Ignition," SAE paper 982454.
[2] Christensen, M., Johansson, B., and Einewall, P., 1997, "Homogeneous Charge Compression Ignition (HCCI) Using Isooctane, Ethanol and Natural Gas—A Comparison with Spark Ignition Operation," SAE paper 972874.
[3] Najt, P. M., and Foster, D. E., 1983, "Compression-Ignited Homogeneous Charge Combustion," SAE paper 830264.
[4] Ulfvik, J., and Johansson, B., 2003, "The Effect of Cooled EGR on Emissions and Performance of a Turbocharged HCCI Engine," SAE paper 2003-01-0743.
[5] Dec, J. E., 2002, "A Computational Study of the Effects of Low Fuel Loading and EGR on Heat Release Rates and Combustion Limits in HCCI Engines," SAE paper 2002-01-1309.
[6] Chen, R., and Milovanovic, N., 2002, "A Computational Study into the Effect of Exhaust Gas Recycling on Homogeneous Charge Compression Ignition Combustion in Internal Combustion Engines Fueled With Methane," Int. J. Therm. Sci., **41**, pp. 805–813.
[7] Peng, Z., Zhao, H., and Ladommatos, N., 2003, "Effects of Air/Fuel Ratios and EGR Rates on HCCI Combustion of *n*-Heptane, a Diesel Type Fuel," SAE paper 2003-01-0747.
[8] Christensen, M., Hultqvist, A., and Johansson, B., 1999, "Demonstrating the Multi-Fuel Capability of a Homogeneous Charge Compression Ignition Engine With Variable Compression Ratio," SAE paper 1999–01–3679.
[9] Law, D., Kemp, D., Allen, J., Kirkpatrick, G., and Copland, T., 2000, "Controlled Combustion in an IC-Engine With a Fully Variable Valve Train," SAE paper 2000-01-0251.
[10] Agrell, F., Angstrom, H. E., Eriksson, B., Wikander, J., and Linderyd, J., 2003, "Integrated Simulation and Engine Test of Closed Loop HCCI Control by Aid of Variable Valve Timings," SAE paper 2003–01–0748.
[11] Yokota, H., Kudo, Y., Nakajima, H., Kakegawa, T., and Suzuki, T., 1997, "A New Concept for Low Emission Diesel Combustion," SAE paper 970891.
[12] Hasegawa, R., and Yanagihara, H., 2003, "HCCI Combustion in DI Diesel Engine," SAE paper 2003-01-0745.
[13] Suzuki, H., Koike, N., Ishii, H., and Odaka, M., 1997, "Exhaust Purification of Diesel Engines by Homogeneous Charge With Compression Ignition Part 1: Experimental Investigation of Combustion and Exhaust Emission Behavior under Pre-mixed Homogeneous Charge Compression Ignition Method," SAE paper 970313.
[14] Suzuki, H., Koike, N., and Odaka, M., 1998, "Combustion Control Method of Homogeneous Charge Diesel Engines," SAE paper 980509.
[15] Simescu, S., Fiveland, S. B., and Dodge, L. G., 2003, "An Experimental Investigation of PCCI-DI Combustion and Emissions in a Heavy-Duty Diesel Engine," SAE paper 2003-01-0345.
[16] Kim, D. S., Kim, M. Y., and Lee, C. S., 2004, "Effect of Premixed Gasoline Fuel on the Combustion Characteristics of Compression Ignition Engine," Energy Fuels, **18**, pp. 1213–1219.
[17] Osses, M. A., Andrews, G. E., and Greenhough, J., 1998, "Diesel Fumigation Partial Premixing for Reduced Particulate Soot Fraction Emissions," SAE paper 980532.
[18] Zaidi, K., Andrews, G. E., and Greenhough, J., 2002, "Effect of Partial Fumigation of the Intake Air With Fuel on a DI Diesel Engine Emissions," SAE paper 2002-01-1156.
[19] Kakoi, Y., Tsutsui, Y., Ono, N., Umezawa, K., and Kondo, N., 1998, "Emission Reduction Technologies Applied to High-Speed Direct Injection Diesel Engine," SAE paper 980173.
[20] Lee, C. S., Lee, K. H., Chon, M. S., and Kim, D. S., 2001, "Spray Structure and Characteristics of High-Pressure Gasoline Injectors for Direct-Injection Engine Applications," Atomization Sprays, **11**, pp. 35–48.
[21] Gray III, A. W., and Ryan III, T. W., 1997, "Homogeneous Charge Compression Ignition (HCCI) of a Diesel Fuel," SAE paper 971676.

A Modular Code for Real Time Dynamic Simulation of Gas Turbines in Simulink

S. M. Camporeale

B. Fortunato

M. Mastrovito

Dipartimento di Ingegneria Meccanica e Gestionale-Sezione di Macchine ed Energetica, Politecnico di Bari, Via Re David 200, 70100 Bari, Italy

A high-fidelity real-time simulation code based on a lumped, nonlinear representation of gas turbine components is presented. The code is a general-purpose simulation software environment useful for setting up and testing control equipments. The mathematical model and the numerical procedure are specially developed in order to efficiently solve the set of algebraic and ordinary differential equations that describe the dynamic behavior of gas turbine engines. For high-fidelity purposes, the mathematical model takes into account the actual composition of the working gases and the variation of the specific heats with the temperature, including a stage-by-stage model of the air-cooled expansion. The paper presents the model and the adopted solver procedure. The code, developed in Matlab-Simulink using an object-oriented approach, is flexible and can be easily adapted to any kind of plant configuration. Simulation tests of the transients after load rejection have been carried out for a single-shaft heavy-duty gas turbine and a double-shaft aeroderivative industrial engine. Time plots of the main variables that describe the gas turbine dynamic behavior are shown and the results regarding the computational time per time step are discussed. [DOI: 10.1115/1.2132383]

1 Introduction

Real-time simulation can be used as a powerful tool in developing, testing and tuning control devices of gas turbines. A high-fidelity computer simulation can be used to substitute a real engine for many applications such as:

- Rapid-prototyping of control or diagnostic systems;
- Verifying the functionality of mechanic and electronic devices;
- Reducing costs and time for control equipment setup.

Moreover, it can be possible to simulate critical transients that should be avoided on the actual plant due to risk of damage. The block diagram in Fig. 1 shows how real-time software can be linked to control devices by means of suitable interfaces. The main features of the real-time simulation are:

- The simulation is carried out in part via software and in part through hardware devices; for such a reason, it is called "hardware-in-the-loop" simulation;
- The computer program outputs have to be generated at least as fast as the predicted physical phenomena impose [1].

Other applications of real-time gas turbine models include the use as onboard observer in aircraft engines or as engine simulator in flight simulators.

For real-time applications, in order to reduce the computational time, techniques based on the linearization of the model have been often adopted [2,3]. However, the computer programs based on linearized models should be used only in the neighborhood of the working point about which the linearization has been carried out.

Recently, real-time engine models based on nonlinear aerothermal relations have been proposed [4,5]. In these works, the set of nonlinear algebraic equations has been solved by means of the Newton-Raphson method, using the Broyden method for updating the Jacobian matrix. This solving procedure, already adopted by the authors in previous works [6], has shown some limits when applied to real-time simulation. The main problem is that the time required by the iterative procedure to complete all the calculations for a given time step cannot be a priori determined, as it is depending on the convergence rate that is variable with the working point.

The present work shows a novel approach for developing a real time simulation code characterized by the following key features:

- The mathematical model and the numerical scheme are specially developed in order to obtain, at the same time, high-fidelity and computational efficiency;
- The code is modular and can be applied to any kind of gas turbine layout.

The program has been developed using an object-oriented approach already adopted by the authors for gas turbine simulation [7]. The code has been developed in Matlab-Simulink® [8] that provides a graphical user interface for developing the program. The proposed mathematical model is also compatible with Real-Time-Workshop®, a software package available in Simulink®. Through this tool, it is possible to automatically generate a source code in C language from the Simulink model of the gas turbine. Such source code can be compiled in order to generate an executable program much faster than the original Simulink program. Moreover it is possible to produce programs capable of driving input/output interfaces for data acquisition and control. It is believed that the time needed for developing new applications or to modify existing ones by means of this procedure will be much shorter than the time required by traditional programming technique.

In the following sections the mathematical model and the solving procedure are described. Then, two gas turbines for power generation are simulated in order to verify the dynamic response and the numerical performance.

2 Gas Turbine Mathematical Model

The mathematical model adopted in this work can be defined as an "aero-thermal model" with a lumped representation of the gas turbine components [2]. This approach has been adopted by many

Contributed by the International Gas Turbine Institute (IGTI) of ASME for publication in the JOURNAL OF ENGINEERING FOR GAS TURBINES AND POWER. Manuscript received December 1, 2001; final manuscript received March 1, 2002. Assoc. Editor: E. Benvenuti. Paper presented at the International Gas Turbine and Aeroengine Congress and Exhibition, Amsterdam, The Netherlands, June 3–6, 2002, Paper No. 2002-GT-30039.

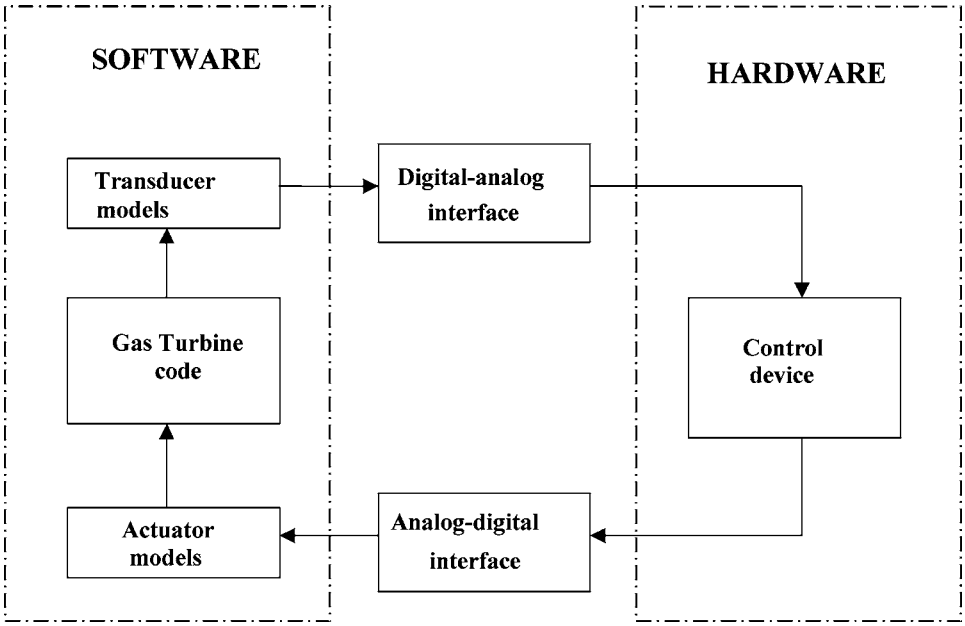

Fig. 1 Real-time simulation software interfaced to hardware control devices

authors in order to obtain a high-fidelity model for aero engines [9], gas turbines for power generation [6,7,10], and cogeneration [11].

Compressors and turbines are modeled as volume-less elements; a capacity (plenum) is introduced between these elements in order to take into account the unsteady mass balance. The burner is modeled as a pure energy accumulator. Other components, such as the cooled turbine module, the bleed air extraction module, the electric load module and so on, have been developed to complete the engine model.

For all the components, the algebraic equations are arranged in such a way that the output values can be obtained from the input variables without iterative calculations. In most cases, the input variables are referred to the entering flow and, similarly, the output variables are referred to the exiting flow. However, in order to determine the matching between compressor and first stage turbine nozzle or the enthalpy drop subdivision among the subsonic turbine stages, it is necessary to take into account the pressure in the downstream blocks. For this reason, in some cases, a variable referred to the inlet flow is evaluated as a function of the properties of the exiting flow.

2.1 Thermodynamic Fluid Properties. Due to the high turbine inlet temperature and fuel-to-air ratio that characterize modern gas turbines for power generation, the variation of the specific heats with temperature and composition should be included in the mathematical model, not only for design and steady-state off-design calculations, but also for the accurate simulations of the transients.

In the model adopted in the present work, the working gas is assumed to behave as a mixture of semi-perfect gases having the following properties:

The specific heats of the individual component gases are only function of temperature;

The pressure of the mixture is the sum of the partial pressures of the individual gas components.

Under such hypothesis the thermodynamic properties of the working fluids are functions of temperature and mixture composition. As a consequence of such an approach, the mass fraction of each chemical component is necessary. Unfortunately, in modern gas turbines with blade air cooling, the composition of the expanding gas is not constant due to the mixing of the hot gas with the cooling air. Consequently, it is necessary to evaluate the mixture composition in every turbine stage.

The number of variables required to determine the composition can be reduced recognizing that the combustion in gas turbine engines is always operated with a large excess of air and that the combustion process can be considered completed at the exit of the combustion chamber. Consequently, the mixtures can be considered in thermodynamic equilibrium and the unburned products are neglected. Therefore, for gas turbines without water or steam injection, it is possible to assume that the expanding gas is composed of only two components that are mixtures of constant composition themselves: stoichiometric combustion products and dilution air [6,7]. The composition of the stoichiometric combustion products can be evaluated before running the simulation, if the fuel composition is known. Therefore, the actual composition of the combustion gas can be identified once either the fraction of stoichiometric products or the fraction of dilution air is known.

In this work, the following variables have been chosen to identify the thermodynamic properties of the working fluids: the stagnation temperature, T, the stagnation pressure, p, the mass flow rate, g, and the fraction of stoichiometric products, x. The stoichiometric combustion product fraction x has been chosen instead of the fuel-to-air ratio f used in Ref. [7], since it seems to give a more understandable representation of the mixing process in the cooled turbine.

For gas turbine power plants with water or steam injection, the water fraction that is not a combustion product can be adopted as third component of the mixture.

The thermodynamic properties of the individual chemical species are evaluated against the temperature using a polynomial law. The gas constant, R, the specific heat, c_p, and the enthalpy, h, of the mixture can be obtained considering the actual gas composition.

2.2 The Compressor. During the transient, the compressor module, considered as a volume-less component, is assumed to behave as a quasi-steady component, so that a steady state compressor map is used. The map provides the mass air flow rate (g) and the isentropic efficiency ($\eta_{is,c}$) as a function of pressure ratio ($\beta_c = p_{out}/p_{in}$), corrected rotational speed ($n/\sqrt{\theta}$), and inlet guide vane position (IGV)

$$\frac{g\sqrt{\theta}}{\delta} = f_1(\beta_c, n/\sqrt{\theta}, \mathrm{IGV}), \quad \eta_{\mathrm{is},c} = f_2(\beta_c, n/\sqrt{\theta}, \mathrm{IGV}) \tag{1}$$

Such functions are numerically evaluated through interpolation on digitized maps. Section 3 will describe the adopted interpolation procedure. The air temperature at the compressor exit is given by

$$T_{\mathrm{out}} = T_{\mathrm{in}} \cdot \left[1 + \frac{1}{\eta_{\mathrm{is},c}} (\beta_c^{(k-1)/k} - 1) \right] \tag{2}$$

where the specific heat ratio k is evaluated at the temperature T_m that is the arithmetic average between the inlet (T_{in}) and the outlet (T_{out}) temperature. In order to avoid an iterative procedure for calculating T_{out}, the specific heat ratio k is evaluated using the value of the temperature T_{out} determined at the previous time step. This assumption does not introduce an appreciable error because the temperature T_{out} has low influence on specific heat ratio; moreover, the error by the suggested procedure can be considered negligible because of the very small time step used in real time simulation. The compressor mechanical power is given by

$$P_c = g(h_{\mathrm{out}} - h_{\mathrm{in}}) \tag{3}$$

where the enthalpy values h_{out} and h_{in} are evaluated at the temperatures T_{out} and T_{in}, respectively.

2.3 Plenum. Since turbomachinery, compressor and turbine units are considered as volume-less elements, the unsteady mass balance is modeled through an adiabatic capacity (plenum). A plenum is placed at the compressor outlet in order to take into account the unsteady mass balance within compressor ducts, compressor discharge and combustion chamber. Other plena are placed between the turbine stages.

The flow speed is assumed to be negligible inside the plenum, while temperature and pressure are supposed to vary with a polytropic law with exponent m. Applying the mass conservation law, results in

$$\frac{V_p}{mRT_{\mathrm{out}}} \cdot \frac{dp_{\mathrm{out}}}{dt} = g_{\mathrm{in}} - g_{\mathrm{out}} \tag{4}$$

where V_p is the volume of the plenum. The polytropic coefficient m can be approximated by the specific heat ratio k. The energy accumulation inside the plenum is neglected, therefore

$$T_{\mathrm{out}} = T_{\mathrm{in}} \tag{5}$$

Moreover, since neither pressure losses nor momentum effects are considered in the plenum,

$$p_{\mathrm{in}} = p_{\mathrm{out}} \tag{6}$$

This value is needed to provide the pressure datum to the component placed upstream of the compressor plenum. The volume V_p influences the pressure p_{out} variation due to the amount of the mass accumulated in the plenum. Using the gas state equation, Eq. (4) can be rearranged in the form

$$\tau_p \frac{dp_{\mathrm{out}}}{p_{\mathrm{out}} dt} = \frac{g_{\mathrm{in}}}{g_{\mathrm{out}}} - 1 \tag{7}$$

where the characteristic time τ_p is given by

$$\tau_p = \frac{M_p}{m g_{\mathrm{out}}} \tag{8}$$

and M_p represents the mass inside the plenum.

2.4 Splitter. The compressed air extracted for turbine cooling is evaluated in a module called splitter. According to experimental data available about gas turbine cooling systems [12], the air mass flow, is evaluated from

$$\frac{g_{\mathrm{cool}}\sqrt{T_{\mathrm{in}}}}{p_{\mathrm{in}}} = K\sqrt{1 - \frac{p'_{\mathrm{out}}}{p_{\mathrm{in}}}} \tag{9}$$

where K represents the discharge coefficient, p_{in} and T_{in} are the pressure and the temperature at the bleed point, respectively, and p'_{out} is the static pressure at the exit of the cooling circuit. The K coefficient is estimated on the basis of the cooling air mass flow rate, needed for blade cooling at the gas turbine design point. For simplicity, in this work, the value of p'_{out} is approximated by the value of the pressure at the stage exit.

The main flow mass flow rate exiting from the splitter is evaluated by subtracting the cooling flow rate from the entering mass flow.

2.5 Burner. The burner has been represented as a pure energy accumulator, neglecting the mass balance that is instead attributed to the upstream plenum block. The inside temperature and pressure have been assumed homogeneous and equal to the combustor respective outlet values.

The equation that describes the burner dynamics is obtained from the unsteady energy conservation

$$\frac{d(M_{\mathrm{cc}} u_{\mathrm{cc}})}{dt} = g_{\mathrm{in}} h_{\mathrm{in}} + g_b(h_b + \eta_b \mathrm{LHV}) - g_{\mathrm{out}} h_{\mathrm{out}} \tag{10}$$

where M_{cc} and u_{cc} are the mass inside the burner and the internal specific energy, respectively; LHV is the lower heating value of the fuel. Neglecting the variations of the mass and of the specific heat functions, Eq. (10) can be rearranged thus obtaining

$$\tau_{\mathrm{cc}} \frac{dT_{\mathrm{out}}}{dt} = \frac{[g_{\mathrm{in}} h_{\mathrm{in}} + g_b(h_b + \eta_b \mathrm{LHV}) - g_{\mathrm{out}} h_{\mathrm{out}}]}{g_{\mathrm{out}} c_{p_{\mathrm{out}}}} \tag{11}$$

where the time constant τ_{cc} can be evaluated from

$$\tau_{\mathrm{cc}} = \frac{M_{\mathrm{cc}}}{K g_{\mathrm{out}}} \tag{12}$$

A time delay $\varepsilon_{\mathrm{CR}}$ has been introduced to take into account of the flame delay that exists from the fuel injection to the heat release.

Under the hypothesis of negligible variation of the mass present in the combustor, the continuity equation gives

$$g_{\mathrm{out}} = g_{\mathrm{in}} + g_b \tag{13}$$

This equation is rearranged in order to obtain the feedback signal going from the turbine first stage to the compressor plenum

$$g_{\mathrm{in}} = g_{\mathrm{out}} - g_b \tag{14}$$

The pressure drop across the burner has been evaluated from

$$p_{\mathrm{out}} = y_{\mathrm{cc}} p_{\mathrm{in}} \tag{15}$$

where the loss coefficient, y_{cc}, depending on the square mass flow rate is evaluated by means of the value of the mass flow at the previous time step.

2.6 Multistage Turbine With Blade Cooling. In modern gas turbines, either "heavy-duty" or "aero-derivative," the gas expansion is distributed on more stages, characterized by blade cooling systems. Under the hypothesis that the turbine module behavior can be considered quasi-steady, the turbine characteristic curves can be used in order to estimate the mass flow parameter Γ as a function of the expansion ratio $\beta_t = p_{\mathrm{out}}/p_{\mathrm{in}}$ and the turbine corrected speed. Knowing the value of mass flow parameter Γ, it is possible to evaluate the mass flow rate across turbine as a function of temperature and pressure at the turbine inlet

$$g_{\mathrm{in}} = \Gamma \frac{p_{\mathrm{in}}}{\sqrt{T_{\mathrm{in}}}} \tag{16}$$

In order to subdivide the enthalpy drop among more stages, the mass flow parameter has been evaluated for each stage using the

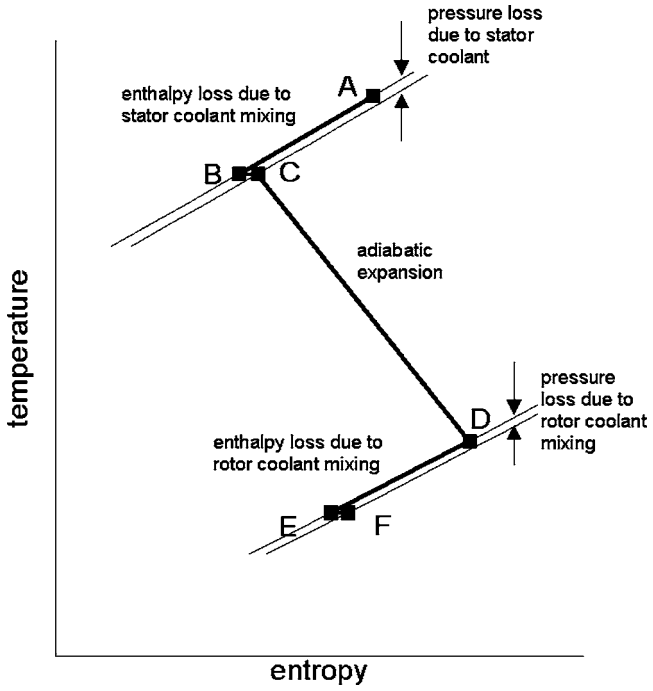

Fig. 2 Expansion model adopted for the cooled stages

method described in Ref. [6] and in Ref. [13]. A plenum is placed between two consecutive stages in order to model the unsteady mass balance.

For each stage the cooled turbine expansion has been modeled according to the scheme proposed by El Mastri [14] and already adopted both for steady-state off-design simulation [13,15] and for dynamic simulation [6]. A graphical representation of the cooled expansion is provided in Fig. 2. The model can be represented using three distinguishable phases as follows:

- the mixing between main flow and cooling air of the stator blades (from point *A* to point *C* in Fig. 2);
- the expansion of such mixed gas flow (from point *C* to point *D*);
- the mixing between the new main flow and rotor cooling air (from *D* to *F*).

These three phases have been represented by three components; in particular there are two mixing unit (one for the stator cooling air and the other for the rotor cooling air), and a component representing the adiabatic gas expansion. These two components are called "mixer" and "adiabatic turbine," respectively. Figure 3 shows the Simulink representation of these blocks as they have been implemented in the cooled stage block. The mathematical models are described below.

2.6.1 Mixer. The mixer block is used to evaluate the enthalpy and the pressure drop due to the mixing of the main gas flow with the cooling air. The mass flow at the mixer outlet is given by the continuity equation

$$g_{\text{out}} = g_{\text{in}} + g_{\text{cool}} \tag{17}$$

The composition of the gas exiting the mixer, considering that the stoichiometric product fraction in the air is nil, is obtained from the relation

$$x_{\text{out}} = g_{\text{in}} x_{\text{in}} / g_{\text{out}} \tag{18}$$

The outlet gas enthalpy h_{out} after the mixing process is evaluated from the enthalpy balance

$$h_{\text{out}} = \frac{[g_{\text{in}} h_{\text{in}} + g_{\text{cool}} h_{\text{cool}}]}{g_{\text{out}}} \tag{19}$$

The stagnation temperature T_{out} is obtained as a function of the outlet enthalpy h_{out} and of the dilution air x_{out}.

The pressure drop in the mixer is evaluated from the momentum loss equation

$$p_{\text{out}} = p_{\text{in}} \cdot \left[1 - \frac{g_{\text{cool}}}{g_{\text{in}}} \cdot (1 - Y) \cdot K \cdot \text{Ma}^2 \right] \tag{20}$$

where Y is the momentum loss coefficient depending on blade geometry, and Ma is the Mach number of the gas. For the stator row, the Mach number is evaluated from absolute velocity in the throat section while in the rotor row, the Mach number is evaluated from the relative velocity in the rotor throat section. For simplicity, it has been assumed that the Mach numbers remain constant during the simulations.

2.6.2 Adiabatic Expansion. In order to evaluate the final temperature of the adiabatic expansion, a suitable expression for the isentropic efficiency η_t as a function of the expansion ratio β_t and of the corrected rotational speed is needed. The adopted expression provides a law for isentropic efficiency variation as a function of the efficiency of both stator and rotor rows. Such row efficiencies are evaluated in relation to the main flow angle of attack.

The temperature at the end of expansion is given by the relationship

$$T_{\text{out}} = T_{\text{in}} [1 - \eta_t (1 - \beta_t^{(k-1)/k})] \tag{21}$$

where the specific heat ratio k is evaluated, for the actual gas composition, at the mean temperature T_m between T_{in} and T_{out}

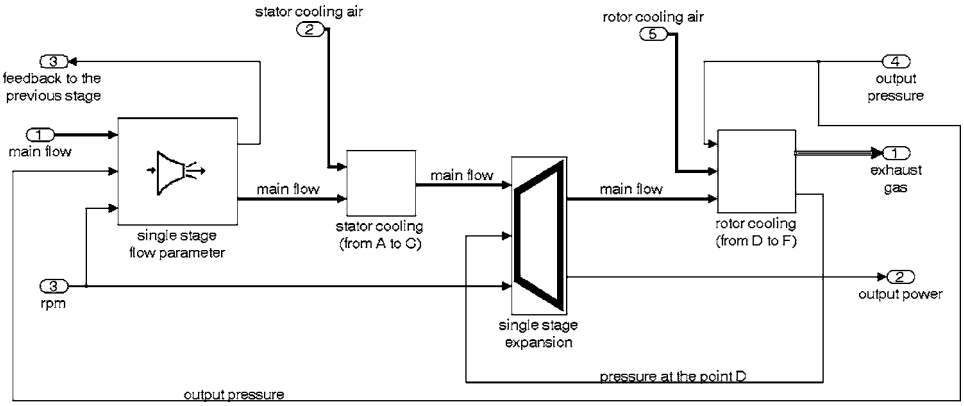

Fig. 3 Simulink scheme of a cooled turbine stage

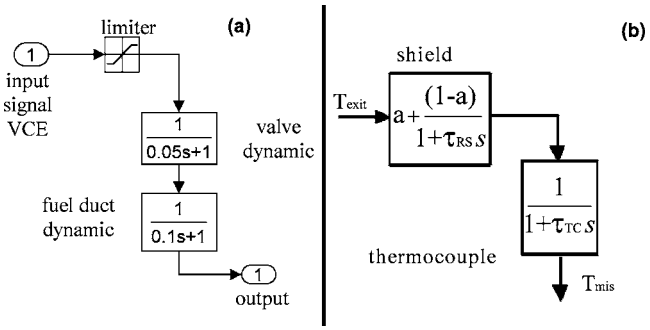

Fig. 4 Transfer functions for transducers and actuators: (*a*) fuel system actuator, (*b*) exhaust temperature transducer

using, for this last temperature, the value obtained at the previous time step.

The power P_t produced by the expanding gas is given by

$$P_t = g_{\text{in}}(h_{\text{in}} - h_{\text{out}}) \tag{22}$$

where the enthalpy values h_{in} and h_{out} are evaluated from the temperatures T_{in} and T_{out}, respectively.

2.7 Shaft Dynamic. The angular acceleration of the shaft joining compressor, turbine and, eventually, applied load is given by the angular momentum equilibrium, depending on moment of inertia J which includes the inertia effects of the shaft and of the other connected devices. Thus

$$\frac{d\omega}{dt} = \frac{1}{J\omega}(P_t - P_c - P_f - P_E) \tag{23}$$

where P_t represents the internal mechanical power of the turbine, P_c is the internal mechanical power required by the compressor, P_E is the mechanical power required by the electrical load and, finally, P_f represents a sum of power losses due to mechanical friction, friction on the rotor disks, and power to drive auxiliary equipments.

For gas turbines with two or more shafts, Eq. (23) is to be applied to each shaft. Arranging Eq. (23) in nondimensional form, the characteristic time constant τ_I is obtained

$$\tau_I \frac{dn}{dt} = \frac{n_{\text{des}}^2}{P_{u,\text{des}} n}(P_t - P_c - P_f - P_E) \tag{24}$$

where τ_I is given by

$$\tau_I = \frac{J \cdot \omega_{\text{des}}^2}{P_{u,\text{des}}} \tag{25}$$

and ω_{des} and $P_{u,\text{des}}$ are the shaft angular speed and the turbine output power at the design point, respectively. The power losses considered in the term P_f are estimated by a loss-factor that is a function of the angular speed. This formulation has been preferred to that involving the mechanical efficiencies, in order to gain numerical accuracy especially in idle condition or during the gas turbine startup when the output power is negative or zero.

2.8 Dynamic Behavior of Actuators and Transducers. As shown in Fig. 1, the real time simulation software includes the models for mechanical actuators such as the fuel system, the actuator moving the inlet guide vanes of the compressor or of the turbine, the actuator of the bleed valves an so on.

The fuel system scheme proposed by Rowen [16], and already used by other authors [17,18] has been adopted. The scheme is presented in Fig. 4(*a*) in terms of Laplace transfer functions. Two first order transfer functions act on the input signal: the first transfer function takes into account the fuel valve positioning system dynamic; the second transfer function represents the fuel flow dynamic in the fuel admission duct.

The temperature transducer has also a great importance to achieve good results since the control device makes use of temperature as an input. To obtain a good agreement with the physical system, the temperature signal is related to the stack temperature through the shielded thermocouple model described in Fig. 4(*b*), following a scheme already adopted by many authors [16–18].

3 Solving Method

The dynamic simulation model of the gas turbine consists of a mixed set of ordinary differential and nonlinear algebraic equations. In order to obtain a real time execution of the code, the integration of this set of equations, at each time step, must be completed by the computer within a time shorter than the assumed time step.

A fixed time step of 1 ms could be a reasonable value for gas turbine applications in order to use the simulator in connection with control devices.

As far as concerns the solution of the differential equations, the small time step addresses towards an explicit solver instead of an implicit scheme that requires an uncertain number of iterations until the convergence has been reached. The choice of an explicit solver requires that physical phenomena with characteristic time smaller than the time step cannot be considered in order to avoid numerical instabilities. For such a reason, for example, the insertion of small plena should be carefully considered.

Dealing with the solution of the algebraic equations, the constraints about iterative methods make it impossible to use a solution scheme like the Newton-Raphson one. As has been shown in the previous section, the algebraic equations are arranged in order to explicitly generate the output values. It will be shown that if the algebraic equations are properly ordered, it is possible to obtain the solution by forward substitution. Supposing that the system consists of N ordinary differential equations and M algebraic equations, the equations are arranged and sorted as follows

$$\begin{aligned} \frac{dy_i}{dt} &= f_i(y_1, \ldots, y_{N+M}) \quad i = 1, N \\ y_i &= g_i(y_1, \ldots, y_{i-1}) \quad i = N+1, N+M \end{aligned} \tag{26}$$

At each time step, the differential equations are integrated by means of an explicit scheme, thus obtaining the new values of the first N variables. Then, through the scheme in Eq. (26), the remaining M variables are sequentially evaluated by forward substitution. In other words, any variable y_i is calculated as an explicit function of the variables $y_1, \ldots, y_{i-1}$ that are already known.

Most of the algebraic equations of the proposed mathematical model result to be properly ordered without numerical manipulation, if they are ordered in accordance with the stream direction in the components that compose the gas turbine model. The Matlab-Simulink environment offers the possibility of easily ordering the equations by means of a graphical user interface [7].

To illustrate how the solution proceeds, a simple single-shaft gas turbine is considered. The model, shown in Fig. 5, consists of the following components: compressor, plenum, burner, adiabatic turbine, and a simple proportional-integral (PI) speed governor. The aim is to show how it is possible to deal with the matching between the compressor and the turbine without using an iterative solver. The arrows in the Simulink scheme represent the transfer of the data values from one block to the other. Bold arrows represent the transfer of multiple data referred to the variables that identify the fluid properties: the stagnation temperature, T, the stagnation pressure, p, the mass flow rate, g, and the fraction of dilution air, x. Often, the transfer of the data has the same direction as the gas stream but, in some cases, since the downstream block interacts with the upstream one, one datum may be transferred in the opposite direction to the stream one. Examples of

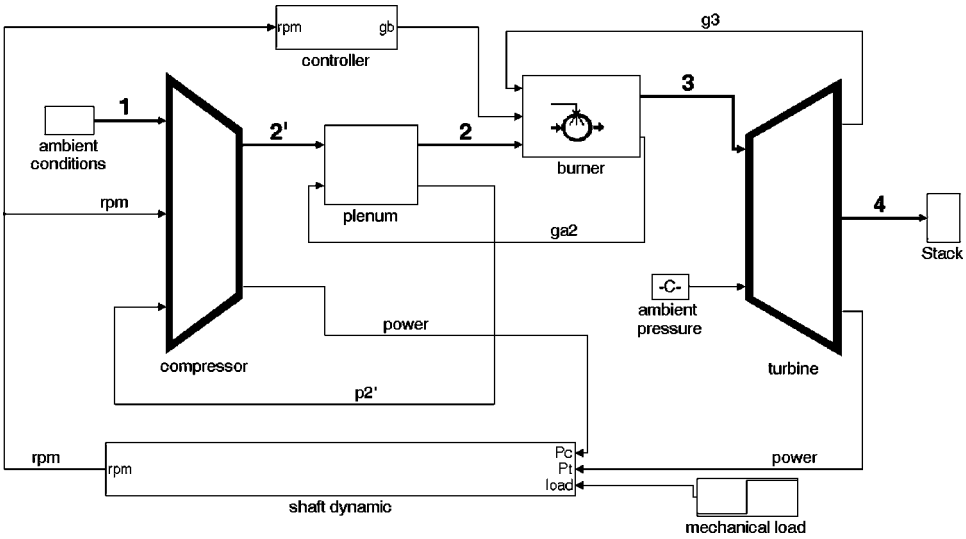

Fig. 5 Simplified scheme of a single-shaft gas turbine

these feedbacks are the plenum discharge pressure p_2, the mass flow rate entering the turbine g_3, the mass flow rate entering the combustion chamber g_2.

The flow chart given in Fig. 6 shows how the sequential solution proceeds. At each time step, the ordinary differential equations are integrated. For sake of simplicity, in this example, the Euler scheme is considered. Specifically, the pressure p_2 at the compressor discharge, which is equal to the pressure $p_{2'}$ at the plenum exit, is obtained from the unsteady mass balance of the plenum. The temperature T_3 at the combustor outlet is obtained from the unsteady energy balance of the combustor. The rotational speed, n, is obtained from the shaft dynamics. The fuel rate, g_b, is determined from the speed governor equations. Once these variables are known, it is possible to evaluate all the other unknown quantities by substitution in the algebraic equations, as is shown by the flow chart. It can be observed that the working point of the compressor is determined by the values of the rotational speed, n, and the pressure ratio $\beta c = p_2/p_1$. The mass flow rate entering the turbine, g_3, is determined, from the known mass flow parameter, the temperature T_3 and the pressure p_3.

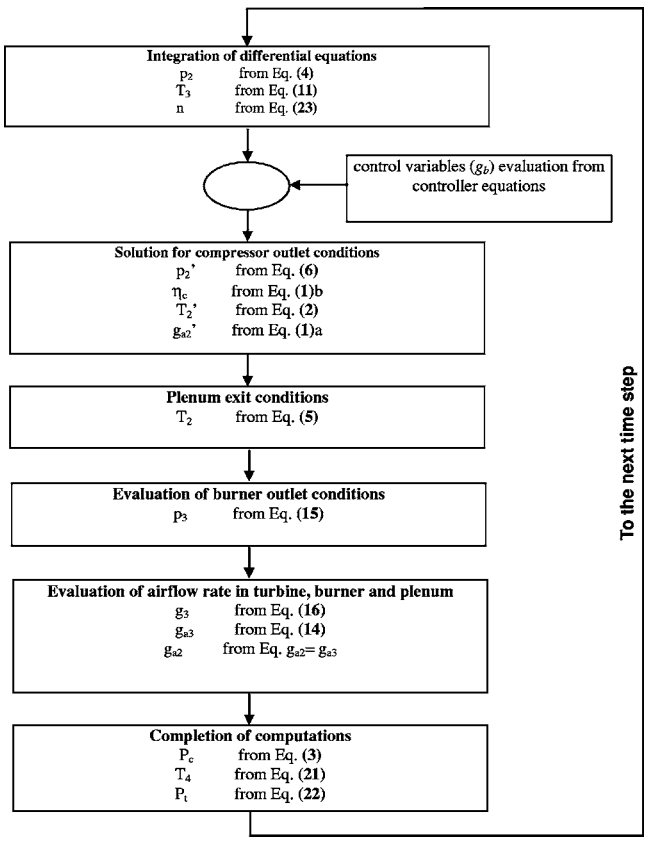

Fig. 6 Sequential solving technique for the gas turbine model in Fig. 5

In turbines with more stages, for all the stages following the first one, the inlet pressure is determined from Eq. (16), instead of the mass flow rate, since the pressure is necessary to evaluate the pressure ratio in the upstream stage.

The flow chart in Fig. 6 shows that the solution has been reached without the iterative procedure that is generally required for the solution of the nonlinear equation system. It should be observed that this result is made possible by means of the approximations that are applicable to real-time gas turbine dynamic models in consideration of the very short time-step. Specifically, as has been shown in the mathematical model, the specific heats are determined on the basis of temperature and composition evaluated at the previous time step. To this purpose the "Memory Block," available in Simulink, has been used. The Simulink environment is able to check if iterative calculations are needed to determine the value of one or more variables: this procedure is useful also to verify if the assembly of the components or a new component is compatible with real-time operations.

The proposed formulation is also compatible with the Real-Time-Workshop® toolbox, that is a toolbox available in Matlab-Simulink environment able to automatically generate a source code in C language from the Simulink scheme. This feature can be useful for developing a code for hardware-in-the-loop applications.

Finally, it is useful to describe the method adopted for loading the data of the compressor map in the computer code. This method has been developed in order to make as short as possible the computation time needed for interpolation and to make this time independent from the number of points of the experimental map. This technique, similar to the so-called "beta-lines" method [1], is applied to a map in terms of nondimensional groups in order to take into account the effects of ambient air conditions.

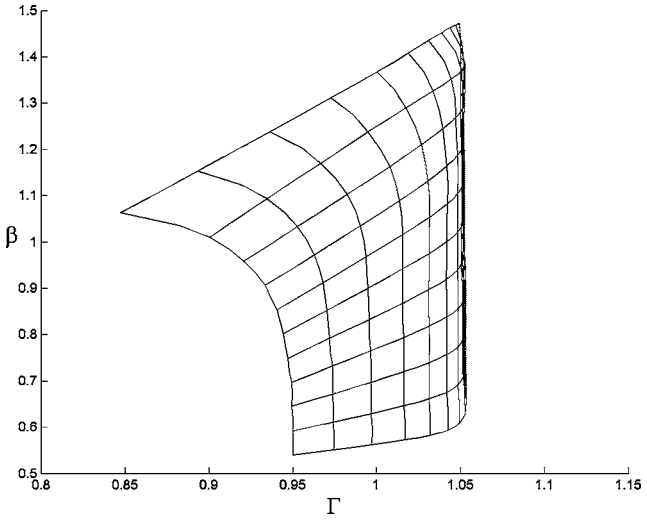

Fig. 7 Computational grid for the compressor map interpolation

This technique is based upon two distinct phases: the first phase consists of off-line calculation on the digitized map and it is done only once; the second phase is executed at every time step. The preliminary analysis strives for obtaining efficiency in the data extraction and consists of transforming the domain of the physical variables, in which the map is defined, into a Cartesian uniform domain. The transformation adopted in this work associates any point (β_c, n) of the map with a point (ξ, η) in the transformed domain by means of the relations

$$\eta = \frac{n - n_{\min}}{n_{\max} - n_{\min}} \qquad \xi = \frac{\beta_c - \beta_{c,\min}(n)}{\beta_{c,\max}(n) - \beta_{c,\min}(n)} \tag{27}$$

where:

$n_{\min}$ = minimum rotational speed in the compressor map;

$n_{\max}$ = maximum rotational speed;

$\beta_{c,\min}(n)$ = pressure ratio at intersection between the chocking line and the constant speed curve referred to the speed n;

$\beta_{c,\max}(n)$ = pressure ratio at intersection between the surge line and the constant speed curve referred to n.

In this way, the compressor working range can be represented by a grid as shown in Fig. 7. The transformed domain (ξ, η) results in a uniform Cartesian grid in which is possible to interpolate, by means of a bilinear technique, with a small computational effort. Moreover, since the computational effort is not dependent of the number of point of the map, it is possible to make use of very refined map only charging the computer memory but not increasing the computation time. This technique has been generalized for the map of a compressor with variable inlet guide vanes.

4 Simulation Results

The aim of this section is to show that the code is able to accurately simulate the dynamic behavior of a gas turbine under very large load variations.

Two gas turbines for power generation have been chosen in order to test the code: the first one is a large heavy duty gas turbine and the second one is an aero-derivative double-shaft engine. Preliminarily steady-state off-design behavior of the large heavy duty gas turbine has been simulated in order to show that the nonlinear mathematical model characteristics of the code make it able to reproduce the behavior of the gas turbine under working conditions varying from idle to full-load.

4.1 Single Shaft Gas Turbine. In order to overcome the lack of complete experimental data from transient tests in the open literature, the code has been undertaken to a validation against steady-state off-design data, by simulating a very slow transient. The experimental data given by Jansen et al. in [19] concerning the gas turbine V64.3 manufactured by Siemens have been chosen. The gas turbine has a single shaft gas arrangement for electric power generation (Fig. 8); it consists of 17 stages axial flow compressor, of which four stages are provided of variable inlet guide vanes (IGV) in order to vary the air mass flow. Seven of the eight turbine rows are cooled, although, for sake of simplicity, only the

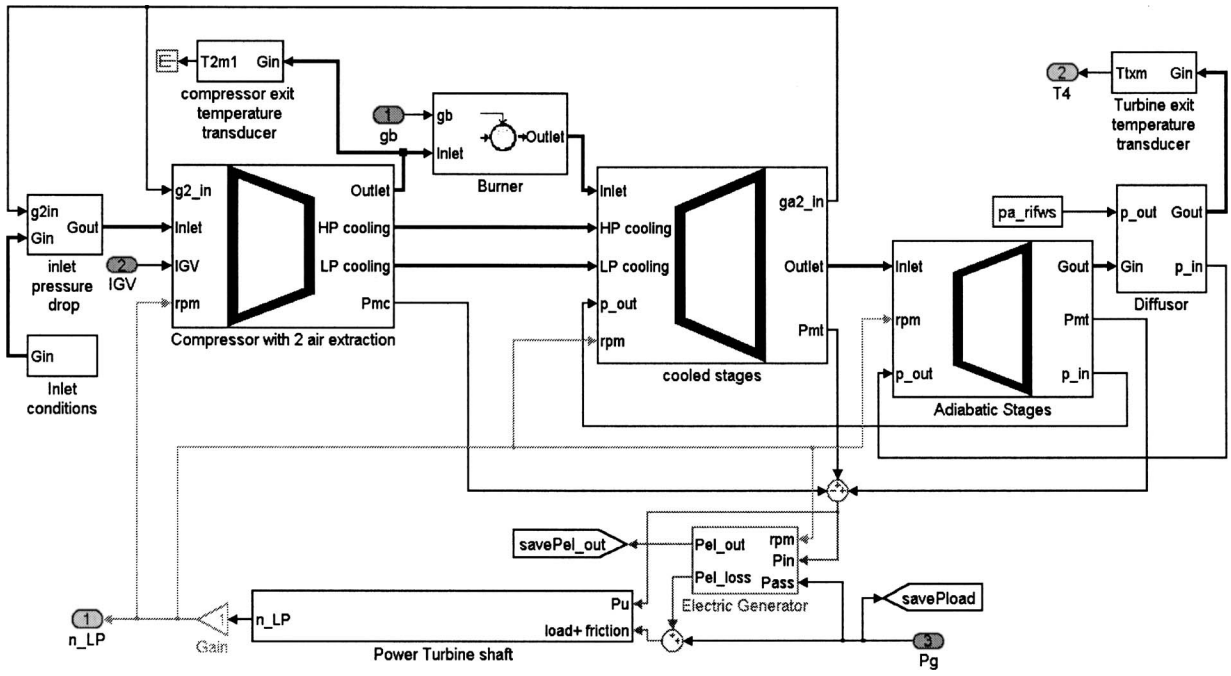

Fig. 8 Simulink scheme of the heavy duty single shaft gas turbine

Table 1 Design specifications assumed for the gas turbine Siemens V64.3

Shaft speed, rpm	5400
Electrical power, MW	61.5
Cycle efficiency, %	35.8
Inlet air flow, kg/s	185
Pressure ratio	15.6
Turbine inlet temperature, °C	1250
Turbine exit temperature, °C	534

first two stages are assumed to be cooled in the code. As given in Ref. [20], the design specifications of the engine are summarized in Table 1. The turbine expander has been represented by making use of three different blocks: the first two blocks represent two cooled stages while the third one simulates the adiabatic expansion. Subsequently the code has been developed under the Simulink environment, some parameters needed for the simulation have been determined on the basis of the off-design performance given in Ref. [19] by making use of an adaptive procedure, needed to obtain that the design parameters can produce a reasonable fitting to the experimental data, on the basis of the technological characteristics of the considered engine. The simulation results given by Kim et al. [20], as well as the results obtained by using a code previously developed in FORTRAN by two of the authors [6,13] have been provided as useful for comparison. The part-load simulation form null load to 110% of nominal load is presented in nondimensional form in Fig. 9. The IGV control system keep the exit temperature constant from 50% to 100% of nominal load; for lower power output, the IGV position is kept constant. The illustrated parameters concern compressor pressure ratio, exhaust gas mass flow and temperature, turbine inlet temperature and overall LHV efficiency. A good agreement between simulation and experiments is obtained for all the measured variables, as well as with the numerical results obtained with the other two above mentioned codes that are, instead, not suitable for real time applications. Moreover it clearly appears that, due to its intrinsic nonlinear features, the code is able to accurately simulate the whole transient from idle to full load, while the linearized real time codes are able to model only a limited region around the working point chosen for linearization.

A load rejection test from full load to idle is simulated in order to verify that the code is able to reliably reproduce very hard dynamics. Figure 10(*a*) shows the time-plot of the electrical power demand (P_{load}) in nondimensional form, which is obtained by dividing the power demand by its design point value. The time unit for the x axis is the second. The power demand variation is supposed to occur instantaneously following the imposed law. In Fig. 10(*b*) the controlled variables are represented: the rotational shaft speed (RPM in the legend) and the measured exhaust temperature (T_{TXM}). The curve clearly shows the plant behavior in the two different stages of load drop and load rising. The curves representing the control variables are drawn in Fig. 10(*c*). The fuel mass flow rate (g_b) is normalized to its design point value, while the inlet guide vane position (IGV), varying from 0 to 1, is given by the rotation angle of inlet guide vanes and is normalized to its value at full open position. It appears that the fuel flow rate rapidly decreases as a consequence of the electric power drop since the fuel system has a short characteristic time; on the other side, the IGV variation is quite slow since the temperature transducer characteristic time is quite long as shown by observing the curve of T_{TXM} in Fig. 10(*b*). Figure 10(*d*) finally shows temperature and pressure at the compressor plenum exit (T_2 and p_2) and at the turbine inlet (T_3 and p_3), respectively. The important information that can be predicted by using a complete thermo-fluid dynamic code, like the proposed one, which can take into account the dynamic matching among the turbomachinery components of the engine, may be very useful for the setup of the control system, such as the anti-surge control system.

In order to evaluate the numerical accuracy of the code, the simulation has been repeated using a Heun second order scheme: the results concerning the most important variables have been compared showing that the maximum relative difference between the solutions obtained adopting the Euler scheme and that obtained adopting the Heun one is smaller than $5 \cdot 10^{-4}$.

4.2 Double Shaft Gas Turbine. A double shaft aeroderivative gas turbine for power generation is considered. The main engine characteristics adopted for developing the simulation model are referred to the gas turbine LM2500 by General Electric [21]: specifically, suitable values of efficiencies, compressor mass flow rate and pressure ratio, turbine inlet temperature, have been chosen in order to allow the simulation model to meet the engine performance given by the manufacturer. Moreover, such values can be adapted to take into account the degradation of the engine performance due, for example, to the compressor fouling.

The model developed for simulating such an engine is shown in Fig. 9. For the sake of clarity, the gas turbine model is displayed as an ensemble of subsystems composed of many blocks. The compressor block is a subsystem composed of two compressor units with an intermediate air extraction for turbine blade cooling; it includes also two plena and two splitter blocks for the cooling air flows. The high-pressure turbine block is a subsystem composed of two air-cooled stages. The power turbine, that is considered not to be cooled, is modeled by a single adiabatic expander. A plenum, placed between the exit of the HP turbine and the inlet of the power turbine, takes into account the volume of both the turbines and the connecting ducts. The map of the compressor, including variable inlet guide vanes varying with the rotational speed, has been adapted from Ref. [22]. The control variable is the fuel flow rate, g_b, and a PI controller (not shown in the figure) has been designed to control the power turbine rotational speed. Similar to the previously shown models, numbers in the scheme are given to identify the different engine sections.

As far as concerns the specific features of the real-time model, Fig. 11 shows that the value of the mass flow, g_3, at the HP turbine inlet, is addressed backwards from the HP turbine block to the burner. Then, from this block, the air mass flow, g_2, is addressed backwards to the compressor subsystem, where it is needed for the mass balance of the plenum. It can be observed also that the pressure at the power turbine inlet is addressed upstream to the HP turbine block, in order to determine the enthalpy drop on the HP turbine.

A varying electric load, Fig. 12(*a*), has been applied in order to describe the dynamic behavior of the gas turbine. First, starting from the design point condition, a load rejection of 50% of full-load at $t=5$ s is simulated. Then, 25 s later, a load rising ramp is applied bringing back the power to full load. Figure 12(*b*) shows the time plots of the rotational speed of gas generator and power turbine. Figure 12(*c*) shows the control signal VCE sent by the controller to the fuel system. In the same figure, the fuel flow rate, g_b, appears to be slightly delayed in comparison to the fuel signal due to the dynamics of the fuel system. The simultaneous variations of the compressor speed and the pressure ratio on the compressor working point are described in Fig. 12(*d*) where part of the compressor map is plotted. The three curves are referred to the load rejection (inverted triangles), to the load rising ramp (circles), and to a quasi-steady load variation (crosses). Finally, time plots of temperature and pressure referred to the main points of the gas turbine are plotted in Figs. 12(*e*) and 12(*f*). These figures show that the program provides a detailed representation of the gas turbine dynamics, including the effects on the intermediate temperature and pressure. The plotted results have been obtained using the Euler explicit first order scheme for integrating the ordinary differential equations. Also for this gas turbine, the simulation has been repeated using the Heun second order scheme; the

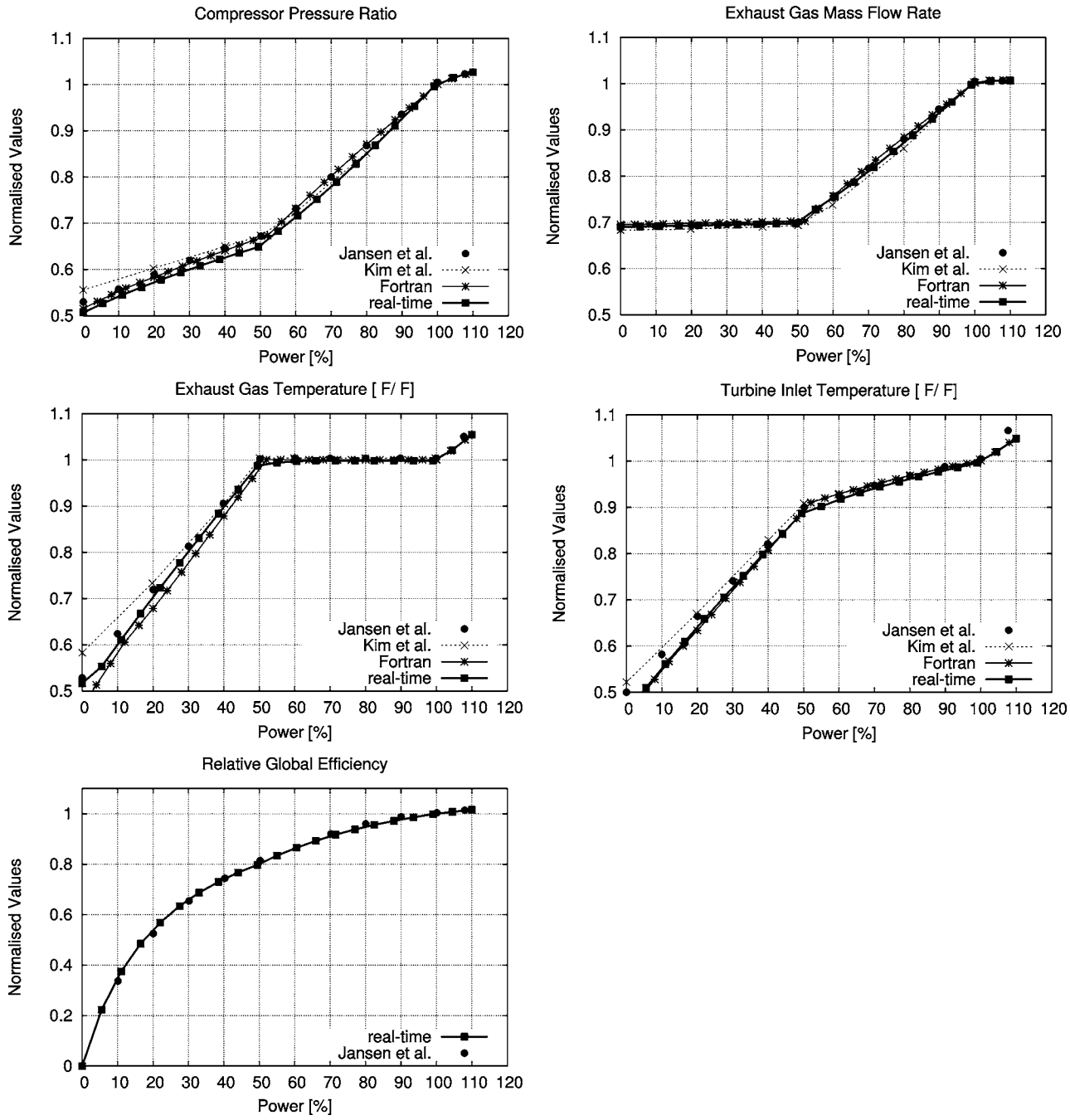

Fig. 9 Simulation results for a slow load increase for the Siemens V64.3 gas turbine comparison of the real-time Simulink model with experimental data by Jansen et al. [19], results by Kim et al. [20], and, finally, with the result obtained by using a proven FORTRAN code [6]

results obtained confirm that the small time step guarantee accurate solutions even adopting a first order scheme. Further tests carried out using a previously developed simulation code making use of a fully implicit solving procedure have given again results undistinguishable from the above described ones.

4.3 Computer Time Performance. The Simulink scheme has been used to produce a source code in C-language by means of the RealTimeWorkshop toolbox. This code has been compiled to obtain an executable program that has been tested to verify the real time capability.

The bar chart in Fig. 13 outlines the average single step calculation time measured on a personal computer based on Pentium III® 800 MHz with a 128 Mbyte memory. The results are referred to the simple single shaft gas turbine in Fig. 5, to the single shaft gas turbine in Fig. 8, and to the aero-derivative engine in Fig. 11. For these last two simulations the comparison between the results obtained by means of the Euler and the Heun schemes is given in order to evaluate the computational effort resulting by using a higher order scheme.

The average computer time per time step has been evaluated dividing the overall calculation time, measured from the start to end of the simulation, by the number of time steps. It should be emphasized that the computational work needed to complete the single step is constant during the simulation and independent from the working conditions (Fig. 13).

Taking into account that a time step of 1 ms was assumed and

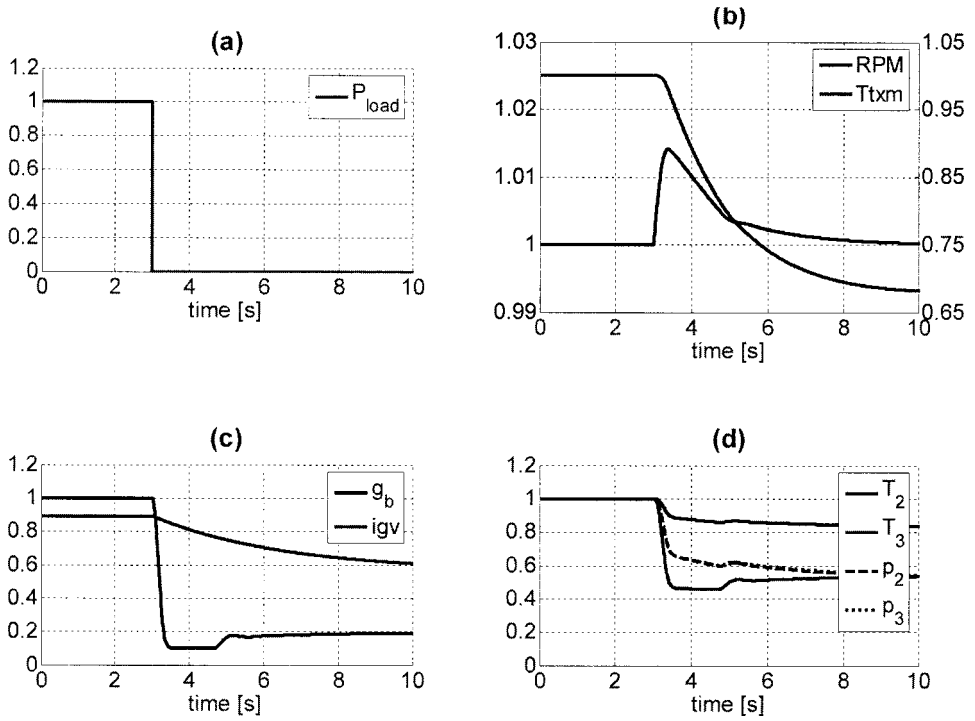

Fig. 10 Dimensionless results for the single-shaft gas turbine; (*a*) applied load; (*b*) controlled variables; (*c*) control variables; (*d*) temperature and pressure at the compressor discharge (T2,p2) and the combustor exit (T3,p3)

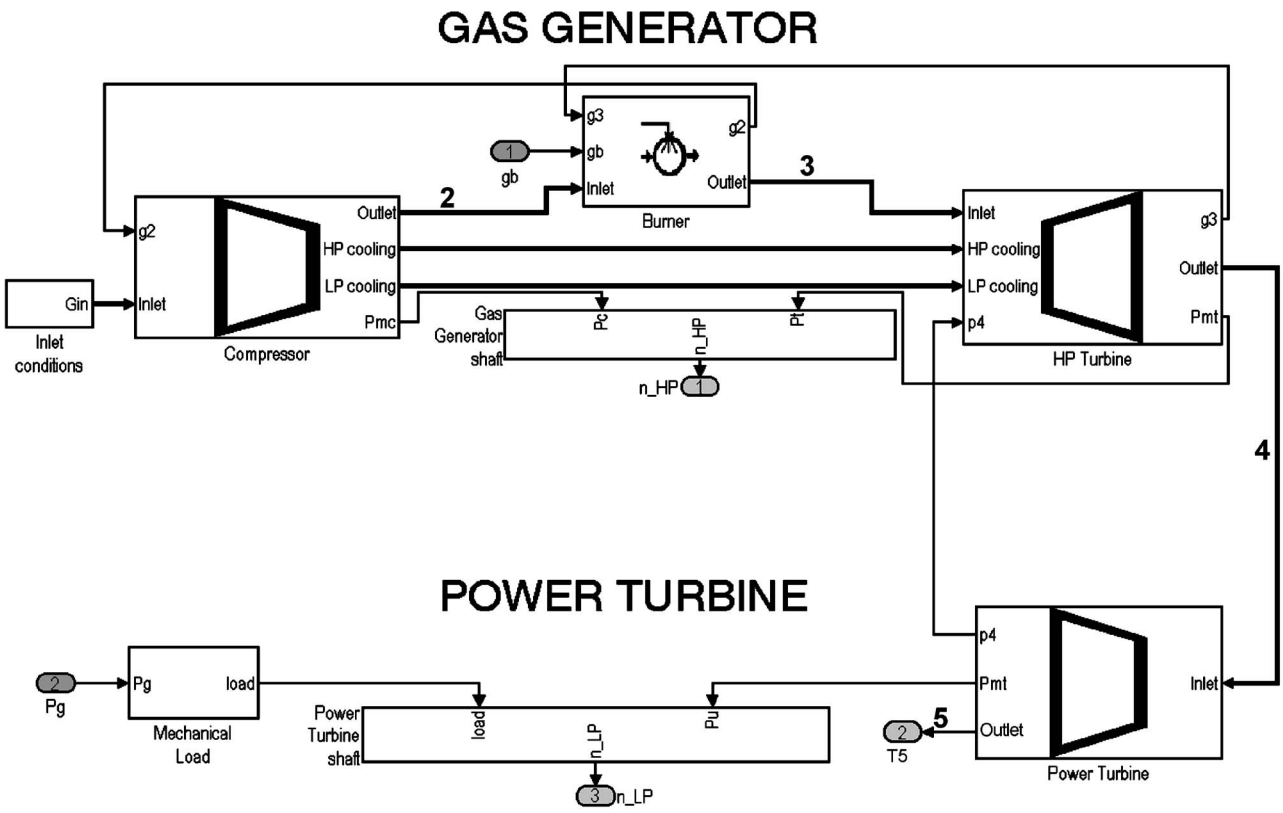

Fig. 11 Double shaft gas turbine scheme

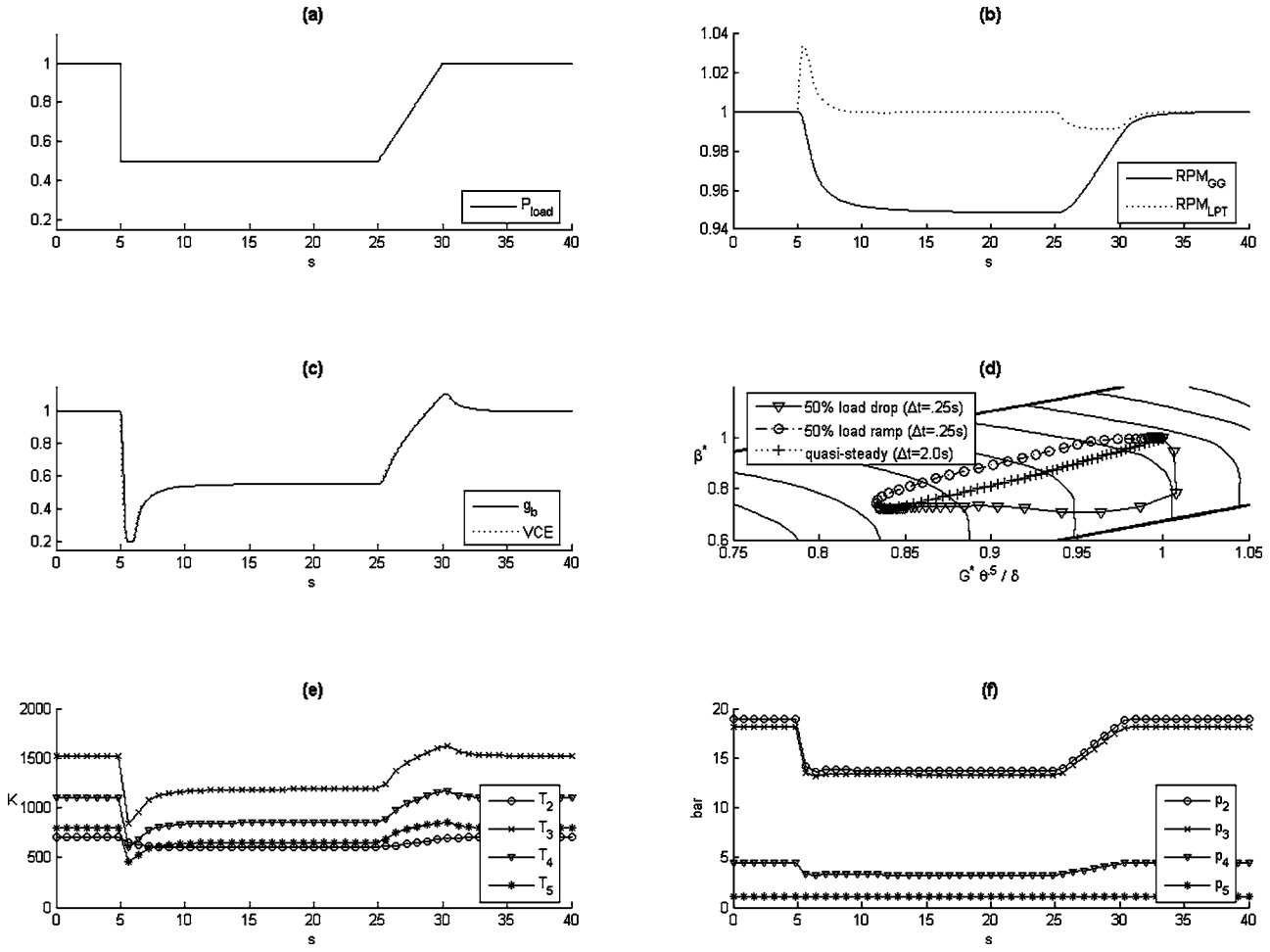

Fig. 12 Simulation results for the double-shaft gas turbine; the subscript numbers are referred as follows: (2) compressor exit; (3) burner exit; (4) gas generator exit; (5) power turbine exhaust gas

that the maximum calculation time resulted about 0.17 ms, it appears that the computer simulation runs 6 to 20 times faster than the simulated system. This result allows us to adopt the described technique in "hardware in the loop" applications, since enough time seems to remain available for data exchange through an input-output interface, within the assumed time step.

5 Conclusions

A novel technique for developing a high-fidelity real time code for gas turbine simulation has been presented. It is shown that the set of nonlinear algebraic equations and ordinary differential equations that compose the mathematical model of the gas turbine can be solved by means of a forward substitution procedure. The mathematical model and the solving procedure are described in the paper. The code is based on the object-oriented approach and is realized under the Matlab-Simulink graphical environment: a library of blocks that simulate the gas turbine components has been set up and a description of main blocks has been provided. These blocks can be easily assembled by means of the graphical interface.

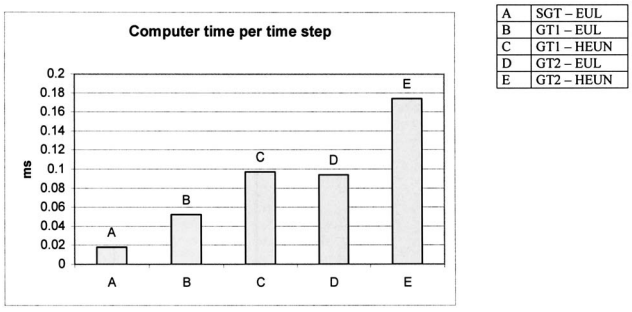

A	SGT – EUL
B	GT1 – EUL
C	GT1 – HEUN
D	GT2 – EUL
E	GT2 – HEUN

Fig. 13 Computer time per time step: SGT simple single-shaft gas turbine; GT1: heavy duty gas turbine; GT2: double shaft gas turbine; EUL: first order Euler scheme; HEUN: second order Heun scheme

The developed code is compatible with the software package called Real-Time-Workshop toolbox. By means of this tool, a source code in C language is automatically generated from the Simulink model and can be compiled. This feature represents an opportunity to modify an existing code or to realize a new one in a relatively short time from models already tested in the Simulink environment.

Two different gas turbines for power generation have been simulated with a relatively high level of details. Some tests have been carried out on the programs obtained by compiling the C codes generated by means of the described procedure. Such tests showed that the codes are able to provide the results in real time, even using a simple personal computer.

The source code in C language can be also modified in order to realize "hardware-in-the-loop" applications for testing control equipments or for control embedded applications or diagnostic purposes.

Acknowledgment

This work has been supported by the Italian Government, Ministry for University and Scientific and Technological Research, under the research project "Dynamic Modeling of Energy Systems."

Nomenclature

Symbols

c_p = specific heat at constant pressure
c_v = specific heat at constant volume
g = mass flow rate
h = specific enthalpy
IGV = normalized inlet guide vane position
K = specific heat ratio=c_p/c_v
LHV = lower heating value
M = mass
Ma = Mach number
m = polytropic coefficient
n = shaft rotational speed
P = power
p = pressure
R = gas constant
t = time
T = temperature
u = internal energy
V = volume
VCE = fuel valve input signal
x = stoichiometric products mass fraction
y = pressure loss coefficient
Y = momentum loss coefficient
β = pressure ratio
δ = p_{amb}/p_0
θ = T_{amb}/T_0
η = efficiency
τ = time constant
Γ = mass flow parameter

Subscripts

a = air
amb = ambient conditions
b = fuel
c = compressor
cc = combustion chamber
cool = cooling air
des = design-point
in = inlet
is = isentropic
mis = measured
out = outlet
p = plenum
t = turbine
0 = standard conditions

References

[1] SAE 1996–05, "Gas Turbine Engine Real Time Performance Model Presentation for Digital Computers," Aerospace Recommended Practice ARP4148 Rev. A.
[2] Walsh, P. P., and Fletcher, P., 1998, *Gas Turbine Performance*, Blackwell Science, Oxford, Chap. 8, p. 468.
[3] Smith, D. L., and Stammetti, V. A., 1990, "Sequential Linearization as an Approach to Real Time Marine Gas Turbine Simulation," J. Eng. Gas Turbines Power, **112**, pp. 187–191.
[4] Visser, P. J., Broomhead, M. J., and van der Vorst, J., 2001, "TERTS, A Generic Real-Time Gas Turbine Simulation Environment," ASME Paper No. 2001-GT-0446.
[5] Stamatis, A., Mathioudakis, K., Ruiz, J., and Curnock, B., 2001, "Real Time Engine Model Implementation for Adaptive Control & Performance Monitoring of Large Civil Turbofans," ASME Paper No. 2001-GT-0362.
[6] Camporeale, S. M., Fortunato, B., and Dumas, A., 1998, "Dynamic Modeling and Control of Regenerative Gas Turbines," ASME Paper No. 98-GT-172.
[7] Agresti, M., Camporeale, S. M., and Fortunato, B., 2000, "An Object-Oriented Program for the Dynamic Simulation of Gas Turbines," ASME Paper No. 2000-GT-42.
[8] Simulink: "User's Guide," The MathWorks, Inc., 1998.
[9] Schobeiri, M. T., Attia, M., and Lippe, C., 1994, "GETRAN: A Generic Modularly Structured Computer Code for Simulation of Dynamic Behaviour of Aero- and Power Generation Gas Turbine Engines," Trans. ASME: J. Eng. Gas Turbines Power, **116**, pp. 483–494.
[10] Crosa, G., Pittaluga, F., Trucco, A., Beltrami, F., Torelli, A., and Traverso, F., 1998, "Heavy Duty Gas Turbine Plant Aero-Thermodynamic Simulation Using Simulink," Trans. ASME: J. Eng. Gas Turbines Power, **120**, pp. 550–556.
[11] Perez-Blanco, H., and Albright, P., 2001, "Heat Recovery System Control Strategy To Meet Multiple Transient Demands," ASME Paper No. 2001 GT-0210.
[12] McGreehan, W. F., and Schotsch, M. J., 1988, "Flow Characteristics of Long Orifices With Rotation and Corner Radiusing," ASME J. Eng. Gas Turbines Power, **110**, pp. 213–217.
[13] Camporeale, S., and Fortunato, B., 1998, "Performance of a Mixed Gas-Steam Cycle Power Plant Obtained Upgrading an Aeroderivative Gas Turbine," Energy Convers. Manage., **39**, pp. 1683–1692.
[14] El Mastri, M. A., 1988, "On the Thermodynamics of Gas Turbines Cycles: Part 2—A model for Expansion in Cooled Turbines," ASME J. Eng. Gas Turbines Power, **110**, pp. 201–209.
[15] Kim, T. S., and Ro, S. T., 1997, "The Effect of Gas Turbine Coolant Modulation on the Part Load Performance of Combined Cycle Plants. 1. Gas Turbines," Bussei Kenkyu, **211**.
[16] Rowen, W., 1983, "Simplified Mathematical Representations of Heavy Duty Gas Turbines," ASME J. Eng. Power, **105**, pp. 865–869.
[17] Hannet, L. N., and Khan, A., 1993, "Combustion Turbine Dynamic Model Validation From Tests," IEEE Trans. Power Syst., **8**, pp. 152–158.
[18] De Mello, F. P., 1994, "Dynamic Models for Combined Cycle Plants in Power System Studies," IEEE Trans. Power Syst., **9**, pp. 1698–1708.
[19] Jansen, M., Schulenberg, T., and Waldinger, D., 1992, "Shop Test Results for the V64.3A Gas Turbine," Trans. ASME: J. Eng. Gas Turbines Power, **114**, pp. 676–681.
[20] Kim, J. H., Song, T. W., Kim, T. S., and Ro, S. T., 2000, "Model Development and Simulation of Transient Behaviour of Heavy Duty Gas Turbines," ASME Paper No. 2000-GT-0548.
[21] "Industrial Engine Performance-Natural Gas Fuel," 1997, GE Report available from "www.ge.com."
[22] Spector, R. B., and Miller, A. A., 1983, "GE LM 2500 Aircraft-Derivative Gas Turbine System," General Electric Company Report GER 343.

Enhancing Flow Field Measurements Through Adaptive Multidimensional Data Sampling

Arnoud R. C. Franken

Paul C. Ivey

School of Engineering,
Cranfield University,
Cranfield, Bedfordshire MK43 0AL, UK

A way to gain insight into the flow field conditions in turbomachinery is by carrying out a series of point measurements in a cross section of the flow, for example, with a miniature multihole pressure probe. A problem commonly encountered in situations like these is the selection of a suitable measurement grid layout and density for obtaining all essential information in a cost-effective and timely manner. In order to achieve the latter, a novel adaptive multidimensional data sampling technique has been developed at Cranfield University. This paper describes the underlying principles of this technique, the algorithms utilized, and the results obtained during its successful application to data sets of two different flow fields in a high-speed research compressor. [DOI: 10.1115/1.2135822]

Introduction

A way to gain insight into the flow field conditions in turbomachinery is by carrying out a series of point measurements in a cross section of the flow, for example, with a miniature multihole pressure probe (see, [1]). A problem commonly encountered in situations like these is the selection of a suitable measurement grid layout and density for obtaining all essential information in a cost-effective and timely manner. For situations like these, where sometimes several flow parameters are observed simultaneously, each changing differently across the measurement field and dependent on the operating conditions, there exists no generally applicable sampling theorem for predetermining the minimum number and position of grid points needed to accurately and efficiently reconstitute the multidimensional flow field features. Consequently, uniform measurement grids, which might incorporate some a priori knowledge of the flow field and usually form a compromise between acceptable resolution and measurement duration, are typically utilized to obtain the information sought. Depending on the flow conditions, using such grids will (or might) lead to situations in which features are under- or oversampled. This is not only an inefficient use of scarce resources but can also adversely affect information quality in areas of the flow field that are of particular interest. Improving this situation by making measurement grid layout and density adapt automatically to the flow field conditions (i.e., making measurements only where essential) will lead to a better utilization of available resources and to insights that are more valuable. To achieve this, a novel auto-adaptive multidimensional data-sampling technique for application to steady flow field effects has been developed at Cranfield University. In this paper the underlying principle of this novel data-sampling technique, the algorithms utilized, as well as the results obtained with a number of different high-speed multistage axial compressor test data sets will be described. Furthermore, the results obtained with this data-sampling technique are compared to those obtained using a conventional, fixed measurement grid, and efficiency and information quality gains are demonstrated.

Feature Sampling and Reconstruction

Introduction. The minimum number of sample points needed to accurately describe an object to be sampled depends on the shape of this object as well as the technique used to accurately reconstitute this shape from the sample data obtained. For example, if the object measured is a straight line then it is known from mathematics that the coordinates of at least two points lying somewhere on this line must be known in order for it to be accurately described by means of a linear equation. As the shape of the object becomes slightly more complicated then more than one technique for accurately describing it becomes available. Each of these techniques is likely to require a different minimum number of points, thereby making the selection of the necessary number and position of sample points more challenging. This selection problem becomes significantly more difficult when the exact shape of the object to be measured is highly complicated, unknown beforehand, or both, as is the case with the flow field conditions in a cross section of a high-speed multistage axial compressor. The reason that *predetermining* the minimum number and position of sample points for accurately reconstituting these kinds of shapes is so difficult is because there are no theorems available for guidance. The emphasis here is on *pre*determining because theorems do exist for *determining* the minimum number and position of sample points. Such theorems, which are used in fields such as computer and robot vision and biomedical engineering, require the availability of high-density data sets prior to their application because of their development for eliminating redundant data from such data sets (see, e.g., [2–5]). Consequently, these theorems are not usable for determining the minimum number and position of sample points either prior to or during the data acquisition process.

Conventional Measurement Grids. The shape of the flow field features in the cross section of an axial compressor is complicated for many reasons, the discussion of which is beyond the scope of this paper. When the objective is to experimentally characterize these features the necessary data can often, for practical reasons, only be obtained through a series of point measurements. In the absence of a theorem for predetermining the most suitable measurement grid layout and density, the conventional approach is to use a dense, uniform measurement grid. These grids might incorporate a priori knowledge of the flow field and usually form a compromise between acceptable resolution and measurement duration (see Fig. 1 for an example of such a grid).

Measurement grids like the one shown in Fig. 1 are likely to accurately capture all characteristic flow field features present due to their layout and high sample point density. Again utilizing such grids is a very inefficient approach, in particular, when there are large areas present in the flow field in which the flow variables of interest change little, because the number of samples needed to

Contributed by the International Gas Turbine Institute (IGTI) of ASME for publication in the JOURNAL OF ENGINEERING FOR GAS TURBINES AND POWER. Manuscript received August 30, 2005; final manuscript received September 6, 2005. IGTI Review Chair: K. C. Hall. Paper presented at the ASME Turbo Expo 2005: Land, Sea, and Air, Reno, NV, June 6–9, 2005, Paper No. GT2005-68994.

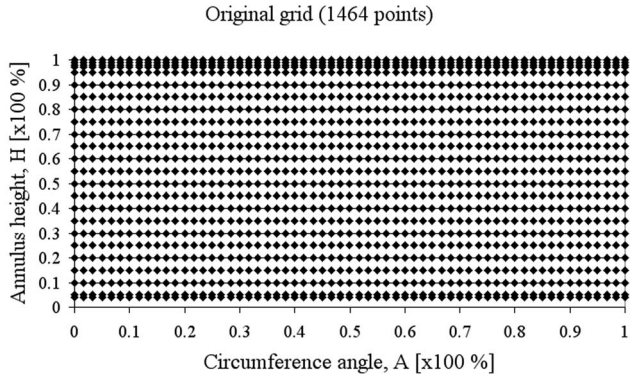

Fig. 1 Measurement grid used to investigate flow field effects in Cranfield University's High-Speed Research Compressor. This measurement grid contains 1464 sample points and is 1 1/2 blade-pitch wide.

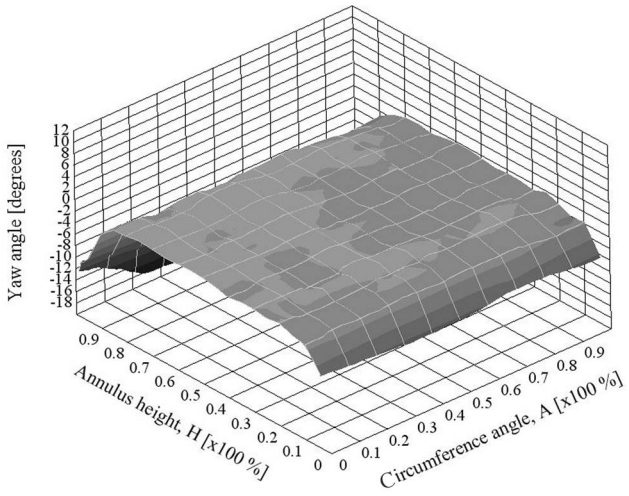

Fig. 2 Yaw-angle distribution obtained with the measurement grid shown in Fig. 1 during a HSRC rig test

accurately describe smooth changes is likely to be smaller than in areas where changes are rapid. That is, it is more than likely that a fewer number of samples are needed to accurately describe, for example, the yaw angle[1] distribution in Fig. 2 than the one in Fig. 3. Despite this fact, which will be proven in a later section, both these distributions were obtained during two different HSRC rig tests with measurement grids like the one shown in Fig. 1 (see also Fig. 4).

Inefficient approaches to obtain essential flow field insights may have been acceptable when time and costs were a lesser issue. Currently with gas turbine engine manufacturers as well as every organization in their value creation chain being continuously forced by their customers to further reduce time and costs while improving product or service performance in order to remain competitive, it is not acceptable anymore. These trends are more than likely to continue unabated in the future thus necessitating research and development of algorithms that allow the layout and density of measurement grids to automatically adapt to the local flow field conditions so that measurements are made only where essential. The latter is the topic of the following section.

Development of an Auto-Adaptive Sampling Algorithm

Introduction. As was stated at the beginning of the previous section, the minimum number of sample points needed to accurately describe an object to be sampled depends on the shape of this object as well as the technique used to accurately reconstitute this shape from the sample data obtained. Therefore, knowledge of the object's shape to be sampled, which in the case of compressor flow field measurements will be the shapes of the distributions of the flow variables of interest, as well as the technique used to reconstitute that shape from the data obtained, will play key roles in the development of algorithms for adaptive measurement grids. Because the latter choice is determined by the former, the shapes of the distributions of the flow variables of interest will be discussed first.

Analyzing Flow Field Features. Detailed information about the flow field features to be sampled is typically not available prior to measurement and thus a justification for carrying out the experimental investigation. Often, however, a limited amount of information may be available and this must be utilized in the development of an algorithm that adapts a measurement grid's layout and density to the local conditions. For example, it is known that due to viscous effects and turbulence, larger changes in the magnitude of flow variables are to be expected near walls and other boundaries than in the bulk of the flow and thus that areas of rapid and smooth change are present. The approximate locations of these areas within the measurement field are known beforehand, although not their exact shapes and sizes. The latter must be established by the adaptive sampling algorithm because they affect the total number and position of sample points necessary to accurately describe the flow field features of interest in a cost-effective and efficient manner. Establishing where these areas are located within the measurement field as well as their shapes and sizes requires the ability to recognize them in the first place, which will have implications for the way the field is sampled. The latter can be seen as follows. In the conventional approach to sampling a flow field, samples are taken sequentially in every point of the grid, as is shown schematically in Fig. 5.

As a result, flow field information embedded in the data obtained becomes available in strings. Unfortunately, these strings of information do not provide any insights into the data trend ahead of the last point sampled or about any other part of the measurement field not yet sampled. Yet such whole-field information is needed to determine where areas of rapid or smooth change are located, their shapes and sizes and thus where point measurements are essential. In order to obtain such information, samples from

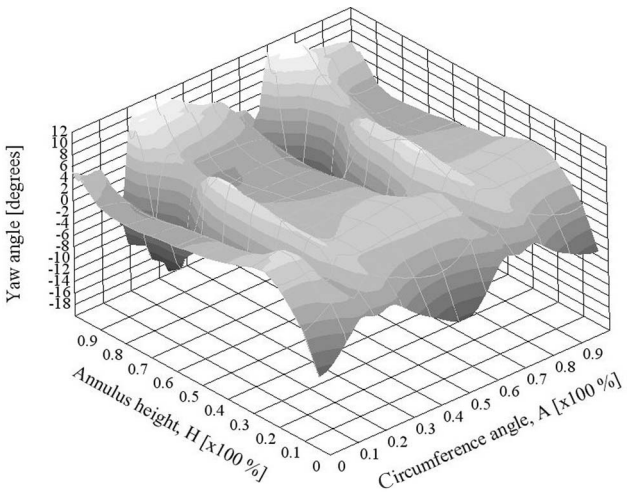

Fig. 3 Yaw-angle distribution obtained with the measurement grid shown in Fig. 1 during a different HSRC rig test

[1]Yaw angle is a flow angle measured in the horizontal plane. See, e.g., Franken and Ivey [1] for a more detailed discussion on the measurement of this flow angle and other flow variables using a multihole pressure probe.

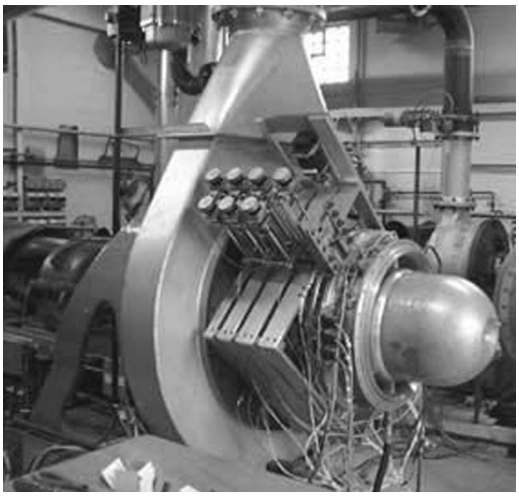

Fig. 4 Cranfield University's high-speed axial research compressor (HSRC) test rig

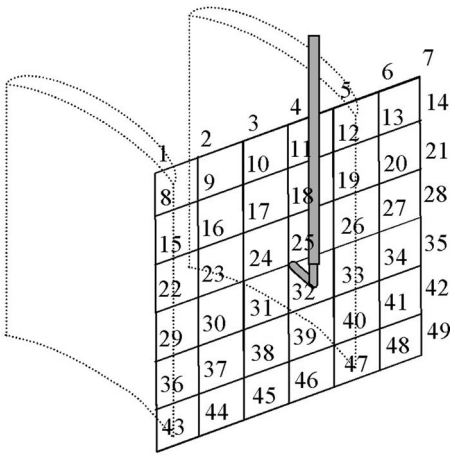

Fig. 5 Schematic of the traversing of a pressure probe through a measurement grid in a compressor cross section

across the entire measurement field are needed. In order to keep the necessary time and costs of obtaining this information to a minimum, this must be achieved with as few samples as possible, i.e., by utilizing the coarsest measurement grid sensible. More will be said about the latter later, but with regard to the grid shown in Fig. 5 it could mean that, for example, samples are only taken in points 1, 3, 5, 7, 15, 17, …, 43, 45, 47, and 49. Of course, the information embedded in these samples will not provide a detailed picture of the flow field features, but it will be clear enough to roughly identify the areas of rapid and smooth change.

Automatically Identifying Areas of Rapid and Smooth Change. In the adaptive multidimensional data-sampling technique utilized in fields such as robot vision or biomedical engineering areas of rapid and smooth change are identified by computing the local surface curvature in every grid point, involving the computation of partial derivates and comparing it to a reference curvature for which the number and position of sample points are known. Such an approach is not recommended here because when more points are added to a cell of a coarse grid (e.g., if points 2 and 9 are added to the cell 1-3-17-15-1), the curvature computations become highly complicated, and local curvature values will change but do not necessarily converge. The latter makes automatic grid refinements using this approach a difficult process. An easier solution to the problem of determining where within the measurement field additional sample points are needed is found by returning to the objective of the measurements: obtaining data to accurately describe the flow field features of interest. In other words, when the flow field features of interest are accurately described, additional data points will only lead to redundant information, which must be avoided in order to enhance cost-effectiveness and efficiency. Therefore, after sampling the coarsest grid sensible, each additional grid point sampled should only add new information. This requires the ability to assess if additional points have provided new information but also where additional grid points are still needed to extract all essential information. The former can be determined by comparing the information *before* and *after* the additional points were added to the data set in conjunction with a specified criterion, for example, an acceptable difference. The latter can be achieved in a similar fashion, but this requires that it is somehow known what the total information embedded is so that currently available information can be compared to it. In a research setting, such detailed information is usually not present, which makes this approach seemingly impossible. In order to make it possible, that situation must be approximated with a suitable model, i.e., a model that can reliably approximate the situation in which all embedded information is known using only currently available information. One modeling approach that meets this requirement is the thin-plate spline method. As is known from the literature on spline regression models (see, e.g., [6]), spline models are approximation/interpolation models that are defined on a particular interval and are composed of pieces of simple functions defined on subintervals and joined at their endpoints with a suitable degree of smoothness. Depending on the application, spline models can be constructed in many ways, its discussion beyond the scope of this paper, and the thin-plate spline approach is one of them. As is stated by Bookstein [7], Franke [8], and Foley and Lane [9], thin-plate splines are particularly well suited for accurately interpolating irregularly sampled data, which may be sparse and/or noise-contaminated, in two- or three-dimensional domains, and evaluation on any defined grid. Furthermore, as Franke [8] and Foley and Lane [9] state, of all the spline models that could be used for such applications, the thin-plate spline approach is one of the most effective and simplest to implement. Because of those reasons, the thin-plate spline method is the most suitable choice for the application discussed here. Before this discussion is continued the algorithm behind thin-plate splines will be briefly described.

Thin-Plate Spline Algorithm. As Bookstein [7] reports, the concept of thin-plate splines is based on a constrained thin steel plate adopting a position of least net bending energy when being slightly bended (i.e., minimization of the bending energy function)

$$\int\int_{\Re^2} (f_{xx}^2 + 2f_{xy}^2 + f_{yy}^2)dxdy \tag{1}$$

As Franke [8] and Foley and Lane [9] state, the interpolant that minimizes this integral has the following form:

$$f(x,y) = \sum_{j=1}^{n} a_j E(r) + b_0 + b_1 x + b_2 y \tag{2}$$

where

$$E(r) = r^2 \log r^2 \text{ and } r^2 = (x - x_j)^2 + (y - y_j)^2 \tag{3}$$

The $n+3$ unknown coefficients a_j, b_0, b_1, and b_2 are determined by solving the $n+3$ linear equations $f(x_i, y_i)$ together with the conditions

$$\sum_{j=1}^{n} a_j = 0 \quad \sum_{j=1}^{n} a_j x_j = 0 \quad \sum_{j=1}^{n} a_j y_j = 0 \tag{4}$$

In matrix form (2) can be written as follows:

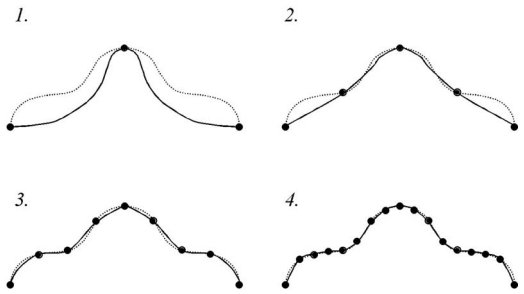

Fig. 6 Improvement of the thin-plate spline approximation (solid line) by adding more sample points (·) to the data set

$$\underline{z} = A\underline{a} + B\underline{b} \tag{5}$$

where $A=[E_{ij}]$ is an $n\times n$ matrix and where B is an $n\times 3$ matrix whose rows are $[\underline{1}\ \underline{x}_i\ \underline{y}_i]$. The conditions in (4) can thus be written as

$$B^T\underline{a} = \underline{0} \tag{6}$$

Equations (5) and (6) can be rewritten to obtain the coefficients a_j, b_0, b_1, and b_2

$$\underline{a} = A^{-1}(\underline{z} - B\underline{b}) \tag{7}$$

$$\underline{b} = (B^TA^{-1}B)^{-1}B^TA^{-1}\underline{z} \tag{8}$$

Thin-plate splines allow the inclusion of a smoothing feature for dealing with noisy data, in which case the interpolation is not exact anymore. To include this feature (5) needs to be modified as follows:

$$\underline{z} = (A + \lambda I)\underline{a} + B\underline{b} \tag{9}$$

Where $\lambda > 0$ is a smoothing parameter and I is the $n\times n$ identity matrix.

Algorithm for Auto-Adaptive Data Sampling. To briefly recap the earlier discussion on the development of a novel adaptive multidimensional data-sampling technique, in order to make only measurements where necessary and extract all essential information in a cost-effective manner, it is necessary to start with the coarsest measurement grid sensible and refine it only where necessary. This requires the ability to assess in which areas of the measurement field sufficient samples have been obtained and where more are still needed, which requires the ability to somehow know what the embedded information is. In a research setting such knowledge is usually not present, but it can be approximated with thin-plate spline models. The latter can be seen as follows. In cross sections of flow fields, the distributions of flow variables can be represented by continuous smooth surfaces (see, e.g., Figs. 2 and 3). Thin-plate splines have the flexibility to approximate such surfaces closely and this approximation improves the more data points are available to prescribe the shape. Figure 6 demonstrates this graphically. Furthermore, as is clearly visible in Fig. 6, after a certain number of data points have been added to the data set, the differences between the approximations/interpolations based on the previous and current data sets become very small in some areas (i.e., adding more points in those areas does not lead to a significant improvement of the approximation). Therefore, these differences can be used in a control loop in conjunction with a specified, application-dependent criterion (e.g., an acceptable minimum difference, for determining where additional sample points are required and where not).

After the areas in the measurement field have been identified where additional sample points are required, a decision must be made regarding their location in these areas. A simple solution is to double the density of the respective grid cells, i.e., placing the additional sample points between previous sample points (see Fig. 7).

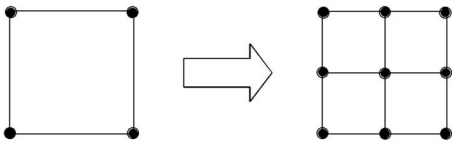

Fig. 7 Adapting the local measurement grid density

Based on the above discussion, the novel adaptive multidimensional data sampling technique developed at Cranfield University can be formulated as follows:

1. Using a priori knowledge of the flow field features at the operating conditions of interest, select the coarsest measurement grid sensible, i.e., a grid density and layout that will at least capture the major features of the underlying data function.
2. Create a second measurement grid that has about double the density of the initial grid.
3. Use the second grid for sampling of the flow field and use the obtained samples (i.e., the *current* data set) to create a data set corresponding to the initial grid (i.e., the *previous* data set).
4. Use the previous and current data sets to create two corresponding thin-plate spline models.[2]
5. Use both models to develop interpolation data sets on the grid of the highest technical resolution and compute the difference between the interpolants in every point of this grid.
6. Double the density of the respective cell in the current grid if the absolute value of this difference is larger than an acceptable minimum difference.[3]
7. Obtain the additional samples and add these to the new current data set. Go back to step 4 and repeat this procedure until either further local grid refinements are not required or the highest technical resolution has been reached.

Results and Discussion

Introduction. In order to keep development time and costs to a minimum, the novel adaptive multidimensional data-sampling technique detailed in the previous section was first tested with flow field data obtained in earlier high-speed axial research compressor (HSRC) rig tests. Utilizing these data sets presented some limitations with regard to the availability of sample data in arbitrary locations within the boundaries of the measuring field. Therefore, the selection of the initial grid and the subsequent grid development were controlled to coincide with physically sampled points (see Fig. 1). In addition, it was assumed that the grid shown in Fig. 1 represented the grid of highest technical resolution possible. Some of the results obtained during these tests are discussed in the following section.

Application of Auto-Adaptive Sampling Algorithm. As stated, the novel sampling algorithm was tested with available data sets. Because of space limitations and the fact that the results obtained are comparable, only the procedure and results obtained with the data set of Fig. 3 will be discussed in detail.

Starting with the first step of the algorithm, prior to the application of the algorithm to the data set, it was known that the position of the two compressor blades within the measuring field would be near $A=0.2$ and $A=0.7$ (see Fig. 3). Furthermore, it was known that rapid changes in yaw angle were to be expected in

[2]In following iterations, only one thin-plate spline model will be developed as the "previous" model is available from the previous iteration.

[3]The acceptable minimum difference is an application-dependent quantity. Factors that should be taken into consideration when setting this difference are, e.g., the measurement inaccuracy of the sensor used and the stability of process variables during measurements.

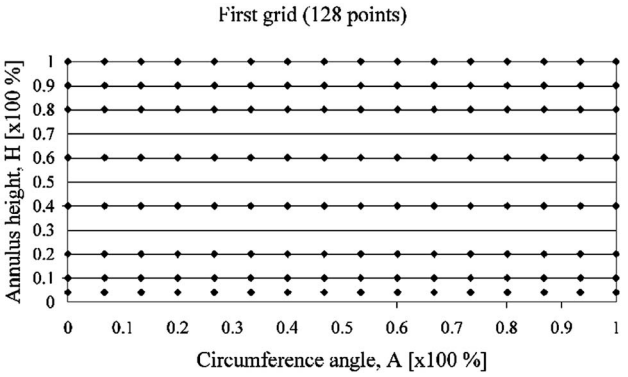

Fig. 8 Initial measurement grid utilizing a priori knowledge of the flow field conditions

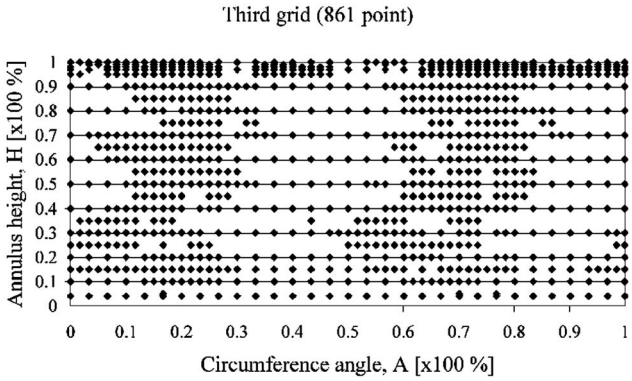

Fig. 10 Third measurement grid. The higher sample point densities near the hub ($H<0.2$), casing ($H>0.9$), and compressor blades ($A=0.2$ and $A=0.7$) clearly indicate the locations, shapes, and sizes of the areas of rapid change.

these areas as well as close to the hub and casing. Therefore, the initial grid was chosen so that more sample points would be located in the bottom and top 20% of the grid (see Fig. 8). This choice was reflected in the second measurement grid (step 2) as can be seen in Fig. 9. Next, using the original data set, two data sets were created that corresponded with the sampled grids (step 3), and corresponding thin-plate spline models were subsequently developed (step 4). In the following step (step 5), both models were evaluated on the grid of highest technical resolution (i.e., the grid shown in Fig. 1). In several areas, in particular near to the hub, casing, and compressor blades, differences between the interpolants were found to be larger than the acceptable minimum difference, which was chosen to correspond with the absolute measurement inaccuracy of the pressure probe used in the actual tests (0.4 deg, see [1]). Therefore, the density of the respective grid cells was doubled (step 6) and 427 additional samples obtained (step 7, see Fig. 10). The procedure was subsequently repeated, and in step 6 areas near the hub, casing and blades were found where the differences between the interpolants were larger than the accepted minimum difference. Therefore, the density of the respective grid cells was doubled and 39 additional samples obtained (see Fig. 11). The procedure was repeated for a third time and, again, in step 6 of the algorithm small areas were found were the differences between the interpolants were larger than the acceptable minimum difference. At this point additional samples could not be obtained as the highest technical resolution had been reached (i.e., the available data set did not contain data at smaller increments). Despite this fact, a comparison between the original measurement results (Fig. 3) and the thin-plate spline interpolations on the same grid (Fig. 12) showed that the fourth measurement grid, containing 38% fewer grid points than the original grid, leads to an accurate approximation.

As is clearly visible in Fig. 13, there are some differences between the measured values and the thin-plate spline approximations. The majority of these differences are very small and perfectly acceptable. Nevertheless, there are some differences that are larger than the acceptable minimum difference of 0.4 deg. There are several reasons that explain these differences. For example, the 1464 measurement values, which were used as a benchmark, are not exact due to, for example, measurement inaccuracies. The final thin-plate spline model, which did not contain a smoothing parameter, is not constrained in all these points, and therefore, small differences will be found in some areas. Furthermore, as was stated earlier, points could only be adaptively sampled for which measurement results were available. As a subsequent analysis of these differences indicated, the larger differences are found in areas that could not be sampled with the available data set but can be sampled during an actual rig test. Therefore, some of the larger differences visible in Fig. 13 cannot be simply attributed to systematic model or algorithmic limitations; the limitations posed by the available data set used for the testing of the algorithm have to be taken into account as well.

Similar results were obtained when the novel data sampling technique was applied to the yaw angle distribution shown in Fig. 2. The flow conditions in that particular HSRC rig test were, of course, significantly different from those that led to the yaw angle distribution shown in Fig. 3. The features are smoother and rapid or steep changes are practically not present. Therefore, the expectation of a fewer number of necessary sample points was met after

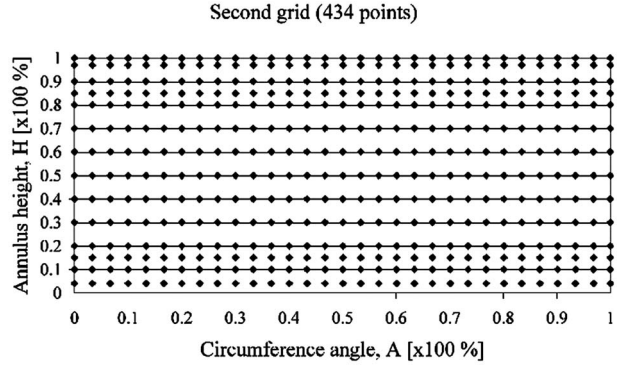

Fig. 9 Second measurement grid

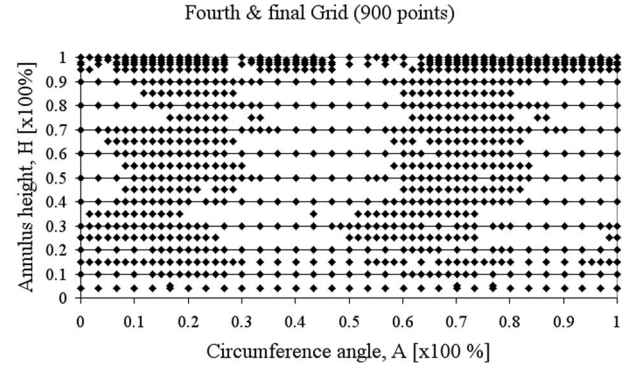

Fig. 11 Fourth and final measurement grid containing 900 grid points. The locations, shapes, and sizes of areas of high and low sample point density clearly correspond with the areas of rapid and smooth change visible in Fig. 3.

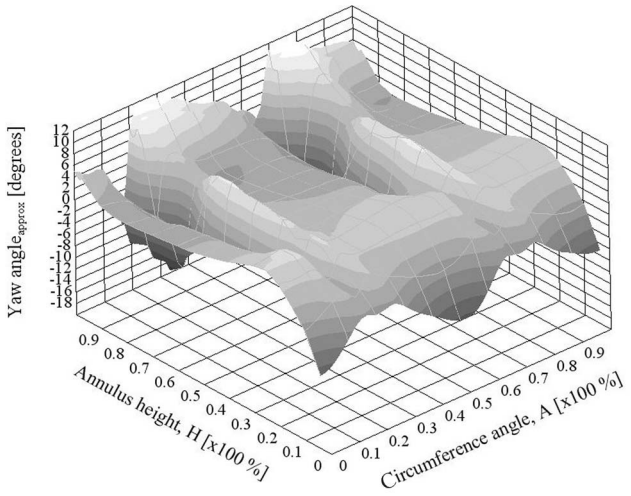

Fig. 12 Thin-plate spline approximation/interpolation of the yaw-angle distribution shown in Fig. 3

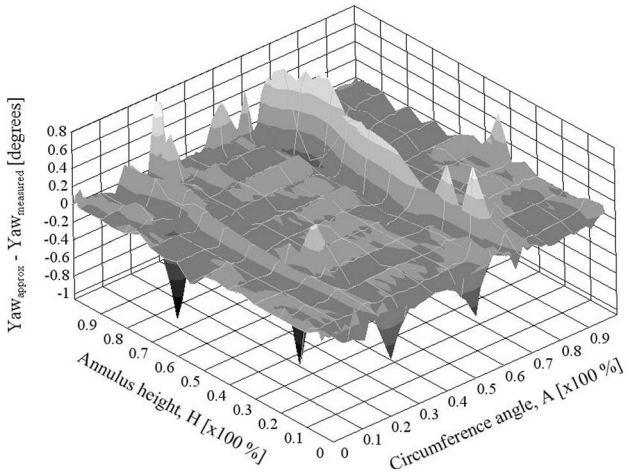

Fig. 13 Differences between the approximated and measured yaw-angle values

the fourth and final iteration of the adaptive sampling procedure was completed; only 639 out of 1403 possible points needed to be sampled, a reduction of 54%.

Implications of Algorithm on Experiments. What sets the auto-adaptive sampling algorithm detailed here apart from the conventional approach to sampling flow field features is that the required local grid resolution is automatically determined in test and driven by feature reconstruction needs instead of time or budgetary constraints. Consequently, point measurements are only made where essential for obtaining an accurate description of the features. Furthermore, as the two examples discussed in the previous section clearly demonstrate, this novel approach offers the capability to substantially reduce the number of points sampled in comparison to a conventional grid and, thus, the duration and running cost of rig tests.[4] These are important advantages when pressures to reduce time and costs are high. Furthermore, the algorithm offers the capability to accurately capture fine flow field features in a shorter period of time than would be possible with a uniform high-density grid by only locally utilizing high sample point densities. This is a great advantage when the time to capture important features is short (e.g., when measuring at or near critical operating conditions). Finally, the novel approach produces as a by-product accurate, easy-to-use approximation/interpolation models of the flow field features sampled. This enhances the ease and accuracy of performance computation carried out posttest, leading to better informed decisions for further tests and developments.

Conclusions

Because of the complexity and multidimensionality of flow fields in turbomachinery as well as the unavailability of suitable multidimensional data-sampling techniques, flow field features are typically sampled utilizing dense uniform measurement grids that might incorporate some a priori knowledge. Furthermore, the grid densities and layouts employed usually form a compromise between acceptable resolution and measurement duration. Consequently, flow field features can be substantially under- or oversampled, thereby affecting information quality in areas of the flow field that are of particular interest for research and development purposes as well as the efficient utilization of scarce resources. Market dynamics and competitive forces do not allow the sustained usage of such inefficient processes, necessitating the development and application of cost-effective and efficient techniques for adaptively sampling multidimensional flow field features. The research project described in this paper has shown that this need can be met through the development and successful application of a novel adaptive data-sampling technique. Utilization of this novel approach offers the following benefits:

- Measurements are only made where necessary to extract all essential flow field information present, thereby improving the cost-effective and efficient utilization of scarce resources
- Local grid resolution is automatically determined and driven by feature reconstruction needs and not time or budgetary constraints
- Improvement of flow field information quality by adapting grid resolution to local flow field conditions
- Accurate, easy-to-use approximation/interpolation models of the flow field features are available posttest for further performance computations

Acknowledgment

The authors would like to thank D.A. Lippett for providing the high-speed compressor test data used in this research project.

Nomenclature

A = circumference angle (deg, %)
A = $n \times n$ matrix
a_j = coefficients ($j=1-n$)
B = $n \times 3$ matrix
b_0, b_1, b_2 = coefficients
H = annulus height (%)
I = identity matrix
n = number of data points

References

[1] Franken, A. R. C., and Ivey, P. C., 2004, "Accelerating the Calibration of Multi-Hole Pressure Probes by Applying Advanced Computational Methods," ASME Paper No. GT2004-53434.
[2] Garcia, M. A., 1994, "Efficient Surface Reconstruction From Scattered Points Through Geometric Data Fusion," *Proc., 1994 IEEE International Conference on Multi-Sensor Fusion and Integration for Intelligent Systems*, IEEE, New York, pp. 559–566.
[3] Garcia, M. A., 1995, "Fast Approximation of Range Images by Triangular

[4]The exact reduction in duration and running cost of rig tests that can be realized is dependent on the design of the test rig, the complexity of the flow field features encountered at the operating conditions of interest, the layout and density of the conventional grid utilized as a benchmark, and the capabilities of the probe positioning system used. These factors are test and/or facility dependent, and therefore, outcomes achieved at one facility are not necessarily comparable to those achieved at another. Because of these reasons, no figures are presented here for indicative purposes.

Meshes Generated Through Adaptive Randomized Sampling," *Proc., 1995 IEEE International Conference on Robotics and Automation*, IEEE, New York, Vol. 2, pp. 2043–2048.
[4] Huang, H-L, and Ho, S-Y., 2001, "Mesh Optimization for Surface Approximation Using an Efficient Coarse-to-Fine Evolutionary Algorithm," *Proc., 2001 IEEE Congress on Evolutionary Computation*, IEEE, New York, Vol. 1, pp. 584–591.
[5] Unser, M., 1995, "Multi-Grid Adaptive Image Processing," *Proc., 1995 IEEE International Conference on Image Processing*, IEEE, New York, Vol. 1, pp. 49–52.
[6] Marsh, L. C., and Cormier, D. R., 2002, *Spline Regression Models*, Sage Publications, University of Iowa.
[7] Bookstein, F. L., 1989, "Principal Warps: Thin-Plate Splines and the Decomposition of Deformations," IEEE Trans. Pattern Anal. Mach. Intell., **11**, pp. 567–585.
[8] Franke, R., 1982, "Smooth Interpolation of Scattered Data by Local Thin-Plate Splines," Comput. Math. Appl., **8**, pp. 273–281.
[9] Foley, T. A., and Lane, D. A., 1990, "Visualization of Irregular Multivariate Data," *Proc., First IEEE Conference on Visualization*, IEEE, New York, pp. 247–254.

Chemical-Looping Combustion for Combined Cycles With CO_2 Capture

Stefano Consonni[1]
e-mail: stafano.consonni@polimi.it

Giovanni Lozza

Giampaolo Pelliccia

Dipartiamento di Energetica,
Politecnico di Milano,
Milan, Italy

Stefano Rossini

Francesco Saviano

Enitecnologie,
San Donato Milanese,
Milan, Italy

Chemical-Looping Combustion (CLC) is a process where fuel oxidation is carried out through an intermediate agent—a metal oxide—circulated across two fluidized bed reactors: a reduction reactor, where an endothermic reaction reduces the metal oxide and oxidizes the fuel, and an oxidation reactor, where an exothermic reaction oxidizes the metal oxide in air. Overall, the system carries out the same job of a conventional combustor, with the fundamental advantage of segregating the oxidation products (CO_2 and H_2O) into an output flow free of nitrogen and excess oxygen. The flow exiting the reduction reactor consists of water and CO_2, the latter readily available for liquefaction, transport and long-term storage. The hot, vitiated air from the oxidation reactor is the means to produce power through a thermodynamic cycle. This paper reports of a study supported by the ENI group to assess the potential of the integration between CLC and combined gas-steam power cycles. More specifically, we focus on four issues: (i) optimization of plant configuration; (ii) prediction of overall efficiency; (iii) use of commercial gas turbines; (iv) preliminary economic estimates. The CLC system is based on iron oxides which, to maintain their physical characteristics, must operate below 900–1000°C. Given the crucial importance of the temperature of the vitiated air generated by CLC on the performance of the combined cycle, we consider two options: (i) "unfired" systems, where natural gas is fed only to the CLC system, (ii) "fired" systems, where the vitiated air is supplementary fired to reach gas turbine inlet temperatures ranging 1000–1200°C. Results show that unfired configurations with maximum process temperature 850–1050°C and zero emissions reach net LHV plant efficiencies ranging 43%–48%. Fired cycles where temperature is raised from 850 to 1200°C by supplementary firing can achieve 52% net LHV efficiency with CO_2 emission about one half of those of a state-of-the-art combined cycles. Fired configurations allow significant capital cost and fuel cost savings compared to unfired configurations; however, a carbon tax high enough to make them attractive (close to 50 €/ton) would undermine these advantages.
[DOI: 10.1115/1.1850501]

1 Background and Scope

The use of fossil fuels is so widespread and deep-rooted in industrial societies (and man's habits) that its reduction as a means to reduce greenhouse gas emissions will require an unprecedented, daunting effort [1]. In the short- and medium-term, substantial reductions of greenhouse gas emissions could still be achieved by sequestering the CO_2 generated by fossil fuels oxidation. The capture and long-term storage of CO_2—or possibly other carbon-laden compounds [2]—could thereby ease the transition toward the long-term goal of a society relying on most environmentally benign energy sources and conversion systems.

CO_2 sequestration appears to make most sense for large-scale power stations, either due to economies of scale and to the complexity of the systems needed for capture and storage. In this case there appear to be three crucial issues:

1. CO_2 capture in fossil fuel-fired power plants;
2. CO_2 transport to storage site;
3. availability of appropriate, long-term storage sites.

This paper focuses on the first issue, assuming that a system does exist for transporting liquid, supercritical CO_2 at 85 bar to a safe, long-term storage site like depleted oil or gas fields, underground caverns, aquifers or deep oceanic waters. Should higher pressures be required, they can easily be achieved with very low pumping energy requirements.

In a fossil fuel-fired power plant, CO_2 capture can be carried out by a variety of processes and technologies. A host of recent studies focus on three concepts involving relatively well-known technologies:

i. CO_2 removal via amine chemical absorption from flue gas [3,4];
ii. fuel decarbonization, i.e. conversion of fossil fuel into hydrogen and CO_2, which is removed ahead of combustion [5,6];
iii. oxy-combustion, where nearly-pure CO_2 is obtained by knocking out the water from the gas generated by burning the fuel into oxygen [7,8].

This paper focuses on yet another technology, often named as Chemical Looping Combustion (CLC), reporting the outcome of a research commissioned by Enitecnologie, a company of the ENI group, to the Energy Department of Energy Engineering Politecnico di Milano.

The CLC concept is illustrated in Fig. 1. Natural gas enters a "reduction reactor" where solid metal oxides are reduced by giving up oxygen to the fuel, which is therefore oxidized to CO_2 and water. Reduced metal oxides then flow into an "oxidation reactor" where they are oxidized in air. The flow of solid, oxygen-rich metal oxides and vitiated air exiting the oxidation reactor enters a cyclone, where the solid oxides are separated from the gas stream

[1]To whom correspondence should be addressed.

Contributed by the International Gas Turbine Institute (IGTI) of ASME for publication in the JOURNAL OF ENGINEERING FOR GAS TURBINES AND POWER. Paper presented at the International Gas Turbine and Aeroengine Congress and Exhibition, Vienna, Austria, June 13–17, 2004, Paper No. 2004-GT-53503. Manuscript received October 1, 2003; final manuscript received March 1, 2004. IGTI Review Chair: A. J. Strazisar.

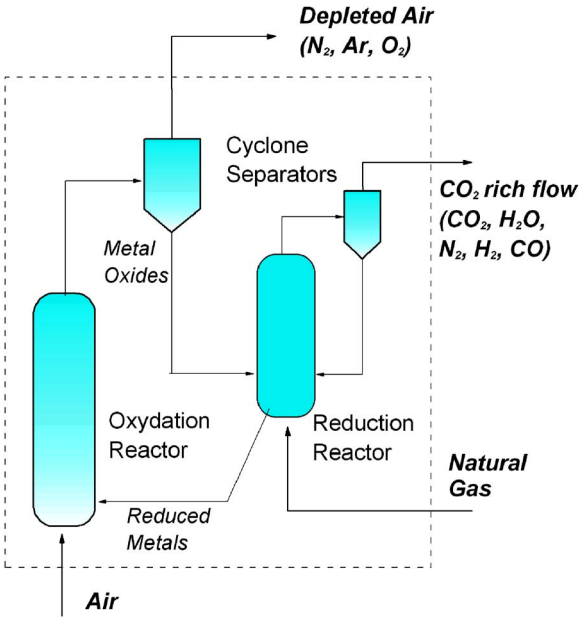

Fig. 1 Chemical looping combustion concept

and recycled (whereby the term "looping") to the reduction reactor [9,10] Altogether, the system is equivalent to a conventional combustor, with the fundamental advantage that the oxidation products (CO_2 and H_2O) are made available in a flow nearly free of diluents.

In order to generate power, the system in Fig. 1 must be coupled to a thermodynamic cycle. This paper addresses the integrated process where CLC is coupled to a combined gas-steam power cycle. More specifically, we aim at:

a. assess plant configuration;
b. show how the operating parameters (gas turbine pressure ratio, CLC temperatures) affect efficiency and specific output;
c. assess the use of commercial gas turbines;
d. carry out a preliminary economic evaluation.

All this while accounting for the limits imposed by the CLC process and by state-of-the-art power plant technology. One first, basic constraint regards the fuel input. CLC requires a clean fuel like natural gas to avoid contamination and degradation of the circulating solids. This is why our attention is restricted to natural gas-fired systems and the results obtained here will be compared to the ones achievable by other NG-fired power plants with CO_2 capture.

2 CLC Technology

The CLC concept depicted in Fig. 1 can be implemented in a number of ways, depending on the type and physical characteristics of the oxide that carries out the chemical loop, the type of reactor, the operating conditions. In this paper we consider a pressurized system where both reactors are fluidized beds. The metal oxide floats (or circulates) in the beds as a relatively fine powder to make available the solid–gas contact surface needed to carry out the heterogeneous reactions with natural gas (in the reduction reactor) and with oxygen (in the oxidation reactor). In addition to the metal oxide, the solid particles comprise also inert material—or possibly a catalyst—to warrant adequate physical, thermal and chemical kinetic characteristics (not investigated here).

Operating temperatures and flow rates crucially depend on the type of metal oxide. In this paper we consider iron oxides because, besides being relatively cheap and easy to supply, their heat of reaction determines—under adiabatic conditions—a temperature decrease in the reduction reactor. Therefore, the maximum temperature reached by the metal oxide equals the temperature of the vitiated air discharged by the oxidation reactor, exactly what is needed to maximize power plant performance for a given maximum temperature of the solid in the beds.

Table 1 Reduction and oxidation reactions for selected metals to be used for CLC, referred to the combustion of one mole of CH_4. ΔH_R^0=heat of reaction at 25°C. For adiabatic reactors, the maximum system temperature is reached at the outlet of the RR when the reduction reaction is exothermic (Cu,Mn), at the outlet of the OR when the reduction reaction is endothermic (Fe,Ni).

Metal		Reactions	ΔH_R^0 (kJ)
Cu	RR	$8\ CuO + CH_4 \leftrightarrow CO_2 + 2\ H_2O + 4\ Cu_2O$	−517.5
	OR	$4\ Cu_2O + 2\ O_2 \leftrightarrow 8\ CuO$	−284.8
Fe	RR	$12\ Fe_2O_3 + CH_4 \leftrightarrow CO_2 + 2\ H_2O + 8\ Fe_3O_4$	230.9
	OR	$8\ Fe_3O_4 + 2\ O_2 \leftrightarrow 12\ Fe_2O_3$	−1033.2
Mn	RR	$12\ Mn_2O_3 + CH_4 \leftrightarrow CO_2 + 2\ H_2O + 8\ Mn_3O_4$	−379.5
	OR	$8\ Mn_3O_4 + 2\ O_2 \leftrightarrow 12\ Mn_2O_3$	−422.8
Ni	RR	$4\ NiO + CH_4 \leftrightarrow CO_2 + 2\ H_2O + 4\ Ni$	175.7
	OR	$4\ Ni + 2\ O_2 \leftrightarrow 4\ NiO$	−978
	overall	$CH_4 + 2\ O_2 \leftrightarrow CO_2 + 2\ H_2O$	−802.3

In a CLC system based on iron oxides and fed with pure methane, the reduction reactor reduces hematite (Fe_2O_3) to magnetite (Fe_3O_4) according to the endothermic reaction:

$$CH_4 + 12\ Fe_2O_3 \rightarrow CO_2 + 2\ H_2O + 8\ Fe_3O_4 - 230.9\ kJ \quad (1)$$

where the 230.9 kJ per mole of CH_4 to be supplied to the reactants are the difference between the heat needed to reduce the metal (for 8 moles of Fe_3O_4, 1033.2 kJ) and the heat released by the oxidation of 1 mole of methane (802.3 kJ). The 1033.2 kJ needed to reduce Fe_2O_3 are given back by the oxidation taking place in the OR:

$$8Fe_3O_4 + 2\ O_2 \rightarrow 12Fe_2O_3 + 1033.2\ kJ \quad (2)$$

If the reactors are adiabatic, the temperature in the reduction reactor decreases; consequently, the maximum temperature is reached at the outlet of the oxidation reactor and coincides with that of the vitiated air exported to the CC.

As an alternative to iron, one may consider copper, manganese and nickel. Table 1 summarizes the reactions taking place in the reduction and oxidation reactors. Fe and Ni are preferable because the reduction reaction is endothermic. Moreover, according to Ref. [11], iron and nickel show very high CH_4 to CO_2 conversion rate in the reduction reactor. On the other hand, Fe looks more attractive than Ni due to its lower cost and higher reactivity. With Cu and Mn the temperature at the outlet of an adiabatic reduction reactor would be higher than the temperature of the vitiated air sent to the power cycle. Thus, the cycle would operate with a maximum temperature lower than the maximum temperature tolerable by the metal oxide—a situation which would penalize performance. This unfavorable situation could be improved by cooling the reduction reactor to generate high-pressure steam—which however would significantly complicate the design of the reduction reactor and increase its cost.

2.1 Approach Adopted to Estimate Performances. Since this paper focuses on the potential of CLC for power generation, we will not deal with the details of reactor chemistry and kinetics, nor with the issues related to the thermo-fluid-dynamic and structural design of the reactors and their ancillary components (cyclones, feeding systems, etc.). These topics are being investigated by Enitecnologie. Here the CLC system is modeled based on simplifying assumptions which are insufficient to define the actual

Table 2 Composition and conditions calculated for the flows at the outlet of the reactors for iron and nickel oxides. In both cases, the reduction reactor is fed with 10 kg/s of natural gas at 15°C (467 MW_{LHV}), pressure is 20 bar, maximum temperature is 1050°C and air enters the oxidation reactor at 300°C.

	Iron	Nickel	Iron	Nickel
Solids	OR outlet		RR outlet	
mass flow, kg/s	2507	353.6	2470	316.6
temperature, °C	1050	1050	986.2	707.5
reduced Me, % wt	0.0	0.0	43.6	43.32
oxidized Me, % wt	50.8	54.86	6.5	6.21
inert material, % wt	49.2	45.14	50.0	50.47
Gaseous flow	OR outlet (vitiated air)		RR outlet (CO_2 rich flow)	
mass flow, kg/s	474.8	498.3	47.2	47.0
temperature, °C	1050	1050	986.2	707.5
N_2, % mol	82.7	82.42	1.087	1.09
O_2, % mol	15.18	15.47	0	0
Ar, % mol	0.98	0.98	0	0
H_2O, % mol	1.11	1.10	65.25	64.72
CO_2, % mol	0.03	0.03	33.64	33.47
CO, % mol	0	0	0.008	0.179
H_2, % mol	0	0	0.009	0.538

design of the CLC components, but are fully adequate to predict the heat/mass balances and thus the overall performance of the integrated CLC-CC system. More specifically, we have assumed the following:

1. Hematite (Fe_2O_3) and magnetite (Fe_3O_4) are the sole reactive solid species, carrying out the chemical loop according to reactions (1) and (2).
2. Both reactors are adiabatic.
3. The composition at the outlet of both reactors is at equilibrium, i.e. the reactant residence times are higher than the characteristic times of chemical kinetics and of heat/mass transport. A catalyst may be needed.
4. Fuel is natural gas with molar composition 92% CH_4, 3.2% C_2H_6, 1.1% C_3H_8, 0.3% CO_2, 3.3% N_2, 0.1% higher hydrocarbons. HHV and LHV are 51.75 and 46.706 MJ/kg, respectively.
5. Excess oxygen, i.e. excess hematite, in the reduction reactor is 10%. Maintaining some excess oxygen is essential to warrant the full oxidation of natural gas.
6. Inert solid material is 50% of the total flow of solids entering the oxidation reactor. This inert material is necessary to achieve appropriate physical characteristics of the solid particles and to realize a favorable temperature distribution across the reactors.

Table 2 exemplifies the CLC operating conditions corresponding to these assumptions. The table also reports the operating conditions obtained, under the same assumptions, with nickel oxide. Due to the lower molecular weight of its reduced and oxidized form, nickel gives a dramatic reduction of the mass flow circulating across the reactors. Despite this advantage, iron is likely to be a better choice than nickel due to: (i) higher reactivity and much lower cost; (ii) narrower temperature range spanned by the solid oxides along the loop (986–1050°C for iron vs 707–1050°C for nickel), which reduces material stresses. The temperature range spanned by nickel could be reduced by increasing the amount of inert material, which however would lessen the benefit of smaller solid oxide flow.

3 Power Cycle

Coupling a CLC system with a combined cycle implies two types of interaction between the CLC island and the power cycle: (i) the CLC system substitutes the gas turbine combustor: compressed air discharged by the gas turbine compressor is fed to the oxidizing reactor and vitiated air is fed to the gas turbine expander, (ii) heat recovery from the pressurized, CO_2-rich flow discharged by the reduction reactor generates steam that adds to the steam generated in the HRSG.

The simplified scheme of the integrated plant considered here is reported in Fig. 2. To reduce heat transfer irreversibilities and maximize electricity production, heat recovery from the CO_2-rich flow takes place across three evaporators (each feeding one of the HRSG drums) and an LP economizer. Downstream of this heat recovery, the CO_2-rich flow is further cooled down to nearly ambient temperature to knock out most of the water, leaving highly concentrated CO_2 (94–96 vol. %) which is further dried and compressed up to 85 bar in an inter-cooled compressor to make it suitable for transport and long-term storage.

In the ''unfired'' scheme, all the NG input goes to the reduction reactor and the gas turbine is fed by hot, vitiated air. In the ''fired'' scheme, a fraction of the NG input goes to a combustor placed between the CLC and the gas turbine expander. Direct firing with NG allows increasing TIT much above the value tolerable by CLC, with major benefits on performance but also significant increase of CO_2 emissions.

As shown in Fig. 2, we have also considered NG preheating with saturated water bled from the HP drum. Although this preheating is always beneficial to the efficiency, it is not fully pursued due to the difficulty of operating fuel control valves above 100–150°C. Since this issue does not apply to CLC plants—at least for ''unfired'' cycles—NG is heated up to about 300°C.

The steam cycle includes three evaporation pressure levels with reheat, a rather complex arrangement representative of large-scale, high-efficiency combined cycles.

3.1 Basic Cycle Parameters. Once it is assumed that efficiencies, pressure drops, temperature differences, thermal losses, etc. of the system components conform to the state-of-the-art of power plant technology, the performances of the integrated CLC-CC plant depend on the following basic cycle parameters:

a. turbine inlet temperature (TIT);
b. gas turbine pressure ratio β;
c. pressure of CO_2-rich flow;
d. steam cycle evaporation pressures.

In unfired plants, TIT is determined by the maximum temperature tolerable by the CLC system. In fired plants, TIT is not subject to optimization (the higher the TIT, the higher the efficiency) but it is determined by constraints imposed by the gas turbine or by the limits on CO_2 emissions. After accounting for pressure losses, the pressure ratio β determines the pressure of CLC reactors. Unlike TIT, β is subject to optimization, because there is a value that maximizes efficiency and another that maximizes specific work. The pressure at which the CO_2-rich flow goes through the evaporators, the economizer and the trim cooler shown between points 9 and 10 in Fig. 2 could be lower than the pressure at the discharge from the reduction reactor, because at point 9 in Fig. 2 one may place a turboexpander. Even after properly accounting for expansion and compressor efficiencies, the power generated by such expander can be greater than the extra-power needed for CO_2 compression, because the flow to be compressed is at much lower temperature and has been deprived of most of the water. However, lowering the pressure of point 10 in Fig. 2 decreases the dew point temperature[2] and ends up in a much lower rate of heat recovered (LP steam, feedwater). In practice, preliminary calculations demonstrated that efficiency and power output are rather insensitive to the pressure at point 10. This is why we assume here that the CO_2-rich flow stays at the pressure of the reduction reactor (except for pressure losses), achieving significant investment cost

[2]With NG as fuel, the mol fraction of water in the flow exiting the reduction reactor is about two thirds. Thus, if the reactor operates at 10 bar, the dew point is about 162°C, i.e., thesaturation pressure of water at 6.6 bar.

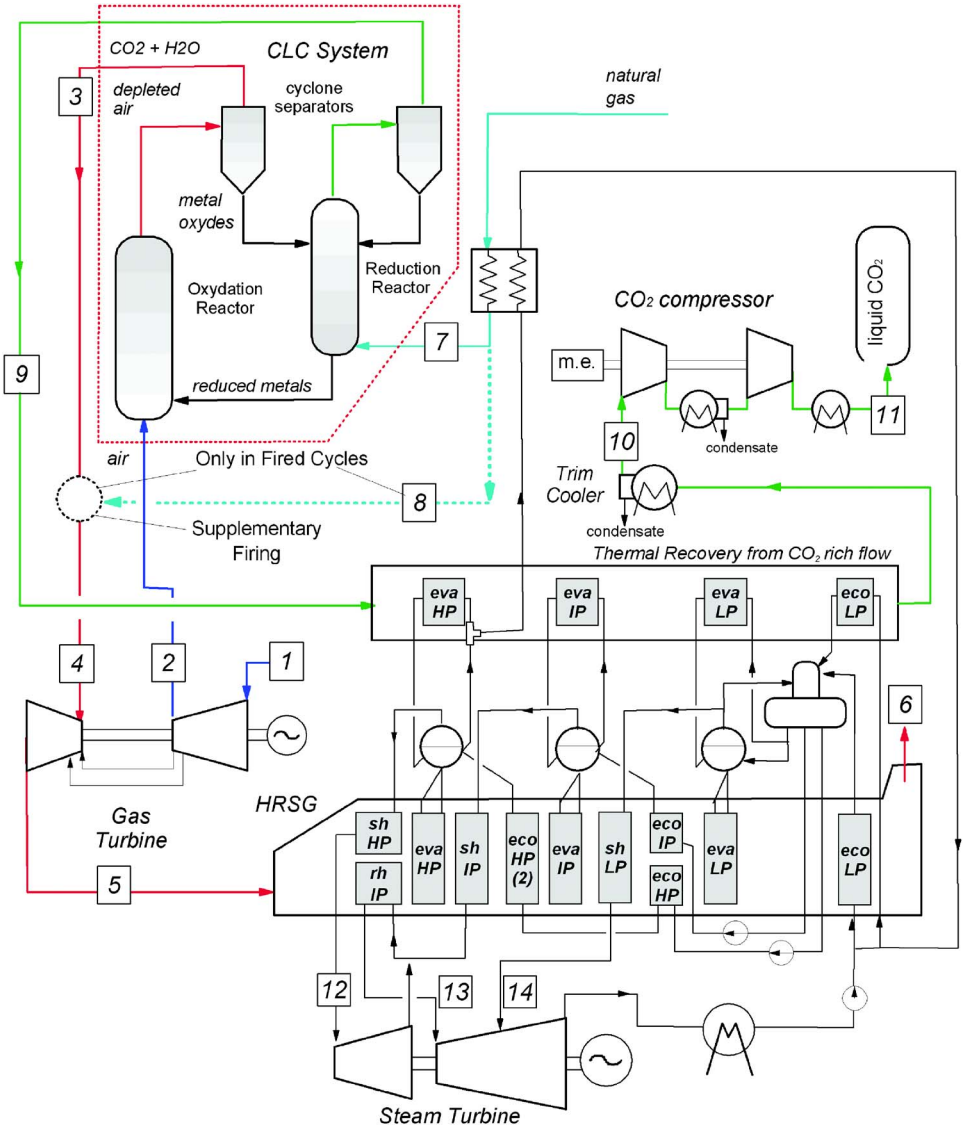

Fig. 2 Simplified scheme of CLC integrated with a combined cycle

reductions (elimination of a gas expander, smaller CO_2 compressor, smaller heat transfer areas for heat recovery due to higher gas density), with negligible efficiency penalties. As for the evaporation pressures of the steam cycle, they have been varied with the outlet temperature of the gas turbine to maximize electric efficiency.

4 Calculation Model and Assumptions

Heat and mass balances of the integrated CLC-CC plants have been estimated by a computer code originally developed to assess the performance of gas/steam cycles for power production [12–15] and later extended to handle gasification of coal and biomass [16], unconventional fuels [17], chemical reactors [18], fuel cells [19] and essentially all processes encountered in advanced power plants.

The system of interest is defined as an ensemble of components, each belonging to one of fourteen basic types: pump, compressor, turbine, heat exchanger, combustor, steam cycle, etc. Basic characteristics and mass/energy balances of each component are calculated sequentially and iteratively until the conditions at all interconnections converge toward stable values. The energy balance of components with reactive flows is solved together with the equations that warrant chemical equilibrium (if required) and the conservation of atomic species. After reaching convergence, the code can perform a full 2nd-law analysis, evaluating the flows of reversible work in and out of each component.

Thermodynamic properties are calculated according to the JANAF tables [20,21], except for water and steam, which conform to S.I. tables [22] and the highly concentrated CO_2, handled by the CO_2 compression and drying system, which is calculated by ASPEN Plus [23] based on the Peng-Robinson model [24]. Chemical equilibria are calculated by a model originally developed by Reynolds [25], included in our code. The performances estimated by the model are for design conditions, i.e. it is assumed that all plant components have been specifically designed "from scratch" to operate at the conditions reached upon convergence. Results presented here are therefore applicable to "greenfield" construction.

Table 3 summarizes the most important assumptions maintained throughout most calculations (exceptions are discussed further below). Those for the power plant are representative of combined cycle technology. The polytropic efficiencies of gas turbine compressor and expander reported in the table are the asymptotic values reached without scale effects; the actual values are calculated by our code based on similarity parameters. Gas turbine cooling flows are calculated based on TIT, the maximum allow-

Table 3 Main assumptions adopted for calculating the performances of the integrated CLC-CC systems. (*) Maximum values; actual values have been optimized depending on GT outlet temperature.

Ambient Conditions	15°C, 1 atm 60% RH
NG supply	15°C, 20 bar
NG flow rate	10 kg/s (476 MWt)
Approach ΔT in NG heater	20°C
Compressor air leakage	0.8% of inlet flow rate
Compressor polytropic efficiency	$\eta_{pc,\infty}=0.90$
Turbine polytropic efficiency	$\eta_{tc,\infty}=0.93$
Max T of turbine nozzles/blades	830°C/800°C
Approach, pinch, subcooling ΔT	25/10/10°C
HRSG Pressure Levels	3 bar/20 bar/110 bar(*)
Condensing pressure	0.05 bar
HRSG thermal losses	0.7% of thermal input
Mechanical losses, compressor/GT/ST	0.3%/0.3%/0.5%
Generator efficiency	99%
Thermal loss of CLC reactors	0.7% thermal input
Composition at reactors outlet	chemical equilibrium
CLC pressure loss,	7.5%
Excess oxygen in reduction reactor	$\varepsilon=10\%$
Inert mass fraction in circulating solids	$\kappa=50\%$
Stage compr ratio of CO_2 compressor	$\cong 2$
Compressor stage isentropic efficiency	85%
Temperature at intercooler outlet	30°C
Mechanical/electric efficiency	96%/96%
Liquid CO_2 to disposal	30°C, 85 bar

able metal temperatures reported in the table, the calculated gas expansion path and a number of parameters interpreting state-of-the-art cooling technology [13,14,26].

The assumptions adopted for the CLC island are reasonable guesses based on the experience of Enitecnologie and a preliminary assessment of CLC technology. Obviously, specific features like pressure drops, excess oxygen, heat losses will have to be verified based on the design and the operating experience of actual plants. Notice that the large 7.5% pressure drop across the CLC system includes all losses from compressor discharge to gas turbine inlet: ducts, reactors, cyclones, valves, etc.

According to Johansson et al. [27], a minor fraction (about 2%) of the CO_2 generated in the reduction reactor leaks to the oxidation reactors. Since this leakage has not been considered here, our predictions tend to underestimate both power output (because we do not considered the contribution of the CO_2 going through the gas turbine expander) and CO_2 emissions.

Maintaining the same NG input for all calculations, i.e., the same power of the CLC island, implies that the gas turbine changes with TIT and β. In practice one would proceed differently because, rather than tailoring the gas turbine to a given CLC system, it is more likely that one would tailor the CLC to an existing gas turbine. Nonetheless, in a parametric analysis aimed at assessing the influence of basic parameters like TIT and β, referring to a given machine makes no sense, and keeping a constant NG input appears the most sensible choice. The issues related to the use of commercial gas turbines are discussed in Sec. 7.

5 Results for Unfired Systems

Figure 3 shows net electric efficiency vs specific power output (referred to the mass flow of air entering the gas turbine compressor) for three $T_{max,CLC}$. At the lowest value of 850°C, the gas turbine is uncooled. As typical of all gas turbine cycles and combined cycles, the pressure ratio yielding maximum efficiency increases with TIT. To appreciate properly the values in the diagram, the reader must consider that efficiency is net of the power for CO_2 compression, i.e. it refers to the net output of a NG-fired system with zero CO_2 emissions.

Table 4 gives the breakdown of the power output and power consumption (also for the fired systems discussed in the next paragraph). At the low TIT considered for these unfired systems, gas turbine power output is slightly higher than 50% of total net

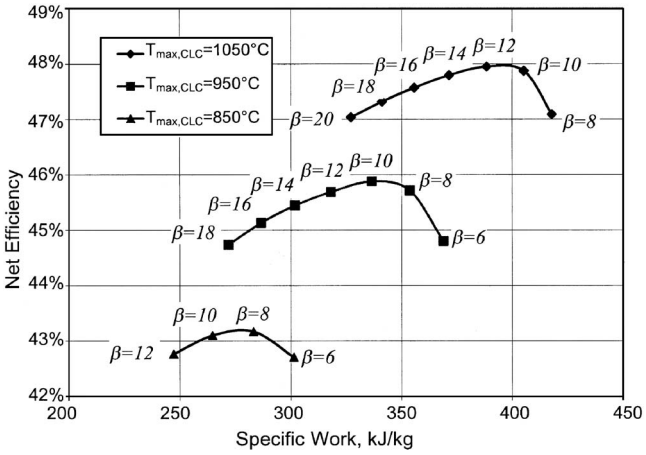

Fig. 3 Efficiency vs specific work of unfired systems

output—significantly less than in conventional, NG-fired CC. CO_2 compression accounts only for few percent of gross power output, not only because specific production is low (due to the low carbon intensity of NG), but especially because CLC makes available CO_2 at the relatively high pressure of the reduction reactor (8–12 bar).

Table 5 gives the detail of the operating conditions at the points marked in Fig. 2 for $T_{max,CLC}=850°C$. The mass flow across the gas turbine expander is smaller than that discharged by the compressor, the difference being the oxygen captured in the oxidation reactor (compare points 2 and 3=4). About half of the mass flow discharged by the reduction reactor (see difference between points 9 and 10) is removed as condensed water, leaving about 2.6 kg of ~97% pure CO_2 per kg of NG, which is then compressed to 85 bar (point 11). Steam conditions at the inlet of the HP and MP steam turbine (see points 12 and 13) are moderate due to the low temperature at the outlet of the gas turbine (443°C, see point 5).

Figure 4 shows the sensitivity to the fraction of inert material circulating in the beds together with the metal oxides. Varying the inert fraction causes significant effects on the temperatures across the reactors, because inert materials provide a means to store thermal energy. With more inert the temperature of the flow exiting the reduction reactor (point 9 in Fig. 2) increases, and a larger fraction of the fuel heating value ends up as heat recovered in the pressurized boiler between points 9 and 10 of Fig. 2.

Since such heat goes only through the steam cycle, the efficiency of its conversion into electricity is lower than the efficiency of the combined cycle; thus, when the inert fraction increases the efficiency of the whole system decreases. This effect however is minimal, unless one goes to very high inert fractions.

Figure 5 shows the results of the 2nd-Law analysis. The top portion of the stacked bars is the exergy of the liquid CO_2 made available at 85 bar.

If CO_2 capture is among the objectives one wishes to achieve with the integrated CLC-CC plant, then such exergy should not be considered a loss, but a useful outcome.

Its value is significant because it includes the work ΔEx_{mix} generated by reversibly mixing CO_2 into the atmosphere [28,29], i.e. by isothermally expanding it to its atmospheric partial pressure of about 35 Pa. ΔEx_{mix} accounts for about two thirds of the exergy of CO_2. Figure 5 shows that the major irreversibilities take place in the reactors and the steam cycle, and that they all decrease when the maximum temperature increases.

6 Results for Fired Systems

In the "fired" system, CLC provides only a fraction of the input to the thermodynamic cycle. The rest is provided by burning natural gas in a supplementary combustor placed between the exit of the oxidation reactor and the gas turbine expander.

Table 4 Power outputs and net efficiency for unfired and fired CLC systems at optimum gas turbine compression ratio. For all fired CLC systems, $T_{max,CLC}$=850°C.

	Unfired			Fired		
$T_{max,CLC}$ or T_{SF}°C	850	950	1050	1000	1100	1200
GT compression ratio	β=8	β=10	β=12	β=10	β=14	β=16
Power Output, MWe						
Gas Turbine	111.1	118.1	122.4	159.5	218.3	270.9
Steam Turbine	98.6	103.9	108.9	136.3	155.4	186
CO_2 Compressor	−4.8	−4.3	−3.9	−4.3	−3.81	−3.5
Auxiliaries	−3.3	−3.4	−3.5	−4.2	−4.8	−5.7
Net Power Output	201.6	214.3	224.0	287.3	365.1	447.7
NG input, MW_{LHV}						
Suppl. firing	–	–	–	135.2	259.5	391.0
CLC system	467.1	467.1	467.1	467.1	467.1	467.1
Net Efficiency, %	43.2	45.9	47.9	47.7	50.25	52.2
CO_2 emission, g/kWh$_e$	0	0	0	94.6	142.8	175.5

Table 5 Thermodynamic conditions at points shown in Fig. 2 for unfired plant with $T_{max,CLC}$=850°C, β=8 and fired plant with $T_{max,CLC}$=850°C, T_{SF}=1200°C, β=14 m in kg/s, p in bar, T in °C

	Unfired-$T_{max,CLC}$=850°C, β=8						
	1	2	3=4		5	6	7
M	712.1	702.5	665.3		669.2	669.2	10
p	1.01	8	7.4		1.03	1.01	8.4
T	15	277.9	850		443.5	107.2	279.2
	8	9	10	11	12	13	14
M	0.0	47.19	26.61	26.56	55.33	72.76	28.65
p	–	7.4	7.17	85	78.2	18.4	1.84
T	–	787.5	30	30	413.9	417.4	260
	Fired-$T_{max,CLC}$=850°C, T_{SF}=1200°C, β=16						
	1	2	3	4	5	6	7
M	987.5	894.9	857.7	866.1	950.7	950.7	10
p	1.01	16	14.8	14.36	1.03	1.01	16.48
T	15	406.2	850	1200	537.2	97.6	303.4
	8	9	10	11	12	13	14
M	8.37	47.19	26.58	26.56	95.25	121.53	31.64
p	16.8	14.8	14.33	85	108.56	18.4	2.76
T	303.4	787.8	30	30	505.6	509.2	260

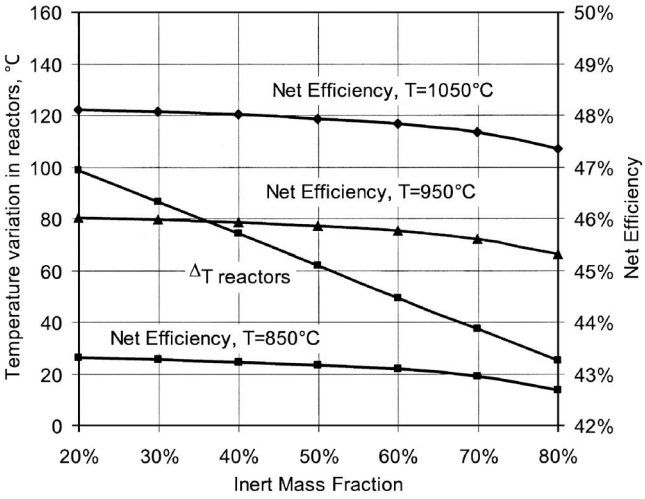

Fig. 4 Sensitivity to the mass fraction of inert material in the solids circulating in the reactors

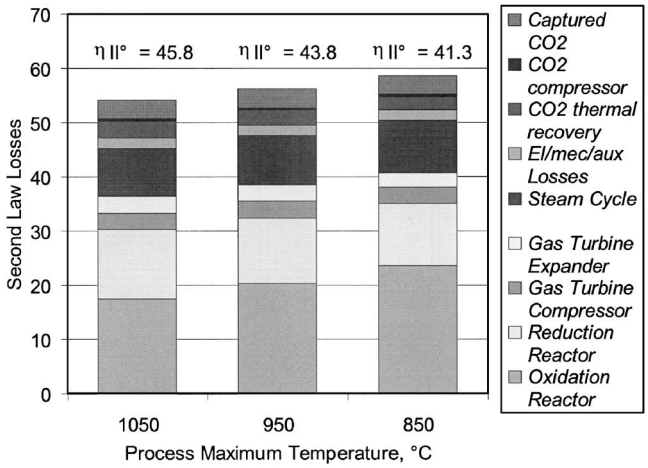

Fig. 5 Second-law losses for unfired cycles

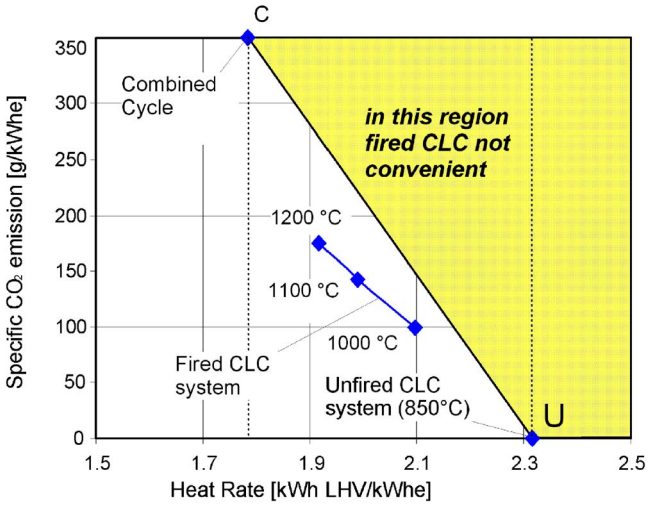

Fig. 6 Comparison between the heat rate and the CO_2 emissions of fired CLC-CC systems with those of unfired CLC-CCs (point "U") and those of conventional NG-fired CC (point "C"). In all cases, the temperature at the outlet of the reduction reactor is 850°C. A generation system comprising unfired CLC-CCs and conventional CCs would lie on the line connecting points C and U.

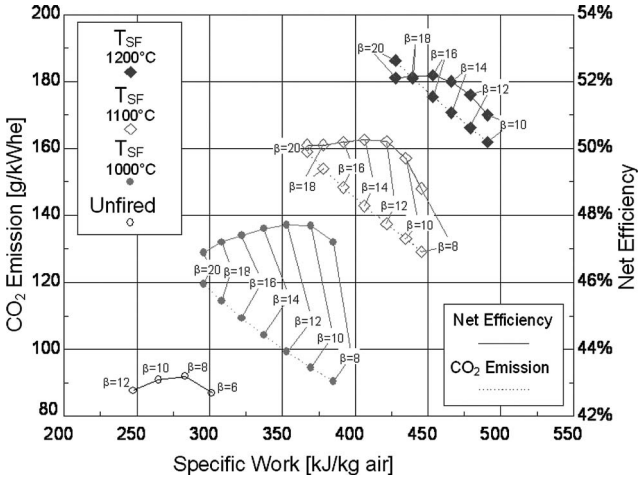

Fig. 7 Net efficiency and CO_2 emission vs specific work of fired CLC-CC systems. In all cases, the temperature at the outlet of the oxidation reactor is 850°C.

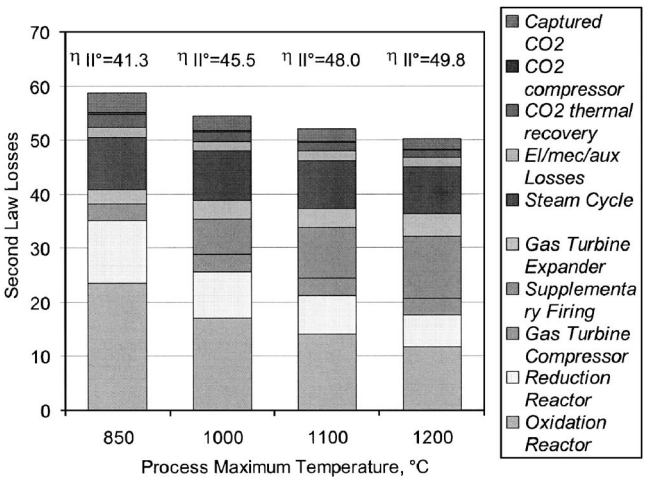

Fig. 8 Second-law losses for fired cycles with $T_{max,CLC}=850°C$

This supplementary combustor allows de-coupling the maximum temperature of CLC from the maximum temperature of the thermodynamic cycle, thus fully exploiting the capabilities of gas turbine technology independently of the constraints posed by CLC.

The ensuing increase of efficiency and power output must be weighed against the CO_2 emissions generated by the fuel burnt in the supplementary combustor. With this regard, the fired system can be considered as a linear combination of an unfired CLC-CC plant (point "U" in Fig. 6) and a NG-fired, conventional CC (point "C" in Fig. 6). The point representing its heat rate and CO_2 emissions will lie on the line connecting points "U" and "C" in Fig. 6, more specifically at a position determined by the ratio between the combustion power (m_{fuel}*LHV) of CLC and the total combustion power. Should the point representative of the fired system lie above line C–U, then the fired system would make no thermodynamic sense, because a combination of unfired CLC-CCs and conventional CCs could generate power with the same CO_2 emissions but higher efficiency—or with the same efficiency but lower CO_2 emissions. Figure 6 show that this is not the case and that fired cycle do make thermodynamic sense.

From the technological point of view, a fired cycle adds to the issues of CLC the challenge of the supplementary combustor. Being fed with an oxidizer at high temperature (in our case vitiated air at 850°C) such combustor would be subject to critical cooling issues. In order to warrant adequate operating conditions to the liner and the other components exposed to the hot gas, it is likely that some cooling fluid (air from compressor discharge or steam bled from the steam turbine) will have to be used. Since such cooling has not been considered in our calculations, our predictions for fired cycles may be somewhat optimistic.

Figure 7 shows net electric efficiency and CO_2 emissions vs specific power output for systems with increasing supplementary firing temperature and constant maximum CLC temperature of 850°C. For $T_{SF}=1200°C$, the fired CLC-CC plant reaches a net efficiency of 52% with CO_2 emissions about one half of conventional NG-fired CC.

The optimum pressure ratio increases from about 8 for the unfired plant to about 16 for the plant with $T_{SF}=1200°C$.

Table 4 gives the breakdown of power outputs, as well as efficiency and CO_2 emissions. The improvement brought about by supplementary firing can be appreciated by comparing the unfired case with $T_{max,CLC}=850°C$, $\beta=8$ with the fired case with the same $T_{max,CLC}$, $T_{SF}=1200$ and $\beta=14$: supplementary firing increases net power output by 447.7–201.6=246.1 MW_e at the expense of 391 MW_{LHV} of NG. This implies a "marginal efficiency" of 63%, about 7 percentage more than a state-of-the-art combined cycle.

Table 5 gives the details of the operating conditions (also for $T_{SF}=1200$, $\beta=14$). With supplementary firing, the operating conditions of the gas turbine (TIT, β, TOT) and of the steam cycle (evaporation pressures, superheat and reheat temperatures) can be kept much closer to those adopted in conventional CCs. Figure 8 reports the breakdown of 2nd-Law losses. The losses of CLC and the exergy of the CO_2 captured decrease when supplementary firing increases because their absolute value stays constant, while NG input increases.

7 Use of Commercial Gas Turbines

Unless CLC becomes the technology of choice for power generation, it is unlikely that manufacturers will ever offer a gas turbine designed to operate at the optimum conditions (β, TIT, mass flows) of an integrated CLC-CC plant. Instead, actual implementations of CLC will have to resort to commercial gas turbine designed for conventional, NG-fired CC. Given the outcome of the analysis illustrated in the previous chapters, using such "conventional" gas turbine should not imply great handicaps, because the optimum cycle parameters of integrated CLC-CC plants are not too far from those of commercial "second generation" heavy-duty machines, i.e., the large engines introduced in the 1980s and upgraded in the early 90s ("E" technology by General Electric, ".2" by Siemens).

When a gas turbine designed for NG-fired operation is fed by a CLC system, its pressure ratio would decrease to compensate the lower mass flow through the turbine. In fact, the gas turbine expander typically operates in "choked" conditions, i.e. at constant reduced mass flow. The turbine reduced mass flow G (a nondimensional quantity) is defined as:

$$G = m_{in,T} \cdot \sqrt{R \cdot T_0}/(p_0 \cdot A)$$

where $m_{in,T}$ is the flow at the turbine inlet, R the gas constant, T_0 and p_0 the total temperature and pressure at turbine inlet, A an equivalent flow cross section. To understand the turbine behavior under CLC conditions, one can assume that the compressor air flow is the same of the NG-fired engine (the compressor operates at the same speed and with similar β). Therefore: $m_{in,T}$ decreases, because in CLC there is no fuel addition and part of the oxygen is given up in the oxidation reactor; TIT and thus T_0 are lower; R is slightly lower, because the molecular weight of air is slightly higher than the weighted average of CO_2 and H_2O generated by the combustion of NG; for the same pressure ratio β, p_0 is lower

Table 6 Performance and cost (1 Euro=1.2 USD) of the gas turbines considered for integration in unfired CLC (Siemens V94.2) and in fired CLC (Siemens V94.2A)

	Siemens V94.2			Siemens V94.2A		
	Natural gas		CLC unfired	Natural gas		CLC fired
GT inlet air flow, kg/s	508.9	508.9	508.9	519.8	519.8	519.8
Compression ratio	11.3	11.3	10.31	13.8	13.8	13.9
Turbine inlet flow, kg/s	–	463.7	477.1	–	427.2	456.5
TIT, °C	–	1105	847	–	1245	1178
Turbine inlet pressure bar	–	11.44	9.63	–	13.56	12.6
Turbine cooling flow, %	–	10.0	2.95	–	18.54	8.1
1st nozzle cross section, m^2	–	0.430	0.430	–	0.378	0.378
Turbine outlet flow, kg/s	–	518.2	480.1	–	531.2	498.4
TOT, °C	537.2	537.8	404.9	584.4	583.9	565.0
Net power output, MW	157.0	157.4	77.7	190.0	190.0	146.5
Net LHV efficiency, %	34.4	34.4	24.99	35.3	35.7	30.94
Total Cost, M€	20.6	20.6	20.6	25.2	25.2	25.2
Specific Cost, €/kW	131.1	130.8	264.9	132.5	132.5	171.8
Source	GTW 2003	our predictions		GTW 2003	our predictions	

because the pressure loss across the CLC system (we have assumed 7.5% in Table 3) is higher than the 2%–3% typical of heavy-duty gas turbine combustors.

While the decrease of $m_{\text{in},T}$, R and T_0 tends to decrease G, the decrease of p_0 gives an opposite effect. The former typically prevails and thus β must decrease to maintain the same value of G (the actual variation depends on the specific situation). To exemplify the application of CLC with existing, commercial gas turbines we have considered two large heavy-duty machines offered by Siemens, which feature cycle parameters not too far from the optima shown in Figs. 3 and 7: V94.2 for the unfired cycle with $T_{\text{max,CLC}}=850°\text{C}$; V94.2A for the fired cycle with $T_{\text{SF}}=1200°\text{C}$.

First, these machines have been modeled to reproduce the performance quoted by the manufacturer [30]. Then, the same model has been used to predict the performances of the integrated CLC-CC plant. The results are reported in Table 6, showing that: in the unfired cycle with $T_{\text{max,CLC}}=850°\text{C}$, the V94.2 decreases its pressure ratio from 11.3 to 10.3, a value giving performance very similar to those at optimum pressure ratio (Fig. 3); in the fired cycle with $T_{\text{max,CLC}}=850°\text{C}$ and $T_{\text{SF}}=1200°\text{C}$, the V94.2A maintains its pressure ratio, which is very close to the optimum for fired CLC (Fig. 7).

The overall picture emerging from Table 6 indicates that there should be no major technical issue preventing the use of existing heavy-duty machines in CLC-CC plants. On the other hand, the last two rows of Table 6 show that the derating (i.e., lower power output following reduced TIT and smaller turbine mass flow) causes a large increase in the gas turbine specific cost (€/kW), which increases by about 30% for the fired cycle and more than doubles for the unfired cycle.

8 Economic Estimates and Comparison With Other Low-CO_2 Emission Technologies

Whether CLC will actually play a role in the mitigation of the greenhouse problem will ultimately depend on the cost of the CO_2 it can deliver for long-term storage. At the current stage of CLC development, costs are obviously very uncertain, because the experience gained so far is just at the laboratory scale [9,11]. Nonetheless, it is possible to develop preliminary comparative estimates that can give a sense of the conditions under which CLC can be competitive with other low-CO_2 emission technologies.

Table 7 summarizes the performance assumed for the plants considered for the comparative economic analysis. SC-CA refers to a Semi-Closed cycle with Chemical Absorption of CO_2 from enriched flue gases, analyzed in [18]; PO-CA refers to the plant with Partial Oxidation and Chemical Absorption of CO_2 from synthesis fuel, discussed in Ref. [6].

The CLC plants considered for the economic assessment are sized to a power output of about 400 MWe, to avoid discrepancies coming from different scales. Their performance are taken from Table 4: the unfired CLC plant is the one with $T_{\text{max,CLC}}=850°\text{C}$ and $\beta=8$, while the fired plant is the one with $T_{\text{SF}}=1100°\text{C}$ and $\beta=14$.

Investment costs have been estimated by the methodology described in [6], with some variation to account for modified market conditions and some additional assumption specific to CLC plants:

1. For fired gas turbines (NGCC,SC-CA,PO-CA) specific cost is 160 €/kWe, somewhat higher than that in Table 6 to account for turn-key installation and auxiliaries. For CLC applications the cost is made specific to the air flow (i.e., same airflow, same hardware), with a 20% reduction for unfired systems to account for the absence of the combustor and the downsizing of the electric generator.
2. For the steam section and the balance of plant (including cost of engineering and contingencies), the base specific cost is 475 and 125 €/kWe, respectively, with a scale factor of 2/3 with respect to a base 380 MW NGCC plant.
3. For plants other than CLC, we assumed the same cost of the additional hardware given in previous works [6,18], adapted to an exchange rate 1.2 USD/euro.
4. For the CLC island we have assumed a cost of 42 M€ for the unfired plant, 34 M€ for the fired plant. These figures were evaluated after preliminary estimations and must simply be regarded as an educated guess based on the authors' experience. The lower cost of the fired plant accounts for the lower volumetric flow to be handled by CLC as a consequence of higher pressure ratio and specific power output.

An additional 5% for contingencies was added for non-mature technologies, i.e., all but NGCC.

Other assumptions relevant to cost evaluation are listed in Table 8: we have considered a relatively high natural gas cost to conform to midterm projections. Investment costs are summarized in Table 9, together with the resulting Cost of Electricity (COE) and the cost of avoided CO_2.

Table 7 Reference plants for economic analysis

	NG-fired CC	SC-CA	PO-CA	Unfired CLC	Fired CLC
Net power output, MW_e	373.2	331.6	394.0	403.3	365.1
Net efficiency, %	56.10	51.09	48.47	43.17	50.25
GT output, MW_e	237.6	226.3	233.4	222.6	218.3
ST output, MW_e	139.8	121.6	177.1	197.3	155.4
Air flow rate, kg/s	625	625	625	1424.2	898.5
CO_2 emission, g/kWh	356	35.6	41.7	~0	145.7

Table 8 General assumptions for cost evaluations

Discount rate	10%/yr
Inflation rate	2%/yr
Operating plant life	25 years
Mortgage plan duration	20 years
Revenues tax rate	40%
Capital charge rate	14.91%/yr
Capacity factor	7000 h/yr
Annual insurance cost and O&M	3% of plant cost
Natural gas cost	4.50 €/GJ
Cost of storage of CO_2	10 €/ton

Given the high uncertainties in the estimates of investment cost, in Fig. 9 we have reported the specific investment cost that could make low-CO_2 emission technologies competitive with NG-fired CC without CO_2 capture as a function of a carbon tax.

The points marked on the lines show the investment cost of low-CO_2 plants as depicted by Table 9: if the carbon tax is higher than that corresponding to these points, then the plant in Table 9 would be cost-effective with respect to the NG-fired CC without capture; the opposite is true if the carbon tax is lower.

Figure 9 is not very encouraging for CLC, because the carbon tax needed to make them competitive (48–52 €/ton) is higher than that required for the competitiveness of the other technologies. However, one must also notice that capital cost estimates are very preliminary, and that the picture given in Fig. 9 may change significantly once more accurate estimates will be available. Fired CLC is not much better than the unfired cycle, but this consideration crucially depends on the cost of natural gas.

Nonetheless, Fig. 9 shows that an unfired system reaching 1050°C would represent the winning solution, calling for a relatively low carbon tax (30 €/ton), mainly due to its interesting cycle efficiency. Considering that such a solution would be much simpler to develop, operate and maintain than PO-CA and SC-CA (once the critical design issues of the CLC island are solved) and that it would benefit of the virtual absence of NO_x and CO emission, the potential of CLC systems should not be underestimated.

9 Conclusions

Integrated CLC-CC plants offer the potential for generating electricity with near-zero emissions, since the working fluid of the thermodynamic cycle—vitiated air—is segregated from the combustion products.

Unfired configurations with maximum process temperature 850–1050°C can reach net efficiencies ranging 43%–48%. Fired configurations where temperature is raised from 850 to 1200°C by supplementary firing can achieve 52% net efficiency with CO_2 emission about one-half of those of a modern combined cycle.

A preliminary economic analysis indicates that the cost of CO_2 avoided by integrated CLC-CC plants with maximum CLC temperature 850°C is about 50 €/ton for both the fired and unfired version. On one hand, this compares unfavorably with the cost of alternative technologies like Semi-Closed Cycles or Partial Oxidation with Chemical Absorption (35 €/ton); on the other, these economic estimates are subject to great uncertainty and could change significantly once more accurate estimates will be available. An important potential exists for unfired CLC systems operating at higher temperatures (i.e., over 1000°C), provided that their technical feasibility can be demonstrated by further R&D developments.

Table 9 Investment costs, cost of electricity (COE) and cost of avoided CO_2 for the same plants listed in Table 7

	NG-CC	PO-CA	SC-CA	Unfired CLC	Fired CLC
Gas Turbine M€	38.02	37.34	41.64	69.31	54.66
Steam section M€	66.44	77.78	60.54	83.58	71.29
Power plant BOP M€	46.93	58.98	52.21	61.64	56.55
Other Equipment M€	0.00	42.58	31.08	42.00	33.88
Net Capital Cost M€	151.38	216.69	185.47	256.52	216.38
Specific Cost	405.6	550.0	559.3	636.1	592.7
COE investment €/MWh	8.69	11.79	11.99	13.63	12.70
COE o&m €/MWh	2.04	2.45	3.35	2.45	2.45
COE fuel €/MWh	29.46	34.11	32.35	38.29	32.90
COE CO_2 storage €/MWh	0	3.78	3.62	4.72	2.59
COE Total €/MWh	40.19	52.12	51.31	59.09	50.64
Cost of Avoided CO_2 €/ton	–	37.14	34.04	52.06	48.10

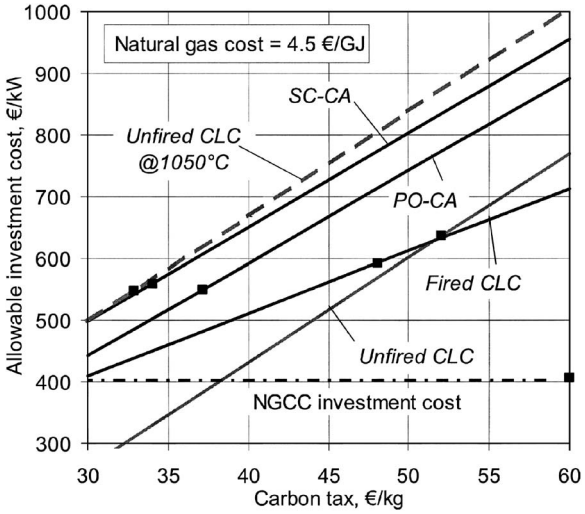

Fig. 9 Specific investment cost of a power plant with CO_2 capture that gives the same COE of a NG-fired CC without CO_2 capture. The points marked on the lines identify the situation of the plants in Table 8.

Acknowledgment

The authors gratefully acknowledge the support of the ENI group for the development of the research presented in this paper.

Nomenclature

G = Reduced mass flow, see equation in Sec. 7
m = Mass flow, kg/s
p = Pressure, bar
T = Temperature, °C
$T_{max,CLC}$ = Maximum temperature of CLC
T_{SF} = Temperature of supplementary firing, °C
β = Gas turbine pressure ratio

Acronyms

CC = Combined cycle
COE = Cost of electricity
GT = Gas turbine
HHV, LHV = Higher/lower heating value, MJ/kg
HP, MP, LP = High/medium/low pressure
HRSG = Heat recovery steam generator
NG = Natural gas
OR = Oxidation reactor
PO-CA = Partial oxidation-chemical absorption
RR = Reduction reactor
SC-CA = Semi-closed cycle chemical absorption
ST = Steam turbine
TIT = Turbine inlet temperature
TOT = Turbine outlet temperature

References

[1] Williams, R. H., 2002, "Toward Zero Emissions for Trasnportation Using Fossil Fuels," in VIII Biennal Asilomar Conference on Transportation, Energy and Environmental Policy Managing Transtions, edited by K. S. Kurani and D.

Sperling, Trasnprotaion Research Board, Washington, D.C.
[2] Lackner, K. S., 2002, ''Carbonate Chemistry for Sequestering Fossil Carbon,'' Annual Rev. Energy and Environment, **27**, pp. 193–232.
[3] Chapel, D. G., and Mariz, C., 1999, ''Recovery of CO_2 From Flue Gases: Commercial Trends,'' presented at the Canadian Society of Chemical Engineers annual meeting, October 4–6, 1999, Saskatoon, Saskatchewan, Canada.
[4] Shrikar, C., Amitabh, G., and Balazs, H., 2001, ''Advanced Technology for the Capture of Carbon Dioxide From Flue Gases,'' First National Conference on Carbon Sequestration Washington, DC, May 15–17, 2001.
[5] Andersen, T., Kvamsdal, H. M., and Bolland, O., 2000, ''Gas Turbine Combined Cycle With CO_2 Capture Using Auto-Thermal Reforming of Natural Gas,'' ASME paper 2000-GT-0162.
[6] Lozza, G., and Chiesa, P., 2002, ''Natural Gas Decarbonization to Reduce Low CO_2 Emission From Combined Cycles. Part A: Partial Oxidation—Part B: Steam-Methane Reforming,'' J. Eng. Gas Turbines Power, **124**, pp. 82–95.
[7] Kiga, T., Takano, S. et al., 1997, ''Characteristic of Pulverized-Coal Combustion in the System of Oxygen/Recycled Flue Gas Combustion,'' Energy Convers. Manage., **38**, Suppl., pp. S129–S134.
[8] Wilkinson, M. B., Boden, J. C., Gilmartin, T., Ward, C., Cross, D. A., Allam, R. J., and Ivens, N. W., 2002, ''CO_2 Capture From Oil Refinery Process Heaters Through Oxyfuel Combustion,'' paper B4-1, Kyoto, Japan, October 2002.
[9] Ishida, M., and Jin, H., 1997, ''CO_2 Recovery in a Power Plant With Chemical Looping Combustion,'' Energy Convers. Manage., **38**, suppl., pp. S187–S192.
[10] Mattison, T., Lyngfelt, A., and Cho, P., 2001, ''The Use of Iron Oxide as an Oxygen Carrier in Chemical-Looping Combustion of Methane With Inherent Separation of CO_2,'' Fuel, **80**, pp. 1953–1962.
[11] Mattison, T., and Lyngfelt, A., 2001, ''Capture of CO_2 Using Chemical-Looping Combustion,'' presented at First Biennial Meeting of the Scandinavian-Nordic Section of the Combustion Institute, April 18–20, Göteborg, Sweden.
[12] Lozza, G., 1990, ''Bottoming Steam Cycles for Combined Gas-Steam Power Plants: a Theoretical Estimation of Steam Turbine Performance and Cycle Analysis,'' Proc. 1990 ASME Cogen-Turbo, New Orleans, LA, pp. 83–92.
[13] Consonni, S., 1992, ''Performance Prediction of Gas/Steam Cycles for Power Generation,'' Ph.D thesis 1983-T, Mechanical and Aerospace Engineering Dept., Princeton University, Princeton, NJ.
[14] Chiesa, P., Consonni, S., Lozza, G., and Macchi, E., 1993, ''Predicting the Ultimate Performance of Advanced Power Cycles Based on Very High Temperature Gas Turbine Engines,'' ASME Paper No. 93-GT-223.
[15] Macchi, E., Consonni, S., Lozza, G., and Chiesa, P., 1995, ''An Assessment of the Thermodynamic Performance of Mixed Gas-Steam Cycles. Part A: Intercooled and Steam-Injected Cycles,'' J. Eng. Gas Turbines Power, **117**, pp. 489–498.
[16] Consonni, S., and Larson, E. D., 1996, ''Biomass-Gasifier/Aeroderivative Gas Turbine Combined Cycles. Part A and B,'' J. Eng. Gas Turbines Power, **118**, pp. 507–525.
[17] Consonni, S., Larson, E. D., Kreutz, T. G., and Berglin, N., 1998, ''Black Liquor Gasifier/Gas Turbine Cogeneration,'' J. Eng. Gas Turbines Power, **120**, pp. 442–449.
[18] Chiesa, P., and Consonni, S., 2000, ''Natural Gas Fired Combined Cycles With Low CO_2 Emissions,'' J. Eng. for Gas Turbine and Power, Trans. ASME, **122**, no. 4, pp. 429–436, July.
[19] Campanari, S., and Macchi, E., 1998, ''Thermodynamic Analysis of Advanced Power Cycles Based Upon Solid Oxide Fuel Cells, Gas Turbines and Rankine Bottoming Cycles,'' ASME Paper No. 98-GT-585.
[20] Stull, D. R., and Prophet, H. (Project Directors), 1971, *JANAF Thermochemical Tables*, 2nd ed., U.S. National Bureau of Standards, Washington, DC.
[21] Gardiner, W. C., ed., 1984, *Combustion Chemistry*, Springer-Verlag, New York.
[22] Schmidt, E., 1982, *Properties of Water and Steam in S.I. Units*, Springer-Verlag, Berlin.
[23] AspenTech, 2002, ''Aspen Plus rel. 11.1,'' Reference Manual.
[24] Reid, R. C., Prausnitz, J. M., and Poiling, B. E., 1987, *The Properties of Gases and Liquids*, 4th ed., McGraw–Hill, New York.
[25] Reynolds, W. C., 1986, ''The Element Potential Method for Chemical Equilibrium Analysis: Implementation in the Interactive Program STANJAN. Version 3,'' Deptartment of Mechanical Engineering, Stanford University, Stanford, CA.
[26] Chiesa, P., and Macchi, E., 2002, ''A Thermodynamic Analysis of Different Options to Break 60% Electric Efficiency in Combined Cycle Power Plants,'' ASME Paper No. GT-2002-30663.
[27] Johansson, E., Lyngfelt, A., Mattison, T., and Johnsson, F., 2003, ''Gas Leakage Measurements in a Cold Model of an Interconnected Fluidized Bed for Chemical-Looping Combustion,'' Powder Technol., **134**, pp. 210–217.
[28] Bejan, A., 1988, *Advanced Engineering Thermodynamics*, John Wiley and Sons, New York.
[29] Consonni, S., 1990, ''Entropy Analysis of Mixed Gas/Steam Cycles,'' Proc. 45th ATI Congress (Cagliari, Sept. 1990), pp. IIID-49-60, SGE Publisher, Padova, Italy.
[30] Gas Turbine World Handbook 2003, Pequot Publishing, Southport, CT.

Richard Knight
e-mail: richard.knight@rolls-royce.com

Mitsuru Obana
e-mail: mitsuru.obana@rolls-royce.com

Rolls-Royce plc,
Derby, UK

Christer von Wowern
e-mail: christer.von.wowern@power.alstom.com

Athanasios Mitakakis
e-mail: athanasios.mitakakis@power.alstom.com

Demag Delaval Industrial Turbomachinery

Erhard Perz
Sim Tech Simulation Technology,
Austria
e-mail: e.perz@simtechnology.com

Mohsen Assadi
e-mail: mohsen.assadi@vok.1th.se

Björn F. Möller
e-mail: bjorn.fredriksson@vok.1th.se

Lund Institute of Technology,
Lund, Sweden

Pratyush Sen
e-mail: pratyush.sen@ncl.ac.uk

Ian Potts
e-mail: ian.potts@Newcastle.ac.uk

University of Newcastle,
Newcastle, UK

Alberto Traverso
e-mail: alberto.traverso@unige.it

Leonardo Torbidoni
e-mail: torbidoni@unige.it

Università di Genova,
Genova, Italy

GTPOM: Thermo-Economic Optimization of Whole Gas Turbine Plant

Trends towards distributed power generation and the deregulation of energy markets are increasing the requirement for software tools that optimize power generation plant design and operation. In this context, this paper describes the GTPOM (thermo-economic optimization of whole gas turbine plant) European project, funded in part through the European Commission's 5th Framework Programme, focusing on the development and demonstration of an original software tool for the thermo-economic analysis and optimization of conventional and advanced energy systems based on gas turbine plant. PSEconomy, the software tool developed during the GTPOM project, provides a thermo-economic optimization capability for advanced and more-conventional energy systems, enabling the complex trade-offs between system performance and installed costs to be determined for different operational duties and market scenarios. Furthermore, the code is capable of determining the potential benefits of innovative cycles or layout modifications to existing plants compared with current plant configurations. The economic assessment is performed through a complete through-life cycle cost analysis, which includes the total capital cost of the plant, the cost of fuel, O&M costs and the expected revenues from the sale of power and heat. The optimization process, carried out with a GA-based algorithm, is able to pursue different objective functions as specified by the User. These include system efficiency, through-life cost of electricity and through-life internal rate of return. Three case studies demonstrating the capabilities of the new tool are presented in this paper, covering a conventional combined cycle system, a biomass plant and a CO_2 sequestration gas turbine cycle. The software code is now commercially available and is expected to provide significant advantages in the near and long-term development of energy cycles.
[DOI: 10.1115/1.1850511]

Introduction and Objectives

In the current energy market environment of increasing liberalization there is a growing need for analysis tools that combine elements of power generation plant thermodynamic performance and through-life economic performance. In addition, the ability to enable detailed trade-off analysis to be performed between performance and cost to maximize through-life economics of power generation plant is becoming critical for station owners and developers. A need was therefore identified for an integrated software design tool that provides:

1. Full thermodynamic performance evaluation capability;
2. Detailed through-life economic performance evaluation capability based on User-selected economic, operational and market scenarios;
3. Complex through-life economic and performance optimization capability.

The objective of the GTPOM project reported in this paper was therefore to specify, design and implement a software tool delivering this functionality.

Contributed by the International Gas Turbine Institute (IGTI) of ASME for publication in the JOURNAL OF ENGINEERING FOR GAS TURBINES AND POWER. Paper presented at the International Gas Turbine and Aeroengine Congress and Exhibition, Vienna, Austria, June 13–17, 2004, Paper No. 2004-GT-54200. Manuscript received October 1, 2003; final manuscript received March 1, 2004. IGTI Review Chair: A. J. Strazisar.

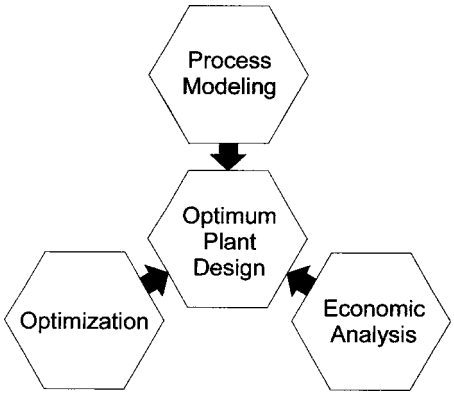

Fig. 1 Basic system structure

PSEconomy: General Structure

The goal of the GTPOM project was to integrate the following capabilities into a single software package, as shown in Fig. 1:

a. *process modeling capability*
b. *economic analysis capability*
c. *optimization capability*

These integrated capabilities make it possible to analyze the trade-off between high efficiency, typically requiring higher investment costs and lower performance with higher operating costs. The ability to analyze this trade-off systematically can radically improve the economic performance of a power plant project.

Basic Concept. The basic concept of PSEconomy requires the calculation of the following data for individual components: *investment costs and operating costs and revenues*.

A plant model can then be established, where individual component results are summated to produce the respective costs for the complete plant (it is also possible to calculate costs on assembly level overriding results from component level). Such a plant model also allows the calculation of fuel mass flow, delivered electricity and other parameters under given operating conditions. When fuel prices and tariffs are known, this enables the determination of operating costs and revenues for given operating conditions. By defining an operational scenario, it is possible to determine all system costs and revenues. This means that the models of a process component include investment cost correlations for the design models and operating cost correlations for the operating models of the component.

Operating Scenarios. In order to allow the assessment of the economic aspects of plant operation, it is necessary to define the operational scenarios under which the system will operate in service. It is possible to define the operating scenario via operating data over a specified period with good granularity.

In PSEconomy a number of representative operating cases are provided in order to make operational scenario definition more straightforward, although the software is sufficiently flexible to enable the User to specify their own scenario as required. All operating cases share the same set of input and output variables which are distinguished by the *values for the input variables and annual operating hours*.

Input variables will frequently change over the operating years. For example, fuel cost might be subject to an annual escalation. PSEconomy provides several rules that allow the User to define these changes in a convenient way.

Implementation. The commercially available heat balance and process modeling package IPSEpro was chosen as the basis for the development because it provides functionality that is essential for integrating the capabilities described above.

Like other heat balance programs, IPSEpro allows plant models to be assembled graphically from individual component models. However, IPSEpro does not limit the User to predefined component models. Instead, it organizes the component models in model libraries, and provides MDK, Model Development Kit, for creating new model libraries and component models. This functionality is used for implementing the component cost correlations.

PSE, IPSEpro's Process Simulation Environment, also provides well-defined interface functions that allow its integration with other software modules. This functionality was required for integrating PSE and PSEconomy.

PSEconomy has been implemented as a general applicable program that is independent from any particular field of application. This guarantees a high level of flexibility and the capability to adjust it for the requirements of a particular user.

The adjustment for a particular field of application, like gas turbine plants, is done via a specialized IPSEpro model library and PSEconomy project templates.

Component Capital and Noncapital Cost Modeling

A key part of the GTPOM project was the development of a library of new component models dealing with the simulation of thermodynamic performance and the calculation of through-life cycle costs. The modeling work was performed using IPSEpro-MDK. MDK provides all capabilities required for describing the process components mathematically and to compile them into a special component model library (the GTPOM library).

The components that were developed can be grouped into the following categories.

1. *Gas Turbine*:
   Including: Inlet Duct/Compressor/Diffuser/Combustor/Turbine/Exhaust volute/Gas Turbine Gearbox/Gas Turbine Generator;
2. *Steam Turbine*:
   Including: Steam Turbine/Steam Condenser/Deareator/Steam Turbine Gearbox/Steam Turbine Generator;
3. *Heat exchangers*:
   Including: Intercooler/Aftercooler/Recuperator/Economizer/Superheater/Evaporator/Humidifier/Exhaust Gas Condenser;
4. *Biomass related components*:
   Including: Gasifier and Cyclone/Fuel Drier/Combustion Reactor/Hot Gas Filter;
   Other novel components:
5. Including: CO_2 plant/Synthetic gas combustor.

A small number of additional performance and cost models were created which effectively summate/combine the individual component models in order to enable the calculation of overall cycle parameters such as total cycle efficiency and cost of electricity. Special components were also included to specify and determine external costs such as fuel cost, the value of heat and electricity costs/prices. These elements also facilitated the exchange of information between IPSEpro-PSE and PSEconomy.

The GTPOM library enables the User to build an extensive number of gas turbine based cycles and to analyze all related thermodynamic as well as economic issues. The gas turbine modules were built with particular focus on single shaft industrial engines, while all components were specifically intended to work in gas turbine based thermodynamic cycles.

The level of complexity of the components has been a trade off between the level of accuracy that is expected from such a tool and its operability. In particular, it was found that although a high level of complexity would increase the accuracy of the result, it would also have a detrimental effect on the robustness of the models and simultaneously it would increase the calculation time to unacceptable levels.

For all components, models have been made available that allow their performance calculation at both design point and off design conditions. Additionally, in the design point models, an

approximate calculation of the ''hardware'' features of the components has been included. The computed geometric characteristics in conjunction to the thermodynamic properties of the components were employed for the estimation of their respective capital cost. The cost correlations for each of the components are based on the industrial experience of the consortium members and are intended to provide a preliminary estimation of component economics. Examples of the component cost correlations are as follows:

GT expander cost=*f*(geometrical size, number of stages, firing temperature)

CO_2 plant cost=*f*(vol % CO_2, gas flow)

HEX cost=*f*(area, material, type of HEX).

The part load performance models also include correlations for estimating the through-life maintenance costs of the plant. Computation of these costs can take place at a component level in principle but it is also possible to calculate them on an assembly level in order to provide a greater level of accuracy. For instance, the maintenance cost for the ''gas turbine assembly'' has been correlated in terms of the GT power output and its firing temperature.

Component costs represent just a fraction of the final Total Capital Investment (TCI). TCI is nominally divided into three categories:

i. Direct Costs (DC), which are the costs of all the permanent equipment such as hardware components and devices, instrumentation and controls, architectural and civil work.
ii. Indirect Costs (IC), that relate to the completion of the plant, e.g., engineering, supervision, and financial contingencies.
iii. Other Outlays (OO), which include items such as the startup costs, licensing costs and working capital (fuel stocks, etc.) [1–3].

The calculation of all these additional expenditures can be performed in the tool either by imposing known costs for each item or through an estimating function based on component costs. In this way, a very flexible cost platform is available to the user who can apply it to a very wide range of possible cases from the construction of a new power plant to the re-powering of existing plants.

Unlike fuel and maintenance costs, which are continuous or repetitive in nature, the TCI cost is a one-time cost or is split between those years at the start of the project. In this case, the allowances for funds used during construction paid to the shareholders or banks need to be included in the TCI.

Investment Analysis

Once all the capital costs have been assessed and fixed, the full-life cycle cost analysis is necessary to estimate the economic performance of the plant during its operating life.

The main capabilities of the economic analysis are to model economic and market scenarios under which the plant will operate, and to determine throughlife operational costs based on a corresponding User-defined plant operational scheduling scenario. The through-life costs are calculated using off-design performance analysis and User-specified financial assumptions [4–6].

Depreciation and Capital Costs. The first element of costs that must be recovered by the production of heat and electrical power is the fixed capital costs. In this respect, depreciation reflects the fact that the value of an asset tends to decrease with age (or use) due to deterioration that will ultimately lead to the retirement of the asset. In addition, depreciation is an accounting mechanism for repaying the original cost of the plant, serving to reduce applicable taxes during the plant's operating life. In the economic analysis module within PSEconomy, several predefined depreciation methods can be chosen or customized by the User to best reflect the actual economic and industrial environment for the operation of the plant.

Interest paid on borrowed capital is also critical in determining the overall project economics, and this is therefore an integral part of the economic analysis software. In PSEconomy a general approach has been implemented such that the User can select a number of funding sources each of which could have a different borrowing rate. As has already been mentioned, any interest paid to investors during the construction phase of the project is considered in the calculation of TCI.

Finally, additional items such as insurance or property taxes have been included in the capabilities of the economic analysis.

Table 1 Investment parameters

Global Financial Parameters
• Average Rate of Return
• Payback Period
• Discounted Payback Period
• Net Present Value
• Benefit-Cost Ratio Method
• Internal Rate of Return

Variable Costs and Revenues. The fuel consumption of the system and other materials of supply such as ammonia or water are provided to the economic analysis module as inputs since they are derived by the thermodynamic performance analysis. User-specified escalation rates are used to determine variable costs over the project life unless otherwise specified by the User. In this way, the economic scenario can reflect actual or forecast trends of tariffs for gas, diesel fuel, electricity and heat. Moreover, the economic scenario in different countries all over the world can be easily implemented and the economic performance of the same plant under different energy and environment policies can therefore be simulated.

Finally, if taxation is imposed on plant emissions, the environmental costs can be ''internalized'' into the economic calculation and the effect of different carbon tax levels on the optimal plant configuration can be assessed [8,9].

Maintenance costs, derived from the operational scenario of the plant and the component O&M cost models, are also included in the calculations.

Investment Assessment. Before capital is invested in a project, it is necessary to estimate the expected profit from the investment. Most capital expenditure decisions involve choosing the ''best'' of a number of alternative solutions that, often, are mutually exclusive. Thus, calculating the profitability of an investment and choosing the best alternative are important objectives of the economic analysis. In the GTPOM project a *deterministic investment analysis* has been employed, where all the cost coefficients or discount rates can be varied year by year but are set by the User.

The flexible economic platform allows the User to define the annual tariff scenario for the revenues expected from the sale of electricity and heat. These are then compared with the annual capital and variable costs to give the global economic performance of the plant. Within PSEconomy, this can be assessed by the use of the standard financial parameters listed in Table 1.

Current/Constant Money. The economic analysis module provides the facility to switch between current and constant money analysis. This option distinguishes between ''nominal'' and ''real'' interest rates and monetary value. In general, a current-money analysis makes the plant appear more costly than would be expected in today's cost values, whereas a constant money analysis presents the plant as less expensive than it ultimately will be. An economic analysis can be carried out either in current money by including the effect of inflation in projections of capital expen-

ditures, fuel costs, O&M costs, etc., or in constant money by excluding inflation and considering only the real escalation rate. The choice between the two different methods depends on the purpose of the analysis.

The relationship between the real interest rate (r_r) and the nominal interest rate (r_n) is

$$(1+r_n)=(1+r_i)(1+r_r), \tag{1}$$

where r_i is the general inflation rate.

The thermo-economic optimization [10] of power plants using PSEconomy becomes feasible in practice since all of the economic parameters described above can be used as the objective function for the optimization procedure.

Optimization Algorithm

The optimization module enables the user to optimize a selected criterion through varying a number of system parameters that he/she selects. The optimization module can be used in two ways:

1. operational optimization
2. life cycle optimization

Operational Optimization. The task in the case of operational optimization is to "operate a given plant in the best way." It is always restricted to the optimization of an individual point of operation. The objective is to find the best values for one or more operating parameters.

Life Cycle Optimization. The task in the case of life cycle optimization is to "find the best design parameters for a given load profile." The objective is to find the best value for one or more design parameters so that one of a number of preselectable financial measures is optimized. These measures include internal rate of return, payback period and net present value of investment.

Life cycle optimization always involves evaluation of a complete operating profile.

Implementation. As part of the GTPOM project, an optimization module with evolutionary search algorithm was developed. The optimizer was required to adjust a relatively large number of decision variables, up to 17 in the studies reported in this paper, whilst the objective functions to be optimized were available only as discrete calculated values. The evolutionary search method chosen was a Genetic Algorithm (GA), which generates improved solutions by mimicking the biological processes of natural selection. In this method, pioneered by Holland [7], a population of solutions is allowed to evolve over a number of generations. Here populations of 300–500 individual solutions were typically allowed to evolve over 50–100 generations. The initial population is generated by random distribution over the prescribed range of the decision variables. All the decision variables for each population member solution are coded as a binary string, analogous to a chromosome in a biological system. For the present application each real or integer variable could be adequately represented by an 8 bit substring, giving a total string length of 136 bits for a 17 variable problem. The PSE/PSEconomy solver is then run to evaluate the objective function, be it thermal efficiency, cost of electricity or internal rate of return, for each population member. A "breeding pool" of relatively good or "fit" solutions is then selected from the current population, and pairs of individuals are randomly selected from this pool and "mated" to produce pairs of "child" individuals for the next generation. This process of selection and "mating" is repeated, maintaining the population size, for a specified number of generations or until the difference between the best and average fitness values of the population falls to a specified level, at which stage the best individual is taken to be close to optimum.

Various methods of selecting the "breeding pool" of fit solutions from the current population are described in the literature [11,12], but tests showed a two challenge tournament method to be very effective for the present class of problem. In this method, successive trios of individuals are drawn randomly from the population and their fitness is compared, the best of the trio being passed to the mating pool. "Mating" of solution pairs is effected by two operations: crossover and mutation. In single point crossover, the binary string chromosomes of the two parents are cut at some random position and the final sub-strings are interchanged to produce two new "child" chromosomes. Mutation is a secondary operator that introduces a small probability that part of the coding of any new "child" chromosome may be deliberately changed to maintain diversity of the population. Each child string is then decoded to produce the physical decision variables for the new population member.

Because of the nature of the thermoeconomic problem, it is entirely possible that some combinations of decision variable values in the search space will be incompatible, and will cause the solver to fail. In such cases a failure flag is sent to the optimizer, which then allocates an arbitrary low fitness to this population member so that it is subsequently discarded in the selection process. This robust fault tolerance of the GA is essential for the present application.

Test Cases: CCGT, Biomass Plant and CO_2 Sequestration Plant

In order to understand the benefit of PSEconomy in practical applications, a number of thermoeconomic optimization demonstration case studies were performed as part of the program. These are based on a conventional combined cycle system, a biomass plant and a CO_2 sequestration gas turbine cycle.

The conventional combined cycle plant (Fig. 2) is a standard two-pressure nonreheat system where a single gas turbine is used as the topping cycle and the heat from the exhaust is recovered via a series of heat exchangers.

The biomass plant model (Fig. 3) uses a pressurized gasifier model, integrated into a combined cycle plant where the cooled and filtered synthetic gas is fired in a gas turbine. Gasification takes place in a gasification reactor without the presence of air, thus giving a higher heating value of the fuel gas. Heat is supplied in a second (combustion) reactor where char and nonvolatile material in the fuel is burnt with air. Cooling of the fuel gas and the exhaust is made before the gases are separately cleaned in hot gas filters.

The CO_2 sequestration cycle (Fig. 4) is modeled as a standard two-pressure combined cycle system with postcombustion CO_2 separation. All the steam produced at the lower pressure is used for the separation of carbon dioxide, resulting in a significant efficiency reduction compared with a conventional combined cycle system. The separation system is based on chemical absorption using amines as the absorbent for the carbon dioxide.

In order to determine the potential economic merits of each of these cycles prior to, and following, optimization by the new software, a representative operational and economic scenario is required within which the three cycle configurations are required to operate. However, in view of the fact that the prediction of future market parameters is highly speculative, a simplified through-life operational and economic scenario was developed for the purposes of this exercise in order to

a. Demonstrate the capability of the software to handle both design point and off-design engine operation;
b. Model market price fluctuations and volatility;
c. Model realistic variations in future gas prices;
d. Demonstrate the ability of the software to make trade-offs between capital cost and operations and maintenance cost in order to achieve the optimal through-life performance.

The outline of the selected operational scenario is shown in Fig. 5. Four operating cases are specified over a year, and this is assumed to repeat over the operational life of the plant, in this case

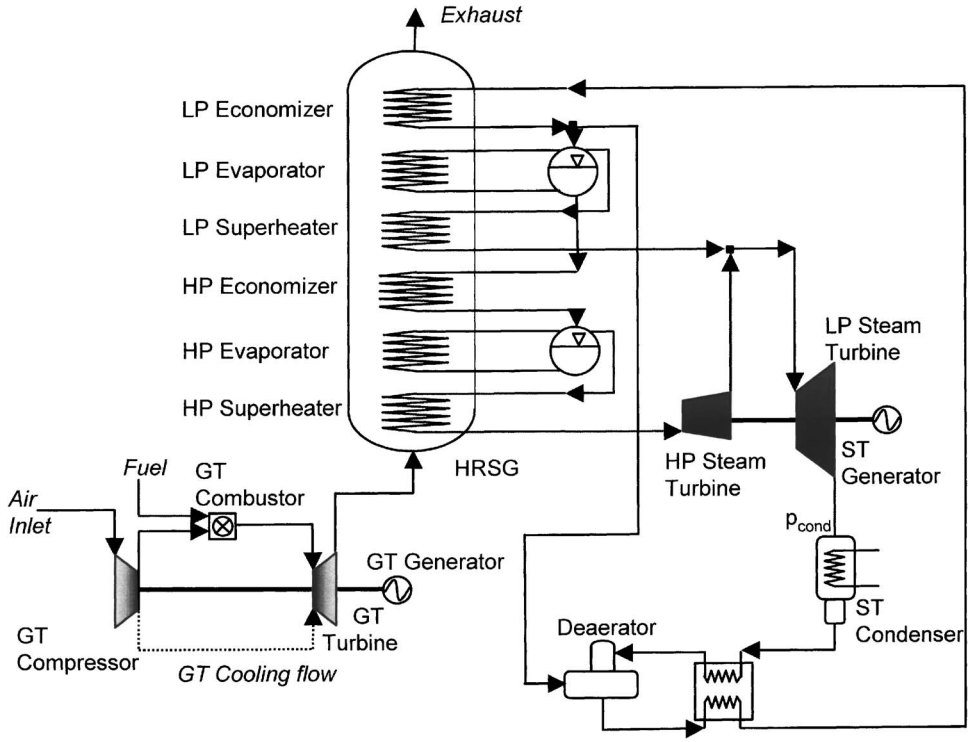

Fig. 2 CCGT cycle configuration

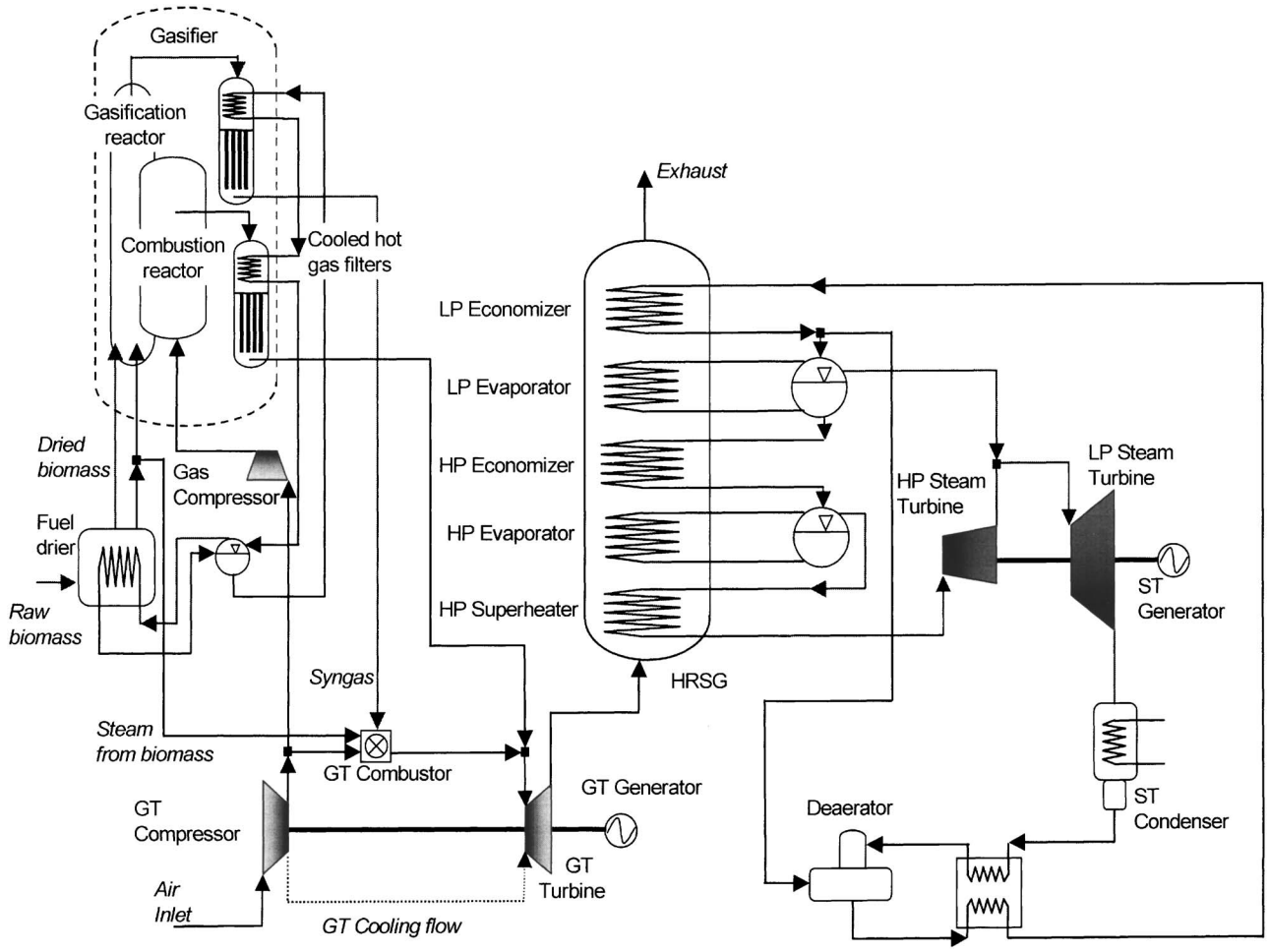

Fig. 3 Biomass cycle configuration

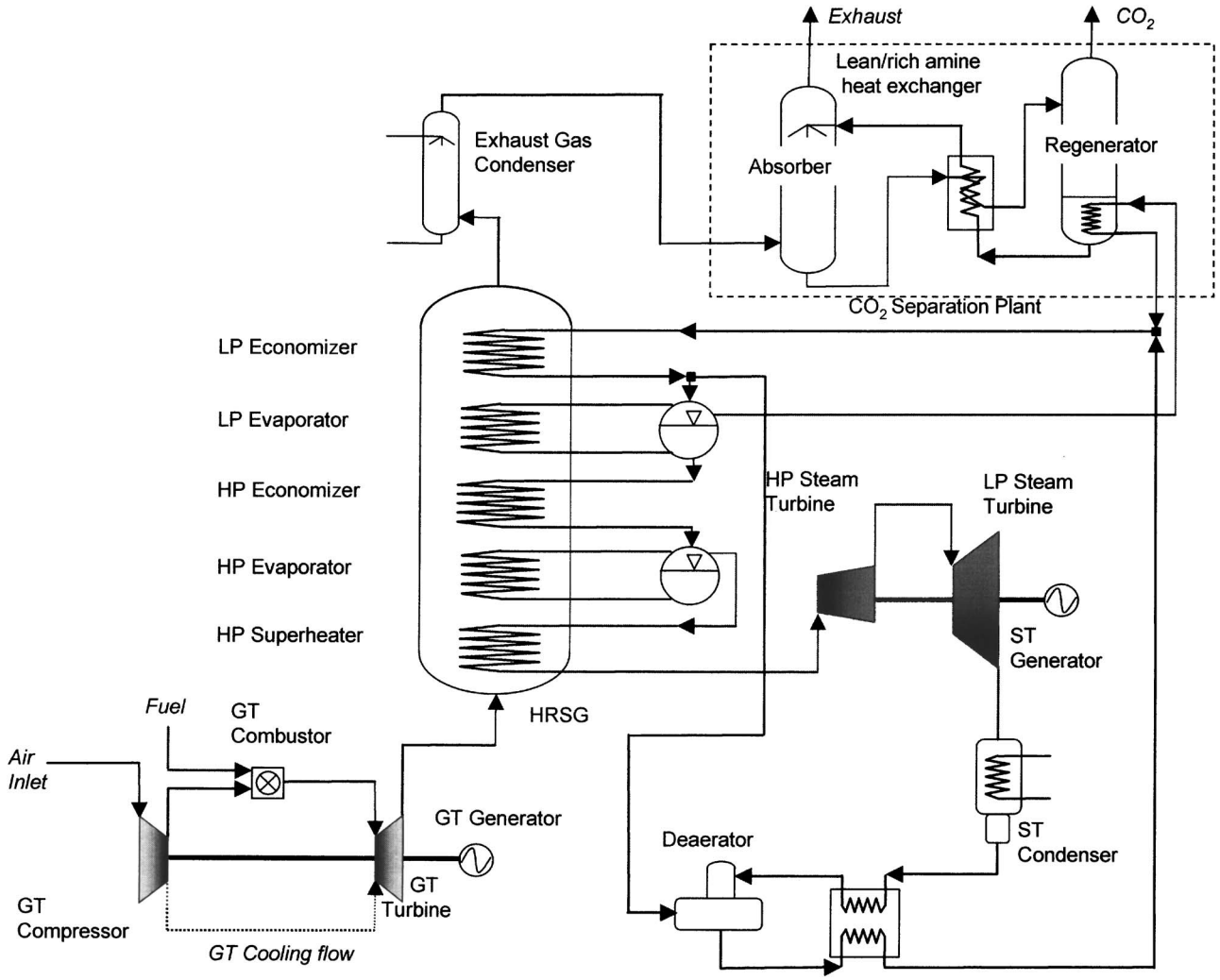

Fig. 4 CO_2 sequestration cycle configuration

15 years. The operation of the three systems are specified at two power outputs (100% and 70%) in order to model the design-point and part-load behavior of the systems. Furthermore, in order to model market price volatility, for the majority of yearly operation the selling price of energy generated by the systems into the energy market is assumed to be 5 € c/kWh, a typical market value for exported energy within Europe. However, for some periods of the year this figure is assumed to increase to 10 € c/kWh as shown to reflect the types of price surge that may occur, for example, as a result of power shortfalls.

Throughout the case studies it was assumed that each power generation system achieves an average availability of 95%, hence the total number of hours in Fig. 5 is 8322 over the period of 12 months. A financial discount rate of 6.5% was assumed throughout the case studies.

A key component of the operational costs of the power plants over their 15 year assumed operational life is fuel costs. The software determines the fuel costs based on the fuel price and the co-incident consumption of the power plant based on the instantaneous point of operation on the operating characteristic. For the CCGT and the CO_2 sequestration plant cases, the natural gas prices assumed over the 15 years of the project, whilst speculative, were derived from a number of gas price predictions taken from published sources within EU Member States, which average out at the equivalent of around 1.5 € c/kWh. For the biomass case, the assumed price of biomass fuel (wood chippings) was around 1 € c/kWh equivalent.

The studies described in this paper relate to the optimization of through-life internal rate of return (IRR), this being one of the standard financial parameters selectable by the User within PSEconomy for the optimizer objective function. For each of the cycle cases up to seventeen decision variables were used for the optimization process. These included major component parameters from the cycles, suitably selected to ensure that the design optimization process was performed appropriately. For example, 9 parameters from gas turbine components and 8 parameters from steam turbine and heat exchanger components were selected as the decision variables for the CCGT case study, and these included GT compressor stage loading, GT compressor pressure ratio, GT turbine inlet temperature and various heat exchanger temperatures and pressures. Similar (or equivalent) parameters were selected for the biomass and CO_2 sequestration examples.

As previously mentioned, populations of 300–500 individual solutions were allowed to evolve typically over 50–100 generations. This population range ensures (in most cases) that software convergence is captured in the first generation. The number of generations (50–100) generally provides sufficient confidence that the optimal solution is captured during the optimization process.

The impact of the optimization process can be clearly seen from the results shown in Tables 2, 3, and 4.

For these studies, operating within the bounds of the financial and operating assumptions detailed earlier, the IRR improvements have been achieved through sizeable capital cost reductions at the expense of some reduction in system efficiency (Table 2).

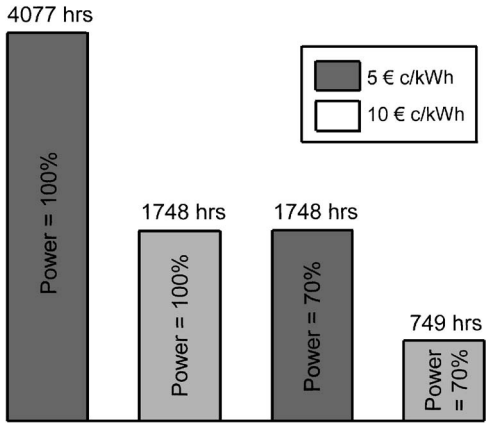

Fig. 5 Outline annual operational scenario

Taking the biomass system as an example, closer inspection of the cycle parameters before and after optimization reveals a significant improvement in gas turbine efficiency (Table 3) and a significant reduction in the capital costs of the biomass and heat exchanger components of the system (Table 4). As the biomass plant components are the most expensive parts of the cycle (they were modeled as a function of fuel flow to the gas turbine), the optimization process has rightly targeted this area as a focus for cost reduction by improving gas turbine efficiency. The gas turbine efficiency improvement was achieved through an increase in overall pressure ratio with a coincident reduction in mean turbine diameter in order to keep the turbine cost down. The heat exchanger cost reductions were achieved through pinch-point temperature optimizations and as a result of the lower gas turbine exhaust temperature arising from the higher gas turbine efficiency. This trade-off provides the most favorable arrangement in terms of through-life cycle economic performance for this particular biomass system.

Importantly, the values of all system parameters (around 1000 in these cases) can be exported from the software in spreadsheet form for more detailed analysis, enabling the User to assess the practical implications of the optimization process. The particular trade-offs made by the optimizer during any study are of course directly affected by the accuracy of the performance and cost models built within PSEconomy. They are also affected by the way in which the optimizer search criteria are set. With a complex system like a gas turbine power generator, there is a risk of the optimizer determining optimal configurations that in reality are impossible to build for practical reasons. PSEconomy therefore provides the User with the facility to set constraints on the decision variables thus ensuring that output system configurations are within practical limitations.

As the software comprises a detailed through-life economic performance analysis tool in conjunction with a robust genetic algorithm-based optimizer, computational times of several hours can be required depending on the particular problem being solved and the complexity of the optimization process. Given the powerful functionality offered by the software, computational times of this order are not considered unduly large for preliminary design analysis.

Table 2 Overall optimization results

	Before optimization			After optimization		
	€/kW	η%	IRR %	€/kW	η%	IRR %
CCGT	741	53.69	17.8	514	51.01	27.0
Biomass	1279	44.21	10.1	1048	43.66	13.7
CO_2 seq	1186	48.56	5.3	986	47.36	8.7

Table 3 Impact of optimization on efficiency (η)

	Before optimization			After optimization		
	CCGT	Bio-mass	CO_2 seq	CCGT	Bio-mass	CO_2 seq
GT η (%)	36.33	30.49	35.17	34.45	34.11	33.58
ST[a] η (%)	17.36	15.67	13.39	16.56	11.78	13.78
Net η (%)	53.69	44.21	48.56	51.01	43.66	47.36

[a]Steam turbine efficiency on GT source fuel basis

Table 4 Impact of optimization on capital costs (all values in € million apart from final two rows)

	Before optimization			After optimization		
	CCGT	Bio-mass	CO_2 seq	CCGT	Bio-mass	CO_2 seq
Genset[a]	20.00	21.92	20.00	14.45	18.02	14.84
ST[b]	4.36	5.38	3.05	3.45	3.47	3.15
HTX[c]	7.22	10.38	6.31	3.56	3.29	3.95
Bio[d]	0	43.31	0	0	36.22	0
CO_2[e]	0	0	23.83	0	0	24.10
Other[f]	17.59	28.03	17.99	12.55	17.35	15.18
TOTAL	49.17	109.0	71.18	34.01	78.35	61.22
Plant MW	66.36	85.25	60.02	66.21	74.74	62.11
€/kW	741	1279	1186	514	1048	986

[a]Genset, genset costs.
[b]ST, steam turbine costs.
[c]HTX, heat exchangers costs.
[d]Bio, biomass plant costs.
[e]CO_2, CO_2 sequestration plant costs.
[f]Other, includes engineering costs, construction costs, electrical interconnection plant and building costs.

Conclusions

This paper has described the successful development and integration of a software system for gas turbine power generation plant economic performance analysis and optimization. The software program PSEconomy, based on the commercial process modeling package IPSEpro, and the GTPOM component library successfully combine gas turbine power generation thermodynamic and economic performance analysis. The robust genetic-algorithm optimizer allows full through-life cycle optimization of gas turbine cycle configurations.

This approach provides system designers with an additional degree of design flexibility when developing new cycle configurations, and allows the economic benefits of new approaches applied to existing power generation systems to be assessed and maximized.

While the economic improvements provided by the application of the new tool are dependent on the particular plant configuration, the accuracy of the component models used during the modeling process, and the economic scenarios selected for plant operation, indications from the case studies reported in this paper suggest significant benefits are achievable.

Acknowledgment

The support of GTPOM project by the European Commission is gratefully acknowledged. The authors wish to sincerely thank Darren Watson for having successfully proposed and pursued the GTPOM project in its early stages, and for his excellent management of the consortium during the first part of the project. Special acknowledgments also go to Ulf Linder and Aristide Massardo for their very significant contributions to the project.

Nomenclature

COE = cost of electricity
GT = gas turbine
HEX = heat exchanger
IRR = internal rate of return
MDK = model development kit
O&M = operating and maintenance
PSE = process simulation environment
r = interest rate
TCI = total capital investment

References

[1] Peters, M., and Timmerhaus, K., 1991, *Plant Design and Economics for Chemical Engineers*, 4th ed., McGraw–Hill, New York.
[2] Chadwick, L., 1991, "The Essence of Management Accounting," Adrian Buckley, ed., Prentice–Hall, Englewood Cliffs, NJ.
[3] Bejan, A., Tsatsaronis, G., and Moran, M., 1995, "Thermal Design and Optimization," Wiley–Interscience, New York.
[4] Parking, M., Powell, M., and Matthews, K., 1997, *Economics*, Addison–Wesley, Reading, MA.
[5] Nellis, J. G., and Parker, D., 1992, *The Essence of Business Economics*, Adrian Buckley, Series editor, Prentice–Hall, Englewood Cliffs, NJ.
[6] Weston, J. F., and Brigham, E. F., 1974, "Finanza Aziendale," Il Mulino.
[7] Holland, J. H., 1975, "Adaptation in Natural and Artificial Systems," University of Michigan Press, Ann Arbor, MI.
[8] Frangopoulus, C. A., 1983. "Thermoeconomic Functional Analysis: A Method for Optimal Design or Improvement of Complex Thermal Systems," Ph.D. thesis, Georgia Institute of Technology, Atlanta, GA.
[9] Agazzani, A., Massardo, A. F., and Frangopoulos, C. A., 1998, "Environmental Influence on the Thermoeconomic Optimization of a Combined Plant With NO_x Abatement," J. Eng. Gas Turbines Power **120**, pp. 557–565.
[10] El-Sayed, M., and Tribus, M., 1983, "Strategic Use of Thermoeconomics for System Improvement," J. Eng. Power **92**, pp. 27–34.
[11] Goldberg, D. E., 1989, "Genetic Algorithms in Search, Optimization and Machine Learning," Addison–Wesley, Reading, MA.
[12] Mitchell, M., 1996, *An Introduction to Genetic Algorithms*, The MIT Press, Cambridge, MA.

Design Study of a Humidification Tower for the Advanced Humid Air Turbine System

Hidefumi Araki
Shinichi Higuchi
Shinya Marushima
Shigeo Hatamiya

Hitachi Ltd.,
Power and Industrial Systems
R&D Laboratory,
7-2-1 Omika-cho,
Hitachi-shi, 319-1221, Japan

The advanced humid air turbine (AHAT) system, which can be equipped with a heavy-duty, single-shaft gas turbine, aims at high efficiency equal to that of the HAT system. Instead of an intercooler, a WAC (water atomization cooling) system is used to reduce compressor work. The characteristics of a humidification tower (a saturator), which is used as a humidifier for the AHAT system, were studied. The required packing height and the exit water temperature from the humidification tower were analyzed for five virtual gas turbine systems with different capacities (1, 3.2, 10, 32, and 100 MW) and pressure ratios ($\pi = 8$, 12, 16, 20, and 24). Thermal efficiency of the system was compared with that of a simple cycle and a recuperative cycle with and without the WAC system. When the packing height of the humidification tower was changed, the required size varied for the three heat exchangers around the humidification tower (a recuperator, an economizer, and an air cooler). The packing height with which the sum total of the size of the packing and these heat exchangers became a minimum was 1 m for the lowest pressure ratio case, and 6 m for the highest pressure ratio case. [DOI: 10.1115/1.2132384]

1 Introduction

The advanced humid air turbine (AHAT) system which utilizes humid air has been studied [1] to improve thermal efficiency of gas turbine power generation. It is an original gas turbine power generation system which substitutes the water atomization cooling (WAC) system for the intercooler system of the HAT [2] cycle. The advantage of the AHAT system is its high thermal efficiency obtained through a heat recovery system; neither an extremely high combustion temperature nor pressure ratio is needed.

As for studies on the gas turbine itself, an experiment with the combustor which burns high humidity air [3] and an analysis of turbine blade cooling with humid air [4] have been carried out. Moreover, for system equipment, a water recovery system from the exhaust gas has been studied experimentally [5].

The humidifier is a distinctive component of the AHAT system. As a humidification means, a spray-type humidifier [6] was studied other than the humidification tower which is the subject of this paper.

Inside the humidification tower, the difference of the vapor pressure between the surface of the liquid film and the airflow serves as a driving force for humidification. Therefore, the structural specifications required for the humidification tower depend greatly on the pressure, temperature, and flow rate of the air or the feed water. For example, Swedish researchers have designed a HAT cycle pilot plant which has a pressure ratio of 8 and has a humidification tower with a packing height of 0.9 m and tower height of about 3 m [7,8]. On the other hand, a feasibility study by EPRI [9] indicated that a HAT cycle plant with a pressure ratio of 23 requires a humidification tower of 24 m height. Recently, researchers at the University of Genoa proposed a Micro HAT of the 100–500 kW class [10]. They compared the sizes of the humidification tower for pressure ratios ranging from 2 to 8.

The performance of tower packing has been steadily improved since the packing is commonly used in chemical plants. Then, it is important to know the specifications of the humidification tower for the AHAT system of various pressure ratios when the latest packing is used.

The purpose of this study is to investigate the specifications and the characteristics of the humidification tower for the AHAT system according to the pressure ratio which is a basic characteristic of the gas turbine. The sizes of major components around the humidification tower such as the recuperator, air cooler, and economizer are evaluated, and the relationship between the pressure ratio of the gas turbine and required capacity of the humidification system is clarified.

2 AHAT System and Humidification Equipment

Figure 1 shows a schematic of the AHAT system. An advantage of the system is that it can use a single-shaft gas turbine which is commonly used for power generation. There is no intercooler; instead power reduction of the compressor is achieved by the WAC system. The heat is recovered by the air cooler installed in the compressor exit and by the economizer installed downstream from the recuperator. Then, circulated water is heated and fed to the humidification tower and compressed air is humidified to saturation. By adding the humidity of about 15–20 wt %, the working fluid of the turbine can be increased without increasing the power of the compressor. As a result, shaft power and thermal efficiency can be improved greatly compared with the recuperated cycle without humidification. The water vapor contained in the exhaust gas is recovered at the water recovery system and purified at the water treatment system. The removal of the sulfur and alkali metals from recovered water is important to prevent hot corrosion of the gas turbine [11].

Depending on the pressure ratio of the gas turbine, the degree of humidification differs because the temperatures of compressed air and exhausted gas and saturated vapor pressure of the compressed air are all different at different pressure ratios. Moreover, the required height of packing and the diameter of the humidification tower depend on the gas turbine since the density of compressed air is different at different pressure ratios.

In order to evaluate the size of the humidification tower, and the capacity of heat exchangers around it, the heat and material balance of the entire system is calculated. In that process, the poly-

Contributed by the International Gas Turbine Institute (IGTI) of ASME for publication in the JOURNAL OF ENGINEERING FOR GAS TURBINES AND POWER. Manuscript received August 25, 2005; final manuscript received September 28, 2005. IGTI Review Chair: K. C. Hall. Paper presented at the ASME Turbo Expo 2005: Land, Sea, and Air, Reno, NV, June 6–9, 2005, Paper No. GT2005-68671.

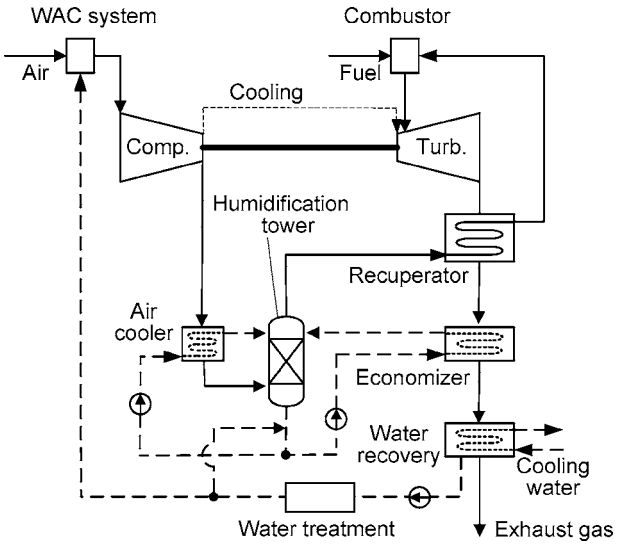

Fig. 1 Schematic of AHAT (advanced humid air turbine) system

tropic efficiency of the compressor and the turbine, the amount of WAC, etc., are assumed for each pressure ratio of the gas turbine.

3 Evaluation Method

3.1 Input Conditions for Gas Turbine and Plant. Since the recovery heat of the air cooler and the economizer which influences the humidification rate is decided by the heat mass balance of the entire plant, the evaluation of gas turbine performance is required.

The conditions assumed for each gas turbine with different pressure ratios are shown in Table 1. The power output and polytropic efficiency of the compressor and the turbine were set to become larger for a larger pressure ratio case. The WAC flow ratio (ratio to suction airflow rate) was assumed to increase by raising the pressure ratio. This is because the number of stages of the compressor increases with the pressure ratio, and the temperature of air within the compressor becomes high, also.

An advanced cooling technology or rather expensive material is needed for the combustor and the turbine blade when the combustion gas temperature becomes high. So, the upper limit of combustion gas temperature was chosen to be 1350 °C based on past research [4]. However, for a low pressure ratio gas turbine (for instance, $\pi=8$), if the combustion temperature were 1350 °C, the exhaust gas temperature would be 800 °C or more, which would exceed the maximum allowable temperature for the uncooled turbine blades or the stainless steel recuperator. From these limitations, the maximum values of the combustion gas temperature and exhaust gas temperature were set as 1350 and 650 °C, respectively, as shown in Table 1. The relation between the pressure ratio and the number of gas turbine stages was decided after referring to actual data for marketed gas turbines.

Table 1 Assumptions for each gas turbine case

Case name		$\pi=8$	$\pi=12$	$\pi=16$	$\pi=20$	$\pi=24$
Pressure ratio π [-]		8	12	16	20	24
Power output [MW]		1	3.2	10	32	100
WAC flow ratio[%] (Inlet air mass basis)		1.1	1.9	2.7	3.5	
Comp.	Polytropic eff [%]	84	87	90	93	
Turbine	Entry temp [°C]	Calculated			1350	
	Exhaust temp [°C]	650			Calculated	
	Polytropic eff [%]	86	88	90	92	
	Number of stages	2		3		4

Table 2 Common conditions for all gas turbines

Equipment	Item	Value
Comp	Ambient cond	101.3 kPa, 15 C, 60% RH
	Inlet pres loss	1.12 kPa (4.5 in. H_2O)
Comb	Efficiency	99.99%
	Pres loss	4%
Turbine	Bearing and wind losses	1.5% of shaft power
Gearbox	Gearing loss	1.5% of shaft power
Generator	Electrical eff	95%

Common conditions applied for all gas turbines cases are shown in Table 2.

Table 3 shows the boundary conditions for the AHAT system equipment. Outlet air temperature of the air cooler should be low to decrease the outlet water temperature of the humidification tower, which minimizes sizes of the economizer and the air cooler. However, to avoid cooling compressed air below the dew point temperature, which is about 110 °C when the pressure ratio is 24, the outlet air temperature of the air cooler was set to be higher than the dew point by 5 °C. This temperature was fixed at 115 °C for all calculation cases to allow comparison of the size of the air coolers required for heat recovery to the same temperature. The pressure loss caused in the air piping in front of and behind the air cooler is not considered.

The packing in the humidification tower was assumed to be RSR#2 manufactured by the Raschig Co. This is a fourth generation packing material and it has the merit of a very small pressure drop [12]. When the feed water temperature to the packing is high, the driving force of the mass transfer at the liquid film surface becomes large and the required height of the packing will be low. Then, the feed water temperature was assumed to be the evaporation temperature minus 10 °C, considering the margin to steaming.

Temperature effectiveness of the recuperator was assumed to be 95.2% the same as in past research [4]; the terminal temperature difference at the hot end corresponds to 20 °C when the pressure ratio is 20. Even though this temperature effectiveness is larger than that of a conventional recuperator for gas turbine use, the temperature difference between the inlet and the outlet air is larger in the AHAT system since the inlet temperature of the humidified air is lower than that of an ordinary recuperated cycle. Thus temperature effectiveness tends to become larger in the AHAT system. However, the size of the recuperator does not become excessively large, because when the hot end terminal temperature difference is

Table 3 AHAT system conditions

Equipment	Item	Value
Air cooler	Outlet air temp	115 °C
	Pres. loss (air)	1%
Humidification tower	Packing type	Raschig Super Ring No. 2
	Packing height	Input parameter
	Inlet water temp	Evaporation temp. −10 °C
	Inlet water pres	Comp. discharge pres. +300 kPa
	Tower pres loss	0.50%
Recuperator	Temp eff	95.20%
	Pres loss (air)	3%
	Pres loss (gas)	3%
Economizer	Pres loss (gas)	0.50%
	Exhaust gas temp	100 °C
Water treatment sys	Outlet water temp	15 °C

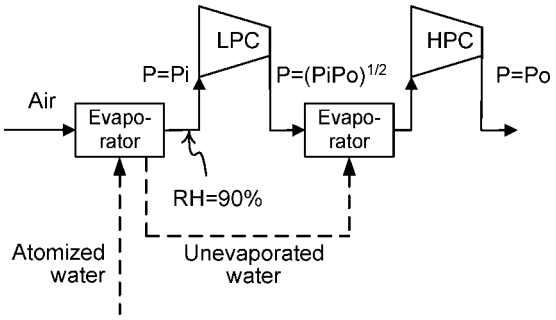

Fig. 2 Simplified model of WAC system

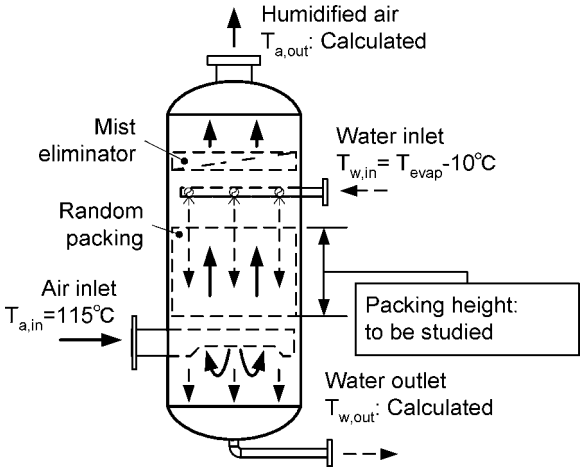

Fig. 3 Schematic of humidification tower

20 °C, the cold end terminal temperature difference is about 100 °C and consequently the logarithmic mean temperature difference becomes 40 or 50 °C.

The exhaust gas temperature at the exit of the economizer was assumed to be 100 °C, the same as in past research. Because this temperature is lower than that of the air cooler outlet air (115 °C), the mixture of cold make-up water and hot drained water from the humidification tower is distributed to these heat exchangers in parallel.

3.2 Modeling of WAC. In the past study [4], as the pressure ratio and the number of compressor stages were fixed, evaporation of atomized water at each compressor stage was calculated using a Lagrangian model. However, a simpler model as shown in Fig. 2 was used in this study to deal with various pressure ratio cases. Regardless of the number of stages of the actual compressor, this model consists of LPC (low pressure compressor) and HPC (high pressure compressor). A part of the atomized water evaporates at the inlet duct of the LPC until relative humidity at the LPC inlet becomes 90%. Unevaporated water passes through to the LPC outlet as liquid water and it is mixed with hot compressed air to evaporate. Humidity of the mixed air at the inlet of the HPC is not saturated in any calculation cases; however, some qualification tests are needed to verify whether such water flow rate can surely be evaporated.

3.3 Estimation of Cooling Airflow Rate. Cooling of the gas turbine blade requires a complex design procedure because it depends on the temperature of the hot gas, the selected material, and cooling mechanism. Torbidoni [13] presented a new method to calculate the cooling flow that considers the heat flux of a small section at given span and chord locations. However, a simpler design procedure was needed in this study because the pressure ratio and number of turbine stages were different for each calculation case. So the same procedure as shown in Jordal's thesis [14] was adopted; the cooling effectiveness, the allowable blade surface temperature, and the ratio of the blade surface area to the flow area were assumed for each turbine stage, and the required amount of cooling airflow was calculated.

Some studies have shown that the cooling airflow was reduced greatly when humidified air was used as coolant [4,14]. However, blade cooling by the compressor exit air was assumed in the present study.

3.4 Characteristics of Humidification Tower Packing. In the humidification tower, the liquid film flows down from the top of the packing as shown in Fig. 3. Air is supplied from the bottom side of the packing, and it makes contact with the falling liquid film. Then, the surface part of the liquid film evaporates and air is humidified. The process was modeled by dividing the packing into 40 cells in the vertical direction as shown by Fig. 4. The height of a cell was changed when the effect of the packing height was surveyed.

Heat and mass transfers on the surface of the liquid film were solved as one-dimensional simultaneous difference equations as follows.

- Mass conservation of moisture content in humid air

$$\frac{\rho_a \partial Y}{\partial t} + \frac{\rho_a u_a \partial Y}{\partial x} = m \tag{1}$$

- Enthalpy conservation of humid air

$$\frac{\rho_a \partial h_a}{\partial t} + \frac{\rho_a u_a \partial h_a}{\partial x} = q_S + q_L \tag{2}$$

- Mass conservation of liquid film

$$\frac{\partial \rho_w}{\partial t} + \frac{\partial (\rho_w u_w)}{\partial x} = -m \tag{3}$$

- Enthalpy conservation of liquid film

$$\frac{\partial \rho_w h_w}{\partial t} + \frac{\partial (\rho_w u_w h_w)}{\partial x} = -(q_S + q_L) \tag{4}$$

- Mass transfer equation

$$m = k_Y a (Y_w - Y_a) \tag{5}$$

- Heat transfer equation

$$q_S = h_G a \times (T_w - T_a) \tag{6}$$

$$q_L = h_v \times m \tag{7}$$

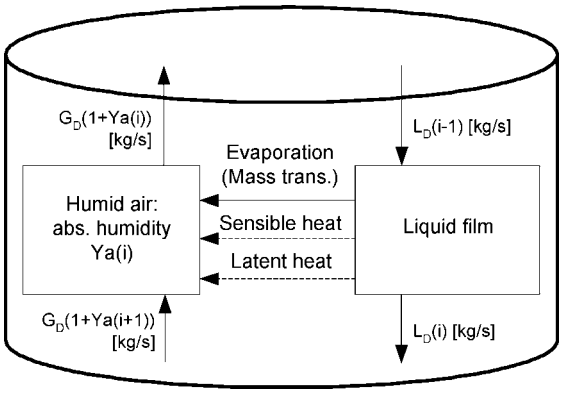

Fig. 4 Heat and mass transfer model inside the humidification tower packing

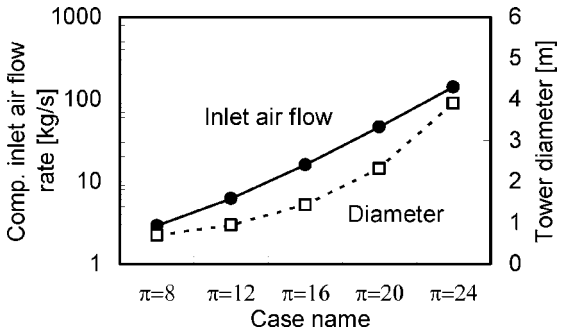

Fig. 5 Compressor inlet airflow rate and diameter of packing for each calculation case

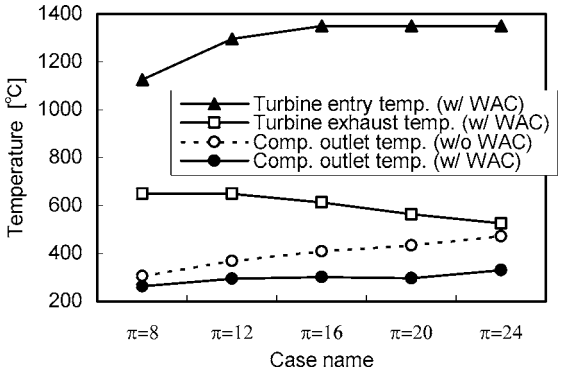

Fig. 6 Compressor outlet temperature and turbine entry/exhaust temperature

Some studies solve for the interface temperature between the liquid film and humid air to calculate heat and mass transfers [8,15]. However, the liquid film temperature was substituted for the liquid film surface temperature in this study for simplicity. Ackerman's correction, which corrects mass transfer coefficient at high mass transfer rate, as considered by Parente et al. [16], was not used in this study for the same reason. The boundary conditions such as temperature, pressure, and flow rate of the humid air and liquid film are automatically inputted from and outputted to the plant system calculation code. It is the main feature of this calculation code that the characteristic of the humidification tower can be automatically linked with the plant system conditions.

The mass transfer coefficient on the surface of the liquid film is related by the performance of the packing. Since H_{OG} (height of the overall transfer unit of the gas phase) for the air-water system is unpublished, H_G (height of the transfer unit of the gas phase) for ammonia-air-water system was calculated using a calculation program [17]. Then this value was converted into H_{OG} for the air-water system at the high temperature and high pressure conditions as shown by Eq. (8)

$$H_{OG,\mathrm{wat}} = \left(\frac{D_{\mathrm{NH3}}}{D_w}\right)^{0.5} H_{G,\mathrm{NH3}} \tag{8}$$

The diameter of the humidification tower was estimated by using the given flooding curve of the packing for each pressure ratio case. Flooding is the phenomenon in which the falling liquid film does not flow downwards and accumulates when the upward airflow velocity is increased. In this study, the tower diameter was chosen so that the airflow velocity was 60% of the flooding velocity.

As shown in Fig. 5, the required tower diameters for $\pi=8$ (1 MW) and $\pi=24$ (100 MW) were 0.70 and 3.91 m, respectively. The diameter becomes relatively small for the higher pressure ratio case because specific power is larger. Velocities of the gas and the liquid film were determined for these diameters and mass transfer in the packing was calculated.

4 Results

4.1 Pressure Ratio and Cooling Airflow Rate. Figure 6 shows the air temperature at the compressor exit, and combustion gas temperatures at the turbine inlet and turbine exit. When WAC system is not used, the air temperature at the compressor exit increases with the increasing pressure ratio. On the other hand, when WAC system is used, the rise of the compressor exit air temperature is suppressed because the amount of WAC is increased with the pressure ratio.

Similarly, the ratio of the cooling airflow to compressor intake airflow is shown in Fig. 7. In this figure, the ratio of the cooling airflow increases with the pressure ratio because the surface area increases with the number of turbine stages and the combustion gas temperature rises with the pressure ratio. However, the cooling airflow rate for the pressure ratio of 20 is smaller than that for the pressure ratio of 16 because the compressor exit air temperature is lower when the pressure ratio is 20 and WAC system is used.

4.2 Pressure Ratio and Humidification. Figure 8 shows the relationships between the pressure ratio and the humidification ratio by WAC system combined with the humidification tower and by the humidification tower alone. The humidification ratio by the humidification tower is larger when WAC system is not used since a larger amount of hot water is produced by the air cooler using the higher temperature of the compressor exit air. On the other hand, when the pressure ratio is 20 and WAC system is used, as a result of the compressor exit temperature becoming low as mentioned above, the humidification ratio by the humidification tower

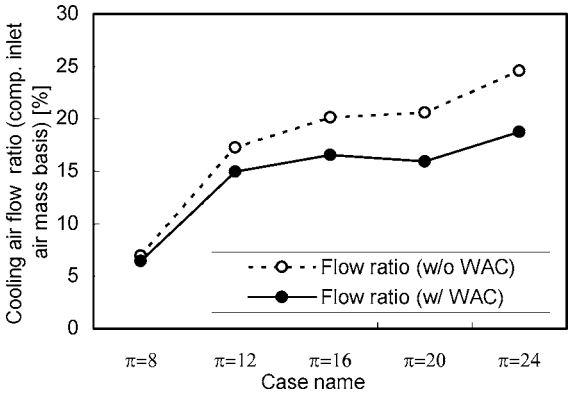

Fig. 7 Cooling airflow ratio

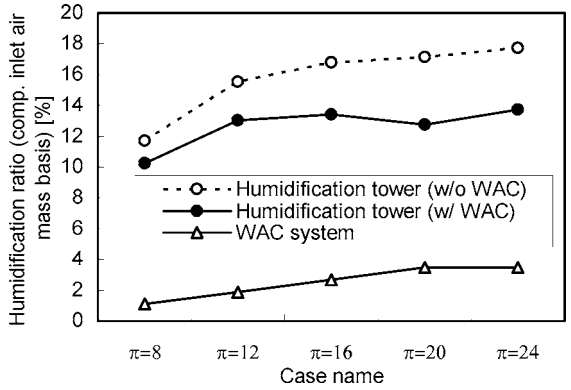

Fig. 8 Humidification ratio by WAC system and humidification tower

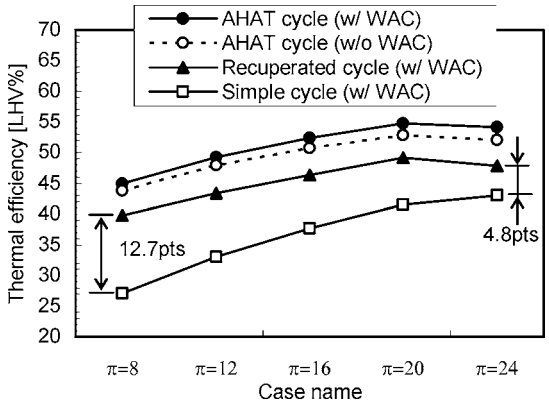

Fig. 9 Comparison of thermal efficiency

decreases.

Figure 9 shows the relation between the pressure ratio and the thermal efficiency. For comparison with the AHAT system, the thermal efficiency of a recuperated cycle which has a recuperator with the same temperature effectiveness, a simple cycle which has a gas turbine of the same polytropic efficiency is described.

Although the recuperated cycle efficiency is dominant at a pressure ratio of 8 by 12.7 points compared with the simple cycle, the difference drops to 4.8 points at a pressure ratio of 24. The reason is that when the pressure ratio is high, heat recovery by the recuperator is decreased because the compressor exit air temperature becomes high and the turbine exhaust gas temperature is low.

The difference between AHAT and the recuperated cycle with WAC system ranges from 5.1 to 6.3 points according to the pressure ratio. As for the HAT cycle (including AHAT), the hot air coming from the compressor exit is humidified and cooled down to its saturation temperature, and the air is fed to the recuperator and the heat of the exhaust gas can be effectively recovered.

The effect of WAC system is clear for high pressure ratio cases when the atomization water flow rate is increased. For the pressure ratio of 20, thermal efficiency with WAC system is improved 1.9 points over the case with no WAC system.

For the pressure ratio of 20, the AHAT system has the 54.7% LHV of the highest efficiency when WAC system is used. The reason why the thermal efficiency has decreased at pressure ratio of 24 is that the temperature of the turbine exhaust gas is the lowest, and that the number of turbine stages and the cooling airflow rate are the maximum.

Although blade cooling by the compressor exit air was assumed in this study, the cooling airflow can be decreased by using humidified air, and a further improvement of the thermal efficiency is possible as described in past studies [4,14].

4.3 Size of Humidification Tower and Heat Exchangers. When the sole purpose is to humidify compressed air regardless of the cost of the equipment, the height of the packing of the humidification tower is not so important. However, by increasing the packing height, the contact area between the liquid film and air increases, the exit water temperature falls, and heat recovery becomes more effective.

Figure 10(*a*) shows the temperature and the humidity profile inside the packing of 2 m height for the $\pi=16$ case. The air of 115 °C rises from the lower side, and the hot water of 190 °C (evaporation temperature minus 10 °C) flows down from the upper side. The difference between the bulk air humidity and the humidity on the liquid film surface which corresponds to a saturation pressure of the liquid film temperature works as the driving force of the diffusion phenomenon, and water is evaporated from the liquid film surface. Humid air is saturated in the latter half of the packing when its height is 2 m as shown in the figure.

The latent heat transferred from the hot water to humid air is proportional to the evaporation rate, and the sensible heat transfer is proportional to the temperature difference between liquid film and humid air. Therefore, air is cooled down on the lower side of the packing, and air is heated on the upper side. The air exit temperature becomes a saturation temperature corresponding to the steam partial pressure when the height of the packing is high enough. On the other hand, the exit water temperature changes continuously depending on the packing height. Therefore optimizing the exit water temperature leads to the choice of the packing height.

Figure 10(*b*) is the temperature-enthalpy diagram of the same calculation case, which is commonly used to show operation of the humidification tower. The operating line corresponds to the temperature of the falling liquid film and specific enthalpy of humid air at the same location. The air line indicates the temperature of actual humid air and specific enthalpy; the equilibrium line indicates the specific enthalpy of air when assuming saturation. The pinch point temperature difference between the equilibrium line and the operating line, which is an index of performance, is 5.4 °C for this case.

Figure 11 shows the humidification tower exit water temperature when the height of the packing is changed. When the pressure ratio is the same and the height of the packing is high, the exit water temperature falls. At this time, the feed water flow rate to the economizer and the air cooler decreases since the amount of heat recovered in the system is the same.

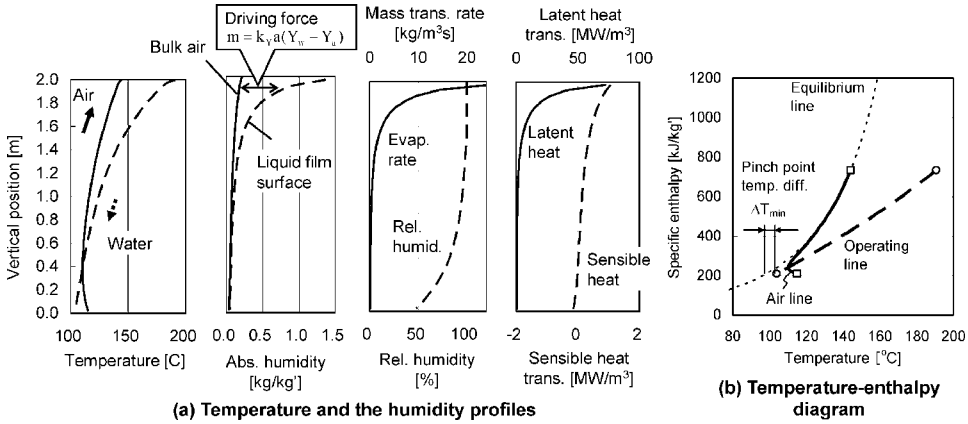

Fig. 10 (*a*) Temperature and the humidity profiles and (*b*) temperature-enthalpy diagram inside the packing of 2 m height for $\pi=16$ case

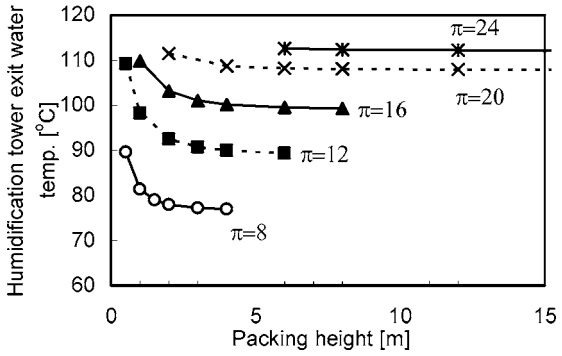

Fig. 11 Temperature of water at the humidification tower exit

For the pressure ratio, the exit water temperature becomes low for the lower pressure ratio. The reason is that the steam partial pressure in humid air becomes small for the same absolute humidity when the pressure ratio is low, and that the driving force necessary for evaporation from the liquid film surface becomes larger. In addition, since the flow rate of WAC is increased at the high pressure ratio, the steam partial pressure of the air and the exit water temperature become high.

In order for the exhaust gas temperature after the economizer to reach 100 °C, the feed water temperature at the economizer inlet must be lower than 100 °C. The feed water temperature is determined by the weighted average of the humidification tower exit water temperature and the make-up water (recycled water or external water) temperature. From this, the packing height of 6 m or more is needed when the pressure ratio is 24.

Figure 12 shows the relationships between the packing height and the terminal temperature difference, the log-mean temperature difference, and the KA value of the economizer when the pressure ratio is 16.

When the packing height is high, the water temperature at the bottom of the packing becomes low and ΔT_l (the terminal temperature difference at the cold end) of the economizer becomes large. Since ΔT_h (the terminal temperature difference at the hot end of the economizer) is almost invariable, ΔT_{lm} (the logarithmic mean temperature difference) grows with the height of the packing. The heat exchanger duty Q is calculated by $Q=KA\Delta T_{lm}$. Therefore, by increasing the packing height, ΔT_{lm} of the economizer is enlarged and the required heat transfer surface area A becomes smaller when the exhaust gas temperature is the same.

Similarly, the calculation results for all pressure ratios of the *KA* values of the economizer, the air cooler, and the recuperator are shown in Fig. 13. These *KA* values are standardized by the inlet airflow rate of the compressor. According to this, it is understood that the size of the economizer and the air cooler become smaller when the packing height is raised, and the pressure ratio

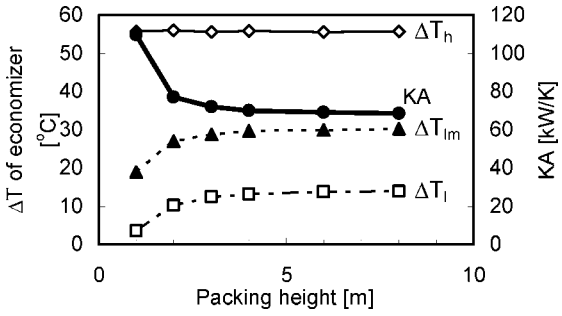

Fig. 12 Packing height and log-mean temperature difference, and the *KA* value of the economizer for $\pi=16$ case

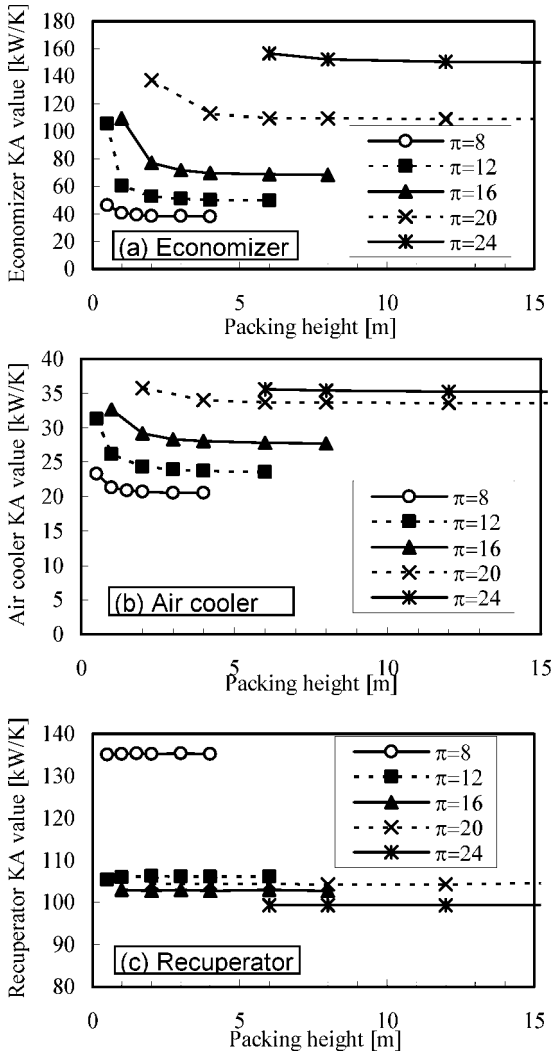

Fig. 13 *KA* values of (*a*) economizer, (*b*) air cooler, and (*c*) recuperator

of the gas turbine is lowered.

The size of the recuperator mostly becomes smaller for higher pressure ratio cases. The first reason is that when the pressure ratio is high, the turbine exhaust temperature becomes low and the heat recovery in the recuperator becomes small. The second reason is that the cooling airflow rate of the turbine blade increases for higher pressure ratio cases and that the flow rate of the exhaust gas fed to the recuperator becomes larger than that of the compressed air. Consequently, the exhaust gas from the recuperator is at a high temperature and the terminal temperature difference at the cold end becomes large. As a result, the logarithmic mean temperature difference grows bigger and the *KA* value becomes smaller as $Q=KA\Delta T_{lm}$.

Conversion factors shown in Table 4 were used to derive the volume of these three heat exchangers from the *KA* values obtained by the above-mentioned method. To decide the conversion factors, actual data were used which showed the relation between the volume and the *KA* value of heat exchangers. A compact plate-fin heat exchanger was assumed for the recuperator. On the other hand, a finned-tube type heat exchanger was assumed for the air cooler and the economizer, because highly pressurized water is fed to these heat exchangers in order to avoid steaming. The conversion factor for the air cooler is smaller than that of the economizer because heat transfer coefficient of compressed air is larger than that of exhaust gas. The change in the heat exchanger tube

Table 4 Criteria for volume estimation

Equipment	Type	Volume estimation formula
Recuperator	Corrugated plate-fin, block type	$Vol[m^3]=KA[kW/K]\times 0.03$
Economizer	Finned-tube type	$Vol[m^3]=KA[kW/K]\times 0.2$
Air cooler	Finned-tube type	$Vol[m^3]=KA[kW/K]\times 0.1$

thickness or the change in heat transfer coefficient, which is affected by the pressure ratio, was neglected in determining the conversion factor.

Figure 14 shows the volume of the three heat exchangers and the packing of the humidification tower when the packing height is changed for each pressure ratio case using these conversion factors. This figure indicates that the total volume of these heat exchangers and the humidification tower has a local minimum for each pressure ratio case. Moreover, since the volume ratio of the tube-type economizer is large, it is effective to make this compact.

When paying attention to the pressure ratio, the volume of the components necessary to build the AHAT system is small when the pressure ratio is low. However, the difference will decrease if the economizer is more compact since its influence is large. The heights of the packing of the humidification tower with which the entire volume becomes the minimum are 1, 2, 3, 4, and 6 m for pressure ratios of 8, 12, 16, 20 and 24, respectively.

Figure 15 illustrates the size and shape of the packing when the volume of the components becomes the minimum for each calculation case. When the electric power increases from 1 to 100 MW, the packing height increases from 1 to 6 m and the diameter increases from 0.70 to 3.91 m. Since the required height of the packing is low for the lower pressure ratio cases, the application of the AHAT system to the small-sized gas turbine is possible as well as the middle-sized one from the viewpoint of the equipment size.

5 Conclusions

The size and the humidification characteristics of the humidification tower were examined in order to understand the plant equipment size of the AHAT system. Five virtual gas turbine systems with different capacities (1, 3.2, 10, 32, and 100 MW) and pressure ratios (π=8, 12, 16, 20, and 24) were assumed.

The required tower diameters for π=8 (1 MW) and π=24 (100 MW) cases were 0.70 and 3.91 m, respectively. The diameter became relatively small for the higher pressure ratio case because specific power was larger.

When the packing height was high, the water temperature at the bottom of the packing was low and the required heat transfer surface area of the economizer became smaller for the same pressure ratio. Similarly, the heat transfer surface area of the economizer, the air cooler, and the recuperator were calculated. The packing height was found with which the sum total of the size of the humidification tower and these heat exchangers became the minimum.

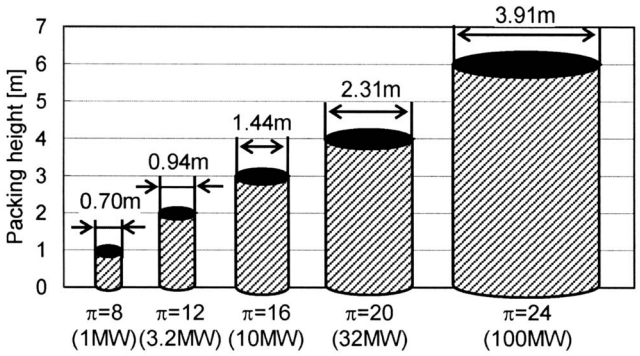

Fig. 15 Size and shape of the packing required for each calculation case

When the pressure ratio was low, the required packing height was low because the steam partial pressure in humid air became small for the same absolute humidity and because the driving force necessary for evaporation from the liquid film surface became larger. When the pressure ratio was changed from 8 to 24, the height of the packing of the humidification tower with which the total volume of the packing and the three heat exchangers became a minimum increased monotonically within the range from 1 to 6 m.

Acknowledgment

This research was made possible by the assistance of the Ministry of Economy, Trade and Industry of Japan, Agency for Natural Resources and Energy. The authors wish to express their deep gratitude.

Nomenclature

- a = effective interfacial mass transfer area of packing (m^2/m^3)
- D = diffusion coefficient (m^2/s)
- G_D = mass flow rate of dry air (kg/s)
- h = specific enthalpy (kJ/kg)
- h_G = gas phase heat transfer coefficient ($kW/m^2\,K$)
- $h_G a$ = volumetric gas phase heat transfer coefficient ($kW/m^3\,K$)
- H_G = height of transfer unit of gas phase (m)
- h_v = specific enthalpy of steam (kJ/kg)
- H_{OG} = height of overall transfer unit of gas phase (m)

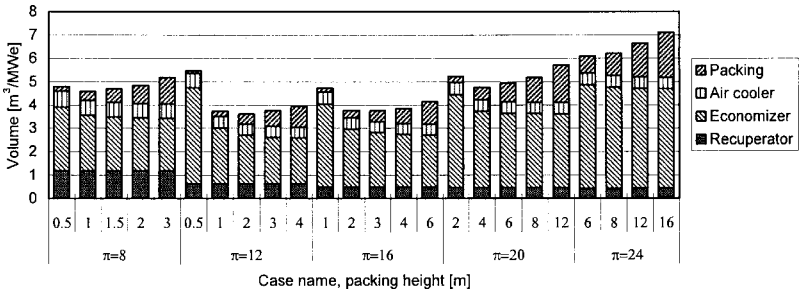

Fig. 14 Volume of the three heat exchangers and the packing of the humidification tower required for 1 MW of electric power output

KA = product of specific conductance and area of heat transfer surface (kW/K)
k_Y = gas phase mass transfer coefficient ($kg/m^2\ s\Delta Y$)
k_Ya = volumetric gas phase mass transfer coefficient ($kg/m^3\ s\Delta Y$)
L_D = mass flow rate of liquid film (kg/s)
LHV = lower heating value (kJ/kg)
m = amount of mass transfer per volume ($kg/m^3\ s$)
Q = rate of heat transfer (kW)
q_L = rate of latent heat transfer per volume (kW/m^3)
q_S = rate of sensible heat transfer per volume (kW/m^3)
t = time (s)
T = temperature (°C)
ΔT_h = terminal temperature difference at the hot end (°C)
ΔT_l = terminal temperature difference at the cold end (°C)
ΔT_{lm} = logarithmic mean temperature difference (°C)
u = velocity (m/s)
$w/$ = with
w/o = without
Y = absolute humidity (kg/kg')
π = pressure ratio
ρ = density (kg/m^3)

Subscripts

a = air
i = ith position of cell
NH3 = ammonia
w = water

References

[1] Hatamiya, S., 2002, "Gas Turbine Power Generation Technology Utilizing High Humidity Air" [in Japanese], Thermal Nuclear Power, **53**, pp. 1031–1038.
[2] Nakamura, H., and Yamamoto, K., 1992, "HAT(Humid Air Turbine) Cycle" [in Japanese], Thermal Nuclear Power, **43**, pp. 1587–1592.
[3] Koganezawa, T., Inoue, H., and Kobayashi, N., 2002, "Experimental Study on Diffusion Flame Combustor for Advanced Humid Air Turbine" [in Japanese], JSME Annual Meeting, **4**, pp. 187–188.
[4] Higuchi, S., Hatamiya, S., Seiki, N., and Marushima, S., 2003, "A Study of Performance on Advanced Humid Air Turbine Systems," Paper No. IGTC-03 TS-090.
[5] Numata, S., Yokota, O., and Hatamiya, S., 2002, "Analysis of Condensation Heat Transfer to Water Spray for Water Recovery System" [in Japanese], JSME the 39th National Heat and Mass Transfer Symposium pp. 661–662.
[6] Hatamiya, S., Araki, H., and Higuchi, S., 2004, "An Evaluation of Advanced Humid Air Turbine System With Water Recovery," ASME Paper No. GT2004–54031.
[7] Rosén, P., 2000, "Evaporative Cycles—in Theory and in Practise," Licentiate thesis, Lund Institute of Technology, Sweden, ISBN 91-7874-078-9.
[8] Lindquist, T. O., Thern, M., and Torisson, T., 2002, "Experimental and Theoretical Results of a Humidification Tower in an Evaporative Gas Turbine Cycle Pilot Plant," ASME Paper No. GT-2002–30127.
[9] Rao, A. D., Francuz, V. J., Shen, J. C., and West, E. W., 1991, "A Comparison of Humid Air Turbine (HAT) Cycle and Combined-Cycle Power Plants," EPRI IE-7300 Project 2999–7 Final Report.
[10] Parente, J. M. O. S., Traverso, A., and Massardo, A. F., 2003, "Micro Humid Air Cycle Part A: Thermodynamic and Technical Aspects," ASME Paper No. GT-2003–38326.
[11] Bartlett, M., 2002, "Developing Humidified Gas Turbine Cycles," Doctoral thesis, Royal Institute of Technology, Sweden, ISSN 1104–3466.
[12] Nittetu Chemical Engineering Ltd., 2001, *Raschig's Packing & Internals* [in Japanese].
[13] Torbidoni, L., and Horlock, J. H., 2004, "A New Method to Calculate the Coolant Requirements of a High Temperature Gas Turbine Blade," ASME Paper No. GT-2004–53729.
[14] Jordal, K., 2000, "Gas Turbine Cooling Modeling—Thermodynamic Analysis and Cycle Simulations," Licentiate thesis, Lund Institute of Technology LUTMDN/TMVK-7034-SE.
[15] Aramayo-Prudencio, A., and Young, J. B., 2003, "The Analysis and Design of Saturators for Power Generation Cycles: Part II—Heat and Mass Transfer," ASME Paper No. GT-2003-38946.
[16] Parente, J. M. O. S., Traverso, A., and Massardo, A. F., 2001, "Saturator Analysis for an Evaporative Gas Turbine Cycle," Appl. Therm. Eng., **23**, pp. 1275–1293.
[17] Raschig GmbH, 2001, *WINSORP* [Computer Program], ver.4.02.

Safe Dynamic Operation of a Simple SOFC/GT Hybrid System

Christoph Stiller
e-mail: christoph.stiller@ntnu.no

Bjørn Thorud

Olav Bolland

Department of Energy and Process Engineering,
The Norwegian University
of Science and Technology,
Kolbjørn Hejes vei 1B,
N-7491 Trondheim, Norway

The current work shall prove the feasibility and show methods to safely operate a simple SOFC/GT hybrid system under part-load and load change. Dynamic and steady state studies on a detailed model of a SOFC/GT hybrid system have been performed. A design point is selected. Steady-state part-load behavior is shown by means of performance maps. An operation line with fairly constant temperatures in the upper part-load regime and an almost constant efficiency down to approximately 25% part-load is proposed and the dynamic behavior of the system on rapid load changes is investigated. Strategies for the dynamic controlling of power by manipulating fuel flow are shown that might enable the system to adapt to a new setpoint power quite quickly. [DOI: 10.1115/1.2132385]

Keywords: SOFC, hybrid system, dynamic model, part-load

Introduction

A large amount of modeling work [1–4] and a demonstration plant [5] have proven that a solid oxide fuel cell (SOFC) integrated with a gas turbine (GT) has a potential for high efficiency electricity production with low environmental emissions. However, these types of systems face many challenges when it comes to load change and part-load operation. A gas turbine alone has good dynamic properties compared to the SOFC, but part-load performance can be rather poor. In any operational point, compressor surge must be prevented. A SOFC is generally able to respond quickly to load changes [6], but it might be destroyed or seriously degraded either due to thermally induced stresses caused by different thermal expansion coefficients in the cell materials or from carbon deposition at the anode. Another phenomenon that may occur during load change is backflow of gas from the burner to the anode cycle. These incidents must not occur in any operation instance.

Results from part-load operation modeling have already been discussed by some authors. Costamagna et al. [7] investigated a hybrid system using a non-dimensional tubular SOFC model. In all simulations they assumed constant fuel utilization (FU). If shaft speed was assumed constant, power output could only be controlled by varying the fuel flow. These simulations showed large variations in air utilization (AU) and loss of efficiency for fixed shaft speed when operating at part-load. For variable shaft speed, however, AU and FU as well as SOFC inlet temperatures could remain fairly constant in part-load operation with only a small penalty on system efficiency. This effect was mainly due to increased recuperator efficiency owing to reduced air flow rate.

Campanari [8] also used a non-dimensional tubular SOFC model to investigate the hybrid system. Assuming constant FU of 80%, for constant shaft speed they suggested reducing AU and current density for part-load. This approach will reduce power output of the SOFC as well as the turbine inlet temperature (TIT) and consequently the power output of the GT. For variable shaft speed they suggested to reduce air flow rate and current density to maintain a constant AU. However, a reduction in air flow rate leads to pressure reduction and therewith higher turbine outlet temperature (TOT) and thus higher recuperator outlet temperatures. They concluded that for maintaining constant TIT, the current density has to be reduced further.

Chan et al. [3] also investigated a non-dimensional tubular SOFC-type in a hybrid system. In their system, power is reduced by shifting the load from the SOFC to the GT through introducing fuel to the combustor, which results in strong reduction of the system efficiency. This method also implies that a SOFC bypass should be implemented for both fuel and air. Due to the low part-load efficiency, they state that this method is mainly for short term load reduction. The aim was to maintain a relatively high SOFC temperature.

Pålsson and Selimovic [9] used a two-dimensional planar SOFC model for part-load studies. Design point was set where the compressor flow matched the cooling requirement of the SOFC. They introduced an air heater/cooler prior to the SOFC entry in order to meet the requirements for the air inlet temperatures at part-load operation. TIT was kept constant and shaft speed was varied. At part-load operation, increased FU and low GT part-load efficiency led to increased power contribution from the SOFC. Due to the problems associated with matching of the system components, they concluded that the load range for hybrid systems should be limited to 55–100%, corresponding to a load variation of the GT of 20–100%.

Kimijima and Kasagi [10] studied part-load of a 30 kW simple recuperated cycle using a non-dimensional SOFC model. Variable and fixed shaft speed operations are compared. FU is kept constant, even though it is mentioned that FU could be increased at part-load operation. They conclude that variable shaft speed operation is favorable in terms of part-load performance; however the higher TOT could cause problems.

All the above-mentioned authors have identified inlet and outlet gas temperatures as well as air and fuel utilization of the SOFC as important parameters for part-load operation of hybrid systems. Maintaining a constant SOFC operation temperature is important to avoid thermal cracking, but this might be difficult to achieve at reduced pressure as the TOT increases and consequently the recuperator outlet temperatures.

We have recently investigated a SOFC system with recycle and pre-reformer to be fitted into a hybrid system [11]. Performance maps were introduced to illustrate the relationships between the most important SOFC parameters over air flow and either FU or AU, while keeping the other of the two latter parameters constant. Based on these maps, it was found out that strategies with fairly constant temperatures in the SOFC seem feasible. Due to the lack of a GT model, SOFC inlet temperature was assumed constant and the pressure was assumed proportional to the air flow. This was the main limitation of this work.

The current work presents a detailed dynamic model of a tubular SOFC system integrated into a simple recuperated GT cycle. It

Contributed by the International Gas Turbine Institute (IGTI) of ASME for publication in the JOURNAL OF ENGINEERING FOR GAS TURBINES AND POWER. Manuscript received August 30, 2005; final manuscript received September 6, 2005. IGTI Review Chair: K. C. Hall. Paper presented at the ASME Turbo and Expo 2005: Land, Sea, and Air, Reno, NV, June 6–9, 2005, Paper No. GT2005-68481.

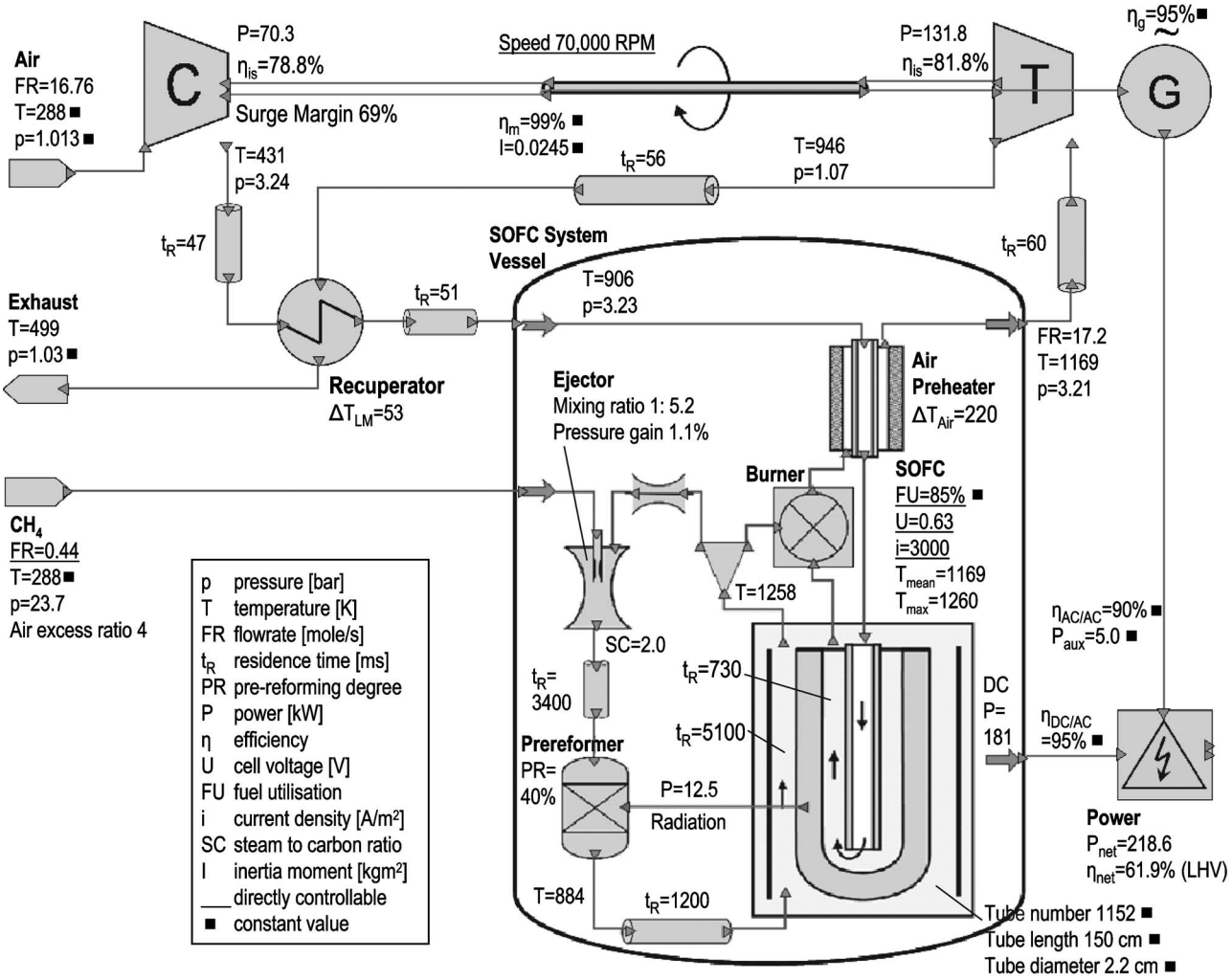

Fig. 1 Cycle layout and design point values (square-marked values remain always constant)

shall prove the feasibility and show methods to operate such a system in part-load and load change without any of the critical phenomena to occur. The system is designed for a certain nominal performance. The selection of the design point is discussed and vital parameters are highlighted. Furthermore, part-load behavior as a function of the controllable parameters, i.e., fuel flow and shaft speed, is investigated. The dependency of crucial system parameters on the controllable parameters is displayed in steady state performance maps. From the maps, valid ranges of the controllable parameters and advantageous operation lines are derived. Applying the derived operation lines, transient behavior of the crucial parameters during load-changes is investigated. Considering steady state and transient results, a strategy for safe operation of the investigated system is proposed. Finally, an overview on further opportunities is given.

SOFC and GT-Cycle Model

The investigated hybrid cycle is shown in Fig. 1. The ducts account for time delay of the flows under transient conditions. The SOFC system design (inside the vessel in Fig. 1) is similar to that of Siemens-Westinghouse. This type of design has been described by other authors [12,13]. The model incorporates pre-reformer, afterburner, and recirculation and mixing chamber, where part of the anode exhaust gas is admixed to the fresh fuel in an ejector in order to supply steam to the steam reforming and shift reaction. Required valves for start-up, shut-down, and failure have not been included. The whole model is implemented in the equation based modeling tool gPROMS [14]. The sub-models comprise the following:

- The SOFC model is spatially discretized and fully dynamic in terms of gas transport and heat transfer, allowing the study of temperature distributions. Gas flows are treated as one-dimensional plug flows, while the solid structures are modeled by a two-dimensional (2D) discretization scheme in axial and radial direction, neglecting effects in the circumferential direction. The model accounts for the effects of internal reforming, activation and concentration polarization, ohmic resistance, and pressure losses. A more detailed description of the model is given in Appendix A.
- As the temperature distribution inside the pre-reformer is of minor interest, it is modeled as a non-dimensional Gibbs equilibrium reactor where reforming and water-gas shift reactions take place. It is thermally connected to the fuel cell tube. The consumed heat is supplied by radiation from the anode surface, adjusted by a shape factor to meet a certain pre-reforming degree at the design case. Gas residence time in the pre-reformer is accounted for by ducts up- and downstream the pre-reformer.
- The afterburner is non-dimensional and adiabatic and completely combusts the remaining anode exhaust gas together with the cathode air. By mixing cathode and anode exhaust

streams, it causes pressure equalization of these flows upstream.
- The afterburner exhaust is preheating the inlet air by a counter-flow tube-shell setup, where the tube is the prolongation of the fuel cell air supply tube. The model accounts for thermal inertia, pressure loss, and gas residence times. The approaches are equal to the SOFC model.
- The pressure loss in the anode loop is overcome by an ejector. High induced (recycle) flow rates at low pressure differences are typically achieved by subsonic mixing ejectors. The actuating flow is accelerated to supersonic speed in a Laval nozzle before it enters the mixing chamber. The ejector model is based on section-wise momentum balances and has been validated against data from Marsano et al. [15]. Pressure losses are included by a fixed throttle valve.
- The ducts are adiabatic and frictionless. Their only purpose is to account for gas residence time.
- The HEX is a stack of counter-flow plate-fin type. A 2D distributed model is applied that accounts for thermal inertia, pressure loss, and gas residence times. The approaches are equal to the SOFC model.
- Generator and power electronics account for transformation efficiencies which are assumed to be constant. A constant power sink accounts for power consumption of auxiliaries and transformation efficiency decrease at low load.
- The compressor is based on the performance map of a small centrifugal research compressor by the German Aerospace Centre [16]. The map is understood as a generic radial compressor map and therefore it has been scaled in terms of reduced mass flow, pressure ratio and shaft speed to fit the design case. The map has been modeled using polynomials of fourth and fifth order for reduced mass flow, pressure and efficiency as functions of reduced shaft speed and operation (β) line. A surge margin (SM) is calculated as follows

$$\mathrm{SM} = \frac{\pi_{\mathrm{surge}}(\dot{m}) - \pi(\dot{m},n)}{\pi(\dot{m},n)} \tag{1}$$

  where $\pi(\dot{m},n)$ is the actual pressure ratio at the actual mass flow and reduced shaft speed and $\pi_{\mathrm{surge}}(\dot{m})$ is the surge pressure ratio at the actual mass flow. An iso-line representation of the compressor characteristics is shown in Appendix B.
- The turbine is based on the performance map of a small radial turbine [16] which is, similar to the compressor map, scaled to fit the design case. An ellipse approach has been used for the relationship between reduced mass flow, reduced shaft speed, and operation (β) line. Pressure ratio and efficiency have been modeled through polynomials. An isoline representation of the turbine characteristics is shown in Appendix B.

The shaft model includes acceleration/deceleration of the shaft through moment of inertia of the moving parts

$$\frac{d\omega}{dt} = \frac{P_B}{I \cdot \omega} \tag{2}$$

where ω is the angular shaft speed in $[\mathrm{rad}\cdot\mathrm{s}^{-1}]$, I is the moment of inertia in $[\mathrm{kg}\cdot\mathrm{m}^2]$, and P_B is the power balance

$$P_B = \eta_m P_{\mathrm{turb}} - P_{\mathrm{comp}} - P_{\mathrm{gen}} \text{ in } [\mathrm{W}] \tag{3}$$

The resulting whole model consists of approximately 9,000 algebraic and 2,000 state variables. The simulations were performed on a 2.5 GHz Intel Pentium-4 processor PC. Calculation time for a steady state point was approximately 5–10 s. The solver for dynamic calculations uses flexible time increments, thus calculation time depends on the momentary fluctuation rate of the variables. A calculation time of about 5 min was required for the dynamic performance studies shown below.

Design Point

Before part-load behavior can be studied, a design point has to be defined. All relevant cycle data are displayed in Fig. 1. Most of the data are similar to recent literature on hybrid cycles [3,7,8,10] and public data from Siemens-Westinghouse. Values in the figure marked with a square are constant during all simulations. The design point and system dimensioning is furthermore based on the following assumptions:

- The system size is determined based on the Siemens-Westinghouse stack design which incorporates 1152 tubular cells [17].
- Pure methane is supplied as fuel.
- A length of 0.5 m was chosen for the air preheat tube, yielding a temperature increase of 220 K at design point.
- The ducts have a length of 1 m and are dimensioned for gas velocities around 20 m/s at design point. The residence times are calculated utilizing the ideal gas law. Therefore they will vary slightly in other operation points. Residence times before and after the pre-reformer account for the actual pre-reformer residence time.
- The fuel utilization (FU) is determined from current and fuel flow, as these parameters can be measured in a real system. Setting FU constant hence means maintaining a constant ratio of current to fuel flow. While this in steady state provokes a constant content of combustibles in the anode exhaust gas, the content may vary during dynamic operation due to pressure change and gas transport delay. Due to the variations of the heating value of the exhaust gas, this may cause severe oscillations in burner temperature during load change. The common fuel utilization value of 85% has been chosen.
- The ejector has been dimensioned for supplying a steam to carbon ratio of 2 in the design point. The difference in static pressure of induced and actuating gas flow in the mixing zone is vital for the ejector performance. According to Johannesen [18], a lower actuating flow pressure than induced flow pressure, causes a strong reduction in induced flow rate, while a higher actuating flow pressure does not significantly increase induced fluid flow rate. For being able to reduce the fuel flow rate for part-load operation while maintaining a high recycle ratio, the inlet pressure of the actuating fluid at design point must be high. A value of 23.7 bar was chosen for design point.
- The recuperator is dimensioned in order to achieve a high amount of heat recuperation at tolerable size and pressure drop.
- The rotating parts of turbine, compressor, generator, and shaft have together a moment of inertia of 0.025 $\mathrm{kg}\cdot\mathrm{m}^2$. This is equivalent to a rotating mass of 20 kg and a mean radius of 5 cm. The moment of inertia influences the power output during shaft acceleration and deceleration.
- The generator is assumed to have a constant efficiency of 95%. The power electronics have constant efficiencies of 90% for ac/ac and 95% for dc/dc conversion. In order to account for power consumption of auxiliaries and the decreasing conversion efficiencies at load reduction, a constant sink term of 5 kW was applied.

Steady-State Performance

With the given design, three degrees of freedom remain for off-design operation:

1. Shaft speed variation
2. Fuel flow variation
3. Fuel utilization/current/voltage variation.

Variation of the shaft speed can be controlled by the power electronics, i.e., generator power. Dependent on the power balance

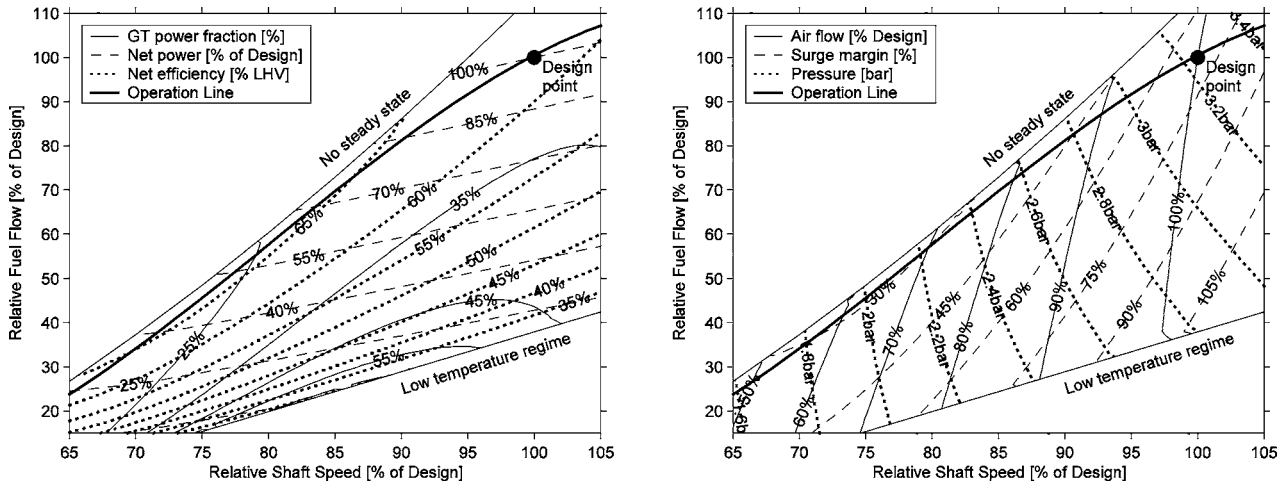

Fig. 2 Power parameters (left) and turbomachinery parameters (right) in steady state

at the shaft, it runs steadily, accelerates or decelerates. Fuel flow variation can be achieved by a control valve. For the dynamic simulations we assume that the flow rate can instantaneously be adjusted to a desired value.

Fuel utilization and current are coupled via the fuel flow rate, while current and voltage are coupled via the fuel cell characteristics. However, large variations in FU are not recommendable, as low FU leads to low steam content in the anode recycle and high TIT, while high FU leads to steep internal temperature gradients in the fuel cell. Therefore, we chose to operate at constant FU by setting the current proportional to the fuel flow rate.

The remaining free parameters, shaft speed and fuel flow, may be varied independently from each other within certain limits. Each combination determines a certain operation point of the system. Thus, two-dimensional matrices of the interesting process parameter steady state values over the two free parameters can be produced and displayed in performance maps. We have previously introduced similar maps for a SOFC stack system [11]. In that work we used air utilization and air flow rate as free parameters. Due to absence of a GT cycle model, in that work simplified assumptions for gas inlet temperature and operating pressure had to be made. These data are in the present work being calculated by the GT cycle model, representing a more comprehensive study.

For easy reading, we give dimensionless values for shaft speed (RSS) and fuel flow (RFF), related to the design point values. RSS is varied between 65% and 105%, representing the valid range for the compressor and turbine map. RFF is varied between 15% and 110%.

Figures 2 and 3 show the steady-state behavior of the parameters of interest as a function of RSS and RFF. For easier reading, each diagram shows only the fields of three parameters.

The blinded out area on the upper left (low shaft speed and high fuel flow) represents an area where no steady state exists. Transient experiments have shown that the temperature in this regime is steadily climbing far beyond the valid ranges and furthermore eventually causing compressor surge. This is because enhanced effectiveness of the heat recuperation loop and lower air excess ratio at lower airflow causes TIT to increase. Concurrently, the increased TIT causes decrease of airflow, originating from compressor and turbine characteristics.

In the lower right area (high shaft speed and low fuel flow), the cell is cooled down strongly and therefore the voltage is low. As it is not recommendable to operate in this regime, it is blinded out for cell voltages lower than 0.3 V.

A first result from the performance map is that reducing fuel flow at constant shaft speed (and therewith fairly constant air flow), i.e., going down a vertical line from design point, results in a strong reduction in temperatures and therewith efficiencies.

The figures also show that a load reduction by linearly reducing

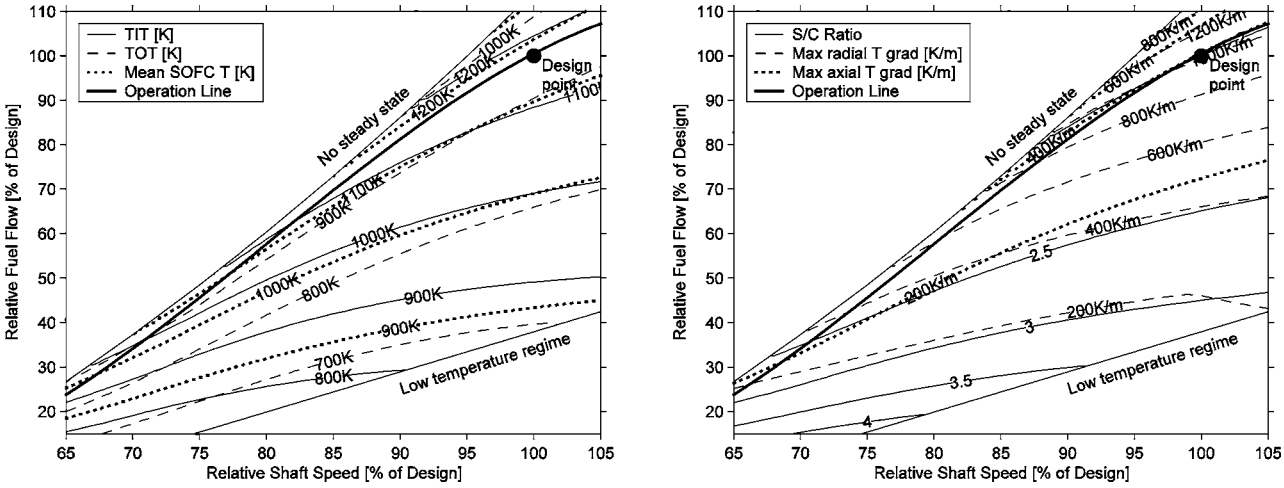

Fig. 3 Significant temperatures (left) and steam to carbon ratio and SOFC temperature gradients (right) in steady state

fuel flow and air flow will lead into the unstable region. Remaining in the stable regime therefore implies larger percentual reduction in fuel flow than air flow. This is a consequence of the lower pressure ratio at reduced shaft speed which results in an increased TOT. The same behavior is also confirmed in a study by Costamagna et al. [7].

Surge margin and steam to carbon ratio do not reach any alarming values in the shown operation range.

Steady-State Operation Line

The main parameter of interest for the power plant is simply the power output. Using the performance maps, we find lines of constant dimensionless net power in Fig. 2. For a certain desired power in steady state, each point of its line is basically a valid operation point. However, in order to decide which point is optimal, the following objectives need to be considered:

1. High efficiency
2. Safe operation: Distance from invalid regimes and alarming values for safety-relevant parameters
3. Fairly constant SOFC temperature level

The latter point is the most restrictive requirement, as thermal cycling affects the lifetime of SOFCs. It is also the most important in terms of load following behavior and thermal gradients in the fuel cell during dynamic operation.

From Fig. 3 it can be seen that isolines of the most significant temperatures are almost parallel and linear in the area of interest.

At a given current, the mean SOFC temperature is strongly influencing voltage and thus power output of the SOFC. Due to high thermal inertia, the SOFC is quite slow in reaching a new steady temperature state after a load change, causing power to vary over a long time. The most favorable operation line in terms of quick load following would therefore be along a line of constant mean SOFC temperature. However, in Fig. 3 (left, red lines), it can be seen that reducing shaft speed at constant mean SOFC temperature results in approaching the regime where no steady state exists. We assume there is an indifferent regime close to the steady-state boundary, where the same values of air and fuel flow may cause different operation temperatures depending on the initial temperatures. However, if no reliable temperature feedback to the control system exists, the system cannot be operated safely in this regime. Hence the temperature must be decreased when strongly decreasing the load. The proposed operation line therefore follows a line of constant mean SOFC temperature for relative shaft speed between 90% and 100%. Below 90%, the operation line departs from the constant mean SOFC temperature line and instead pursues a parallel line to the steady-state border down to the minimum RSS of 65%. The resulting operation line can be developed as a third order polynomial and is plotted in the maps. Its equation is

$$\mathrm{RFF} = -7.21 \cdot \mathrm{RSS}^3 + 17.31 \cdot \mathrm{RSS}^2 - 11.45 \cdot \mathrm{RSS} + 2.34 \quad (4)$$

With this strategy, a fairly constant mean SOFC temperature of approximately 1170 K can be maintained in a range of relative net power (RP) from 80% to 105%. The minimum part load operation at 65% RSS yields a relative power of 24% and a mean SOFC temperature of 970 K. Knowing a desired output power (in steady state), the required shaft speed can be estimated through

$$\mathrm{RSS} = 0.674 \cdot \mathrm{RP}^3 - 1.08 \cdot \mathrm{RP}^2 + 0.930 \cdot \mathrm{RP} + 0.478 \quad (5)$$

The net LHV-based efficiency increases from 62% at design point to 66% at relative power of 50% and decreases again to 63% at minimum part load. TIT decreases from 1170 K at design point slowly to approximately 930 K at minimum part load. This decrease helps in keeping the surge margin wide. Trends and values of all other parameters can be estimated from the performance maps. Including an air bypass around the SOFC system may facilitate constant mean SOFC temperature over the whole range. This will be studied further.

The shown behavior certainly depends on the characteristics of all applied components and assumptions of the cycle. The displayed quantitative data represent only the current system. However, the trends are expected to be similar in a real system. Hence, the demonstrated methods can be applied on a real system, once an accurate model of its true behavior is available.

Dynamic Performance

In the following study, the control parameters of fuel flow and shaft speed are changed between several points and the behavior of the crucial system parameters is investigated. There is no controller including a feedback loop of measured output parameters as normally found in control system designs. The purpose of this method is to show the straight, non-controlled behavior of the system following a load change.

In order to study dynamic load changes, a strategy for changing shaft speed and fuel flow is required. Speed changes of the shaft are calculated by its inertia and power balance; see Eqs. (2) and (3). In case of reduced generator load the shaft accelerates, and vice versa. We manipulate the shaft power balance in a way that the shaft acceleration/deceleration is either a constant value or zero

$$\frac{P}{I \cdot \omega} = \frac{d\omega}{dt} = R \cdot \mathrm{sgn}(N_{\text{set point}} - N) \quad (6)$$

where $N_{\text{set point}}$ is the set point shaft speed in $[\mathrm{s}^{-1}]$ and R is the shaft speed change rate in $[\mathrm{rad} \cdot \mathrm{s}^{-2}]$. The sgn function yields

$$1 \text{ if } N < N_{\text{set point}}$$

$$0 \text{ if } N = N_{\text{set point}}$$

$$-1 \text{ if } N > N_{\text{set point}}$$

Therewith the shaft speed is either constant at set point or moving linearly towards a new set point. The value of 52.4 $\mathrm{rad} \cdot \mathrm{s}^{-2}$, corresponding to a speed change rate of 500 rpm/s, is set for R. This approach only represents a theoretical investigation method; for practical speed control systems, additional requirements apply.

The relative fuel flow is coupled to the actual relative shaft speed via the operation line Eq. (4), i.e., a speed change will result in fuel flow following an approximate ramp function.

The time from initiation of a load change until the new steady state is reached, called relaxation time, is an important parameter in dynamic studies. Figure 4 shows relaxation behavior for a quick load change between 100% and 24% RP (respectively, 100% and 65% RSS). At time equals 1, the shaft speed set point is changed by a step.

As can be seen from Fig. 4, with the reset of the set point shaft speed at time equals 1, power performs an immediate step into the inverse direction due to the shaft deceleration/acceleration. It takes very long until the power reaches its steady value after the load changes, calling for a control strategy incorporating feedback loops for exact load following.

The surge margin has a minimum during load decrease and a maximum during increase. This behavior is different from regular gas turbine cycles. It is caused by the fairly constant TIT during speed change, which is caused by thermal inertia of the air preheater inside the SOFC system.

The maximum temperature gradients in the cell show unsteadiness along the relaxation time, indicating that the cell temperature profile is changing and the location of maximum gradients are moving. However, no global minima or maxima can be observed during the relaxation process.

During load decrease, the steam to carbon ratio reaches a minimum of 1.8 after approximately 50 s, but this is not regarded as a critical value. During load increase, the anode exhaust gas recycle ratio increases temporarily to a very high value. This represents a

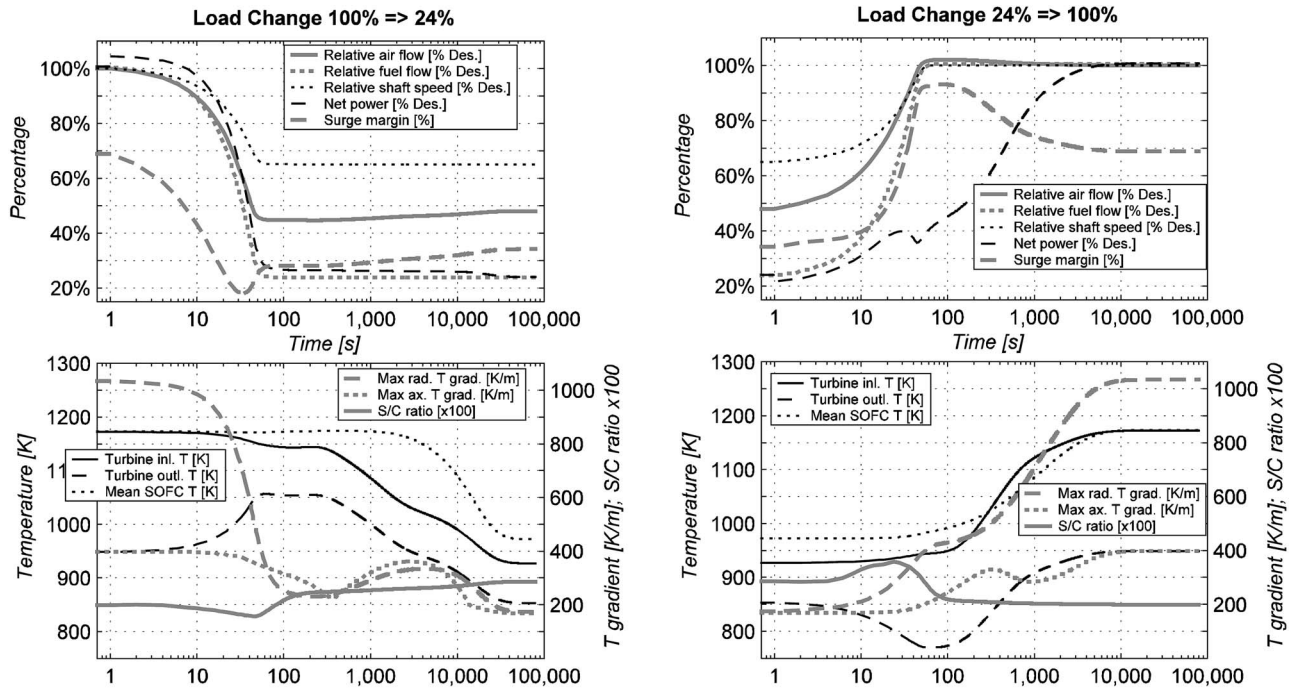

Fig. 4 Load change between 24% and 100% (left: decrease; right: increase)

danger, as it may cause backflow from the burner to the anode exhaust gas recycle loop. Thereby the anode may be exposed to oxygen.

Figure 5 shows the fuel flow into the burner for a load increase at different speed change rates. The minima occur because during load change, the pressure is increasing and with it the gas mass in the fuel cell. Hence, less gas is leaving the cell than entering it during pressure increase. Furthermore, more fuel is being introduced, improving ejector performance. Anode backflow is hence restricting the maximum possible speed/pressure increase rate.

Another problem with quick pressure increase is the temporarily high depletion of the anode outlet gas due to the constant current to fuel flow ratio. In other words, the "true" fuel utilization may temporarily come very close to 100% and the voltage must be decreased to very low values in order to keep the current to fuel flow ratio constant. The simulation with 750 rpm/s in Fig. 5 could not be finished due to numerical problems associated to this phenomenon. It may in practice lead to fuel cell degradation or burner extinguishing. However, it can be omitted by a more sophisticated current/voltage control (i.e., setting a minimum boundary for the voltage). The break in the power curve during load increase at a time of approximately 50 s (see Fig. 4) is also a result of a temporarily too low voltage.

Table 1 lists the time required from the set point reset until the margin of ±2% of the new steady state value of power and radial gradient has been reached for load change between three different points. The maximum radial thermal gradient is taken as a measure for the thermal steady state, simply because it shows the strongest variation of all temperature-related parameters. Steady power is always reached somewhat quicker.

It can be observed that between 80% and 100% relative net power, steady state is reached quicker. This is because of the fairly constant mean SOFC temperature in this regime, with the SOFC comprising the highest thermal inertia in the system. Beside the mean SOFC temperature, relaxation time is strongly influenced by the end point of the load change. Higher load end points cause quicker relaxation as a consequence of the higher gas and energy turnover. This has been reported previously by Achenbach [6] and is the reason why load increases relax generally faster than load decreases.

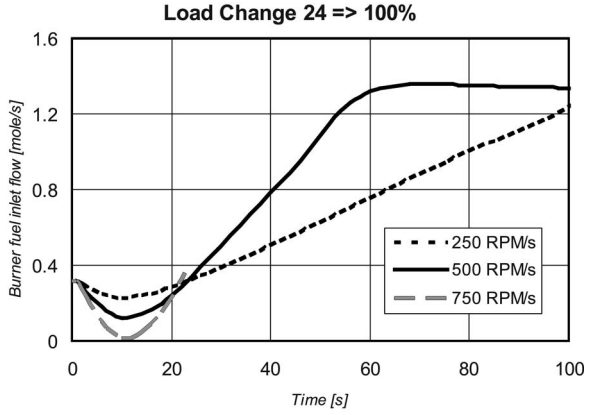

Fig. 5 Burner fuel flow at different speed change rates

Table 1 Relaxation times for load changes

Relaxation time [s]		to 24%	to 80%	to 100%
From RP=24%	Power		5400	3800
	Radial Grad.		11000	6200
From RP=80%	Power	26000		360
	Radial Grad.	38000		2650
From RP=100%	Power	28000	40	
	Radial Grad.	40000	5300	

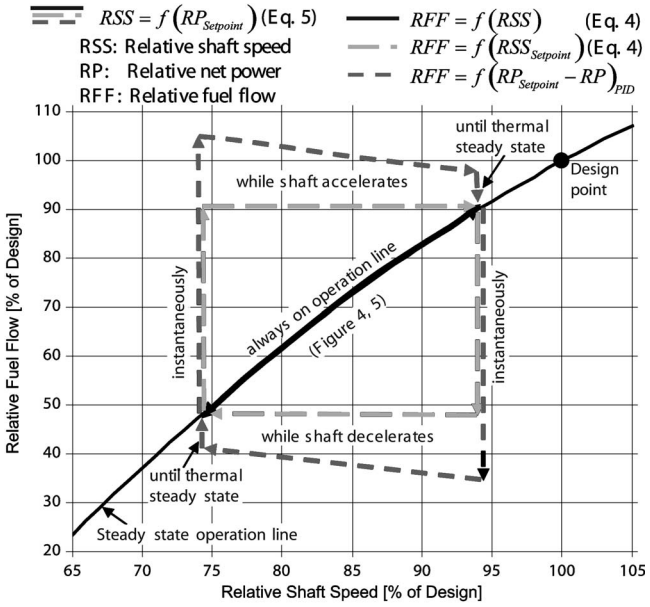

Fig. 6 Control strategies for fuel flow

Control Strategy

The dynamic performance study revealed slow relative power change and long time until power steady state is reached when moving along the proposed operation line. This might be sufficient for a power plant connected to the grid. However, a remote power plant without grid connection is required to follow load curves very quickly, thus load compensation units such as batteries or large capacitors would be required.

On the other hand, other methods of operating the hybrid cycle may be advantageous. At present, the fuel flow, which influences power output to great extent and which can be controlled quite quickly, is coupled to the rather slowly moving parameter of shaft speed via Eq. (4). Furthermore, during a load change, the system may be operated at any combination of RSS and RFF, as long as the end point is within the stable regime of the performance maps.

In an advanced control strategy, the set point shaft speed could be directly coupled to the set point power output via Eq. (5), ensuring that the system in steady state is always on the proposed operation line.

The fuel flow could then be coupled to the set point shaft speed instead of the actual shaft speed in the same way as in Eq. (4), resulting in a much faster power change. The most efficient way though would be to control fuel flow by comparing the feedback measured actual power with the set point power.

Figure 6 shows the proposed strategies in a RFF-over-RSS diagram (same as Figs. 2 and 3). The red line indicates the movement of the parameters if fuel flow is coupled to actual shaft speed (strategy pursued for the above dynamic performance study). The rectangular lines indicate the movement of parameters if fuel flow is coupled to set point shaft speed, and the outer lines sketch the possible behavior if the power output is controlled a feedback loop. With the latter strategy, it should be possible to follow load curves with a very short delay between set point and actual power. However, the mentioned critical phenomena could be a restriction to very quick load variation with the proposed system.

Where quick load following is required, alternative systems with constant shaft speed and other means to control the air flow, such as variable inlet guide vanes or an air bypass, may be even more suitable, as these control means can be manipulated much quicker than the inertia-affected shaft speed. Another option would be introduction of an auxiliary burner in the current system directly upstream the turbine for quick TIT control.

Conclusions

A powerful full dynamic model of a simple hybrid system has been developed and the hybrid system performance has been characterized. The following main conclusions can be drawn:

1. The system power is mainly controlled by fuel flow, shaft speed, and current.
2. Setting the ratio of current to fuel flow (and therewith fuel utilization) constant, the part-load behavior of the system shows the presence of unstable regimes (no steady state exists) at high fuel flow and low shaft speed, and regimes with very low SOFC temperatures at high shaft speed and low fuel flow.
3. In steady-state part-load, the air-to-fuel ratio must increase in order not to operate in an unstable regime.
4. Operation lines with constant mean SOFC temperature exist, but approximate the unstable regime. An operation line is proposed where the mean SOFC temperature is constant in a load range from 80% to 100%. Below 80% load, temperature must decrease if no temperature feedback controller is applied.
5. Load changes in the regime of constant mean SOFC temperature reach a new thermal steady state quite quick, while it takes much longer when the temperature is varied.
6. The effect of gas from the burner flowing back into the anode cycle restricts the pressure increase rate under load increase.
7. Quicker load changes may be performed when the fuel flow and SOFC current are varied quicker than the shaft speed.
8. With the present tool, a coherent design for control of the whole system may be developed.

The depicted quantitative data are only valid for the studied model. However, the qualitative trends are expected to be similar in a genuine system. Hence, the demonstrated methods can be applied on a real system, given that relevant data of its behavior are available.

Acknowledgment

We thank the Norwegian Research Council, Shell Technology Norway and Statkraft for their financial support.

Nomenclature

FU = fuel utilization
GT = gas turbine
HEX = heat exchanger
RFF = fuel flow relative to design point
RP = net power relative to design point
RPM = rounds per minute
RSS = shaft speed relative to design point
SM = surge margin
SOFC = solid oxide fuel cell
TIT = turbine inlet temperature
TOT = turbine outlet temperature

Appendix A: SOFC Model (Figs. 4–7, Table 2)

Figure 7 shows a breakdown of the cell geometry. The numbers refer to the equations for the thermal model which are listed in Table 2. The following features are included:

- Heat transfer between the fuel cell tube walls and the fluids are calculated using Newton's law of cooling. Heat transfer coefficients are calculated from Nusselt numbers for laminar flow and for constant heat flux.
- Thermal radiation is incorporated between the air supply tube and the cathode surface by using a shape factor for

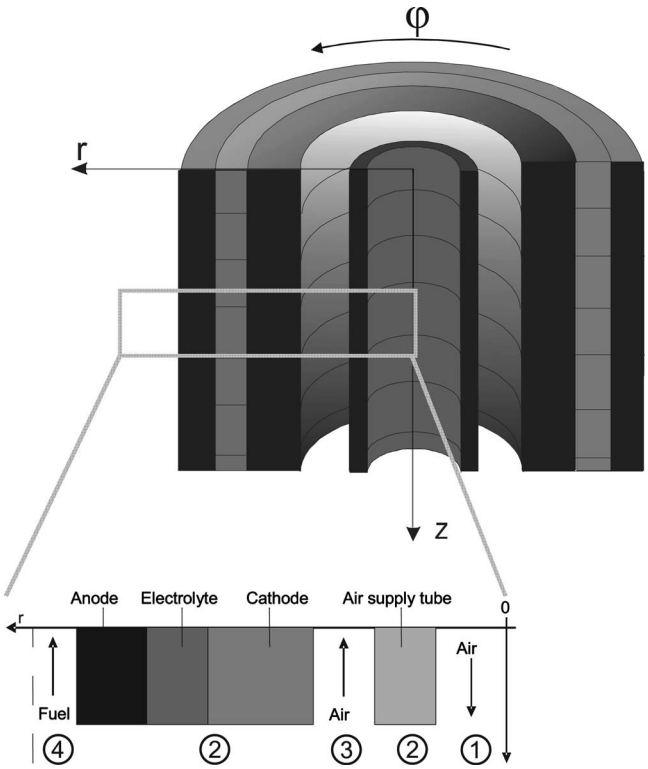

Fig. 7 Break down of the cell geometry

radiation between two tubes, neglecting axial spreading effects and absorption in the gas.

- To reduce calculation time, the solid structure of the anode, electrolyte and the cathode is treated as one single material with weighted mean values for the thermal and electrical properties.
- As the total thickness of anode and electrolyte (0.14 mm) is very small compared to the cathode (2.2 mm), heat sources and sinks related to the electrochemical and methane reforming kinetics are located at the anode surface.
- For steam reforming kinetics, Achenbach's approach is used [19], while the water-gas shift reaction is assumed to be always in equilibrium.
- The local electrical potential is calculated by the Nernst equation, an approach for polarization losses by Karoliussen et al. [20], an analytical expression for the ohmic resistance developed by Nisancioglu [21] and diffusion losses. For the latter, Knudsen-diffusion is applied using diffusion coefficients determined from the Fuller method [22] and correction factors for multicomponent diffusion coefficient calculation. Electrochemical oxidation of CO is neglected.

Friction losses in the air delivery tube, cathode and anode channels are accounted for by the Reynolds number approach and under the assumption of laminar flow [23].

Appendix B: Compressor and Turbine Map

See Figs. 8 and 9.

Table 2 Equations for heat transfer in the SOFC tube

Ref. No. in Fig. 7	Equation	Comment
1	$\frac{\partial(T_{\text{air}}c_p\rho_{\text{air}})}{\partial t}+v_{\text{air}}\frac{\partial(T_{\text{air}}c_p\rho_{\text{air}})}{\partial z}=\frac{2\alpha}{r_{\text{AST},i}}(T_{\text{AST}}-T_{\text{air}})$	Heat transfer between air supply tube and air within the tube
2	$\frac{dT}{dt}=\frac{k}{c\cdot\rho}\nabla^2T$	Heat conduction in solid structures (Air supply tube and SOFC membrane)
3	$\frac{\partial(T_{\text{air}}c_p\rho_{\text{air}})}{\partial t}+v_{\text{air}}\frac{\partial(T_{\text{air}}c_p\rho_{\text{air}})}{\partial z}=\frac{2r_{\text{AST},o}\alpha_{\text{AST},o}}{(r_{c,i}^2-r_{\text{AST},o}^2)}(T_{\text{AST},o}-T_{\text{air}})+\frac{2r_{c,i}\alpha_{c,i}}{(r_{c,i}^2-r_{\text{AST},o}^2)}(T_{c,i}-T_{\text{air}})$	Heat transfer between air supply tube, cathode air and cathode
4	$\frac{\partial(T_{\text{fuel}}\rho_{\text{fuel}}c_{p,\text{fuel}})}{\partial t}+v_{\text{fuel}}\frac{\partial(T_{\text{fuel}}\rho_{\text{fuel}}c_{p,\text{fuel}})}{\partial z}$	Heat transfer between anode surface and fuel
	$=\frac{2\alpha_{\text{fuel}}r_{a,o}}{((r_{a,o}+\Delta r)^2-r_{a,o}^2)}(T_{a,o}-T_{\text{fuel}})$	
	$\frac{\partial(T_{\text{fuel}}c_{p,\text{fuel}}\rho_{\text{fuel}})}{\partial t}+v_{\text{fuel}}\frac{\partial(T_{\text{fuel}}c_{p,\text{fuel}}\rho_{\text{fuel}})}{\partial z}=\frac{2r_{a,o}\alpha_{\text{fuel}}}{((r_{a,o}+\Delta r)^2-r_{a,o}^2)}(T_{a,o}-T_{\text{fuel}})$	

Nomenclature	T	Temperature [K]	k	Thermal conductivity [W/mK]
	c/c_p	Heat capacity [J/kg K]	α	Convective heat transfer coeff. [W/m^2 K]
	ρ	Density [kg/m^3]	Δr	Thickness of fuel plenum [m]
	v	Gas velocity [m/s]	r	Radius [m]
	t	Time [s]	z	Axis direction [m]
Subscripts	AST	Air supply tube	c	Cathode
	a	Anode	i	Inner radius
	o	Outer radius		

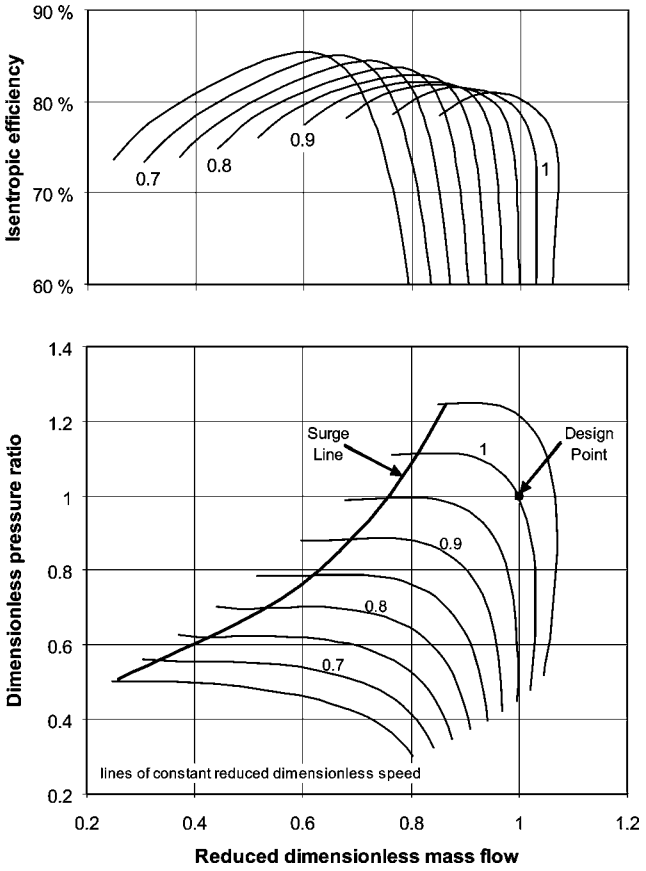

Fig. 8 Normalized compressor map

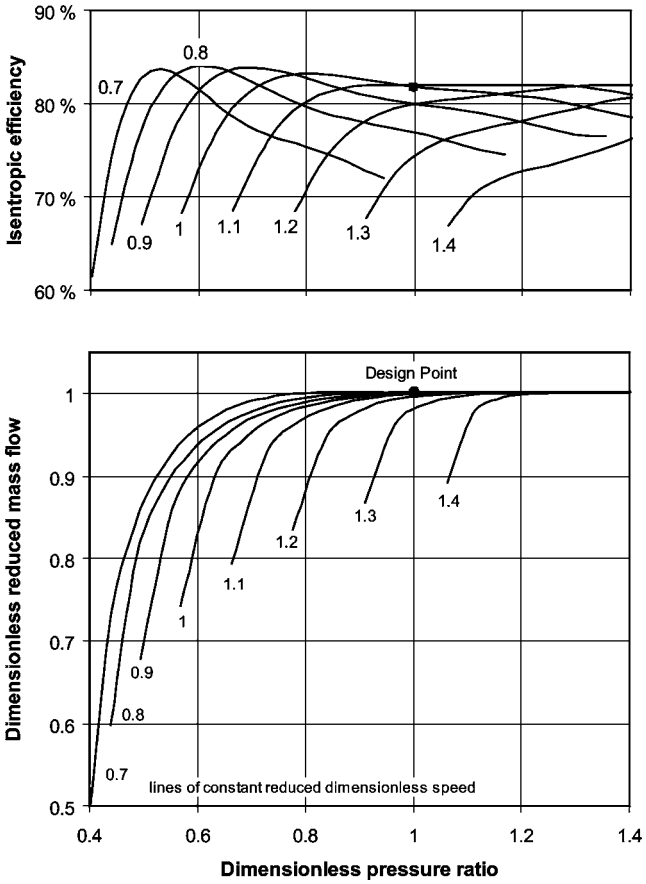

Fig. 9 Normalized turbine map

References

[1] Stiller, C., Thorud, B., Seljebø, S., Mathisen, Ø., Karoliussen, H., and Bolland, O., 2004, "Finite-Volume Modeling and Hybrid-Cycle Performance of Planar and Tubular Solid Oxide Fuel Cells," J. Power Sources (to be published).

[2] Rao, D., and Samuelsen, G. S., 2001, "A Thermodynamic Analysis of Tubular SOFC Based Hybrid Systems," ASME Paper 2001-GT-0522.

[3] Chan, S. H., Ho, H. K., and Tian, Y., 2003, "Modeling for Part-Load Operation of Solid Oxide Fuel Cell-Gas Turbine Hybrid Power Plant," J. Power Sources, **114**, pp. 213–227.

[4] Pålsson, J., Selimovic, A., and Sjunnesson, L., 2000, "Combined Solid Oxide Fuel Cell and Gas Turbine Systems for Efficient Power and Heat Generation," J. Power Sources, **86**, pp. 442–448.

[5] Veyo, S. E., Lundberg, W. L., Vora, S. D., and Litzinger, K. P., 2003, "Tubular SOFC Hybrid Power System Status," ASME Paper 2003-GT-38943.

[6] Achenbach, E., 1995, "Response of a Solid Oxide Fuel Cell to Load Change," J. Power Sources, **57**, pp. 105–109.

[7] Costamagna, P., Magistri, L., and Massardo, A. F., 2001, "Design and Part-Load Performance of a Hybrid System Based on a Solid Oxide Fuel Cell Reactor and a Micro Gas Turbine," J. Power Sources, **96**, pp. 352–368.

[8] Campanari, S., 2000, "Full Load and Part Load Performance Prediction for Integrated SOFC and Microturbine Systems," J. Eng. Gas Turbines Power, **122**, pp. 239–246.

[9] Pålsson, J., and Selimovic, A., 2001, "Design and Off-Design Predictions of a Combined SOFC and Gas Turbine System," ASME Paper 2001-GT-0379.

[10] Kimijima, S., and Kasagi, N., 2002, "Performance Evaluation of Gas Turbine-Fuel Cell Hybrid Micro Generation System," ASME Paper 2002-GT-30111.

[11] Thorud, B., Stiller, C., Weydahl, T., Bolland, O., and Karoliussen, H., 2004, "Part-Load and Load-Change Simulation of Tubular SOFC Systems," Sixth European Solid Oxide Fuel Cell Forum, Lucerne, Switzerland.

[12] Rao, A. D., and Samuelsen, G. S., 2002, "Analysis Strategies for Tubular Solid Oxide Fuel Cell Based Hybrid Systems," J. Eng. Gas Turbines Power, **124**, pp. 503–509.

[13] Song, T. W., Sohn, J. L., Kim, J. H., Kim, T. S., Ro, S. T., and Suzuki, K., 2004, "Parametric Studies for a Performance Analysis of a SOFC/MGT Hybrid Power System Based on a Quasi-2D Model," ASME Paper 2004-GT-53304.

[14] gPROMS (General Process Modelling and Simulation Tool), v.2.3.3, Process Systems Enterprise Ltd., London, http://www.psenterprise.com/.

[15] Marsano, F., Magistri, L., and Massardo, A. F., 2004, "Ejector Performance on a Solid Oxide Fuel Cell Anodic Recirculation System," J. Power Sources, **129**, pp. 216–228.

[16] Kurzke, J., 2004, *Compressor and Turbine Maps for Gas Turbine Performance Computer Programs—Component Map Collection 2*, Joachim Kurzke, Dachau, Germany.

[17] Yi, Y., Smith, T. P., Brouwer, J., Rao, A. D., and Samuelsen, G. S., 2003, "Simulation of a 220 Kw Hybrid SOFC Gas Turbine System and Data Comparison 2003," Proc.-Electrochem. Soc., **7**, pp. 1442–1454.

[18] Johannesen, N. H., 1951, "Ejector Theory and Experiments," Dissertation, Danish Academy of Technical Sciences, Copenhagen, Denmark.

[19] Achenbach, E., and Riensche, E., 1994, "Methane/Steam Reforming Kinetics for Solid Oxide Fuel Cells," J. Power Sources, **52**, pp. 283–288.

[20] Karoliussen, H., Nisancioglu, K., Solheim, A., and Ødegård, R., 1992, "SOFC Stack Modeling With Internal Reforming," Fourth IEA Workshop on SOFC, Lausanne, Switzerland.

[21] Nisancioglu, K., 1989, "Ohmic Losses," Natural Gas Fuelled Solid Oxide Fuel Cells and Systems, IEA Workshop on Mathematical Modelling, Charmey, Switzerland.

[22] Reid, R. C., Prausnitz, J. M., and Poling, B. E., 1987, *The Properties of Gases and Liquids*, McGraw-Hill, New York.

[23] Mills, A. F., 1995, *Heat and Mass Transfer*, Irwin, Chicago.

Steven Chambers
Horia Flitan
Paul Cizmas[1]

Department of Aerospace Engineering,
Texas A&M University,
College Station, TX 77843

Dennis Bachovchin
Thomas Lippert

Siemens-Westinghouse Power Corporation,
Pittsburgh, PA 15235

David Little
Siemens-Westinghouse Power Corporation,
Orlando, FL 32826

The Influence of In Situ Reheat on Turbine-Combustor Performance

This paper presents a numerical and experimental investigation of the in situ reheat necessary for the development of a turbine-combustor. The flow and combustion were modeled by the Reynolds-averaged Navier-Stokes equations coupled with the species conservation equations. The chemistry model used herein was a two-step, global, finite rate combustion model for methane and combustion gases. A numerical simulation was used to investigate the validity of the combustion model by comparing the numerical results against experimental data obtained for an isolated vane with fuel injection at its trailing edge. The numerical investigation was then used to explore the unsteady transport phenomena in a four-stage turbine-combustor. In situ reheat simulations investigated the influence of various fuel injection parameters on power increase, airfoil temperature variation, and turbine blade loading. The in situ reheat decreased the power of the first stage, but increased more the power of the following stages, such that the power of the turbine increased between 2.8% and 5.1%, depending on the parameters of the fuel injection. The largest blade excitation in the turbine-combustor corresponded to the fourth-stage rotor, with or without combustion. In all cases analyzed, the highest excitation corresponded to the first blade passing frequency. [DOI: 10.1115/1.2135812]

1 Introduction

In the attempt to increase the thrust-to-weight ratio and decrease the thrust specific fuel consumption, turbomachinery designers are facing the fact that the combustor residence time can become shorter than the time required to complete combustion. As a result, combustion could continue in the turbine, which is often considered to be undesirable. A thermodynamic cycle analysis, however, demonstrated a long time ago the benefits of using reheat in the turbine in order to increase specific power and thermal efficiency. Even better performance gains for specific power and thermal efficiency were predicted for power generation gas turbine engines when the turbine is coupled with a heat regenerator [1]. Starting in the 1960s, several patents were awarded for different inventions that addressed various aspects related to turbine reheat [2–4].

In spite of these advances, the technological challenges and the difficulty of predicting and understanding the details of the transport phenomena inside the reheat turbine precluded the development of turbine-combustors. Herein, a turbine-combustor is defined as a turbine in which fuel is injected and combustion takes place. The process of combustion in the turbine is called in situ reheat.

Several challenges are associated with the combustion in the turbine-burner: mixed subsonic and supersonic flows, flows with large unsteadiness due to the rotating blades, hydrodynamic instabilities, and large straining of the flow due to the very large three-dimensional acceleration and stratified mixtures [1]. The obvious drawback associated with the strained flows in the turbine-burner is that widely varying velocities can result in widely varying residence time for different flow paths and, as a result, there are flammability difficulties for regions with shorter residence times. In addition, transverse variation in velocity and kinetic energy can cause variations in entropy and stagnation entropy that impact heat transfer. The heat transfer and mixing may be enhanced by increasing interface area due to strained flows.

Experimental data for conventional (i.e., without in situ reheat) gas-turbines have shown the existence of large radial and circumferential temperature gradients downstream of the combustor [5,6]. These temperature nonuniformities, called hot streaks, have a significant impact on the secondary flow and wall temperature of the entire turbine. Since the combustor exit flow may contain regions where the temperature exceeds the allowable metal temperature by 460–930 K [7], understanding the effects of temperature nonuniformities on the flow and heat transfer in the turbine is essential for increasing vane and blade durability. It is estimated that an error of 100 K in predicting the time-averaged temperature on a turbine rotor can result in an order of magnitude change in the blade life [8,9].

Temperature nonuniformities generated by the upstream combustor can be amplified in a turbine-burner. Consequently, it is expected that not only will the secondary flow and wall temperature be affected but also the blade loading due to the modified pressure distribution. Temperature nonuniformities in a turbine-burner can also affect the location of hot spots on airfoils and, as a result, can affect the internal and film cooling schemes.

Numerous experimental [7,10–14] and numerical [15–19] investigations explored the influence of temperature nonuniformities on the flow and heat transfer in a conventional turbine. To the best knowledge of the authors, there are no data, however, available in the open literature that illustrate the effects of in situ reheat on turbine-burners. The objective of this paper is to evaluate a numerical model for in situ reheat against experimental data for a single-vane burner and to use this numerical model to investigate the effects of combustion on the performance of a four-stage turbine-combustor. This numerical simulation is crucial for the development of turbine-burners which, in spite of their challenges, can provide significant performance gains for turbojet engines and power generation gas turbine engines.

Section 2 presents the physical model used for the simulation of flow and combustion in a turbine-combustor. The governing equations and the chemistry model are presented. Section 3 describes

[1]To whom correspondence should be addressed.

Contributed by the International Gas Turbine Institute (IGTI) of ASME for publication in the JOURNAL OF ENGINEERING FOR GAS TURBINES AND POWER. Manuscript received October 1, 2003; final manuscript received March 1, 2004. IGTI Review Chair: A. J. Strazisar. Paper presented at the International Gas Turbine and Aeroengine Congress and Exhibition, Vienna, Austria, June 13–17, 2004, Paper No. GT2004-54071.

the numerical model. This section includes information about the grid generation, boundary conditions, and numerical method. The comparison against experimental data and the results for a four-stage turbine are presented in Sec. 4.

2 Physical Model

The effects of in situ reheat on (i) a single vane-burner, and (ii) a multirow turbine-burner are modeled by the Reynolds-averaged Navier-Stokes equations and the species conservation equations. The model is three-dimensional for the single vane, and quasi-three-dimensional for the four-stage turbine-combustor, in order to reduce the computational time. This section will present the details of the governing equations and the chemistry model.

2.1 Governing Equations. The unsteady, compressible flow through the turbine-combustor was modeled by the Reynolds-averaged Navier-Stokes equations. The flow was assumed to be fully turbulent and the kinematic viscosity is computed using Sutherland's law. The Reynolds-averaged Navier-Stokes equations and species conservation equations were simplified by using the thin-layer assumption [20].

In the hypothesis of unity Lewis number, both the Reynolds-averaged Navier-Stokes and species equations were written as [21]

$$\frac{\partial Q}{\partial \tau}+\frac{\partial F}{\partial \xi}+\frac{\partial G}{\partial \eta}=\frac{\sqrt{\gamma_\infty}M_\infty}{\mathrm{Re}_\infty}\frac{\partial S}{\partial \eta}+S_{ch} \tag{1}$$

Note that Eq. (1) was written in the body-fitted curvilinear coordinate system (ξ, η, τ).

The state and flux vectors of the Reynolds-averaged Navier-Stokes equations in the Cartesian coordinates were

$$q^{ns}=\begin{bmatrix}\rho\\ \rho u\\ \rho v\\ e\end{bmatrix},\quad f^{ns}=\begin{bmatrix}\rho u\\ \rho u^2+p\\ \rho uv\\ (e+p)u\end{bmatrix},\quad g^{ns}=\begin{bmatrix}\rho v\\ \rho uv\\ \rho v^2+p\\ (e+p)v\end{bmatrix}$$

The state and flux vectors of the species conservation equations in the Cartesian coordinates were

$$q^{sp}=\begin{bmatrix}\rho y_1\\ \rho y_2\\ \vdots\\ \rho y_N\end{bmatrix},\quad f^{sp}=\begin{bmatrix}\rho u y_1\\ \rho u y_2\\ \vdots\\ \rho u y_N\end{bmatrix},\quad g^{sp}=\begin{bmatrix}\rho v y_1\\ \rho v y_2\\ \vdots\\ \rho v y_N\end{bmatrix}$$

Further details on the description of the viscous terms and chemical source terms are presented in [22].

2.2 Chemistry Model. The purpose of this investigation was to determine the influence of in situ reheat on the performance of a turbine-combustor, as opposed to predicting the complete set of combustion products. Consequently, the chemistry model used herein was a two-step, global, finite rate combustion model for methane and combustion gases [23,24]

$$\begin{aligned}\mathrm{CH_4}+1.5\mathrm{O_2}&\rightarrow \mathrm{CO}+2\mathrm{H_2O}\\ \mathrm{CO}+0.5\mathrm{O_2}&\rightarrow \mathrm{CO_2}\end{aligned} \tag{2}$$

This reduced kinetics model was tuned to match the flame speed and heat released, as opposed to species concentrations [23]. The rate of progress (or Arrhenius-like reaction rate) for methane oxidation was given by

$$q_1=A_1\exp(-E_1/\mathcal{R}/T)[\mathrm{CH_4}]^{-0.3}[\mathrm{O_2}]^{1.3} \tag{3}$$

where $A_1=2.8\times10^9\ \mathrm{s^{-1}}$, $E_1/\mathcal{R}=24{,}360$ K. The reaction rate for the $\mathrm{CO/CO_2}$ equilibrium was

$$q_2=A_2\exp(-E_2/\mathcal{R}/T)[\mathrm{CO}][\mathrm{O_2}]^{0.25}[\mathrm{H_2O}]^{0.5} \tag{4}$$

with $A_2=2.249\times10^{12}\ (\mathrm{m^3/kmol})^{0.75}\ \mathrm{s^{-1}}$ and $E_2/\mathcal{R}=20{,}130$ K. The symbols in square brackets represent local molar concentrations of various species. The net formation/destruction rate of each species due to all reactions was $\hat{\dot{w}}_i=\Sigma_{k=1}^{N_r}\mathcal{M}_i\nu_{ik}q_k$, where ν_{ik} were the generalized stoichiometric coefficients. Note that the generalized stoichiometric coefficient is $\nu_{ik}=\nu''_{ik}-\nu'_{ik}$, where ν'_{ik} and ν''_{ik} are stoichiometric coefficients in reaction k for species i appearing as a reactant or as a product. Additional details on the implementation of the chemistry model can be found in [20].

3 Numerical Model

The numerical model used herein to simulate the flow and combustion in the four-stage turbine-combustor was implemented in the CORSI code [20] and was based on an algorithm developed for unsteady flows in turbomachinery [25]. The Reynolds-averaged

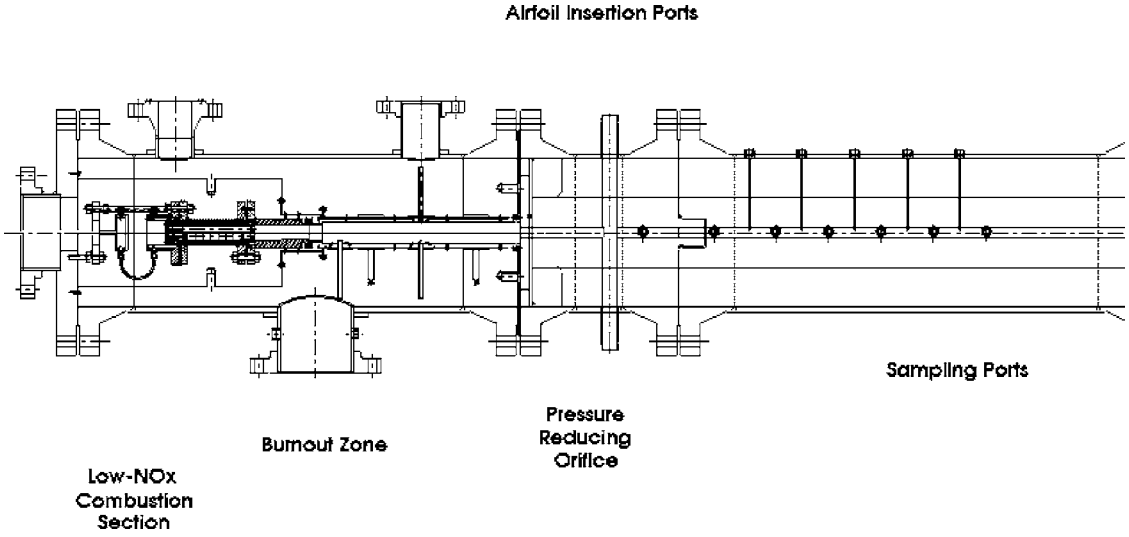

Fig. 1 Experimental setup for a single-vane burner

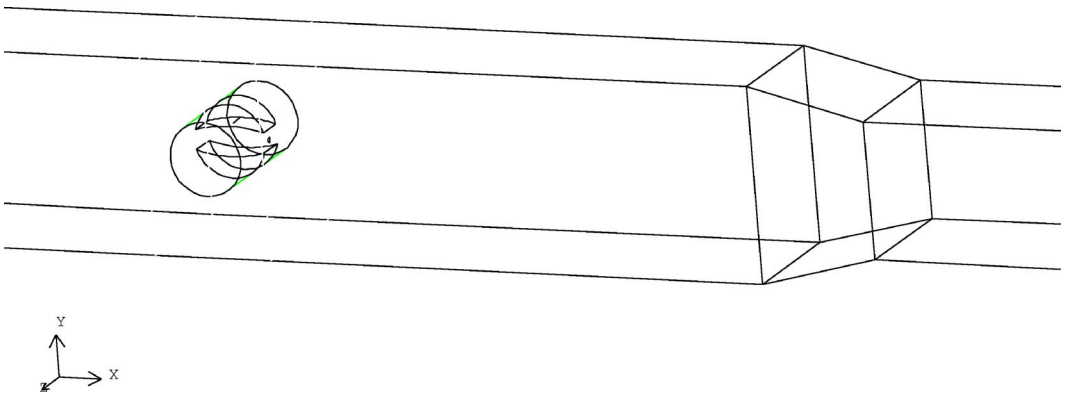

Fig. 2 Detail of the computational domain of the single-vane burner

Navier-Stokes equations and the species equations were written in strong conservation form. The fully implicit, finite-difference approximation was solved iteratively at each time level, using an approximate factorization method. Three Newton-Raphson subiterations were used to reduce the linearization and factorization errors at each time step. The convective terms were evaluated using a third-order accurate upwind-biased Roe scheme [26]. The viscous terms were evaluated using second-order accurate central differences. The scheme was second-order accurate in time.

The size of the computational domain used to simulate the flow inside the turbine-combustor was reduced by taking into account flow periodicity. Two types of grids were used to discretize the flow field surrounding the rotating and stationary airfoils, as shown later in Fig. 10. An O-grid was used to resolve the governing equations near the airfoil, where the viscous effects were important. An H-grid was used to discretize the governing equations away from the airfoil. The O-grid was generated using an elliptical method. The H-grid was algebraically generated. The O- and H-grids were overlaid. The flow variables were communicated between the O- and H-grids through bilinear interpolation. The H-grids corresponding to consecutive rotor and stator airfoils were allowed to slip past each other to simulate the relative motion.

The transport of chemical species was modeled by the mass, momentum, energy, and species balance equations. The governing equations of gas dynamics and chemistry were solved using a fully decoupled implicit algorithm [21,27–29]. A correction technique was developed to enforce the balance of mass fractions [20]. The governing equations were discretized using an implicit, approximate-factorization, finite difference scheme in delta form [30]. The discretized operational form of both the Reynolds-averaged Navier-Stokes and species conservation equations, combined in a Newton-Raphson algorithm [31], were described in [20,22] where additional details on the implementation of the intercell numerical fluxes and on the Roe's approximate Riemann solver were presented.

Two classes of boundary conditions were enforced on the grid boundaries: (i) natural boundary conditions, and (ii) zonal boundary conditions. The natural boundaries included inlet, outlet, periodic, and the airfoil surfaces. The zonal boundaries included the patched and overlaid boundaries.

At the inlet boundary conditions, the flow angle, average total pressure, and downstream propagating Riemann invariant were specified. The upstream propagating Riemann invariant was extrapolated from the interior of the domain. At the outlet, the average static pressure was specified, while the downstream propagating Riemann invariant, circumferential velocity, and entropy were extrapolated from the interior of the domain. Periodicity was enforced by matching flow conditions between the lower surface of the lowest H-grid of a row and the upper surface of the topmost H-grid of the same row. At the airfoil surface, the following boundary conditions were enforced: the no-slip condition, the adiabatic wall condition, and the zero normal pressure gradient condition.

Data were transferred from the H-grid to the O-grid along the O-grid's outermost grid line to impose the zonal boundary conditions of the overlaid boundaries. Data were then transferred back to the H-grid along its inner boundary. At the end of each iteration, an explicit, corrective, interpolation procedure was performed. The patch boundaries were treated similarly, using linear interpolation to update data between adjoining grids [32].

4 Results

This section starts with the evaluation of the combustion model against experimental data for a single-vane burner. Selected results of the numerical simulation of unsteady transport phenomena inside a four-stage turbine-combustor are subsequently presented. The section describing the four-stage turbine-combustor begins with a description of the geometry and flow conditions, followed by a brief discussion of the accuracy of numerical results. The last part of this section presents the effects of in situ reheat on the unsteady flow, blade loading, and power increase in the turbine-combustor.

4.1 Single-Vane Burner. To verify the validity of the methane combustion model for in situ reheat applications, a single-vane burner was experimentally investigated and numerically simulated. In situ reheat tests were run in the Siemens Westinghouse small-scale, full-pressure, combustion test facility, shown in Fig. 1. Preheated air (0.20 kg/s) and natural gas were delivered to a low-NO_x burner section, which was run at full pressure (typically 14 bar). Air preheat temperature and fuel/air ratio were adjusted to give an exhaust gas stagnation temperature and composition corresponding to a selected location in a turbine cascade. The exhaust gas was then passed through a pressure-reducing orifice to increase the Mach number in the injection and sampling sections to typical turbine levels. A back-pressure control valve was used to set the sampling section pressure.

Using a calibrated orifice plate, airflow to the system was measured with an accuracy of 2%. Natural gas flow was regulated with a mass flow controller with an accuracy of 1%. Gases were sampled at various locations downstream of the injection point, and compositions determined using a gas chromatograph, with error limits of ±5%. The temperature was measured with thermocouples, with error limits of ±2 K. Upstream of the vane burner, the mass flow rate of gases was 0.134 kg/s, the total temperature was 1507 K and the total pressure was 6.26 bar. The vane burner was placed in a 17.8 mm×25.4 mm pipe. The 17.8 mm ×25.4 mm pipe reduces to a 17.8 mm×17.8 mm pipe at ~69.8 mm downstream from the vane burner, as shown in Fig. 2.

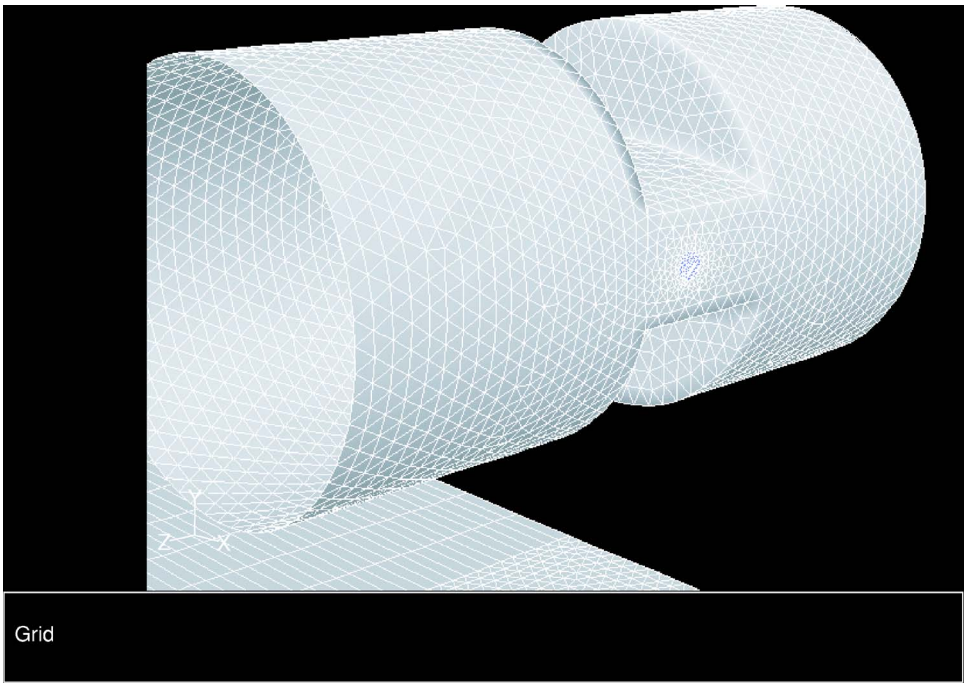

Fig. 3 Detail of the single-vane burner grid

The static pressure upstream of the 17.8 mm × 17.8 mm pipe was 5.44 bar and at the exit was 4.6 bar. The composition by volume of the gas mixture upstream of the vane burner was N_2 73.48%, H_2O 10.59%, O_2 10.21%, CO_2 4.84%, and Ar 0.88%. The Ar was not modeled by the combustion model. The composition by volume of the fuel injected through the vane burner was CH_4 96.1%, C_2H_6 2.0%, C_3H_8 0.9%, CO_2 0.5%, and N_2 0.5%. The fuel was injected at the temperature of 289 K and static pressure of 5.84 bar. The mass flow rate of fuel was 0.416 g/s.

The flow and combustion in the single-vane burner were three-dimensionally modeled. The computational domain extended 0.115 m upstream from the vane injection location and 1.071 m downstream. A detail of the computational domain is shown in Fig. 2. The shape of the vane burner was defined by the intersection of two radii. The injection hole had a diameter of 0.66 mm. The injection hole was located at the center of the pipe, however, the shoulders of the vane were not equally spaced with respect to the injection hole. A detail of the computational grid of the single-vane burner is shown in Fig. 3.

Wall functions were utilized to reduce the number of grid points in the boundary layer regions. Consequently, the number of grid cells was limited to ~2.2 million. The grid was unstructured and was generated with Gambit [33].

The chemistry model used to simulate the in situ reheat was a two-step finite rate combustion model for methane and combustion gases described by Eqs. (2)–(4). The flow and combustion in the single-vane burner were modeled with FLUENT [34] as opposed to the four-stage turbine-burner, which was modeled with the CORSI code described in the previous sections. Both FLUENT and CORSI codes had an identical chemistry model.

At inlet, the input data specified total pressure, initial static pressure, total temperature, turbulence intensity, hydraulic diameter, and the composition of the gas mixture, as shown in Table 1. The input data at the injector location specified the same list of variables as at inlet. The values of these variables are also shown in Table 1. Note that the small quantities of ethane and propane were lumped into methane in order to be able to use the two-reaction model presented above. The mass fraction of N_2 was not an input datum for the problem. The value of the N_2 was calculated such that the sum of all mass fraction species equaled 1. At the outlet, the static pressure value of 4.6 bar was specified.

The numerical results shown herein illustrate the spatial variation of methane and carbon monoxide mass fractions, and total temperature. Figure 4 shows the variation of methane mass fraction along the $z=0$ plane of the combustor and at four planes perpendicular to the x-axis located at 12, 15, 20, and 35 mm downstream of the injector. The methane completely burned at ~70 mm downstream of the injector. Figure 5 shows methane mass fraction variation in the four planes described above. The lack of symmetry of the contour plots of methane mass fraction was due to the off-center position of the vane. All other variables show a similar lack of symmetry.

Figure 6 shows the variation of CO along the $z=0$ plane of the combustor and at five planes perpendicular to the x-axis located at 12, 35, 45, 79, and 94 mm downstream of the injector. The flame was off center and closer to the lower wall. Figure 7 shows CO variation in the five planes described above. Note that the last plane, located at 94 mm downstream of the injector, was situated in the smaller section part of the pipe (17.8 mm × 17.8 mm).

Figure 8 shows the variation of total temperature along the $z=0$ plane of the combustor and at five planes perpendicular to the x-axis located at 12, 35, 79, 94, and 120 mm downstream of the injector. The maximum total temperature was ~1970 K. Figure 9

Table 1 Input data for the vane burner

Parameter	Inlet	Injection
Total pressure (bar)	6.26	7.95
Initial static pressure (bar)	5.93	5.84
Total temperature (K)	1507	311
Turbulence intensity (%)	10	10
Hydraulic diameter (m)	0.0254	0.00066
Mass fraction		
CH_4	0.0	0.9778
O_2	0.115	0.0
CO_2	0.0754	0.01355
CO	0.0	0.0
H_2O	0.06755	0.0
N_2	0.74205	0.00865

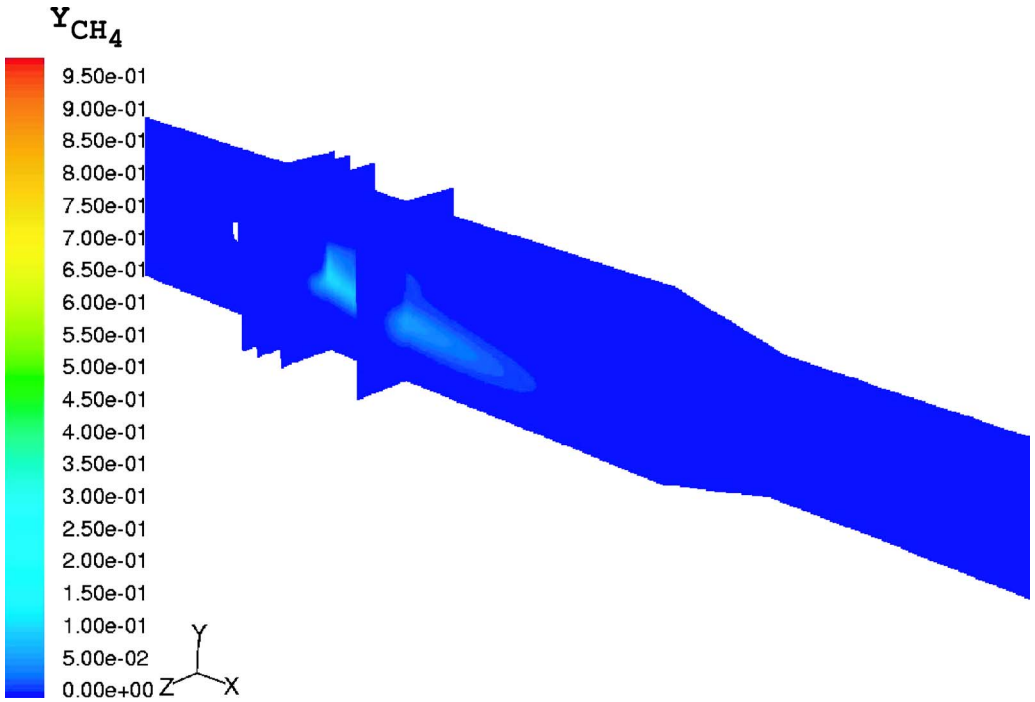

Fig. 4 Contour plots of methane mass fraction

shows total temperature variation in the five planes described above. The total temperature predicted by the numerical simulation along the centerline at 836 mm downstream of the injector was 1602 K. The measured total temperature at the same location was 1544 K. The predicted temperature was 58 K higher than the measured temperature. There are several possible reasons for the temperature difference, such as: (i) simplified kinetics scheme, (ii) limitations of the k-ϵ turbulence model, (iii) approximations due to using binary diffusion coefficients, and (iv) adiabatic boundary conditions used in the simulation neglected the wall surface heat transfer that occurred in the experiment.

To improve temperature prediction, the combustion model was extended to include the backward reaction of the carbon monoxide oxidation. The rate of the backward reaction of the CO/CO_2 equilibrium was

$$q_{2b} = A_{2b} \exp(-E_2/\mathcal{R}/T)[CO_2] \tag{5}$$

with $A_{2b}=5\times10^8$ $(m^3/kmol)^{0.75}$ s^{-1} and $E_2/\mathcal{R}=20{,}130$ K. The total temperature predicted with this improved kinetics model

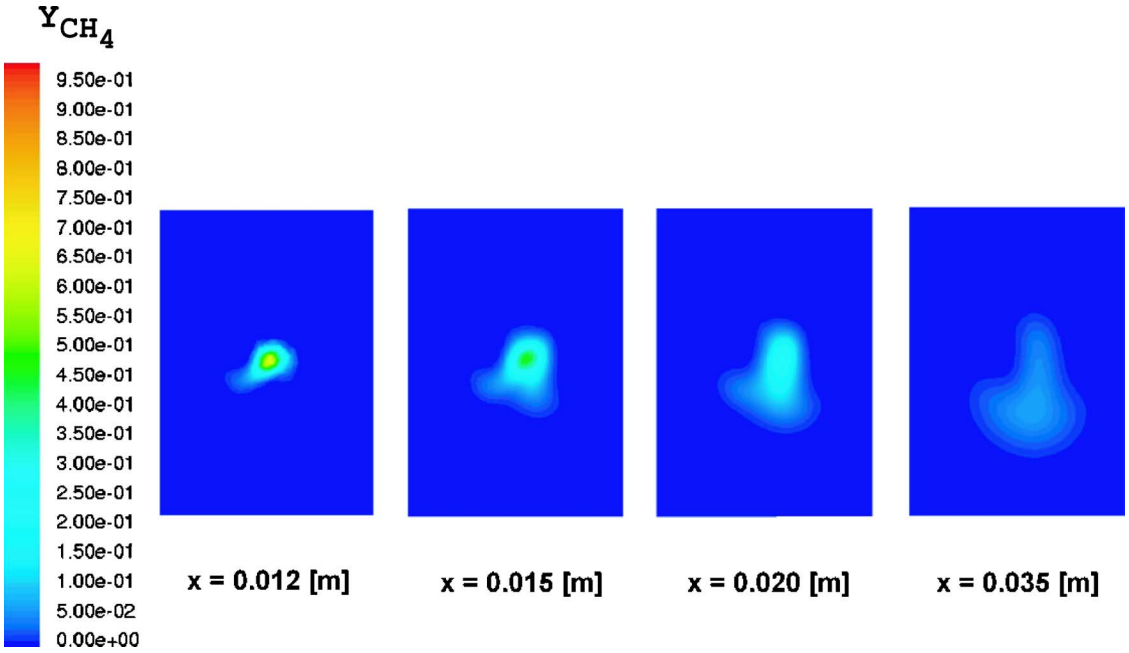

Fig. 5 Contour plots of methane mass fraction at x=constant planes

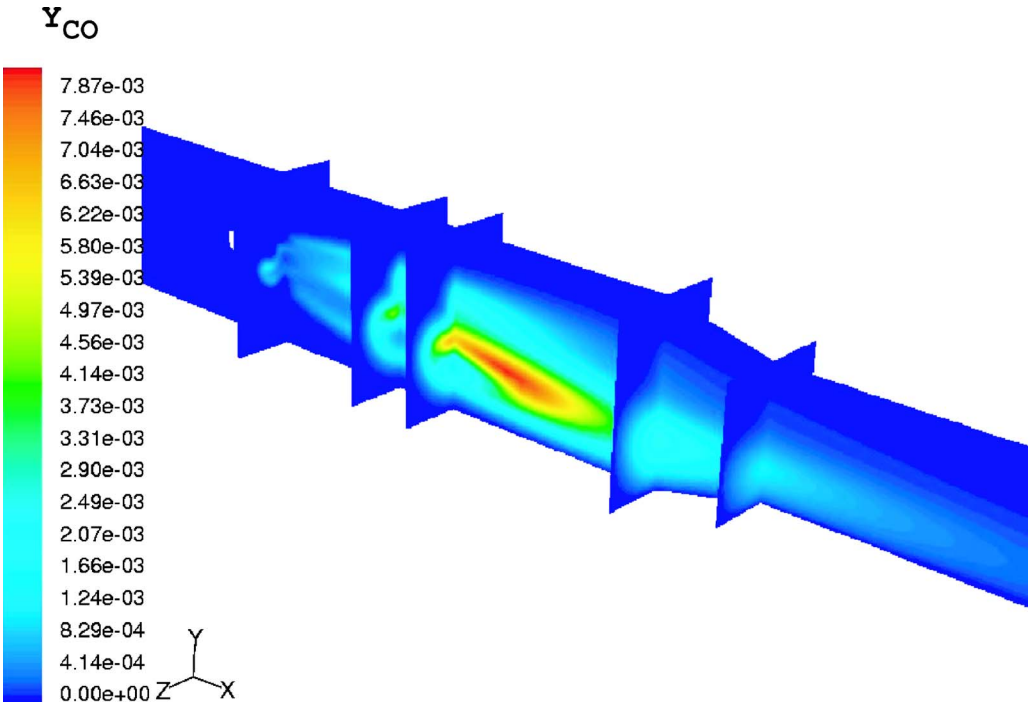

Fig. 6 Contour plots of carbon monoxide mass fraction

along the centerline, at 836 mm downstream of the injector, was 1562 K. Consequently, the temperature difference between the experimental results and the numerical results was reduced to 18 K. Note that the modeling of the backward reaction did not require solving for additional species, and as a result, the increase of the computational time was insignificant.

The accuracy of numerical prediction could also be increased by improving turbulence modeling. The standard k-ϵ model used herein produced better results than the renormalization group or the realizable k-ϵ models [35]. It has been reported that either the standard k-ω or the shear stress transport k-ω model produced slightly better results than the k-ϵ model, without requiring additional computational time [36]. The Reynolds-stress turbulence model would probably produce more accurate results than the k-ϵ model, but with a higher computational cost. However, the overall agreement between the measurements and the predictions obtained with both the k-ϵ and Reynolds-stress turbulence models are reasonably good [37]. Regardless of the turbulence model used, the uncertainty caused by turbulence modeling grows as the distance downstream of the flame increases.

Gas chromatograph measurements at 0.311 m downstream of the injector found that the volume fraction of CH_4 was 0.35%, and the volume fraction of CO was 0.16%. At the same location, the numerical simulation predicted values close to zero (smaller than 10^{-4}%) for methane. The carbon monoxide volume fraction predicted by the chemical model (2) was 3×10^{-4}%, whereas the model that included the backward reaction predicted 0.69%. This discrepancy between the numerical and experimental results indi-

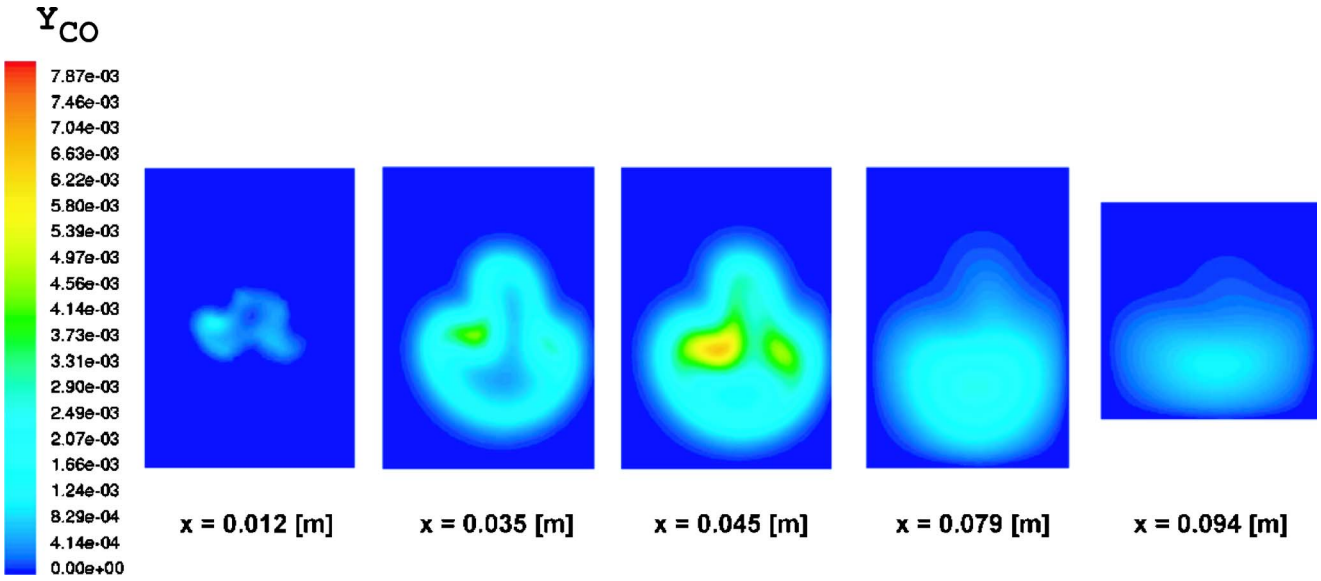

Fig. 7 Contour plots of carbon monoxide mass fraction at x=constant planes

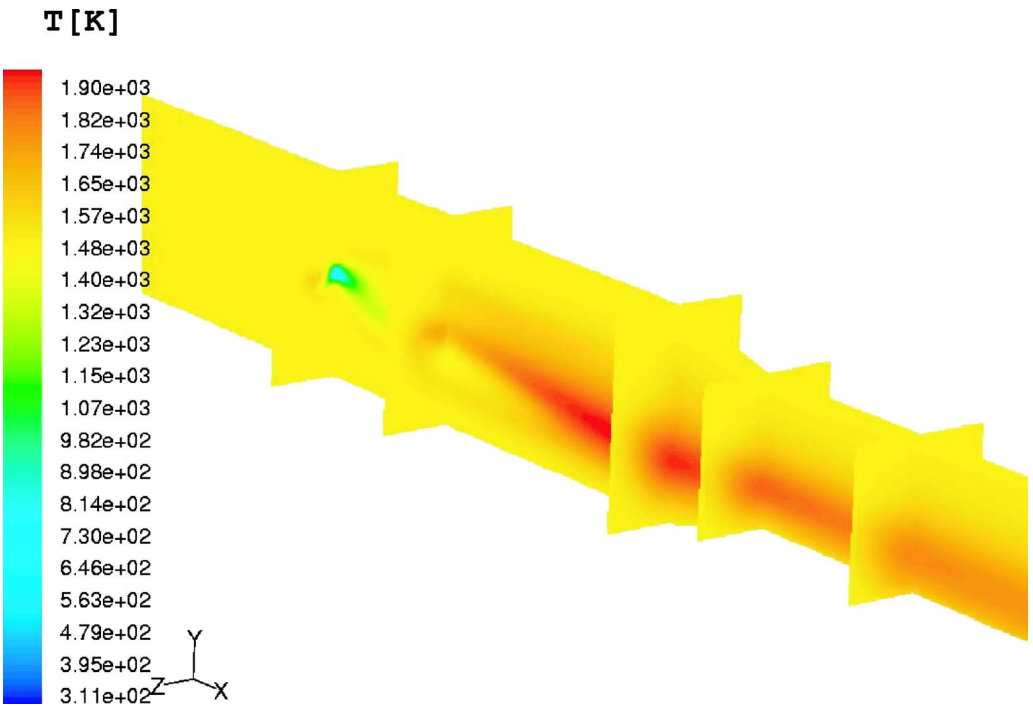

Fig. 8 Contour plots of total temperature

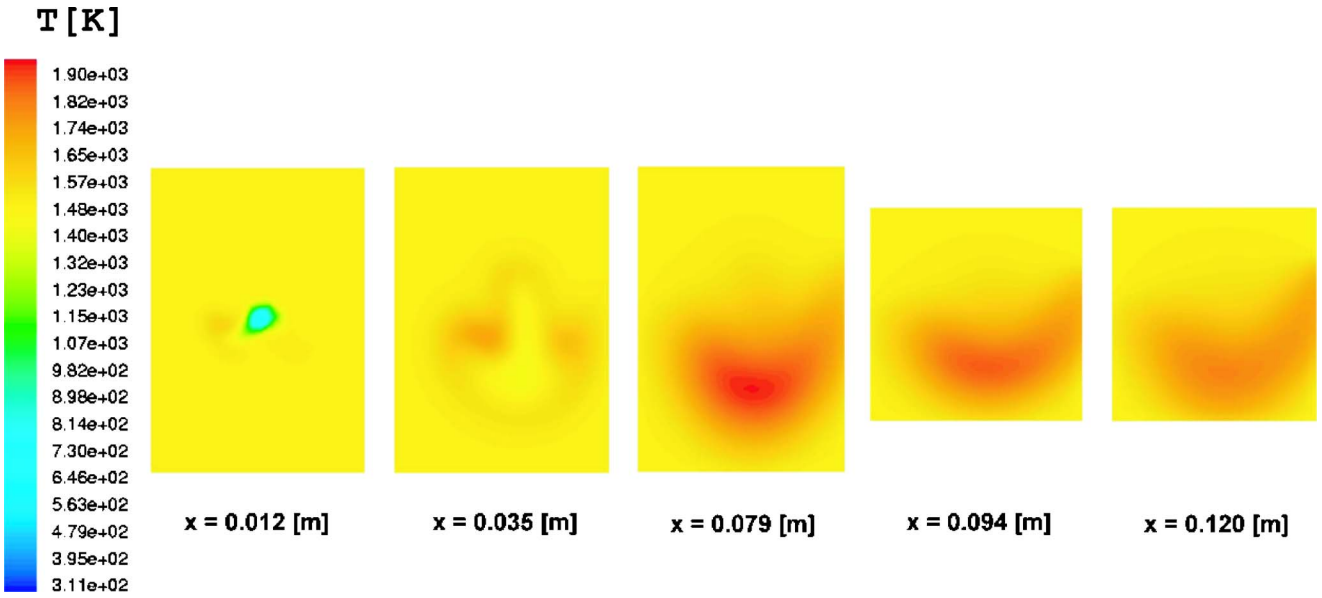

Fig. 9 Contour plots of total temperature at *x*=constant planes

Table 2 Parameters of fuel Injection

Parameter	Case 1	Case 2	Case 3
Injection velocity (m/s)	270.6	270.6	77
Pressure (bar)	14.88	14.88	14.88
Temperature (K)	313	590	313
Injection slot size (mm)	0.54	0.54	1.36
Fuel mass flow rate ($\times 10^{-4}$ kg/s/vane/mm)	13.5	7.2	9.6

cates that the methane oxidation happened more rapidly in the simulation than in the experiment. The species prediction can be improved by using a reduced chemical kinetics model that includes more reactions [38–40]. The computational cost of such a simulation, however, will increase several times, depending on the additional number of species modeled. Since the purpose of this simulation was the prediction of the influence of heat release on turbine-combustor performance, as opposed to predicting the detailed composition of the combustion products, the two-reaction model was adopted herein.

The numerical simulation was done on an IBM Regatta pSeries 690 computer using four processors. The computation converged in ~3500 iterations. The wall clock time for this run was ~195 h.

4.2 Four-Stage Turbine Burner. Once the combustion model was tested for the single-vane burner, the next step was to investigate a four-stage turbine-burner. The purpose of this numerical investigation was to determine the influence of several fuel injection parameters on the unsteady flow and combustion in the turbine-burner. Since the computational time of a three-dimensional model for the four-stage turbine-burner would exceed the computational time of the single-vane burner by a factor of four, and since a parametric analysis of the turbine-burner was necessary, it was decided to replace the three-dimensional model by a less computational expensive quasi-three-dimensional model. A quasi-three-dimensional, as opposed to a two-dimensional model, was needed in order to take into account the large radial variation of the four-stage turbine. Since FLUENT did not have a quasi-three-dimensional model, the CORSI code was used instead.

4.3 Geometry and Flow Conditions. The blade count of the four-stage turbine-combustor required a full-annulus simulation for a dimensionally accurate computation. To reduce the computational effort, it was assumed that there were an equal number of airfoils in each turbine row. As a result, all airfoils except for the inlet guide vane airfoils were rescaled by factors equal to the number of airfoils per row divided by the number of airfoils of row one. An investigation of the influence of airfoil count on the turbine flow showed that the unsteady effects were amplified when a simplified airfoil count 1:1 was used [41]. Consequently, the results obtained using the simplified airfoil count represent an upper limit for the unsteady effects.

The inlet temperature in the turbine-combustor exceeded 1800 K and the inlet Mach number was 0.155. The inlet flow angle was 0 deg and the inlet Reynolds number was 7,640,000/m, based on the axial chord of the first-stage stator. The values of the species mass fractions at inlet in the turbine-burner were $y_{CO_2}=0.0775$, $y_{H_2O}=0.068$, $y_{CO}=5.98\times10^{-06}$, $y_{H_2}=2.53\times10^{-07}$, $y_{O_2}=0.1131$, $y_{N_2}=0.7288$, and $y_{Ar}=0.0125$. The rotational speed of the test turbine-burner was 3600 rpm.

The effects of in situ reheat were investigated by comparing the performances of a turbine-combustor for several cases of fuel injection against the performance of the same turbine without combustion. Three of the most representative cases are presented herein. Pure methane was injected at the trailing edge of the first vane in all the cases of in situ reheat presented herein. The parameters that varied in the turbine-combustor were the injection velocity, methane temperature, and injection slot dimension. These parameters and the fuel mass flow rate per vane and span length are presented in Table 2.

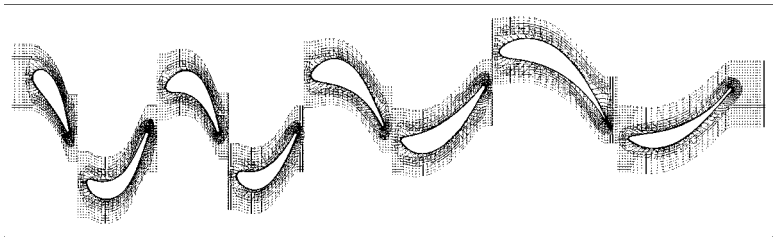

Fig. 10 Detail of the medium grid (every other grid point in each direction shown)

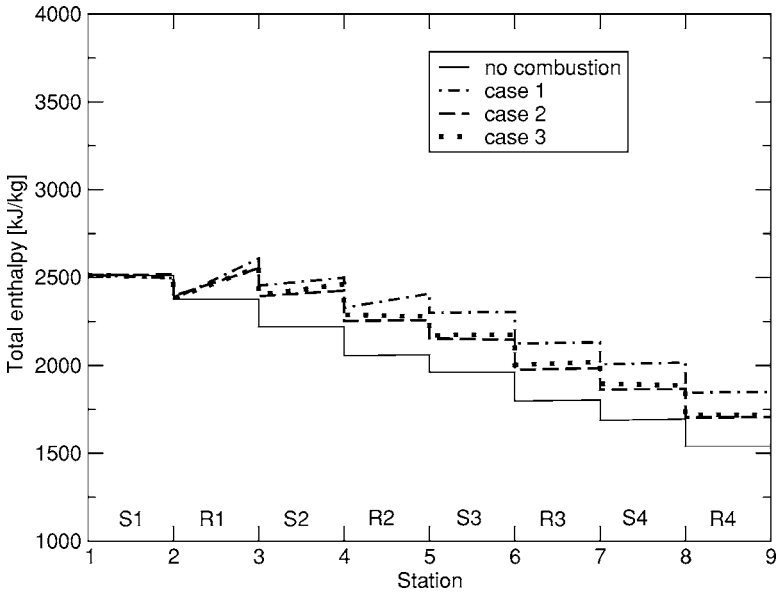

Fig. 11 Variation of averaged total enthalpy (absolute or relative)

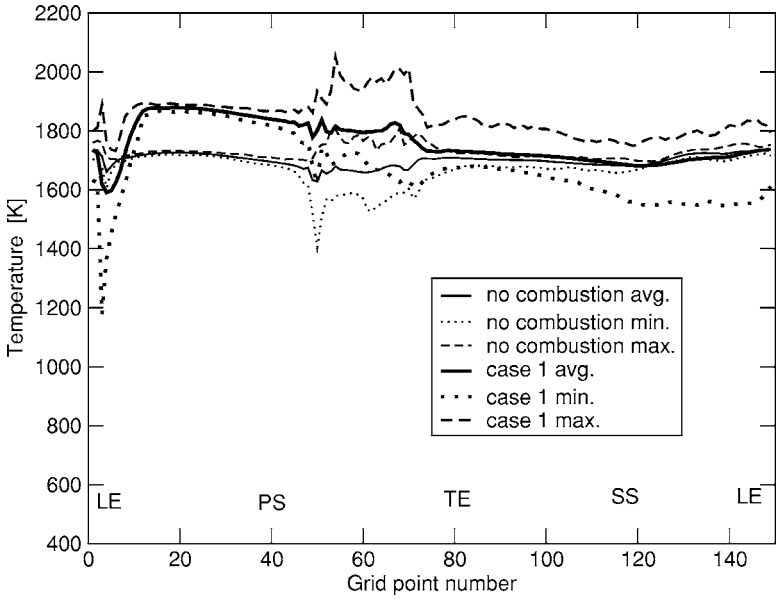

Fig. 12 Variation of stagnation temperature along first row of rotors for the case without combustion and case 1 of in situ reheat

4.4 Accuracy of Numerical Results. To validate the accuracy of the numerical results corresponding to the governing equations used, it was necessary to show that the results were independent of the grid that discretizes the computational domain. The verification of grid independence results was presented in [20], where a one-stage turbine-combustor was simulated. Note that the grids were generated such that, for the given flow conditions, the y^+ number was <1. Approximately 20 grid points were used to discretize the boundary layer regions.

Based on the conclusions of accuracy investigation presented in [20], the medium grid was used herein since it provided the best compromise between accuracy and computational cost. This grid had 53 grid points normal to the airfoil, 225 grid points along the airfoil in the O-grid, 75 grid points in the axial direction, and 75 grid points in the circumferential direction in the H-grid. The stator airfoils and rotor airfoils had the same number of grid points. The inlet and outlet H-grids each had 36 grid points in the axial direction and 75 grid points in the circumferential direction. The grid is shown in Fig. 10, where for clarity every other grid point in each direction is shown.

The results presented in this paper were computed using three Newton subiterations per time step and 2700 time steps per cycle. Here, a cycle is defined as the time required for a rotor to travel a distance equal to the pitch length at midspan. To ensure time periodicity, each simulation was run in excess of 80 cycles. The numerical simulation was done on a 64-processor SGI Origin 3800 computer. The computational time for a run was ~160 h.

4.5 Unsteady Temperature Variation. The variation of total enthalpy for the three in situ reheat cases and for the no combustion case is shown in Fig. 11. The abscissa indicates the axial location. S1 denotes stator 1, R1 denotes rotor 1, etc. The total enthalpy was calculated at the inlet and outlet of each row. Depending on the row type, that is, stator or rotor, the total enthalpy was calculated using either the absolute or the relative velocity. The switch between using absolute or relative velocities generated discontinuities between rows. As shown in Fig. 11, for all fuel injection cases, the total enthalpy increased compared to the no combustion case. The largest enthalpy increase was located on the first rotor, where most of the combustion takes place. The combustion and heat release continued throughout the second stator and rotor, as indicated by the total enthalpy variation shown in Fig. 11 [42].

The stagnation temperature variation along the first row of rotors was strongly influenced by the in situ reheat, as shown in Fig. 12. Figure 12 shows the averaged, minimum, and maximum stag-

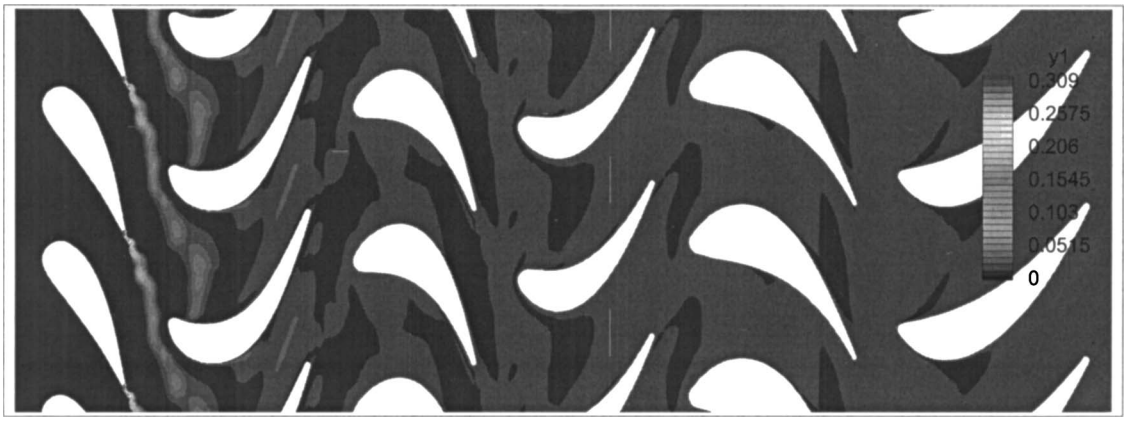

Fig. 13 Contour plots of methane mass fraction (case 1, first three stages)

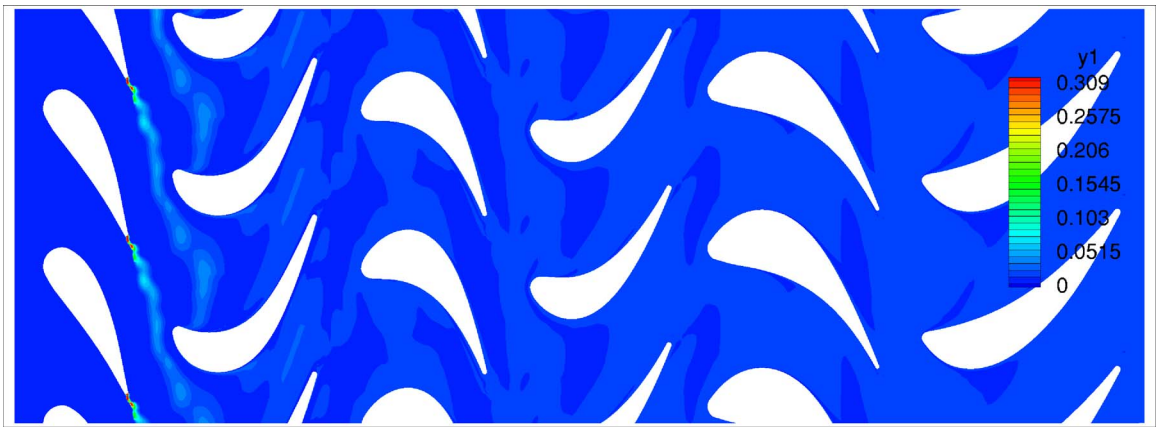

Fig. 14 Contour plots of oxygen mass fraction (case 1, first three stages)

nation temperatures for the flow without combustion and for case 1 of flow with combustion. On the pressure side, the averaged temperature of case 1 was ~180 K larger than the no combustion case temperature. At the leading edge, however, the averaged temperature of case 1 was ~70 K lower than in the no combustion case. On the suction side, the averaged temperature of case 1 was slightly higher than in the no combustion case. On most of the suction side, the averaged temperature of case 1 was approximately 15 to 20 K larger than the no combustion case temperature.

The averaged temperature indicates that combustion took place on the pressure side of the rotor airfoil. This conclusion is also supported by snapshots of contour plots of methane and oxygen mass fraction shown in Figs. 13 and 14. The existence of small regions where the averaged temperature of the case with combustion was lower than the average temperature of the case without combustion indicates that combustion was not completed. Consequently, the low enthalpy of the fuel injected reduced the airfoil temperature locally. The maximum temperature of the case with combustion was larger than the maximum temperature of the no combustion case over the entire airfoil. On the pressure side, the minimum temperature of the case with combustion was larger than the minimum temperature of the case without combustion. On most of the suction side, however, the minimum temperature of the case with combustion was smaller than the minimum temperature of the case without combustion, indicating that the unburned, cold fuel injected was affecting this region [42].

4.6 Unsteady Force Variation. The fuel injection in the turbine-combustor modified the tangential forces in the turbine, as shown in Table 3. In situ reheat decreased tangential force F_y on the first blade row but increased tangential force on the subsequent rows. Since the tangential force decrease on the first stage was smaller than the increase on the subsequent stages, the power of the turbine-combustor increased for all cases with combustion. The largest power increase was 5.1% and corresponded to case 1. Power increased by 2.8% in case 2 and 4.6% in case 3. Although the variation of the averaged blade force F_{tot} was rather small, as shown in Table 3, the power increase was significant.

The time variation of the rotor blade tangential forces, shown in Fig. 15, indicates that the largest amplitudes occurred in the last rotor row and the smallest amplitudes occurred in the first rotor row. This conclusion is valid for every combustion or no combustion case.

A phase shift caused by fuel injection is visible for the first and second rotor blades. The larger unsteadiness within the second rotor makes this phenomenon more clearly distinguishable in Fig. 15(*b*). The patches of burning mixture and the reduced degree of mixedness were the probable causes for this tangential force phase shift in the upstream region.

Figure 16 shows the fast Fourier transform of the tangential forces. They have been nondimensionalized by the average tangential force obtained from the case without fuel injection. The blades of the fourth rotor were excited the most. This excitation occurred at the first blade passing frequency (BPF), which was 1920 Hz. For the rest of the blades, the excitation due to the second BPF was comparable in amplitude to the excitation of the first BPF. Except for the first rotor in case 1 and the third rotor in case 3, the fuel injection increased the excitation of the first BPF. The largest amplitude increase was 216% and occurred on the third-row blades in case 2. The unsteady force, however, was ~50% of the maximum amplitude value that occurred on the fourth rotor blade at BPF [42].

5 Conclusions

A two-reaction, global, finite rate combustion model was evaluated against experimental data for a single-vane burner. This combustion model has been utilized to explore the effects of in situ reheat in a four-stage turbine-combustor. The complexity of the transport phenomena in a multistage turbine-combustor generated a challenging numerical simulation. The large unsteadiness and straining of the flow along with the wide range of velocity variation lead to a wide range of local characteristic time scales for flow and combustion, which strongly impacted the ongoing reactions.

The numerical simulation was used to predict the airfoil temperature variation and the unsteady blade loading in a four-stage turbine-combustor. The largest excitation of the four-stage turbine-combustor corresponded to the fourth-stage rotor, with or

Table 3 Forces on blades

	No Combustion	Case 1	Case 2	Case 3
F_{tot1} (kN)	18.28	18.21	18.71	18.67
α_1 (deg)	38.4	36.4	36.1	36.3
F_{y1} (kN)	11.36	10.81	11.03	11.05
F_{tot2} (kN)	11.87	12.27	12.17	12.31
α_2 (deg)	60.3	61.7	61.9	62.7
F_{y2} (kN)	10.31	10.81	10.74	10.94
F_{tot3} (kN)	12.62	13.19	12.75	13.08
α_3 (deg)	62.2	65.0	63.9	63.8
F_{y3} (kN)	11.17	11.95	11.45	11.73
F_{tot4} (kN)	11.41	13.03	12.31	12.58
α_4 (deg)	65.5	65.5	65.7	66.1
F_{y4} (kN)	10.38	11.85	11.21	11.51

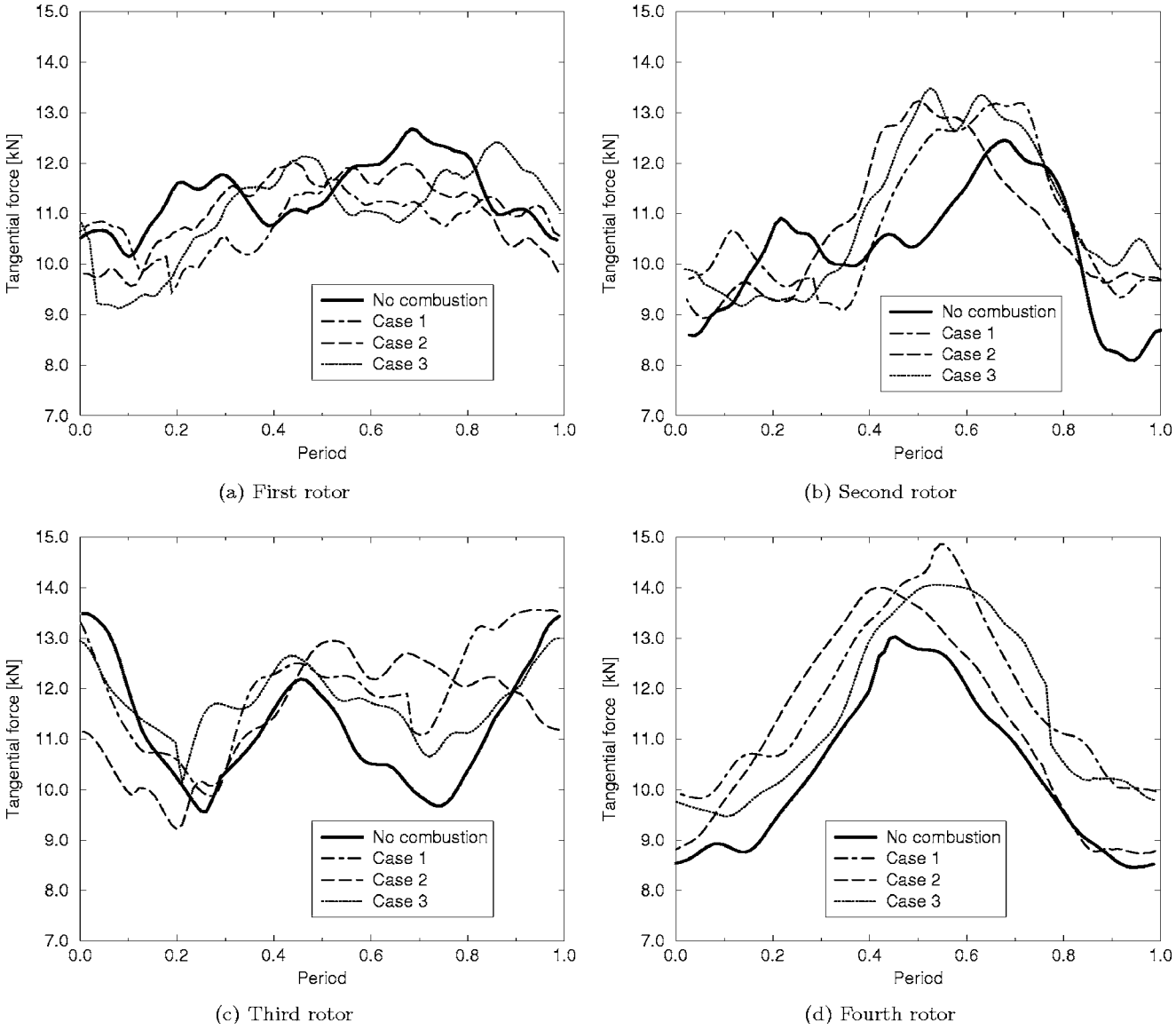

Fig. 15 Variation of tangential forces on the rotors

without combustion. The highest excitation corresponded to the first blade passing frequency, for all cases analyzed.

The in situ reheat decreased the power of the first stage, but increased more the power of the following stages. The power of the turbine increased between 2.8% and 5.1%, depending on the parameters of the fuel injection.

Acknowledgment

This paper was prepared with the support of the U.S. Department of Energy (DOE), under Award No. DE-FC26-00NT40913. However, any opinions, findings, conclusions, or recommendations expressed herein are those of the authors and do not necessarily reflect the views of the DOE. The Government reserves for itself and others acting on its behalf a royalty-free, nonexclusive, irrevocable, worldwide license for Governmental purposes to publish, distribute, translate, duplicate, exhibit, and perform this copyrighted paper. Additional funding was provided by Siemens Westinghouse Power Corporation. The authors gratefully acknowledge the support of Charles Alsup, the DOE project manager. The authors also appreciate the support of the Texas A&M Supercomputing Center and the Super-Computing Science Consortium (SC)^2 who generously provided access to the computing resources of the Pittsburgh Supercomputing Center.

Nomenclature

A = Arrhenius factor
E = activation energy
e = total intrinsic internal energy per unit volume
(F,G) = inviscid flux vector in curvilinear coordinates
(f,g) = inviscid flux vector in Cartesian coordinates
M = Mach number
$\mathcal{M}$ = molar mass
N_r = number of reactions
p = pressure
Q = state vector in curvilinear coordinates
q = state vector in Cartesian coordinates or rate of progress
$\mathcal{R}$ = universal gas constant
Re = Reynolds number
S = viscous flux vector
u = fluid velocity in the x direction
v = fluid velocity in the y direction
y_i = mass fraction of species i

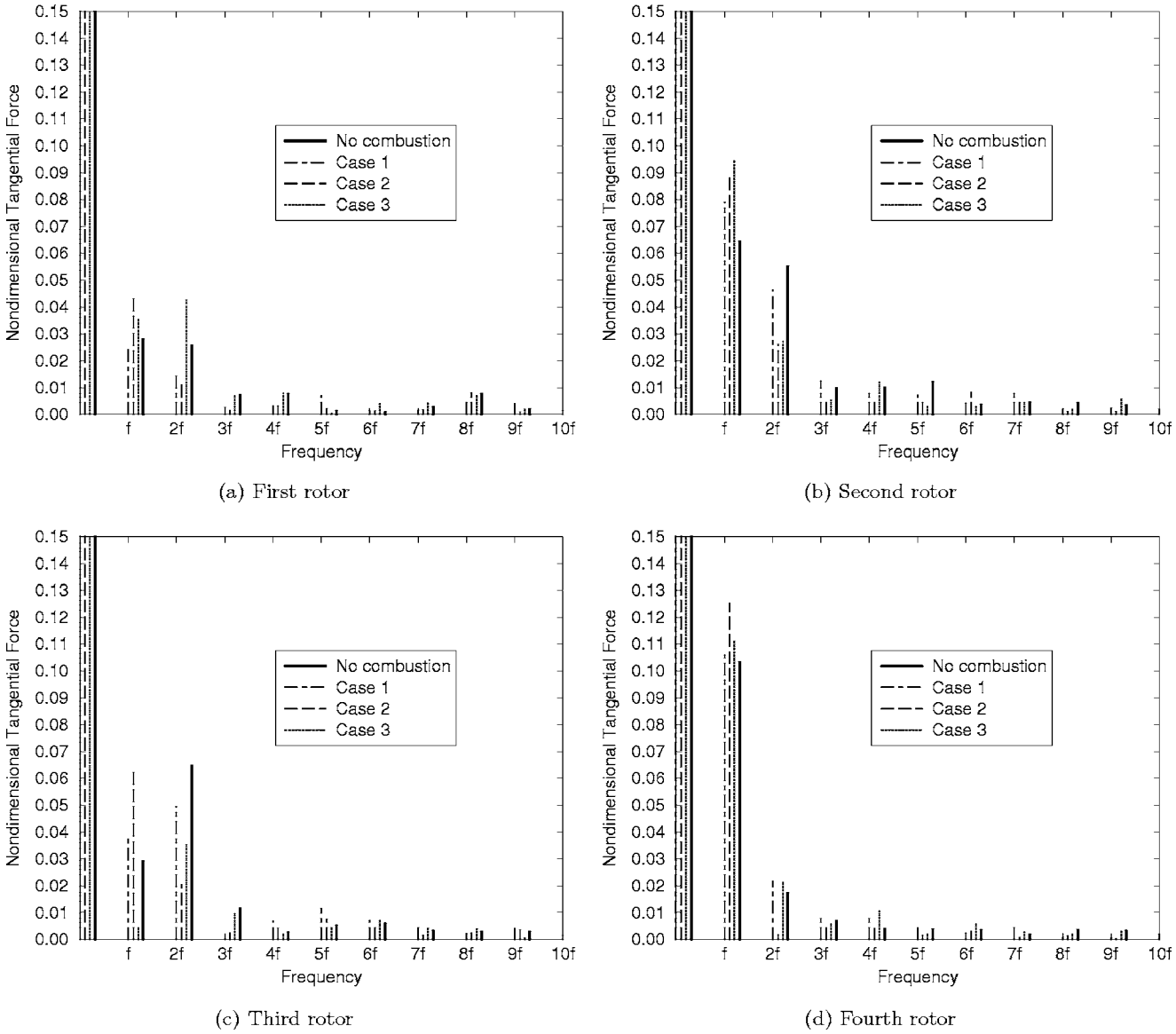

Fig. 16 Fast Fourier transform of tangential forces

$\dot{w}$ = species net production rate
γ = adiabatic exponent (ratio of specific heats)
ν = stoichiometric coefficient
ρ = density
τ = nondimensional time
(ξ, η) = curvilinear coordinates

Subscripts

ch = chemical source term
i = species index
∞ = upstream infinity

Superscripts

ns = Navier-Stokes
sp = species
$''$ = products
$'$ = reactants

References

[1] Sirignano, W. A., and Liu, F., 1999, "Performance Increases for Gas-Turbine Engines Through Combustion Inside the Turbine," J. Propul. Power, **15**(1), pp. 111–118.

[2] Simpson, J. R., and May, G. C., 1964, "Reheat Apparatus for a Gas Turbine Engine," U.S. Patent No. 3,141,298, Rolls-Royce Ltd., Derby, England.

[3] Witt, S. H. D., 1967, "Reheat Gas Turbine Power Plant With Air Admission to the Primary Combustion Zone of the Reheat Combustion Chamber Structure," U.S. Patent No. 3,315,467, Westinghouse Electric Corp., Pittsburgh.

[4] Althaus, R., et al., 1995, "Method of Operating Gas Turbine Group With Reheat Combustor," U.S. Patent No. 5,454,220, Asea-Brown-Boveri Baden, Switzerland.

[5] Dills, R. R., and Follansbee, P. S., 1979, "Use of Thermocouples for Gas Temperature Measurements in a Gas Turbine Combustor," Tech. Rep., National Bureau of Standards, Special Publication No. 561.

[6] Elmore, D. L., Robinson, W. W., and Watkins, W. B., 1983, "Dynamic Gas Temperature Measurement System," Tech. Rep., NASA, Contractor Report No. 168267.

[7] Butler, T. L., Sharma, O. P., Joslyn, H. D., and Dring, R. P., 1989, "Redistribution of an Inlet Temperature Distortion in an Axial Flow Turbine Stage," J. Propul. Power, **5**, pp. 64–71.

[8] Graham, R. W., 1980, "Fundamental Mechanisms That Influence the Estimate of Heat Transfer to Gas Turbine Blades," Heat Transfer Eng., **2**(1), pp. 39–47.

[9] Kirtley, K. R., Celestina, M. L., and Adamczyk, J. J., 1993, "The Effect of Unsteadiness on the Time-Mean Thermal Loads in a Turbine Stage," SAE Paper No. 931375.

[10] Whitney, W. J., Stabe, R. G., and Moffitt, T. P., 1980, "Description of the Warm Core Turbine Facility and the Warm Annular Cascade Facility Recently Installed at NASA Lewis Research Center," Tech. Rep., NASA, Technical Memorandum 81562.

[11] Schwab, J. R., Stabe, R. G., and Whitney, W. J., 1983, "Analytical and Experimental Study of Flow Through and Axial Turbine Stage With a Nonuniform Inlet Radial Temperature Profile," AIAA Paper No. 83–1175.

[12] Stabe, R. G., Whitney, W. J., and Moffitt, T. P., 1984, "Performance of a High-Work Low Aspect Ratio Turbine Tested With a Realistic Inlet Radial Temperature Profile," AIAA Paper No. 84–1161.
[13] Sharma, O. P., Pickett, G. F., and Ni, R. H., 1992, "Assessment of Unsteady Flows in Turbomachines," ASME J. Turbomach., **114**(1), pp. 79–90.
[14] Shang, T., Guenett, G. R., Epstein, A. H., and Saxer, A. P., 1995, "The Influence of Inlet Temperature Distortion on Rotor Heat Transfer in a Transonic Turbine," AIAA Paper No. 95–3042.
[15] Rai, M. M., and Dring, R. P., 1990, "Navier-Stokes Analyses of the Redistribution of Inlet Temperature Distortions in a Turbine," J. Propul. Power, **6**(3), pp. 276–282.
[16] Krouthen, B., and Giles, M. B., 1988, "Numerical Investigation of Hot Streaks in Turbines," AIAA Paper No. 88–3015.
[17] Takahashi, R. K., and Ni, R. H., 1991, "Unsteady Hot Streak Migration Through a 1-1/2 Stage Turbine," AIAA Paper No. 91–3382.
[18] Shang, T., and Epstein, A. H., 1996, "Analysis of Hot Streak Effects on Turbine Rotor Heat Load," ASME Paper No. 96-GT-118.
[19] Dorney, D. J., Sondak, D. L., and Cizmas, P. G. A., 2000, "Effects of Hot Streak/Airfoil Ratios in a High-Subsonic Single-Stage Turbine," Int. J. Turbo Jet Engines, **17**(2), pp. 119–132.
[20] Isvoranu, D. D., and Cizmas, P. G. A., 2003, "Numerical Simulation of Combustion and Rotor-Stator Interaction in a Turbine Combustor," Int. J. Rotating Mach., **9**(5), pp. 363–374.
[21] Balakrishnan, A., 1987, "Application of a Flux-Split Algorithm to Chemically Relaxing, Hypervelocity Blunt-Body Flows," AIAA Paper No. 87–1578.
[22] Cizmas, P., Flitan, H., and Isvoranu, D., 2003, "Numerical Prediction of Unsteady Blade Loading in a Turbine-Combustor," 8th National Turbine High Cycle Fatigue Conference, Monterey, CA.
[23] Westbrook, C. K., and Dryer, F. L., 1981, "Simplified Reaction Mechanisms for the Oxidation of Hydrocarbon Fuels in Flames," Combust. Sci. Technol., **27**, pp. 31–43.
[24] Hautman, J., Dryer, F. L., Schug, K. P., and Glassman, I., 1981, "A Multiple-Step Overall Kinetic Mechanism for the Oxidation of Hydrocarbons," Combust. Sci. Technol., **25**, pp. 219–235.
[25] Cizmas, P. G. A., and Subramanya, R., 1997, "Parallel Computation of Rotor-Stator Interaction," Eighth International Symposium on Unsteady Aerodynamics and Aeroelasticity of Turbomachines, pp. 633–643.
[26] Roe, P. L., 1981, "Approximate Riemann Solvers, Parameter Vectors, and Difference Schemes," J. Comput. Phys., **43**, pp. 357–372.
[27] Eberhardt, S., and Brown, K., 1986, "A Shock Capturing Technique for Hypersonic, Chemically Relaxing Flows," AIAA Paper No. 86–0231.
[28] Yee, H. C., 1987, "Construction of Explicit and Implicit Symmetric Schemes and Their Applications," J. Comput. Phys., **68**, pp. 151–179.
[29] Li, C. P., 1987, "Chemistry-Split Techniques for Viscous Reactive Blunt Body Flow Computations," AIAA Paper No. 87–0282.
[30] Warming, R. F., and Beam, R. M., 1978, "On the Construction and Application of Implicit Factored Schemes for Conservation Laws," *SIAM-AMS Proceedings*, Vol. 11, pp. 85–129.
[31] Rai, M. M., and Chakravarthy, S., 1986, "An Implicit Form for the Osher Upwind Scheme," AIAA J., **24**, pp. 735–743.
[32] Rai, M. M., 1985, "Navier-Stokes Simulation of Rotor-Stator Interaction Using Patched and Overlaid Grids," AIAA Paper No. 85–1519.
[33] FLUENT INC., 2002, Gambit 2.0: Training Notes, January.
[34] FLUENT INC., 2003, Fluent 6.1: Training Notes, March.
[35] Christo, F., and Dally, B., 2005, "Modeling Turbulent Reacting Jets Issuing Into a Hot and Diluted Coflow," Combust. Flame, **142**, pp. 117–129.
[36] Engdar, U., Nilsson, P., and Klingmann, J., 2004, "Investigation of Turbulence Models Applied to Premixed Combustion Using a Level-Set Flamelet Library Approach," ASME J. Eng. Gas Turbines Power, **126**, pp. 701–707.
[37] German, A., and Mahmud, T., 2005, "Modelling of Non-Premixed Swirl Burner Flows Using a Reynolds-Stress Turbulence Closure," Fuel, **84**, pp. 583–594.
[38] Nicol, D. G., Malte, P. C., Hamer, A. J., Roby, R. J., and Steele, R. C., 1999, "Development of a Five-Step Global Methane Oxidation: No Formation Mechanism for Lean-Premixed Gas Turbine," ASME J. Eng. Gas Turbines Power, **121**(2), pp. 272–280.
[39] Sung, C. J., Law, C. K., and Chen, J.-Y., 2001, "Augmented Reduced Mechanisms for NO Emission in Methane Oxidation," Combust. Flame, **125**, pp. 906–919.
[40] Barlow, R. S., 2003, "International Workshop on Measurement and Computation of Turbulent Nonpremixed Flames," http://www.ca.sandia.gov/TNF, Sandia National Laboratories.
[41] Cizmas, P. G. A., 1999, "Transition and Blade Count Influence on Steam Turbine Clocking," Tech. Rep., Texas Engineering Experiment Station, College Station.
[42] Flitan, H. C., and Cizmas, P. G. A., 2003, "Analysis of Unsteady Aerothermodynamics Effects in a Turbine Combustor," *10th International Symposium on Unsteady Aerodynamics and Aeroelasticity of Turbomachines*, Durham, NC.

A Study on Transient Performance Characteristics of the Canard Rotor Wing Type Unmanned Aerial Vehicle Propulsion System During Flight Mode Transition

Changduk Kong[1]
e-mail: cdgong@mail.chosun.ac.kr

Jongha Park
e-mail: jjonga29@nate.com

Myoungcheol Kang
e-mail: k0914@stmail.chosun.ac.kr

Department of Aerospace Engineering,
Chosun University,
#375 Seosuk-dong, Dong-gu,
Kwangju 501-759,
Republic of Korea

A propulsion system of the CRW (Canard rotor wing) type UAV (unmanned aerial vehicle) was composed of the turbojet engine, exhaust nozzles (including some tip jet nozzles and a main nozzle), and the duct system (including straight ducts, curved ducts, and master valve). The CRW-type UAV has three different flight modes, such as the rotary wing mode for takeoff and landing, the high-speed forward flight mode with the fixed wing, and the transition flight mode between the previously mentioned two flight modes. In order to evaluate transient performance characteristics of the CRW-type UAV propulsion system during flight mode transition, the propulsion system was modeled using SIMULINK®, which is a user-friendly graphical-user-interface-(GUI) type dynamic analysis tool provided by MATLAB, in this study. The transition flight mode between the rotary wing mode and the fixed wing mode was simulated by considering area variation of the master valve and the main exhaust nozzle. In order to verify acceptability of the main turbojet engine model, performance simulation results using SIMULINK were compared to results using the commercial program GSP. Through this simulation, proper operation of the master valve and the variable area main nozzle can be found for safe flight transition. Therefore, performance characteristics were investigated depending on various angle positions of the master valve. [DOI: 10.1115/1.2135821]

Introduction

A smart unmanned aerial vehicle (UAV), which has been developed by KARI (Korea Aerospace Research Institute), has some new technologies, such as a Canard rotor wing (CRW) concept for both vertical takeoff and landing (VTOL) and high-speed forward flight, highly reliable and intelligent flight capability, and light vehicle structure [1].

The CRW concept, using the hot cycle, is suitable for the smart UAV because of fulfilling the VTOL UAV mission requirement. This concept uses tip-jet nozzles driven by hot gas of the main jet engine to rotate the rotary wing for the vertical flight mode as well as the turbojet engine for high-speed forward flight as the conventional engine. The propulsion system for this concept flight can be operated by dividing into three flight modes, such as the rotary wing mode for takeoff and landing, the fixed wing mode for the high-speed forward flight, and the transition flight mode between two flight modes. In order to establish safe operation regions of the propulsion system, the performance simulation should be needed. The performance simulation can provide important data not only to confirm performance characteristics in a much wider safe-flight envelope (which cannot be provided by experimental tests) but also to design the engine controller or the integrated flight control system. In the previous study, steady-state and transient performance analysis of this CRW-type UAV propulsion system was partially performed [2].

In this study, in order to obtain transient performance characteristics of the CRW-type UAV propulsion system during flight mode transition, the propulsion system was modeled and simulated using SIMULINK® [3]. Moreover, performance characteristics of the propulsion system was investigated depending on various angle positions of the master valve at both the rotary and fixed wing modes.

Propulsion System Modeling

The studied propulsion system is mainly composed of a turbojet engine, a duct system, and a nozzle system. The turbojet engine is used as a major engine, and the duct system is divided into a straight duct, curved ducts, and a master valve. The nozzle system is divided into tip-jet nozzles for the rotary wing mode and the main nozzle for the fixed wing mode. The hot pressure jet cycle was selected to rotate two rotary wings by tip-jet nozzles driven by hot gas delivered from the main turbojet engine.

In the takeoff and landing mode, the vehicle can hover using the rotary wing with tip-jet nozzles driven by hot gas ejected through the curved and straight ducts from the engine, but the main nozzle should be closed to prevent forward flight. However, if the flight velocity reaches to proper forward velocity more than stall speed, then the vehicle can fly using the only main nozzle thrust, but the master valve should be closed to prevent the rotary flight mode.

The main nozzle is a variable convergent type, but the tip-jet nozzle is a fixed convergent type. Figure 1 shows a schematic layout of the smart UAV propulsion system. The overall model is composed of modular blocks represented by individual components, such as intake subsystem, compressor subsystem, combustor subsystem, compressor turbine subsystem, duct subsystem, nozzle subsystem, and rotor dynamics subsystem.

The overall SIMULINK model is expressed by Fig. 2. The duct subsystem is divided into the straight and bend subsystem, the

[1]Corresponding author.

Contributed by the International Gas Turbine Institute (IGTI) of ASME for publication in the JOURNAL OF ENGINEERING FOR GAS TURBINES AND POWER. Manuscript received August 25, 2005; final manuscript received September 28, 2005. IGTI Review Chair: K. C. Hall. Paper presented at the ASME Turbo Expo 2005: Land, Sea, and Air, Reno, NV, June 6–9, 2005, Paper No. GT2005-68400.

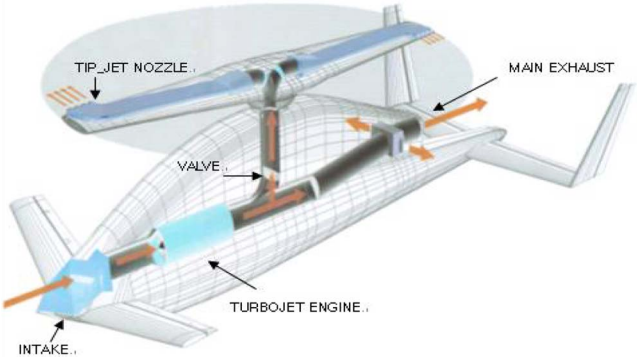

Fig. 1 Schematic layout of smart UAV propulsion system

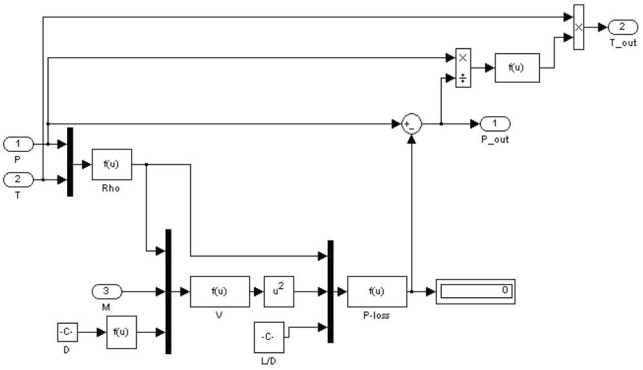

Fig. 3 Straight and bend duct subsystem

valve subsystem, and the ICV (inter component volume) subsystem shown as Figs. 3–5, respectively.

Intercomponent Volume (ICV) Method

In order to establish a transient performance model for the CRW-type UAV propulsion system using SIMULINK, the ICV model was used. In this method, mismatches of both work and mass flow rate between components are assumed during transient engine operation [4].

The mass-flow-rate mismatch between components must be used to calculate change rate of pressure at each station of the study engine, by taking values of intercomponent volumes and applying the perfect gas law. Time derivative of pressure in the combustion chamber can be expressed by

$$\dot{P}_2 = \frac{RT_2}{V_1}\dot{m}_1 \tag{1}$$

By the same manner, time derivative of pressure in the duct system with the main nozzle or the tipjet nozzles can be derived by,

$$\dot{P}_4 = \frac{RT_4}{V_2}\dot{m}_2 \tag{2}$$

Also, the work mismatch is utilized to estimate the variation of rotational speed by integrating difference work between compressor and turbine during transient operation. The rotational speed increase during acceleration of the rotor can be expressed by

$$\frac{dN}{dt} = \left(\frac{30}{\pi}\right)^2 \frac{J}{NI} \quad [\mathrm{TW} - \mathrm{CW}] \tag{3}$$

In this study, the fourth order Runge-Kutta method is applied for integration.

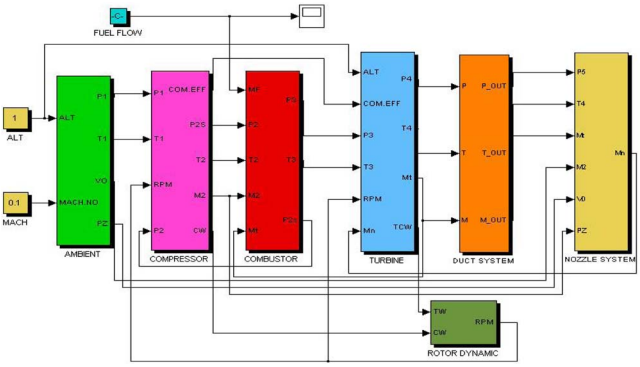

Fig. 2 Overall SIMULINK model

Duct System Modeling

The proposed propulsion system has ducts between the gas generator and the tip-jet nozzle, as well as the main nozzle. The duct loss should be estimated to simulate a precise propulsion system model depending on its length and shape.

In the case of the straight duct, the pressure drop due to friction at constant pipe cross sections is given by [5]

$$\Delta p = 4 f \frac{L}{D}\frac{1}{2}\rho V^2 \tag{4}$$

In order to predict friction coefficients in the duct, the Reynolds number is defined as

$$\mathrm{Re} = \frac{\rho V D}{\mu} = \frac{VD}{\nu} \tag{5}$$

Therefore internal duct friction coefficients have the following value at each Re range [1]:

$$f = \frac{0.0791}{\mathrm{Re}^{0.25}} \quad (3000 < \mathrm{Re} \leqslant 10{,}000)$$

$$f = \frac{0.0460}{\mathrm{Re}^{0.2}} \quad (10{,}000 < \mathrm{Re} \leqslant 200{,}000)$$

$$f = 0.0014 + \frac{0.0125}{\mathrm{Re}^{0.32}} \quad (200{,}000 < \mathrm{Re} \leqslant 3{,}000{,}000) \tag{6}$$

In case of the curved duct, the pressure drop can be calculated by [6]

$$\Delta p = \frac{1}{2}\rho V^2 \left[K_{S,G} + 4f\frac{(L_u + L_D)}{D} \right] \tag{7}$$

In case of the master valve, the pressure drop can be calculated by

$$\Delta p = \frac{1}{2}\rho V^2 \left[C_K + 4f\frac{(L_u + L_D)}{D} \right] \tag{8}$$

The flow past a valve can be calculated by [7]

$$w = \frac{0.532(C_d A)_v (N_{CS})}{\sqrt{T}} P_1 \tag{9}$$

If the butterfly valve is used, the geometric area of the valve is given by

$$A_v = \frac{\pi D^2}{4}(1 - \cos\theta) \tag{10}$$

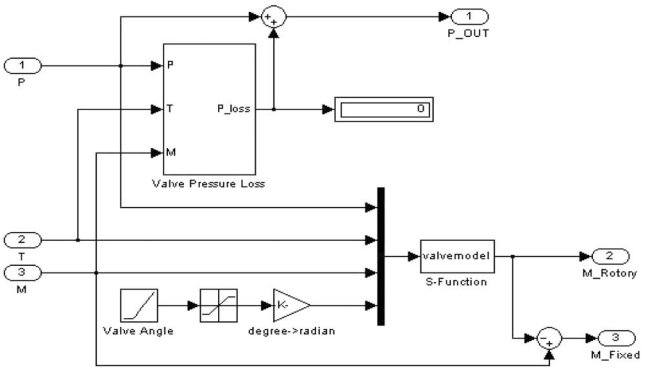

Fig. 4 Valve subsystem

Transient Performance Analysis

Transient performance analysis was performed at flight mode transition with valve angle change. In order to determine initial input values for transient analysis, steady-state analysis results obtained by the previously developed program were used. In this analysis, four cases are considered.

Case 1: Transition Behaviors of Main Turbojet Engine. Transient behaviors of the main turbojet engine were investigated to verify acceptability of the proposed model. Transient analysis results of the only turbojet engine without duct systems are shown in Figs. 6(*a*)–6(*c*). A fuel schedule with step increase is selected to accelerate the engine speed from idle (75%) to maximum (100%) at sea level static standard atmospheric condition. As shown in Fig. 6, analysis results using the proposed SIMULINK model agree well, with them using the commercial program GSP. It means that the developed SIMULINK model [3] is acceptable for transient performance analysis of the study turbojet engine.

Case 2: Transient Behaviors of Propulsion System During Rotary Wing Flight Mode. Transient analysis results of the turbojet engine with the curved duct system in Figs. 7(*a*)–7(*f*). There are three linear fuel increase schedules with 0.5, 1, 2, and 3 s (fuel increase rate) from idle (75% of the revolutions per minute) to maximum rotational speed (100%) at 1 km altitude and Mach No. 0.1 flight velocity.

As shown at Fig. 7(*c*), the faster the fuel increase, the more turbine inlet temperature overshoot occurs, as in the bare engine performance characteristics.

In case of the duct exit pressure (Fig. 7(*d*)) and the net thrust at tip jet nozzles (Fig. 7(*f*)), the pressure and the thrust decrease rapidly at initial condition then increase rapidly to the converged steady-state conditions. It is considered that there are instantly mismatches of air mass flow and work between each component. Therefore, in order to operate the engine safely during the rotary wing flight mode, the fuel throttling should be performed slowly.

Case 3: Flight Mode Transition From Rotary Wing Mode to Fixed Wing Mode. During flight mode transition from the rotary wing mode to the fixed wing mode, the propulsion system has an operation condition with maximum rotational speed (100%) at 1 km altitude and Mach No. 0.1 flight velocity. Master valve angle variation of the duct system is scheduled from 90 to 0 deg during times of 100, 150, and 200 s, respectively.

When the master valve is linearly closed from full opening position, as shown in Fig. 8(*a*), the main nozzle exit area is gradually increased with chocking condition, as shown in Fig. 8(*b*). Therefore, gas mass flow at the tip-jet nozzle decreases gradually. On the other hand, gas mass flow at the main nozzle is increasing to maximum flow condition some what quickly, as shown in Fig. 8(*c*). At this condition, pressure at the tip-jet nozzle inlet falls down to atmospheric pressure, but pressure at variable main nozzle inlet is dropped with very small value due to friction loss by flowing, as shown in Fig. 8(*d*).

In this case, it has a tendency that total net thrust is oscillatorilly increasing, but the specific fuel consumption (SFC) is decreasing, as shown in Figs. 8(*e*) and 8(*f*). Therefore, even though operation of the master valve is slowly scheduled, thrust fluctuation should be considered for safe flight during flight mode transition.

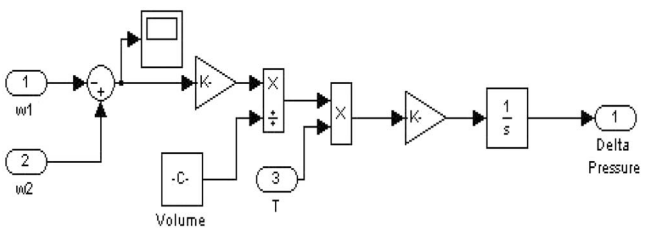

Fig. 5 ICV subsystem

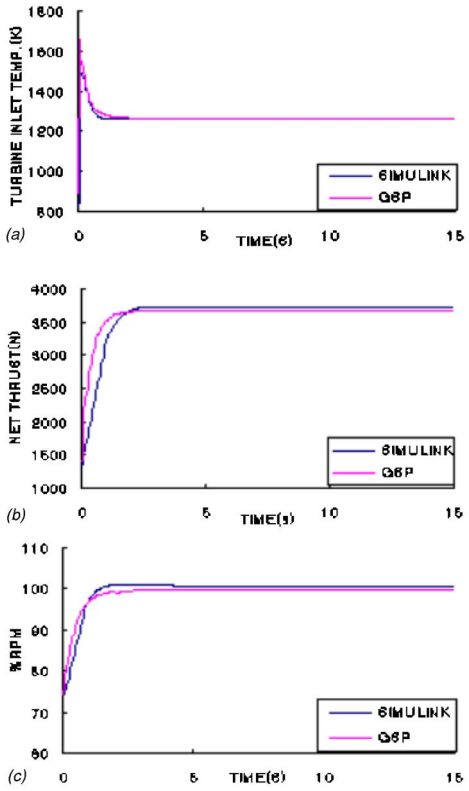

Fig. 6 Comparison of transient analysis results of turbojet engine by SIMULINK and GSP

Case 4: Flight Mode Transition Case From Fixed Wing Mode to Rotary Wing Mode. In this case, inverse flight mode transition from the fixed wing mode to the rotary wing mode is the condition. The propulsion system has the same operation condition as in case 3. Master valve angle variation is scheduled from 0 to 90 deg during times of 100, 150, and 200 s, respectively. While the master valve is linearly opening from the closed position as shown in Fig. 9(*a*), the main nozzle exit is gradually closing with chocking condition, as shown in Fig. 9(*b*). Therefore, gas mass flow at the tip-jet nozzle is rapidly increasing (to a small degree), but the flow at the main nozzle is gradually decreasing, as shown

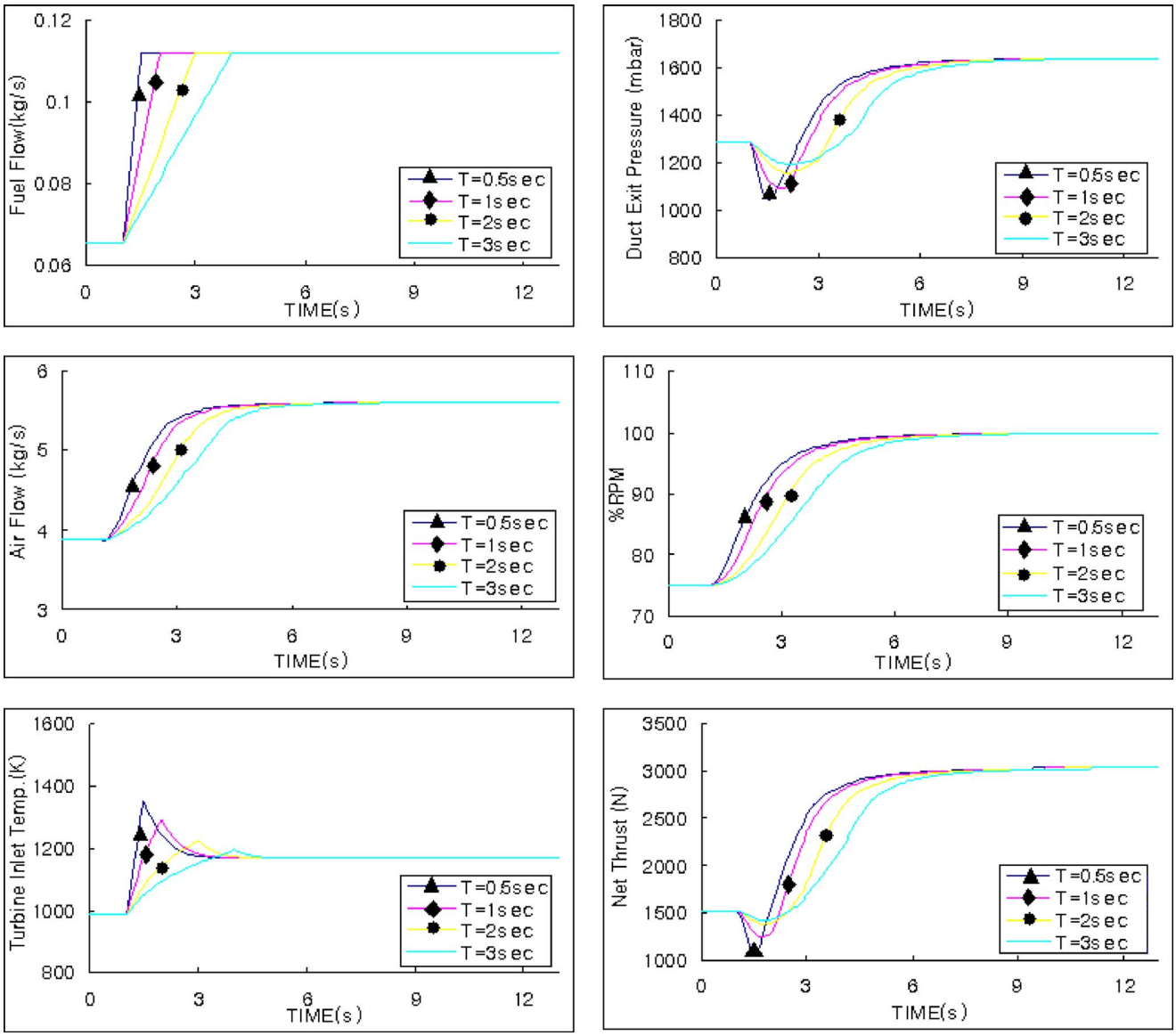

Fig. 7 Transient analysis result of rotary wing flight mode

in Fig. 9(*c*). At this operation, pressure at tip jet nozzle inlet is increased, but pressure at the main nozzle inlet is mostly maintained, as shown in Fig. 9(*d*).

In this case, it has a different tendency from case 3, that total net thrust is oscillatorilly decreasing but the specific fuel consumption (SFC) is increasing as in Figs. 9(*e*) and 9(*f*).

Therefore, this case thrust oscillation should also be considered for safe flight during flight mode transition.

Conclusion

In order to obtain transient performance characteristics of the CRW-type UAV propulsion system during flight mode transition, the propulsion system was modeled and simulated using the SIMULINK®. Moreover the performance characteristics of the propulsion system were investigated depending on position angle variation of the master valve at both the rotary and fixed wing modes.

In case 1, transient behaviors of the main turbojet engine were safely investigated to verify acceptability of the proposed model. According to comparison results, analysis results of the proposed model agreed well, with them using the commercial program GSP.

In case 2, transient performance behaviors at the rotary wing flight mode were investigated with three linear fuel increase schedules from idle to maximum rotational speed. According to analysis results, the faster the fuel increase, the more turbine inlet temperature overshoot occurs, and the net thrust at the tip-jet nozzles decrease rapidly at initial condition then increase quickly to the converged steady-state condition. In order to operate the engine safely, the fuel throttle showed to be performed slowly.

In case 3, during flight mode transition from the rotary wing mode to the fixed wing mode; the master valve position of the duct system was linearly closed and the variable main nozzle exit area was gradually increased with chocking condition. At this condition, the tip-jet nozzle inlet pressure fell down to atmospheric pressure, but the main nozzle inlet pressure was mostly maintained, except for friction loss. Total net thrust was oscillatorilly increased.

In case 4, during flight mode transition from the fixed wing mode to the rotary wing mode, the master valve was linearly opened and the main nozzle exit area was gradually closed with

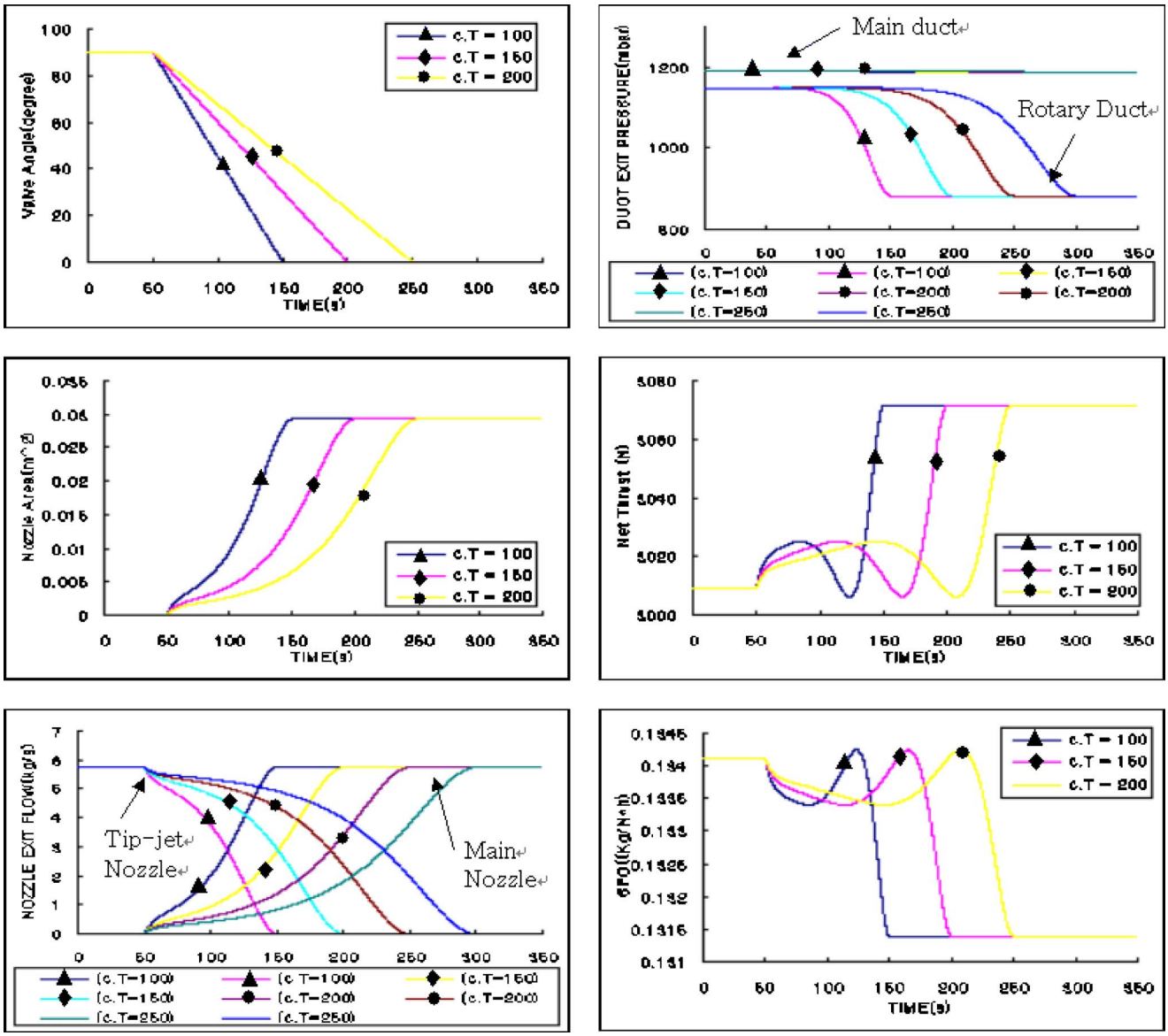

Fig. 8 Transient propulsion system performance characteristic during flight mode transition (from rotary wing mode to fixed wing mode)

chocking condition. At this condition, the tip-jet nozzle inlet pressure was rapidly increased, but main nozzle inlet pressure was mostly maintained. Total net thrust also was oscillatorilly decreased.

Through this investigation, it was found that severe thrust fluctuation should be considered for safe flight during flight mode transition even though operation of the master valve is scheduled slowly.

Acknowledgment

This study was supported by research funds from Chosun University, 2005.

Nomenclature

$\dot{P}_2$ = time derivative of pressure in the combustor
$\dot{P}_4$ = time derivative of pressure in the duct
R = gas constant
$V_{1,2}$ = component volume
$\dot{m}_1$ = accumulation of mass flow rate in the combustor
$\dot{m}_2$ = accumulation of mass flow rate in the nozzle
J = Joulean mechnical equivalent of heat
I = polar moment of inertia of rotor spool
N = shaft rotational speed
TW = turbine work
CW = compressor work
f = friction factor
Re = Reynolds number
μ = dynamic viscosity coefficient
ρ = density
V = gas velocity
D = diameter
L = length
$K_{S,G}$ = pressure loss coefficient
L_u = upstream tangent length
L_D = downstream tangent length
C_K = corrected pressure loss coefficient
C_dA_v = effective open area of valve
N_{cs} = chester smith function
θ = valve angle

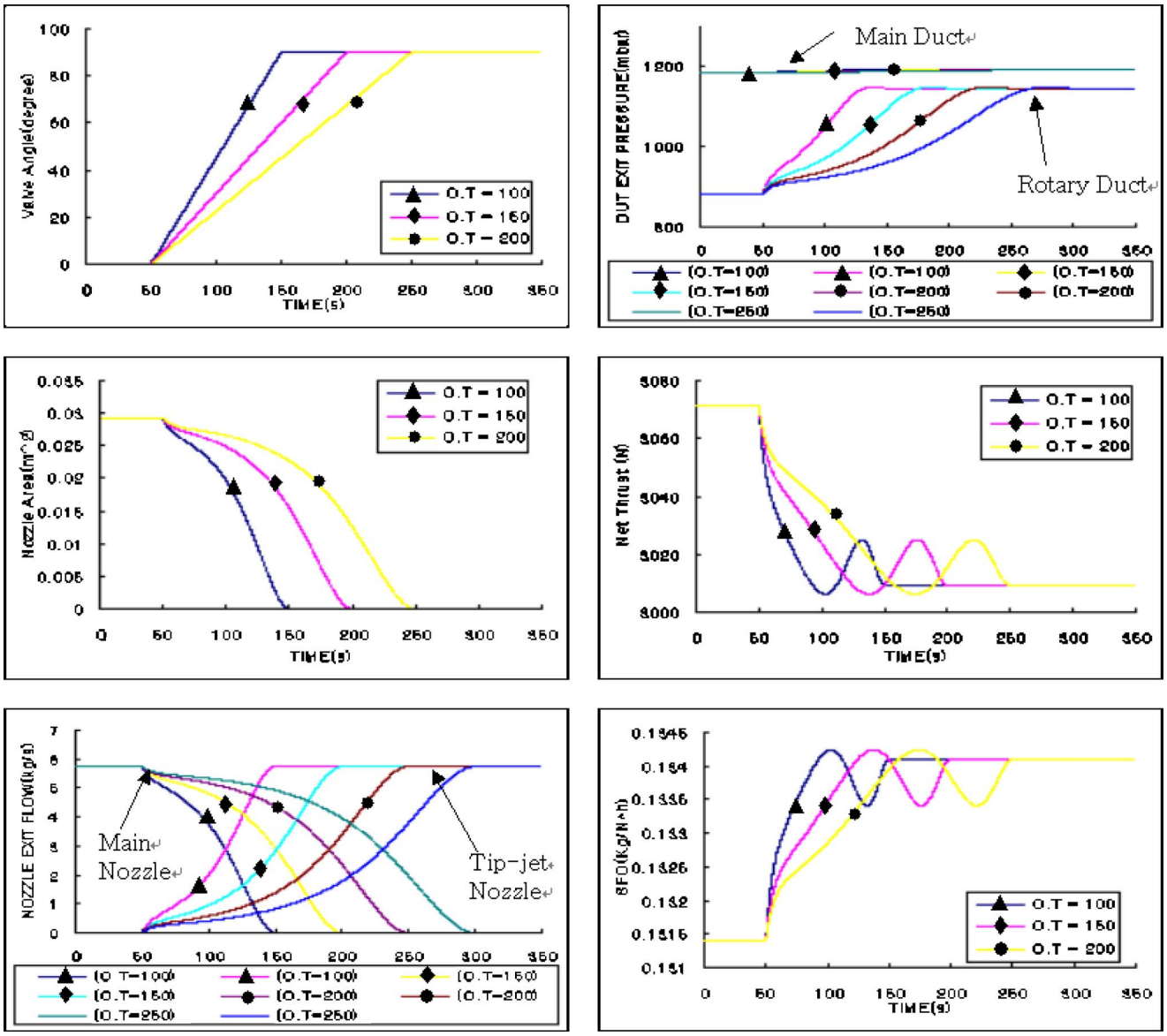

Fig. 9 Transient propulsion system performance characteristic during flight mode transition (from fixed wing mode to rotary wing mode)

References

[1] Tai, J. C. M., 1998, "A Multidisciplinary Design Approach to Size Stopped Rotor/Wing Configurations Using Reaction Drive and Circulation Control," Georgia Institute of Technology, Ph.D. thesis.

[2] Changduk, K., 2004, "Steady-State/Transient Performance Simulation of the Propulsion System for the Canard Rotor Wing UAV During Flight Mode Transient," *Proceedings of ASME TURBO EXPO 2004, ASME, NY.*

[3] Math Works, 1997, *SIMULINK: Dynamic System Simulation for MATLAB, Ver.2*, The Math Works, Inc.

[4] Fawke, A. J., 1970, "Digital Computer Simulation of Gas Turbine Dynamic Behavior," Ph.D. thesis, University of Bristol, UK.

[5] ESDU, 1966, *Friction Losses for Fully-Developed Flow in Straight Pipes*, Engineering Sciences Data Item No. 66027.

[6] ESDU, 1977, *Pressure Losses in Curved Ducts: Single Bends*, Engineering Sciences Data Item No. 83037.

[7] The Boeing Company, 2000, *EASY5: Environmental Control System Library User Guide*.

A Fully Integrated Approach to Component Zooming Using Computational Fluid Dynamics

Vassilios Pachidis[1]
e-mail: v.pachidis@cranfield.ac.uk

Pericles Pilidis
e-mail: p.pilidis@cranfield.ac.uk

Department of Power, Propulsion and Aerospace Engineering, Gas Turbine Engineering Group, Cranfield University, Cranfield, Bedfordshire MK43 0AL, UK

Fabien Talhouarn
Ecole Polytechnique de l'Universiti d'Orlians, 8 rue Lionard de Vinci, 45072 Orlians Cedex 2, France
e-mail: talhouarnf@yahoo.com

Anestis Kalfas
Turbomachinery Laboratory, ETH Zurich, Swiss Federal Institute of Technology, Sonneggstrasse 3, 8092 Zurich, Switzerland
e-mail: kalfasa@asme.org

Ioannis Templalexis
Hellenic Air Force Academy, Section of Thermodynamics, Power and Propulsion, Dekeleia Air Base, Greece
e-mail: templalexis@hafa.gr

Background. *This study focuses on a simulation strategy that will allow the performance characteristics of an isolated gas turbine engine component, resolved from a detailed, high-fidelity analysis, to be transferred to an engine system analysis carried out at a lower level of resolution. This work will enable component-level, complex physical processes to be captured and analyzed in the context of the whole engine performance, at an affordable computing resource and time.* ***Approach***. *The technique described in this paper utilizes an object-oriented, zero-dimensional (0D) gas turbine modeling and performance simulation system and a high-fidelity, three-dimensional (3D) computational fluid dynamics (CFD) component model. The work investigates relative changes in the simulated engine performance after coupling the 3D CFD component to the 0D engine analysis system. For the purposes of this preliminary investigation, the high-fidelity component communicates with the lower fidelity cycle via an iterative, semi-manual process for the determination of the correct operating point. This technique has the potential to become fully automated, can be applied to all engine components, and does not involve the generation of a component characteristic map.* ***Results***. *This paper demonstrates the potentials of the "fully integrated" approach to component zooming by using a 3D CFD intake model of a high bypass ratio turbofan as a case study. The CFD model is based on the geometry of the intake of the CFM56-5B2 engine. The high-fidelity model can fully define the characteristic of the intake at several operating condition and is subsequently used in the 0D cycle analysis to provide a more accurate, physics-based estimate of intake performance (i.e., pressure recovery) and hence, engine performance, replacing the default, empirical values. A detailed comparison between the baseline engine performance (empirical pressure recovery) and the engine performance obtained after using the coupled, high-fidelity component is presented in this paper. The analysis carried out by this study demonstrates relative changes in the simulated engine performance larger than 1%.* ***Conclusions***. *This investigation proves the value of the simulation strategy followed in this paper and completely justifies (i) the extra computational effort required for a more automatic link between the high-fidelity component and the 0D cycle, and (ii) the extra time and effort that is usually required to create and run a 3D CFD engine component, especially in those cases where more accurate, high-fidelity engine performance simulation is required.* [DOI: 10.1115/1.2135815]

Introduction

It is widely believed that research and development (R&D) in gas turbine systems is becoming very expensive. The recent economic recession and global competition in the commercial gas turbine industry led academia and industry to initiate pioneering research for the reduction of development costs and time and the improvement of engine performance, efficiency, reliability, etc. Large-scale hardware tests contribute significantly to the high development costs [1].

Design and development costs could potentially be reduced by replacing some of the large-scale tests, currently required for product development, with high-resolution, highly integrated component-system computational simulations. A more extensive use of sophisticated simulation tools would certainly save a large portion of the costs directly associated with testing and also enable the effects of design changes to be studied, in detail, before a commitment to a final design is made. By simulating full gas turbine systems in sufficient detail early in the design process, critical design and cost issues can be resolved before hardware is built [2]. Moreover, the recent rapid development of gas turbine diagnostic techniques, such as linear and nonlinear gas path analysis, fuzzy logic, neural networks, genetic algorithms, etc., demands more accurate engine models (higher level of fidelity) and shorter simulation times. During engine diagnosis, using any of the above techniques an engine model is required to run off-design hundreds or even thousands of times. For the time being, however, "high-fidelity simulation" and "faster simulation" are two contradictory concepts.

The majority of today's engine simulation software is of a low fidelity zero-dimensional (0D). Such an engine simulation tool is also available at Cranfield University with the name PYTHIA. In these 0D cycle simulations, individual components are usually represented via nondimensional look-up tables (maps) of experimental or "default" data, with adjustments for off-design effects, such as variable geometry, Reynolds effects, gamma correction, clearances, etc. Conventional gas turbine performance simulation tools can offer a good prediction of the performance of a whole engine but are incapable of analyzing the performance of individual engine components, in detail, or "capturing" extreme/complex physical phenomena (i.e., inlet flow distortion). On the other hand, computational fluid dynamics (CFD) tools can predict the performance of individual engine components satisfactorily,

[1]Corresponding author.

Contributed by the International Gas Turbine Institute (IGTI) of ASME for publication in the JOURNAL OF ENGINEERING FOR GAS TURBINES AND POWER. Manuscript received October 1, 2003; final manuscript received March 1, 2004. IGTI Review Chair: A. J. Strazisar. Paper presented at the International Gas Turbine and Aeroengine Congress and Exhibition, Vienna, Austria, June 13–17, 2004, Paper No. GT2005-68458.

under various operating conditions, but do not offer whole engine performance prediction.

In many cases, simulating individual engine components alone is not sufficient. In the simulation of a complete gas turbine system, the presence of upstream and downstream engine components (compressor, bypass duct, etc.) affects the flow through a given component; therefore, the "presence" of the remaining engine components must be brought in the simulation to account for inter-component effects.

By modeling the entire geometry of a propulsion system at the highest level of resolution (3D), all the information necessary to access engine life, reliability, and performance could be collected. Two issues, however, prevent this from being a practical solution. First, for a complete three-dimensional (3D) system simulation, the amount and level of detailed information needed as boundary and initial conditions would be extremely difficult to obtain. Second, the computational time and cost will be extremely high for effective and practical use in an industrial or academic research environment. Given the current computational and financial resources, a fast method of combining different levels of analysis seems to be necessary.

Other research efforts with similar focus have been reported in the past. Turner et al. [3] discussed a multifidelity simulation by NASA and GE of a turbofan engine with component characteristics zoomed into "partial" performance maps for a 0D cycle simulation. AuBuchon and Follen [1] described another collaborative effort between NASA and Pratt & Whitney on one-dimensional (1D) compressor zooming. Within the context of the Cranfield-Rolls Royce UTC collaboration, Yin [4,5] has carried out significant research on high bypass ratio (HBR) two-dimensional (2D) fan zooming. Reed and Afjeh [6–8] have also published on numerical zooming techniques, in the context of the NPSS program. In July 1997 Reed and Afjeh [9] published a paper on a comparative study of high- and low-fidelity fan models for turbofan engine system simulation. Smith [10] reported a collaborative research effort between NASA and GE on fan and compressor high-fidelity zooming.

Simulation Strategy

As mentioned before, this project focuses on the investigation of the appropriate simulation strategies that will allow the performance characteristics of a gas turbine engine component, resolved from a detailed, high-fidelity 3D analysis, to be integrated into an engine system analysis performed at a lower level of detail.

This paper discusses a simulation strategy with the potential to (i) "match" the fidelity of the simulation according to the needs of the analysis for each component individually, (ii) investigate relevant physical processes occurring in an engine component in more detail, and (iii) assess the effects of various isolated flow phenomena on overall engine performance in a timely and affordable manner. The strategy described in this paper is called "fully integrated zooming" [11,12].

This is a rather automatic and fully integrated approach to high-fidelity analysis with the 3D CFD component model being directly linked to the 0D engine model via the 0D component. The 3D and 0D models communicate with each other by means of inlet and outlet boundary conditions. For the purposes of this preliminary investigation and for the determination of the correct component operating point, boundary conditions are exchanged between the two models following a semi-manual process.

After selecting engine operating conditions and power setting, a 0D engine model simulation is carried out to generate a first set of component operating conditions. The established component inlet and outlet boundary conditions from the 0D cycle simulations are used to define component boundary conditions in the 3D model simulation. Operating characteristics of the three-dimensional component model are then compared against the initial 0D solution.

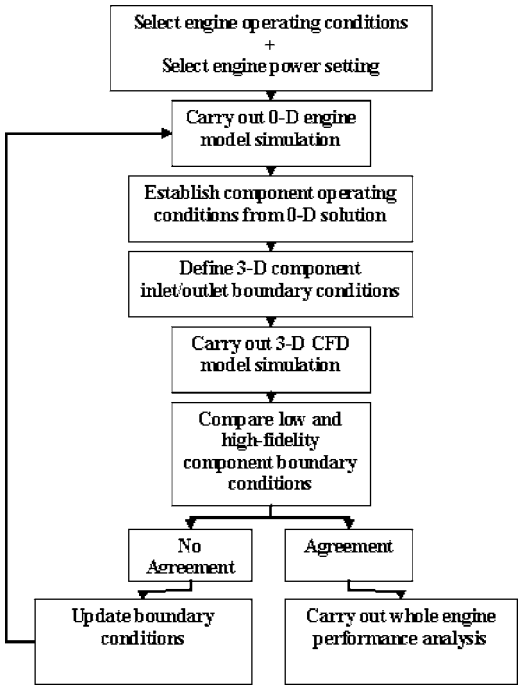

Fig. 1 Fully integrated zooming strategy

Determining the correct component operating point generally involves an iterative process. Initially the 0D component will not match the high-fidelity component for various reasons, such as 0D component being of low fidelity, geometry not taken into account in 0D simulations, intercomponent effects not taken into account in the high-fidelity simulations, etc. Boundary conditions need to be updated and exchanged between the two component representations, in an iterative process, until a converged component performance is achieved at the selected engine operating conditions and power setting.

If the 0D and 3D flow solutions are in agreement, within a preestablished error margin, the averaged 3D flow solution establishes the correct component operating point to be used in the whole engine performance simulation. If the flow solutions are not in agreement, the 3D boundary conditions are communicated back to the 0D engine model as a second "guess." The 0D engine model simulation is carried out again to provide new, updated boundary conditions for the 3D CFD simulation. The process is repeated many times, until the two solutions agree within the preestablished error margin and a converged operating point is found. The same process can be repeated for all engine operating conditions and power settings. Generation of a complete component characteristic map is not required.

The high-fidelity component can fully define the characteristic of the engine component at several operating conditions and can be used to provide a more accurate, physics-based estimate of the component's performance and hence, engine performance, replacing the empirical values within the 0D cycle model. This technique is called fully integrated zooming and can be applied to all engine components that can be modeled in 2D or 3D. It requires the iterative execution of the 0D engine cycle and the high-fidelity model to establish the correct component operating characteristic at given flight conditions and engine power setting (Fig. 1).

Simulation Tools

Using the CFM56-5B2 HBR turbofan engine as a case study, this work looked into intake pressure recovery effects on whole engine performance, following the fully integrated zooming approach described above. The study utilized two different simula-

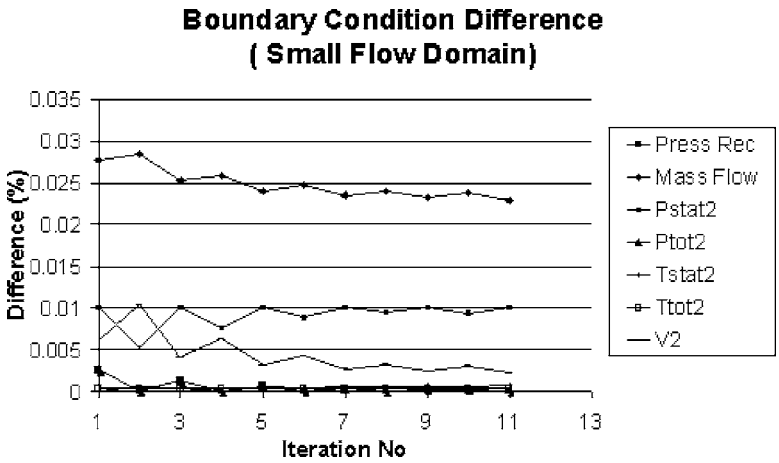

Fig. 2 Convergence history using a small flow domain

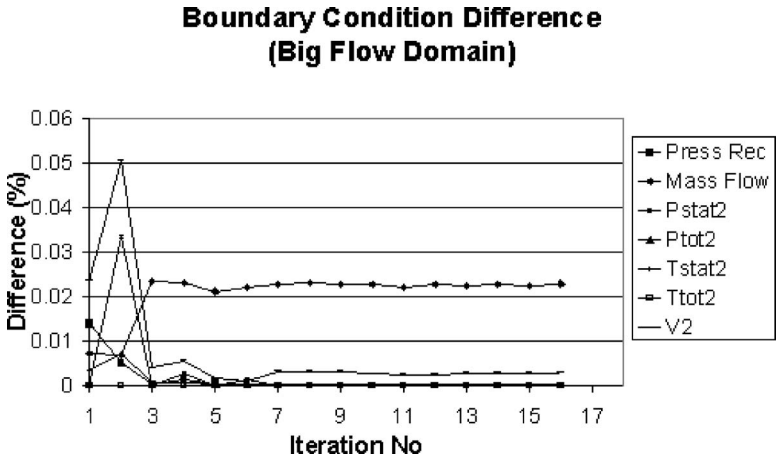

Fig. 3 Convergence history using a big flow domain

tion software: (i) a 0D gas turbine modeling and performance simulation system, developed at Cranfield University in the UK, called PYTHIA, and (ii) the commercial CFD package GAMBIT/FLUENT. The PYTHIA scheme has been developed by the Gas Turbine Engineering Group at Cranfield University [13]. Based on Cranfield's previous "generation" engine simulation software, called TURBOMATCH [14], it has been specifically developed to be a fully modular, object-oriented, engine cycle simulator that can perform steady-state design, off-design, and degraded performance analysis of civil aero, industrial, and military engines. PYTHIA is also a versatile engine diagnostics tool. A PYTHIA engine model is assembled from a collection of interconnected elements and controlled by an appropriate numerical solver. By means of engine component icons and via an engine component toolbar, various preprogramed routines can be called up to simulate the action of the different components of the engine, resulting finally in output of engine thrust or power, fuel consumption, specific fuel consumption, etc., together with details of individual component performance and of the gas properties at various stations within the engine.

For the purposes of this investigation, an engine model was built in PYTHIA that resembles the CFM56-5B2 HBR turbofan engine in both configuration and performance. The modeling was based on engine performance data available in the public domain. Moreover, a 3D CFD intake model, based on the geometry of the intake of the CFM56-5B2 HBR turbofan engine, was created and meshed in the commercial package GAMBIT using approximately 300,000 cells. The optimum number of cells was established by a "grid-independence" study. The commercial CFD solver, FLUENT, was used to carry out the CFD analysis. The geometry of the intake was similarly obtained from the public domain.

Typically, a PYTHIA engine model uses performance maps for turbines and compressors to obtain a balanced, steady-state engine condition. Intake pressure recovery is simplistically simulated by means of an empirical total pressure drop at both design point and off-design conditions.

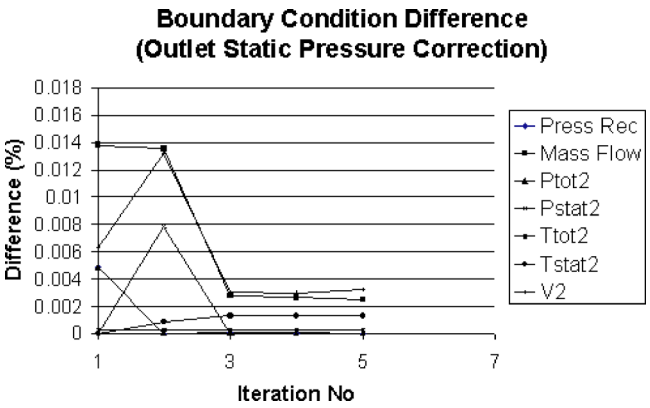

Fig. 4 Convergence history using a big flow domain and intake outlet static pressure correction

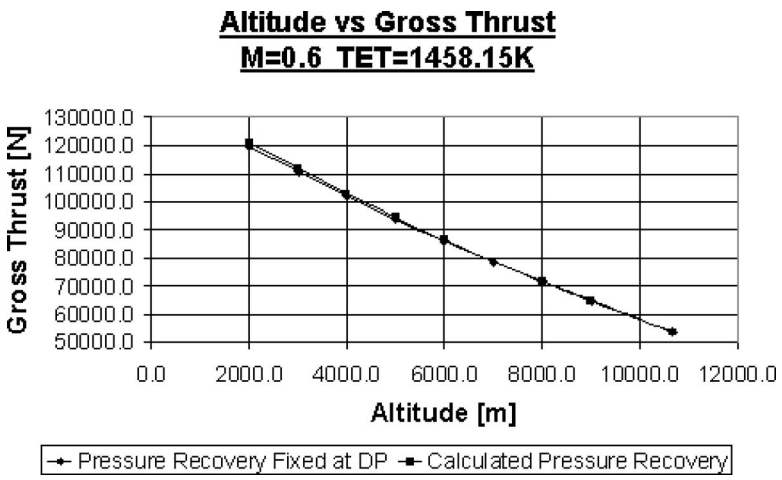

Fig. 5 Altitude versus gross thrust

In order to establish the baseline intake and engine performances for the zooming analysis, the 0D intake characteristics were calibrated such that at the baseline conditions (DP) there was no difference between the 0D intake performance (i.e., pressure recovery, mass flow etc.) and the performance predicted by the full, 3D CFD intake model.

Analysis

During off-design (OD) analysis, establishing a converged intake operating point involved the iterative process described in the section on Simulation Strategy. After selecting engine operating conditions and a power setting, the 0D turbofan engine model of the CFM56-5B2 was run in PYTHIA to generate a first set of intake operating conditions. The established intake inlet/outlet boundary conditions from the 0-D cycle simulations were used to define boundary conditions in the 3D model simulation. Operating characteristics of the three-dimensional intake model were then compared against the initial 0D solution. Initially, the 0D component did not match the high-fidelity component for the reasons stated before. Boundary conditions were exchanged between the two component representations, in an iterative process, until a converged component performance was achieved at the given engine operating conditions and power setting.

In those cases where the 0D and 3D flow solutions were in agreement, within a 0.25% difference approximately, the averaged 3D flow solution established the operating point of the intake for the given power setting, to be used at a later stage for the whole engine performance simulation. In those cases where flow solutions were not in agreement, the 3D boundary conditions were "fed" back to the 0D engine model as a second guess. The 0D engine model simulation was carried out again to provide new, updated boundary conditions for the 3D CFD simulation. The process was repeated many times until the two solutions agreed within the preestablished "difference margin" and a converged intake operating point was found.

The zooming analysis reported in this paper looked into different Mach numbers and operating altitudes for a fixed engine power setting and incidence angle. Varying altitude and Mach number gave a satisfactory range of different intake inlet operating conditions and allowed for a thorough engine performance comparison. More analytically, the engine's power setting was kept at the DP value of 1458.15 K turbine entry temperature (TET) and incidence angle was kept at 0 deg. Intake operating points were obtained for Mach numbers between 0.8 (DP value) and 0.3 and for a range of altitudes between 10,670 m (DP value) and 2000 m. Results in this paper are presented only for the altitude variation.

Repeating the process for different engine operating conditions, power settings, and incidence angles establishes the full engine performance using the fully integrated approach. At this stage however, it was outside the scope and requirements of the investigation to repeat the same methodology for a larger number of different cases.

The high-fidelity intake model defined the performance characteristics of that particular intake geometry fully, at the simulated

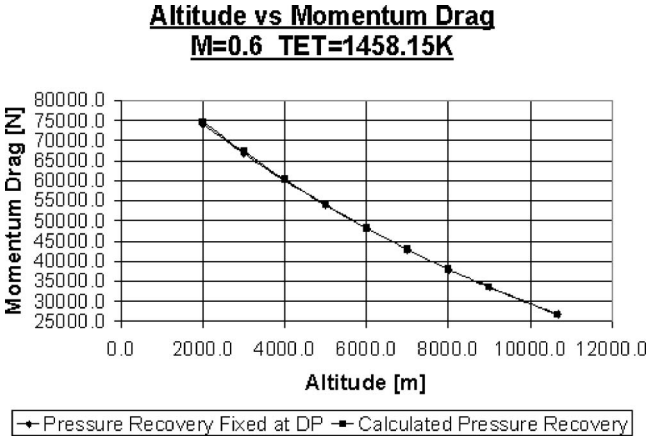

Fig. 6 Altitude versus momentum drag

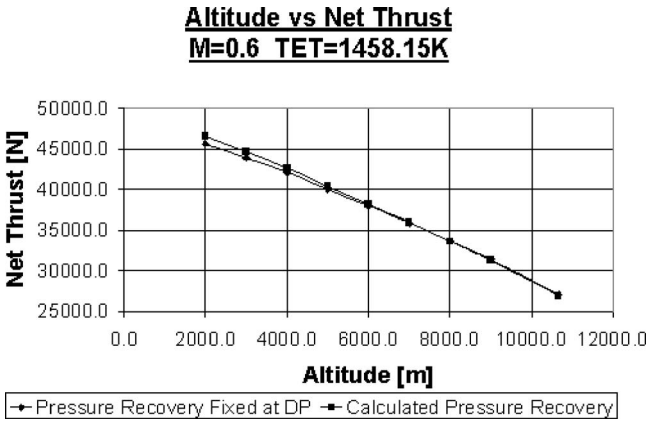

Fig. 7 Altitude versus net thrust

operating conditions, and was then used to provide a more accurate, physics-based estimate of the intake's performance (i.e., pressure recovery) and hence, engine performance, replacing the empirical pressure recovery values within the PYTHIA cycle model.

For the purposes of this preliminary investigation and for the determination of the correct operating point, boundary conditions were exchanged between the two models following an iterative, semi-manual process. A CFD model, fully embedded in the 0D cycle analysis, would require the additional programing of an appropriate iterative routine so that, during an OD analysis, appropriate boundary conditions can be communicated automatically.

Convergence

As mentioned before, matching the boundary conditions of the 3D CFD intake model to those of the 0D intake component required an iterative execution of PYTHIA and FLUENT. Initial 0D cycle and 3D CFD test runs, using a small, localized domain revealed a very poor convergence probability. Figures 2–4 illustrate some convergence history samples of intake boundary conditions for PYTHIA-FLUENT iterative runs close to DP conditions.

In several occasions and particularly in those cases where extreme operating conditions were selected (resulting in unrealistic boundary conditions), the percentage difference between boundary conditions seemed to oscillate and/or even diverge. Figure 2 is representative of this sort of unstable computational solution. In this particular case, the outlet static pressure difference initially diverged and then oscillated around 1.0%. The difference in mass flow remained also fairly large, even after 11 iterations, ~2.3%. Iterating for other points demonstrated similar unstable computational behavior.

Improving the CFD intake model (denser grid) and using a bigger flow domain, which also accounted for the flow outside the engine's nacelle, improved the computational stability of the solution and the chances for convergence. Figure 3 is representative of this group of iterative runs between PYTHIA and FLUENT. The difference in mass flow remained at a ~2.3% after 16 iterations; however, the difference in all other boundary conditions dropped below an acceptable 0.3% after seven iterations.

Applying a correction factor to the outlet static pressure prediction of the 0D intake component, in every iteration, to take into account the presence of the fan and its effects on the flow field, improved the relatively large difference in mass flow even further and led to a much faster convergence. For this type of iterative runs, all boundary conditions converged after three to four iterations within an acceptable 0.4%. Figure 4 demonstrates the above observation and is representative of the final group of iterative runs.

Engine Performance Simulation

Subsequent engine performance analysis demonstrated differences in the simulated engine performance between using the standard, empirical intake pressure recovery values and using the CFD-coupled approach. At cruise conditions and DP power setting the simulation results, using the CFD-coupled method, matched the baseline engine performance very well. As expected, only third-decimal-place differences were observed.

The largest differences in engine performance were observed at operating conditions other than those at cruise (OD conditions). The following paragraphs attempt to demonstrate this point by discussing the trends observed in some of the engine simulation results, as examples. Because of the inherent "uncertain" accuracy of the public domain data used for the modeling of the engine and the intake, results presented in this paper are to be taken only qualitatively.

Lowering the altitude from 10,670 m to 2000 m, at a constant Mach number ($M=0.6$) and power setting (TET=1458.15 K) gave a 0.5% reduction in engine gross thrust at 10,670 m and a 1.2% increase at 2000 m compared to the baseline engine performance (empirical pressure recovery). Similarly momentum drag

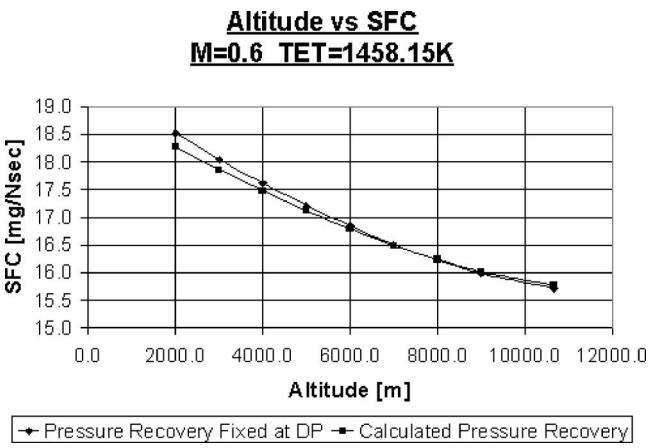

Fig. 8 Altitude versus SFC

was reduced by 0.3% at 10,670 m and increased by 0.7% at 2000 m. Net thrust went down by 0.6% at 10,670 m and up by 2.0% at ~2000 m. This also resulted in SFC going up by 0.3% at 10,670 m and down by 1.3% at 2000 m. Figures 5–8 illustrate the above observations.

Conclusions

This work demonstrated the potentials of the fully integrated approach to component zooming by using a 3D CFD intake model of a high bypass ratio turbofan, directly coupled to a 0D engine performance simulation software. The CFD model was based on the geometry of the intake of the CFM56-5B2 engine and was used in the 0D cycle analysis to provide a more accurate, physics-based estimate of intake performance (i.e., pressure recovery) and, hence, engine performance replacing the default empirical values.

For the purposes of this preliminary investigation, the high-fidelity component communicated with the lower fidelity cycle via an iterative, semi-manual process for the determination of the correct operating point. This technique has the potential to become fully automated, can be applied to all engine components, and does not involve the generation of a component characteristic map.

This work showed that establishing the correct component operating point through this iterative process successfully, depends strongly on the quality of the CFD model geometry, grid fidelity, and the soundness of the operating conditions selected.

The above analysis was carried out only at a zero incidence angle and fixed power setting. Following exactly the same simulation strategy, other power settings and incidence angles can be included in the analysis, for an even more realistic intake/engine performance prediction, especially under takeoff and landing conditions.

This paper presented a detailed comparison between the simulated baseline engine performance and the one obtained by using the CFD-coupled approach. Gross thrust, net thrust, momentum drag, and SFC were compared at different altitudes and Mach numbers. Results presented in this report, for the case of altitude variation, are to be taken only qualitatively, because of the inherent uncertain accuracy of public domain data. However, in the cases examined, the analysis carried out by this study, demonstrated relative changes in the simulated engine performance larger than 1%.

For this reason, this investigation proves the value of the simulation strategy followed in this paper and completely justifies (i) the extra computational effort required for a more automatic link between the high-fidelity component and the 0D cycle, and (ii) the extra time and effort that is usually required to create and run a 3D CFD engine component, especially in those cases where more accurate, high-fidelity engine performance simulation is required.

References

[1] AuBuchon, M. and Follen, G., 2000, "Numerical Zooming Between a NPSS Engine System Simulation and a One-Dimensional High Compressor Analysis Code," Computational Aerosciences Workshop, High Performance Computing and Communications Program, Moffett Field, CA, NASA/TM-2000-209913, February.

[2] Evans, A., Follen, G., Naiman, C., and Lopez, I., 1998, "Numerical Propulsion System Simulation's National Cycle Program," NASA Lewis, Cleveland, AIAA-98-3113, July.

[3] Turner, M. G., Reed, J. A., Ryder, R., and Veres, J. P., 2004, "Multi-Fidelity Simulation of a Turbofan Engine with Results Zoomed Into Mini-Maps for a Zero-D Cycle Simulation," ASME Paper No. GT2004-53956.

[4] Yin, J., 1999, "High Bypass Ratio Fan Modeling" (WP2), Performance Engineering UTC Annual Review Report, School of Mechanical Engineering, Cranfield University, March.

[5] Yin, J., 1999 "Proposed Calculation Procedures for the Generation and Application of 2-D Fan Characteristics," *Performance Engineering UTC Document PE005. Version 2*, School of Mechanical Engineering, Cranfield University, August.

[6] Reed, J. A., and Afjeh, A. A., 1994, "Development of an Interactive Graphical Propulsion System Simulator," 30th AIAA/ASEE Joint Propulsion Conference, University of Toledo June, AIAA Paper No. AIAA-94-3216.

[7] Reed, J. A., and Afjeh, A. A., 1994, "Distributed and Parallel Programming in Support of Zooming in Numerical Propulsion System Simulation," *NASA Proceedings of Symposium on Applications of Parallel and Distributed Computing*, Columbus, April.

[8] Reed, J. A., and Afjeh, A. A., 1995, "An Interactive Graphical System for Engine Component Zooming in a Numerical Propulsion System Simulation," University of Toledo, 33rd Aerospace Sciences Meeting and Exhibit January, AIAA Paper No. A1AA-95-0118.

[9] Reed, J. A., and Afjeh, A. A., 1997, "A Comparative Study of High and Low Fidelity Fan Models for Turbofan Engine System Simulation," *Proceedings of the IASTED International Conference on Applied Modeling and Simulation*, Banff, Canada, July.

[10] Smith, L. H., 1994, "NASA/GE Fan and Compressor Research Accomplishments," ASME J. Turbomach., **116**(4), pp. 554–568.

[11] Talhouarn, F., Pachidis, V., and Pilidis, P., 2004, "Partially Integrated Approach to 3-D Component Zooming Applied to the Intake," Cranfield Technical Report, Cranfield University, School of Engineering, Department of Power, Propulsion, and Aerospace Engineering, Gas Turbine Performance Group, July.

[12] Guideuil, G., Pachidis, V., and Pilidis, P., 2004, "Iterative Approach to 2D Component Zooming Applied to a Turbofan Intake," Cranfield Technical Report, Cranfield University, School of Engineering, Department of Power, Propulsion, and Aerospace Engineering, Gas Turbine Performance Group, July.

[13] Pachidis, V., 2004, "Gas Turbine Simulation—PYTHIA Workshop Guide, Part I and II," Cranfield University, Department of Power, Propulsion and Aerospace Engineering, ASME/IGTI Aero Engine Life Management Conference, London, March.

[14] Palmer, J. R., 1990, "The TURBOMATCH Scheme For Aero/Industrial Gas Turbine Engine Design Point/Off Design Performance Calculation," SME, Thermal Power Group, Cranfield University.

Effects of Manufacturing Tolerances on Regenerative Exchanger Number of Transfer Units and Entropy Generation

Wei Shang
e-mail: wes153@mail.usask.ca

Robert W. Besant

Department of Mechanical Engineering,
University of Saskatchewan,
57 Campus Drive,
Saskatoon, S7N 5A9, Canada

A prime concern with the design of ultra-compact heat exchangers is the impact on performance of flow channel variations due to flow channel hydraulic diameter variations caused by manufacturing tolerances. This paper uses analytical methods to show that as the standard deviation in flow channel sizes, caused by manufacturing tolerances in a rotary regenerative exchanger, is increased compared to the average flow channel diameter the effective number of transfer units decreases. Depending on the operating conditions, the entropy generation number either increases or decreases with increasing flow channel size variations. These findings extend previous findings that showed that flow channel variations cause lower pressure drops and effectiveness.
[DOI: 10.1115/1.2132380]

1 Introduction

Most regenerative exchangers are designed with small flow channels. They can be used to transfer both heat (sensible energy) and water vapor (latent energy) in energy recovery applications.

Figure 1 shows a typical regenerative exchanger rotor and several different flow channel geometries used in wheels employed for energy recovery. In this kind of counterflow rotary regenerators energy is transferred by convection from one duct gas flow to the wheel matrix surface where it is stored in the wheel matrix which is then rotated to the opposite side where an equal amount of energy is transferred to the other gas flow. The matrix flow channels can be parallel surface, equilateral triangle, square geometry, hexagonal, circular flow channels, or corrugated geometry as shown in Figs. 1(*a*)–1(*f*). These exchangers usually have a large heat and mass transfer surface area per unit volume, e.g., 4000 m^2/m^3, and a large number of flow channels per unit surface area of face, e.g., 40,000 pores per m^2 [1]. For typical manufacturing processes, significant variations occur in these flow channel hydraulic diameters. Shang and Besant [2] showed that these variations lower both the effectiveness and the pressure drop.

It was found by Shang and Besant [1] that the manufacturing tolerances can cause wide range variation of flow channel sizes. The ratio of the standard deviation in flow channel hydraulic diameters with respect to the mean value, σ/D_0, can be employed as the criteria to quantify the manufacturing tolerances in rotary regenerator industry. Shang and Besant [1] used optical and micrometer method to measure four different rotary regenerators and showed a range of σ/D_0 from 0.064 to 0.234. The corresponding pressure drop and effectiveness ratios, $\Delta p/\Delta p_0$ and $\varepsilon/\varepsilon_0$, for the regenerators compared to their ideal identical ones (or $\sigma=0$) were found to range from 0.982 to 0.859 and 0.986 to 0.867, respectively.

First the purpose of this paper is to extend the above studies to include the effects of flow channel hydraulic diameter variation on the effective number of transfer units, Ntu, which is defined as [3]

$$\mathrm{Ntu} = \frac{UA}{(\dot{m}c_p)_{\min}} \tag{1}$$

The number of transfer units, Ntu, is one of the most important dimensionless factors for heat exchanger design which is often treated as an independent operating factor in heat exchanger analysis. Second, the entropy generation number, N_S, which combines irreversible heat rate and pressure drop effects, is studied for the impacts of flow channel hydraulic diameter variation caused by manufacturing tolerances.

2 Performance of Regenerative Exchangers

To characterize the performance of a regenerative exchanger several performance factors are needed to be determined. According to the ASHRAE Std 84-91R [4], they are effectiveness, ε (including sensible, latent or moisture, and total or enthalpy), pressure drops, Δp (for both the supply and exhaust side), EATR (exhaust air transfer ratio), OACF (outside air correction factor), and RER (recovery efficiency ratio). Among these factors, the effectiveness, ε, and pressure drop, Δp, are often of most concern to manufacturers and designers for energy recovery applications.

The effects of variations in flow channel hydraulic diameter are outlined in the next section but first the effectiveness is defined.

The calculation of the effectiveness of a regenerative exchanger is presented in ASHRAE Std 84-91R [4]. To determine the regenerator effectiveness the gas flow properties must be measured at the four stations as shown in Fig. 2. For the case of negligible specific heat changes, the effectiveness is defined as

$$\varepsilon = \frac{\dot{m}_s(X_1 - X_2)}{\dot{m}_{\min}(X_1 - X_3)} \tag{2}$$

where

- ε = sensible, latent, or total energy effectiveness,
- X = either product of dry-bulb temperature (°C) and specific heat, c_p[kJ/(kg·K)], or humidity ratio (kg water/kg air), or total enthalpy (kJ/kg of dry air) corresponding to the sensible, latent (or moisture), and total effectiveness, respectively,
- $\dot{m}_s$ = mass flow rate of dry air in the supply stream (kg/s),
- $\dot{m}_e$ = mass flow rate of dry air in the exhaust stream (kg/s),

Contributed by the International Gas Turbine Institute of ASME for publication in the JOURNAL OF ENGINEERING FOR GAS TURBINES AND POWER. Manuscript received November 8, 2004; final manuscript received July 28, 2005. Assoc. Editor: J.-C. Han.

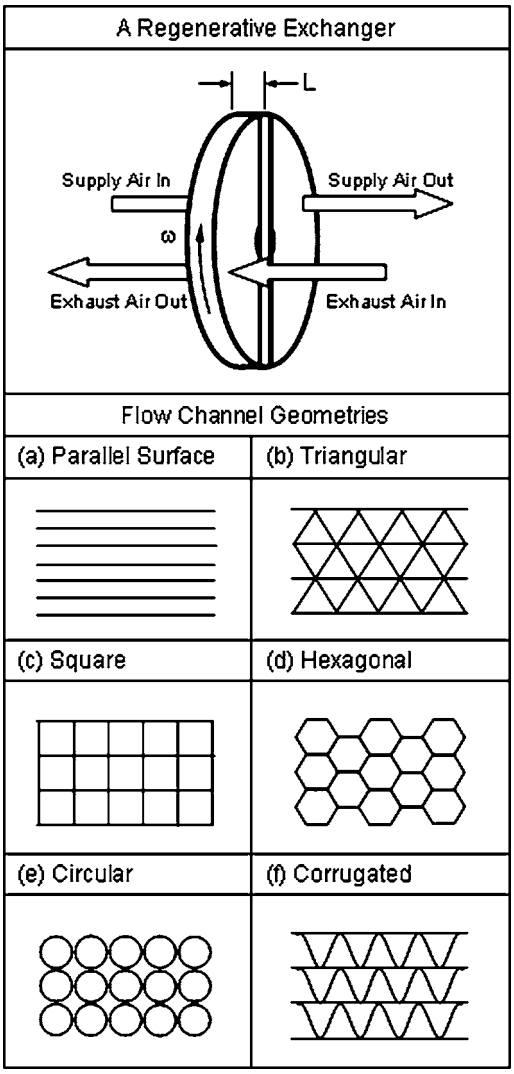

Fig. 1 A typical regenerative exchanger rotor and six different flow channel geometries

$$\dot{m}_{\min} = \text{minimum value of either } \dot{m}_s \text{ or } \dot{m}_e \text{ (kg/s)}.$$

For balanced flows in the supply and exhaust streams, $\dot{m}_s = \dot{m}_e = \dot{m}_{\min}$, Eq. (1) can be simplified as

$$\varepsilon = \frac{(X_1 - X_2)}{(X_1 - X_3)} \tag{3}$$

3 Manufacturing Tolerance Effects on Regenerative Exchanger Performance

The performance of a rotary regenerator will be altered by flow channel hydraulic diameter variations. These variations caused by manufacturing tolerances in the gas flow channels can be characterized by several different performance factors including: pressure drop, effectiveness, Ntu, and entropy generation number. All of them will be altered when the variations in hydraulic diameters of the flow channels are finite.

3.1 Pressure Drop Ratio. Shang and Besant [2] show that an analytical equation can be employed to relate the pressure drop across the flow channels with flow channel hydraulic diameter variations, Δp, to the pressure drop in an identical or ideal wheel without flow channel size variations, Δp_0. This pressure drop ratio for parallel surface flow channels as shown in Fig. 1(*a*) or symmetrical cylinder flow channels (i.e., equilateral triangle, square geometry, hexagonal, and circular flow channels as shown in Figs. 1(*b*)–1(*e*)) can be expressed in the functional form

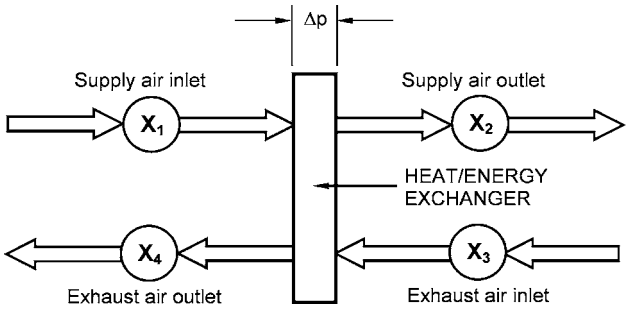

Fig. 2 Schematic for counter-flow regenerative exchangers

$$\frac{\Delta p}{\Delta p_0} = f_{p,1}\left(\frac{\sigma}{D_0}\right) \tag{4a}$$

or for corrugated flow channels as shown in Fig. 1(*f*)

$$\frac{\Delta p}{\Delta p_0} = f_{p,2}\left(\frac{\sigma}{D_0}, \eta_0\right) \tag{4b}$$

where σ/D_0 is the ratio of the standard deviation in flow channel hydraulic diameters with respect to the mean value. The mean corrugated aspect ratio, η_0, is defined as the ratio of mean wave-height and mean wavelength for a corrugated geometry as shown in Fig. 1(*f*). For rotary regenerators the range of η_0 is typically within $0.2 < \eta_0 < 1.0$.

Equations (4*a*) and (4*b*) consider only flow channel manufacturing tolerance effects. The reader is referred to the Appendix for more detailed analytical expressions of these equations.

Figure 3 illustrates the relationship between pressure drop ratio, $\Delta p/\Delta p_0$, and the standard deviation in flow channel hydraulic diameters with respect to the mean value, σ/D_0, for different flow channel geometries as shown in Fig. 1. Figure 3(*a*) shows the pressure drop ratio as a function of σ/D_0 with solid line for parallel surface matrix as shown in Fig. 1(*a*) and with dashed line for symmetrical cylindrical flow channels as shown in Figs. 1(*b*)–1(*e*). Figure 3(*b*) shows the case of corrugated flow channels as shown in Fig. 1(*f*) when the mean aspect ratio of the flow channels, η_0, is 0.2, 0.5, 1.0, and 1.5.

It is interesting to note that when the aspect ratio, $\eta_0 \to 0$, the pressure drop ratio curves for corrugated flow channels in Fig. 3(*b*) will be close to the curve for parallel surface flow channels as shown in Fig. 3(*a*) with solid line. Also, the pressure drop ratio curve for corrugated flow channels with aspect ratio $\eta_0 = 0.7$ is close to the pressure drop ratio curve with dashed line for symmetrical cylinders.

3.2 Effectiveness Ratio. At any operating condition the effectiveness ratio, $\varepsilon/\varepsilon_0$, of the regenerative exchanger with flow channel pore size variations compared to a wheel without variations can be expressed in the functional form

$$\frac{\varepsilon}{\varepsilon_0} = f_{\varepsilon,1}\left(\frac{\sigma}{D_0}, \partial\varepsilon_m\right) \tag{5a}$$

for a parallel surface or symmetrical cylinder flow channels and

$$\frac{\varepsilon}{\varepsilon_0} = f_{\varepsilon,2}\left(\frac{\sigma}{D_0}, \eta_0, \partial\varepsilon_m\right) \tag{5b}$$

for a corrugated flow channel wheel matrix. Again, the reader is referred to the Appendix for more detailed analytical expressions of Eqs. (5*a*) and (5*b*).

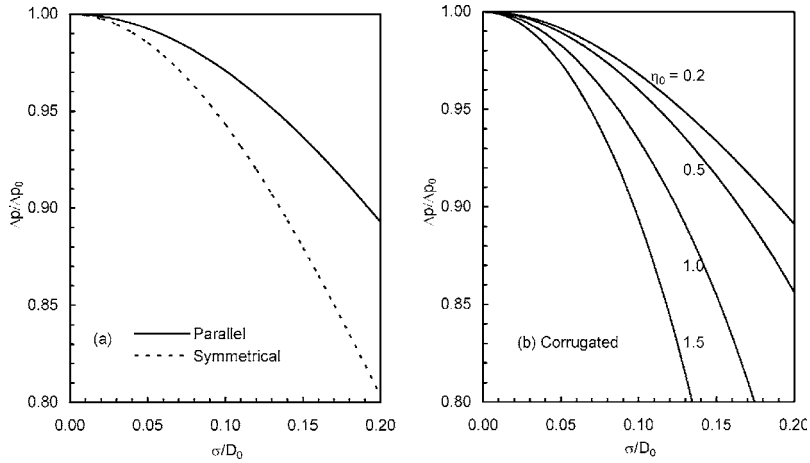

Fig. 3 Pressure drop ratio, $\Delta p/\Delta p_0$, for regenerative exchangers with a matrix of (*a*) parallel surface flow channels as shown in Fig. 1(*a*) and symmetrical cylinder flow channels as shown in Figs. 1(*b*)–1(*e*) and (*b*) corrugated geometries as shown in Fig. 1(*f*) with random variations in flow channel sizes to one without versus σ/D_0

$\partial\varepsilon_m$ is the effectiveness sensitivity coefficient [2] and defined by

$$\partial\varepsilon_m = \left.\frac{\dot{m}_0}{\varepsilon_0}\frac{\partial\varepsilon}{\partial\dot{m}}\right|_{\dot{m}=\dot{m}_0} \tag{6}$$

which is a constant that is dependent only on the operating condition.

Figure 4(*a*) shows this effectiveness ratio, $\varepsilon/\varepsilon_0$, versus the standard deviation in flow channel hydraulic diameters with respect to the mean value σ/D_0 for parallel surface with solid lines and for symmetrical cylinder flow channels with dashed lines for three different operating conditions $\partial\varepsilon_m=-0.1$, -0.3, and -0.5. For corrugated flow channels Fig. 4(*b*) illustrates this relationship for $\partial\varepsilon_m=-0.3$ but with the aspect ratio, η_0, as a parameter where η_0 is 0.2, 0.5, 1.0, and 1.5. For rotary regenerator applications, $\partial\varepsilon_m$ will be close to -0.3 [5].

3.3 Ntu. In heat exchanger applications, the effectiveness-Ntu method of design is preferrable because this method does not require knowledge of the outlet flow properties. Ntu is usually regarded to be constant for applications with specified operating conditions. However, it will be shown that the effective Ntu decreases when tolerances in the manufacturing process cause a significant increase in the ratio of flow channel standard deviation to mean hydraulic diameter (σ/D_0).

For rotary regenerators, Lambertson [6] correlated effectiveness, ε, with the total regenerative exchanger heat capacity rate ratio, C_r^*, Ntu, and Cr. Kays and London [3] modified this correlation for parallel flow channels in the wheel matrix of counterflow rotary regenerators for balanced flows (Cr=1):

$$\varepsilon = K\frac{\text{Ntu}}{1+\text{Ntu}} \tag{7}$$

where K is the rotational capacitance coefficient for rotary regenerators defined as

$$K = 1 - \frac{1}{9(\text{Cr}^*)^{1.93}} \tag{8}$$

where

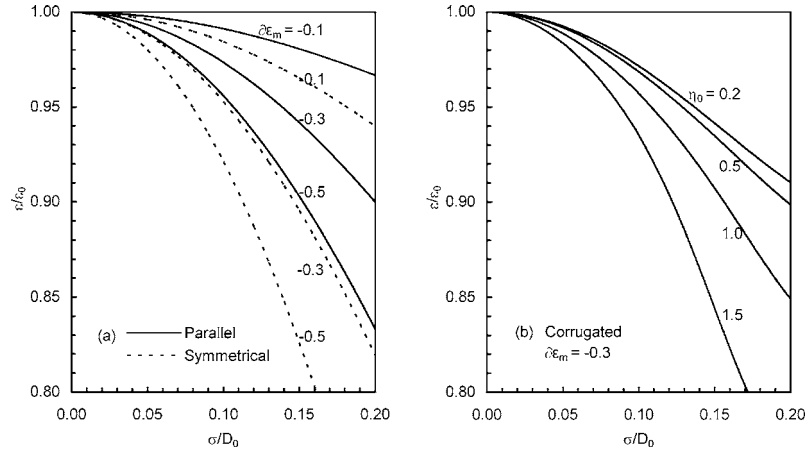

Fig. 4 Effectiveness ratio, $\varepsilon/\varepsilon_0$, for regenerative exchangers with a matrix of (*a*) parallel surface flow channels and symmetrical cylinder flow channels and (*b*) corrugated geometries for aspect ratio, $\eta_0=0.2$, 0.5, 1.0, and 1.5, with random variations in flow channel sizes to one without versus σ/D_0

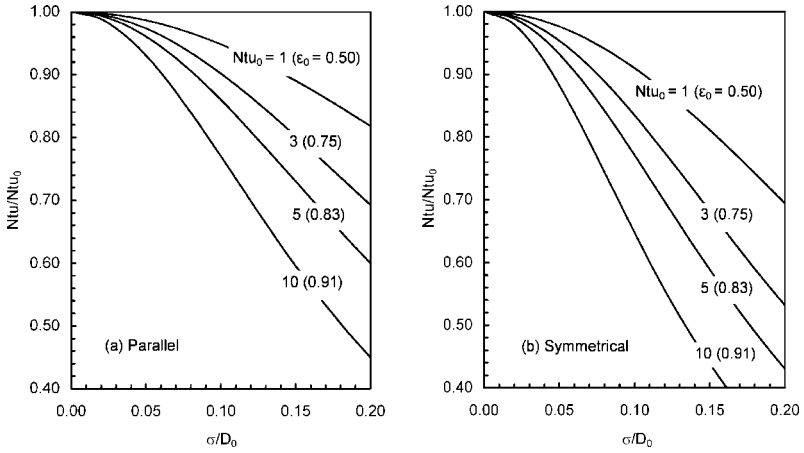

Fig. 5 Ntu ratio, Ntu/Ntu_0, for regenerative exchangers with a matrix of (*a*) parallel surface flow channels and (*b*) symmetrical cylinder flow channels with random variations in flow channel sizes to one without versus σ/D_0

$$Cr^* = \frac{(Mc_p)_w n}{(\dot{m}c_p)_{g,\min}} \tag{9}$$

and

$$Cr = \frac{(\dot{m}c_p)_{\min}}{(\dot{m}c_p)_{\max}} \tag{10}$$

This correlation is restricted to $Cr=1.0$ and $Cr^* > 1.25$. When $Cr^* \geq 4.0$, as it is in most heat wheels, $0.99 < K < 1.0$, indicating that it has little effect on the effectiveness [3].

Using Eqs. (5) and (7) the ratio of effective Ntu for a rotary regenerator with flow channel size variations and Ntu_0 for the same ideal regenerator without variations can be expressed as

$$\frac{Ntu}{Ntu_0} = f_{N,1}\left(\frac{\sigma}{D_0}, Ntu_0, \partial\varepsilon_m\right) \tag{11a}$$

for parallel and symmetrical cylinder flow channels and

$$\frac{Ntu}{Ntu_0} = f_{N,2}\left(\frac{\sigma}{D_0}, \eta_0, Ntu_0, \partial\varepsilon_m\right) \tag{11b}$$

for corrugated flow channels.

When both heat and moisture transfer occur in rotary regenerators coated with a desiccant as manufactured for energy recovery applications, the effectiveness correlations for both sensible energy and water vapor transfer with balanced mass flows of dry air have dominant terms similar to Eq. (7) [5]. These correlations imply that we can use Eq. (7) to estimate the effect of flow channel variations on rotary regenerator effectiveness for sensible energy (ε_s) and latent energy (ε_l) transfer. Since the total energy (or enthalpy) effectiveness (ε_t) is related to $\varepsilon_s, \varepsilon_l$, and an operating condition factor, it too will vary with mass face velocity, which is the mass velocity of the flow just before it enters the rotary regenerator, in the same manner as ε_s and ε_l. These relationships show that, for any particular operating condition, $\partial\varepsilon_m$ will be constant [2].

The Ntu ratios in Eq. (11*a*) for parallel surface and symmetrical cylinders under the same operating condition $\partial\varepsilon_m = -0.3$ are presented in Figs. 5(*a*) and 5(*b*), respectively. The Ntu ratios in Eq. (11*b*) for corrugated geometry are presented in Fig. 6. These curves show that the effectiveness ratio Ntu/Ntu_0 for any finite values of $\partial\varepsilon_m$ is inversely proportional to σ/D_0 and Ntu_0. When the airflow rate through a regenerator is decreased, the duration of exposure for a quantity of air and the adjacent matrix will be extended so that the effectiveness or number of transfer units, Ntu, is increased. However, the penalty for restoring the effectiveness of the exchanger to its original design value, ε_0, is a loss in the energy transfer rate or total energy recovery. For example, for a regenerator with symmetrical cylinder flow channels with σ/D_0

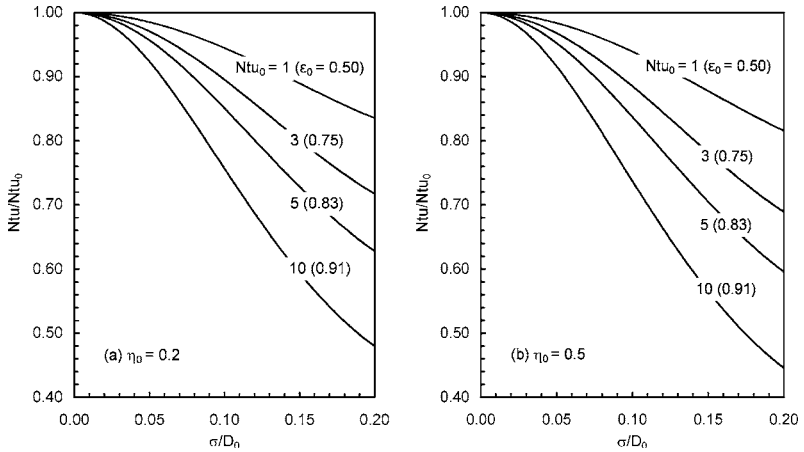

Fig. 6 Ntu ratio, Ntu/Ntu_0, for regenerative exchangers with a matrix of corrugated flow channels with random variations in flow channel sizes to one without versus σ/D_0 for η_0 at (*a*) 0.2 and (*b*) 0.5

$=0.1$ and $\partial\varepsilon_m=-0.3$ the $\mathrm{Ntu}/\mathrm{Ntu}_0=0.84$ for $\mathrm{Ntu}_0=3$ the corresponding effectiveness is $\varepsilon=0.72$ in Fig. 5(*b*) while the design effectiveness is $\varepsilon_0=0.75$—so to return the effectiveness to $\varepsilon=0.75$, the airflow rate and energy transfer rate would have to be reduced by nearly 20% so that $\mathrm{Ntu}_0=3.72$, giving a new $\mathrm{Ntu}/\mathrm{Ntu}_0=0.81$ corresponding to $\varepsilon=0.75$ and $\varepsilon_0=0.79$.

It is concluded from these results that the design of exchangers for a high design Ntu_0 brings with it increased sensitivity to flow channel size variations. Conversely, exchangers designed with a low Ntu_0 will be less sensitive to flow channel size variations. For example, for a rotary regenerator with symmetrical cylinder flow channels with $\sigma/D_0=0.05$ the drop in $\mathrm{Ntu}/\mathrm{Ntu}_0$ will be larger than 10% when $\mathrm{Ntu}_0=10$ but it will be less than 5% when $\mathrm{Ntu}_0=3$.

In practical applications the designer of rotary regenerators should know, not only the total surface area of the regenerator matrix, but the variations in the flow channels if the effective Ntu is to be predicted. These results show that the decrease in the effective Ntu will be most pronounced for large variations in the flow channel hydraulic diameter and large total surface areas or, more exactly, Ntu_0.

3.4 Entropy Generation. The entropy generation rate for ideal gases flowing through counterflow heat exchangers was developed by Bejan [7,8]. It is an important design consideration when only energy transfers are considered for convective heat transfer due to forced flow and is written

$$\dot{S}_{\mathrm{gen}}=(\dot{m}c_p)_s\ln\frac{T_2}{T_1}+(\dot{m}c_p)_e\ln\frac{T_4}{T_3}-(\dot{m}R)_s\ln\frac{p_2}{p_1}-(\dot{m}R)_e\ln\frac{p_4}{p_3} \tag{12}$$

This equation shows that the entropy generation rate depends on both the temperature changes and pressure drops. This rate can be written as the dimensionless entropy generation number, N_S, for balanced flow rates [9]

$$N_S=\frac{1}{\dot{m}c_p}\dot{S}_{\mathrm{gen}} \tag{13}$$

Substituting Eq. (12) into Eq. (13) for balanced flows with $\dot{m}_s=\dot{m}_e$ and c_p constant, we get

$$N_S=\ln\frac{T_2}{T_1}+\ln\frac{T_4}{T_3}-\frac{R}{c_p}\left(\ln\frac{p_2}{p_1}+\ln\frac{p_4}{p_3}\right) \tag{14}$$

Equation (14) can be expressed as the combination of temperature term and pressure term

$$N_S=N_{S,T}+N_{S,p} \tag{15}$$

The two terms, $N_{S,T}$ and $N_{S,p}$, in Eq. (15) can be expanded into infinite series and rewritten using more convenient dimensionless ratios respectively as

$$N_{S,T}=\left\{\varepsilon\theta-\sum_{i=2}^{\infty}(-1)^i\frac{(\varepsilon\theta)^i}{i}[(-1)^i\theta_m^i+\theta_M^i]\right\} \tag{16}$$

and

$$N_{S,p}=\frac{R}{c_p}\left[\sum_{j=1}^{\infty}\frac{2}{j}\left(\frac{\Delta p}{p}\right)^j\right] \tag{17}$$

where it is assumed that

$$\Delta p=p_1-p_2=p_3-p_4 \tag{18}$$

and

$$p=p_1=p_3 \tag{19}$$

as it is for practical energy recovery applications. The non-dimensional temperatures, θ_M, θ_m, and θ, are defined by

$$\theta_M=\text{maximum of}\left\{\frac{T_1}{\Delta T_M},\frac{T_3}{\Delta T_M}\right\} \tag{20a}$$

$$\theta_m=\text{minimum of}\left\{\frac{T_1}{\Delta T_M},\frac{T_3}{\Delta T_M}\right\}=\theta_M-1 \tag{20b}$$

$$\theta=\frac{1}{\theta_M}\cdot\frac{1}{\theta_m} \tag{20c}$$

Equations (20*a*)–(20*c*) imply that only one independent dimensionless temperature term need be considered (e.g., θ_M), where

$$\Delta T_M=|T_1-T_3| \tag{21}$$

is, in effect, the dimensional size of one temperature step used to non-dimensionalize each temperature.

It is found that, for most practical applications with gases, several terms are needed for accurate results in the series for $N_{S,T}(\varepsilon,\theta)$ and $N_{S,p}(\Delta p/p)$. Then Eqs. (16) and (17) gives Eqs. (22) and (23). For the case that only one term is needed for $N_{S,p}$ ($\Delta p/p<0.01$) gives Eq. (23*a*) but when several terms are needed Eq. (23*b*) is used

$$N_{S,T}=\theta\varepsilon-\tfrac{1}{2}(\theta_M^2+\theta_m^2)(\theta\varepsilon)^2+\tfrac{1}{3}(\theta_M^3-\theta_m^3)(\theta\varepsilon)^3-\tfrac{1}{4}(\theta_M^4+\theta_m^4)(\theta\varepsilon)^4 \tag{22}$$

$$N_{S,p}=\frac{R}{c_p}\cdot\frac{2\Delta p}{p} \tag{23a}$$

$$N_{S,p}=\frac{R}{c_p}\left[2\left(\frac{\Delta p}{p}\right)+\left(\frac{\Delta p}{p}\right)^2+\frac{2}{3}\left(\frac{\Delta p}{p}\right)^3+\frac{1}{2}\left(\frac{\Delta p}{p}\right)^4\right] \tag{23b}$$

This implies that the entropy generation number due to pressure drop variations is proportional to the pressure drop across the exchanger as it will be for HVAC applications (i.e., Eq. (23*a*)) but for gas turbine applications [10] more terms will be needed as in Eq. (23*b*) to get accurate results.

Figure 7 shows that $N_{S,T}$ decreases with increasing θ_M so that small values of ΔT_M, which occur in HVAC energy recovery applications, cause small values of $N_{S,T}$ while large values of ΔT_M, which occur in gas turbine and power applications, cause large values of $N_{S,T}$. For gas turbine applications typical values of $N_{S,T}$ will be slightly greater for θ_M close to 10 [10].

Equation (22) can be used to determine the entropy generation number when the effectiveness and operating temperature ratios are known. Figure 8 shows the entropy generation number for different operating conditions. The non-dimensional temperature $\theta_M=9.5$ (or $\theta_m=8.5$), shown as a parameter in Fig. 8, corresponds

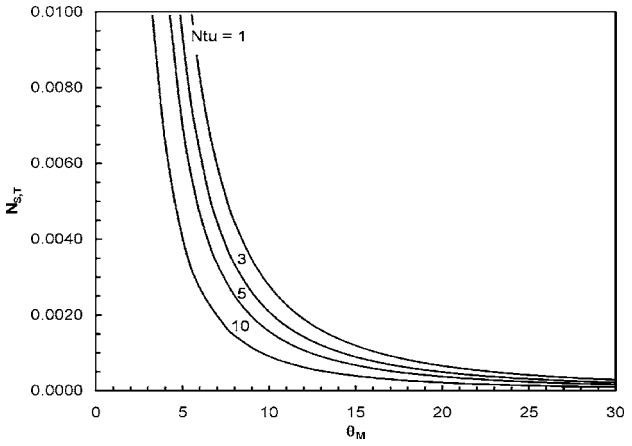

Fig. 7 Entropy generation number due to thermal conductance versus non-dimensional temperature

to the operating condition in gas turbines for power generation [10]. The temperatures $\theta_M=27.8$ (or $\theta_m=26.8$) and $\theta_M=15.2$ (or $\theta_m=14.2$) correspond to HVAC-ARI summer cooling certification test conditions and winter heating certification test conditions, respectively (see Table 1) [11]. This figure shows that $N_{S,T}$ is a maximum at $\varepsilon=0.5$ and goes to 0 as $\varepsilon\rightarrow 0$ or 1.0 (as shown in Fig. 9).

This same result, when plotted versus Ntu in place of ε in Fig. 9 (i.e., using Eq. (7) for a counterflow rotary regenerator), indicates that $N_{S,T}$ has a peak value when Ntu=1.0 and decreases towards zero as Ntu$\rightarrow$0 and the heat rate goes to zero or Ntu becomes a very large number because $\Delta T_M\rightarrow 0$.

Now it is convenient to compare the size of irreversible heat transfer effects, $N_{S,T}$, and the pressure drop effects, $N_{S,p}$, and to include the effective or actual performance factors (e.g., Ntu/Ntu_0 and $\Delta p/\Delta p_0$). For a regenerative heat exchanger, the thermal conductance-area ratio or Ntu/Ntu_0 and pressure drop ratio $\Delta p/\Delta p_0$ will decrease when the flow channel hydraulic diameter variations increase as shown in Fig. 3 and Figs. 5 and 6; however, their impacts are different. Figures 10–13 show the ratio of entropy generation number due to heat transfer, $N_{S,T}$, and pressure drop, $N_{S,p}$, versus hydraulic diameter variations for different types of flow channel geometries for certain ranges of Ntu_0 and $\Delta p_0/p$. The ranges of Ntu_0 and $\Delta p_0/p$ shown represent the range of typical design conditions for most HVAC applications. The operating condition for the regenerative exchanger is at $\partial\varepsilon_m=-0.3$. Comparable results for two typical gas turbine applications are shown in Figs. 14–17. As shown in Figs. 14(*a*), 15(*a*), 16(*a*), and 17(*a*) the ratio of $N_{S,T}/N_{S,p}$ is of order one, just as it is for the selected HVAC operating conditions. However, the ratio is 10 times smaller for gas turbines applications with $\Delta p_0/p=0.1$ as shown in Figs. 14(*b*), 15(*b*), 16(*b*), and 17(*b*).

These results show that the pressure term $N_{S,p}$ is always important with respect to $N_{S,T}$ for practical energy recovery applications and its effect increases with increasing σ/D_0. For gas turbine applications, with $\Delta p_0/p$ of order 0.1, $N_{S,p}$ is dominant. It is concluded from these results that the entropy generation number for heat transfer divided by the entropy generation number for forced flow ($N_{S,T}/N_{S,p}$) depends on the operating conditions as illustrated in Figs. 10–17. Furthermore as the design Ntu_0 is increased, there is an increased sensitivity to flow channel size variations such that, as σ/D_0 increases from 0 to 0.2, $N_{S,T}/N_{S,p}$ increases by about 10% for $\text{Ntu}_0=1.0$ ($\Delta p_0/p=10^{-3}$) but this ratio approximately doubles for $\text{Ntu}_0=10$ ($\Delta p_0/p=10^{-3}$) for both HVAC applications as shown in Figs. 10–13 and gas turbine applications as shown in Figs. 14–17, respectively.

Table 1 Certification operating conditions for heat and energy exchanger tests, ARI Std 1060-2001

Item	Test conditions	
	Summer cooling	Winter heating
1. Entering supply air		
a. Dry bulb temperature	35±1°C (95±1.8°F)	1.7±1°C (35±1.8°F)
b. Relative humidity	47.4% ±2%	82.5% ±2%
2. Entering exhaust air		
a. Dry bulb temperature	23.9±1°C (75±1.8°F)	21.1±1°C (70±1.8°F)
b. Relative humidity	51.2% ±2%	49.2% ±2%

Comparing the effective entropy generation number, N_S, for a manufactured rotary heat exchanger with flow channel variations and, N_{S0}, for a similar ideal design exchanger with no variations, N_S/N_{S0} can be expressed as

$$\frac{N_S}{N_{S0}}=W_T\cdot\left(\frac{N_{S,T}}{N_{S,T0}}\right)+W_p\cdot\left(\frac{N_{S,p}}{N_{S,p0}}\right) \tag{24}$$

where W_T and W_p are design weighting factors for the temperature and pressure terms defined by

$$W_T=\frac{N_{S,T0}}{N_{S,T0}+N_{S,p0}} \tag{25}$$

and

$$W_p=\frac{N_{S,p0}}{N_{S,T0}+N_{S,p0}}=1-W_T \tag{26}$$

Using Eq. (22) we can write

$$\frac{N_{S,T}}{N_{S,T0}}=\frac{[1-(\theta_M^2+\theta_m^2)(\theta\varepsilon)/2+(\theta_M^3-\theta_m^3)(\theta\varepsilon)^2/3-(\theta_M^4+\theta_m^4)(\theta\varepsilon)^3/4](\varepsilon/\varepsilon_0)}{1-(\theta_M^2+\theta_m^2)(\theta\varepsilon_0)/2+(\theta_M^3-\theta_m^3)(\theta\varepsilon_0)^2/3-(\theta_M^4+\theta_m^4)(\theta\varepsilon_0)^3/4} \tag{27}$$

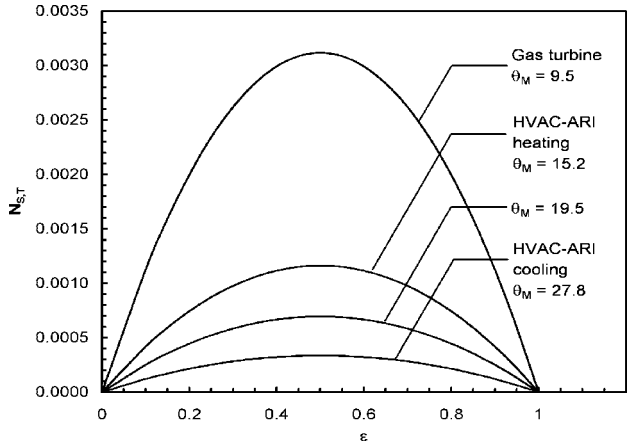

Fig. 8 Entropy generation number due to thermal conductance effects versus effectiveness for various operating conditions

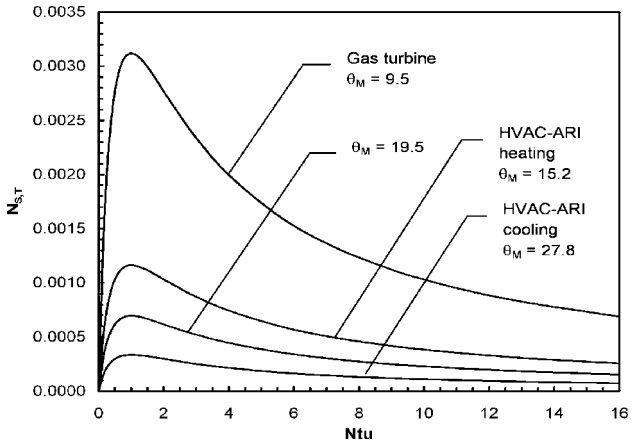

Fig. 9 Entropy generation number due to thermal conductance effects versus Ntu for various operating conditions

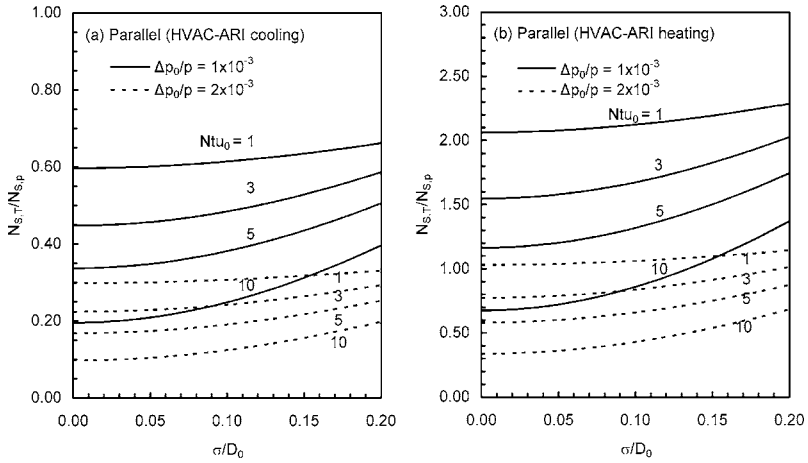

Fig. 10 Ratio of $N_{S,T}/N_{S,p}$ for regenerative exchangers with a matrix of parallel surface flow channels with random variations in flow channel sizes to one without versus σ/D_0 under ARI (*a*) summer cooling (θ_M=27.8) and (*b*) winter heating (θ_M=15.2) operating conditions

which is the entropy generation number ratio, $N_{S,T}/N_{S,T0}$, due to thermal conductance variations. In Eq. (27) $\varepsilon/\varepsilon_0$ is given by Eq. (4).

Similarly, using Eq. (23*a*) we get

$$\frac{N_{S,p}}{N_{S,p0}} = \frac{\Delta p}{\Delta p_0} \tag{28a}$$

while Eq. (23*b*) gives

$$\frac{N_{S,p}}{N_{S,p0}} = \frac{2(\Delta p/p) + (\Delta p/p)^2 + 2(\Delta p/p)^3/3 + (\Delta p/p)^4/2}{2(\Delta p_0/p) + (\Delta p_0/p)^2 + 2(\Delta p_0/p)^3/3 + (\Delta p_0/p)^4/2} \tag{28b}$$

In Eq. (28*a*) the ratio $\Delta p/\Delta p_0$ is shown in Fig. 3 for various types of flow channels.

Figures 18–25 show the total entropy generation number ratio (N_S/N_{S0}) versus flow channel size variations (σ/D_0) with the design Ntu_0 and pressure drop ratio ($\Delta p_0/p$) as parameters. Similar to the $N_{S,T}/N_{S,p}$ ratio, these results imply a sensitivity to operating conditions as well as the above design parameters. They tend to show the least sensitivity to σ/D_0 when Ntu_0 is in an intermediate range, e.g., 3–5 ($\Delta p_0/p = 1\times10^{-3}$), and greatest sensitivity when Ntu_0=1 or 10 ($\Delta p_0/p = 1\times10^{-3}$). Increasing σ/D_0 tends to decrease N_S/N_{S0} for Ntu_0=1 as shown in Figs. 18–21 for HVAC applications.

It is interesting to note that if only one term was considered $N_{S,T}$ in Eq. (22), then $N_{S,T}/N_{S,T0}$ in Eq. (27) simply equals $\varepsilon/\varepsilon_0$, which is given by Eq. (4) and shown in Fig. 4. If this assumption (i.e., $N_{S,T}/N_{S,T0}=\varepsilon/\varepsilon_0$) is adopted, it would lead to very large errors in the values of N_S/N_{S0}. If Figs. 18–21 were replotted using $N_{S,T}/N_{S0}$, all values of N_S/N would be less than 1.0 with increasing σ/D_0.

Figures 22–25 show the comparable N_S/N_{S0} versus σ/D_0 results for the two typical operating conditions for a gas turbine. These two operating conditions give results showing a very different trend than the HVAC results. For gas turbine applications, the total entropy generation number ratio (N_S/N_{S0}) tends to show the least sensitivity to σ/D_0 when Ntu_0 is close to 5 for $\Delta p_0/p$ =0.01 as shown in Figs. 22(*a*), 23(*a*), 24(*a*), and 25(*a*). However,

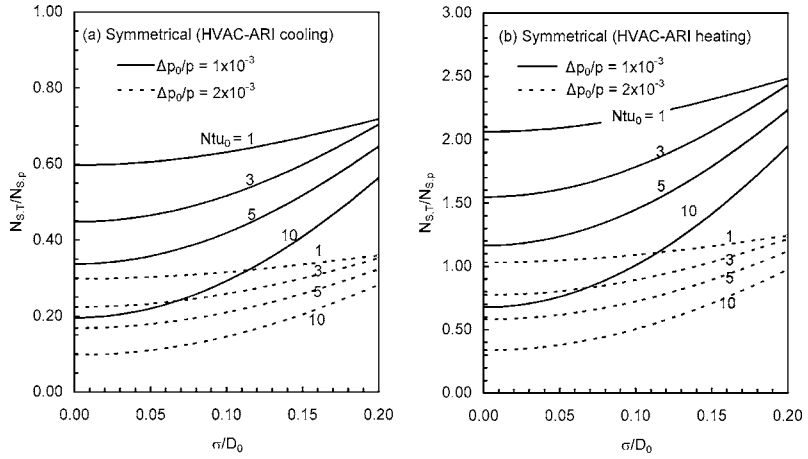

Fig. 11 Ratio of $N_{S,T}/N_{S,p}$ for regenerative exchangers with a matrix of symmetrical cylinder flow channels with random variations in flow channel sizes to one without versus σ/D_0 under ARI (*a*) summer cooling (θ_M=27.8) and (*b*) winter heating (θ_M=15.2) operating conditions

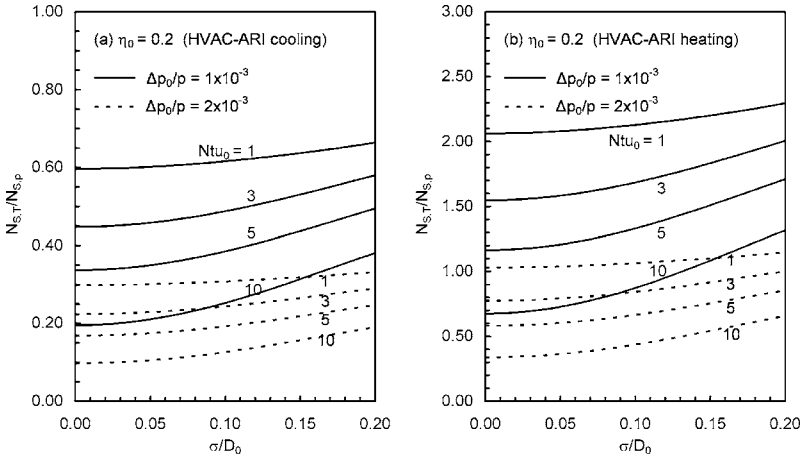

Fig. 12 Ratio of $N_{S,T}/N_{S,p}$ for regenerative exchangers with a matrix of corrugated flow channels with random variations in flow channel sizes to one without versus σ/D_0 for η_0=0.2 under ARI (*a*) summer cooling (θ_M=27.8) and (*b*) winter heating (θ_M=15.2) operating conditions

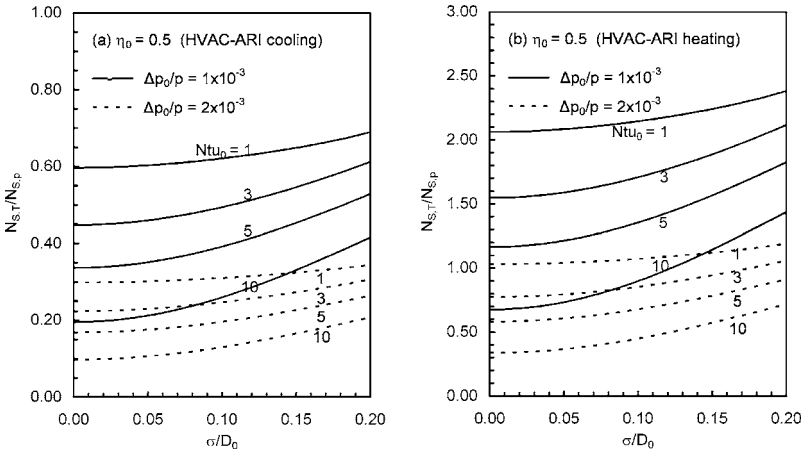

Fig. 13 Ratio of $N_{S,T}/N_{S,p}$ for regenerative exchangers with a matrix of corrugated flow channels with random variations in flow channel sizes to one without versus σ/D_0 for η_0=0.5 under ARI (*a*) summer cooling (θ_M=27.8) and (*b*) winter heating (θ_M=15.2) operating conditions

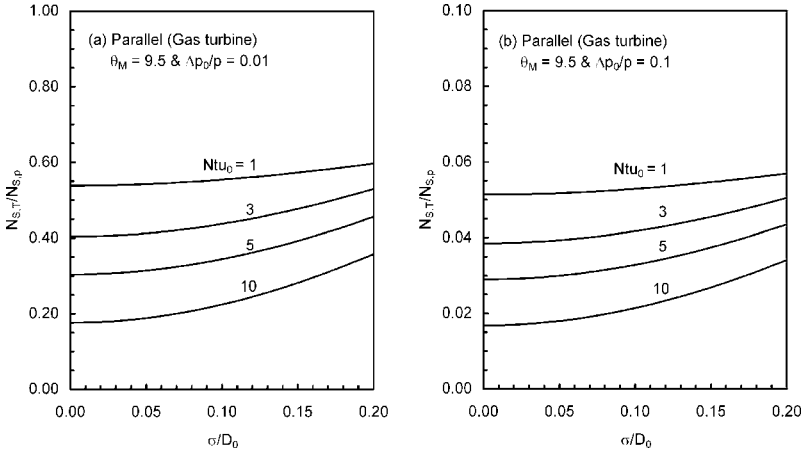

Fig. 14 Ratio of $N_{S,T}/N_{S,p}$ for regenerative exchangers with a matrix of parallel surface flow channels with random variations in flow channel sizes to one without versus σ/D_0 for two gas turbine operating conditions

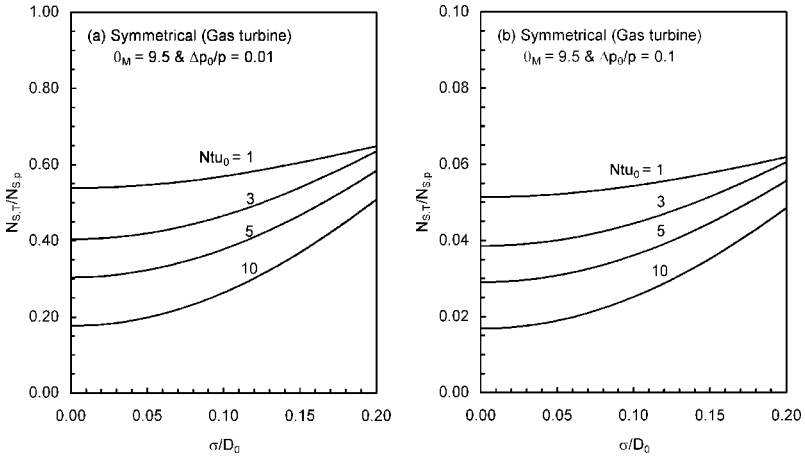

Fig. 15 Ratio of $N_{S,T}/N_{S,p}$ for regenerative exchangers with a matrix of symmetrical cylinder flow channels with random variations in flow channel sizes to one without versus σ/D_0 for two gas turbine operating conditions

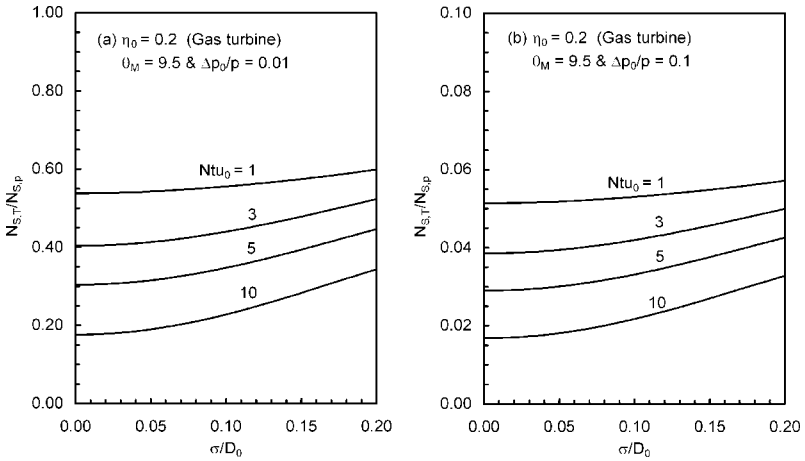

Fig. 16 Ratio of $N_{S,T}/N_{S,p}$ for regenerative exchangers with a matrix of corrugated flow channels with random variations in flow channel sizes to one without versus σ/D_0 for η_0=0.2 for two gas turbine operating conditions

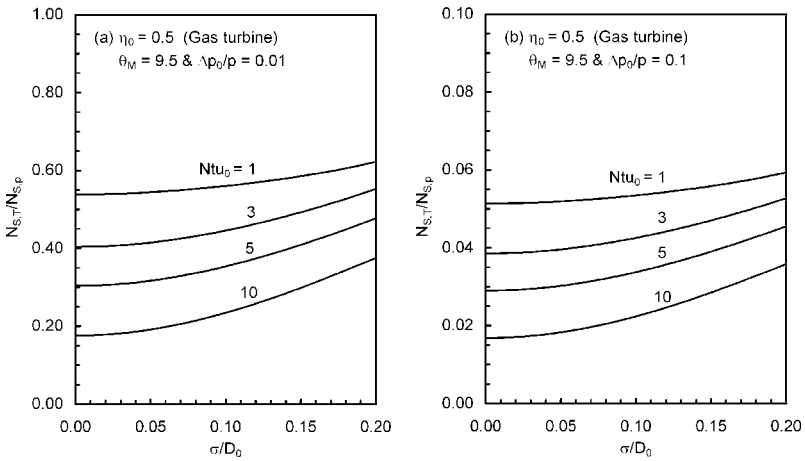

Fig. 17 Ratio of $N_{S,T}/N_{S,p}$ for regenerative exchangers with a matrix of corrugated flow channels with random variations in flow channel sizes to one without versus σ/D_0 for η_0=0.5 for two gas turbine operating conditions

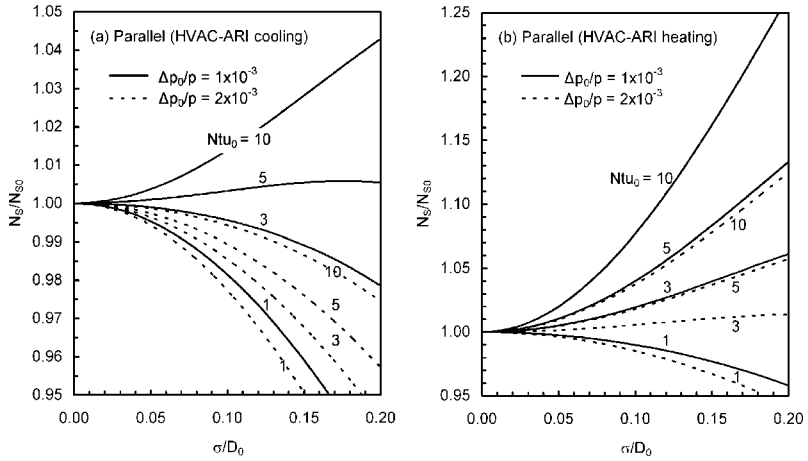

Fig. 18 Ratio of N_S/N_{S0} for regenerative exchangers with a matrix of parallel surface flow channels with random variations in flow channel sizes to one without versus σ/D_0 under ARI (*a*) summer cooling (θ_M=27.8) and (*b*) winter heating (θ_M=15.2) operating conditions

with a higher value of $\Delta p_0/p$, such as $\Delta p_0/p=0.1$, these ratios are very sensitive to σ/D_0 as shown in Figs. 22(*b*), 23(*b*), 24(*b*), and 25(*b*).

4 Summary and Conclusions

Ntu is one of the most important dimensionless parameters used in the design and selection of regenerative exchangers. From this study of Ntu_0 as a design parameter for a regenerative exchanger, it is concluded that:

1. The effective number of transfer units (Ntu) for regenerative exchangers decreases with increasing variations in the flow channel hydraulic diameter (i.e., σ/D_0) and design number of transfer units (Ntu_0). Results show significant performance degradation effects when typical flow channel size variations occur.

   The entropy generation number (N_S) for regenerative exchangers is a dimensionless factor which accounts for irreversible energy dissipation due to heat transfer and fluid flow. For N_S as a design parameter for a regenerative exchanger, it is concluded that:
2. Both temperature and pressure affect the entropy generation in regenerative exchangers. In regenerative exchanger entropy analysis temperature and pressure can be considered independently.
3. Several terms must be included in the expansion of the irreversible heat transfer component of N_S ($N_{S,T}$) and only one term is required for the pressure drop component ($N_{S,p}$) for HVAC applications but more terms are required for gas turbine applications because high mass flow rates cause high pressure drops across a regenerator.
4. The pressure drop term of N_S ($N_{S,p}$) should always be included in the total for practical applications because it is always significant for practical applications, i.e., the ratio of $\Delta p_0/p$ cannot be neglected. For some gas turbine operating conditions this term may be dominant.
5. Increasing flow channel size variations (i.e., σ/D_0) will cause the entropy generation number (N_S) to increase for the case of small design number of transfer units (e.g., $\mathrm{Ntu}_0=1$). For gas turbine applications the entropy generation number (N_S) will increase with increasing flow channel size variations for a high design number of transfer units (e.g., $\mathrm{Ntu}_0=10$) with a low pressure drop (e.g., $\Delta p_0/p=0.01$) but will

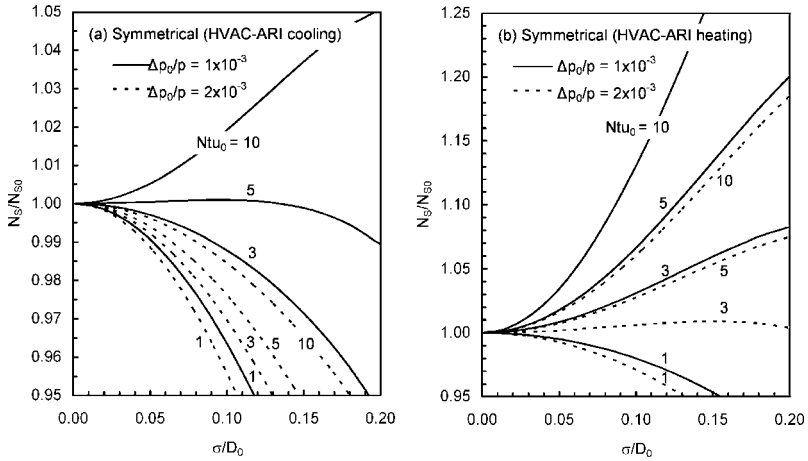

Fig. 19 Ratio of N_S/N_{S0} for regenerative exchangers with a matrix of symmetrical cylinder flow channels with random variations in flow channel sizes to one without versus σ/D_0 under ARI (*a*) summer cooling (θ_M=27.8) and (*b*) winter heating (θ_M=15.2) operating conditions

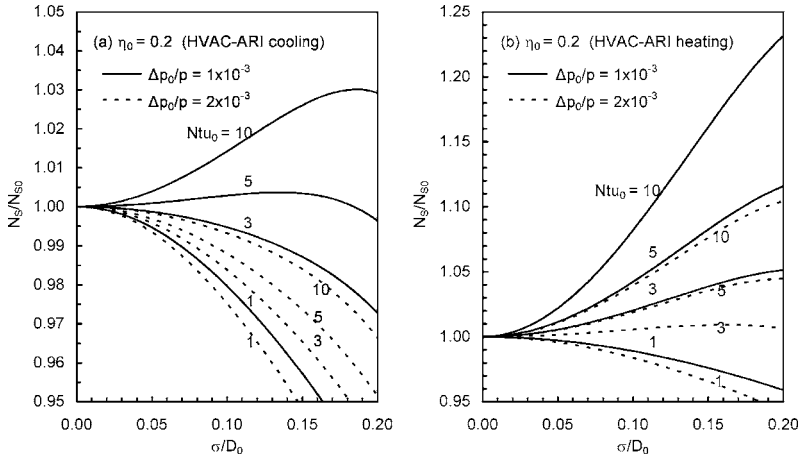

Fig. 20 Ratio of N_S/N_{S0} for regenerative exchangers with a matrix of corrugated flow channels with random variations in flow channel sizes to one without versus σ/D_0 for η_0=0.2 under ARI (*a*) summer cooling (θ_M=27.8) and (*b*) winter heating (θ_M=15.2) operating conditions

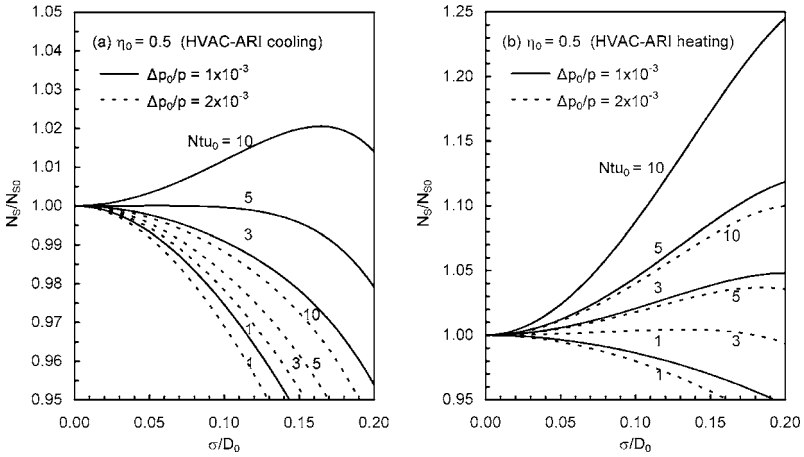

Fig. 21 Ratio of N_S/N_{S0} for regenerative exchangers with a matrix of corrugated flow channels with random variations in flow channel sizes to one without versus σ/D_0 for η_0=0.5 under ARI (*a*) summer cooling (θ_M=27.8) and (*b*) winter heating (θ_M=15.2) operating conditions

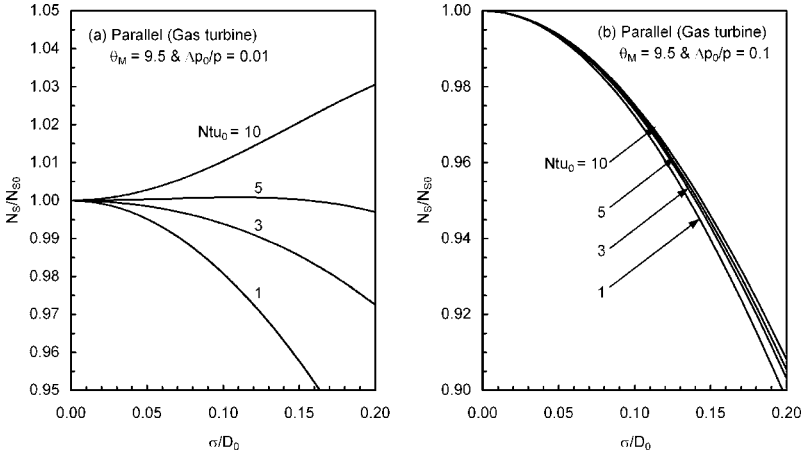

Fig. 22 Ratio of N_S/N_{S0} for regenerative exchangers with a matrix of parallel surface flow channels with random variations in flow channel sizes to one without versus σ/D_0 for two gas turbine operating conditions

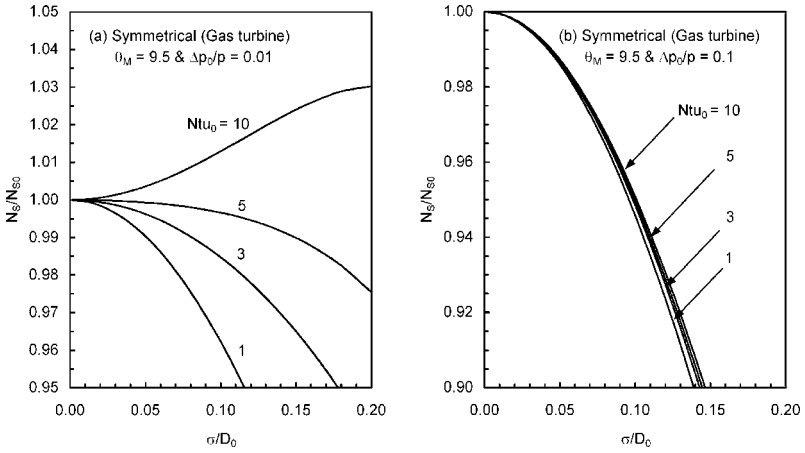

Fig. 23 Ratio of N_S/N_{S0} for regenerative exchangers with a matrix of symmetrical cylinder flow channels with random variations in flow channel sizes to one without versus σ/D_0 for two gas turbine operating conditions

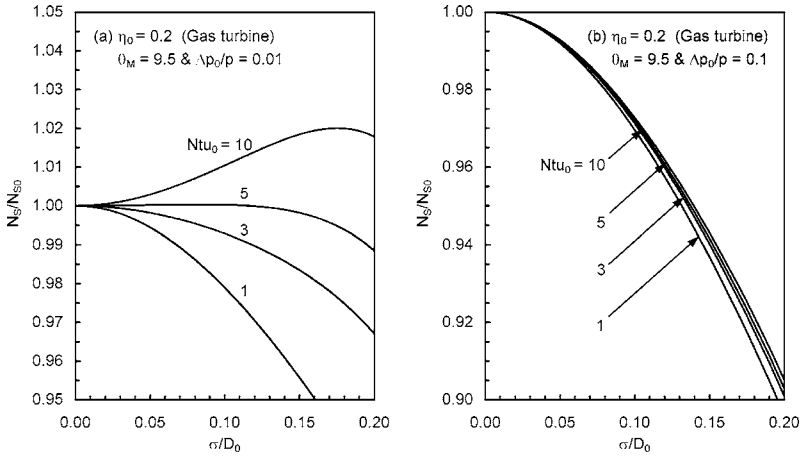

Fig. 24 Ratio of N_S/N_{S0} for regenerative exchangers with a matrix of corrugated flow channels with random variations in flow channel sizes to one without versus σ/D_0 for η_0=0.2 for two gas turbine operating conditions

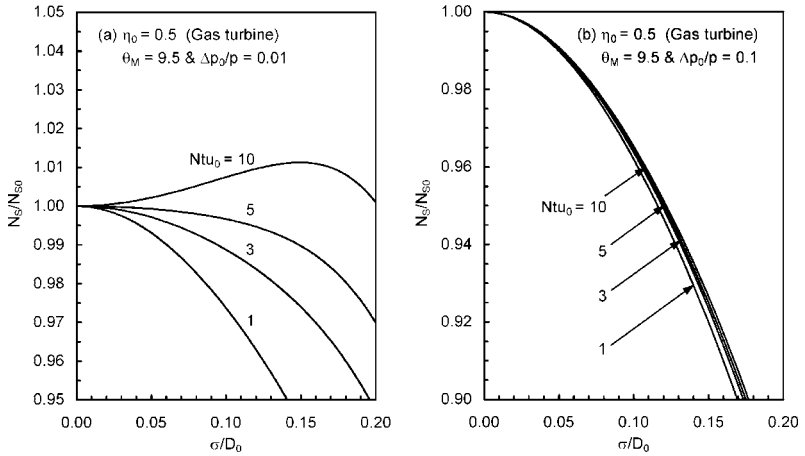

Fig. 25 Ratio of N_S/N_{S0} for regenerative exchangers with a matrix of corrugated flow channels with random variations in flow channel sizes to one without versus σ/D_0 for η_0=0.5 for two gas turbine operating conditions

decrease with increasing flow channel size variations for a higher pressure drop (e.g., $\Delta p_0/p=0.1$).

Acknowledgment

This research work was financially supported by Venmar CES, Saskatoon, SK, Canada and NSERC, Canada.

Nomenclature

A = flow surface area of heat exchanger, m^2
c_p = specific heat, J/(kg·K)
Cr = regenerative exchanger heat capacity rate ratio, defined by Eq. (10), dimensionless
Cr^* = regenerative exchanger heat capacity rate ratio, defined by Eq. (9), dimensionless
D_0 = mean hydraulic diameter of flow channels, m
$f_{N,1}$ = number of transfer units ratio function for parallel surface or symmetrical cylinder flow channels, dimensionless
$f_{N,2}$ = number of transfer units ratio function for corrugated flow channels, dimensionless
$f_{p,1}$ = pressure drop ratio function for parallel surface or symmetrical cylinder flow channels, dimensionless
$f_{p,2}$ = pressure drop ratio function for corrugated flow channels, dimensionless
$f_{\varepsilon,1}$ = effectiveness ratio function for parallel surface or symmetrical cylinder flow channels, dimensionless
$f_{\varepsilon,2}$ = effectiveness ratio function for corrugated flow channels, dimensionless
i = 2,3,…, dimensionless
j = 1,2,…, dimensionless
K = rotational capacitance coefficient for regenerative exchanger, dimensionless
M = total mass of a regenerative exchanger, kg
$\dot{m}$ = phase change rate or mass flow rate, $kg/(m^3\cdot s)$ or kg/s
N_S = entropy generation number, dimensionless
Ntu = number of transfer units, dimensionless
n = rotational speed, rev/s
p = atmospheric pressure, Pa
Δp = pressure drop across a regenerative exchanger with nonuniform flow channels, Pa
Δp_0 = pressure drop across a regenerative exchanger with uniform flow channels, Pa
R = gas constant, J/(kg·K)
$\dot{S}$ = entropy generation rate, W/K
t = time, s
T = temperature, K
U = overall heat transfer coefficient, $W/(m^2\cdot K)$
W = weighting factor, dimensionless

Greek

ε = effectiveness, dimensionless
$\partial\varepsilon_m$ = effectiveness sensitivity coefficient, dimensionless
η = aspect ratio, dimensionless
θ = non-dimensional temperature, dimensionless
ω = wheel speed, rad/s
σ = standard deviation of hydraulic diameters, m

Subscripts

e = exhaust air
g = gas
gen = entropy generation
k = 1, 2, 3, and 4
l = latent energy or moisture mass
M = maximum value
max = maximum value
min = minimum value
m = mass flow rate or minimum value
p = pressure
S = entropy
s = supply air or sensible energy
T = relating to temperature variation
t = total energy or enthalpy
w = wall of flow channels
0 = mean value for all flow channels
1 = station 1
2 = station 2
3 = station 3
4 = station 4

Appendix: Pressure Drop Ratio and Effectiveness Ratio

Pressure Drop Ratio. For a rotary regenerator manufactured with parallel surface airflow channels as shown in Fig. 1(*a*), the equation for the pressure drop ratio, $\Delta p/\Delta p_0$, is only a function of σ/D_0 and given by

$$\frac{\Delta p}{\Delta p_0}=f_{p,1}\left(\frac{\sigma}{D_0}\right)=\left[1+3\left(\frac{\sigma}{D_0}\right)^2\right]^{-1} \tag{A1}$$

and for a matrix with symmetrical cylinder airflow channels (i.e., equilateral triangle, square, hexagonal, and circular flow channels as shown in Figs. 1(*b*)–1(*e*))

$$\frac{\Delta p}{\Delta p_0}=f_{p,1}\left(\frac{\sigma}{D_0}\right)=\left[1+6\left(\frac{\sigma}{D_0}\right)^2+3\left(\frac{\sigma}{D_0}\right)^4\right]^{-1} \tag{A2}$$

For a rotary regenerator with a matrix containing corrugated airflow channels as shown in Fig. 1(*f*) the pressure drop ratio, $\Delta p/\Delta p_0$, can be expressed as

$$\begin{aligned}\frac{\Delta p}{\Delta p_0}&=f_{p,2}\left(\frac{\sigma}{D_0},\eta_0\right)\\&=\left[1+6\left(\frac{\sigma}{D_0}\right)^2+3\left(\frac{\sigma}{D_0}\right)^4+(4\beta_1+\beta_2)\left(\frac{\sigma}{D_0}\right)^2\right.\\&\quad+(12\beta_1+18\beta_2+12\beta_3+3\beta_4)\left(\frac{\sigma}{D_0}\right)^4\\&\quad\left.+(15\beta_2+60\beta_3+90\beta_4)\left(\frac{\sigma}{D_0}\right)^6\right]^{-1}\end{aligned} \tag{A3}$$

where β_k (k=1, 2, 3, and 4) are constants which depend only on the mean value of the aspect ratio, η_0 and presented in Table 2.

Effectiveness Ratio. The effectiveness ratio for a rotary regenerator with parallel surface flow channels can be expressed as

$$\begin{aligned}\frac{\varepsilon}{\varepsilon_0}&=f_{\varepsilon,1}\left(\frac{\sigma}{D_0},\partial\varepsilon_m\right)\\&=1+\partial\varepsilon_m\left\{\left(\frac{\Delta p}{\Delta p_0}\right)^2\left[1+15\left(\frac{\sigma}{D_0}\right)^2+45\left(\frac{\sigma}{D_0}\right)^4+15\left(\frac{\sigma}{D_0}\right)^6\right]\right.\\&\quad\left.-\left(\frac{\Delta p}{\Delta p_0}\right)\left[1+3\left(\frac{\sigma}{D_0}\right)^2\right]\right\}\end{aligned} \tag{A4}$$

Table 2 For corrugated flow channels with selected values of η_0 corresponding values of β_k (k=1, 2, 3, and 4)

η_0	β_1	β_2	β_3	β_4
0.2	−0.8192	0.7431	−3.1253	4.200
0.5	−0.6532	0.9470	−4.8442	8.114
1.0	−0.0734	1.3341	−11.127	28.787
1.5	0.7540	1.6455	−20.016	84.966

where $\partial\varepsilon_m$ is the effectiveness sensitivity coefficient defined by

$$\partial\varepsilon_m = \left.\frac{\dot{m}_0}{\varepsilon_0}\frac{\partial\varepsilon}{\partial\dot{m}}\right|_{\dot{m}=\dot{m}_0} \tag{A5}$$

and for a regenerator with symmetrical cylinder flow channels can be expressed as

$$\begin{aligned}\frac{\varepsilon}{\varepsilon_0} &= f_{\varepsilon,1}\left(\frac{\sigma}{D_0}, \partial\varepsilon_m\right)\\ &= 1 + \partial\varepsilon_m\left\{\left(\frac{\Delta p}{\Delta p_0}\right)^2\left[1 + 28\left(\frac{\sigma}{D_0}\right)^2 + 210\left(\frac{\sigma}{D_0}\right)^4 + 420\left(\frac{\sigma}{D_0}\right)^6\right]\right.\\ &\quad\left. - \left(\frac{\Delta p}{\Delta p_0}\right)\left[1 + 6\left(\frac{\sigma}{D_0}\right)^2 + 3\left(\frac{\sigma}{D_0}\right)^4\right]\right\}\end{aligned} \tag{A6}$$

For a regenerator with corrugated flow channels the effectiveness ratio is given by

$$\begin{aligned}\frac{\varepsilon}{\varepsilon_0} &= f_{\varepsilon,2}\left(\frac{\sigma}{D_0}, \eta_0, \partial\varepsilon_m\right)\\ &= 1 + \partial\varepsilon_m\left\{\left(\frac{\Delta p}{\Delta p_0}\right)^2\left[1 + B_{2,2}\left(\frac{\sigma}{D_0}\right)^2 + B_{2,4}\left(\frac{\sigma}{D_0}\right)^4 + B_{2,6}\left(\frac{\sigma}{D_0}\right)^6\right]\right.\\ &\quad\left. - \left(\frac{\Delta p}{\Delta p_0}\right)\left[1 + B_{1,2}\left(\frac{\sigma}{D_0}\right)^2 + B_{1,4}\left(\frac{\sigma}{D_0}\right)^4 + B_{1,6}\left(\frac{\sigma}{D_0}\right)^6\right]\right\}\end{aligned} \tag{A7}$$

where the coefficients, $B_{i,j}$ ($i=1,2$ and $j=2,4,6$), can be calculated by

$$B_{1,2} = 6 + 4\beta_1 + \beta_2 \tag{A8}$$

$$B_{1,4} = 3 + 12\beta_1 + 18\beta_2 + 12\beta_3 + 3\beta_4 \tag{A9}$$

$$B_{1,6} = 15\beta_2 + 60\beta_3 + 90\beta_4 \tag{A10}$$

$$B_{2,2} = 28 + 16\beta_1 + 2\beta_2 + \beta_1^2 \tag{A11}$$

$$B_{2,4} = 210 + 336\beta_1 + 168\beta_2 + 48\beta_3 + 6\beta_4 + 48\beta_1\beta_2 + 6\beta_1\beta_3 + 84\beta_1^2 + 3\beta_2^2 \tag{A12}$$

and

$$\begin{aligned}B_{2,6} &= 420 + 1680\beta_1 + 2100\beta_2 + 1680\beta_3 + 840\beta_4 + 1680\beta_1\beta_2\\ &\quad + 840\beta_1\beta_3 + 240\beta_1\beta_4 + 240\beta_2\beta_3 + 30\beta_2\beta_4 + 1050\beta_1^2\\ &\quad + 420\beta_2^2 + 15\beta_3^2\end{aligned} \tag{A13}$$

References

[1] Shang, W., and Besant, R. W., 2004, "Measurement of Pore Size Variation and Its Effect on Energy Wheel Performance," ASHRAE Trans., **110**(1), pp. 410–421.

[2] Shang, W., and Besant, R. W., 2005, "Effects of Pore Size Variations on Regenerative Wheel Performance," ASME J. Eng. Gas Turbines Power, **127**, pp. 121–135.

[3] Kays, W. M., and London, A. L., 1984, *Compact Heat Exchangers*, McGraw-Hill, New York, pp. 19–33.

[4] ASHRAE, 1991, *ANSI/ASHRAE Standard 84–1991R: Method of Testing Air-to-Air Heat Exchangers*, American Society of Heating, Refrigerating and Air-Conditioning Engineers, Inc., Atlanta.

[5] Simonson, C. J., and Besant, R. W., 1999, "Energy Wheel Effectiveness, Part I: Development of Dimensionless Groups; Part II: Correlations," Int. J. Heat Mass Transfer, **42**(12), pp. 2161–2185.

[6] Lambertson, T. J., 1958, "Performance Factors of a Periodic-Flow Heat Exchanger," Trans. ASME, **80**, pp. 586–592.

[7] Bejan, A., 1982, *Entropy Generation through Heat and Fluid Flow*, Wiley, New York.

[8] Bejan, A., 1996, "Entropy Generation Minimization: The New Thermodynamics of Finite-Size Devices and Finite-Time Processes," J. Appl. Phys., **79**, pp. 1191–1218.

[9] Bejan, A., 1997, *Advanced Engineering Thermodynamics*, Wiley, New York.

[10] Dellenback, P. A., 2002, "Improved Gas Turbine Efficiency Through Alternative Regenerator Configuration," ASME J. Eng. Gas Turbines Power, **124**, pp. 441–446.

[11] ARI, 2001, *ARI Standard 1060: Rating Air-to-Air Energy Recovery Ventilation Equipment*, Air-Conditioning & Refrigeration Institute, Arlington, VA.

Brush Seal Temperature Distribution Analysis

Yahya Dogu[1]
Department of Mechanical Engineering,
Kirikkale University,
Yahsihan, Kirikkale 71451, Turkey
e-mail: ydogu@kku.edu.tr

Mahmut F. Aksit
Faculty of Engineering and Natural Sciences,
Sabanci University,
Tuzla, Istanbul 34956, Turkey
e-mail: aksit@sabanciuniv.edu

Brush seals are designed to survive transient rotor rubs. Inherent brush seal flexibility reduces frictional heat generation. However, high surface speeds combined with thin rotor sections may result in local hot spots. Considering large surface area and accelerated oxidation rates, frictional heat at bristle tips is another major concern especially in challenging high-temperature applications. This study investigates temperature distribution in a brush seal as a function of frictional heat generation at bristle tips. The two-dimensional axisymmetric computational fluid dynamics (CFD) analysis includes the permeable bristle pack as a porous medium allowing fluid flow throughout the bristle matrix. In addition to effective flow resistance coefficients, isotropic effective thermal conductivity as a function of temperature is defined for the bristle pack. Employing a fin approach for a single bristle, a theoretical analysis has been developed after outlining the brush seal heat transfer mechanism. Theoretical and CFD analysis results are compared. To ensure coverage for various seal designs and operating conditions, several frictional heat input cases corresponding to different seal stiffness values have been studied. Frictional heat generation is outlined to introduce a practical heat flux input into the analysis model. Effect of seal stiffness on nominal bristle tip temperature has been evaluated. Analyses show a steep temperature rise close to bristle tips that diminishes further away. Heat flux conducted through the bristles dissipates into the flow by a strong convection at the fence-height region. [DOI: 10.1115/1.2135817]

1 Introduction

Proven performance of brush seal applications in rotating machinery over the past two decades has led to extensive research on extending brush seal usage to more challenging locations subject to elevated pressure load, temperature, rotor speed, and transient rotor-stator closure. Backed by numerous experimental data, modeling and analysis efforts have identified various physical phenomena underlying seal dynamic behavior. From the beginning, design tools have been developed in the light of these experimental and analytical findings. Leakage and life are defined as the two main performance parameters of brush seals.

The brush seal is designed to work in contact with the rotor. Typically, the seal is installed with some assembly interference, which is expected to reach a line-to-line condition at steady-state operation after some initial wear-in/break-in period. However, it is common for brush seals to wear beyond line-to-line condition due to transient rotor excursions or bristle blow-down caused by a radial pressure distribution.

Friction between bristle tips and the rotor causes heat generation and wear, which are strongly related to each other. Seal life and leakage are directly dominated by the amount of wear. Heat generation and the resulting temperature significantly affect the bristle wear mechanism and mechanical properties.

Blow-down is favorable to achieve steady leakage performance. It helps maintain bristle-rotor contact and eliminate seal clearance. On the other hand, blow-down enhances seal contact force by pushing the bristles toward the rotor and results in increased heat generation and wear.

During operation, hot spots may form at the bristle tips and local temperatures may reach the bristle melting point. High-temperature exposure degrades mechanical properties; therefore, bristle tips wear out at an accelerated rate. In addition, a local temperature increase over a thin rotor section may lead to rotor instability problems. As a result, the level of temperature increase will dictate limits of brush seal applications.

From the beginning of brush seal usage, heat generation has been stated as a significant parameter; nevertheless, less attention has been paid to thermal issues. Only a few studies have appeared in the literature, in spite of the significance of the issue.

In one of the pioneering brush seal publications, Gorelov et al. [1] showed that with the decrease of airflow rate, there is a marked heating of the brush. At the same time, very little airflow is sufficient for cooling at low-pressure differentials.

Hendricks et al. [2] were the first to consider the frictional heat flux by employing a formula as products of spring force, surface speed, and interface coefficient. They calculated increasing heat flux as a function of interference.

Owen et al. [3] developed a formula to calculate the heat generation; however, their analysis requires the rotor surface temperature as an input. It was assumed that heat was conducted toward bristles and dissipated to the airflow. They also measured temperature under the rotor rim by utilizing infrared detectors. Temperature readings were taken with 20 s time intervals, which is a very short duration to reach maximum frictional heat generation and steady-state conditions. They calculated the rotor temperature field using a finite element model.

Chew and Guardino [4] developed a computational model for flow between the bristle tips and the rotor to calculate tip force, wear, and temperature. The model included heat conduction and heat generation due to contact friction.

Demiroglu [5] developed a closed-form equation to calculate heat generation. He measured the temperature field over the rotor rim and fence-height region using an infrared thermography technique. The heat flux was calculated in a finite element model for the rotor by matching the measured temperature distribution.

Apart from research with gaseous working fluids, Aksit et al. [6] studied the temperature rise in oil brush seal applications. Their findings indicated that oil temperature levels at high speeds were due to shear thinning.

The extent of bristle and rotor temperature rise is one of the primary concerns in brush seal applications. Bristles are subjected

[1]To whom correspondence should be addressed.

Contributed by the International Gas Turbine Institute (IGTI) of ASME for publication in the JOURNAL OF ENGINEERING FOR GAS TURBINES AND POWER. Manuscript received August 30, 2005; final manuscript received September 6, 2005. IGTI Review Chair: K. C. Hall. Paper presented at the ASME Turbo Expo 2005: Land, Sea, and Air, Reno, NV, June 6–9, 2005, Paper No. GT2005-69120.

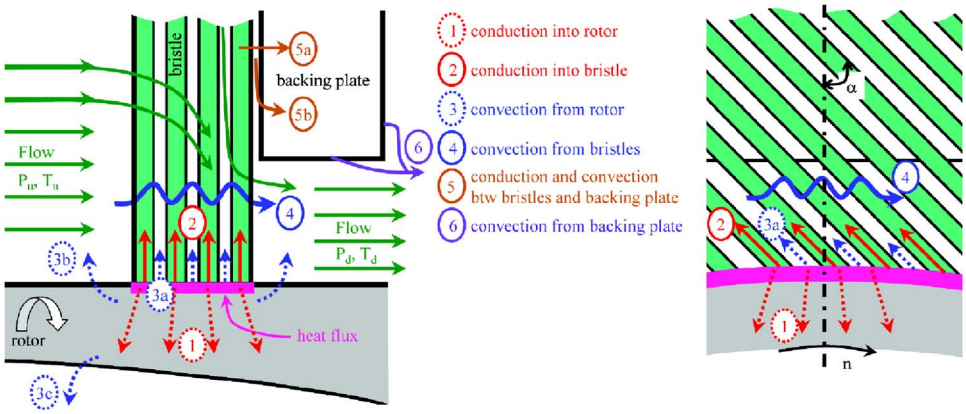

Fig. 1 Schematic of brush seal heat transfer

to excessive bending stress at the backing plate corner due to high-pressure load at fence height. High-temperature exposure in the fence-height region decreases bristle mechanical strength leading to premature bristle failure. Except Demiroglu's [5] thermal camera measurements, there has been no study showing the temperature distribution in the bristle pack.

This study presents analytical and numerical investigations of brush seal temperature distribution after providing an outline for the seal heat transfer mechanism. The full flow and temperature field solution has been obtained using a two-dimensional axisymmetric computational fluid dynamics (CFD) model. The CFD model employs a bulk porous medium approach with defined flow resistance coefficients [7] and a thermal conductivity for permeable bristle pack. Thermal conductivities of all sections (air, bristle, and front and backing plates) are considered as a function of temperature since temperature variation is high in the problem domain. After evaluating brush seal heat transfer mechanisms and possible frictional heat generation levels, a wide range of frictional heat generation is considered to ensure coverage of all practical heat flux inputs in the model. Frictional heat generation is calculated using overall brush pack stiffness. Temperature fields have been identified as a function of seal heat flux input values. To serve as a benchmark, a theoretical analysis has been developed employing a simple fin approach. Analytical results have been compared to the CFD model. The investigation covers various pressure loads representing a range of brush seal operational conditions.

2 Outline of Brush Seal Heat Transfer Mechanism

Brush seals are located between high- and low-pressure cavities. Frictional heat generation between the bristle tips and rotor surface occurs during line-to-line or interference operations. High-speed sliding with bristle-rotor interface produces frictional heat as a function of the tip force, sliding velocity, and friction coefficient. Coupled effects of initial build interference and blow-down produce large bristle tip forces, which may result in excessive frictional heat.

Frictional heat generation at the bristle-rotor interface can be treated as an area of a circumferential heat source all around the rotor and across the bristle pack thickness. As a result of this heat flux input, the temperature rises around heat source region. As illustrated in Figs. 1 and 2, frictional heat is dissipated primarily through surrounding materials, by conduction through the rotor and bristles and by convection to the fluid from both the rotor and bristle surfaces. Examination of heat transfer mechanisms leads to several heat transfer paths as shown in Fig. 1.

The frictional heat at the bristle-rotor interface is, primarily, conducted through the rotor and bristles, which are marked as numbers 1 and 2, respectively, and convectively transferred to the surrounding fluid (3 and 4). In addition, once the temperature rise reaches up to backing plate, additional heat transfer paths are introduced, as illustrated in Figs. 1 and 2. There will be conduction transfer to backing plate 5a through line bristle contacts and

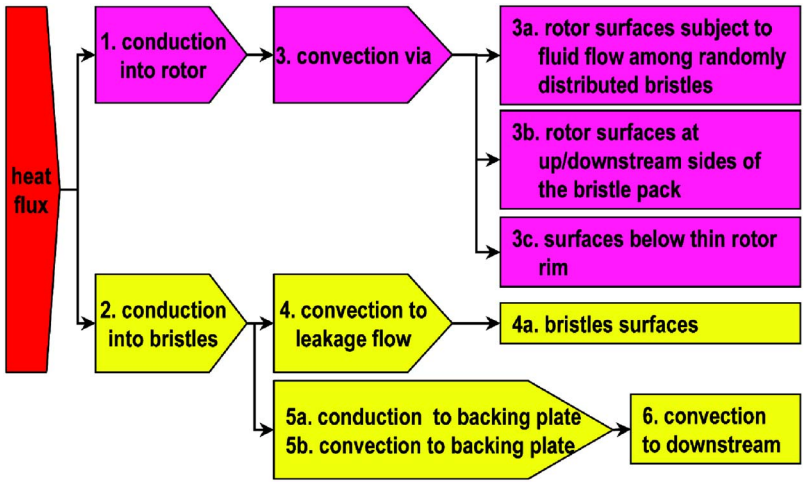

Fig. 2 Schematic of brush seal heat partition mechanism

convection to inward radial flow between backing plate and bristle 5b. The heat will also convectively transferred from backing plate to downstream air 6 as listed below:

1. Conduction into rotor 1
2. Conduction into bristles 2
3. Convection from rotor 3 [=3a+3b+3c]
4. Convection from bristles 4
5. Conduction and convection between bristles and backing plate 5 [=5a+5b]
6. Convection from backing plate 6

The heat conduction through the rotor at the interface 1 is dissipated to the rotor surroundings by convection. Rotor convection occurs by means of several surfaces 3; rotor surfaces subject to the fluid flow among randomly distributed bristles 3a, rotor surfaces at up- and downstream sides of the bristle pack 3b, and surfaces below the thin rotor rim 3c.

The voids among the bristles are very small as the bristle pack compacts under pressure load. The convection surface among bristles over the rotor is practically negligible; however, high fluid velocity formed by axial leakage flow and rotor speed may yield a sizeable amount of heat convection. There is also convection over the rotor surfaces subject to up- and downstream flows. Convection from these surfaces is driven again by axial flow and rotor speed. The rotor also dissipates heat to the surroundings below its thin rim.

The dominant heat transfer mechanism is driven by the leakage flow forming a cross flow around bristles as well as the inward radial flow near the backing plate. The heat conducted through bristles is convectively transferred to the leakage flow 4. Most of the generated frictional heat is carried away by leakage flow in the fence-height section. Each bristle (or entire bristle pack if treated as a bulk) acts as a fin carrying the base heat to fluid flow. The leakage flow is heated up by convection from both the rotor and bristle surfaces. Examination of flow field shows that upstream flow smoothly approaches the seal and penetrates into the bristle pack over the entire upstream face [7]. In the upper region supported by backing plate, the penetrating fluid accumulates near the backing plate as it flows toward the rotor. The inward radial flow merges with the axial flow in the fence-height region and discharges downstream. The leakage flow through the fence-height section carries the heat conducted by the bristles downstream.

In reality, the heat transfer mechanism is three-dimensional and a conjugate form of conduction and convection. In order to calculate the bristle temperature distribution, a full solution of the flow and temperature fields through randomly formed voids among bristles is required in addition to solving conduction along bristles. It is very difficult to obtain a closed-form analytical solution for such a complicated geometry. It is also not an easy task to employ CFD codes to solve three-dimensional Navier-Stokes and energy equations for the real brush geometry. One way to simplify this otherwise complicated problem is to neglect circumferential temperature variations. Tangentially uniform heat generation assumption means a concentric and uniform seal interference with uniform seal and rotor material properties. However, temperature varies in both radial and axial directions.

The present study considers fluid and heat flow within the up- and downstream cavities and the bristle pack, in addition to front and backing plates, and omits the rotor. The two-dimensional (2D) axisymmetric CFD analysis involves a bulk porous-medium approach applied to the permeable bristle pack. Because of solid-fluid friction, the flow within the bristle pack is subject to additional resistance forces, which are defined throughout a calibration procedure [7]. The temperature-dependent thermal conductivity of the solid bristle material is also defined for the porous bristle pack filled by the sealing fluid. This approach overcomes the difficulty of dealing with an undefined flow path and related complicated formulations in order to obtain a full solution for flow and temperature fields within the bristle pack.

Another difficulty arises from the fact that the amount of frictional heat generation varies with respect to several parameters: interference, blow-down, material pair, surface speed, friction coefficient, etc. In addition, partitioning of total heat generation between the rotor and bristles is a complicated problem, and there has been no established procedure.

The main concern in this study is to determine temperature distribution and maximum temperature through the bristle pack for various heat flux inputs. Therefore, a wide range of heat flux rates are studied to cover possible heat-generation cases that can be practically achieved in common applications. A detailed discussion and outline of the calculation procedure for the frictional heat generation is presented below.

3 Frictional Heat Generation

Frictional work due to rotor rub at the bristle tips can be calculated from the product of frictional force and sliding velocity. Assuming all the frictional work is converted into heat, the total frictional heat generation at the bristle-rotor interface is stated as follows:

$$Q = \mu F_b V \tag{1}$$

where μ is the interface friction coefficient, F_b is the normal force acting at bristle tips, and V is the rotor surface speed.

Although this frictional power relation is very simple, determining the defining factors proves difficult. In a typical design problem, sliding velocity is known. Because many interacting factors from seal design to operating pressure affect the bristle tip force, determining the friction coefficient at the bristle-rotor interface is quite difficult. There is a range of reported friction coefficient values from 0.08 to 0.47 under various test conditions [8–12]. A cobalt alloy, Haynes 25, is a common industry standard bristle material. For the common Haynes 25-Inco 718 and Haynes 25-ChromeCarbide pairs, Fellenstein and DellaCorte [8] and Fellenstein et al. [9,10] reported friction coefficient values of 0.25–0.47. Crudgington and Bowsher [12] obtained steady friction coefficient readings of 0.28 when running against stainless steel. In the present thermal study, the approach is to analyze a range of heat input cases rather than calculating thermal distribution of any specific design or rotor material. Therefore, a representative friction coefficient of 0.3 is considered for all cases.

Determining bristle tip force is much more complicated because it is a function of many parameters: geometry, interference level, flow and pressure field, blow-down, material, seal stiffness, etc. Brush deflection coupled with pressure loads and interbristle interactions becomes very complicated in nature and does not lend itself to an accurate analytical formulation. Starting with Flower [13], simple beam theory has been used in many analyses to calculate bristle tip forces. Hendricks et al. [2] presented a comprehensive analytical model including mechanical, aerodynamic, and pressure loads. The loads calculated from a bulk flow model were applied on beams representing the bristles to calculate their deflection in both the axial and radial directions. The model addressed interbristle interactions through propped points, however, did not fully capture frictional coupling, lateral support, and torsional effects. Modi [14] used results from linear elasticity as initial guess for the large deformation solutions. However, the model did not include backing plate friction. Later, some researchers [15–18] combined porous media flow models with beam theory to estimate bristle loads. More recently nonlinear beam solutions have also been implemented in bristle force analyses [19,20]. On the other hand, other groups of researchers used detailed finite-element-based numerical models to calculate bristle forces [12,21–23]. Recently, Demiroglu [5] has developed an empirical expression covering a variety of parameters.

Selecting the correct bristle tip force value to define the right range of heat flux values for practical applications is difficult with so many different approaches to find the beam forces. Therefore, an approach based on overall seal stiffness [12,23–27] is chosen

Table 1 Limits of operational variables considered for defining heat flux analysis domain

Variable	Mild	Severe
Stiffness (K_s)	0.2 psi/mil 54.3 kPa/mm	4 psi/mil 1085.8 kPa/mm
Speed (V)	40 ft/s 12 m/s	984 ft/s 300 m/s
Interference (Δr)	4 mil 0.102 mm	30 mil 0.762 mm

for the frictional heat generation calculations. Stiffness values calculated through the beam theory does not reflect stiffness experienced during actual rotor incursions. Published experimental data indicate that typical seal stiffness without pressure load may vary from 54.3 kPa/mm (0.2 psi/mil) [12] to 230.7 kPa/mm (0.85 psi/mil) [23]. Brush seals are known to experience strong friction pressure coupling. Chupp et al. [26] reported a two- to threefold increase, whereas Short et al. [27] reported up to a sixfold increase in the overall seal stiffness with increasing pressure loads. The aim in the presented study is to cover common applications ranging from mild to severe heat-generation cases. Therefore, a general seal stiffness range from 54.3 kPa/mm (0.2 psi/mil) (to represent a soft seal with light pressure load) to 1085.8 kPa/mm (4 psi/mil) (hard seal with large pressure load) is employed to obtain heat input estimates.

Seal stiffness K_s is defined by measuring contact pressure per unit radial interference/deflection Δr [12,23–27]. Contact pressure at bristle tips is calculated by multiplying the seal stiffness by the bristle deflection as follows:

$$P_c = K_s \Delta r \tag{2}$$

Then, frictional heat flux per unit contact area can be calculated as

$$q_f = \mu P_c V \tag{3}$$

In order to identify the limits of the frictional heat flux that may exist in common applications, extreme ranges of seal stiffness, surface speed, and radial rotor interference are considered, as listed in Table 1. Using mild and severe condition parameters, minimum and maximum heat-generation values are calculated as $q_{f\min}=20$ kW/m^2 and $q_{f\max}=74{,}464$ kW/m^2. A difficulty arises from the unknown heat rates transferred into the rotor and bristles. If half of the generated heat is assumed to be transferred to the bristles while other half is conducted through rotor, then the problem domain is identified as $q_{f\min}=10$ kW/m^2 and $q_{f\max}=37{,}232$ kW/m^2. For the sake of simplicity, five heat flux cases with $q_f=10$, 100, 1000, 5000, and 10,000 kW/m^2 have been analyzed in this work. In terms of investigating the temperature distribution as a function of the heat flux, the assumption of a 50-50 heat portioning by the rotor and bristles becomes insignificant since a wide range of heat flux values are covered in the scope of the investigation.

4 Heat Transfer Analysis Employing Fin Approach

A bristle acts like a fin attached to the rotor surface as shown in Fig. 3. The heat flux is applied at the base representing the frictional heat generation at bristle-rotor interface. The heat is conducted within the bristle and convectively transferred to airflow. The heat conduction through the bristle can be assumed as one-dimensional in the radial direction because of its high conductivity and small diameter. The Biot number ($\mathrm{Bi}=hd/2k_b$), which is the ratio of convection and conduction heat transfer, is much less than unity for the tiny bristle.

Although bristles subjected to cross flow in the fence-height region are well represented with the simple fin approach, the heat transfer mechanism becomes more complicated at the outer sections. Packed against the backing plate under pressure load,

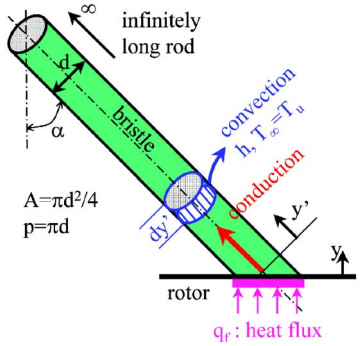

Fig. 3 Schematic of bristle heat transfer as an infinitely long fin

bristles may form numerous interbristle and bristle-backing plate line contacts. The fin heat transfer approach yields a closed-form solution for calculating the temperature distribution along each individual bristle.

By employing the energy equation for the differential element (Fig. 3) and combining it with the Fourier conduction law for a single bristle, the heat transfer equation becomes [28]

$$\frac{d^2\theta}{dy'^2} - m^2\theta = 0 \tag{4}$$

where y' denotes the radial distance from the rotor surface along the bristle axis and θ is the normalized temperature defined as $\theta = T - T_\infty$. The fluid temperature is taken as equal to the upstream inlet temperature, $T_\infty = T_u$. The term m^2 for the cylindrical bristle stands for

$$m^2 = \frac{hp}{k_b A} = \frac{h\pi d}{k_b \pi d^2/4} = \frac{4h}{k_b d} \tag{5}$$

The bristle diameter is denoted as d, and h is the convective heat transfer coefficient around the bristle. Bristle perimeter for convectional area is denoted with p, and bristle cross-sectional area for conduction is shown as A. Equation (4) is derived assuming constant bristle thermal conductivity.

Two boundary conditions are required for the solution of the second-order linear differential equation to obtain the temperature distribution along the bristle. The first boundary condition is applied at the base of the fin at the bristle-rotor interface, where the frictional heat generation is introduced as heat flux. The second boundary condition is defined using an infinitely long fin approach, which is the case for a highly convective surrounding. Because of high convective heat transfer, the bristle temperature exponentially approaches the surrounding fluid temperature when moving away from the bristle-rotor interface. These applied boundary conditions can be stated as

$$y' = 0 \Rightarrow q_f = -k_b \left(\frac{dT}{dy'}\right)\bigg|_{y'=0}$$

$$y' \to \infty \Rightarrow \theta = 0 \tag{6}$$

The solution of the differential equation for conduction in the bristle under these prescribed boundary conditions yields the temperature distribution along the bristle as follows:

$$\theta(y') = \frac{q_f}{mk_b} e^{-my'} \tag{7}$$

Substituting $y'=0$, a closed-form solution for the maximum temperature on rotor surface can be obtained as

$$T_{\max}|_{y'=0} = \frac{q_f}{mk_b} + T_\infty. \tag{8}$$

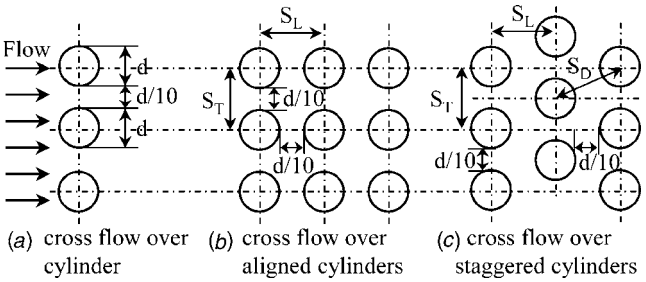

Fig. 4 Bristle layout for calculation of convective heat transfer coefficient

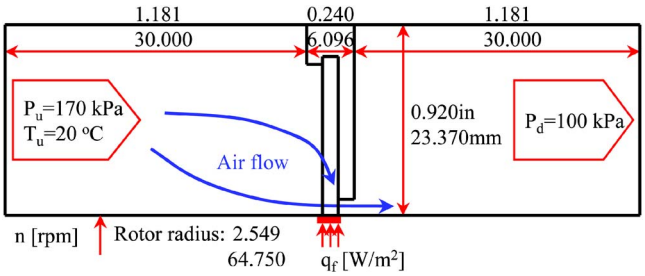

Fig. 5 Brush seal CFD model domain

4.1 Convective Heat Transfer Coefficient Within Bristle Pack. Equations (7) and (8) require the convective heat transfer coefficient around the bristle as an input. The convection coefficient is set by the flow-through voids among randomly packed bristle matrix.

When the flow field within the bristle pack is considered, cross flow among bristles and inward radial flow over the backing plate are the two main flow types in addition to tangential flow due to rotor rotation. The cross flow is very effective at the fence-height section, where the fin approach is well applicable. For a simplified analysis, the convective heat transfer coefficient can be calculated by employing the approximation of following flow types as illustrated in Fig. 4:

1. cross flow over cylinders
2. cross flow through bank of aligned tubes
3. cross flow through bank of staggered tubes

The Nusselt number correlations for these kinds of flows are very well established [28]. For cross flow around cylinders,

$$\mathrm{Nu}_d = \frac{hd}{k} = C\,\mathrm{Re}_d^m\,\mathrm{Pr}^{1/3}$$

$$\text{where } \mathrm{Re}_d = \frac{\rho V d}{\mu} \tag{9}$$

For cross flow around a bank of aligned/staggered tubes,

$$\mathrm{Nu}_d = \frac{hd}{k} = C_1\,\mathrm{Re}_{d,\max}^m \tag{10}$$

Details and calculations of the parameters in Eqs. (9) and (10) are available in most heat transfer textbooks [28]. The convective heat transfer coefficient h is calculated using total leakage obtained from CFD analysis and experimental data. All leakage is assumed to cross flow among bristles at the fence-height section. First, the average flow velocity V_{FH} through the fence-height opening is obtained using the continuity equation

$$\dot{m} = \rho V_{FH} A_{\text{flow}} \Rightarrow V_{FH} = \frac{\dot{m}}{\lfloor \rho\pi[(r+h_{FH})^2 - r^2]\rfloor} \tag{11}$$

where r is rotor radius and h_{FH} is the fence height, which is the distance between rotor surface and backing-plate inner edge.

Bristle spacing is needed to calculate flow velocity for Re. Bristles are randomly compacted under a pressure load and touch each other at many locations. For a representative calculation, interbristle space is taken as one-tenth of the bristle diameter [4,23], which is 0.102 mm (0.004 in.). The effective flow area is calculated by taking the interbristle space between two neighboring bristles and multiplying this value by the total number of bristles per row along the seal circumference. When the total leakage rate is applied to this effective area, the flow velocity is calculated. For configuration of cylinder row in cross flow (type 1), the flow velocity is defined with the following relation:

$$V_1 = \frac{\dot{m}}{\left(\rho \frac{d}{10} \frac{2\pi r}{11d/10} h_{FH}\right)} \tag{12}$$

This procedure has been repeated for both aligned (type 2) and staggered (type 3) bristle configurations (Fig. 4), which involve different spacing relations [28]. The flow velocity is calculated as follows: For aligned bristle configuration,

$$V_2 = \frac{V_{FH} S_T}{S_T - d} \tag{13}$$

For staggered tube configuration,

$$\text{if } S_D = \left[S_L^2 + \left(\frac{S_T}{2}\right)^2\right]^{1/2} < \frac{S_T + d}{2}$$

$$\Rightarrow V_3 = \frac{V_{FH} S_T}{2(S_D - d)}$$

$$\text{otherwise} \Rightarrow V_3 = V_2 \tag{14}$$

For 70 kPa (10.2 psi) pressure load, the total leakage rate is calculated as 0.003 kg/s using the CFD model. Based on this average flow rate, the flow velocity has been calculated as 24.1 m/s for a single row of bristles in cross flow and 23.7 m/s for aligned/staggered tube banks with the bristle spacing values discussed above. These flow velocities are used in Re calculations. Air properties are evaluated at upstream conditions except for density, which is calculated using the ideal gas equation at average pressure of up- and downstream sides.

The convective heat transfer coefficients are calculated for brush seal representative parameters using various Nu correlations for cross flow around cylinders and through the bank of aligned and staggered tubes. The resulting h values from different correlations are fairly comparable (ranging between 1400 and 2200 W/m^2°C for the range of parameters considered), and h is evaluated for the approximation of cross flow around a cylinder. The thermal conductivity of bristle material is taken as a constant in the fin analysis. The CFD analysis and analytical solutions are compared in the Results and Discussion section.

It should also be noted that convective heat transfer coefficient within bristle pack varies with respect to leakage rate and interbristle spacing that are primarily dictated by pressure load. In order to identify effects of these two parameters, the h coefficient is also evaluated for a range of the parameters as presented in Sec. 6.

5 CFD Model

A representative brush seal CFD model domain is selected as shown in Figs. 5 and 6. The model is built in two-dimensional axisymmetric coordinates with a domain consisting of the up- and downstream cavities, the bristle pack, and the front and backing plates. In order to ensure fully developed flow conditions, the up- and downstream cavities are axially extended. The rotor surface is included in the model as a solid boundary. Other than the porous

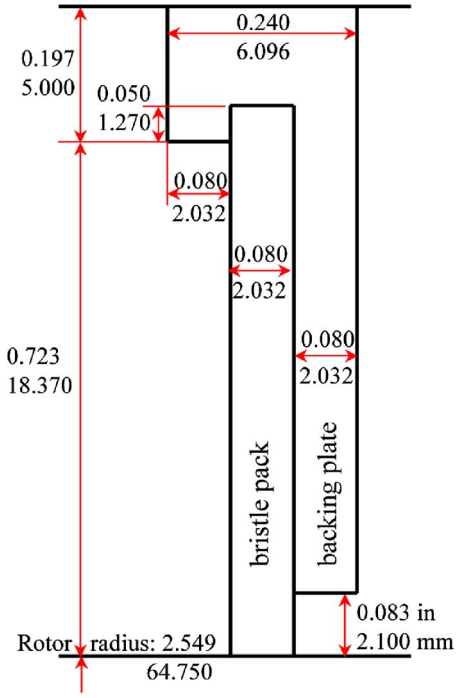

Fig. 6 Typical brush seal dimensions used in CFD model

bristle pack and the front and backing plates, solid sections are omitted in the present investigation by using an adiabatic boundary assumption. As discussed above, since the primary concern of the present analysis is to determine bristle temperature, the heat transfer to the rotor is not included in the model. Meanwhile, considering possible effects of backing plate thermal conductivity on bristle temperature patterns under low-pressure loads with minimal leakage flow, the backing plate is also included in the analysis.

The Newtonian airflow is assumed to be compressible, complying with the ideal gas law ($P=\rho RT$) and turbulent following $k-\varepsilon$ turbulence model. The Navier-Stokes and energy equations for steady flow through the model domain can then be written in Cartesian tensor notation as Continuity equation

$$\frac{\partial}{\partial x_j}(\rho u_j) = 0 \tag{15}$$

Momentum equation

$$\frac{\partial(\rho u_i u_j)}{\partial x_j} = -\frac{\partial P}{\partial x_i} + \frac{\partial}{\partial x_j}\left[\mu\left(\frac{\partial u_i}{\partial x_j} + \frac{\partial u_j}{\partial x_i}\right)\right] - \frac{\partial}{\partial x_i}\left(\frac{2}{3}\mu\frac{\partial u_k}{\partial x_k}\right) \tag{16}$$

Energy equation

$$\frac{\partial(\rho u_j c T)}{\partial x_j} = -P\frac{\partial u_j}{\partial x_j} + \frac{\partial}{\partial x_j}\left(k\frac{\partial T}{\partial x_j}\right) + \Phi$$

where

$$\Phi = \mu\frac{\partial u_i}{\partial x_j}\left(\frac{\partial u_i}{\partial x_j} + \frac{\partial u_j}{\partial x_i}\right) - \frac{2}{3}\mu\left(\frac{\partial u_k}{\partial x_k}\right)^2 \tag{17}$$

The energy flow within the solid front and backing plates is conduction heat transfer, defined as

$$\frac{\partial}{\partial x_j}\left(k_p\frac{\partial T}{\partial x_j}\right) = 0 \tag{18}$$

The bristle pack is considered to be a porous medium in the model by applying a bulk porous medium approach, as defined by Dogu [7]. For the porous bristle pack, fluid flow is subject to additional resistance forces due to fluid friction at solid bristle surfaces other than inertial and viscous forces as given in Eq. (16). Among the many transport models for porous media, the following non-Darcian equation has been employed for the brush seal [7,15–18]:

$$-\frac{dP}{dx_i} = (\alpha_i|u_i| + \beta_i)u_i \tag{19}$$

where α and β represent effective inertial and viscous flow resistance throughout the bristle pack. Frictional forces for the porous bristle pack, described on the right-hand side of Eq. (19), are added to the right-hand side of the momentum equation (Eq. (16)). However, as in the case for a compact bristle pack under pressure load, inertial and viscous forces in Eq. (16) for a highly resistive porous medium become negligibly small relative to frictional forces because of fluid-solid interaction (Eq. (19)). Therefore, Eq. (19) stands alone for flow transport in the porous bristle pack for the present bulk porous medium approach.

Flow resistance coefficients α and β are functions of many parameters: geometric configuration, operating conditions, and bristle-pack dynamic issues. To account for all these parameters in a balanced manner, these flow-resistance coefficients are calculated using experimental data [15,18]. For a comprehensive calculation, axial pressure on rotor and radial pressure on backing plate are used in addition to leakage flow. The bulk porous-medium approach employed incorporates of all the parameters in a balanced manner in matching the experimental data. Details of calibration procedure are presented by Dogu [7].

The energy equation (Eq. (17)) is also valid for the porous bristle pack with the supplied temperature-dependent thermal conductivity for the bristle pack evaluated for the bristle material. Together with other properties, air conductivity is also defined as a function of temperature. Sutherland law is employed for temperature-dependent air viscosity. The conduction heat transfer equation (Eq. (18)) within the solid front and backing plates is also solved using temperature-dependent thermal conductivity of plate materials.

A typical brush seal geometry is shown in Fig. 6. Dimensions are representative of a brush seal as given by Demiroglu [5]. The bristle diameter is 0.102 mm (0.004 in.) with a lay angle of 45 deg.

The solution domain is finely meshed to ensure a mesh independent solution. The typical meshing is plotted in the brush seal region in Fig. 7. A single mesh thickness is considered in the tangential direction at an angle, which is selected to conserve a moderate aspect ratio for meshes in that direction. In a 2D axisymmetric model, in order to take into account the effect of tangential velocity due to the rotor speed, mesh boundaries are cyclically matched in the tangential direction forming pairs of geometrically and physically identical boundaries. By means of

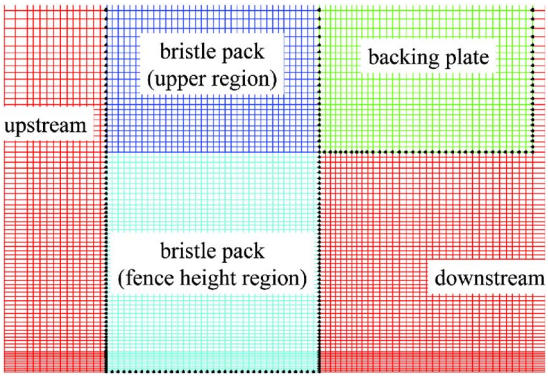

Fig. 7 Sample meshing

cyclic matching for flow repetition on identical faces, the size of computational domain and associated computing time is reduced in the 2D axisymmetric model.

Conservation equations describing the mass, momentum, and energy transfer within the fluid are discretized by the finite volume method. Upwind differencing discretization schemes are employed for all flow variables except density, for which a central differencing scheme is used. The resulting form of the discrete-algebraic finite-volume equations is implicitly solved employing the well-known SIMPLE solution algorithm.

5.1 Boundary Conditions and CFD Model Specifications.

1. Pressure boundary conditions are applied at up- and downstream faces of the model domain. A representative pressure load of 70 kPa (10.2 psi) is chosen. In addition, the analysis is extended to cover effect of several pressure loads as 200, 350, and 700 kPa (29.0, 50.8, and 101.5 psi). Downstream pressure is kept constant at atmospheric pressure of 100 kPa.
2. Temperature at the upstream inlet is imposed at 20°C. In addition, in order to accurately involve the swirl effect, a linear variation of the tangential velocity is prescribed at the upstream face. It is mainly equal to rotor surface speed at the rotor and zero at the stator.
3. No-slip and impenetration boundaries are imposed for all solid walls, surfaces of the rotor and stator and the front and backing plates.
4. At fluid-solid interface for front and backing plate surfaces, conjugate heat transfer is applied to take full account of convection over the surface and conduction through the wall. In addition to defining a single temperature at the wall, the imposed boundary condition equates the convection heat flux over the surface to the conduction heat flux through the wall. In fact, details of the thermal mechanism, where bristles have intermittent line contacts on the backing plate surface with some air gaps in between, cannot be fully represented. The tiny voids among the bristles and backing plate are not considered in the porous medium treatment. Voids are random and too small to fill with micromeshes. However, the porous model includes a porous brush pack in contact with the solid conductive backing plate, allowing a radial inward flow to develop over the backing plate, while modeling the heat transfer between the porous pack, inward radial flow, and the backing plate. The model aims to simulate random conduction and convection zones, which may be present between the bristles and the backing plate to some extent.
5. Stator and rotor surfaces except the bristle-rotor interface are assumed to be adiabatic.
6. Heat flux is determined at bristle-rotor interface. A 50-50 heat portioning is assumed, and only half of the frictional heat is applied to the bristle tips. The heat flux values are varied over a practical, wide range as outlined in frictional heat generation discussed above. The aim is to determine the bristle temperature profile for various representative heat inputs. Heat flux is assumed to be uniformly distributed over the bristle pack thickness. However, it should be noted that blow-down is not uniform in the axial direction over the bristle pack that causes nonuniform heat generation. Nevertheless, this distribution is not yet fully established.
7. Rotor surface speed is defined as the tangential velocity for the rotor wall. Rotor speed is chosen at 3000 rpm, which yields a rotor surface speed of 20.34 m/s for all of the presented analysis cases.
8. Mesh faces in the tangential direction are cyclically matched to consider the tangential flow velocity due to rotor speed. The flow properties, such as velocity components, pressure, and temperature, are identically matched at corresponding meshes on cyclic boundaries.
9. Bristle thermal conductivity is found to follow a linear relationship with respect to temperature. The temperature-dependent thermal conductivity for the widely used bristle material Haynes 25 is

$$k_b(\mathrm{W/m}\,^\circ\mathrm{C}) = 8.84 + 0.02\ T(^\circ\mathrm{C}) \tag{20}$$

valid for temperatures from 0 to 1000°C [5]. This equation gives the thermal conductivity of bristle material itself. However, the bristles are treated as a porous medium in the model. When considering packed bristle matrix under pressure load, the bristles are randomly distributed within the pack. They touch at many points with small voids remaining. In order to consider the effect of voids and contact resistance, bristle pack thermal conductivity could be evaluated by decreasing its magnitude depending on the porosity and thermal contact resistance. Because there is no interruption to heat flow along the bristle axis, bristle conductivity can be used in the radial direction omitting the voids among bristles. However, in the rotor axial direction, the intermittent bristle-bristle line contacts and voids forming among bristles make calculation of heat transfer much more complicated. Unfortunately, there is no available thermal data to estimate the unisotropic thermal conductivity. Therefore, in the model, the isotropic-effective conductivity of the porous bristle pack is assumed to be equal to the thermal conductivity of bristle material as a starting point. The heat flow within the bristle matrix in the rotor axis direction is dominated by conduction through intermittent bristle contacts and flow convection through voids between the bristles. When evaluating heat conduction in the axial direction, depending on the magnitude of convection among bristles, the total axial heat conductance of bristle matrix could be higher or lower than the bristle material thermal conductivity. As the axial conductance of bristle pack gets smaller, the bristle pack would be subject to higher axial temperature gradient.
10. The front and backing plate material is taken as common stainless steel of AISI 304 whose temperature-dependent thermal conductivity is defined as [28]

$$k_p(\mathrm{W}/m\,^\circ\mathrm{C}) = 13.68 + 0.015\ T(^\circ\mathrm{C}) \tag{21}$$

11. Air thermal conductivity is also defined as a function of temperature [28]. The viscosity is calculated as a function of temperature complying the Sutherland law defined as

$$\mu = \frac{\mu_0 (T/T_0)^{3/2}(T_0 + S)}{T + S} \tag{22}$$

where $\mu_0 = 1.716 \times 10^{-5}$ kg/m s, $S = 116$ K, and $T_0 = 273$ K.
12. In addition to use of calculated flow-resistance coefficients in axial and radial directions [7], tangential flow resistance is assumed to be the arithmetic average of the radial and axial flow resistances. This assumption is applied by considering the common 45 deg lay angle.

6 Results and Discussion

In all analysis cases, typical parameters are as follows: pressure load is constant at 70 kPa; air inlet temperature is 20°C, rotor surface speed is 20.34 m/s. The frictional heat generation is varied from 10 to 10,000 kW/m^2. A heat generation of 100 kW/m^2 is chosen as the baseline case. From CFD analysis, mass flow rate under these conditions is calculated as 0.003 kg/s, which is comparable to experimental data in the literature [15,18].

6.1 Leakage and Convective Heat Transfer Coefficient. The mass flow rates for the four pressure loads are calculated as illustrated in Fig. 8. The flow rate increases almost linearly with respect to pressure load within the range considered. The convective heat transfer coefficient is also calculated with the increasing mass flow rate as outlined in Sec. 4 using Eqs. (9) and (10). Higher flow rates yielding higher velocities enhance the heat convection. The bristle spacing also varies with pressure loads. In

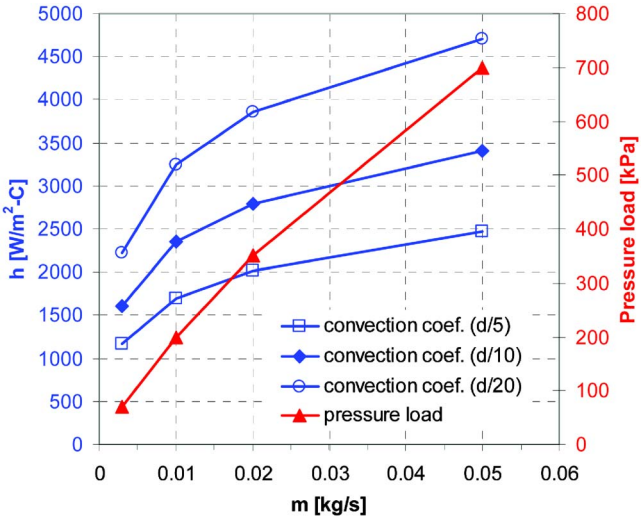

Fig. 8 Convective heat transfer coefficient versus mass flow rate/pressure load

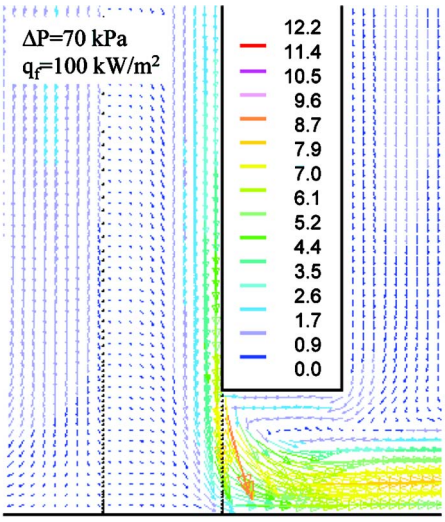

Fig. 10 Velocity vectors (in meters per second) for ΔP =70 kPa, q_f=100 kW/m²

order to evaluate the effect of bristle spacing on the heat convection, the h coefficient is calculated for three values of interbristle space as $d/5, d/10$ [4], and $d/20$. The thinner gap between bristles yields higher velocities and resulting higher h coefficients as plotted in Fig. 8. h is considered at bristle spacing of $d/10$ in the presented results for comparison purposes.

6.2 Contour Plots of Pressure, Temperature, and Velocity Vectors. For a heat generation of 100 kW/m², pressure contours, velocity vectors, and temperature contours are shown in Figs. 9, 10, and 11(*a*)–11(*d*), especially focused near the fence height. Pressure contour lines are plotted at 5 kPa intervals (Fig. 9). Examination of pressure field shows that pressure drop mostly occurs around the fence region closer to the downstream side, as commonly observed in brush seal applications. This type of pressure gradient has been attributed to discharging flow with a contributed effect of expansion.

A velocity vector plot is produced combining the radial and axial velocity components, omitting the tangential velocity component (Fig. 10). This velocity vector plot shows the excessive inward radial flow over the backing plate. The contribution of inward flow on leakage is considerably higher than the direct axial flow at the fence-height region. The inward flow merges with axial flow at the fence region and discharges downstream. A small recirculation forms underneath the backing plate. This is a typical flow field formation for brush seal contact operation. The velocity reaches 12.2 m/s just around the backing plate inner corner, while the rotor surface speed is 20.34 m/s. Combined with the leakage, the velocity used in convective heat transfer coefficient reasonably matches with these velocities.

Temperature contours are shown in Fig. 11(*a*)–11(*d*). The findings indicate that a maximum temperature is reached at the bristle-rotor interface as a result of heat flux input. The temperature at the bristle tips reaches to 54.4°C for the frictional heat input of 100 kW/m² (Fig. 11(*a*)). The temperature exponentially decreases to inlet air temperature in the radial direction. As a result of leakage flow at the fence height, the temperature variation is higher at the fence-height region relative to the upper region. Another observation is that temperature drop over bristle pack thickness in the axial direction is negligibly small. The uniform axial temperature distribution is attributed to the effective convective cooling mechanism of leakage flow in addition to high bristle conductivity. Temperature is ~37.1 °C at the fence-height line corresponding to the backing-plate inner edge. Once temperature rise reaches to backing plate, it caries the heat by conduction toward downstream and dissipates heat to downstream air. As also plotted in Fig. 11(*b*), more temperature rise and heat diffusion is observed throughout the bristle pack for higher heat flux of 1000 kW/m².

Figures 11(*c*) and 11(*d*) show the temperature contours for heat flux of 1000 kW/m² at higher pressure loads of 200 and 350 kPa, respectively. When compared to Fig. 11(*b*), the temperature rise reduces for increasing pressure loads as a result of increased leakage. More leakage flow caries more heat away from the bristle pack. Another observation is that the magnitude of inward radial flow over backing plate increases with pressure load. This accelerated flow also prevents heat diffusion further into the upper region as seen in the temperature contours.

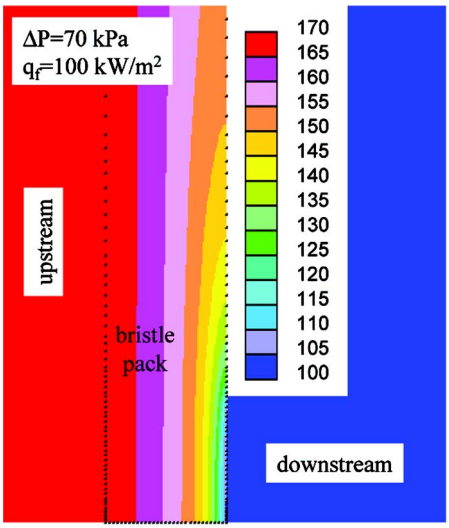

Fig. 9 Pressure contours (in kilopascal) for ΔP=70 kPa, q_f =100 kW/m²

6.3 Radial Temperature Distribution. The radial temperature distribution at the middle section of the bristle pack is plotted for various values of pressure loads and frictional heat inputs in Fig. 12. The temperature in Fig. 12 is nondimensionalized with respect to minimum and maximum temperature in the domain as $T^*=(T-T_{\min})/(T_{\max}-T_{\min})$. The minimum temperature is equal to inlet air temperature at 20°C for all cases. The radial position is

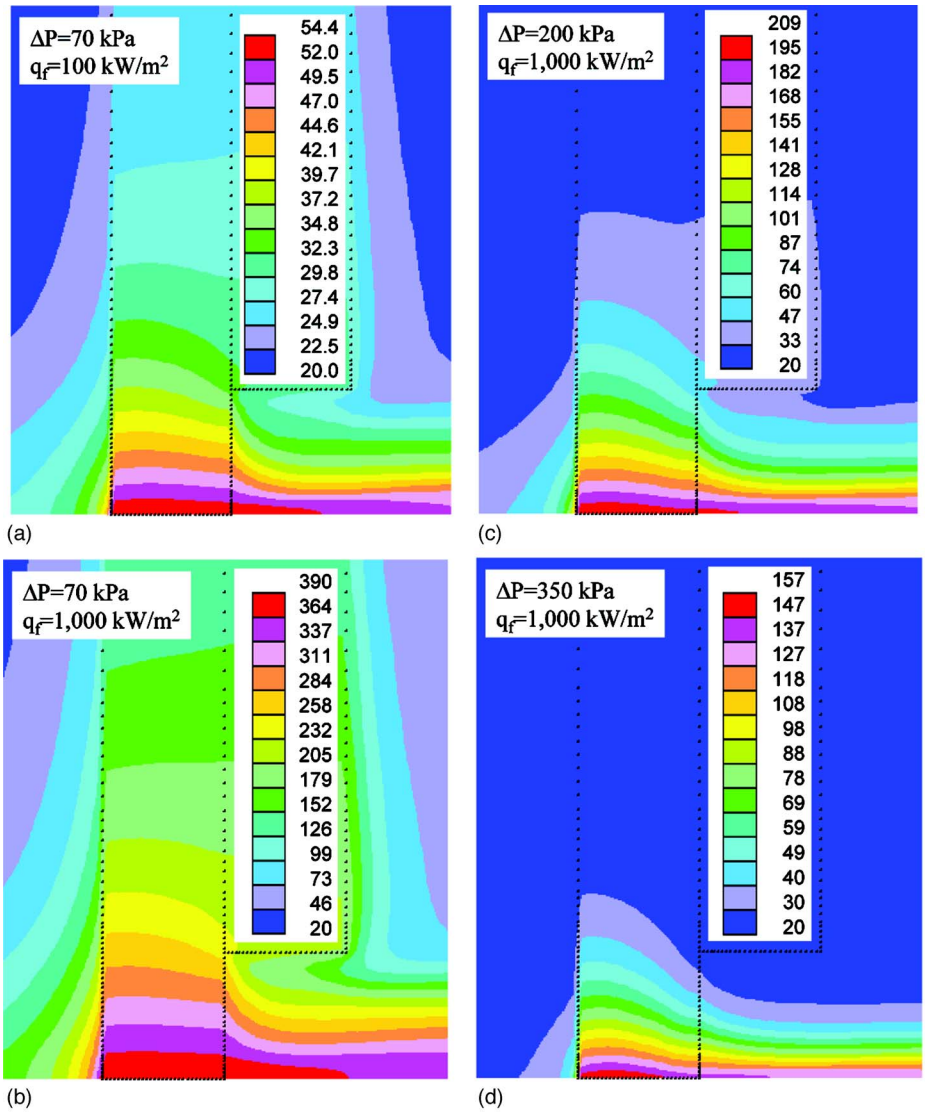

Fig. 11 Temperature contours (in degrees Celsius)

also evaluated as a measure of distance from rotor surface y relative to total bristle free height h_b, as $y^*=y/h_b$. Fence height corresponds to the value of $y^*=0.114$.

An analytical temperature distribution for a single bristle, as given in Eq. (7), is also included in Fig. 12. All the analytical results fall onto same curve when plotted with respect to the nondimensional temperature and radial distance from rotor surface.

Radial temperature exponentially decreases down to inlet air temperature. Most of the temperature drop occurs in the fence-height region for smaller heat flux values. As also seen in temperature contour plots, the radial diffusion of temperature rise is more distributed toward the bristle root with increasing heat flux. CFD results are comparable to the fin analysis for smaller heat flux values. The larger differences at higher heat flux values are attributed to the effect of inward radial flow. It should also be noted that the fin analysis and the CFD model utilize different thermal approaches for the bristle matrix. The fin analysis is based on a single-bristle case, assuming a constant convective heat transfer coefficient. In the calculation of convective heat transfer coefficient, all the leakage is assumed to flow through fence-height section. This yields higher velocity that overestimates h, resulting in a fast cooling mechanism and steep temperature drop along the bristle. On the other hand, the CFD model employs a bulk porous-medium approach that deals with mass, momentum, and energy transfer in the bristle matrix. Therefore, differences in temperature profiles are reasonable while both models gave a similar trend.

In addition to results for 70 kPa pressure load plotted in Fig. 12(a), Figs. 12(b)–12(d) present the radial temperature for pressure loads of 200, 350, and 700 kPa including all five heat flux cases. Temperature lines have the similar trend, as in the case of 70 kPa; however, the effects of increasing leakage and inward radial flow are more pronounced for higher pressure loads. Temperature rise due to heat flux is getting trapped close to the fence-height section for increasing pressure loads, especially for 700 kPa.

6.4 Maximum Temperature. In Fig. 13, maximum temperatures are plotted with respect to heat flux input obtained from both analytical solution (Eq. (8)) and CFD model. Maximum temperature occurs at the bristle-rotor interface. For very high heat flux input cases (which are discussed in Sec. 4), results indicate maximum temperature values beyond 1000°C are possible. This confirms field observations of an orange flash of hot brush fragments during engine start-up [29]. The magnitude of the maximum temperatures exponentially increases with increasing heat flux. Analytical and CFD results follow a similar increasing trend with heat flux. Magnitude of the maximum temperature considerably de-

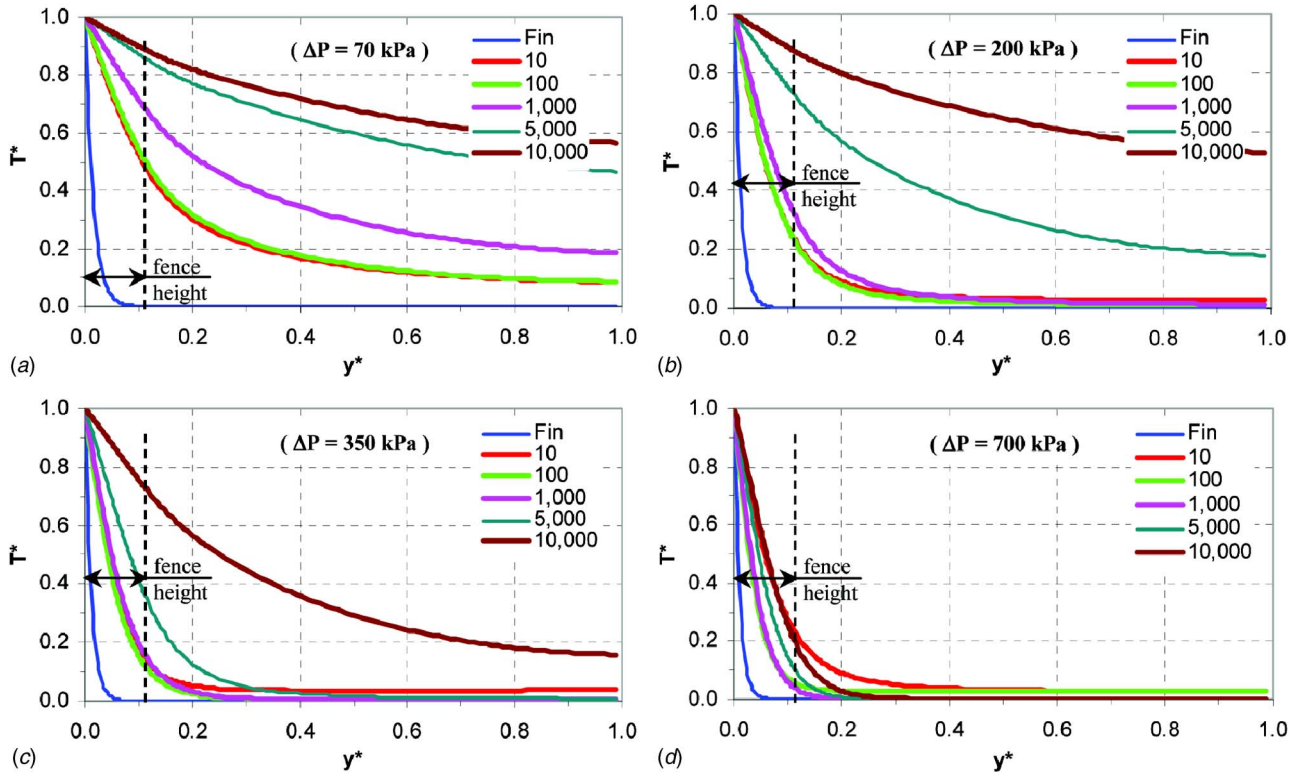

Fig. 12 Radial temperature distribution at the middle of the bristle pack for various pressure loads and frictional heat generations: (*a*) ΔP=70 kPa, (*b*) ΔP=200 kPa, (*c*) ΔP=350 kPa, and (*d*) ΔP=700 kPa

creases with increasing pressure load due to higher convectional cooling and heat removal capacity of increasing leakage flow.

7 Conclusions

Frictional heat in advanced brush seal applications is a major concern. High bristle tip temperatures will cause accelerated oxidation rates even tip melting at extreme cases. Bristle temperature near backing-plate corner is also critical to determine creep behavior of highly loaded seals operating at elevated temperatures. Temperature measurement through the bristle pack has been an open area of interest. More emphasis would be expected based on experimental work using thermocouples among bristles.

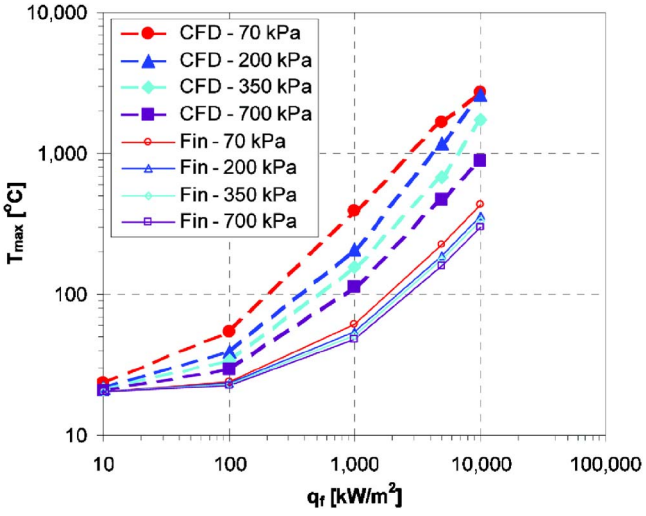

Fig. 13 Maximum temperature for various pressure loads and frictional heat generations

In this study, after outlining the brush seal heat transfer mechanism, both fin heat transfer analysis and porous CFD model have been employed to investigate the bristle temperature distribution. The analytical solution has been developed by treating bristles as fins. The CFD model is based on a bulk porous medium approach for mass and heat transfer in the bristle pack. The study of brush seal thermal analysis can be outlined as follows:

1. Brush seal heat transfer mechanism has been outlined.
2. Frictional heat generation has been calculated based on overall seal stiffness.
3. A closed-form solution has been obtained for the temperature distribution along the bristle using heat transfer relations developed for fins. The convective heat transfer coefficient within the bristle matrix has been evaluated by employing various cross-flow correlations.
4. A bulk porous medium approach has been employed in the thermal CFD analysis.
5. Temperature field in the bristle pack has been obtained with respect to various frictional heat generation rates. A maximum temperature is reached at bristle tips, and this temperature exponentially decreases to air inlet temperature as moved radially away from the rotor surface. Temperature is almost uniform through the bristle pack in the axial direction due to high conductivity and effective cooling of leakage flow. Most of the radial temperature drop occurs in the fence-height region.
6. The maximum temperature exponentially increases with the frictional heat generation.
7. At higher heat flux rates, radial temperature rise along the bristle pack tends to spread toward the bristle root.
8. For higher pressure loads, increasing leakage enhances the convective cooling and heat removal capacity; therefore,

less temperature rise is observed. In addition, temperature rise is trapped closer to the fence-height section due to accelerated inward radial flow over the backing plate.

9. CFD model and fin analyses reasonably match field experience. The fin approach underestimates the bristle temperature relative to CFD analysis.

Nomenclature

A = bristle cross-sectional area [$=\pi d^2/4$], m^2
A_{flow} = flow area, m^2
Bi = Biot number [$=hd/2k_b$]
c = specific heat, J/kg °C
C/C_1 = constant
d = bristle diameter, m
F_b = normal bristle tip load, N
h = convective heat transfer coefficient, W/m^2 °C
h_b = bristle free height, m
h_{FH} = fence height, m
k, k_b, k_p = thermal conductivity of air, bristle, front and backing plate, W/m °C
K_s = bristle pack stiffness, Pa/mm
m = constant/group of terms [$(4h/kd)^{0.5}$], $1/m$
$\dot{m}$ = mass flow rate, kg/s
n = rotor speed, rpm
Nu = Nusselt number
p = bristle perimeter [$=\pi d$], m
P = static pressure, Pa
P_c = bristle contact load, Pa
Pr = Prandtl number
q_f = frictional heat flux, W/m^2
Q = total frictional heat generation, W
r = rotor radius, m
R = ideal gas constant, J/kg K
Re = Reynolds number
$S_{L,T,D}$ = bristle spacing, m
T = temperature, °C
T^* = nondimensional temperature [$(T-T_{min})/(T_{max}-T_{min})$]
u = spatial velocity component, m/s
u_i = superficial velocity, m/s
V = flow velocity and rotor surface speed, m/s
V_{FH} = average velocity at fence-height section, m/s
x = spatial coordinate direction
y = radial distance from rotor surface, m
y' = radial distance from rotor surface along bristle axis
y^* = normalized radial coordinate
α = bristle lay angle, deg
α, β = inertial and viscous flow resistance coefficient
Δr = interference, mm
μ = friction coefficient at bristle-rotor interface and dynamic viscosity, kg/m s
ν = kinematic viscosity, m^2/s
ρ = density, kg/m^3
θ = normalized temperature (=$T-T_\infty$), °C
Φ = viscous dissipation term

Subscripts

i, j, k = spatial coordinate direction
u/d = up-downstream

References

[1] Gorelov, G. M., Reznik, V. E., and Tsibizov, V. I., 1988, "Experimental Study of Brush Seal Flow Characteristics and Comparison With a Labyrinth Seal," Izv. Vyssh. Uchebn. Zaved., Aviatsion. Tekh., **31**(4), pp. 43–46.

[2] Hendricks, R. C., Schlumberger, S., Braun, M. J., Choy, F., and Mullen, R. L., 1991, "A Bulk Flow Model of a Brush Seal System," ASME Paper No. 91-GT-325.

[3] Owen, A. K., Jones, T. V., Guo, S. M., and Hogg, S., 2003, "An Experimental and Theoretical Study of Brush Seal and Shaft Thermal Interaction," ASME Paper No. GT-2003-38276.

[4] Chew, J. W., and Guardino, C., 2004, "Simulation of Flow and Heat Transfer in the Tip Region of a Brush Seal," Int. J. Heat Fluid Flow, **25**(4), pp. 649–658.

[5] Demiroglu, M., 2004, "An Investigation of Tip Force and Heat Generation Characteristics of Brush Seals," Ph.D. thesis, Rensselaer Polytechnic Institute, Troy, NY.

[6] Aksit, M. F., Bhate, N., Bouchard, C., Demiroglu, M., and Dogu, Y., 2003, "Evaluation of Brush Seal Performance for Oil Sealing Applications," AIAA Paper No. AIAA-2003-4695.

[7] Dogu, Y., 2005, "Investigation of Brush Seal Flow Characteristics Using Bulk Porous Medium Approach," ASME J. Eng. Gas Turbines Power, **127**(1), pp. 136–144.

[8] Fellenstein, J. A., and DellaCorte, C., 1996, "A New Tribological Test for Candidate Brush Seal Materials Evaluation," Tribol. Trans., **39**(1), pp. 173–179.

[9] Fellenstein, J. A., DellaCorte, C., Moore, K. D., and Boyes, E., 1996, "High Temperature Brush Seal Tuft Testing of Metallic Bristles Versus Chrome Carbide," AIAA Paper No. AIAA-96-2908.

[10] Fellenstein, J. A., DellaCorte, C., Moore, K. D., and Boyes, E., 1997, "High Temperature Brush Seal Tuft Testing of Selected Nickel-Chrome and Cobalt-Chrome Superalloys," AIAA Paper No. AIAA-97-2634.

[11] Hawthorne, H. M., 1994, "Brush-on-Disc Simulation Tribo-Testing of Materials for Gas Turbine-Compliant Seal Components," Tribol. Int., **27**, pp. 87-95.

[12] Crudgington, P. F., and Bowsher, A., 2002, "Brush Seal Pack Hysteresis," AIAA Paper No. AIAA-2002-3794.

[13] Flower R., 1990, "Brush Seal Development System," AIAA Paper No. AIAA-90-2143.

[14] Modi, V., 1992, "Modelling Bristle Lift-Off in Idealized Brush Seal Configurations," *Proceedings of 4th International Symposium on Transport Phenomena and Dynamics of Rotating Machinery (ISROMAC-4)*, Honolulu, HI, Begell House, New York, pp. 623–632.

[15] Bayley, F. J., and Long, C. A., 1993, "A Combined Experimental and Theoretical Study of Flow and Pressure Distributions in a Brush Seal," ASME J. Eng. Gas Turbines Power, **115**(2), pp. 404–410.

[16] Chew, J. W., Lapworth, B. L., and Millener, P. J., 1995, "Mathematical Modeling of Brush Seals," Int. J. Heat Fluid Flow, **16**(6), pp. 493–500.

[17] Chew, J. W., and Hogg, S. I., 1997, "Porosity Modeling of Brush Seals," ASME J. Tribol., **119**, pp 769–775.

[18] Turner, M. T., Chew, J. W., and Long, C. A., 1998, "Experimental Investigation and Mathematical Modeling of Clearance Brush Seals," ASME J. Eng. Gas Turbines Power, **120**(3), pp. 573–579.

[19] Stango, R. J., Zhao, H., and Shia, C. Y., 2003, "Analysis of Contact Mechanics for Rotor-Bristle Interference of Brush Seal," ASME J. Tribol., **125**, pp. 414–421.

[20] Zhao, H., and Stango, R. J., 2004, "Effect of Flow-Induced Radial Load on Brush Seal/Rotor Contact Mechanics," ASME J. Tribol., **126**, pp 208–215.

[21] Aksit M. F., and Tichy, J. A., 1996, "A Computational Model of Brush Seal Bristle Deflection," AIAA Paper No. AIAA-96-2909.

[22] Sharatchandra, M. C., and Rhode, D. L., 1996, "Computed Effects of Rotor Induced Swirl on Brush Seal Performance: Part 2-Bristle Force Analysis," ASME J. Tribol., **118**, pp. 920–926.

[23] Aksit, M. F., 1998, "A Computational Study of Brush Seal Contact Loads with Friction," Ph.D. thesis, Rensselaer Polytechnic Institute, Troy, NY.

[24] Derby, J., and England, R., 1992, "Tribopair Evaluation of Brush Seal Applications," AIAA Paper No. AIAA-92-3715.

[25] Basu, P., Datta, A., Johnson, R., Loewenthal, R., and Short, J., 1993, "Hysteresis and Bristle Stiffening Effects of Conventional Brush Seals," AIAA Paper No. AIAA-93-1996.

[26] Chupp, R. E., and Prior, R. J., 1997, "Advanced Seal Development for Large Industrial Gas Turbines," AIAA Paper No. AIAA-97-2731.

[27] Short, J. F., Basu, P., Datta, A., Loewenthal, R. G., and Prior, R. J., 1996, "Advanced Brush Seal Development," AIAA Paper No. AIAA-96-2907.

[28] Incropera, F. P., and De Witt, D. P., 1990, *Introduction to Heat Transfer*, 2nd ed., Wiley, New York.

[29] Hendricks, R. C., Griffin, T. A., Bobula, G. A., Bill, R. C., and Howe, H. W., 1993, "Integrity Testing of Brush Seal in Shroud Ring of T-700 Engine," ASME Paper No. 93-GT-373.

Remaining Life Prediction of Thermal Barrier Coatings Based on Photoluminescence Piezospectroscopy Measurements

Mei Wen
Department of Metallurgy and Materials Engineering, University of Connecticut, Storrs, CT 06269

Eric H. Jordan[1]
Department of Mechanical Engineering, University of Connecticut, Storrs, CT 06269
e-mail: Jordan@engr.uconn.edu

Maurice Gell
Department of Metallurgy and Materials Engineering, University of Connecticut, Storrs, CT 06269

*Nondestructive determination of the remaining life of thermal barrier coatings (TBCs) is highly desirable for components removed from service engines. Remaining life predictions for EB-PVD/Pt-Al TBCs cycled at two temperatures (*1151°C *and* 1121°C*) were made based on the thermally grown oxide stresses measured by the photoluminescence piezospectroscopy technique without knowing the test temperature. The predictions were compared using regression methods and neural network methods. It was found that both methods produce accurate life remaining predictions, but the neural network methods were superior. The lowest root-mean-square (rms) error and maximum absolute error for the prediction was 6.1% and 8.2%, respectively. For a data set with a 48.7% rms spallation life variation about the mean, the prediction results obtained are highly encouraging.* [DOI: 10.1115/1.2135820]

1 Introduction

Thermal barrier coatings (TBCs) are widely used in gas turbine engines to protect metal components from hot gases [1–4]. Since the use of thermal barrier coatings enables gas turbine engines to operate at gas temperatures well above the melting temperature of metallic components, spallation of coatings will lead to reduced component lifetime. It is highly desirable to nondestructively evaluate the TBC condition and to assess its remaining life to determine whether engine components can be reliably used for another service interval. Current approaches involve using laboratory and/or engine part statistical data from groups of samples and determining minimum properties. One incentive for approaches based on nondestructive inspection is the prospect of using individual part behavior rather than statistical minimums. This may allow many parts with properties above the minimum to be more fully utilized.

The feasibility of nondestructively measuring the residual stress in the thermally grown oxide detected optically through the overlaying ceramic layer in TBCs was first demonstrated by Clarke et al. using the photoluminescence piezospectroscopy (PLPS) technique [5]. Stress is rapidly and reliably measured by a noncontacting optical method described further in Sec. 3.1. Since that time, many measurements have been made and systematic changes in the measured stress and other related spectral characteristics with cyclic thermal exposure have been demonstrated [6–16]. The potential for using this behavior to make life predictions or assess damage has been described [16,17]. In at least one case, the correspondence between the location of early damage and features on maps of spectral characteristics has been demonstrated [16].

In the present work, we are concerned with the quantitative prediction of remaining life from the measurement of optical features arising from PLPS. The primary purpose of making remaining life predictions is for use in making retirement for cause decisions of individual parts in gas turbines. To date, such predictions have been made for two TBCs tested at a single temperature [17]. Specifically, remaining life was predicted to within ±7% for EB-PVD TBCs with Pt-modified NiAl bond coats and ±2% for EB-PVD TBCs with MCrAlY bond coats. The predictions in that study [17] were made by both direct-regression and neural-network methods. For the Pt-modified NiAl bond-coated systems, predictions were of similar accuracy for both regression and neural-network methods, while neural-network methods were superior for the MCrAlY-coated systems. It is worth noting that the neural-network prediction methods appeared to be superior when more than one spectral characteristic changes systematically with cycles, as was the case for the MCrAlY bond-coated samples.

The predictions made to date are encouraging. However, in component retirement for cause situations, there is typically a variation of temperature from part to part and within a part. These temperature variations are the most common cause for varied spallation lives. In the present study, we attempt to make temperature-blind remaining life predictions for samples tested at two temperatures (1151 and 1121°C). The prediction task chosen is to make remaining life predictions based on measurement data taken up to but not after a selected time to simulate a situation where a part replacement decision has to be made. The relative merits of eight different strategies for making such predictions are compared.

2 Experimental Procedure

Disk-shaped (2.54 cm dia and 0.32 cm thick) TBC specimens investigated in this study were supplied by an engine manufacturer. They consist of a 140 μm thick electron beam physical vapor deposited (EB-PVD) 7 wt. % Y_2O_3-stabilized ZrO_2 (YSZ) coating, a 50 μm grit blasted platinum-modified nickel-aluminide bond coat [(Ni, Pt)Al] and a single-crystal CMSX-4 superalloy substrate.

One-hour cyclic durability tests on EB-PVD Pt-Al TBCs were conducted at two temperatures, 1151 and 1121°C. Cyclic furnace testing is carried out in such a way that only relatively small gradients are expected (<40°C during the cooling transient). Re-

[1]To whom correspondence should be addressed.

Contributed by the International Gas Turbine Institute (IGTI) of ASME for publication in the JOURNAL OF ENGINEERING FOR GAS TURBINES AND POWER. Manuscript received November 19, 2004; final manuscript received October 4, 2005. Review conducted by J. Daleo.

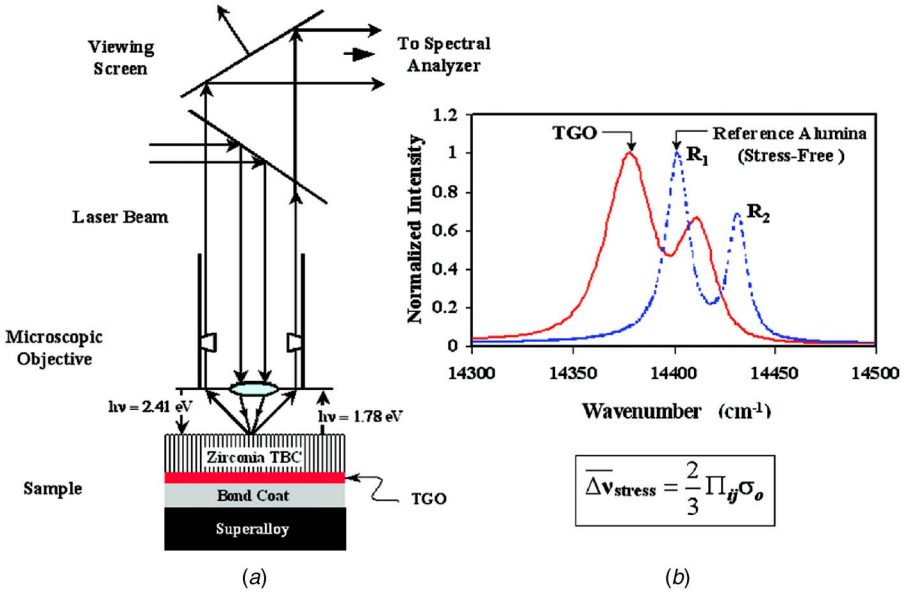

Fig. 1 (*a*) **Schematic illustration of the photostimulated luminescence piezospectroscopy technique, and** (*b*) **typical R_1/R_2 fluorescence spectra for chromium-containing stress-free and stressed α-Al_2O_3**

alistic gradient testing involves very high heat fluxes and is both difficult and expensive [18] and beyond the scope of the present work. In spite of this, simple furnace tests are widely used in industry because they have a good track record of reproducing observed failure modes. The temperature of 1121°C was selected because it corresponded to the sponsor's goal temperature for the future, and 1151°C was selected to correspond to local hot spots and to obtain results without having tests of excessive duration.

Specimens were removed at specified intervals to perform PLPS measurements. Experimental details concerning thermal cycling tests and PLPS measurements can be found in Refs. [8–10,19]. Failure of the specimen was defined by spallation of more than 50% of the total area of coatings.

3 Analysis Procedure

3.1 Description of Data Set. The data consist of seven samples tested to failure: five samples were tested at 1151°C and two samples were tested at 1121°C. PLPS data consist of the fluorescence spectra coming from the thermally grown oxide (TGO) layer. For a homogeneous stress state, two peaks designated R_1 and R_2 are recorded and these peaks shift linearly with the magnitude of the hydrostatic stress in the TGO (Fig. 1). Because damage to the oxide can result in a nonuniform stress, various features of the spectra can change, including: the peak position related to stress, the standard deviation of the stress from multiple measurements at different locations on a given sample, peak width related to stress homogeneity, the R_1/R_2 peak area ratio, and the Gaussian/Lorentzian fraction used to fit the peaks. In the present study, the measured stress and its standard deviation and the R_1/R_2 peak area ratio are the only spectral characteristics that changed systematically with cycles. In addition, the lifespan of each sample is known (Table 1). By dividing the corresponding cycles at which measurements were made by the lifespan of each sample, the corresponding life fraction at which the measurements were taken was obtained. Thus, the original data set has the following features: stress, standard deviation of stress, R_1 and R_2 peak area ratio, and the corresponding life fraction at which measurements were taken. In addition, we can extract other features from the original data set such as the first derivative and second derivative of stress with respect to life fraction.

3.2 Prediction Methods. There are, in principle, many ways in which the features mentioned in Sec. 3.1 can be combined or used separately to make predictions. Two methods were used to estimate the remaining life. First, a straightforward regression approach was used to make remaining life predictions based on a single signal feature. The features used were stress, standard deviation of the stress, or the R_1 and R_2 peak area ratio. Second, a method based on training a neural network was examined. Neural networks have some very useful properties that are suitable for prediction problems, such as nonlinearity, input-output mapping, and adaptivity [20]. Neural networks are composed of simple elements operating in parallel. As in nature, the network function is determined largely by the connections between elements. We can train a neural network to perform a particular function by adjusting the weights between elements. Neural networks are adjusted, or trained, so that a particular input leads to a specific target output. Such a situation is shown in Fig. 2. There, the network is adjusted, based on a comparison of the output and the target, until the network output best matches the target. Typically, many such input/target pairs are used, in this supervised learning, to train a

Table 1 Remaining life prediction based on average stress versus life fraction

Temperature (°C)	Sample	Life (cycles)	Actual life fraction at stress S=1.79 GPa[a]	Actual remaining life fraction[b]	Error in remaining life prediction
1151	1	190	0.648	0.352	−0.148
	2	200	0.694	0.306	−0.194
	3	200	0.469	0.531	+0.031
	4	150	0.361	0.639	+0.139
	5	150	0.378	0.622	+0.122
1121	1	610	0.404	0.596	+0.096
	2	550	0.556	0.444	−0.056
Average					0.112
RMS					0.124
Maximum					0.194

[a]Life fraction from master curve at S=1.79 GPa, LF=0.50
[b]Predicted remaining life fraction from master curve, RLF=0.50

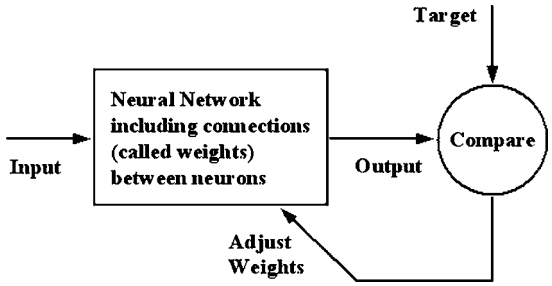

Fig. 2 Schematic flow chart of neural network (adopted from The Mathworks)

network [21]. The neural-network approach easily allows simultaneous use of multiple signal features. The advantage is that there is no need to decide a priori how the various signal features are to be combined. The training of the neural network yields an optimum combination approach within the limits of neural network performance.

In the present work, two different neural networks are used. One is a radial basis function network, the other is a generalized regression neural network (GRNN) [20,21]. They are both two-layer networks. A radial basis function network consists of a hidden radial basis layer of neurons and an output linear layer of neurons. Both layers have bias. The GRNN has a radial basis layer similar to radial basis network and a special linear layer. Only the first layer has bias in the GRNN.

3.3 Leave-One-Out Cross-Validation. Leave-one-out cross-validation [22] was adopted as a means of assessing the predictive capabilities of the neural-network approaches. In this approach, all data sets except one are used to train the neural network, and the predictive capacity of the network is tested by making a prediction of the data set left out. By repeating the procedure, leaving out each data set, in turn, prediction accuracy measures (such as average error, root-mean-square (rms) error, and maximum error of prediction) can be determined in an unbiased way. The hypothetical prediction task provides a basis for making a decision whether to reuse or replace a given part during a regular inspection. The PLPS measurements are used to make the life prediction. Accordingly, the data for test sample must be based on the PLPS measurements up to but not after the chosen inspection time.

4 Experimental Results and Discussion

4.1 Remaining Life Prediction Based on Regression

4.1.1 Prediction Using Stress versus Life Fraction. The assessment of the predictive ability of the simple regression approach using stress data only was based on a retirement for cause task in which a part replacement opportunity is available at half

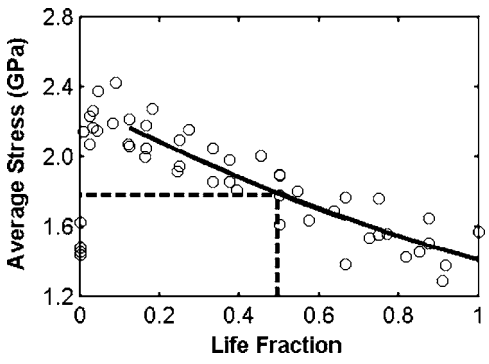

Fig. 3 Quadratic fit for stress versus life fraction for all samples

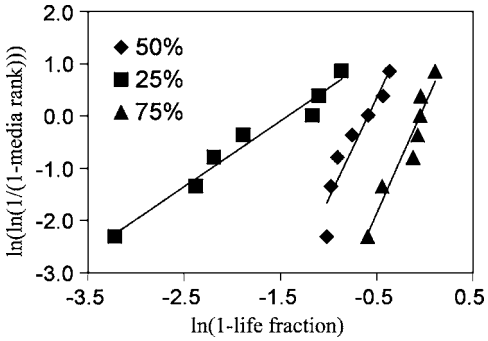

Fig. 4 Weibull plot of life fraction data for PLPS inspections at life fraction 25%, 50%, and 75% from master curve

the expected life. Accordingly, the whole data set was fit to a quadratic function by regression (Fig. 3) and the stress level at half-life was determined (1.79 GPa). Then each individual data set was fit to a quadratic function by regression and the actual remaining life fraction at the threshold stress $S=1.79$ GPa was determined and compared to the ideal value of a remaining life fraction of 0.5. The error of prediction was then calculated and the results are shown in Table 1. The rms error of the prediction is 12.4%, and the maximum absolute error is 19.4%. The prediction accuracy is fairly good considering the nonconstant temperature and the simplicity of the regression method. It is worth noting that the above results are only an example showing the prediction at around half-life. In fact, depending on the stress level obtained from inspection (one stress is the extreme case), corresponding life fraction predicted from master curve can be obtained and the total life can be calculated from this life fraction and the number of cycles at which the sample is inspected.

There is inevitably uncertainty in prediction using the regression mean curve. In an engineering context, one is interested in how much reduction in expected usable life is required to achieve reduced probability of an unexpected failure. Statistical methods were used to study this uncertainty on the limited specimens available. It was found that a two-parameter Weibull distribution represented life data pretty well (Fig. 4). The resulting cumulative distribution from this Weibull distribution is shown in Fig. 5. Using this distribution function, it is possible to estimate the reduction in expected remaining life fraction that is required to have various levels of increased reliability against having a failure before the end of the expected remaining life fraction. This, for example, could be used to determine when the next inspection should be done or in making a decision to remove a part or continue running it. Table 2 shows results for PLPS inspections running at life fraction 25%, 50%, and 75% from the master curve. The values in the table show the allowable remaining life if the

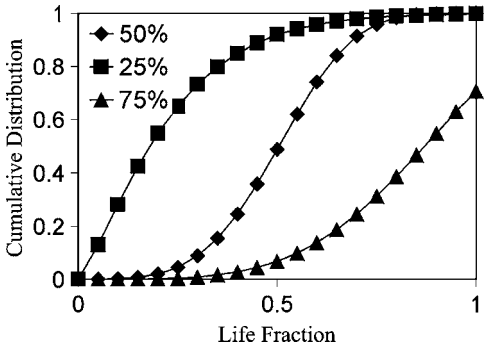

Fig. 5 Cumulative distribution of life fraction data for PLPS inspections at life fraction 25%, 50%, and 75% from master curve

Table 2 Remaining life fraction at different reliability levels for PLPS inspections at life fraction 25%, 50%, and 75% from master curve

Life fraction from master curve	Remaining life fraction from master curve	Reliability		
		50%	90%	95%
0.25	0.75	0.817	0.536	0.416
0.50	0.50	0.496	0.314	0.260
0.75	0.25	0.131	0	0

chance for a part reaching that life is to be 50%, 90%, or 95% according to the Weibull analysis. For example, at the measurement at 50% of life, there is 50% of reliability that the remaining life is equal to or more than 49.6%, while the reliability that the remaining life is equal to or more than 31.4% is 90%. We note that for a sample set as small as the present one, these are just engineering estimations that will be increasingly questionable for tail ends of the distributions, such as for prediction of very high reliabilities.

4.1.2 Prediction Using Peak Area Ratio and Standard Deviation of Stress versus Life Fraction. Figures 6 and 7 show the peak area ratio and standard deviation of stress as a function of life fraction for all samples, respectively. Following the same procedure of Sec. 4.1.1, the prediction can be made using R_1 and R_2 peak area ratio versus life fraction and standard deviation of stress versus life fraction separately. The corresponding results are shown in Tables 3 and 4. It is shown that the predictions using the peak area ratio (rms error 23.9%), and standard deviation of stress (rms error 30.3%), versus life fraction were worse than those using the stress versus life fraction (rms error 12.4%). This is probably because the changes of area ratio and standard deviation of stress as a function of life fraction are relatively temperature sensitive, which makes the data more scattered. In contrast, the change of stress as a function of life fraction is nearly temperature independent, which leads to a master curve representing all sample behavior fairly well; thus, the predicted results are better.

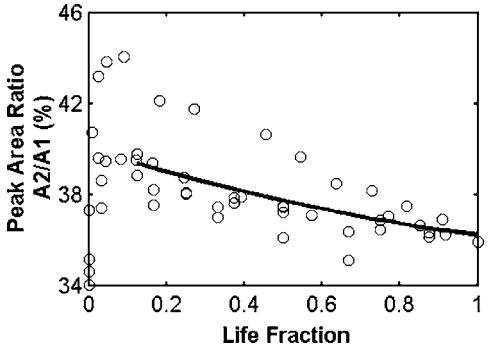

Fig. 6 Quadratic fit for peak area ratio versus life fraction for all samples

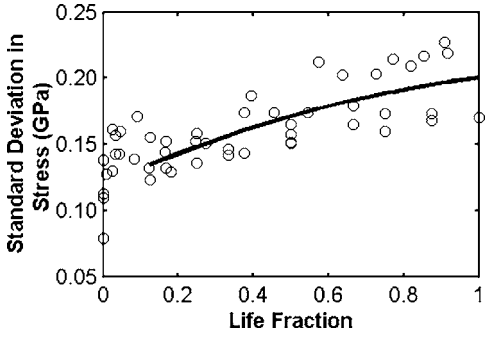

Fig. 7 Quadratic fit for standard deviation of stress versus life fraction for all samples

Table 3 Remaining life prediction based on peak area ratio versus life fraction

Temperature (°C)	Sample	Actual life fraction at area ratio A2/A1=37.7%[a]	Actual remaining life fraction[b]	Error in remaining life prediction
1151	1	0.341	0.659	0.159
	2	0.445	0.555	0.055
	3	0.411	0.589	0.089
	4	0.156	0.844	0.344
	5	0.013	0.987	0.487
1121	1	0.477	0.523	0.023
	2	0.584	0.416	−0.084
Average				0.177
RMS				0.239
Maximum				0.487

[a]Life fraction from master curve at peak area ratio A2/A1=37.7%, LF=0.50
[b]Predicted remaining life fraction from master curve, RLF=0.50

4.1.3 Prediction Using the Weighted Average of Three Features. The regression approach was used to make remaining life predictions based on all three features: TGO stress, peak area ratio, and standard deviation of stress versus life fraction. A simple weighted-average method was used to combine the three features, and the results are shown in Table 5. The weighting factors for a given data feature were selected to be inversely proportional to the root-mean-square error found in regression predictions using that particular feature alone. As would be expected, the results were better than those based on the area ratio and standard deviation of stress versus life fraction, but worse than those based on the stress versus life fraction. The rms error of the

Table 4 Remaining life prediction based on standard deviation of stress versus life fraction

Temperature (°C)	Sample	Actual life fraction at deviation in stress DS=0.171 GPa[a]	Actual remaining life fraction[b]	Error in remaining life prediction
1151	1	0.669	0.331	−0.169
	2	0.985	0.015	−0.485
	3	0.142	0.858	0.358
	4	0.426	0.574	0.074
	5	0.878	0.122	−0.378
1121	1	0.214	0.786	0.286
	2	0.354	0.646	0.146
Average				0.271
RMS				0.303
Maximum				0.485

[a]Life fraction from master curve at deviation in stress DS=0.171 GPa, LF=0.50
[b]Predicted remaining life fraction from master curve, RLF=0.50

Table 5 Remaining life fraction using weighted average method

Error (%)	Stress versus life fraction	Peak area ratio versus life fraction	Deviation in stress versus life fraction	Weighted average of 3 attributes
Average	11.2	17.7	27.1	16.3
RMS	12.4	23.9	30.3	19.3
Maximum	19.4	48.7	48.5	33.4

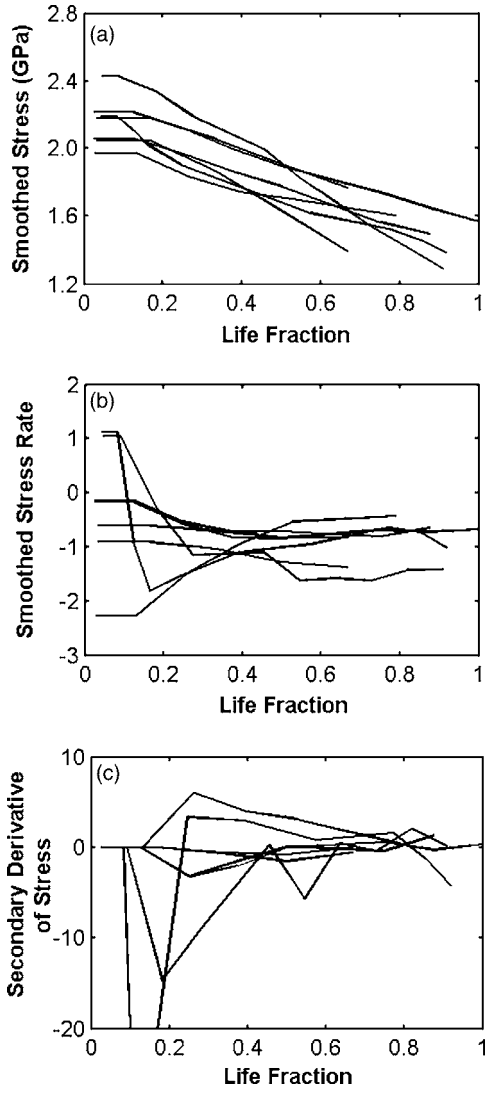

Fig. 8 (*a*) Smoothed stress, (*b*) first derivative of stress, and (*c*) second derivative of stress

prediction was 19.3%. Therefore, predictions based on a combination of multiple features by simple weighted average were inferior to those made using stress alone.

4.2 Remaining Life Prediction Based on Neural Network. In order to get the first and second derivatives of stress, we preprocess the stress data using an α-β filter. The maneuvering index of the α-β filter [23] has been chosen to be equal to 1 to provide moderate noise reduction. The smoothed stress after using the α-β filter is shown in Fig. 8(*a*). The first and second derivative of stress are shown in Figs. 8(*b*) and 8(*c*), respectively. Several different neural-network methods have been implemented for prediction purposes and will be described below.

4.2.1 First Neural Network Method. The input features into the training network are:

- stress (smoothed)
- first derivatives of stresses (smoothed)
- standard deviation of stresses
- R_1 and R_2 peak area ratio
- second derivatives of stresses (smoothed)

The output is the predicted remaining life fraction at certain time points of measurements.

Table 6 Prediction results using neural network method 1

	Using three measurements		Using five measurements	
Error (%)	Radial basis network	Generalized regression neural network	Radial basis network	Generalized regression neural network
Average	7.2	7.2	14.3	13.1
RMS	10.0	8.2	16.0	15.1
Maximum	22.1	13.3	22.7	21.4

The objective of training the network is to match the outputs of the network with the target (the actual remaining lifetime for the samples at certain time points of measurements). After training the network, we can input the measurement data for the test sample to the network and predict its remaining lifetime. Finally, we evaluate the performance of neural networks using the leave-one-out cross-validation technique. Because different samples have different life spans, the total number of measurements from the start of the cyclic test prior to failure for each sample is different. Moreover, we eliminated the first measurement at 0 cycle because the initial cycling period is a transient period. The smallest number of measurements after cycling has begun is five, whereas the largest number of measurements is ten. Here, we use both a radial basis function network and a generalized regression neural network (GRNN) to make predictions using the spectral characteristics from the first three measurements after cycling has begun and compare those predictions to predictions using the first five measurements. The results are shown in Table 6. It was found that the prediction is better for reduced measurements (three measurements) than for full measurements (five measurements). One possible reason for this is that the measurements prior to failure may be more noisy than those at the beginning of test. The comparison of the radial basis function network and GRNN did not show a significant difference in performance. Compared to the simple regression method or weighted-average method, we can see we have some accuracy improvement by using neural networks, which allow simultaneous use of multiple features. For the data containing three measurements, the rms error is 10.0% for radial basis function network and 8.2% for GRNN, respectively. However, the benefit of using neural network with this method is modest. As we mentioned before, we think it is probably because the change of area ratio and standard deviation of stress as a function of life fraction is relatively temperature sensitive, which makes the data more scattered. This increases the difficulty of pattern recognition by neural network and decreases the accuracy of prediction.

4.2.2 Second Neural Network Method. Realizing the temperature sensitivity of area ratio and standard deviation of stress, another method was developed. In addition we wished to allow the neural network to recognize trends over time. First the stress versus life fraction data was fit with a quadratic polynomial function to get the master curve (dashed line in Fig. 9), as was done before in the regression method. Second, the stress and the pseudo life fraction (pseudo LF) derived from the master curve were used in training neural networks and fit to the actual life fraction of samples at various times of measurement. So the input features used in training the network are stress and the pseudo life fraction (pseudo LF) at which the stress was measured (that we derived from the master curve). The output is the predicted remaining life fraction at certain points in time.

After training the network, we can input the measurement data for the test samples and predict the remaining life fraction. As in the first method, we use both the radial basis function network and generalized regression neural network (GRNN) to make predictions using three measurements and five measurements. The results are shown in Table 7. The prediction, again, is better for reduced measurements (three measurements) than for full mea-

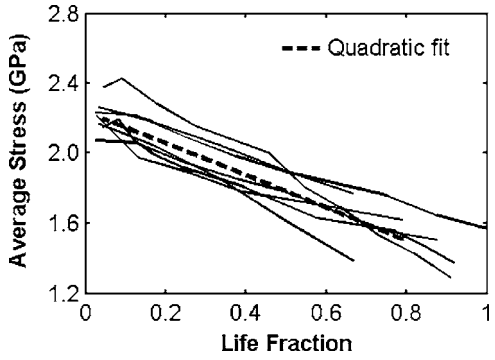

Fig. 9 Stress versus life fraction for neural network method 2

surements (five measurements). Compared to the first method, it is shown that the accuracy of prediction is significantly better. We conclude that with the reduced measurements of current data, radial basis function network combined with master curve give the best prediction results. The rms error is 6.1%, and the maximum absolute error is 8.2%, both of which are encouraging.

Finally, the performance of predictions was compared to the inherent variation in spallation lives of all samples tested at two temperatures and the results are shown in Fig. 10. The standard deviations of predictions using the trained neural-network and regression methods are 6.1% and 12.4%, respectively, which are much less than the inherent variation of spallation lives of 48.7%. It should be pointed out that the neural network was trained using a relatively small data set of seven samples, and the possibility exists that some of the predictive accuracy is due to the network utilizing features unique to this data set. Only more extensive testing can show the extent of this problem, if it exists. However, we note that simple regression gives very respectable predictions. The accuracy of predictions was not dramatically improved by the use of multiple signal attributes or neural networks by themselves (Table 5 versus Table 6). Thus the possibility that neural networks are merely exploiting eccentric features of the data sets to make

Table 7 Prediction results using neural network method 2

	Using three measurements		Using five measurements	
Error (%)	Radial basis network	Generalized regression neural network	Radial basis network	Generalized regression neural network
Average	5.5	7.2	6.5	12.2
RMS	6.1	8.8	7.4	13.1
Maximum	8.2	18.6	10.9	20.5

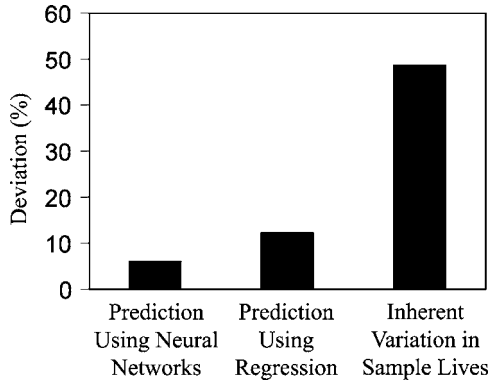

Fig. 10 Comparison of predictions performance with inherent variation of sample lives

predictions seems unlikely. Only when the neural networks are trained on data that makes possible the recognition of trends (via the pseudo life fraction) are the predictions significantly improved (Table 7). Although a larger data set is needed to make more definitive statements, to date the results are consistent with the notion that recognition of trends over time and not the use of neural-network approaches, per se, are mainly responsible for the improved prediction using neural networks shown in Table 7.

4.3 Discussion of Predictions at Two Temperatures. This is the first attempt at remaining life predictions for samples at two different temperatures, without using knowledge of the temperatures. We note that in service hardware the temperatures at critical locations where spallation occurs can vary from component to component within a given engine and between engines. The ability to make predictions in a temperature-blind manner over the limited ranges of temperatures that were practical to test in the current program is promising. If the temperature independence proves true over a wider range of temperatures, then knowledge of local temperatures will not be needed for good life prediction, whereas if temperature dependence is shown to exist for larger temperature differences, the low sensitivity to temperature shown in the present predictions will reduce the sensitivity of the predictions to errors in knowledge of the actual local part temperatures. Because the variation of temperature from one part to another is one of the most important features leading to variation in part lives, it is thus important in practice to have a prediction method that does not require precise knowledge of temperatures. To make life predictions of parts, it is necessary to construct a database for the exact coating/substrate system to be used and to select component relevant temperature ranges and cycle times. With such a database and a few measurements (one in the extreme case) over time for the engine parts, life prediction could be done. Considering the complexity of nonconstant temperatures, the radial basis network prediction with the rms error of 6.1% is encouraging.

The present results have only been proven for the particular system tested. In the present predictions, the samples involved failed primarily due to rumpling that directly influences the stress measured [24] and the present results are expected to be applicable primarily to systems failing in this way. The failure mode of TBCs highly depends on the specifics of the alloy-bond-coated TBC system being tested. Other failure modes can and do occur [2,4]. These failure modes may be influenced by aluminum depletion, local variations in bond coat, and TBC thickness by local mechanical strains, which are affected by surface geometry [25] and other factors. In such cases additional information may be needed to make predictions; for example, for a different system, failure was shown to be associated with measured TGO stress, TGO thickness, and the local radius of curvature [25]. The present authors are developing a prediction method for that system [25] based on curvature maps and stress measurement. In a third group of TBCs, the occurrence of bimodal stress distributions may be predictive [8,26]. The present results show promise for remaining life prediction for the particular type of coating system, whereas other systems may require additional measured data and produce different levels of accuracy of prediction.

5 Conclusions

Remaining life predictions for EB-PVD TBCs on a Pt-modified NiAl bond coat cycled at two temperatures were made based on the data using photoluminescence piezospectroscopy without knowledge of the test temperature. It is important to note that the photoluminescence behavior versus cycles and temperature upon which the present predictions are based has been observed for another similar system [10] but not for the MCrAlY bond-coated system [8]. The predictions using regression methods and neural-network methods were compared, and it was found that the neural-network methods were superior. For the data set considered, the radial basis function network gives the best prediction

results. The rms error and the maximum absolute error are 6.1% and 8.2%, respectively, making such predictions of significant engineering use. For the direct regression method, prediction using measured stress alone, the rms error and the maximum absolute error are 12.4% and 19.4%, respectively. The rms error in the 6–8% range compares favorably to the 48% rms scatter about the mean spallation lives for these tests showing that the PLPS method is truly predictive.

Acknowledgment

This research was funded by Department of Energy under Grant No. UTSR 02-01-SR097, administrated by the South Carolina Institute for Energy Studies, Clemson University, with Dr. Richard Wenglarz as the program monitor. The authors want to thank Dr. Fang Tu for helpful discussions and initial coding work on neural networks.

References

[1] Miller, R. A., 1987, "Current Status of Thermal Barrier Coatings: An Overview," Surf. Coat. Technol., **30**(1), pp. 1–11.
[2] Padture, N. P., Gell, M., and Jordan, E. H., 2002, "Thermal Barrier Coatings for Gas-Turbine Engine Applications," Science, **296**(5566), pp. 280–284.
[3] Jones, R. L., 1996, "Metallurgical and Ceramic Protective Coatings," K. H. Stern, ed., Chapman and Hall, London, pp. 194–235.
[4] Evans, A. G., Mumm, D. R., Hutchinson, J. W., Meier, G. H., and Pettit, F. S., 2001, "Mechanisms Controlling the Durability of Thermal Barrier Coatings," Prog. Mater. Sci., **46**(5), pp. 505–553.
[5] Christensen, R. J., Lipkin, D. M., Clarke, D. R., and Murphy, K. S., 1996, "Nondestructive Evaluation of the Oxidation Stresses Through Thermal Barrier Coatings Using Cr^{3+} Piezospectroscopy," Appl. Phys. Lett., **69**(24), pp. 3754–3756.
[6] Gell, M., Sridharan, S., Wen, M., and Jordan, E. H., 2004, "Photoluminescence Piezospectroscopy: A Multi-Purpose Quality Control and NDI Technique for Thermal Barrier Coatings," Int. J. Appl. Ceram. Technol., **1**(4), pp. 316–329.
[7] Clarke, D. R., Christensen, R. J., and Tolpygo, V., 1997, "The Evolution of Oxidation Stresses in Zirconia Thermal Barrier Coated Superalloy Leading to Spalling Failure," Surf. Coat. Technol., **94–95**(1–3), pp. 89–93.
[8] Sohn, Y. H., Vaidyanathan, K., Ronski, M., Jordan, E. H., and Gell, M., 2001, "Thermal Cycling of EB-PVD/MCrAlY Thermal Barrier Coatings: II. Evolution of Photo-Stimulated Luminescence," Surf. Coat. Technol., **146–147**(1), pp. 102–109.
[9] Xie, L., Sohn, Y. H., Jordan, E. H., and Gell, M., 2003, "The Effect of Bond Coat Grit Blasting on the Durability and Thermally Grown Oxide Stress in an Electron Beam Physical Vapor Deposited Thermal Barrier Coating," Surf. Coat. Technol., **176**(1), pp. 57–66.
[10] Sridharan, S., Xie, L., Jordan, E. H., and Gell, M., 2004, "Stress Variation With Thermal Cycling in the Thermally Grown Oxide of an EB-PVD Thermal Barrier Coating," Surf. Coat. Technol., **179**(2–3), pp. 286–296.
[11] Lipkin, D. M., and Clarke, D. R., 1996, "Measurement of the Stress in Oxide Scales Formed by Oxidation of Alumina-Forming Alloys," Oxid. Met., **45**(3/4), 267–280.
[12] Nychka, J. A., and Clarke, D. R., 2001, "Damage Quantification in TBCs by Photo-Stimulated Luminescence Spectroscopy," Surf. Coat. Technol., **146–147**(1), pp. 110–116.
[13] Clarke, D. R., 2002, "Stress Generation During High-Temperature Oxidation of Metallic Alloys," Curr. Opin. Solid State Mater. Sci., **6**(3), pp. 237–244.
[14] Tolpygo, V. K., and Clarke, D. R., 2003, "Morphological Evolution of Thermal Barrier Coatings Induced by Cyclic Oxidation," Surf. Coat. Technol., **163**(1), pp. 81–86.
[15] Lipkin, D. M., Clarke, D. R., Hollatz, M., Bobeth, M., and Pompe, W., 1997, "Stress Development in Alumina Scales Formed Upon Oxidation of (111) NiAl Single Crystals," Corros. Sci., **39**(2), pp. 231–242.
[16] Selcuk, A., and Atkinson, A., 2003, "The Evolution of Residual Stress in the Thermally Grown Oxide on Pt Diffusion Bond Coats in TBCs," Acta Mater., **51**(2), pp. 535–549.
[17] Jordan, E. H., Sohn, Y. H., Xie, W., Gell, M., Xie, L., Tu, F., Pattipati, K. R., and Willet, P., 2001, "Residual Stress Measurement of Thermal Barrier Coatings Using Laser Fluorescence Technique and Their Life Prediction," *Autotestcon*, Valley Forge, PA, pp. 593–603.
[18] Zhu, D., Choi, S. R., and Miller, R. A., 2004, "Development and Thermal Fatigue Testing of Ceramic Thermal Barrier Coatings," Surf. Coat. Technol., **188–189**, pp. 146–152.
[19] Wen, M., Jordan, E. H., and Gell, M., 2005, "Evolution of Photo-Stimulated Luminescence of EB-PVD/(Ni,Pt)Al Thermal Barrier Coatings," Mater. Sci. Eng., A, **398**(1–2), pp. 99–107.
[20] Tsoukalas, L. H., and Uhrig, R. E., 1997, *Fuzzy and Neural Approaches in Engineering*, Wiley, New York.
[21] www.mathworks.com
[22] Michie, D., Spiegelhalter, D. J., and Taylor, C. C., 1994, *Machine Learning, Neural and Statistical Classification*, Ellis Horwood, Chap. 7.
[23] Bar-Shalom, Y., and Li, X. R., 1993, *Estimation and Tracking: Principles, Techniques and Software*, Artech House, Dedham, MA.
[24] Wen, M., Jordan, E. H., and Gell, M., 2005, "Effect of Temperature on Rumpling and Thermally Grown Oxide Stress in an EB-PVD Thermal Barrier Coating," Surf. Coat. Technol., in press.
[25] Vaidyanathan, K., Jordan, E. H., and Gell, M., 2004, "Surface Geometry and Strain Energy Effects in the Failure of a (Ni,Pt)Al/EB-PVD Thermal Barrier Coating," Acta Mater., **52**(5), pp. 1107–1115.
[26] Wen, M., Jordan, E. H., and Gell, M., 2005, "Analysis of Localized Damage in EB-PVD/(Ni,Pt)Al Thermal Barrier Coatings," Surf. Coat. Technol., in press.

Aerodynamic Instability and Life-Limiting Effects of Inlet and Interstage Water Injection Into Gas Turbines

Klaus Brun
Mechanical and Materials Engineering Division,
Southwest Research Institute,
P. O. Drawer 28510,
San Antonio, TX 78228-0510
e-mail: kbrun@swri.org

Rainer Kurz
Solar Turbines Incorporated,
9330 Sky Park Court,
San Diego, CA 92123-5398
e-mail: kurz_rainer_x@solarturbines.com

Harold R. Simmons
Mechanical and Materials Engineering Division,
Southwest Research Institute,
P. O. Drawer 28510,
San Antonio, TX 78228-0510
e-mail: hsimmons@swri.org

Gas turbine power enhancement technologies, such as inlet fogging, interstage water injection, saturation cooling, inlet chillers, and combustor injection, are being employed by end users without evaluating the potentially negative effects these devices may have on the operational integrity of the gas turbine. Particularly, the effect of these add-on devices, off-design operating conditions, nonstandard fuels, and compressor degradation/fouling on the gas turbine's axial compressor surge margin and aerodynamic stability is often overlooked. Nonetheless, compressor aerodynamic instabilities caused by these factors can be directly linked to blade high-cycle fatigue and subsequent catastrophic gas turbine failure; i.e., a careful analysis should always proceed the application of power enhancement devices, especially if the gas turbine is operated at extreme conditions, uses older internal parts that are degraded and weakened, or uses nonstandard fuels. This paper discusses a simplified method to evaluate the principal factors that affect the aerodynamic stability of a single-shaft gas turbine's axial compressor. As an example, the method is applied to a frame-type gas turbine and results are presented. These results show that inlet cooling alone will not cause gas turbine aerodynamic instabilities, but that it can be a contributing factor if for other reasons the machine's surge margin is already slim. The approach described herein can be employed to identify high-risk applications and bound the gas turbine operating regions to limit the risk of blade life reducing aerodynamic instability and potential catastrophic failure.
[DOI: 10.1115/1.2135819]

Introduction

As the widespread introduction of inlet cooling and water injection technologies for gas turbines is a relatively recent development, only limited historical field operating data and information on the affect on parts life is available. Nonetheless, because of the strong commercial advantage these technologies may bring to the operator, a large number of the devices have been installed over the past five years. Since the introduction of inlet cooling and water injection technologies for ground-based gas turbines, over 800 gas turbine installations worldwide have been built or retrofitted with these technologies. However, inlet air cooling, in combination with off-design operating conditions, nonstandard fuels, combustion dilution, and compressor blade degradation, can lead to compressor aerodynamic instabilities and subsequent gas turbine high-cycle fatigue blade failures. Namely, if the axial compressor's surge margin is significantly reduced by aberrant gas turbine application and operation, the machine may well be in an operating region of localized rotating stall and blade flutter. Flutter has a very strong potential to cause blade damage due to high-cycle metal fatigue.

A number of different gas turbine power augmentation technologies are currently available. They can be generally classified into two categories:

1. *Evaporative Cooling*: These include wetted media, fogging, wet compression, overspray, and interstage injection.
2. *Chillers*: Mechanical and absorption chillers with or without thermal energy storage.

In general, chillers only affect the gas turbine by directly cooling the inlet air temperature. This increases the gas turbines output power, but has otherwise minimal effects on the gas turbine's internal aerodynamics (i.e., the gas turbine is behaving as if it is running on a cold-weather day). Other than some cases where ice formation on the turbine inlet has caused problems with casing distortion, rubbing, and foreign object damage, few gas turbine failures have been directly linked to inlet chilling. However, inlet chillers are generally very large, expensive to operate, and rarely offer more than marginal economic benefits. Thus, they are not widely employed.

On the other hand, evaporative inlet cooling relies on injecting water droplets or vapor into the gas turbine's compressor (either upstream or interstage). Within the context of this paper, we will treat fogging and conventional evaporative cooling as having the same thermodynamic effect on the gas turbine. However, two different principles are employed: evaporative coolers utilize a wetted media that is exposed to the inlet airflow while inlet fogging sprays water mist into the gas turbine inlet system. Either system is normally designed to avoid liquid water carryover into the engine inlet, but fogging systems can sometimes (unintentionally or intentionally) "overspray" (i.e., a significant amount of water does not evaporate before entering the gas turbine inlet). Overspraying has a similar effect as interstage water injection in that water droplets will be present inside the first stages of the axial compressor.

Evaporative cooling has been demonstrated to provide between 5–10% power augmentation on hot/dry days and is, thus, commercially attractive. The principal difference between the various commercially available evaporative cooling technologies is the

Contributed by the International Gas Turbine Institute (IGTI) of ASME for publication in the JOURNAL OF ENGINEERING FOR GAS TURBINES AND POWER. Manuscript received October 1, 2003; final revision March 1, 2004. IGTI Review Chair: K. C. Hall. Paper presented at the ASME Turbo Expo 2005: Land, Sea, and Air, Reno, NV, June 6–9, 2005, Paper No. GT2005-68007.

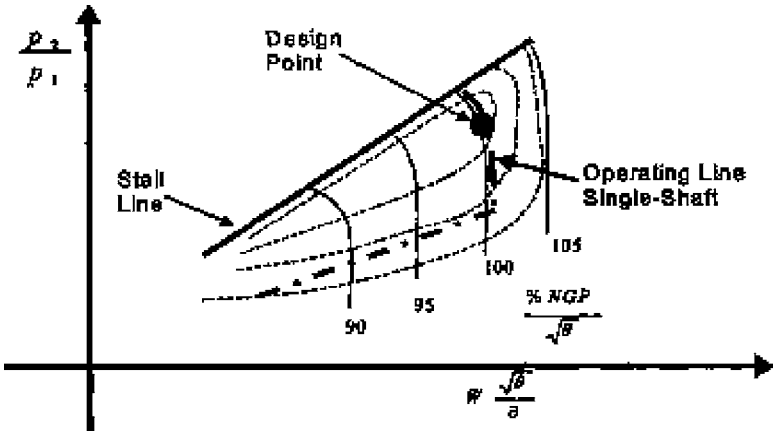

Fig. 1 Axial compressor performance map

quantity of water (percent air saturation), the water droplet size, and the location of the water injection ports into the gas turbine. However, the basic functional principle of all inlet water augmentation technologies is that they effectively reduce the gas turbine's inlet air temperature from the air's dry bulb temperature to the wet bulb temperature of the ambient air. This effective temperature difference depends on the ambient air's relative humidity and temperature, as well as the evaporative cooler's efficiency. The efficiency of evaporative devices is typically measured as the percent of the difference between dry and wet bulb temperature achieved; efficiencies of 80–95% have been reported.

When discussing gas turbine compressor aerodynamic instability, one must also address the issues of combustor diluent injection and low heating value fuels. Although these technologies are primarily concerned with NO_x reduction and fuel flexibility, gas turbine power output is increased and the gas turbine's aerodynamic stability can be severely affected. Most combustor diluent injection applications employ steam or water as the medium, but in some process power plants, CO_2 or nitrogen has successfully been utilized for NO_x reduction. Similarly, the use of low heating value fuels in a gas turbine produces the same net aerodynamic effect as combustor diluent injection. Thus, the influence of diluent injection and low heating value fuel combustion on gas turbine operational stability is also briefly discussed in this paper.

Previous Work on Evaporative Cooling and Wet Compression

Because of the recent popularity of water inlet injection, a number of researchers have studied the effects of the various technologies available on the market. For example, Horlock [1], Zheng et al. [2], Chaker et al. [3,4], Bhargava et al. [5,6], Hartel and Pfeiffer [7], White and Meacock [8], and Bhargava and Meher-Homji [9] all studied various aspects of wet compression in gas turbines. Most of this analysis was focused on thermodynamic effects and did not evaluate the long-term effects on the gas turbine operation and life, or the effects of water injection in combination with other nonstandard gas turbine conditions.

The study of wet compression technology in gas turbines dates back to the 1940s and 1950s, as is evident from the work on jet-engine water injection by Kleinschmidt [10] and Wilcox and Trout [11]. However, detailed thermodynamic analysis of wet compression in ground-based gas turbines is more recent. For example, Utamura et al. [12] studied the impact of droplet size in an industrial gas turbine. Later, Zheng et al. [2] and Hartel and Pfeiffer [7] performed an analysis of the thermodynamic effects of wet compression inside a gas turbine. Also, interstage water injection methods for gas turbine compressors were discussed by Ingistov [13,14].

Operational Effects of Evaporative Cooling

On standard gas turbine applications, such as natural gas power generation, few operational problems have been reported in the public domain that were directly attributed to inlet evaporative cooling. Ingistov [14] even documented that water injection has reduced compressor fouling and improved maintenance intervals. However, in a number of cases where excessive inlet water injection was combined with other factors, such as low heating value fuels, combustor steam injection, highly degraded blades, and off-design operating conditions (load, speed, and ambient temperatures), performance issues and failures have been anecdotally reported. Thus, prior to installing an evaporative cooling system on an existing gas turbine plant or determining the feasibility of water augmentation for a greenfield plant, a proper design review should be performed to prevent any damaging gas turbine operation.

The two most critical effects of gas turbine inlet evaporative are the influence on the aerodynamic stability of the gas turbine's axial compressor and the increased heat transfer of the air-water vapor-fuel mixture on the gas turbine hot-section vanes and buckets. These two effects are separately treated herein for single shaft gas turbines. Namely, detailed discussion is provided on:

1. The onset of aerodynamic compressor instabilities, such as rotating stall and surge that can result from the usage of evaporative cooling power augmentation technologies in gas turbines, is analyzed. A simple method is discussed to determine the compressors operational safety margin. This method can be employed as a design tool for new installations or as a safety check on existing facilities to assure that the gas turbines operate with a proper margin from potentially detrimental conditions.
2. The increased heat transfer due to the higher water vapor content of the exhaust mix is analyzed. A life fraction curve that can be used to estimate the hot-section parts life reduction is presented. This curve can aid the operator to evaluate increased operating costs and maintenance intervals of gas turbines with water inlet injection.

Compressor Aerodynamic Instability

A typical performance map for an axial compressor shows pressure ratio as a function of inlet volumetric flow (or mass flow) for a range of compressor speeds; this compressor map indicates that there are limits on the operating range of such a compressor (see Fig. 1). The limit for low-flow (or high-pressure ratio) operation is set by a flow instability known as surge. The exact location on the compressor map at which surge occurs can range widely depending on operating condition, and as a result, a surge control line is

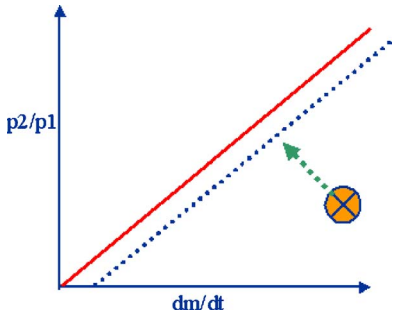

Fig. 2 Operating point moving toward surge line

Fig. 3 Compressor blade failed due to flutter-induced high-cycle fatigue

established with a significant margin above the flow at which surge is expected to occur. A typical surge margin is 10–15% or more of the design flow. Although in driven centrifugal compressors, surge is actively avoided using a recycle loop and valve, most axial compressors in a gas turbine have no actively controlled surge devices other than startup compressor discharge bleed.

Axial compressors will surge when forward flow through the compressor can no longer be maintained due to an increase in pressure across the compressor, and a momentary flow reversal occurs. Once surge occurs, the reversal of flow reduces the discharge pressure or increases the suction pressure, thus allowing forward flow to resume again until the pressure rise again reaches the surge point. This surge cycle continues at a low frequency until some change is made in the process or compressor conditions.

Thus, surge is a global instability in a compressor's flow that results in a complete breakdown and reversal of flow through the compressor. Surge occurs just below the minimum flow that the compressor can sustain against the existing suction to discharge pressure rise (head). When surge occurs, both flow rate and head decrease rapidly and air flows backward within the compressor. Full surge is a source of large axial dynamic forces applied to the gas turbine's elements and, hence, a flow phenomena that must be avoided.

Prior to reaching a surge event, a number of other aerodynamic flow instabilities are likely to occur within an axial compressor. These phenomena include rotating stall and blade flutter. Rotating stall is a localized flow separation (and/or reversal) cell that rotates at about 30–70% rotor speed in the direction of the compressor blades. As the compressor's operation condition moves close to the surge line, rotating stall typically initiates in the stator first and then, once fully developed, also enters the rotating blades.

Compressor rotating stall is a well-understood instability phenomenon in axial compressor aerodynamics. Rotating stall occurs when aerodynamic stability margins are exceeded, and results in a periodic excitation of blade loading. Emmons et al. [15] described rotating stall as a momentary aerodynamic overloading of an already highly loaded blade, which causes this particular blade to exhibit separation and blockage. This blockage restricts the flow through a blade passage and, consequently, diverts the incoming streamlines, causing an increase in incidence on one side of the blade passage and reduced incidence on the other. The increased incidence on the adjacent blade row will cause separation and blockage there, and a stall cell will propagate from blade to blade at a speed different from the compressor running speed.

Thus, rotating stall occurs when the flow's kinetic and pressure (potential) energy cannot overcome the required differential pressure across a blade passage to maintain forward flow and the flow locally "stalls out." As the surge line is passed, multiple rotating stall cells from both the rotor and stator elements combine to generate a full surge event with fully reversed and oscillating flows throughout the entire compressor. Rotating stall has to be distinguished from violent surge, where the flow pattern through the entire compressor breaks down. In many machines, rotating stall may manifest itself only by elevated vibration levels, but the dynamic flow instability leads to blade forces at frequencies other than multiples of running speed or blade pass frequency. The frequencies of rotating stall forces are typically not identified in a Campbell diagram.

Rotating stall is, thus, a precursor to full surge in which the flow locally, significantly deviates from its design magnitudes and angles. Rather than cleanly following the rotor and stator blades, the flow tends to separate on both the leading and trailing edges of the vanes, and periodic vortex shedding is initiated at a frequency determined by the flow's Strouhal number. (Strouhal number is a vortex shedding frequency multiplied by a characteristic length divided by the freestream flow velocity.) If this frequency coincides with any natural frequency of the blade, the blade will oscillate in harmony with the vortex shedding and begin to "flutter." Clearly, flutter imposes significant aerodynamic lateral and torsional forces on the blades at subsynchronous frequencies that can have a very detrimental effect on the life of the blades. For example, Fig. 3 shows a gas turbine compressor blade that failed due to flutter-induced high-cycle fatigue. Both rotating stall and flutter is often experienced when the compressor's operating surge margin is $<5\%$. Standard gas turbine instrumentation is usually not adequate to measure the occurrence of either of these precursors to surge.

Analysis Method

To investigate whether a compressor is operating in a region where rotating stall or flutter may occur, an aerodynamic surge analysis of the compressor must be performed. A basic axial compressor surge analysis consists of a one-dimensional (1D) thermodynamic and two-dimensional (2D) mean streamline flow analysis for each stage of the multistage compressor. The 2D mean streamline analysis yields power absorbed by each stage, total compressor power, and blade-to-blade flow angles. Using the results from the 2D analysis, the 1D thermodynamic analysis results for a particular stage's operating point can be mapped on the stage's characteristic performance curve to determine the local surge margin. Surge margin (SM) for axial compressors is typically defined as

$$\mathrm{SM} = \frac{Q_{\mathrm{design}} - Q_{\mathrm{surge}}}{Q_{\mathrm{design}}} \tag{1}$$

where Q is the volumetric flow rate.

For evaporative cooling, the model assumes that all water instantly vaporizes unless the flow is already saturated, in which case the model assumes that the water is carried by the flow axially through the compressor until the flow can absorb higher moisture content. Evaporative cooling primarily affects the gas turbine's inlet air temperature. Other thermodynamic parameters, such as flow density and specific heat of the air, are also affected by water injection, but the dominant effect is cooling. Nonetheless, although these physical properties play a minimal role in the overall thermodynamic performance of the gas turbine, they do affect the aerodynamic stability of the compressor and must be

included in a surge analysis. Thus, the model locally recalculates the mixture's physical properties based on the moisture content in the air.

Characteristic compressor stage performance curves are typically not available from the gas turbine manufacturer for a particular gas turbine model, so generic single-stage axial compressor curves can be adopted for the application by matching global performance parameters (power, efficiency, and mass flow) with given geometry and operating condition (speed and pressure ratio) information. Namely, using the general thermodynamic equation for stage efficiency

$$\eta_s \approx \frac{T_d - T_i}{T_i\left(\left(\frac{P_d}{P_i}\right)^{k/(k-1)} - 1\right)} \tag{2}$$

the compressors stage power requirements can be determined from

$$W = \Delta h \frac{dm}{dt} = \frac{dm}{dt} c_p (T_d - T_i) \tag{3}$$

and

$$W = \Delta \tau \omega = \omega \frac{dm}{dt} r (V_d^\theta - V_i^\theta) \tag{4}$$

Unless specific information on the compressor stages is available, a 15% original design surge margin is a reasonable and conservative assumption for all stages. Also, mean streamline individual stage compressor blade design angles can be estimated using Euler's turbomachinery equation and flow vector analysis

$$\frac{P_d}{P_s} = \left[1 + \frac{\eta r \omega}{c_p T_s}(c_2 \sin \alpha_2 - c_1 \sin \alpha_1)^{k/(k-1)}\right] \tag{5}$$

The same equation is subsequently used to determine actual blade incidence angles in the surge/flutter analysis. As the aim of the method is to determine changes in surge margin, rather than the total surge margin for a given operating condition, small inaccuracies of the characteristic compressor stage maps do not significantly affect the individual decreases in surge margin calculation.

Aerodynamic Stability Criteria

The results from the characteristic stage curve operating point mapping should assure that the lowest stage surge margin of any stage is always above 5% to conservatively avoid operating the compressor in a region of local aerodynamic instability. Also, from the 2D analysis, the highest local stator and rotor blade incidence angles should not exceed 8 and 12 deg, respectively; high blade incidence angles are an indicator for the potential of rotating stall development.

To avoid high-flow compressor stall, modulated inlet/stator guide vanes are employed on most gas turbines to reduce (throttle) the gas turbine's airflow at low load and start-up/shutdown conditions (see Fig. 1). The gas turbine's axial compressor's surge margin is decreased when operating at these conditions due to high incidence flow on the modulated stage blades. Hence, as compressor aerodynamic instabilities are more likely to occur during off-design operation, the above stability criteria must be met at all gas turbine operating points, including start-up and shutdown.

Factors that can have a significant affect on surge margin in a gas turbine and that should be parametrically evaluated in the surge analysis are:

- inlet water injection (evaporative cooling)
- interstage compressor water injection
- combustor diluent (steam, water, nitrogen, etc.) injection
- compressor blade degradation and fouling
- low or medium equivalent heating value fuels

As each of these factors can individually affect a gas turbine compressor's surge margin, their total impact must be determined for a given gas turbine operating condition. One should note that this analysis treats effects on surge margin as net additive (i.e., if, for example, 5% of surge margin is lost due to degradation and 6% of surge margin is lost due to fogging, the total surge margin decreases by 11%). Namely,

$$\Delta \mathrm{SM} = \sum_{i=1}^{n} \frac{\partial \mathrm{SM}}{\partial \Phi_i} \Delta \Phi_i \tag{6}$$

where Φ is the individually assessed factor influencing the stage surge margin. By parametrically mapping the individual factor effects on surge margin, a global operation limit can be established.

Instability Factor Influence Analysis

Although the above-described surge analysis is based on the sequential application of 1D thermodynamic and 2D mean streamline equations that are readily available in the public domain (see [2] for a comprehensive review), few end users or operators perform this safety check prior to installing water inlet and stage injection on their gas turbine. This has led to some gas turbine operational problems, and even blade failures. Thus, each of the principal factors that can affect the surge margin (evaporative cooling, interstage injection, combustor injection, blade fouling, and low heating value fuels) is individually discussed below. A parametric study of the relative influence of each factor on the axial compressor surge margin is provided for a typical large gas turbine power generation application. Although the analysis results presented herein are based on single-shaft gas turbines, a similar methodology can be developed and applied to two-shaft gas turbines.

Evaporative Cooling

Evaporative cooling of the inlet air into a gas turbine has become a popular method to increase a gas turbine's power. This technology was originally designed to only provide a power boost during peak demand times, but some plants now use fogging even for base load power. Long-term impacts on the gas turbine due to evaporative cooling are not well understood or documented at this time. The primary effect of evaporative cooling is that it reduces the inlet air's temperature to its wet bulb temperature. Typically, a power increase between 5% and 10% can be achieved on hot, dry days using evaporative cooling.

To demonstrate the reduction of surge margin due to evaporative cooling, example results of a surge analysis (as described above) are included herein for a large (>100 MW) industrial frame-type gas turbine. For this case, Fig. 4 shows analysis results for surge margin versus percent inlet fogging. Clearly, inlet evaporative cooling moves the compressor operating point closer to the surge line. At 100% saturation fogging, the surge margin was decreased by ~4% if the ambient relative humidity is about 20–30%. Thus, evaporative cooling techniques, such as inlet fogging alone, will not decrease the surge margin sufficiently to cause aerodynamic instabilities. However, they can be a contributing factor if for other reasons the machine's surge margin is already slim.

Interstage Water Injection

Beyond simple inlet fogging, some users have recently tested injecting water directly into the axial compressor through ports in the first stages of the gas turbine's compressor. Injecting water downstream from the inlet of a gas turbine has a similar effect as overspraying; it locally reduces the airflow temperature to that of the air's wet bulb temperature. This increases gas turbine output power, but also decreases the compressors surge margin. Figure 5

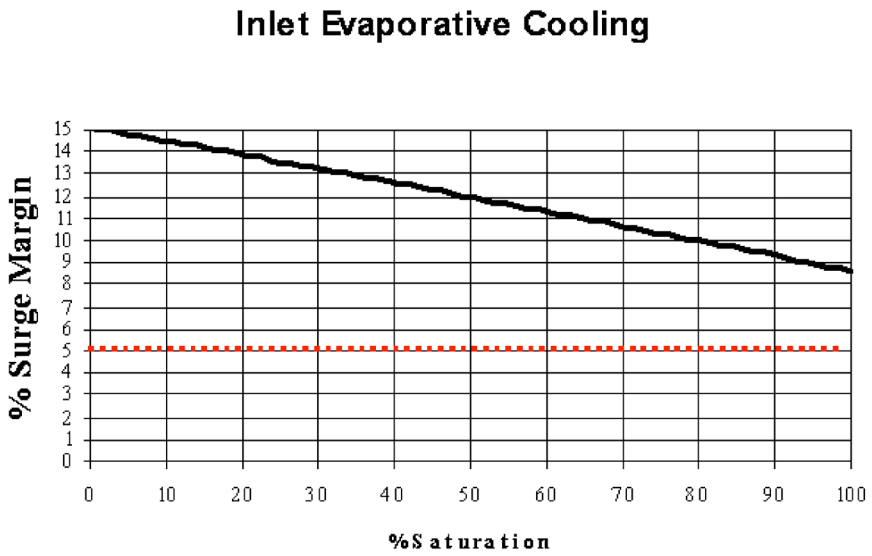

Fig. 4 Surge margin versus percent air saturation

shows a parametric study that evaluates the effect of stage water injection on the frame-type example gas turbine. The cases that are analyzed are:

- compressor stage 1 water injection (spray)
- compressor stage 2 water injection (spray)
- both stage 1 and 2 water injection (spray)

Compressor interstage water injection is seen to have a very strong affect on a compressor's surge margin. Also, study results showed that the further downstream in the compressor water is injected, the larger the loss in compressor surge margin. This is primarily because a stage's aerodynamics sensitivity to physical mixture property increases at higher pressures and temperatures. Specifically, a temperature reduction from dry bulb to wet bulb temperature in a downstream stage has a more significant effect on the blade flow incidence angles (and possible flow separation) than in an upstream stage. Similarly, Fig. 6 shows a parametric study of 100% saturation inlet evaporative cooling *in combination with* interstage water injection. Here, saturation inlet evaporative cooling was assumed for all cases.

Results in Fig. 6 demonstrate that evaporative cooling combined with interstage water injection can move a gas turbine's compressor into aerodynamic instability. Again, the further downstream the injection occurs, the more detrimental the effect on surge margin. The net effect of evaporative cooling and interstage injection is clearly additive.

As previously mentioned, if the compressor's remaining surge margin is $<5\%$, the machine may well be in an operating region of localized rotating stall that can subject the compressor to blade flutter. Flutter has a very strong potential to cause blade damage.

Equivalent Lower Heating Value

When operating a gas turbine with a fuel that has a heating value lower than that of its original design fuel, compressor aerodynamic stability can be affected. Most gas turbine fuel systems are designed for natural gas fuel, which has a heating value of approximately 5×10^7 J/kg, and can handle a Wobbe Index variation of $\pm 10\%$. Steam or water injection into the combustor to reduce NO_x emissions has a similar effect as using lower heating value fuels, since it decreases the equivalent heating value of the

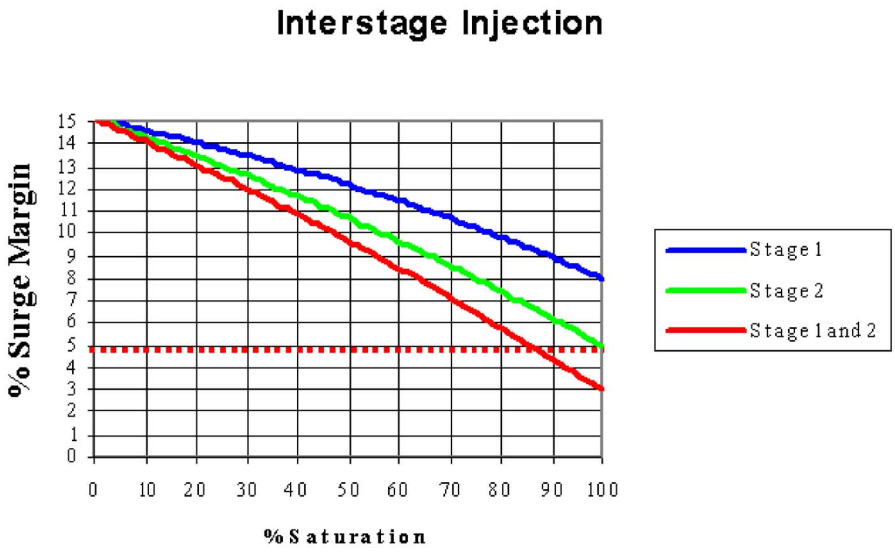

Fig. 5 Surge margin versus interstage injection

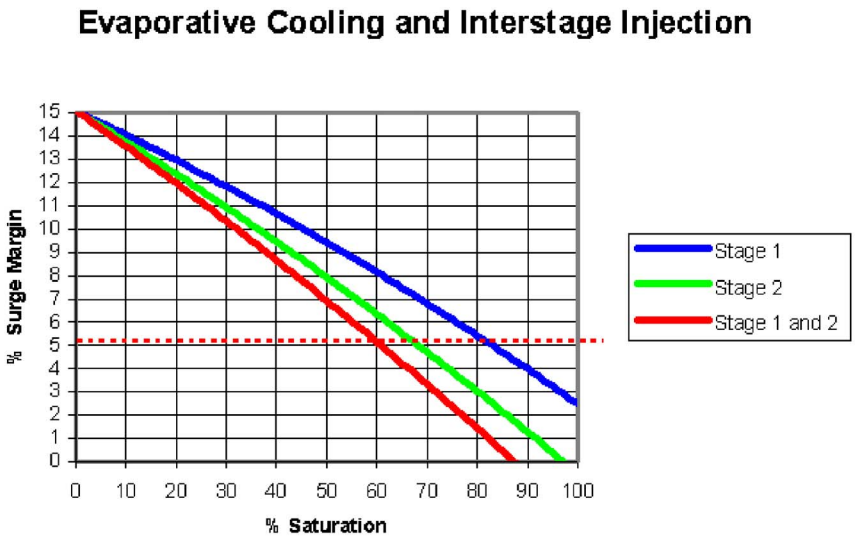

Fig. 6 Surge margin versus inlet evaporative cooling and interstage injection

fuel mixture in the combustor. If the fuel mixture's heating value is significantly lower than that of its design fuel, more fuel must be injected into the combustor to achieve the required equivalent gas turbine heat input and firing temperature. However, the increased volumetric input into the combustor also increases the compressor backpressure (when the gas turbine nozzle is flow choked) and, thus, decreases the compressor's surge margin. Therefore, care must be taken when operating a gas turbine with very low heating value fuels, such as synthesis gas, blast furnace gas, or refinery off gas. Figure 7 shows parametric study results for axial compressor surge margin versus fuel equivalent lower heating value. Equivalent heating value is defined as the resulting net heating value of a fuel/steam/water mixture in the combustor. Results from this analysis show that for a large industrial turbine, the compressor's surge margin can be reduced by about half when burning extremely low heating value fuels. Clearly, other physical effects related to burning low heating value fuels can cause aerodynamic instabilities in the combustor; however, a full discussion on combustion stability is beyond the scope of this paper.

In most standard applications, it is unlikely a user operates a fuel with more than a 10% deviation in heating value than that of natural gas, as most gas turbine's combustion systems could not tolerate that large a variation in Wobbe Index anyway. A 10% swing in heating value only translates into a surge margin decline of about 1%. Thus, the effect of burning lower heating value fuel on the compressor surge margin is probably not an issue for the majority of gas turbine applications.

Compressor Blade Degradation

While all effects discussed above cause the gas turbine compressor operating point to move closer to its surge line, compressor blade degradation due to fouling, erosion, corrosion, and particle fusing, actually moves the surge line toward the operating point. Nonetheless, the net effect is the same in that the gas turbine operates closer to a range of possible aerodynamic instability.

Compressor degradation is principally caused by loss of material on the leading and trailing edges of the blades (corrosion, erosion, and "sand-blasting") and surface fouling (build-up of material and roughening) on the concave and convex sides of the airfoils. Particle fusing and pitting generally does not affect an airfoils aerodynamic performance, and is more related to crack

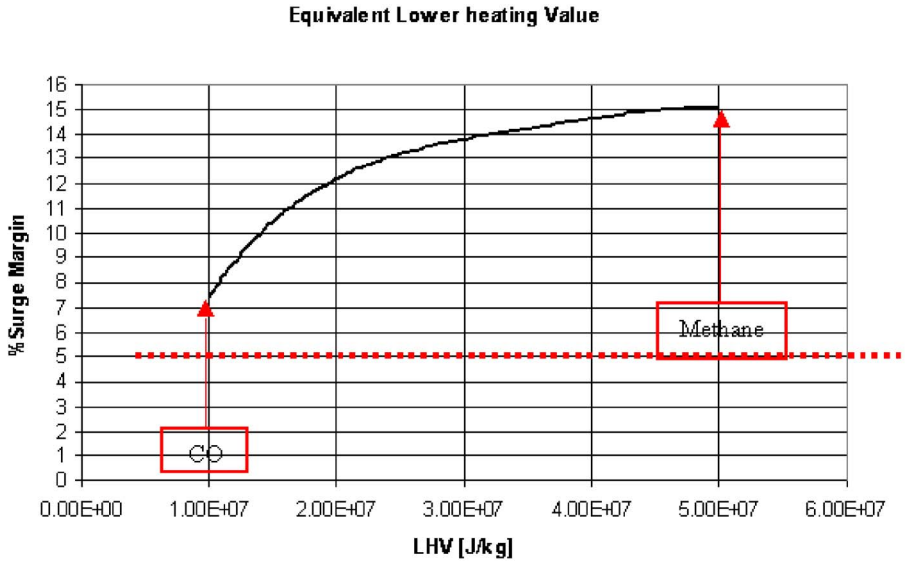

Fig. 7 Surge margin versus equivalent lower heating value

Fig. 8 Degraded compressor blade

formation and other material life limiting issues. Degradation affects a blade's ability to guide the flow. Namely, if the airfoil chord is shortened, the blade profile changed, or the surfaces roughened, the airflow will not follow the blades the same way it would on a new blade; the flow may slip and even separate (see Ref. [16]). Slip is an indicator of how effectively a rotating blade imparts tangential kinetic energy onto the airflow [17–26]. Slip is, thus, a direct function of blade degradation. Figure 8 shows a severely degraded compressor blade.

Compressor flow analysis results for surge margin versus degradation are shown in Fig. 9 for an industrial gas turbine. Here, fouling and corrosion are presented as an equivalent chord loss parameter (ECLP=equivalent chord loss/total chord length). The ECLP is often employed to account for all types of degradation in one convenient parameter. ECLP assumes that aerodynamic degradation due to fouling can be equated to an equivalent decrease of blade chord. Typical values for this parameter range from 0% to 0.3% in frame-type gas turbines, and 0–1% in aero-derivative gas turbines. Surge margin results in Fig. 9 show that even if blades are significantly degraded, a normal industrial gas turbine axial compressor would have had an adequate surge margin to be operating well away from rotating stall and flutter. However, if inlet evaporative cooling is installed on a gas turbine with a severely degraded compressor, the gas turbine could be operating in an area of compressor aerodynamic instability such as rotating stall and flutter.

Hot-Section Effects

The forced heat transfer coefficient between the hot combustion air and the turbine vane and bucket surfaces is a direct function of the air-vapor-fuel product mixture in the turbine. Generally, for a given mixture temperature, the higher the vapor content, the higher its energy content and heat transfer coefficient (i.e., the more water vapor is carried by the mixture, the more heat will transfer to the blades (buckets) and vanes). Since evaporative cooling devices amplify the moisture content of the airflow through a gas turbine, the overall internal heat load must be increased.

In modern gas turbines, the hot-section flow elements are optimized for a design point, where even small increases in surface metal temperature will lead to rapid hot oxidation of the turbine (i.e., these gas turbines are not designed for the increased heat load experienced when utilizing evaporative cooling devices and rapid failure will occur). The added heat transfer from evaporative cooling technologies is, thus, highly problematic for gas turbines with uncooled buckets and vanes (which tend to be older gas turbines).

This effect is somewhat offset in modern air-cooled gas turbines: the internal turbine blade cooling air is bled from the compressor discharge, and as this air also contains a higher water vapor content, it provides increased heat-carrying capacity of the cooling flow. Nonetheless, a detailed analysis shows that this offset does not fully overcome the increased heat transfer into the blades because of the high ratio of forced external versus mostly convective/conductive internal blade heat transfer. Furthermore, for cases of steam/water injection directly into the combustor, the effect is exasperated, as the external flow will clearly have a higher water-vapor content and increased mass flow.

A simplified analysis of the effect of inlet evaporative cooling on a large industrial gas turbine shows that the design life of blades and vanes can be reduced (Fig. 10) unless corrective cooling measures are taken. For example, if saturation evaporative cooling is employed in the industrial gas turbine, the water volume fraction in the exhaust can be as high as 15%. In this case, the hot gas path parts life would be reduced to about 88% of its original design life. Clearly, this is a significant increase of the gas turbine's maintenance costs and a reduced availability.

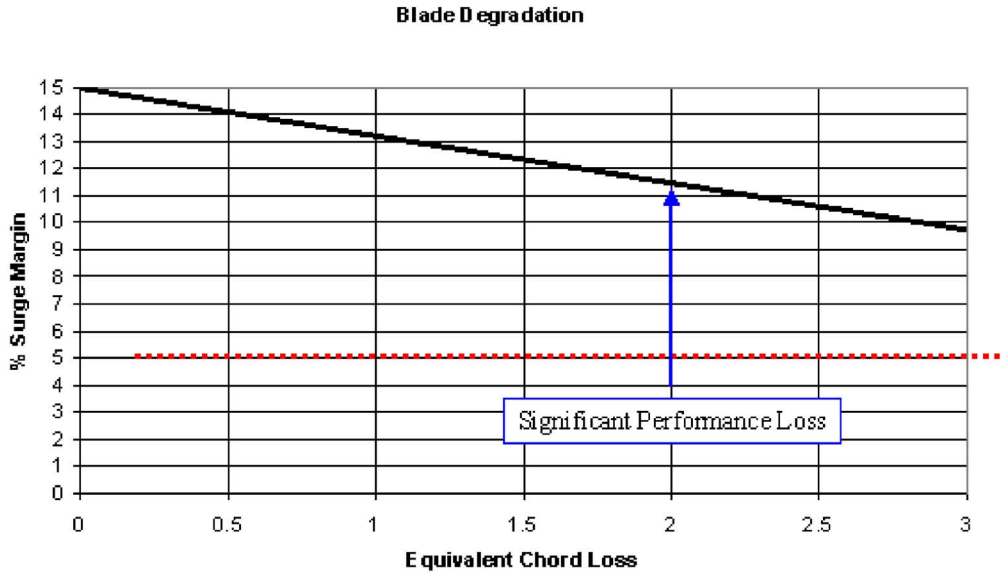

Fig. 9 Surge margin versus blade degradation

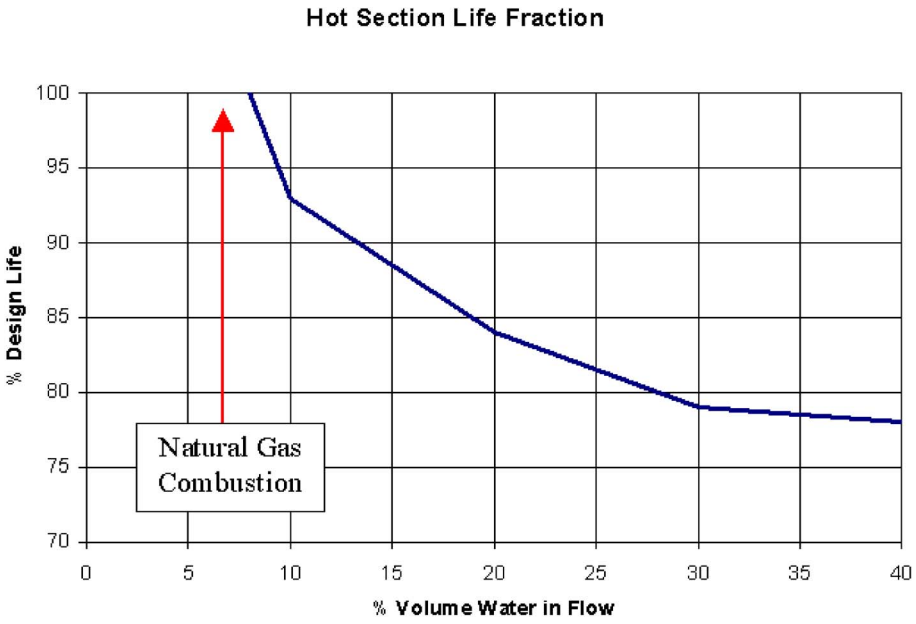

Fig. 10 Hot-section parts life fraction

Summary

Only limited historical field operating data and information on the long-term effect of gas turbine inlet evaporative cooling is available. However, over the past 15 years, more than 800 gas turbine installations worldwide have been built or retrofitted with these technologies. The basic functional principle of all evaporative cooling technologies is that they effectively reduce the gas turbine's inlet air temperature from the air's dry bulb temperature to the wet bulb temperature of the ambient air. Prior to utilizing evaporative cooling systems, a proper gas turbine aerodynamic stability review should be performed to prevent any potential operational and life-limiting problems. This paper discussed a simplified method to evaluate the principal factors that affect the aerodynamic stability of a single shaft gas turbine's axial compressor. As an example, the method was applied to a frame-type gas turbine and results were presented. Results showed that when inlet and interstage water injection is combined with other factors (such as low heating value fuels, combustor steam injection, and highly degraded blades), gas turbine compressor aerodynamic stability problems (such as rotating stall and flutter) will likely occur. These aerodynamic instabilities can be directly linked to blade high-cycle fatigue and possible catastrophic gas turbine failure. Furthermore, any water injection into a gas turbine (inlet, interstage, or combustor) will reduce the hot-section turbine parts life; a curve assessing the overall life reduction was included herein. The method described in this paper can be employed by end users and operators to identify high-risk applications and bound the gas turbine operating range to limit the potential risk of blade life reducing aerodynamic instability and subsequent catastrophic failure. Because the problems described are usually due to the coincidence of several factors, proper and timely engine maintenance can avoid many of the severe problems described herein.

Nomenclature

c_1, c_2 = local velocities
c_p = specific heat
dm/dt = mass flow
h = enthalpy
k = specific heat ratio
P = pressure
Q = volumetric flow
r = radius
SM = surge margin
T = temperature
V = velocity
W = power
ω = angular speed
α = flow incidence angles
η = stage efficiency
τ = torque
$\Delta\tau$ = change of torque
θ = tangential direction

Subscripts

d = discharge
I = inlet
s = suction
1,2 = interstage

References

[1] Horlock, J. H., 2001, "Compressor Performance With Water Injection," ASME Paper No. 2001-GT-0343.
[2] Zheng, Q., Sun, Y., Li, S., and Wang, Y., 2002, "Thermodynamic Analysis of Wet Compression Process in the Compressor of Gas Turbine," ASME Paper No. GT-2002-30590.
[3] Chaker, M., Meher-Homji, C. B., and Mee III, T. R., 2002, "Inlet Fogging of Gas Turbine Engines, Part A: Fog Droplet Thermodynamics, Heat Transfer and Practical Considerations," ASME Paper No. GT-2002-30562.
[4] Chaker, M., Meher-Homji, C. B., and Mee III, T. R., 2002, "Inlet Fogging of Gas Turbine Engines, Part B: Fog Droplet Sizing Analysis, Nozzle Type, Measurement and Testing," ASME Paper No. GT-2002-30563.
[5] Bhargava, R., Bianchi, M., Melino, F., Peretto, A., Meher-Homji, C. B., and Chaker, M. A., 2003, "Inlet Fogging for Gas Turbine Power Augmentation—A State-of-the-Art Review," *Proceedings, International Conference on Power Engineering-03 (ICOPE-03)*, Kobe, Japan, Paper No. C101.
[6] Bhargava, R., Bianchi, M., Melino, F., and Peretto, A., 2003, "Parametric Analysis of Combined Cycles Equipped With Inlet Fogging," ASME Paper No. GT-2003-38187.
[7] Hartel, C., and Pfeiffer, P., 2003, "Model Analysis of High-Fogging Effects on the Work of Compression," ASME Paper No. GT-2003-38117.
[8] White, A. J., and Meacock, A. J., 2003, "An Evaluation of the Effects of Water Injection on Compressor Performance," ASME Paper No. GT-2003-38237.
[9] Bhargava, R., and Meher-Homji, C. B., 2002, "Parametric Analysis of Existing Gas Turbines With Inlet Evaporative and Overspray Fogging," ASME Paper No. GT-2002-30560.
[10] Kleinschmidt, R. V., 1947, "Value of Wet Compression in Gas-Turbine Cycles," Mech. Eng. (Am. Soc. Mech. Eng.), **69**(2), pp. 115–116.
[11] Wilcox, E. C., and Trout, A. M., 1951, "Analysis of Thrust Augmentation of

Turbojet Engines by Water Injection at Compressor Inlet Including Charts for Calculating Compression Process With Water Injection," NACA Report No. 1006.
[12] Utamura, M., Kuwahara, T., Murata, H., and Horii, N., 1999, "Effects of Intensive Evaporative Cooling on Performance Characteristics of Land-Based Gas Turbine," Joint Power Generation Conference, 34.
[13] Ingistov, S., 2001, "Interstage Injection System for Heavy Duty Industrial Gas Turbine Model 7EA," ASME Paper No. 2001-GT-407.
[14] Ingistov, S., 2002, "Interstage Injection Into Axial Compressor, Gas Turbine Model 7EA," ASME Paper No. 2002-30656.
[15] Emmons, H. W., Pearson, C. F., and Grant, H. P., 1955, "Compressor Surge and Stall Propagation," Trans. ASME, **79**, pp. 455–469.
[16] Kurz, R., and Brun, K., 2000, "Degradation in Gas Turbine Systems," ASME Transactions, ASME J. Eng. Gas Turbines Power, **123**(1), pp. 70–77.
[17] Zheng, Q., 2003, "Thermodynamic Analyses of Wet Compression Process in the Compressor of Gas Turbine," ASME J. Turbomach., Transactions of ASME, **125**, pp. 160–165.
[18] Zheng, Q., Wang, G., Sun, Y., Liu, S., and Zhan, Z., 1997, "Experiments on Water Spraying Internal Cooling in Compressor of Gas Turbine," ASME Paper No. 97-GT-158.
[19] Behnken, R. L., and Muray, R. M., 1997, "Combined Air Injection Control of Rotating Stall and Bleed Valve Control of Surge," *Proceedings, 1997 American Control Conference*, Albuquerque, **2**, pp. 987–992.
[20] Behnken, R. L., 1997, "Nonlinear Control and Modeling of Rotating Stall in Axial Flow Compressor," Ph.D. thesis, California Institute of Technology (Tech. Report CDS 96-014).
[21] Greitzer, E. M., 1976, "Surge and Rotating Stall in Axial Flow Compressors: Parts I and II," ASME J. Eng. Power, **98**(2), pp. 190–217.
[22] Bagnoli, M., Bianchi, M., Melino, F., Peretto, A., Spina, P. R., Bhargava, R., and Ingistov, S., 2004, "A Parametric Study of Interstage Injection on GE Frame 7EA Gas Turbine," ASME Paper No. GT2004-53042.
[23] Moore, F. K., and Greitzer, E. M., 1986, "A Theory of Post-Stall Transients in Axial Compression Systems," ASME J. Eng. Gas Turbines Power, **108**, pp. 68–76, and pp. 231–239.
[24] Hill, P. G., 1963, "Aerodynamic and Thermodynamic Effects of Coolant Injection on Axial Compressors," Aeronaut. Q., **14** (Part 4), pp. 331–348.
[25] Jolly, S., 2003, "Inlet Fogging and Wet Compression Technology," ASME Paper No. GT-2003-38209.
[26] Chaker, M., Meher-Homji, C. B., and Mee, T., 2002, "Inlet Fogging of Gas Turbine Engines-Part I, Part II," ASME Paper No. GT-2002-30562.

Experimental Response of Simple Gas Hybrid Bearings for Oil-Free Turbomachinery

Deborah A. Osborne[1]
Honeywell International,
Aerospace/Engineering & Technology,
2525 W. 190th Street,
Torrance, CA 90504-6099
e-mail: deborah.osborne@honeywell.com

Luis San Andrés
Mechanical Engineering Department,
Texas A&M University,
College Station, TX 77843-3123
e-mail: lsanandres@mengr.tamu.edu

Gas film bearings offer unique advantages enabling successful deployment of high-speed microturbomachinery (<0.4 MW). Current applications encompass micropower generators, air cycle machines and turbo expanders. Mechanically complex gas foil bearings are in use; however, their excessive cost and lack of calibrated predictive tools deters their application to mass-produced systems. The present investigation provides experimental results for the rotordynamic performance of a small rotor supported on simple and inexpensive hybrid gas bearings with static and dynamic force characteristics desirable in high-speed turbomachinery. These characteristics are adequate load support, stiffness and damping coefficients, low friction and wear during rotor startup and shutdown, and most importantly, enhanced rotordynamic stability. The test results evidence the paramount effect of feed pressure on early rotor lift-off and substantially higher threshold speeds of rotordynamic instability. Higher supply pressures also determine larger bearing direct stiffnesses, and thus bring an increase in the rotor-bearing system critical speed albeit with a reduction in damping ratio. [DOI: 10.1115/1.1839922]

Introduction

Environmental concerns and extreme operating conditions drive the need for oil-free bearing support elements in small to moderate size turbomachinery (<0.4 MW). While oil-lubricated fluid film bearings provide adequate stiffness and damping characteristics, these support systems are limited by speed and temperature, and require considerable ancillary pumping, sealing, and plumbing. The use of process gas film bearings allows for less complex, lighter weight systems with lower emissions and improved efficiencies. Gas bearings for high-performance turbomachinery should be simple and reliable, load tolerant, and allow for operation at high rotor speeds with good dynamic force properties.

Gas bearings are in use in industrial applications such as auxiliary power units, air-cycle units in aircraft, short-life systems, i.e., cruise missiles and space applications, microturbines and small turbocompressors, and dental hand piece drills. Yet, there are several areas of concern that must be addressed and well understood by industry before gas film bearings become an acceptable and preferred alternative to oil-lubricated bearings [1–3]. The low viscosity of the gas film demands minute clearances to generate adequate load capacity. Damping, necessary to traverse critical speeds and to attenuate rotor response to sudden imbalance and thrust loads, becomes crucial. This requirement demands ever smaller clearances than those in oil film bearings, increasing the need to closely monitor tight manufacturing tolerances and surface finishes, thermal and elastic distortions, mounting, and alignments. Gas bearings also experience excessive drag and damaging wear at start-up and shut down, exhibit a typical hydrodynamic instability in rigid surface configurations, and even induce pneumatic hammer for externally pressurized configurations. In addition, gas bearing force coefficients (stiffness and damping) describing the dynamic forced performance are highly dependent on frequency [4], adding an additional degree of complexity when attempting to quantify bearing performance.

Multiple rigid lobed or pad bearing configurations, modifying a plain cylindrical bearing, can improve their dynamic forced performance by creating a preload (the dimensional difference in clearance between the lobe and the bearing), thereby providing direct stiffness at the bearing centered operating condition. For higher speeds and light loads, multiple-lobe bearings are known to offer a slightly more stable behavior than plain cylindrical journal bearings [5,6].

Excessive drag during the transient rubbing at start-up and shut down can be resolved by increasing the bearing load capacity, in particular at low speeds, by supplementing the hydrodynamic (self-generated) load capacity with pressurized gas fed directly into the bearing clearance. Hybrid (hydrostatic/hydrodynamic) bearings[2] may eliminate wear from solid contact at startup and shutdown and can substantially raise the threshold speed of rotor instability. Shapiro [7] indicates that a substantial increase in load capacity is achieved with a small expenditure of supply gas with the proper hybrid design. Gross [1] categorizes gas bearings by geometry and by type of compensation, i.e., the method by which resistance to lubricant flow is introduced between the pressurized source and the lubricating film. The types of compensation are divided into orifice, capillary, plug type, and inherently compensated (right at the entrance of the flow into the film clearance). Several other practical configurations include hybrid pressure dam bearings and porous bearings, for example.

Lund [8,9] advances the first approximate analysis and results for hybrid gas bearings. Zhang [10] optimizes the pocket geometry present in a hybrid journal bearing with annular and shallow pockets to attain the largest critical mass. Jing [11] finds that surface restriction through multiple axial saw tooth grooves offers more stable performance at the nearly centered journal position. Theoretical predictions and experimental results for the static and dynamic characteristics are included. Greenhill [12] reports experimental results showing the stable performance of prototype hybrid tilting pad gas bearings for speeds to 3 million DN. While offering more stable performance, these bearing configurations are considerably more complex, making low cost mass production difficult.

[1]This was completed during graduate studies with the Mechanical Engineering Department, Texas A&M University.

Contributed by the International Gas Turbine Institute (IGTI) of ASME for publication in the JOURNAL OF ENGINEERING FOR GAS TURBINES AND POWER. Paper presented at the International Gas Turbine and Aeroengine Congress and Exhibition, Atlanta, GA, June 16–19, 2003, Paper No. 2003-GT-38833. Manuscript received Oct. 2002; final manuscript received Mar. 2003. Assoc. Editor: H. R. Simmons.

[2]Hybrid bearings are often termed orifice compensated due to the feeding holes from the external pressurized source into the film lands. Note that in hydrostatic gas bearings, deep recesses or pockets are not recommended to avoid pneumatic hammer instability.

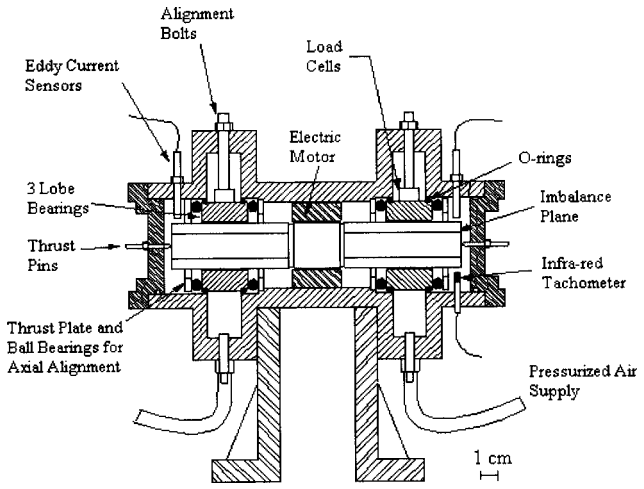

Fig. 1 Cross section view of test rig: rotor supported on three lobe gas bearings

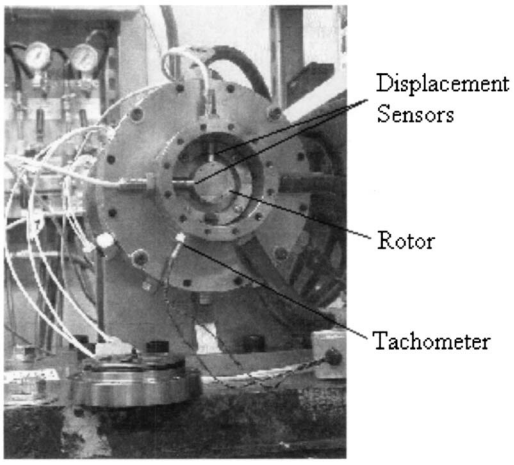

Fig. 2 Test rotor supported on three lobe test bearings showing eddy current sensors and infrared tachometer

Recently, advances concerning gas-lubricated hybrid configurations at high speeds (upwards of 100,000 rpm) have mostly been on the microscale, with application to Microelectromechanical systems (MEMs) and/or microturbomachines. Such systems have millimeter scale geometries and require operating speeds greater than one million rpm. Piekos [13,14] presents a simulation model and design charts for the development of silicon wafer gas-lubricated journal bearings for microfabricated MEMs. Fréchette reports the successful implementation of gas journal bearings supporting an electrostatic induction micromotor to speeds of 15,000 rpm[3] [15].

In the following, comprehensive rotordynamic experiments are conducted on a small rotor supported on three lobed hybrid gas bearings. The objective is to experimentally establish the stability and dynamic forced performance of the rotor-bearing system to assess the limitations of gas hybrid bearings for envisioned applications in oil-free turbomachinery. Experiments recording the rotor bearing run up and coastdown responses for various supply pressures evidence changes in critical speed location and significant variation in system damping ratios. In addition, the bearing "lift-off" characteristics and the identification of the threshold speed of instability and ensuing whirl frequency ratio demonstrate the stable performance of the bearing configuration tested.

San Andrés [16] details the theoretical background for the analysis of hybrid gas bearing dynamic forced performance. Reference [17] is a companion paper to the work reported here and presents correlations between experimental and predicted rotordynamic behavior for the test bearings and rotor detailed below.

Experimental Facility

Figure 1 shows a cross section of the test rig composed of a drive rotor, gas bearings and housings, air feed and discharge ports, and support instrumentation. The rotor weighs 0.827 kg (1.82 lb) and consists of a solid steel shaft, 15 mm diameter and 190 mm long, onto which an integral brushless dc motor and two solid steel sleeves [28.48 mm (1.12 in.) outer diameter] are press fit. Eight 1-mm-diameter holes equally spaced at the rotor ends allow for the placement of imbalance masses.[4] The integral motor maximum speed is 100,000 rpm and offers 0.9 kW of continuous power. A K-type thermocouple monitors the temperature of the motor armature. A rapid rise in motor temperature is a good indicator of sustained solid contact between the rotor and the test bearings. Each bearing housing has two O rings that effectively seal the bearing section and allow that section to be pressurized. The test chamber therefore has six sections with supply air inlet and outlet fittings into each section. Pressure gauges and flow meters record the air flow conditions into each bearing plenum chamber.

Figure 2 shows the end view of the test rig displaying two orthogonal positioned highly sensitive, eddy-current sensors that measure the displacement of the shaft at each end.[5] The displacement sensors have a sensitivity of 39.4 mV/μm (1 V/mil) with a linear range of 400 μm. The sensor recorded voltages are conditioned to remove the large dc bias offset before connection to two separate oscilloscopes and/or the data acquisition system. The oscilloscopes display the rotor orbit at the end monitored.

Force piezoelectric sensors mounted between the bearing housing and the test chamber alignment bolts measure the load transmitted through the bearings (as depicted in Fig. 1). The dynamic force sensors for the left bearing have a sensitivity of 118.8 mV/N (528.5 mV/lbf) and a dynamic range of 44.48 N (10 lbf); the sensors for the right bearing have a sensitivity of 12.0 mV/N (53.2 mV/lbf) and dynamic range of 444.8 N (100 lbf). A high-speed infrared tachometer sensor is rigidly mounted inside the test chamber to indicate the shaft speed and to provide a key phasor signal for data acquisition. Thrust pins mounted rigidly to the test chamber prevent the axial movement of the rotor. Díaz and San Andrés [18] describe the test rig design considerations and features in further detail.

Test Bearings. Table 1 presents the dimensions of the aluminum three-lobed hybrid bearings installed in the test rig. Figure 3 displays the bearing ($L/D=1.05$, $C_r/R=4.6\times10^{-3}$) with three pairs of 1 mm feed holes, spaced 120 deg apart, located at the apex of the lobes. The bearings are installed in the load on pad position (gravity) so that one pair of feed holes is located in the vertical direction above the rotor, and the other orifice pairs are 120 deg away from the vertical position.

Experimental Response of Rotor Supported on Three-Lobe Bearings

The static and dynamic response of the rotor supported on the three lobe bearings characterizes the overall performance of the rotor/bearing system. The feed pressure required to lift the rotor characterizes the static performance. Analysis of the rotor coast

[3]The difficulty with obtaining the appropriate terminal voltage is the speed limiting factor in this application, not the performance of the gas journal bearings.

[4]Note that balancing the rotor to reduce remnant imbalance proved very difficult.

[5]Experimental results refer to the left (L) and right (R) bearings with respect to the view in Fig. 2, having vertical (V) and horizontal (H) sensors at each bearing, i.e., LV refers to the rotor response recorded with the left vertical displacement sensor, for example.

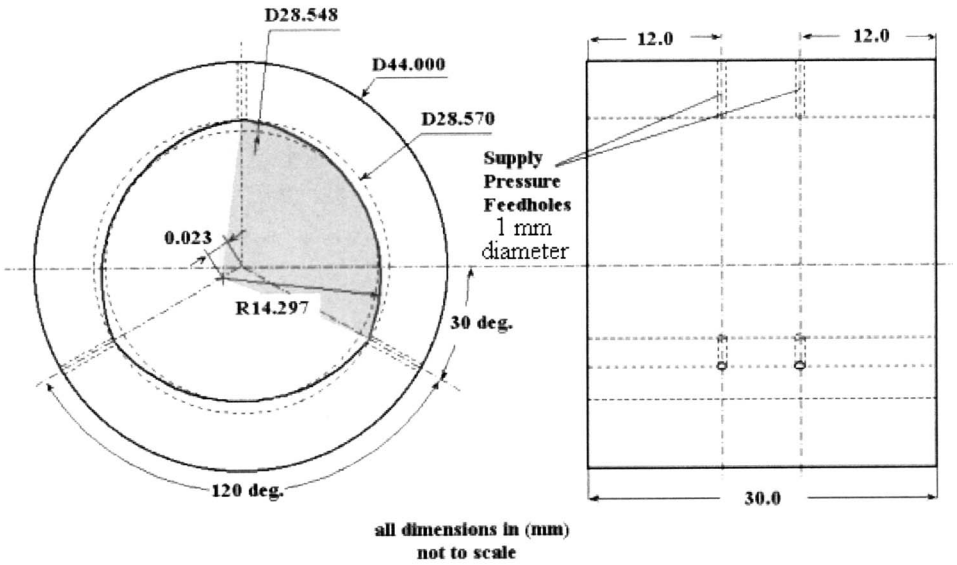

Fig. 3 Geometry of the three lobe test bearing showing preload and feedholes

down response to calibrated imbalance masses, for increasing supply pressures, determines several performance characteristics. The imbalance response at the critical speed gives an overall damping ratio using the bandwidth method. Waterfall plots of the coastdown response show the characteristic vibration patterns identifying the presence of whirl (or whip) instability and evidence the threshold speeds of instability. The transient response at startup demonstrates rotor lift-off characteristics.

Feed Pressure for Rotor Lift-Off. One of the great advantages of gas bearings is their significantly low drag. This advantage is not recognized until a full gas film develops between the rotor and the bearing(s). Therefore, the startup and touchdown stages of a rotor supported on gas bearings are critical due to the great opportunity for wear, and/or more extensive damage, caused by dry friction (hard contact) before the gas film develops between the rotor and the bearing. Ideally, the hybrid configuration provides hydrostatic feed pressure at start and stop conditions, therefore ensuring the presence of a gas film and preventing the rotor from contacting the bearings.

A certain feed pressure, counteracting the downward force due to the rotor weight, lifts the rotor off the bearing and allows a complete gas film to be formed. By observing the position of the shaft indicated by the oscilloscopes, upward motion of the rotor from its static position indicates the feed pressure for rotor lift-off. Opening the supply pressure line to a pressure ratio[6] of 1.27–1.37 ($\pm$0.07) lifts the rotor off the bearing. Upward motion of the shaft centerline and ensuing free rotation verifies rotor lift due to the hydrostatic feed. The shaft normally reaches a steady rotating speed around 2000–4000 rpm, depending on the magnitude of the supply pressure. Once the external pressurization has acted to lift the rotor, there is virtually no friction (drag) preventing the rotor from spinning. Thus, any small perturbation (mainly from the air supply and rotor surface imperfections) causes the rotor to spin either clockwise or counterclockwise.

Rotor Coastdown Responses for Various Supply Pressures. The coastdown response to calibrated imbalance masses gives useful information about the rotordynamic performance of the system. Such information includes the critical speed (the speed at which the response to imbalance is the largest), the overall rotor imbalance (the magnitude of response at high speeds), the overall damping capability, and the threshold speed of instability (should the system become unstable). Measured free-free mode shapes [19] indicate that the rotor is ''nearly'' rigid over the entire operable speed range of the test rig with the first bending mode occurring at 109,200 rpm. The rotor coastdown responses also reveal the effects of increasing feed pressures on the overall performance, the damping ratios, and the system critical speeds and threshold speeds.

Figure 4 shows a waterfall plot for the rotor base line direct response consisting of spectral lines of vibration versus speed while coasting down from a top speed of 60,000 rpm. The results show mainly synchronous vibration and no evidence of rubbing or subsynchronous vibration. The test results correspond to a high feed pressure equal to five times ambient pressure. Figure 5 depicts the rotor synchronous response to remnant imbalance for increasing supply pressures. Note that larger feed pressures generate more bearing direct stiffnesses as evidenced by the increase in critical speeds (from 15,750 to 23,500 rpm for feed pressure ratios equal to 2.36–5.08, respectively). The magnitude of rotor response at the critical speed increases as the supply pressure rises, thus demonstrating a marked reduction in system damping ratio. As the damping ratio decreases, a smaller and broader peak response becomes larger and narrower. The rotor responses show similar values of remnant imbalance (peak-to-peak amplitude of 9.4 μm at 39,000 rpm). The rotor amplitude of response begins to increase at larger speeds (upwards of 60,000 rpm) as it approaches the first bending critical speed.

Table 1 Characteristics of the three lobe bearings

Parameter	Magnitude
Lobe arc length	120°
Length, L	30 mm
Diameter, D	28.5 mm
Nominal Clearance, C_r	66$\pm$1.27 μm
Nominal preload	23$\pm$1.27 μm
Pad offset	50%
Nondimensional preload	0.33
Orifice diameter	1.0 mm
Number of orifices	6
Orifice location	At apex of pads (C_{max})

[6]The pressure ratio is defined as the ratio of the supply pressure to ambient pressure (both in absolute magnitudes).

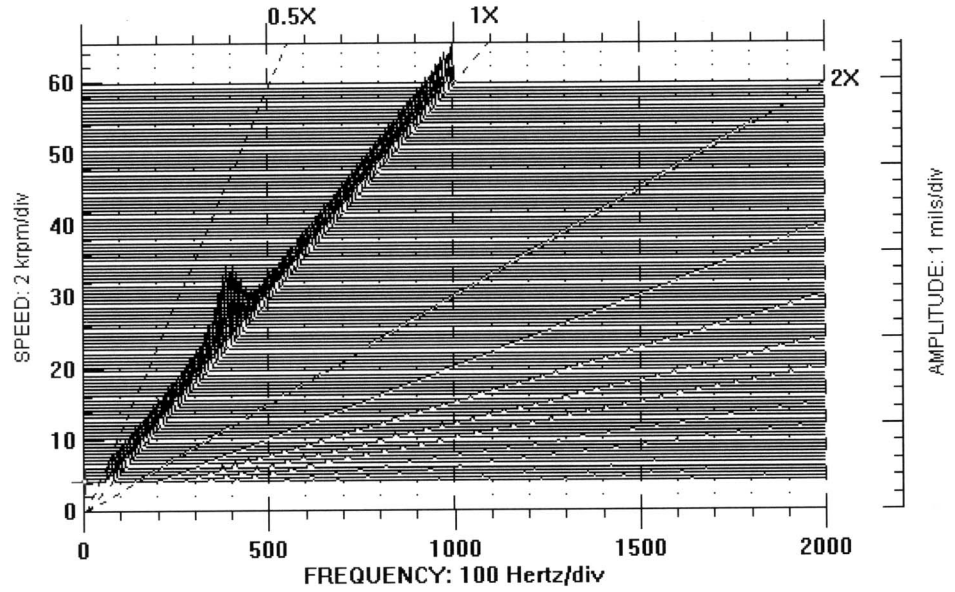

Fig. 4 Waterfall plot of rotor coastdown response at the right vertical eddy current sensor. Supply pressure ratio equal to 5.08 and remnant imbalance.

For increasing feed pressures, Table 2 gives the peak-to-peak amplitudes of synchronous displacement at the critical speed with reference to the nominal clearance. Comparing the response at the left vertical sensor to the response at the right vertical sensor shows a 1:2 relationship of amplitudes at each supply pressure. This large variance between the responses at the left and right bearings is likely due to a complex inherent imbalance in the rotor. Predictions of the system rotordynamic performance presented by Wilde [19] indicate the cylindrical and conical modes to occur very close to each other (within 1200–1700 rpm for increasing pressure ratios). The remnant imbalance condition in the rotor may excite a combination of the modes promoting the 1:2 amplitude relationship. The amplitudes of vibration at both sensors increase for increasing supply pressures and are not larger than the nominal clearance at the left bearings for any feed pressure.

Figure 6 presents the bearing transmitted load recorded during the rotor coastdown due to rotor remnant imbalance. The forces correspond to the bearing load at the sensor located 120 deg clockwise from the vertical plane. The location and magnitude of the peak-to-peak responses indicate an increase in stiffness and a decrease in damping ratio (similar results as with the displacement response). Although not shown here [19], the bearing transmitted forces are of similar magnitude (for a given supply pressure) at the three angular positions of measurement. Values of transmitted forces are as large as 34 N (peak-to-peak) at the critical speeds,

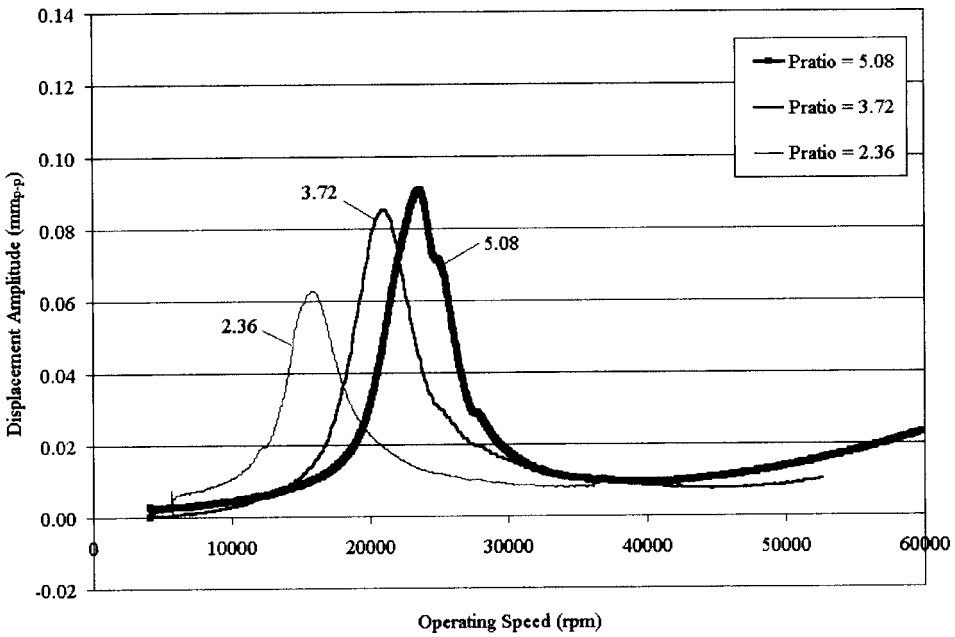

Fig. 5 Synchronous response of rotor supported on gas bearings (remnant imbalance). Measurements at the right vertical eddy current sensor for increasing supply pressure ratios.

Table 2 Peak-peak amplitude of synchronous response and critical speeds for rotor supported on three lobe gas bearings. Remnant imbalance condition (nominal diametral clearance =132 μm).

Sensor location	Supply pressure ratio	Critical speed (rpm)	Peak-to-Peak amplitude at critical speed (mm)	Ratio of amplitudes= amp/nominal clearance
Left vertical	5.08	25,450	0.042	0.318
	3.72	21,500	0.041	0.311
	2.36	16,400	0.030	0.227
Right vertical	5.08	23,500	0.090	0.682
	3.72	20,900	0.085	0.644
	2.36	15,750	0.063	0.477

and nominally 4.3 N (peak-to-peak) at higher speeds. Note that the static load due to rotor weight on each bearing is just 4 N.

Damping Ratios. The bandwidth method allows estimation of the rotor-bearing viscous damping ratio (ξ) while crossing a critical speed region. Figure 7 depicts the identified damping at the two locations of measurement ratios for increasing feed pressures. For low supply pressures, the damping ratio is as high as 12% and decreases towards just ~9% for the high feed pressure condition. The rotor responses in the horizontal direction do not show great variation in damping ratio.

Threshold Speeds of Rotor Instability. In the experiments, the rotor was accelerated to a high speed until a frequency analyzer and oscilloscopes evidenced the onset of violent rotor excursions characterized by a typical subsynchronous frequency. Sustained operation of the rotor at this threshold speed of instability or at even higher speeds is extremely harmful. The waterfall plot in Fig. 8 displays the run up rotor response for remnant imbalance and for a supply pressure ratio equal to 3.72. As the rotor accelerated from rest, the rotor displays its peak synchronous amplitude while crossing the critical speed, and continued in a stable condition until reaching the threshold speed of instability where a subsynchronous frequency just below the natural frequency (critical speed) becomes excited, sending the rotor into whirl instability. For this test, the ratio of the whirl frequency (330 Hz) to the threshold speed (890 Hz), known as the whirl frequency ratio (WFR), is 0.37.

The whirl frequency increases (although not seen in the plot) with speed until reaching the natural frequency (348 Hz), incurring "whip" motion where the whirl frequency remains locked at the natural frequency as the operating speed continues to increase. Once unstable, rotor vibration levels often become violently large making operation above the threshold speed of instability quite dangerous. The threshold speed of instability is a good measure of ultimate system performance, i.e., operation to the highest speed possible while maintaining safe vibration levels. The three lobe bearings operate free from any other subsynchronous vibration, until reaching the threshold speed of instability, for all supply pressure ratios.

As mentioned earlier, the hydrostatic feed tends to stiffen the rotor/bearing system and increases the critical speed for increasing supply pressures. Likewise, the threshold speeds of instability also increase with increasing supply pressures as depicted in Fig. 9. The experimental results clearly show a linear relationship, rendering much higher threshold speeds at higher feed pressures. It is important to note that the threshold speeds in Fig. 9 were obtained as the rotor is run up in speed, as opposed to coastdown. Threshold speeds bringing the rotor back to stable performance as deter-

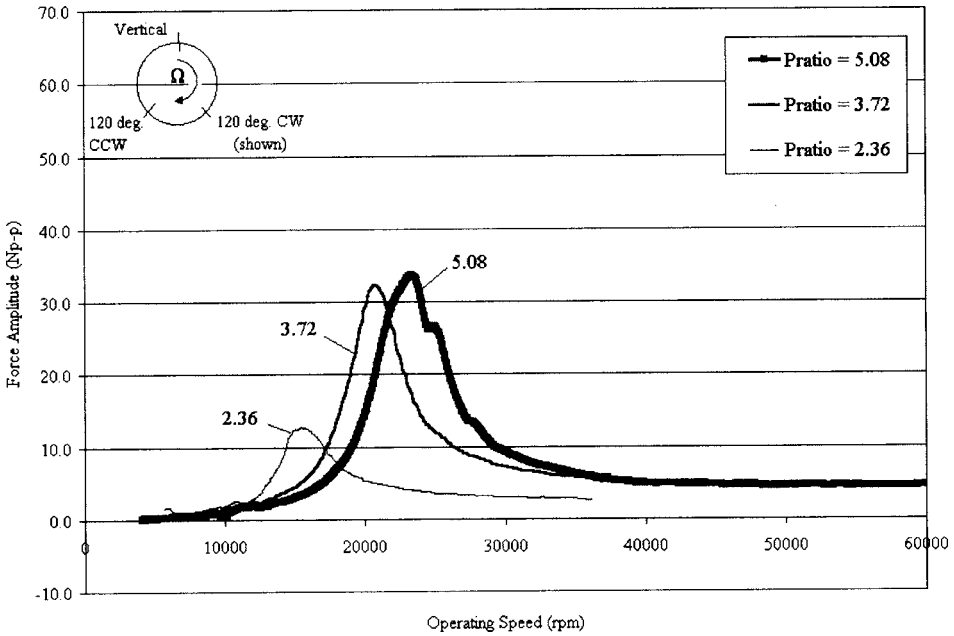

Fig. 6 Bearing forces from coastdown response to remnant imbalance. Measurements at 120 deg clockwise from vertical for increasing supply pressure ratios. Inset shows location of load cells.

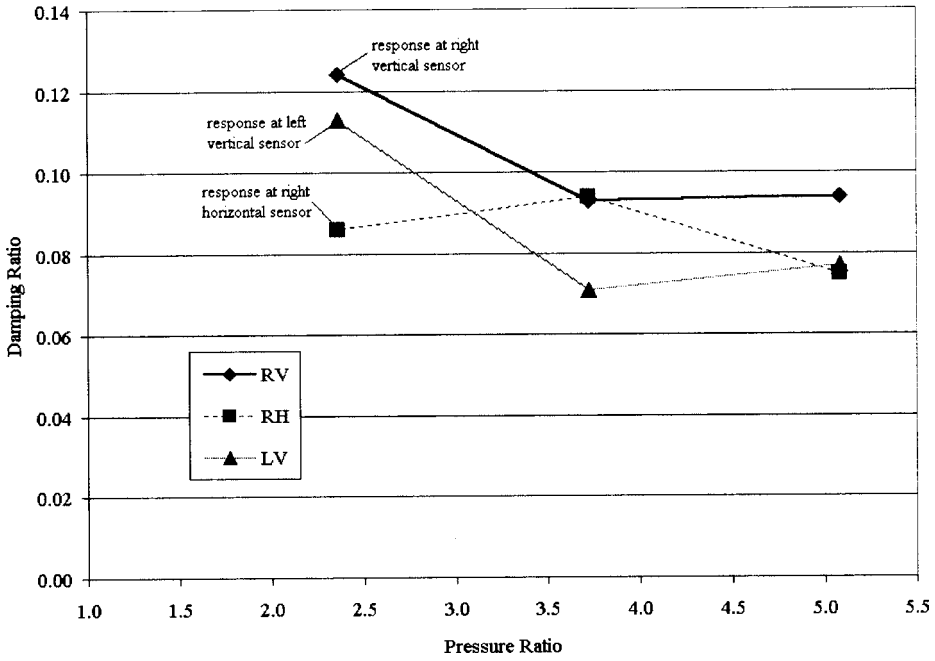

Fig. 7 Damping ratios for increasing supply pressure at three eddy current sensor locations

mined from a coastdown tend to be slightly lower and evidence the characteristics of a soft subcritical bifurcation.

Figure 10 demonstrates that the experimentally derived whirl frequency ratios increase with decreasing supply pressures, and further suggest that a purely hydrodynamic bearing configuration (supply pressure ratio 1.0) should exhibit a WFR of 0.49, i.e., the characteristic half-frequency whirl associated to plain cylindrical fluid film bearings. Note that threshold speeds of instability were not obtained for supply pressure ratios below 1.82 due to sustained rotor rub on its bearings. The experimental results show the major advantage of hybrid gas bearings, i.e., a large hydrostatic feed pressure, for example, pressure ratio equal to 5.08, increases the threshold speed of instability by a factor of 8 as compared to a purely hydrodynamic bearing configuration. This advantage is derived from the large direct stiffness coefficients generated with high feed pressures and also a decrease in cross-coupled stiffness coefficients.

Conclusion

Comprehensive rotordynamic experiments are conducted on a small rotor supported on three lobed hybrid (hydrostatic/hydrodynamic) rigid gas bearings. The rigid bearings comprised of preloaded 120 deg lobes with minute feed holes for external pressurization, for example, bleed off from a turbocharger compressor outlet. The bearing nominal clearance and dimensionless

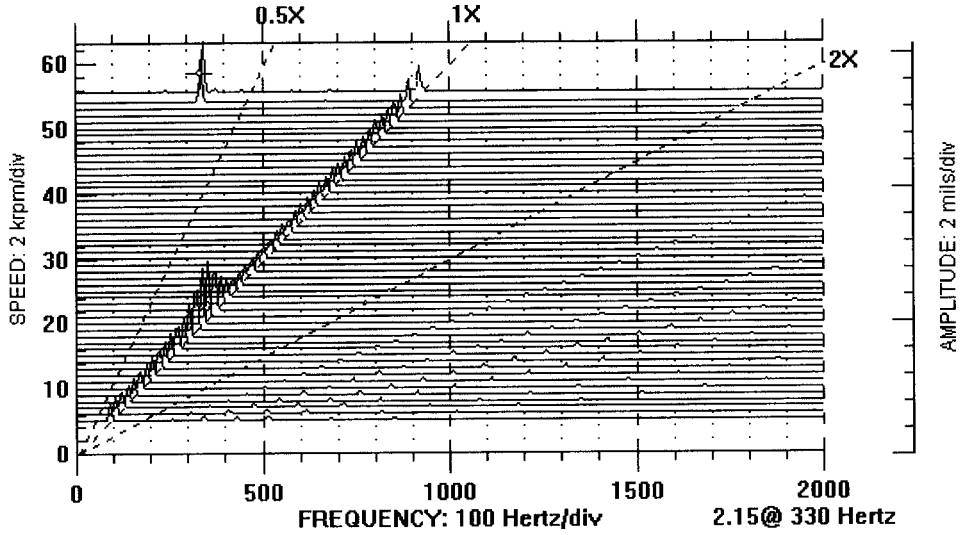

Fig. 8 Waterfall plot of rotor run up response to remnant imbalance at right vertical eddy current sensor with pressure ratio equal to 3.72

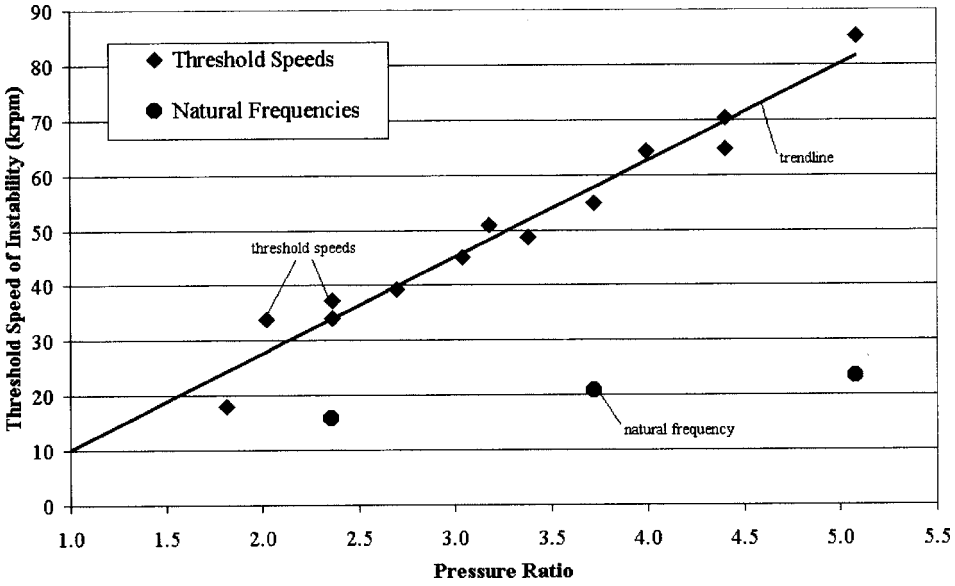

Fig. 9 Threshold speeds of instability and natural frequencies determined from speed run up tests conducted on rotor supported by three lobe gas bearings

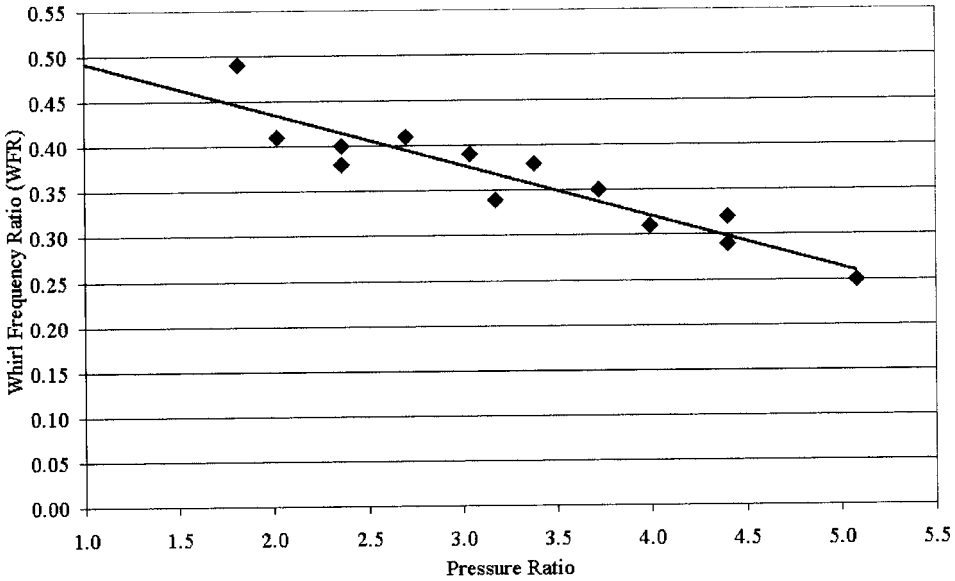

Fig. 10 Whirl frequency ratio determined from speed run up tests for rotor supported on three lobe gas bearings

preload are 66 μm and 0.33, respectively. The test rotor, weighing 827 g, integrates a dc motor and can achieve speeds as large as 100,000 rpm.

Without the rotor spinning, external pressurization lifts the test rotor at 1.36 bar (5 psig). For various imbalance conditions, coast-down tests from 60,000 rpm characterize the rotor response supported on the hybrid gas bearings. As the supply pressure rises, the rotor response shows an increase in critical speed and a noticeable reduction in damping ratio. Threshold speeds of instability also increase with increasing supply pressures, and whirl frequency ratios range from nearly 50% of rotor speed for a purely hydrodynamic condition to 25% for a pressure supply five times ambient. Bearing transmitted loads closely follow the rotor imbalance responses with large peak values while traversing the critical speeds.

Overall, the three lobe bearings offer a simple design, considering cost and manufacturability, with repeatable performance. While the rotor supported on the three lobe bearings does eventually experience rotordynamic instability, the rotor is capable of much higher speeds than if supported on purely hydrodynamic gas bearings. An increase in supply pressure ratio allows for even higher speed stable operation, albeit with less damping ratio while crossing a critical speed region.

A companion paper [17] describes further experimental results and the correlation with rotordynamic predictions.

Acknowledgment

The support of the American Association of University Women (with sponsorship by the Texas State Education Foundation), the Texas A&M University Energy Resources Program (College of Engineering), and the Turbomachinery Research Consortium (Texas A&M University) is gratefully acknowledged.

Nomenclature

C = nominal pad clearance (m)
C_{max} = maximum bearing clearance (m)
C_r = radial bearing clearance (m)
D = journal (rotor) diameter (m)
L = bearing axial length (m)
ζ = damping ratio

References

[1] Gross, W. A., 1969, "A Review of Developments in Externally Pressurized Gas Bearing Technology Since 1959," J. Lubr. Technol., **91**, pp. 161–165.
[2] Barnett, M. A., and Silver, A., 1970, "Application of Air Bearings to High-Speed Turbomachinery," *Proc. Combined National Farm, Construction & Industrial Machinery and Powerplant Meetings*, SAE, No. 700720.
[3] Chen, H. M., Howarth, R., Geren, B. et al., 2001, "Application of Foil Bearings to Helium Turbocompressor," *Proc. 30th Turbomachinery Symposium*, Houston, TX, pp. 103–114.
[4] San Andrés, L., and Vance, J., 2001, "Feasibility Study on Alternative Oil-Less Bearing Technologies for Automotive Turbochargers," Final Research Progress Report, Texas A&M University, College Station, TX.
[5] Garner, D. R., Lee, C. S., and Martin, F. A., 1980, "Stability of Profile Bore Bearings: Influence of Bearing Type Selection," Tribol. Int., **13**, pp. 204–210.
[6] Fuller, D. D., 1969, "A Review of the State-of-the-Art for the Design of Self-Acting Gas-Lubricated Bearings," J. Lubr. Technol., **91**, pp. 1–16.
[7] Shapiro, W., 1969, "Steady-State and Dynamic Analyses of Gas-Lubricated Hybrid Journal Bearings," J. Lubr. Technol., **91**, pp. 171–180.
[8] Lund, J. W., 1964, "The Hydrostatic Gas Journal Bearing With Journal Rotation and Vibration," J. Basic Eng., **86**, pp. 328–336.
[9] Lund, J. W., 1967, "A Theoretical Analysis of Whirl Instability and Pneumatic Hammer for a Rigid Rotor in Pressurized Gas Journal Bearings," ASME J. Lubr. Technol., **89**, pp. 154–166.
[10] Zhang, R. Q., and Chang, H. S., 1995, "A New Type of Hydrostatic/Hydrodynamic Gas Journal Bearing and Its Optimization for Maximum Stability," Tribol. Trans., **38**, pp. 589–594.
[11] Jing, G., Zhang, P., and Hu, Z. Y., 1997, "On Fundamental Characteristics of a Hybrid Gas-Lubricated Journal Bearing With Surface-Restriction Compensation," Tribol. Trans., **40**, pp. 528–536.
[12] Greenhill, L. M., and Lease, V. J., 2001, "Hydrostatic Pivoted Pad Bearings for Oil-Free Turbomachinery," *Proc. ISCORMA Conference*, Lake Tahoe, CA, No. 3005.
[13] Piekos, E. S., and Breuer, K. S., 1999, "Pseudospectral Orbit Simulation of Nonideal Gas-Lubricated Journal Bearings for Microfabricated Turbomachines," ASME J. Tribol., **121**, pp. 604–609.
[14] Piekos, E. S., 2000, "Numerical Simulation of Gas-Lubricated Journal Bearings for Microfabricated Machines," Ph.D. thesis, Massachusetts Institute of Technology, Cambridge, MA.
[15] Fréchette, L. G., Nagle, S. F. et al., 2001, "An Electrostatic Induction Micromotor Supported on Gas-Lubricated Bearings," *Proc. 4th IEEE International Micro Electro Mechanical Systems Conference, MEMS 2001*, Interlaken, Switzerland.
[16] San Andrés, L., and Wilde, D. A., 2001, "Finite Element Analysis of Gas Bearings for Oil-Free Turbomachinery," Revue Européenne des Eléments Finis, **10**, pp. 769–790.
[17] Wilde, D. A., and San Andrés, L., 2003, "Comparison of Rotordynamic Analysis Predictions With the Test Response of Simple Gas Hybrid Bearings for Oil Free Turbomachinery," ASME Paper No. 2003-GT-38859.
[18] Díaz, S., and San Andrés, L., 1999, "High Speed Test Rig for Identification of Gas Journal Bearing Performance: Design, Constraints, and Fabrications," The Turbomachinery Laboratory, Texas A&M University, College Station, TX, Report No. TRC-RD-1-99.
[19] Wilde, D. A., 2002, "Experimental Response of Gas Hybrid Bearings for High Speed Oil-Free Turbomachinery," Masters thesis, Texas A&M University, College Station, TX.

Comparison of Rotordynamic Analysis Predictions With the Test Response of Simple Gas Hybrid Bearings for Oil Free Turbomachinery

Deborah A. Osborne[1]
Honeywell International,
Aerospace/Engineering & Technology,
2525 W. 190th Street,
Torrance, CA 90504-6099
e-mail: deborah.osborne@honeywell.com

Luis San Andrés
Mechanical Engineering Department,
Texas A&M University,
College Station, TX 77843-3123
e-mail: lsanandres@mengr.tamu.edu

Current applications of gas film bearings in high-speed oil-free microturbomachinery (<0.4 MW) require calibrated predictive tools to successfully deploy their application to mass-produced systems, for example, oil-free turbochargers. The present investigation details the linear rotordynamic analysis of a test rotor supported on externally pressurized gas bearings. Model predictions are compared with the test rotordynamic response determined through comprehensive experiments conducted on a small rotor supported on three lobed hybrid (hydrostatic/hydrodynamic) rigid gas bearings. Predictions for the rotor-bearing system synchronous response to imbalance show good agreement with measurements during rotor coastdowns, and manifest a decrease in damping ratio as the level of external pressurization increases. The rotor-bearing eigenvalue analysis forwards natural frequencies in accordance with the measurements, and null damping ratios evidence the threshold speeds of rotordynamic instability. Estimated whirl frequency ratios are typically 50% of rotor speed, thus predicting subsynchronous instabilities at lower rotor speeds than found experimentally when increasing the magnitude of feed pressurization. Rationale asserting the nature of the discrepancies calls for further analysis.
[DOI: 10.1115/1.1839923]

Introduction

Gas-lubricated bearings, as opposed to oil-lubricated bearings, offer many advantages for application to high-speed small-scale turbomachinery. Using process gas as the lubricant offers more cleanliness and the elimination of process contamination by buffer lubricants. Under extreme temperature and speed conditions, gases offer more stability without lubricant vaporization, cavitation, solidification, or decomposition. Gas-lubricated bearings also exhibit lower friction and power usage. In addition, gas bearings do not require the costly, weighty, and complex sealing and lubricant circulation systems required for oil-lubricated systems.

The main disadvantages of gas-lubricated bearings are the lack of damping and low load capacity due to the low viscosity of the gas film. Gas-lubricated bearings therefore require minute clearances demanding tight manufacturing tolerances and surface finishes, and close monitoring of thermal and elastic distortions, mounting, and alignments. In addition, the frequency dependence of gas bearing force coefficients describing their dynamic forced performance [1] adds an additional degree of complexity when attempting to quantify bearing performance.

Fuller [2] reviews the major advances in gas bearing design and modeling reported through the 1960s. Elrod and Malanoski [3] studied the plain cylindrical bearing with a continuous gas film, providing computer-generated solutions. Plain cylindrical bearings offer the best load capacity, but compromise damping characteristics and often experience a dangerous self-excited hydrodynamic instability. Yet, these bearings offer the most affordable design when considering manufacturability and cost. Efficient numerical solutions of the Reynolds equation (predicting the pressure profile within the continuous film) and analyses addressing the major issue of rotor-bearing stability are readily available [4–11].

Supplementing the hydrodynamic (self-generated) load capacity with pressurized gas fed directly into the bearing clearance, resolves the concern of low load capacity at startup, thereby creating a hybrid bearing[2]. Utilizing the proper hybrid bearing design can substantially raise the threshold of instability permitting larger spans of stable response over the rotor/bearing system operating range with a relatively small expenditure of supply gas [12]. Lund [13,14] advances the first approximate analysis and results for hybrid (hydrostatic/hydrodynamic) gas bearings. Piekos [15,16] presents a simulation model and design charts for the application of gas-lubricated journal bearings to Microelectromechanical systems (MEMs) and/or microturbomachines.

San Andrés and Wilde [17] present a finite element (FE) computational analysis for high-speed hybrid gas bearings including external orifice pressurization applied to a three-pad journal bearing. Predictions evidence the strong dependence of the dynamic force coefficients on excitation frequency, which clearly affects the rotordynamics of high-speed rotors supported on air bearings by promoting regions of unstable response with potentially harmful subsynchronous motions.

In a companion paper to the work hereby presented, Wilde and San Andrés [18] present comprehensive rotordynamic experiments conducted on a small rotor supported on three lobed hybrid gas bearings. The rigid bearings comprised of preloaded 120° lobes with minute feed holes for external pressurization, for ex-

[1]This work was completed during graduate studies with the Mechanical Engineering Department, Texas A&M University.

Contributed by the International Gas Turbine Institute (IGTI) of ASME for publication in the JOURNAL OF ENGINEERING FOR GAS TURBINES AND POWER. Paper presented at the International Gas Turbine and Aeroengine Congress and Exhibition, Atlanta, GA, June 16–19, 2003, Paper No. 2003-GT-38859. Manuscript received Oct. 2002; final manuscript received Mar. 2003. Assoc. Editor: H. R. Simmons.

[2]Hybrid bearings are often termed orifice compensated due to the feeding holes from the external pressurization to the film lands [1]. Note that in hydrostatic gas bearings, deep recesses or pockets are not recommended to avoid pneumatic hammer instability.

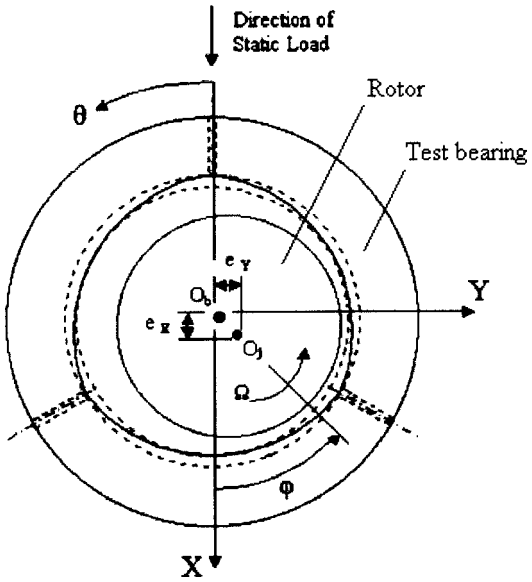

Fig. 1 Schematic view of test three lobe hybrid gas bearing

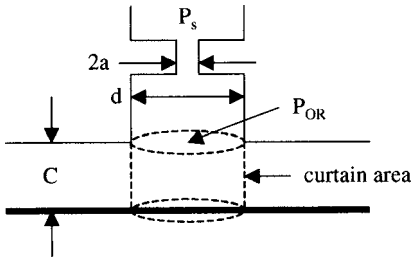

Fig. 2 Geometry of feed orifice in gas hybrid bearing

ample, bleed off from a turbocharger compressor outlet. The test rotor, weighing 827 g, integrates a dc motor and can achieve speeds to 100,000 rpm. For various imbalance conditions, coast-down tests from 60,000 rpm characterize the rotor response supported on the bearings. As the supply pressure rises, the rotor response shows an increase in critical speed and a noticeable reduction in damping ratio. Threshold speeds of instability also increase with increasing supply pressures, and whirl frequency ratios range from nearly 50% of rotor speed for a purely hydrodynamic condition to 25% for a pressure supply five times ambient.

Reported herein, a FE model for hybrid gas bearing analysis predicts frequency dependent stiffness and damping force coefficients at the operating speeds and levels of feed pressure corresponding to experimental values reported in Ref. [18]. Empirical determination of the orifice discharge coefficients is essential for reliable prediction of the gas bearing static and dynamic force performance characteristics. The rotordynamic analysis consists of modeling the test rotor as a collection of mass and spring elements, incorporating the bearings' force (stiffness and damping) coefficients, and determining the linear stability and synchronous response characteristics of the rotor-bearing system. The stability analysis includes examination of the system eigenvalues, and identification of damping ratios and whirl frequency ratio at the threshold speed of instability. Synchronous response predictions evidence the critical speeds and fundamental damping ratio.

Rotordynamic Analysis of Test Rotor Supported on Three Lobe Gas Bearings

Refer to Ref. [18] for a discussion of the test rotor and gas bearings, operating conditions, and major experimental findings. In addition, the reader may find it useful to consult Ref. [19] for detailed coverage of the research program on gas bearings, including test results for other bearing configurations. The test gas bearings are modeled using a FE computational program for solving the ideal gas thin film Reynolds equation [17]. A rotordynamics software suite [20] provides the stability and response predictions for the studied rotor-bearing system.

Gas Bearing Model. Figure 1 shows the test hybrid (hydrostatic/hydrodynamic) gas bearing consisting of three bearing lobes, each with a pair of feed orifices at the lobe apex. The gas film thickness (h) is a function of the nominal clearance (C), pad preload (r_p), pad offset angle (Θ_p), and journal center displacements (e_X, e_Y). The Reynolds equation defines the pressure field (P) in an ideal gas film with constant viscosity [17], i.e.

$$\nabla\cdot\left(\frac{-h^3P}{12\mu}\cdot\nabla(P)\right)+\frac{\Omega\cdot R}{2}\cdot\frac{\partial}{\partial x}(Ph)+\frac{\partial}{\partial t}(Ph)=\frac{(\Re_g T)\cdot\dot{m}_{\mathrm{OR}}}{A}, \tag{1}$$

where ($\dot{m}_{\mathrm{OR}}$), a mass flow source due to local hydrostatic feed, is a function of the pressure ratio $\bar{P}=P/P_s$ and the orifice geometrical configuration (see Fig. 2)

$$\dot{m}_{\mathrm{OR}}=\Phi\cdot m(\bar{p})\cdot g(h),\quad \Phi=\frac{\pi a^2}{\sqrt{\Re_g T}}P_s \tag{2}$$

with

$$m(\bar{P})=\begin{cases}\left(2\cdot\dfrac{k}{k+1}\right)^{1/2}\cdot\left(\dfrac{2}{k+1}\right)^{1/k-1} & \text{for } \bar{P}<\bar{P}_{\mathrm{choke}},\ \bar{P}_{\mathrm{choke}}=\left(\dfrac{2}{k+1}\right)^{k/k-1}\\ \alpha'\cdot\left(2\cdot\dfrac{k}{k-1}\right)^{1/2}\cdot\bar{P}^{1/k}\cdot(1-\bar{P}^{k-1/k})^{1/2} & \text{for } \bar{P}>\bar{P}_{\mathrm{choke}}\end{cases} \quad \text{and} \quad g(h)=\frac{H}{\left(H^2+\dfrac{a^2}{dC}\right)^{1/2}}. \tag{3}$$

In the test bearings, the feed orifices discharge directly to the bearing surface without an expansion volume to prevent the flow versus pressure time lag associated with pneumatic hammer instability. Thus, the orifices are inherent restrictors where the supply to orifice pressure drop occurs at the curtain area (πdC).

In the dynamic analysis of the gas bearings, the journal executes small amplitude motions with frequency (ω) about an equilibrium position determined by a static load. Corresponding perturbations of the film thickness and pressure follow, and the analysis advances Reynolds equations defining the equilibrium (zeroth order) and first-order (dynamic) pressure fields. The equilibrium pressure field renders the bearing static load performance, including orifice flow rates and drag power dissipation. The first-order pressure fields provide the bearing impedances (stiffness and damping force coefficients). Note that the compressibility of the thin film imposes a frequency dependence on the bearing force coefficients. San Andrés and Wilde [17] provide details on the FE numerical method of solution, which utilizes high order shape

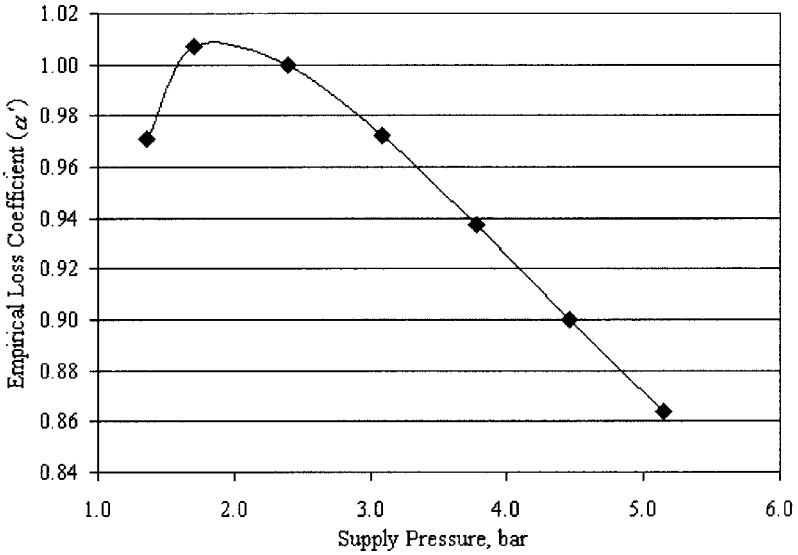

Fig. 3 Empirical loss coefficient versus supply pressure at feed orifice curtain area

functions preventing numerical instability for operation at high-speed numbers[3].

Table 1 details the bearing geometry and the rotor/bearing system operating conditions. The test rotor weighs 0.827 kg and each bearing carries half the rotor weight (4.056 N). Bearing performance predictions are highly dependent on the curtain area feed pressure, which is physically difficult to measure. Thus, an empirical adjustment made to the supply pressure accounts for the flow resistance through the feed orifice and at the feed orifice exit, and determines the actual supply pressure (P_s) at the curtain area. Experiments were conducted to record the mass flow rate with and without the rotor installed on the test bearings for increasing feed pressures. From these measurements, matching mass flow rates establish the actual pressure ratio (curtain area to ambient) at the known feed pressure, thereby establishing the relationship between the feed pressure and the empirical loss coefficient (α') depicted in Fig. 3. In order to determine the actual feed pressure at the curtain area, simply multiply the feed pressure by the loss coefficient. Note that the loss coefficient decreases rapidly as the feed pressure increases.

Predicted Gas Bearing Performance. Figure 4 shows the predicted journal eccentricity and attitude angle versus rotor speed for increasing supply to discharge pressure ratios. In general, journal eccentricities decrease and the attitude angles increase as the rotor speed increases. Hydrostatic pressurization favors small attitude angles and even lower operating rotor eccentricities. Nearly centered rotor operation at high rotor speeds is usually accompanied by poor stability characteristics.

Figures 5 through 8 depict the predicted stiffness and damping (direct and cross-coupled) coefficients versus frequency ratio, FR (ratio of excitation frequency to rotor speed), for a supply to ambient pressure ratio equal to 5.08 and three rotor speeds. In the following discussion, low, medium, and high rotor speeds refer to 20, 40, and 100 krpm, respectively. At this condition of high supply pressure, the static journal eccentricity is small (<2 μm) and thus, the force coefficients show the characteristic features, $K_{yy}=K_{xx}$, $K_{yx}=-K_{xy}$, $C_{yy}=C_{xx}$, $C_{xy}=-C_{yx}$. The predictions indicate that the bearing force coefficients are not largely frequency dependent within the subsynchronous region, $FR<1$, i.e., at those frequencies where the rotor-bearing system is likely to become unstable. At high rotor speeds, the force coefficients do show a marked dependency on excitation frequency.

Predicted direct stiffnesses (K_{xx}) are nearly independent of rotor speeds at excitation frequencies below synchronous, i.e., $FR<1$, evidencing their hydrostatic nature. K_{xx} increases rapidly for $FR>1$ and reaches identical asymptotic values at FR$>$100 for the three rotor speeds shown. In the region $1<FR<10$, higher rotor speeds generate larger direct stiffnesses. Cross-coupled stiffnesses (K_{xy}) are nearly constant for $FR<1$ for the low and medium speeds and with magnitudes proportional to the rotor speed. The coefficient (K_{xy}) decreases rapidly for frequencies above the rotor speed; the fastest rate of decay occurs at the high speed. Recall that large values of cross-coupled stiffnesses promote rotor-bearing instability.

Direct damping coefficients (C_{xx}) show similar frequency dependent characteristics as the cross-coupled stiffness coefficients, decreasing rapidly towards null values as FR grows above 10. For low excitation frequencies, C_{xx} is nearly independent of rotor speed. Cross-coupled damping coefficients (C_{yx}) are proportional to rotor speed and show rapid drops for $FRs>1$. Note that the gas

Table 1 Geometry of test gas bearings and operation conditions

Physical Properties	Magnitude
Diameter, D	28.5 mm
Length, L	30 mm
Number of lobes	3
Lobe length	120 deg
Nominal clearance, C	66 μm
Dimensionless preload, r_p/C	0.346
Lobe offset, Θ_p	60 deg
Feed orifice diameter, d	1.0 mm
Number of feed orifices	6
Operating Conditions	**Magnitude**
Ambient Pressure, P_a	1 bar
Temperature, T	300 K
Viscosity, μ	1.87×10^{-5} Ns/m^2
Density at ambient pressure, ρ	1.224 kg/m^3
Supply pressure, P_s	1.1–5 bar
Rotor speed (maximum)	80 krpm

[3]In the experiments, the bearing speed number $\Lambda=6\mu\Omega/P_a(R/C)^2$ equals 39 at a rotor speed of 80 krpm.

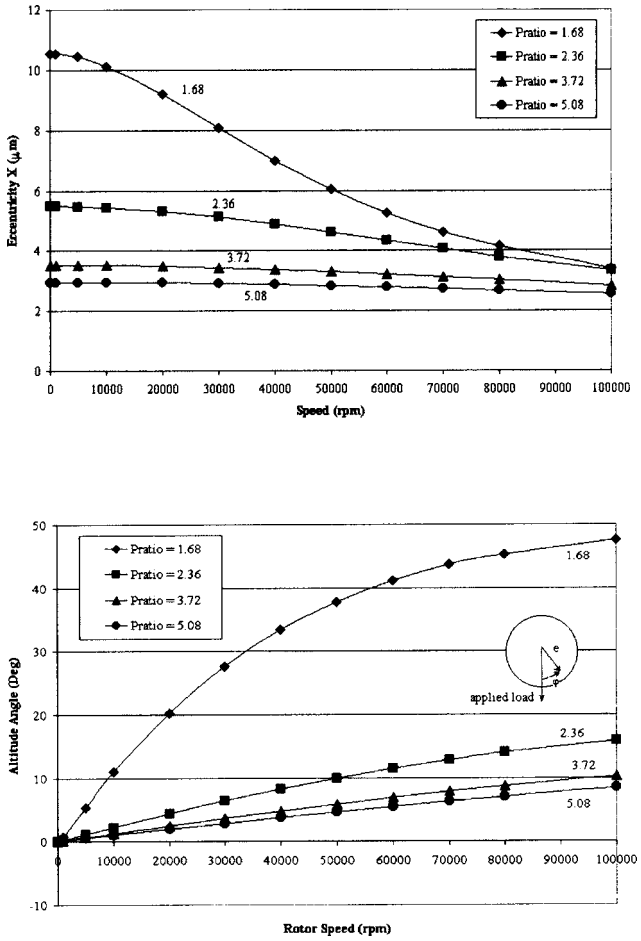

Fig. 4 Predicted journal eccentricity and attitude angle versus rotor speed with feed pressure ratio increasing

bearings lose their damping ability for excitation at very high frequencies while rendering large direct stiffnesses, a typical hardening effect. The most important identifier for rotordynamic analysis, however, is the whirl frequency ratio defined as $(K_{xy}/\Omega C_{xx})$, and for the test bearings, nearly equal to 0.50 for excitation frequencies below synchronous.

Predicted Rotor-Bearing System Performance. The rotordynamics analysis predicts both the synchronous rotor response to imbalance and the system eigenvalues (natural frequencies and damping ratios). Zero or negative damping ratios evidence a loss in dynamic stability, and provide the threshold rotor speeds and ensuing whirl frequency ratios (typically subsynchronous).

Figure 9 shows the multiple station model of the composite rotor comprising a slender steel inner shaft with a press fit dc motor at the middle and two journal sleeves on the sides. The support bearings are represented as spring elements at the appropriate physical locations. The rotor length is 190 mm with a diameter of 28.5 mm. Measurements of the free-free mode natural frequencies and mode shapes of the test rotor were conducted by hanging the rotor from long wires, rapping the rotor at its midplane, and recording the acceleration at different axial locations along the rotor. Miniature accelerometers (1 g) were used in the procedure. Table 2 shows the experimental and predicted first and second natural frequencies. Figures 10 and 11 display the recorded and predicted first and second free-free mode shapes. Adjusting the (unknown) dc motor material properties was necessary to match the first and second natural frequencies. The agreement between predictions and measurements for the first natural mode shape is excellent. Note that the elastic modes of the test rotor are well above the maximum (stable) operating speed of 80,000 rpm. This top speed is largely determined by the type of gas bearing supports, not due to the structural integrity of the rotor assembly.

Figure 5 in the companion paper [18] presents the experimental synchronous rotor response to imbalance for three feed pressure conditions. Presently, Fig. 12 depicts the predicted rotor response using the synchronous force coefficients extracted from the results given in Figs. 5–8 for similar feed pressure conditions. The im-

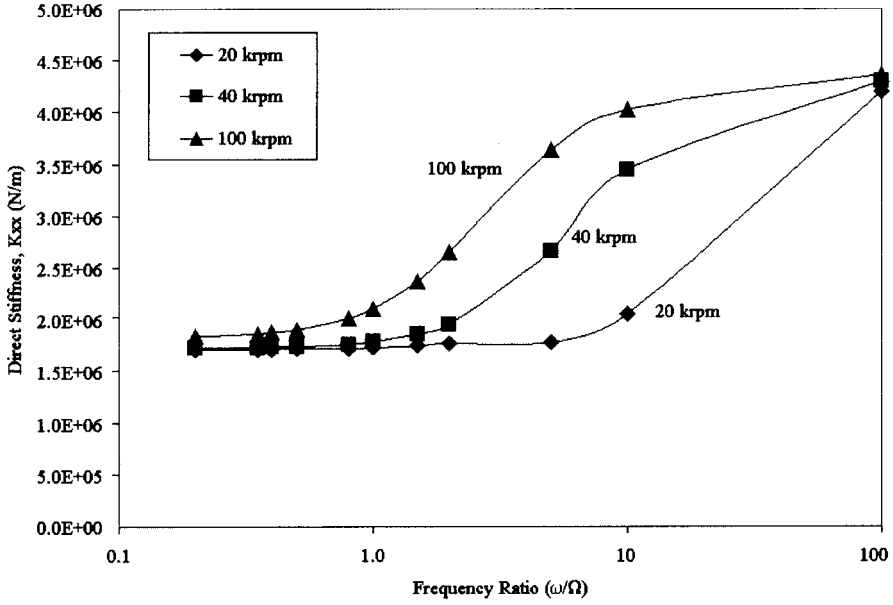

Fig. 5 Predicted gas bearing direct stiffnesses ($K_{xx}=K_{yy}$) versus frequency ratio for feed pressure ratio=5.08 and three rotor speeds

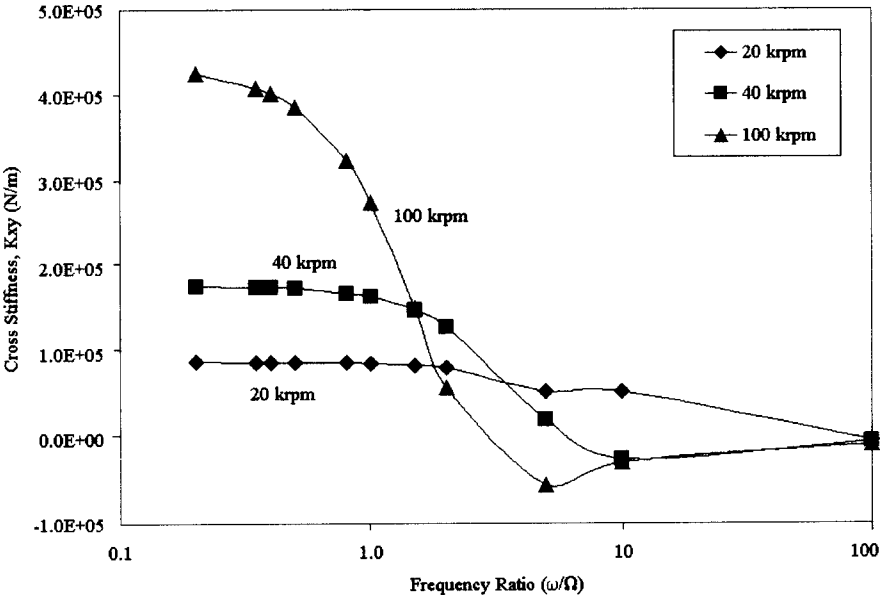

Fig. 6 Predicted gas bearing cross-coupled stiffnesses ($K_{xy}=K_{yx}$) versus frequency ratio for feed pressure ratio=5.08 and three rotor speeds

balance masses used for prediction (2 kg μm)[4] are on the same order of magnitude, and at the same physical location, as those in the experiments. The imbalance distribution is identical on both rotor planes, and thus the rotor responses evidence a cylindrical mode shape. The predicted responses match well with the test responses closely reproducing the critical speed locations, albeit with narrower bands of rapid amplitude growth towards larger motions, thus suggesting predicted viscous damping ratios lower than in the measurements. Note the paramount effect of supply pressure in shifting the critical speed and reducing the effective damping of the rotor-bearing system. It is important to note that the rotor-bearing model does not include any other source of damping but that provided from the gas bearings.

Figure 13 depicts the predicted first two critical speeds increasing as the supply pressure into the bearings increases. Both critical speeds correspond to rigid rotor modes (the lowest being conical and the highest cylindrical) and are close in magnitude to each other. The figure includes the test critical speeds observed from rotor measurements at the bearing supports. The predictions agree well with the measurements.

Figure 14 depicts, as the supply pressure increases, the viscous damping ratios predicted by the rotordynamic model and those extracted from the test imbalance responses while the rotor traversed its critical speed. The experimental values show damping ratios (12.4%–7.1%) at least three times larger than the predic-

[4]The magnitude amounts to a physical rotor off centering (imbalance) of just 5 μm, and inducing a dynamic load ~18 N at a speed of 20 k rpm, i.e., 2.2 times larger than the rotor weight.

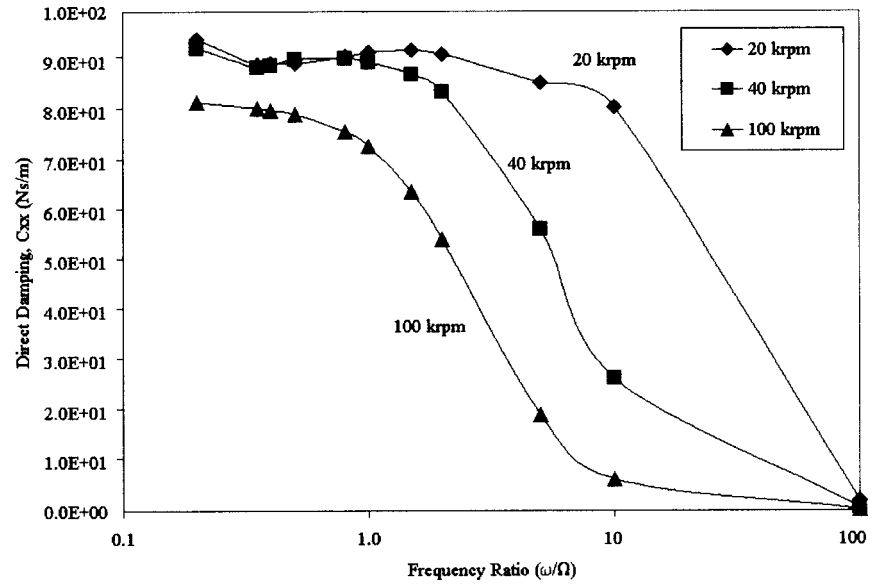

Fig. 7 Predicted gas bearing direct damping coefficients ($C_{xx}=C_{yy}$) versus frequency ratio for feed pressure ratio=5.08 and three rotor speeds

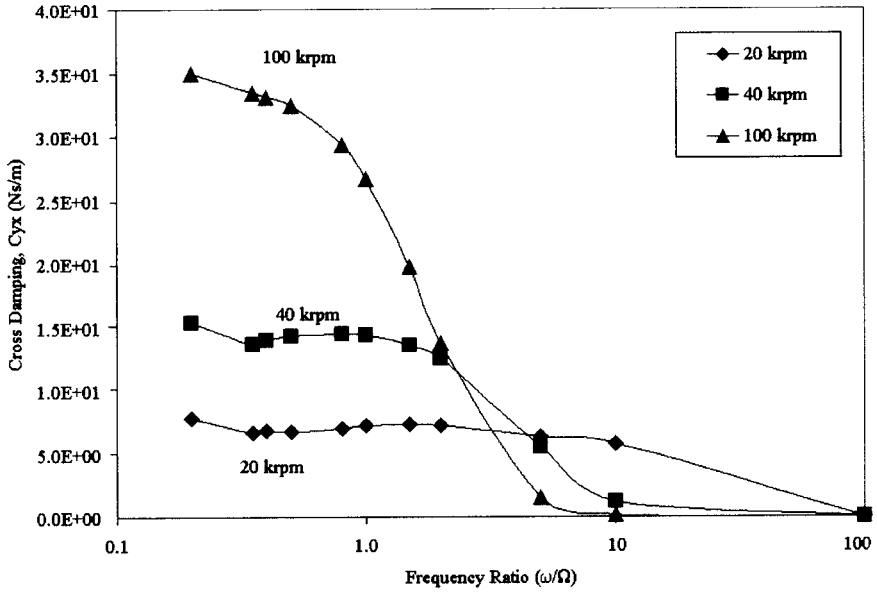

Fig. 8 Predicted gas bearing cross-coupled damping coefficient ($C_{yx}=C_{xy}$) versus frequency ratio for feed pressure ratio=5.08 and three rotor speeds

tions (4.9%–2.7%) and indicate an unknown source of damping not accounted for in the rotor-bearing model. Perhaps, the results also evidence a limitation of the gas bearing analysis predicting force coefficients. Not withstanding the differences, the predictions do show a drop in damping ratio as the hydrostatic feed pressure increases.

A rotor-bearing system mode becomes unstable when its damping ratio drops to a null value at a rotor speed known as the threshold speed of instability. The rotor then shows large amplitudes of vibration at the corresponding natural frequency. The stability whirl frequency ratio (WFR) is defined as the ratio between this natural frequency and the threshold speed. Table 3 shows the experimental and predicted threshold speeds of instability and ensuing WFRs for increasing pressure supply conditions. The predictions show much lower threshold rotor speeds and whirl frequency ratios at typically 50% of rotor speed, independent of the level of external pressurization. This type of instability is the characteristic one of hydrodynamic bearings. On the other hand, the measurements show WFRs decreasing with feed pressure and an extended range of rotor speeds within which the rotor-gas bearing system operates in a stable mode, i.e., free of subsynchronous motions. Note that the (unstable) whirl frequencies are similar for both predictions and experiments since they correspond to the system natural frequencies.

Thus, it is apparent that the test hybrid gas bearings offer more damping than the predictions otherwise show. The experiments demonstrate larger viscous damping ratios at the passage through the (fundamental) critical speed and higher threshold speeds of instability as the feed pressure increases. Thus, the gas bearing physical model needs be closely revised to assert the sources of the discrepancies.

Note that the gas bearing force coefficients are strictly valid for

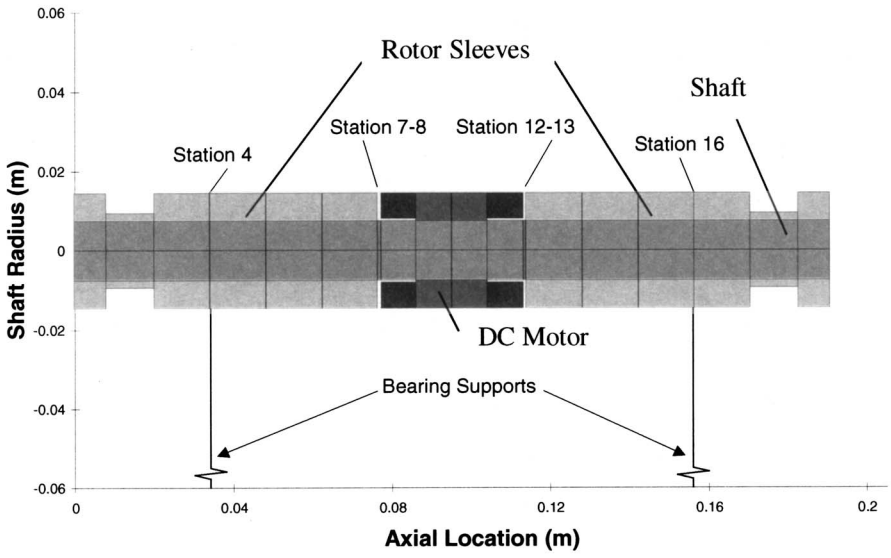

Fig. 9 Geometric model of test rotor

Table 2 Free-free natural frequencies of test rotor

Free-free natural frequencies	Measurement, rpm (Hz)	Predictions, rpm (Hz)	% Difference
1st bending mode	109,200 (1820)	111,942 (1866)	2.4%
2nd bending mode	354,000 (5900)	311,190 (5187)	13.8%

small amplitude rotor motions about an equilibrium position. The test results, on the other hand, show large amplitude rotor motions (a significant portion of the bearing clearance) while the rotor crosses its critical speed. Hence, the discrepancy could be attributed to nonlinear effects from the gas bearing reaction forces. This explanation, of course, does not offer insight to elucidate the large differences in predicted threshold speeds of (linear) instability.

Conclusions

Small scale turbomachinery operating at high speeds are employing gas bearings, thereby eliminating costly mineral lubricant supply systems and allowing for more compact units satisfying severe environmental constraints. The development of gas bearing technology for these applications follows a path of extensive experimentation accompanied by analytical developments able to predict with a degree of accuracy the measurements, thus paving the way for reliable field (industrial) implementation.

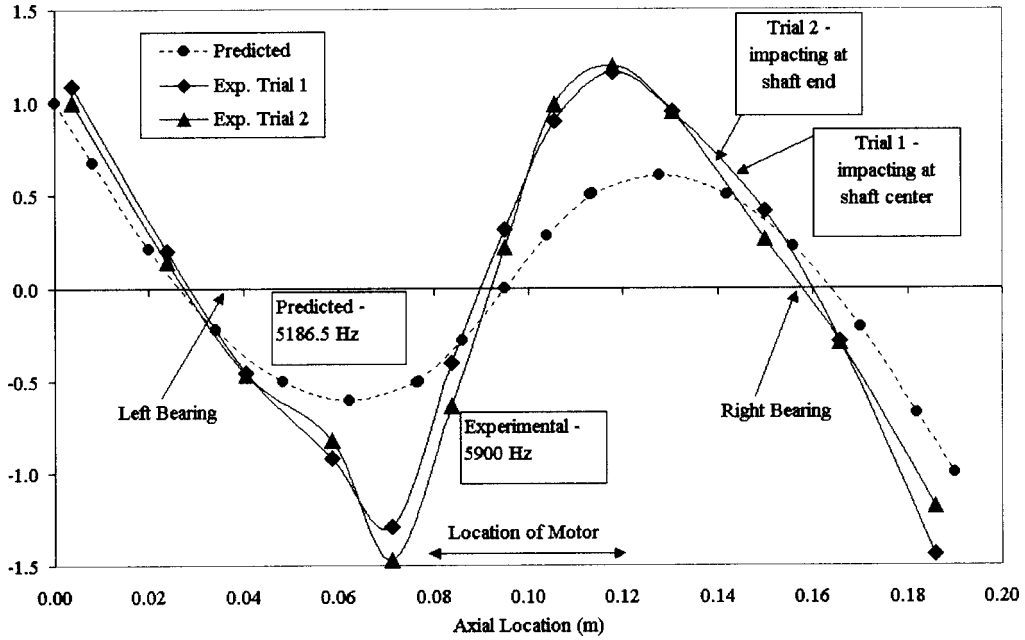

Fig. 10 Measured and predicted first free-free mode shape of test rotor

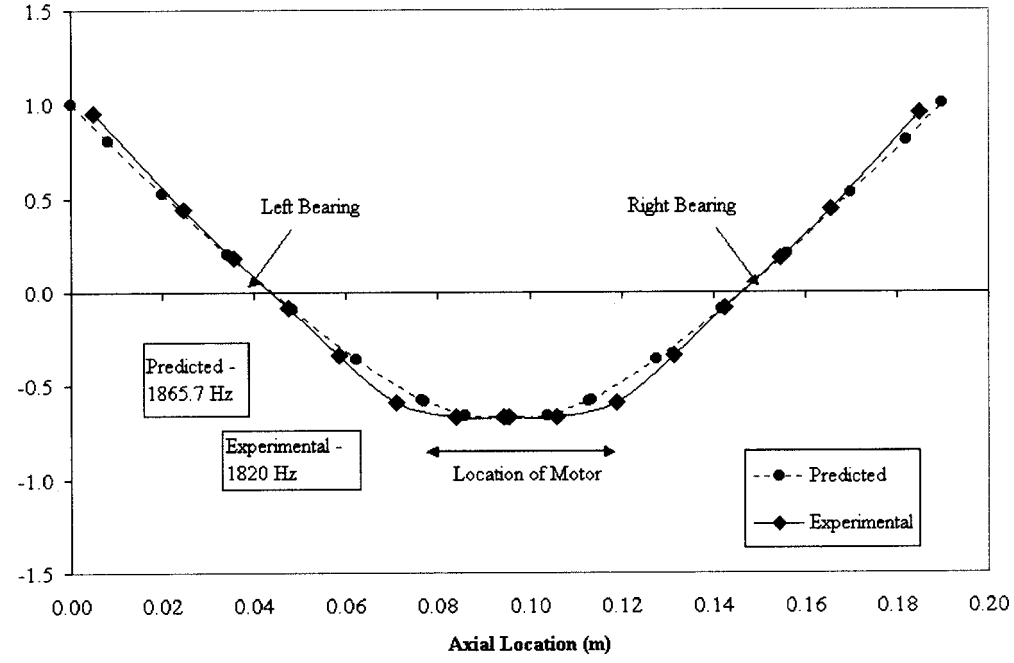

Fig. 11 Measured and predicted second free-free mode shape of test rotor

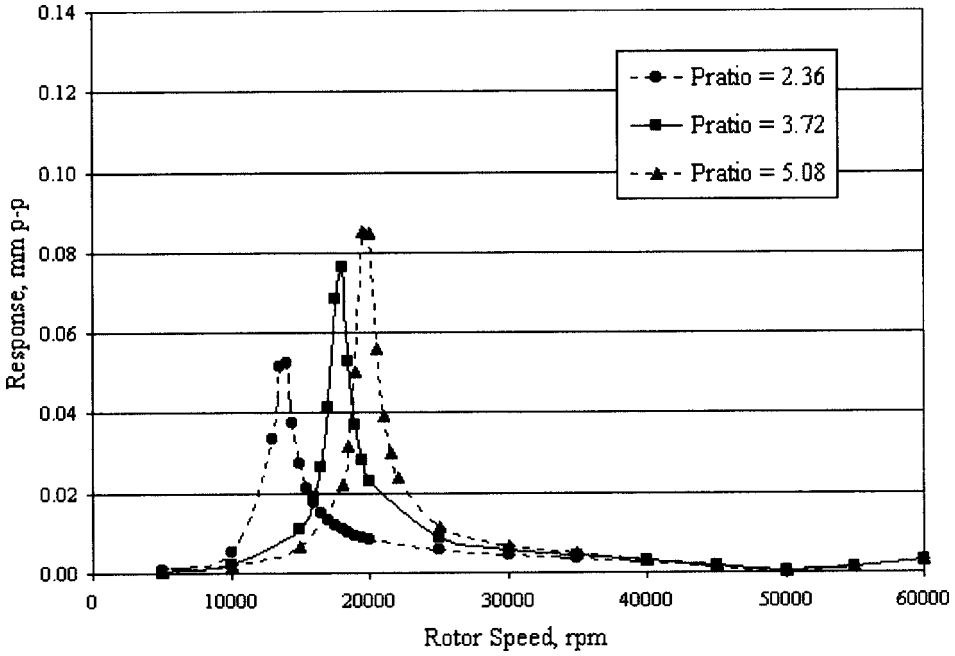

Fig. 12 Predicted (peak-to-peak) imbalance response for rotor supported on gas bearings for synchronous bearing force coefficients and increasing supply pressure ratios

A companion paper [18] presents comprehensive rotordynamic experiments conducted on a small rotor supported on three lobed hybrid (hydrostatic/hydrodynamic) rigid gas bearings operating to speeds as high as 80,000 rpm. Presently, the rotordynamic analysis and predictions for the test rotor and its gas bearings are discussed. The hybrid gas bearings are modeled following classical gas lubrication analysis with numerical predictions advanced by an analytical perturbation FE computational program. Computational software for rotordynamic analysis models the rotor as a collection of mass-elastic stations and incorporates the gas bearing force coefficients for calculation of the rotor-bearing system synchronous response to imbalance, damped eigenvalues showing system damping ratios, natural frequencies, and threshold speeds of instability.

Predicted stiffness and damping coefficients for the gas bearings are frequency dependent, with large variations for frequencies well above the rotor speed. Direct stiffnesses increase to a limiting value while cross-coupled stiffnesses and damping coefficients drop to null values for excitations at very large frequencies. However, the ratio of cross-coupled forces to damping forces, i.e., $Kxy/\Omega Cxx$, remains at 0.50 for subsynchronous excitations irrespective of the level of external pressurization.

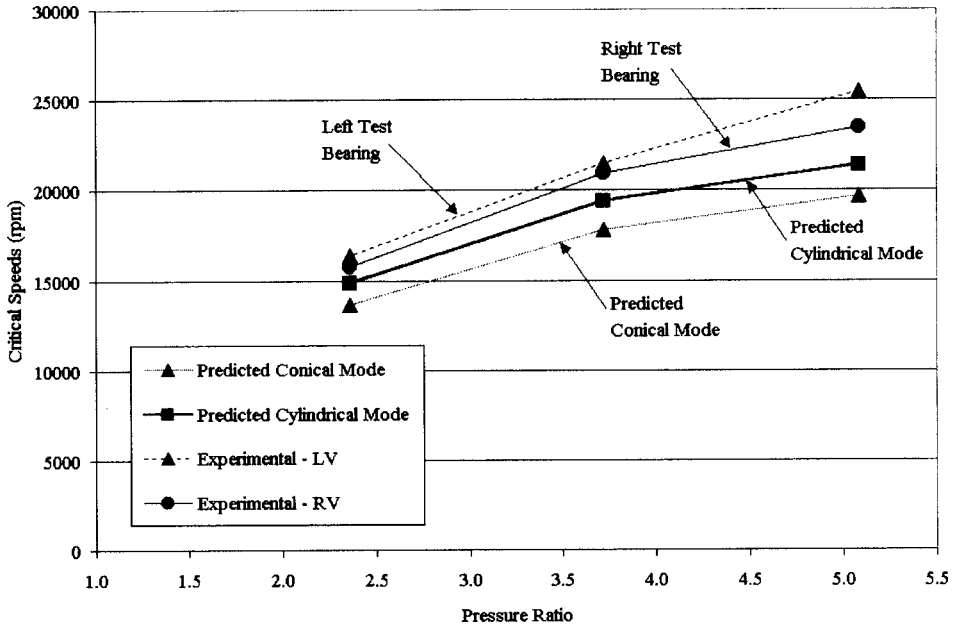

Fig. 13 Measured and predicted critical speeds for rotor supported on gas bearings (supply pressure ratio varies)

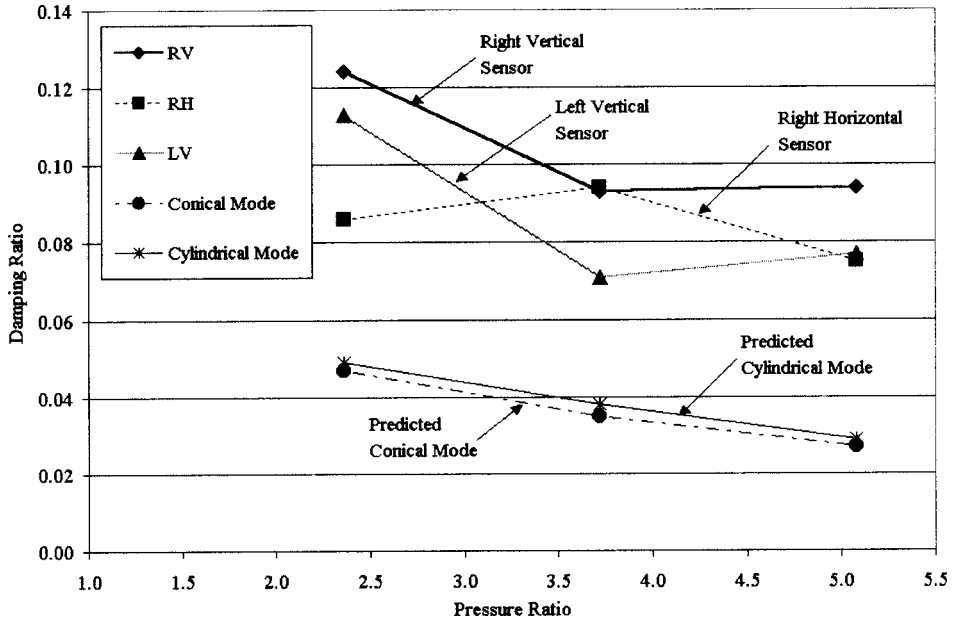

Fig. 14 Experimental damping ratios from synchronous rotor response and predicted (conical and cylindrical modes) damping ratios for rotor supported on gas bearings

Table 3 Experimental and predicted threshold speeds, whirl frequencies, and whirl frequency ratios for test rotor supported on gas bearings

(a) Experimental

Supply pressure ratio	Threshold speed (rpm)	Whirl frequency (rpm)	Whirl frequency ratio
2.36	37,200	13,680	0.40
3.72	54,960	19,440	0.35
5.08	85,184	21,600	0.25

(b) Predictions based on subsynchronous force coefficients (whirl frequency ratio=0.51 for all conditions)

	Conical mode		Cylindrical mode	
Supply pressure ratio	Threshold speed (rpm)	Whirl frequency (rpm)	Threshold speed (rpm)	Whirl frequency (rpm)
2.36	26,760	13,660	28,610	14,610
3.72	34,440	17,710	37,220	18,960
5.08	38,570	19,640	40,710	21,030

The structural model of the composite rotor reproduces with accuracy the experimentally found free-free natural frequencies and mode shapes. Predictions of the synchronous rotor response to imbalance show fundamental critical speeds which correlate well with the measurements. However, the predicted viscous damping ratios are about 30% of those estimated experimentally. Furthermore, the eigenvalue analysis predicts much lower threshold speeds of instability than measured, and thus subsynchronous whirl frequency ratios are higher than the test recorded values. The discrepancy is more notorious for the largest magnitudes of external pressurization. The type of instability predicted has a whirl frequency ratio equal to 0.50 pointing out its hydrodynamic character. The measurements, on the other hand, show whirl ratios decreasing from 0.40 to 0.25 as the feed pressure increases from 2.36 to 5.08 times ambient conditions.

The measurements demonstrate the stable operation of the test rotor-gas bearings to speeds much higher than those predicted by the analysis. Thus, the fundamentals of the physical model, namely classical lubrication and orifice flow equations for gases, must be reassessed to improve the correlation with the test results. Additional experimental verification also becomes mandatory to advance application of gas bearings for current and envisioned applications in oil-free turbomachinery.

Acknowledgment

The support of the American Association of University Women (with sponsorship by the Texas State Education Foundation), the Texas A&M University Energy Resources Program (College of Engineering), and the Turbomachinery Research Consortium (Texas A&M University) is gratefully acknowledged.

Nomenclature

a = orifice restrictor diameter (m)
A = effective orifice area (m^2); (πdh)
C = nominal lobe clearance (m)
$C_{\sigma\beta}$ = damping coefficients (Ns/m); σ, $\beta = X$, Y

d = orifice discharge diameter (m)
e_X, e_Y = journal eccentricity components (m)
h = film thickness (m); $H = h/C$
k = gas specific heat ratio (1.4 for air); $\gamma = (k-1)/k$
$K_{\sigma\beta}$ = stiffness coefficients (N/m); σ, $\beta = X$, Y
L = bearing axial length (m)
$\dot{m}$ = mass flow rate (kg/s)
P = gas absolute pressure (Pa); $p = P/P_*$; $\bar{P} = P/P_s$
R = journal radius (m)
r_p = pad preload (m)
R_g = gas constant (J/kg·K)
T = absolute temperature (K)
t = time (s)
X, Y = inertial coordinate system
$x = R\theta, y$ = coordinate system on plane of bearing
α' = Empirical orifice loss coefficient
Θ_p = Lobe offset angle (rad)
ρ, μ = Gas density (kg/m^3) and viscosity (Pa·s)
Ω = Rotor speed (rad/s)
ω = Excitation frequency (rad/s)

References

[1] San Andrés, L., and Vance, J., 2001, "Feasibility Study on Alternative Oil-Less Bearing Technologies for Automotive Turbochargers," Final Research Progress Report, Texas A&M University, College Station, TX.
[2] Fuller, D. D., 1969, "A Review of the State-of-the-Art for the Design of Self-Acting Gas-Lubricated Bearings," J. Lubr. Technol., **91**, pp. 1–16.
[3] Elrod, Jr., H. G., and Malanoski, S. B., 1960, "Theory and Design Data for Continuous-Film, Self-Acting Journal Bearings of Finite Length," Franklin Institute Laboratories for Research and Development, Report I-A 2049-13.
[4] Raimondi, A. A., 1961, "A Numerical Solution for the Gas-Lubricated Full Journal Bearing of Finite Length," ASLE Trans., **4**, pp. 131–155, Paper No. 60 LC-14.
[5] Castelli, V., and Elrod, H. G., 1965, "Solution of the Stability Problem for 360° Self-Acting, Gas-Lubricated Bearings," J. Basic Eng., **87**, pp. 199–212.
[6] Castelli, V., and Vohr, J. H., 1967, "Performance Characteristics of Herringbone-Grooved Journal Bearings Operating at High Eccentricity Ratios With Misalignment," *Proc. Gas Bearing Symposium*, University of Southampton, Southampton, UK, Paper No. 14.
[7] Elrod, Jr., H. G., McCabe, J. T., and Chu, T. Y., 1967, "Determination of Gas-Bearing Stability Response to a Step-Jump," ASME J. Lubr. Technol., **89**, pp. 493–498.
[8] Czolczynski, K., 1996, "How to Obtain Stiffness and Damping Coefficients of Gas Bearings," Wear, **201**, pp. 265–275.
[9] Faria, M. T. C., 1999, "Finite Element Method of High Speed Grooved Gas Bearings," Ph.D. dissertation, Texas A&M University, College Station, TX.
[10] Faria, M. T. C., and San Andrés, L., 2000, "On the Numerical Modeling of High-Speed Hydrodynamic Gas Bearings," ASME J. Tribol., **122**, pp. 124–130.
[11] Faria, M. T. C., 2001, "An Efficient Finite Element Procedure for Analysis of High-Speed Spiral Groove Gas Face Seals," ASME J. Tribol., **123**, pp. 205–210.
[12] Shapiro, W., 1969, "Steady-State and Dynamic Analyses of Gas-Lubricated Hybrid Journal Bearings," J. Lubr. Technol., **91**, pp. 171–180.
[13] Lund, J. W., 1964, "The Hydrostatic Gas Journal Bearing With Journal Rotation and Vibration," J. Basic Eng., **86**, pp. 328–336.
[14] Lund, J. W., 1967, "A Theoretical Analysis of Whirl Instability and Pneumatic Hammer for a Rigid Rotor in Pressurized Gas Journal Bearings," ASME J. Lubr. Technol., **89**, pp. 154–166.
[15] Piekos, E. S., and Breuer, K. S., 1999, "Pseudospectral Orbit Simulation of Nonideal Gas-Lubricated Journal Bearings for Microfabricated Turbomachines," ASME J. Tribol., **121**, pp. 604–609.
[16] Piekos, E. S., 2000, "Numerical Simulation of Gas-Lubricated Journal Bearings for Microfabricated Machines," Ph.D. thesis, Massachusetts Institute of Technology, Cambridge, MA.
[17] San Andrés, L., and Wilde, D. A., 2001, "Finite Element Analysis of Gas Bearings for Oil-Free Turbomachinery," Revue Européenne des Eléments Finis, **10**, pp. 769–790.
[18] Wilde, D. A., and San Andrés, L., 2003, "Experimental Response of Simple Gas Hybrid Bearings for Oil-Free Turbomachinery," ASME Paper No. GT 2003-38833.
[19] Wilde, D. A., 2002, "Experimental Response of Gas Hybrid Bearings for High Speed Oil-Free Turbomachinery," Masters thesis, Texas A&M University, College Station, TX.
[20] XLTRC^2, 2000, Computational Rotordynamics Software Suite, Turbomachinery Laboratory, Texas A&M University, College Station, TX.

Active Rotor-Blade Vibration Control Using Shaft-Based Electromagnetic Actuation

René H. Christensen

Ilmar F. Santos

Department of Mechanical Engineering,
Technical University of Denmark,
DK-2800 Kgs. Lyngby, Denmark

In this paper the feasibility of actively suppressing rotor and blade vibration via shaft-based actuation is studied. A mathematical model is derived, taking into account the special dynamical characteristics of coupled rotor-blade systems, such as centrifugal stiffened blades and parametric vibration modes. An investigation of controllability and observability shows that if the blades are properly mistuned, it is possible to suppress shaft as well as blade vibration levels by using only shaft-based actuation and sensing; though, in tuned bladed systems, shaft as well as blade actuation and sensing are required. In order to cope with the time-variant dynamics of the coupled rotor-blade system, a periodic time-variant modal controller is designed, implemented, and experimentally tested. A test rig built by four flexible blades is specially designed for this purpose. The rig is equipped with six electromagnetic actuators and different types of sensors (eddy-current displacement transducers, acceleration transducers, and strain gages) with the aim of monitoring and controlling shaft and blade vibration levels. Two different actively controlled rotor-blade system configurations are considered in the present study: (i) a tuned bladed rotor, controlled with help of actuators attached to the rotating blades and shaft-based actuators; (ii) a deliberately mistuned bladed rotor controlled only via shaft-based actuation. Experimental tests are carried out for both configurations. Some experimental problems regarding control implementation are identified and discussed, especially when the controller order and the number of actuators in the centralized control scheme become too high; though, for the mistuned bladed rotor controlled by using only shaft-based actuation, the controller works well. [DOI: 10.1115/1.2056533]

Introduction

Blade faults are a major problem in many types of bladed rotating machines such as for instance turbines and compressors. The increasing demands for lower weight, higher efficiency, and higher speed imply that the blades become continuously more susceptible to vibration problems. Typically, passive damping methods, such as damping wires or frictional damping, are used to reduce vibration problems, working very well at the specific design conditions [1]. However, when the running conditions exceed the design specification, the passive damping devices are no longer sufficient. This might be the case if more critical speeds have to be passed during a start-up phase. Thus, active control might become the only feasible technique to improve performance, suppress vibrations, and prolong machinery lifetime.

Implementing active controls into bladed rotating systems implies that several difficulties have to be considered and dealt with. For instance, it has to be decided where to locate sensors and actuators since it will be very costly to build sensors and actuators into the rotating blades. For practical application, it is of significant interest to study whether blade as well as shaft vibrations can be controlled by using only shaft-based actuators (i.e., active electromagnetic and hydraulic bearings) or whether blade-based actuators are inevitable.

Active control of blade vibrations using shaft-based actuation has been studied by very few researchers. The controllability and observability of a bladed disk controlled via electromagnetic radial and thrust bearings were analyzed in Szász and Flowers [2]. It was shown that full controllability can be achieved by introducing deliberate blade mistuning, and a pattern of mistuning was proposed. In the works of Szász et al. [3] and Szász and Flowers [4], a mistuned bladed disk was controlled by a radial active bearing using a periodic state feedback controller designed using FLOQUET theory. In none of these works was the presence of parametric vibration effects due to vibration coupling among rotors and blades considered. Such effects were studied in the work of Christensen and Santos [5], where the modal controllability and observability of a coupled rotor-blade system, presenting significant vibration coupling among rotor and blades, were investigated. Using time-variant modal analysis, it was shown that rotor and blade vibrations can be controlled by shaft-based actuation if the rotor blades are deliberately mistuned, as it was described by Szász et al. [3] and Szász and Flowers [4]. In the case of tuned rotor blades, it was shown that actuators have to be built into the blades in order to gain full controllability. Moreover, in the paper by Christensen and Santos [5] numerical control results were presented. A modal controller design methodology for periodic time-variant systems, based on time-variant modal analysis, was employed. All the works cited thus far were based, entirely, on numerical results, and no experimental results were presented. In the work of Cho et al. [6] a so-called spin rig (a bladed rotor controlled by electromagnetic bearings) is designed and built. It is intended to study active blade vibration control using this spin rig. However, neither numerical nor experimental results have yet been reported for a rotating blade system.

In this framework the aim of this paper is to give an experimental contribution to the field of active vibration control of rotating bladed systems. The purpose is to demonstrate the feasibility of the periodic modal control scheme, presented in the paper by Christensen and Santos [7], to actively control rotor as well as blade vibrations in practice. A further aim is to experimentally verify the feasibility of controlling rotor-blade coupled vibrations in properly mistuned systems by using only shaft actuation.

The experimental results indicate, in fact, that it may be feasible

Contributed by the International Gas Turbine Institute (IGTI) of ASME for publication in the JOURNAL OF ENGINEERING FOR GAS TURBINES AND POWER. Manuscript received October 1, 2003; final manuscript received March 1, 2004. IGTI Review Chair: A. J. Strazisar. Paper presented at the International Gas Turbine and Aeroengine Congress and Exhibition, Vienna, Austria, June 13–17, 2004, Paper Nos. 2004-GT-53509 and 2004-GT-53512.

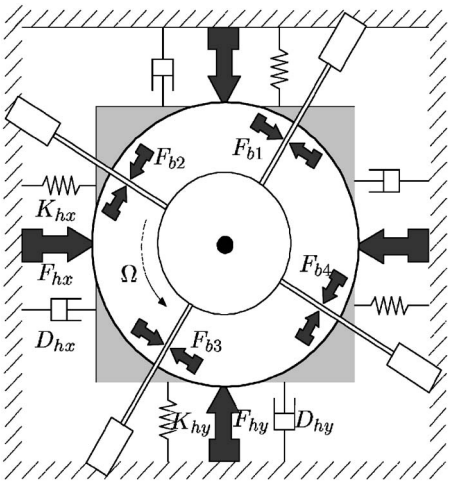

Fig. 1 Mechanical model of the rotor-blade system with actuator forces applied to the rotor as well as to the blades

to control shaft as well as blade vibrations, for example, in gas turbines by means of active magnetic bearings [8,9], active lubricated bearings [10], piezo controlled bearings [11], or bearings controlled by means of hydraulic actuators [12,13]. Such conclusions are obtained using a small test rig built with only four flexible blades.

System Description

For the theoretical study of active rotor-blade vibration control, a simplified rotor-blade system is considered. Figure 1 shows a mechanical model of such a system. The system is composed of a rotating rigid disk. Four equally distributed nontwisted flexible blades are radially clamped to the disk. At the tip end of each blade an additional mass is attached. Such tip masses emphasize the inertia of the blades and increase the vibration coupling among rotor and blades. The disk and shaft are assumed to be rigid. The shaft-disk subsystem is elastically supported, performing only lateral movement in the x_h and y_h directions (planar rigid-body motion). For convenience, such a subsystem will be referred as the "hub" throughout this paper, even though it is not rotating.

Six sets of sensors and actuators are attached to the bladed rotor with the aim of monitoring vibration levels and, additionally, applying active control forces. The locations of sensors and actuators are symbolized by black arrows in Fig. 1. The active forces F_{hx} and F_{hy} are applied to the elastically supported hub, working like an active radial bearing. The four active forces F_{b1}, F_{b2}, F_{b3}, and F_{b4} are applied perpendicularly to each one of the blades, with the intent to control bending movements. Eddy-current transducers and strain gages are assumed to be placed at the same locations, measuring rotor lateral position and blade deflections, respectively.

The parameters describing the physical and geometrical properties of the rotating disk, elastically supported hub, and blades with tip masses are listed in Table 1. Such values are also related to the experimental setup. It is worth mentioning that the rotor/hub mass, stiffness and damping in the x_h and y_h directions are different. These differences result from design solutions adopted for the test rig and the different number of assembly parts of the hub, which are in movement in the orthogonal directions. Nevertheless, in most practical systems rotor/hub mass parameters will be the same.

Mathematical Model

The general equations of motion describing the dynamics of coupled rotor-blade systems are time varying and dependent on the rotor position, the rotational speed and acceleration. Rotating at a constant speed the model complexity reduces to become linear periodic time varying with a periodicity dependent on the rotational speed. The equations of motion are in state-space form expressed as

$$\dot{\mathbf{x}}(t) = \mathbf{A}(t)\mathbf{x}(t) + \mathbf{B}(t)\mathbf{u}(t) + \mathbf{F}(t) \tag{1}$$

$$\mathbf{y}(t) = \mathbf{C}\mathbf{x}(t) \tag{2}$$

where the model matrices are periodic time-variant. The control signals $\mathbf{u}(t)$ denote the actuation forces supplied by the actuators. More details on the mathematical modeling and the specific model can be found in Saracho and Santos [14] and Christensen and Santos [7].

The dynamics of coupled rotor-blade systems are characterized by peculiarities, such as centrifugal stiffened blades, parametric vibration modes, and frequency veering. Before going into detail about transforming the mathematical model into a time-invariant model using time-variant modal formulation, suitable for system analysis and controller design, these peculiarities will be visualized and discussed. Figure 2 shows frequency-response waterfall diagrams of the rotor and blade movement, respectively, as functions of the rotational speed. These diagrams clearly show the centrifugal stiffening of the blades and the parametric vibration modes. The centrifugal stiffening is observed by the increasing blade eigenfrequencies with rotational speed, see A in Fig. 2(*a*). The presence of parametric vibration phenomena, due to the vibration coupling among the rigid rotor and the flexible blades motion [15], is observed by the v-shaped frequency components, see B, C, G, and H in Figs. 2(*a*) and 2(*b*). Components B and C are backward- and forward-rotating contributions from the rotor natural frequencies to the blade movement. The components G and H are contributions from the blade natural frequency to the rotor movement. The remaining frequency components D and I are caused by the rotational speed. Components E and F are related to the natural frequencies of the rotor/hub, where predominately lateral movements in horizontal and vertical direction occur. By a close look in Fig. 2(*b*), the frequency-veering phenomenon can be clearly detected. Basis and parametric frequency components converge toward each other, where a strong dynamic interaction between the modes occurs and veer apart. For instance, G comes closer to E around 350 rpm and closer to F

Table 1 Rotor and blade properties

Rotor/Hub			
Mass	m_{hx}	10.5	[kg]
	m_{hy}	8.6	[kg]
Stiffness	K_{hx}	66×10^3	[N/m]
	K_{hy}	77×10^3	[N/m]
Damping[a]	D_{hx}	1.2×10^{-6}	[N s/m]
	D_{hy}	1.5×10^{-6}	[N s/m]
Excentricity	ϵ	1×10^{-3}	[m]
	κ	0	[rad]
Disk radius	r	0.04	[m]
Mass rotor	m_r	3.0	[kg]
Blades and Tip masses			
Length	L_i	80×10^{-3}	[m]
Distributed mass	ρ_i	0.195	[kg/m]
Elasticity	E_i	2.0×10^{11}	[N/m^2]
Moment of inertia (area)	I_i	2.08×10^{-12}	[m^4]
Damping[a]	D_{bi}	0.8	[N s/m]
Tip mass	m_{ti}	0.108	[kg]
Tip inertia	J_{ti}	3.35×10^{-5}	[kg m^2]
Tip mass length	L_{ti}	30×10^{-3}	[m]

[a]Experimentally obtained from the logarithmic decay

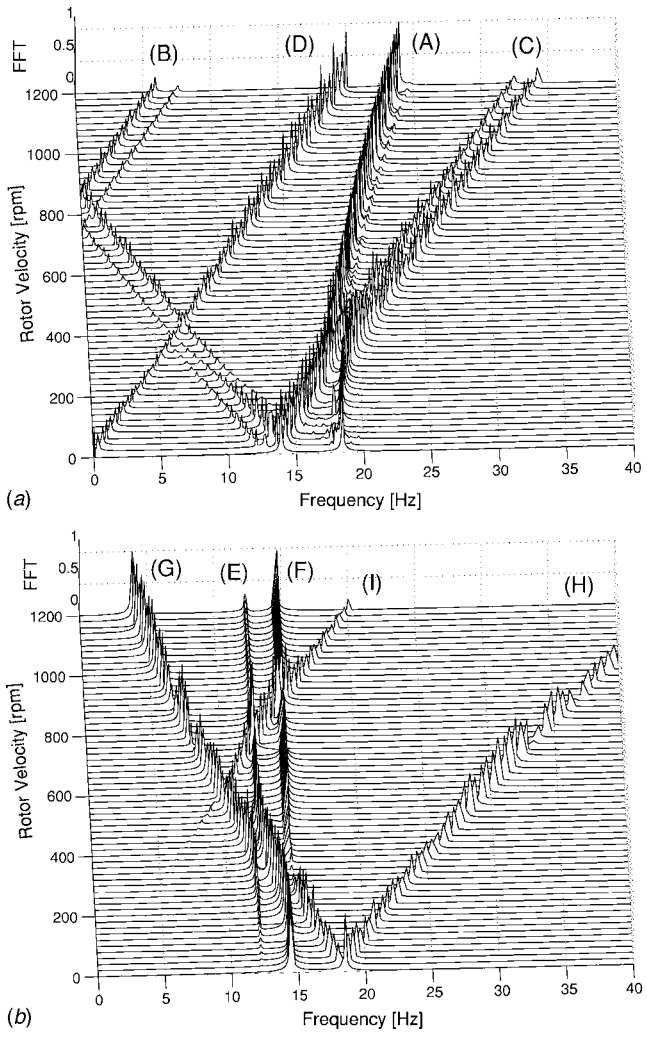

Fig. 2 Theoretical waterfall diagrams showing normalized frequency responses of the (*a*) blade movement and (*b*) rotor movement for a coupled rotor-blade system with identical blades as functions of the rotational speed

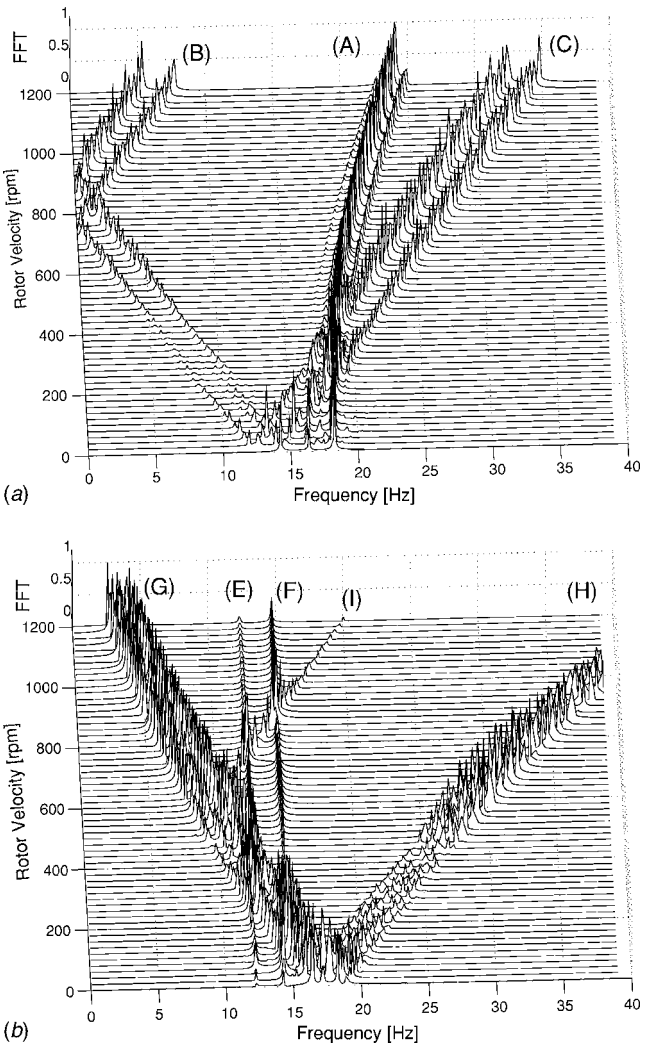

Fig. 3 Theoretical waterfall diagram showing normalized frequency responses of the (*a*) blade movement and the (*b*) rotor movement for a coupled mistuned rotor-blade system as functions of the rotational speed

around 200 rpm. Similarly, such a behavior can be seen in Fig. 2(*a*), where component C comes close to A at the same angular velocities.

As described in the introduction, rotor and blade vibrations can be controlled by using shaft-based actuation if the blades are deliberately mistuned [2]. Figure 3 shows waterfall diagrams of a deliberately mistuned system, mistuned by changing the blade tip masses $m_{t_1}=0.108$ kg, $m_{t_2}=0.119$ kg, $m_{t_3}=0.130$ kg, and $m_{t_4}=0.141$ kg. The most significant changes of the dynamical response due to such blade mistuning, compared to the tuned responses in Fig. 2, can be detected in the rotor movement. Figure 3(*b*) shows that the deliberate blade mistuning results in additional parametric mode components in the rotor movement, G and H. Four forward-rotating and four backward-rotating mode components related to the primarily blade-related modes are observed. This means that all four primarily blade-related mode shapes (mode 3–6) become theoretically detectable and influenceable from the inertial reference frame. For a thorough analysis of the system modal controllability and observability via a mode-shape analysis, see [5].

In order to analyze the system dynamics, explain the parametric mode components, and obtain a mathematical model aided for controller design, the periodic state-space model (1) is transformed into a time-invariant model by using time-varying modal analysis formulation [16]. Such modal decomposition transforms the system of equations with periodic time-varying coefficients into a system of independent equations of motion, where each equation represents one vibration mode. The modal formulation is obtained by introducing a vector of modal state variables $\boldsymbol{\xi}(t)$ defined by $\mathbf{x}(t)=\boldsymbol{\Phi}_R(t)\boldsymbol{\xi}(t)$, where $\boldsymbol{\Phi}_R(t)$ represents the right modal matrix. Introducing this new state vector, the system is rewritten into the form

$$\dot{\boldsymbol{\xi}}(t) = \boldsymbol{\mathcal{A}}\boldsymbol{\xi}(t) + \boldsymbol{\mathcal{B}}(t)\mathbf{u}(t) + \boldsymbol{\mathcal{F}}(t) \tag{3}$$

$$\mathbf{y}(t) = \boldsymbol{\mathcal{C}}(t)\boldsymbol{\xi}(t) \tag{4}$$

where $\boldsymbol{\mathcal{A}}=[\boldsymbol{\Phi}_L^T(t)\mathbf{A}(t)\boldsymbol{\Phi}_R(t)-\boldsymbol{\Phi}_L^T(t)\dot{\boldsymbol{\Phi}}_R(t)]$ is a diagonal matrix containing the eigenvalues of $\mathbf{A}(t)$ along the diagonal, $\boldsymbol{\mathcal{B}}(t)=\boldsymbol{\Phi}_L^T(t)\mathbf{B}(t)$ is the modal control matrix, $\boldsymbol{\mathcal{F}}(t)=\boldsymbol{\Phi}_L^T(t)\mathbf{F}(t)$ is the vector of modal forces, and $\boldsymbol{\mathcal{C}}(t)=\mathbf{C}\boldsymbol{\Phi}_R(t)$ is the modal output matrix. The right $\boldsymbol{\Phi}_R(t)$ and left $\boldsymbol{\Phi}_L^T(t)$ modal matrices, used for the transformation, are periodic time varying and determined using Hill's method of infinite determinants [16]. Using such a method, the modal matrices are expressed in terms of Fourier expansion series; that is,

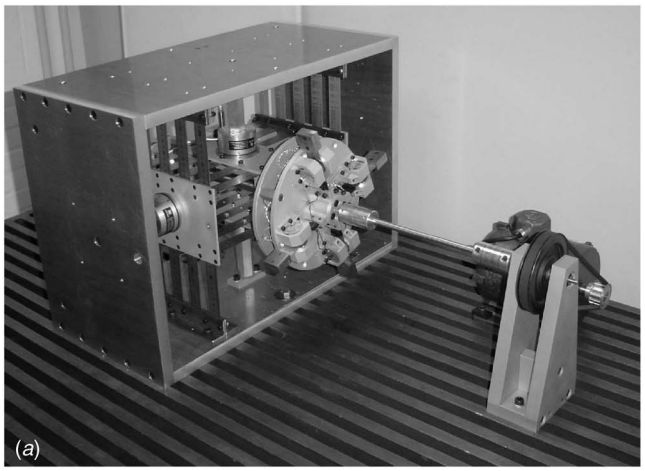

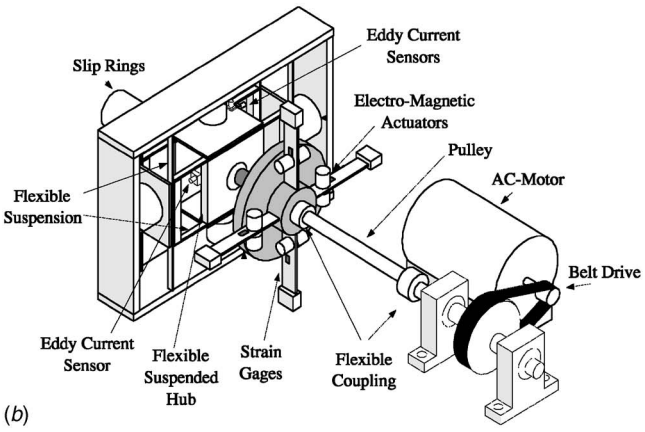

Fig. 4 Photograph and schematic drawing of the test rig

$$\mathbf{\Phi}_R(t) = \sum_{j=-n}^{n} \mathbf{\Phi}_{R,j} e^{ij\Omega t} \tag{5}$$

$$\mathbf{\Phi}_{R(t)} \mathbf{\Phi}_L^T(t) = \mathbf{I} \tag{6}$$

The modal matrices are composed of the eigenvectors of the system. The Fourier coefficients $\mathbf{\Phi}_{R,j}$ represent basis and parametric vibration mode components of the system. Basis modes, corresponding to the basis eigenvalues λ, are given by $\mathbf{\Phi}_{R,0}$. Parametric vibration modes, corresponding to the eigenvalues $\lambda + ij\Omega$, are given by $\mathbf{\Phi}_{R,j}$. That means, analyzing the vibration mode shapes by studying the eigenvectors in terms of the Fourier expansion coefficients, the presence of the parametric vibration modes in the waterfall diagrams in Figs. 2 and 3 can be explained. The modal coordinates $\boldsymbol{\xi}(t)$ of the transformed system address both type of modes, i.e., the basis modes and the associated parametric modes. Therefore, reducing the vibration amplitudes of hub and blades using the representation in the modal state coordinates $\boldsymbol{\xi}(t)$ implies that the basis as well as the parametric modes will be reduced. The efficiency of this modal transformation technique for analyzing the coupled rotor-blade system and for mathematically explaining the presence of parametric vibrations in such a system is carefully investigated in Saracho and Santos [17].

Test Facility

An experimental test setup was specially designed and built for the experimental investigation of active rotor-blade vibration control. Figure 4(*a*) shows a photograph and Fig. 4(*b*), a schematic drawing of the test rig. The rig is composed of a rigid rotating disk mounted on an elastically supported hub. The elastic support is built by a set of flexible beams, allowing the hub to perform only lateral movement. It means that disk angular rotations and gyroscopic effects are avoided. Four flexible blades with the lengths of 80 mm are radially attached to the disk. The four blades are designed as simple Euler-Bernoulli beams with 0.108–0.141 kg masses attached at the tip end. Different schemes of blade configurations, with and without mistuning, can be easily generated by substituting or rearranging the blades or by changing the weight of the tip masses.

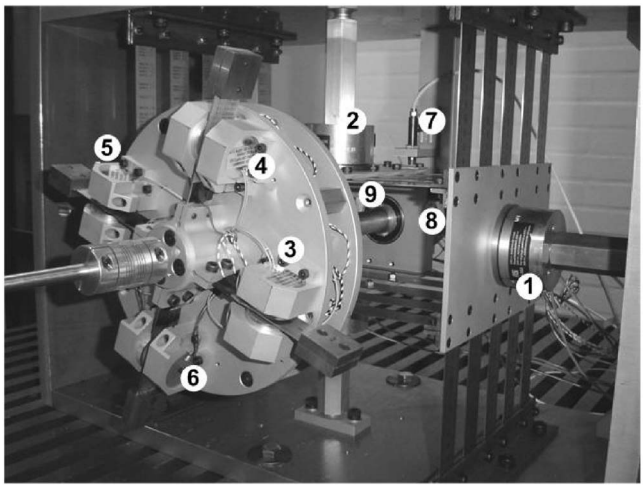

Fig. 5 Close-up photographs of the rotor-blade test rig showing measurement sensors and electromagnetic actuators

To drive the rotor-blade system an AC-motor (0.17 hp) is built into the rig. The motor speed is controlled by a frequency converter. The motor torque is transmitted to the elastically supported bladed rotor with help of an auxiliary subsystem built by a pulley and two flexible couplings. The flexible coupling arrangement allows "free" rotor/hub lateral movement.

Sensors. Various sensors are built into the test rig to monitor the rotor and blade vibration levels. The blade deflections, the rotor lateral movement and the rotor angular position and speed are monitored (see Fig. 5). The rotor/hub lateral movement is monitored by two eddy current displacement probes (elements 7 and 8 in Fig. 5). The rotor angular position and speed are also measured by means of an eddy current displacement probe attached to the hub (element 9). Such a sensor detects a mark at the shaft surface, and its signal is used as trigger. Based on the time history of trigger signals, the rotor angular speed and position can be calculated. To measure the deflections of the blades, each blade is instrumented with a pair of strain gages. The strain gages are connected to analog amplifiers (Wheatstone bridges) and filters. Electronic circuit boards have been developed for this particular test rig and built into the rotating disk. The measured strain gage signals are amplified and transmitted from the rotating disk to an external control unit, located outside the rotor in the inertial nonrotating frame, through an arrangement built by 12 slip rings.

Actuators. Six pairs of noncontact electromagnetic actuators are used to control the blade and rotor vibrations. Four sets of actuators are built into the rotating disk, acting directly onto each one of the blades (elements 3–6 in Fig. 5.) The remaining two sets of actuators (elements 1 and 2), act directly onto the hub and are attached to the inertial reference frame. This means, that these two pairs of actuators work as an active radial magnetic bearing, controlling the rotor lateral movement. All six sets of electromagnetic actuators are built by low-cost holding magnets. The power-amplified control signals to the actuators fixed in the rotating disk as well as the measurement signals are transmitted through the

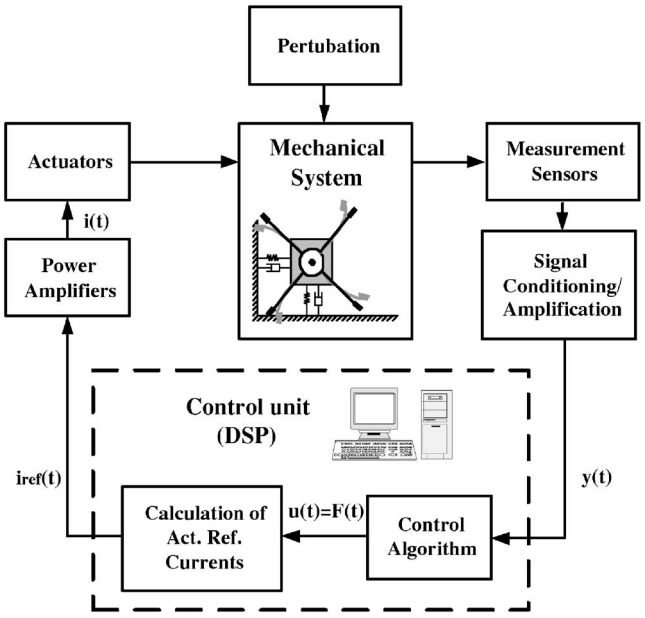

Fig. 6 Control setup for the rotor system

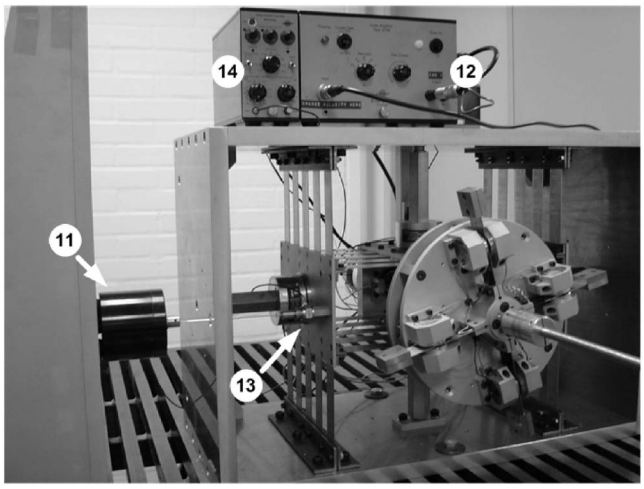

Fig. 7 Experimental rotor-blade system setup: electromagnetic shaker (element 11) power amplifier for the shaker (element 12), force transducer (element 13), and charge amplifier (element 14)

slip-ring assembly.

The static force produced by the magnetic flux between an electromagnetic actuator and the controlled element is nonlinear and dependent on the air-gap area A_a, the magnetic permeability of air μ_a, the number of turns in the magnet coil n, the control current in the coil i and the effective magnetic air gap z_0+z. The force is given by

$$F = \frac{n^2 \mu_a A_a}{4}\left(\frac{i}{z_0+z}\right)^2 \tag{7}$$

The frequency bandwidth of the magnetic actuators will be limited due to magnet coil inductance. Generally speaking, for control purposes the frequency bandwidths of the actuators must be larger than the highest frequency of the rotor-blade system intended to be controlled. Otherwise, the actuator dynamics will significantly limit the performance of the controlled system and threaten stability once it is not included in the mathematical model. In order to incorporate the actuator dynamics into the control algorithm, the frequency response function expressing the relation between a reference current and the produced magnetic force is determined. Combining the theoretical static magnetic force given by Eq. (7) and such frequency response functions, a relation between the desired magnetic forces and the reference control current can be expressed as

$$i_{\text{ref}}^2 = CF(z_0+z)^2 G(s) \tag{8}$$

where C is a constant given by $C_h = 4/(n_m^2 \mu_a A_a) = 2 \times 10^{-3}\ \text{A}^2/(\text{Ns}^2)$ for the hub actuators and by $C_b = 6 \times 10^{-3}\ \text{A}^2/(\text{Ns}^2)$ for the smaller blade actuators. $G(s)$ is a transfer function describing the filter-shaping behavior of the actuator in the frequency domain. The "filter function" $G(s)$ is determined as the inverse of the transfer function describing the dynamics of the magnetic actuator.

Signal Processing and Data Acquisition. The sensors and actuators implemented in the active rotor-blade system are connected to a digital signal processor DSPACE® DS1103 board, hosted on a personal computer. For the active control experiments, the digital signal processor monitors the measurement signals and runs a control algorithm in real time with a sampling rate of 1000 Hz.

Figure 6 shows the experimental control-system setup. The measured and conditioned sensor signals are fed into the digital signal processor. The control algorithm determines the desired control action based on the measured signals, i.e., the required active magnetic forces $F(t)$ to suppress the system vibrations. The compensation of actuator nonlinearities due to the magnetic air gap and operational frequency range is done by calculating the control actions $F(t)$ with the aid of the reshaping filter functions, Eq. (8). Hereby, the control signal $u(t)$, represented by the desired control forces $F(t)$, are transformed into reference current control signals $i_{\text{ref}}(t)$ and sent to the actuator power amplifiers. Such a control signal reshaping implies that a linear control algorithm can be implemented despite the nonlinearity of the electromagnetic actuators.

Experimental Results

The dynamics of the noncontrolled as well as the performance of the actively controlled coupled rotor-blade system are now experimentally analyzed. For this purpose, the test rig is equipped with a shaker for perturbating the system and a force transducer. Figure 7 shows the force transducer (element 13), attached to the hub, and the shaker (element 11) attached to the flexible foundation by means of a wire. The measured perturbation force and the resulting rotor displacement are fed into a signal analyzer to calculate the rotor frequency-response function. The frequency response of a rotating blade is determined by projecting the nonrotating excitation force onto a direction orthogonal to the blade.

Noncontrolled Rotor-Blade System (Tuned Blades). Before the active vibration controllers are implemented and tested, the noncontrolled system is analyzed with the aim of observing the peculiarities of the coupled rotor-blade dynamics and validating the derived mathematical model. The frequency-response spectra of the system operating passively in steady-state condition were measured for various rotational speeds in the span of 0–600 rpm. Figure 8(*a*) shows the measured frequency responses (waterfall diagrams) for the blade movement, and Fig. 8(*b*) shows the rotor horizontal movement for the noncontrolled rotor-blade system. These clearly show the presence of parametric vibration modes due to the rotor and blade vibration coupling, which are described, in detail, in [5]. The waterfall diagram of the blade response (Fig. 8(*a*)) shows the increasing blade natural frequency due to the centrifugal stiffening (A), the backward-rotating parametric mode shape components (B) and the forward-rotating parts (C). The frequency components denoted by D, J, and K represent the rota-

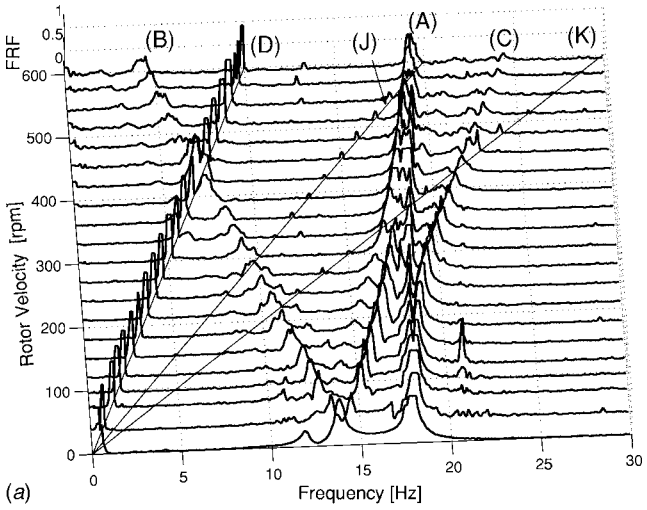

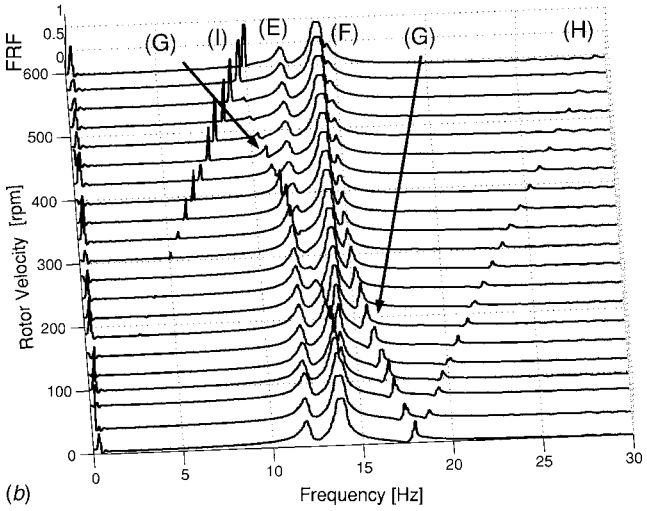

Fig. 8 Experimental frequency response (waterfall diagrams) of the (*a*) blade movement and (*b*) rotor horizontal movement of the noncontrolled rotor-blade system.

tional speeds Ω, 2Ω, and 3Ω, respectively. Observing the rotor response waterfall diagram in Fig. 8(*b*), it is possible to detect the hub lateral motion by the frequency components E and F. The rotor parametric modes are denoted by G and H and the rotational speed by I.

The experimental waterfall diagrams of the coupled rotor-blade system agree very well with the theoretical diagrams in Fig. 2. The general form and the frequency components present in the experimental responses match with the theoretical ones.

Active Control of Tuned Rotor-Blade System. In the paper by Christensen and Santos [5], it was shown that in the case of tuned blades it is required to mount sensors and actuators in all blades as well as on the rotor/hub in order to control all vibration levels. Therefore, six sets of actuators and sensors are applied to the system to control and monitor it.

Decentralized PD Control. First, a control scheme composed of six independent classical decentralized PD controllers are designed and implemented in the experimental setup. The measured rotor positions and blade deflections are numerically differentiated in the control unit to obtain velocities. Subsequently, positions and velocities are fed into independent PD controllers given by

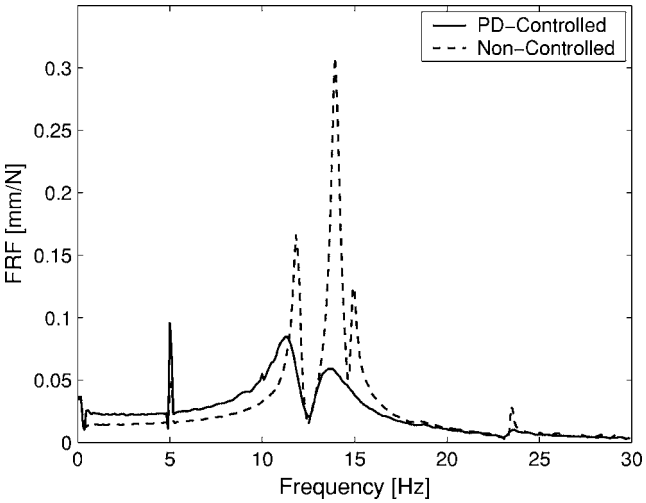

Fig. 9 Experimental frequency response function of the rotor lateral motion for the noncontrolled system and controlled by six decentralized PD controllers

$$u(t) = K_p x(t) + K_d \dot{x}(t) \tag{9}$$

where x and $\dot{x}$ denote the rotor lateral positions and velocities or the blade deflections and velocity. The proportional K_p and derivative K_d controller gains are obtained by simple trial-and-error hand tuning.

Figures 9 and 10 show the experimental frequency responses of the shaft and blade motions, respectively, when the system is controlled by such six decentralized PD controllers. The system rotates at the constant speed $\Omega = 300$ rpm (5 Hz). Compared to the frequency responses of the noncontrolled system, it seems the PD controllers work well and significantly reduce the vibration amplitudes of the rotor and blades. However, in the blade response (Fig. 10), a lack of blade actuation power is detected by the peak at the rotational frequency of 5 Hz caused by gravity. The presence of this peak is not caused because the actuators can not produce static forces large enough to compensate the gravity effect on blade deflection. It is a consequence of the limitation of the actuator dynamics because of magnetic inductance. The combination of the actuators limited dynamics and a very low blade structural damping leads to the control problems. From the blade

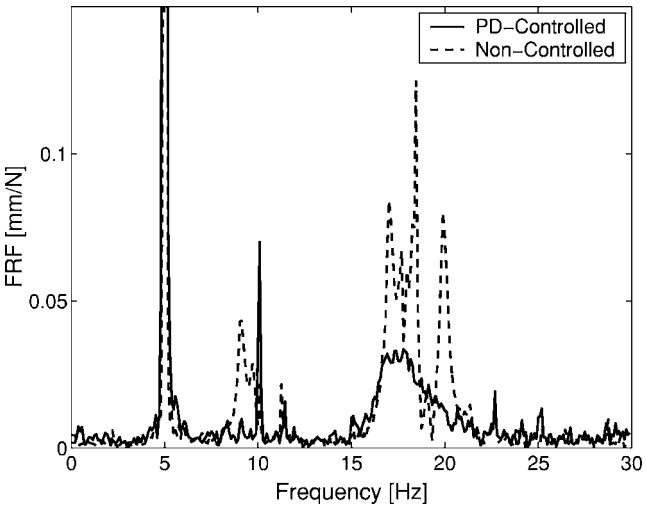

Fig. 10 Experimental frequency response function of a blade motion for the noncontrolled system and controlled by six decentralized PD controllers

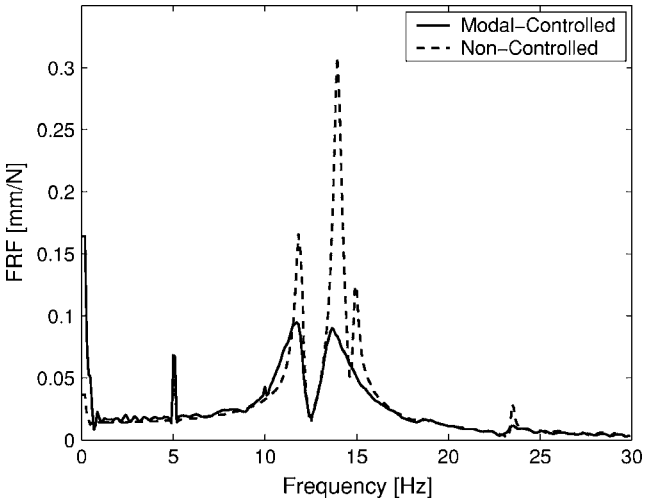

Fig. 11 Experimental frequency response function of the rotor lateral motion for the noncontrolled system and when controlled by a periodic time-variant modal state feedback controller

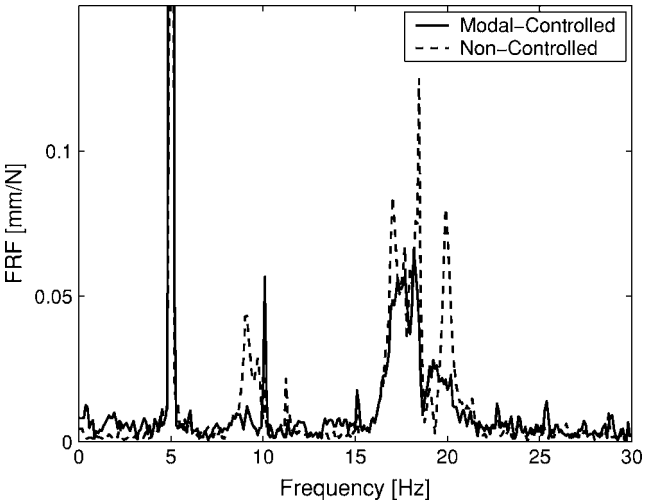

Fig. 12 Experimental frequency response function of a blade motion for the noncontrolled system and when controlled by a periodic time-variant modal state feedback controller

phase diagrams, a very low level of blade structural damping can be detected. This very low blade structural damping results in system open-loop poles being located very close to the imaginary axis. When this happens, a lightly faulty model or slow actuator dynamics can result in closed-loop poles to turn unstable even in the case of very small gains. Therefore, in order to achieve some degree of controller robustness, the gains of the PD-control scheme are detuned on the expense of achieving performance. This is, however, a typical problem controlling very low-damped structures.

Moreover, the blade response peaks related to the rotational speed are detected not only at 5 Hz, but also at the frequencies 10 Hz and 15 Hz. The explanation for these peaks is again the gravity effect resulting in a harmonic excitation of the blades by the frequency of the rotational speed 5 Hz. The dynamic response of a periodic time-variant structure subjected to a harmonic excitation by the frequency Ω is not only built by the frequency component Ω, but also by $2\Omega, 3\Omega, \ldots$ [18]. This corresponds to the frequency components present in the response, i.e., 10 Hz and 15 Hz. However, because of a very poor coherence of the measured frequency-response function at the frequencies 10 Hz and 15 Hz, it is difficult to make any emphatic conclusion related to the amplitude of the measured responses in the controlled and noncontrolled cases at such frequencies.

Periodic Modal State Feedback Control. Next, a centralized periodic time-variant modal state feedback controller is designed to adequately cope with the dynamical behavior of the system. A periodic time-variant modal state feedback controller is designed based on the modal model, for further details see [7]. The controller is designed to suppress the first six modes corresponding to all frequencies below 30 Hz.

Figure 11 and 12 show frequency responses of the bladed rotor controlled by the six pairs of actuators, using such a periodic modal state feedback control scheme. The frequency-response functions are again compared to the responses of the noncontrolled system. Significant reduction of rotor movement is observed, though the blade vibration is only slightly reduced. Compared to the responses of the decentralized PD-controlled system (Fig. 9 and 10), a better performance was achieved using the PD control. The reasons for this poor performance of the modal-controlled system are numerous.

The blade vibrations induced by gravity are noncontrolled, in this case, because these are not addressed by the controller. It is recalled that when the modal controller was designed, the modal force vector was neglected. Therefore, if the gravity effect should be controlled using the modal state control scheme, then a feedforward control loop compensating the gravity will be required. However, for the actual system such compensation is not possible due to the very low-damped poles of the system.

Another reason why the performance of the designed periodic modal state feedback control scheme cannot compete with the classical decentralized PD controllers is modeling uncertainties. It is worthy to mention that the gains of the feedback controller are calculated based on the mathematical model. Moreover, the modal state feedback controller is designed to rely heavily on quantitative mode information. Therefore, if the model is not correct, then the control actions calculated by the controller will not reduce the vibration amplitudes of the real system as much as expected.

One of the drawbacks of designing full state feedback controllers is a high sensitivity to model uncertainties. This is the case because the state controller couples all state variables, meaning that the control signal for a single-blade actuator will be dependent not only on the deflection and velocity of the actual blade, such as in the case of the decentralized PD controller, but also on positions and velocities of the rotor and other blades. In the present rotor-blade system, the modal state controller is given by a 6×12 gain matrix, which couples the positions and velocities of rotor and blades. Because of this quite complex coupling among the control signals and the blade deflections, the periodic modal state feedback controller becomes very sensitive to model imperfections.

For the actual test rig this drawback of using state space control is clearly identified. In order to design a controller and still remain some degree of robustness it was necessary to detune the controller, resulting in poor performance, as observed in Figs. 11 and 12. Using PD controllers, as previously presented, the control effort can be "pushed" much more and still retain control robustness. At the actual stage of this experimental investigation, one can conclude that the periodic modal state feedback controller performance is not as good as the classical decentralized PD control. The modal controller could not be optimized to achieve the same performance as that of the classical decentralized PD control.

Finally, it can be concluded that implementing the complex modal state controller into the system demands a very well-adjusted mathematical model. Otherwise, the model-based modal control algorithm will excite the system instead of reducing the vibration amplitudes.

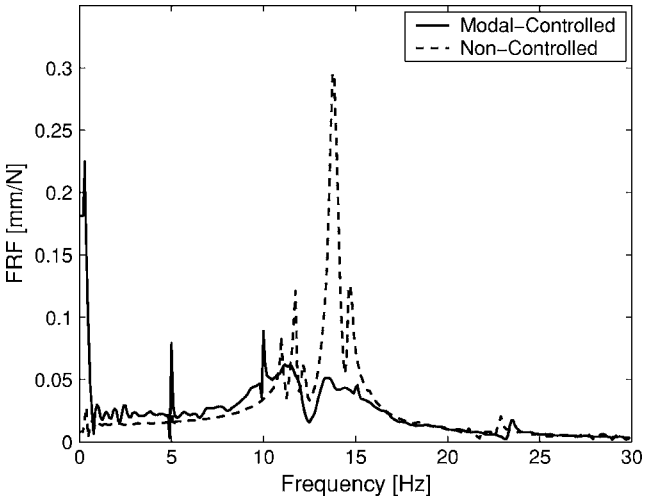

Fig. 13 Experimental frequency response function of the rotor lateral motion for the noncontrolled system and for the rotor-blade system controlled by only shaft actuation

Active Control of Mistuned Rotor-Blade System. As described in the Introduction, the blade vibrations can be controlled by using only the shaft-based actuators if the blades are properly deliberately mistuned. The reason for this is that all blade vibration modes become coupled to the lateral motion of the rotor. Therefore, by controlling the lateral motion of the rotor, the blade vibrations can also be suppressed. In this study a periodic modal controller is designed aiming at suppressing rotor as well as blade vibrations of a mistuned rotor via shaft-based actuation.

Periodic Modal State Feedback Control. The centralized periodic modal controller is designed and implemented into the mistuned test rig. The system is mistuned by adding mass to three of the blade-tip masses. Figures 13 and 14 show the frequency responses of the rotor and blade for the active-controlled mistuned rotor-blade system. Figure 13 shows a very efficient reduction of rotor vibration amplitude. Furthermore, by observing the rotor frequency response in Fig. 13, it is noted that the noncontrolled blade vibration at frequency 5 Hz lead to control spillover. Such spillover can be detected by the peak in the rotor response at the frequency 10 Hz caused by the coupling among the shaft actuator control signals and the blades motion. The vibration amplitude of the blade (Fig. 14), is also significantly reduced. All frequency components related to the family of primarily blade-related modes (modes 3–6) in the interval ~16–17.5 Hz and the two parametric contributions at ~9 Hz and ~20 Hz are efficiently reduced. The blade vibrations induced by the gravity are noncontrolled because these are not addressed by the controller.

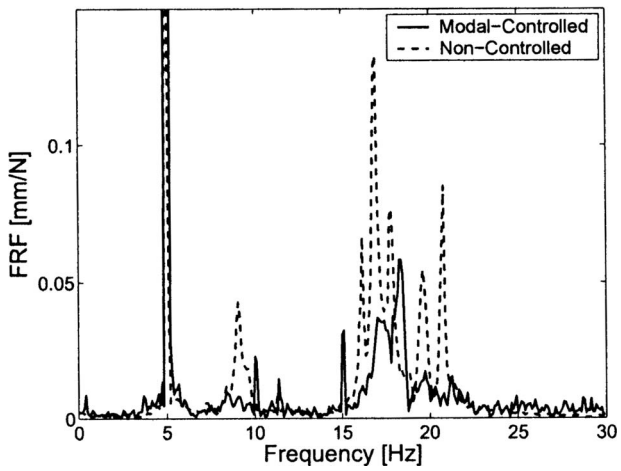

Fig. 14 Experimental frequency response function of a blade motion for the noncontrolled system and for the rotor-blade system controlled by only shaft actuation.

Conclusions

In this paper experimental and practical aspects related to the implementation of active vibration controllers for coupled rotor-blade systems have been studied. In the literature, it has previously been shown that rotor-blade vibrations can be controlled by means of only shaft-based actuation if the blades are properly mistuned.

To experimentally validate such a statement and analyze the system dynamics, an experimental rotor-blade test rig equipped with various sensors and actuators was designed and built. The experimental tests have been split into three parts; (i) experimental tests of a noncontrolled system; (ii) tests of an actively controlled tuned system, and (iii) tests of an actively controlled mistuned system.

i. Experimental tests of the noncontrolled rotor-blade system were carried out and frequency-response functions for the system rotating at speeds in the span of 0–600 rpm were measured. The peculiar characteristics of this special kind of system, such as the presence of parametric vibration modes and frequency veering, were clearly presented.
ii. For a tuned rotor-blade system, two different control strategies were implemented and tested. A scheme of six independent decentralized PD controllers allows the reduction of rotor as well as blade vibrations very efficiently. Until this stage of the experimental research, the implementation of the more complex periodic modal state feedback control scheme has shown its limitations and difficulties. Too many state variables and too many actuators are coupled in the controller design, resulting in a controller very susceptible to model imperfections. Therefore, the performance of the centralized modal controller became poor and it could not compete with the more simple decentralized PD controllers.
iii. A mistuned rotor-blade system was controlled using only radial shaft actuation. The performance of this system shows that blade vibrations can be controlled using only the shaft-based actuation in practice.

Finally, it can be concluded that the results presented reveals the potential of controlling rotor-blade vibrations via shaft-based actuation if the blades are properly mistuned. Moreover, despite the implementation difficulties and high sensitivity to modeling imperfections, it is also possible to conclude that the periodic modal control methodology applied to controller design works in practice and may be applicable to other periodic time-variant systems. Among the future aspects of this ongoing research work is to improve magnetic actuator performance aiming at also achieving a better control performance.

References

[1] Rao, J. S., 1991, *Turbomachine Blade Vibration*, Wiley, New York.
[2] Szász, G., and Flowers, G. T., 2000, "Vibration Suppression in Bladed-Disk Assemblies With Deliberate Mistuning via Magnetic Bearings," J. Vib. Control, **6**, pp. 903–921.
[3] Szász, G., Flowers, G. T., and Hartfield, R. J., 2000, "Hub-Based Vibration Control of Multiple Rotating Airfoils," J. Propul. Power, **16**(6), pp. 1155–1163.
[4] Szász, G., and Flowers, G. T., 2001, "Time Periodic Control of a Bladed Disk Assembly Using Shaft Based Actuation," ASME J. Vibr. Acoust., **123**, pp. 395–401.
[5] Christensen, R. H., and Santos, I. F., 2004, "A Study of Active Rotor-Blade Vibration Control Using Electro-Magnetic Actuation—Part 1: Theory," ASME Paper No. GT2004-53509.
[6] Cho, B., Johnson, D., Provenza, A., and Morrison, C., 2003, "Control Study

for Five-Axis Dynamic Spin Rig Using Magnetic Bearings," ASME Paper No. GT2003-38912.
[7] Christensen, R. H., and Santos, I. F., 2005, "Design of Active Controlled Rotor-Blade Systems Based on Time-Variant Modal Analysis," J. Sound Vib., **280**(3–5), pp. 863–882.
[8] Schweitzer, G., 1998, "Magnetic Bearings as a Component of Smart Rotating Machinery," *Proc. of 5th Int. Conf. on Rotor Dynamics*, Vieweg Verlag, Branschweig, pp. 3–15.
[9] Ulbrich, H., 1998, "Active Vibration Control of Rotors," Proc. of 5th Int. Conf. on Rotor Dynamics, pp. 16–31.
[10] Santos, I. F., and Scalabrin, A., 2003, "Control System Design for Active Lubrication With Theoretical and Experimental Examples," ASME J. Eng. Gas Turbines Power, **125**(1), pp. 75–80.
[11] Alizadeh, A., Ehmann, C., Schönhoff, U., and Nordmann, R., 2003, "Active Bearing of Rotors Utilizing Robust Controlled Piezo Actuators," ASME Paper No. DETC2003/VIB-48850.
[12] Althaus, J., and Ulbrich, H., 1992, "A Fast Hydraulic Actuator for Active Vibration Control," *Proc. of 5th Int. Conf. on Vibrations in Rotating Machinery*, Bath, England, Institute of Mechanical Engineers.
[13] Santos, I. F., 1994, "Design and Evaluation of Two Types of Active Tilting Pad Journal Bearings," *Proc. of IUTAM Symposium on Active Control of Vibration*, Bath, England, IUTAM, Mechanical Engineering Publications Ltd., London, pp. 79–87.
[14] Saracho, C. M., and Santos, I. F., 2001, "Dynamic Models for Coupled Blade-Rotor Vibrations," *Proc. of IX Int. Symposium on Dynamic Problems of Mechanics*, Florianopolis, Brazil, The Brazilian Society of Mechanical Sciences, Rio de Janeiro, pp. 263–268.
[15] Santos, I. F., Saracho, C. M., Smith, J. T., and Eiland, J., 2004, "Contribution to Experimental Validation of Linear and Non-Linear Dynamic Models for Representing Rotor-Blade Parametric Vibrations," J. Sound Vib., **271**, pp. 883–904.
[16] Xu, J., and Gasch, R., 1995, "Modale Behandlung Linearer Periodisch Zeitvarianter Bewegungsgle-Ichungen," Arch. Appl. Mech., **65**(3), pp. 178–193 (in German).
[17] Saracho, C. M., and Santos, I. F., 2003, "Modal Analysis in Periodic, Time-Varying Systems With Emphasis to the Coupling Between Flexible Rotating Beams and Non-Rotating Flexible Structures," *Proc. of X Int. Symposium on Dynamic Problems of Mechanics*, São Paulo, The Brazilian Society of Mechanical Sciences, Rio de Janeiro, pp. 399–404.
[18] Irretier, H., 1999, "Mathematical Foundations of Experimental Modal Analysis in Rotor Dynamics," Mech. Syst. Signal Process., **13**(2), pp. 183–191.

Bump-Type Foil Bearing Structural Stiffness: Experiments and Predictions

Dario Rubio
e-mail: dariorubio10@neo.tamu.edu

Luis San Andrés
e-mail: lsanandres@mengr.tamu.edu

Mechanical Engineering Department,
Texas A&M University,
College Station, TX 77843-3123

Gas foil bearings (FB) satisfy many of the requirements noted for novel oil-free turbomachinery. However, FB design remains largely empirical, in spite of successful commercial applications. The mechanical structural characteristics of foil bearings, namely stiffness and damping, have been largely ignored in the archival literature. Four commercial bump-type foil bearings were acquired to measure their load capacity under conditions of no shaft rotation. The test bearings contain a single Teflon-coated foil supported on 25 bumps. The nominal radial clearance is 0.036 mm *for a* 38 mm *journal. A simple test setup was assembled to measure the FB deflections resulting from static loads. The tests were conducted with three shafts of increasing diameter to induce a degree of preload into the FB structure. Static measurements show nonlinear FB deflections, varying with the orientation of the load relative to the foil spot weld. Loading and unloading tests evidence hysteresis. The FB structural stiffness increases as the bumps-foil radial deflection increases (hardening effect). The assembly preload results in notable stiffness changes, in particular for small radial loads. A simple analytical model assembles individual bump stiffnesses and renders predictions for the FB structural stiffness as a function of the bump geometry and material, dry-friction coefficient, load orientation, clearance and preload. The model predicts well the test data, including the hardening effect. The uncertainty in the actual clearance (gap) upon assembly of a shaft into a FB affects most of the predictions.* [DOI: 10.1115/1.2056047]

Introduction

Gas foil bearing technology has made significant progress during the last 30 years. Foil bearings (FBs) fulfill most of the requirements of novel oil-free turbomachinery by increasing tenfold their reliability in comparison to rolling elements bearings, for example [1]. Foil bearings are made of one or more compliant surfaces of corrugated sheet metal and one or more layers of top foil surfaces. The compliant surface provides bearing structural stiffness and comes in several configurations such as a bump type (see Fig. 1), leaf type, and tape type, among others. Due to the hydrodynamic film created by rotor spinning, the top foil and elastic structure retract resulting in a larger film thickness than with rigid wall bearings [2,3], thus enabling high-speed operation and larger load capacity [1], including a tolerance for shaft misalignment. The underlying compliant structure (bumps) provides a tunable structural stiffness source [4–6], and damping of Coulomb type arises due to the relative motion between the bumps and the top foil, and between the bumps and the bearing wall [7,8].

FBs generally operate with ambient air. However, some specific applications use other fluids such as helium, xenon, liquid nitrogen, and liquid oxygen, among others [9]. Remarkable improvements in high-temperature limits are obtained by using coatings (solid lubricants) [10]. Process gases can operate at very high temperatures without chemically breaking down, as opposed to conventional lubricant oils. Since the later 1960s, gas FBs are common in air cycle machines, the heart of the environment control system in aircraft. Current applications of FBs include oil-free cryogenic turboexpanders for gas separation plants, auxiliary power units for various aerospace and ground vehicles, automotive gas turbine engines, vapor-cycle centrifugal compressors, and commercial air/gas compressors [9].

Recently, Della Corte and Valco [11] proposed a simple empirical formula to estimate the ultimate load capacity in foil bearings in terms of the product of bearing diameter and operating speed. The proportionality constant (D) depends on the FB configuration. The authors define three generations of foil bearings. First generation FBs with simple bump distributions and developed in the 1970s show a load coefficient $D=0.4$. Third generation FBs with controlled bump compliances in the axial and circumferential directions render a much-improved load capacity with a D coefficient up to 1.4.

The measurement of the structural stiffness in bump-foil bearings is the scope of the present study. Ku and Heshmat [4,5] provide the earliest experimental and analytical studies. Bump material and its pitch and height, and to a lesser extent bump thickness, largely determine the bump stiffness. Coatings, surface finish, and tight assembly also produce high values of bump stiffness. The presence or absence of lubrication appears not to make a remarkable difference in the bump stiffness. Ku [12] determines the structural stiffness of bump foil strips while varying test parameters and conditions such as the friction coefficient, surface coating, and lubricant, among others. For all test conditions, the dynamic structural stiffness increases as the static load increases, while becoming smaller as the amplitude of motion increases. Ku et al. [4,7] introduce a model for estimation of the elastic deformation of a bump-foil strip and the prediction of the equivalent structure stiffness and viscous damping coefficient. Iordanoff [6] also advances the analytical formula for an evaluation of the bump foil stiffness for free end and clamped end (welded) conditions. Typical analyses of bump strips include the dry-friction forces between the top foil and bumps, the housing and bumps, and the coupling forces with adjacent bumps.

There is scant information on the structural stiffness of an entire foil journal bearing. Ku and Heshmat [13] performed dynamic force tests on a bump-foil bearing and identified dynamic stiffness

Contributed by the International Gas Turbine Institute (IGTI) of ASME for publication in the JOURNAL OF ENGINEERING FOR GAS TURBINES AND POWER. Manuscript received October 1, 2003; final manuscript received March 1, 2004. IGTI Review Chair: A. J. Strazisar. Paper presented at the International Gas Turbine and Aeroengine Congress and Exhibition, Vienna, Austria, June 13–17, 2004, Paper No. GT2004-53611.

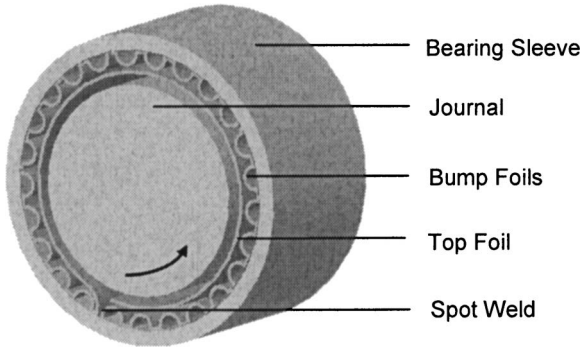

Fig. 1 Bump-type gas foil bearing

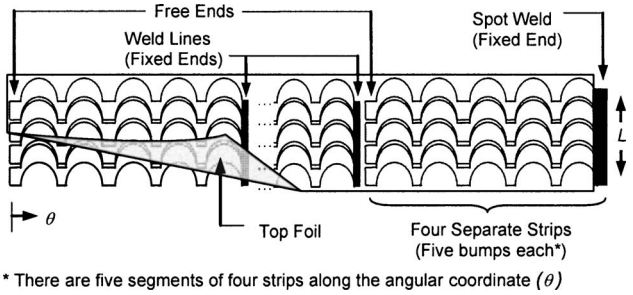

Fig. 2 Schematic view of extended bump strips

and structural damping coefficients for three static loads. The test force coefficients are frequency dependent, increasing with increasing loads. Structural coupling became apparent in spite of unidirectional loads being applied into the test bearing.

The structural stiffness and resulting bearing load capacity are the maximum available since, in operation, hydrodynamic effects merely act as a load path from the rotor to the bearing support casing. Therefore, in this investigation we provide reliable measurements of the static structural stiffness of bump-type foil bearings. The results serve as a benchmark for the calibration of analytical tools under development.

Test Foil Bearing

Four bump-type foil bearings—second generation—were acquired from a manufacturer. The bearings, with length (L) equal to 38.10 mm (1.500 in.), consist of a Teflon-coated foil (0.1016 mm thickness) supported on 25 bumps, whose height (h) and pitch (p) equal 0.381 and 4.57 mm; respectively. The FBs were designed to operate with a shaft of nominal diameter (D) equal to 38.10 mm. The manufacturer recommended a radial clearance of 0.0355 mm (1.4 ml) for the nominal configuration. Table 1 shows the nominal dimensions and parameters of two test foil bearings, identical in construction, hereby referred to as FB1 and FB2. Figure 2 depicts an unwrapped view of the bump strips layout. Refer also to Fig. 15, later, for other bump geometrical parameters. The main components of the bearing are as follows:

(a) *Bearing sleeve*, a rigid cylindrical ring supporting the bump foils and the top foil.

(b) *Top foil*, a thin flat metal sheet welded to the bearing sleeve at one end and free at the other end.

(c) *Bump foil* consisting of four strips, each with five bumps, aligned axially. The end of a strip is welded to the bearing sleeve while the other end is free. A total of five segments are placed around the bearing sleeve. Each segment is welded at one end and free at the other. The test foil bearings have a total of 25 bumps around the bearing sleeve.

(d) *Spot weld* line attaching the top foil and the bump foil strips to the bearing sleeve. At the spot weld location there is a region without bumps, spanning approximately 10 deg. The spot weld constrains the movement of the top foil and the bump foil at one end (fixed end).

Table 1 Nominal dimensions and parameters of test bump foil bearings

Parameters and dimensions	Values
Inner diameter (mm), D	38.17
Axial bearing length (mm), L	38.10
Nominal clearance (mm), $Cnom$	0.0355
Number of bumps, N	25
Bump pitch (mm), p	4.572
Bump length (mm), $2lo$	4.064
Foil thickness (mm), t	0.102
Bump height (mm), h	0.381
Poisson's ratio, υ	0.29
Modulus of elasticity (MPa), E	213.73
Bearing weight (kg)	0.278

Experimental Procedure

A simple test setup is assembled on a lathe. Figure 3 depicts the main components of the test setup, consisting of a test foil bearing, a copper shaft, a dynamometer, and a displacement eddy current sensor. The dynamometer is clamped to the lathe tool holder and moves horizontally by rotating the tool holder positioning mechanism. Two FBs are tested with three different shafts of diameters, $D_1=38.07$ mm (1.499 in.), $D_2=38.1$ mm (1.500 in.), and $D_3=38.13$ mm (1.501 in.). Thus, different assembly bearing preloads are achieved. As per the manufacturer specifications, shaft diameter D_2 should provide a 35.55 μm radial clearance with the foil bearing.

The clearance hereby defined refers to an actual (air) gap between the foil bearing and the journals. It is important to note that most foil bearings are assembled with a preload, i.e., interference between bearing and shaft. Analytical predictions of gas foil bearing performance rely on a predefined air gap, however. Radil et al. [14] and DellaCorte et al. [15] follow an empirical procedure to estimate the linear region of FB structural deflection, and define this overall displacement as the FB clearance. This ad-hoc practice is not followed here.

The load application mechanism consists of moving the dynamometer toward the foil bearing sleeve. Once the dynamometer touches the bearing, the loading process starts from 0 to 224 N (0 to 50 lb). The bearing deflections are irregular for small loads (<44 N), and therefore more collection of data pairs (static load, bearing deflection) are recorded in this load region. A

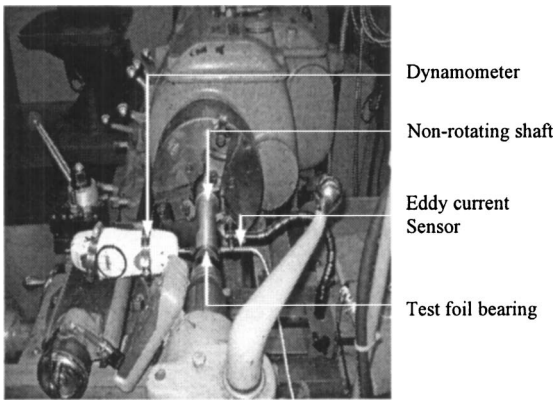

Fig. 3 Test setup for static experiments. Side view.

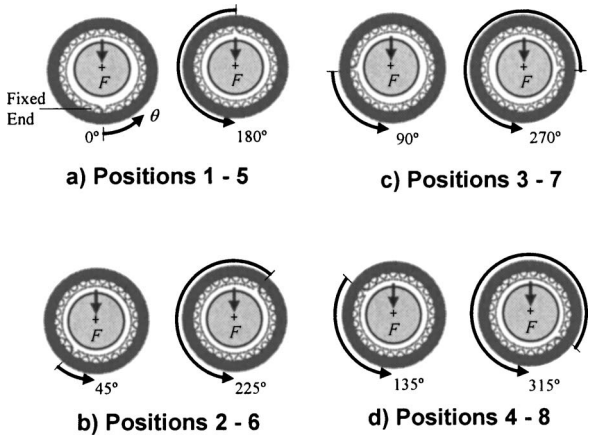

Fig. 4 Load and bearing angular orientations grouped in pairs

reasonable time between individual loading processes is taken to ensure the repeatability of the displacement data. The loading process is performed along eight angular positions 45 deg apart from each other; each angular position is labeled, as shown in Fig. 4. The spot weld on the foil bearing is a reference for the origin of the circumferential coordinate (θ), with angles measured from the free end toward the fixed end.

Identification of FB Structural Stiffness

The FB structural characteristics can be distinguished from the measurements. The static cross-coupled bearing deflection is negligible compared to the deflection along the load direction. Figures 5 display the recorded deflections versus loads for journals of diameter (D_1) through (D_3), i.e., for increasing preloads. Deflection-versus-load curves corresponding to applied loads at opposite sides (180 deg apart) of the bearing sleeve are grouped as paired measurements, i.e., positions 1 and 5, for example. Note that the applied loads are compressive; thus, negative values do not indicate traction but rather their angular orientation. Results shown in Fig. 5 correspond to FB1. Similar results are found for FB2; see [16] for details.

Figures 5 show that the structural deformation mechanism of the test FB1 is nonlinear for all angular orientations. A third-order polynomial, $F=g(X)$, fits best the load and deflection pairs at meridional planes. The correlation coefficients of the polynomials exhibit values larger that 99.3% for all test data pairs. Appendix A shows the coefficients of the polynomial fit functions.

For journal diameters D_1 and D_2, the static load versus the deflection curve at position 1 (0 deg) is distinctly different than those results shown for other angular positions, as shown in Figs. 5(a) and 5(b), and labeled as the spot weld effect. At position 1 (θ=0 deg), the load pushes the bearing into the shaft at the spot weld, as depicted in Fig. 4. Hence, the top foil and bumps around the spot weld are being compressed. The bumps located at the fixed end are more constrained than the bumps located at the free end. The foil bearing, when subjected to small loads applied at the location of the spot weld, tends to move toward the free end since the bumps near this angular position provide less resilience to the movement than the bumps located at the fixed end [7,8]. Once the load increases, the bumps next to the fixed end become active and the bearing develops larger stiffnesses. Although results at position 1 (0 deg) show a different pattern, the deflection-versus-load curves still follows a nonlinear behavior. Conversely, preloading the bearing (using shaft diameter D_3) eliminates the peculiar deformation behavior at position 1 (0 deg), as shown in Fig. 5(c). The bearing preload expands the top foil and compresses (retracts) the bumps even before the loading process starts. Therefore, the bumps at the free and fixed end become active simultaneously.

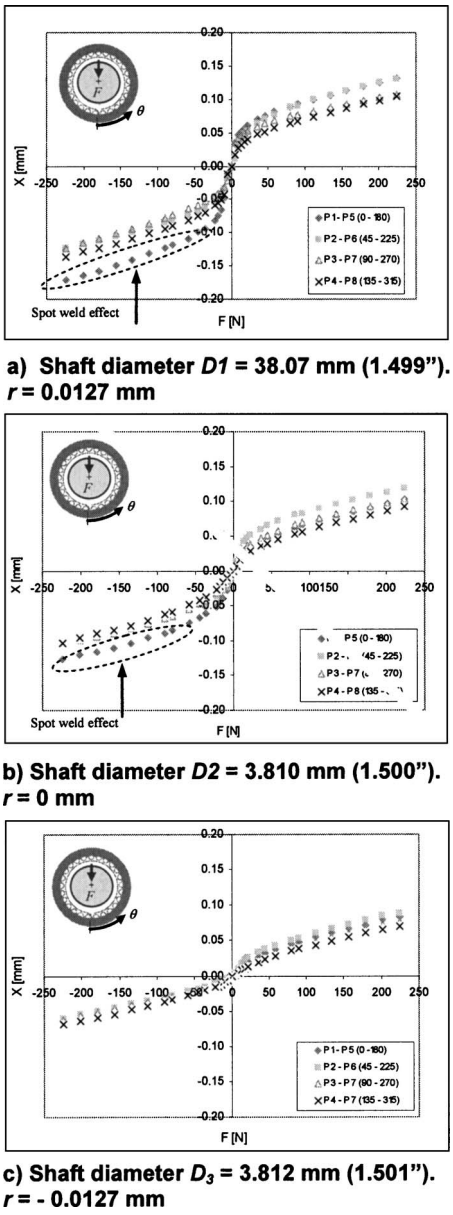

a) Shaft diameter *D1* = 38.07 mm (1.499"). *r* = 0.0127 mm

b) Shaft diameter *D2* = 3.810 mm (1.500"). *r* = 0 mm

c) Shaft diameter D_3 = 3.812 mm (1.501"). *r* = - 0.0127 mm

Fig. 5 Foil bearing deflection versus static load for all angular positions

Bearing structural stiffness is identified for each shaft diameter from $K=\partial F/\partial x$. Figures 6 and 7 depict the identified structural stiffness for angular positions 1–5 (0 deg–180 deg) and 4–8 (135 deg–315 deg), respectively. The graphs show the effects of the three different shaft diameters (assembly preload) on the FB1 structural stiffness. Remarkable differences are distinguished in K as the assembly preload increases. More structural stiffness curves are given later with comparison to analytical predictions. The structural stiffness, derived from the load versus deflection tests, increases nonlinearly as the radial deflection (shaft displacement) increases, thus producing a hardening effect. Similar results are obtained for FB2 and considering other angular positions, see [16].

In general, the FB structural stiffness varies significantly with shaft diameter (preload). When the shaft diameter is D_1 =38.07 mm (1.499 in.), the bearing stiffness exhibits the widest curve and presents the lowest structural stiffness values. For the nominal shaft diameter D_2=38.10 mm (1.500 in.), the bearing stiffness increases relative to the D_1 structural stiffness curve for

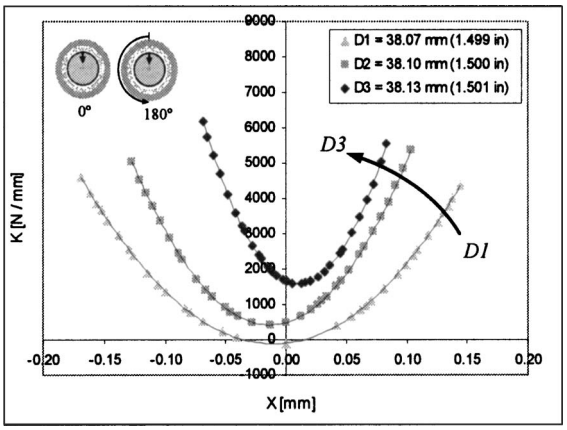

Fig. 6 FB1 structural stiffness versus deflection for three shaft diameters. Positions 1–5 (0 deg–180 deg)

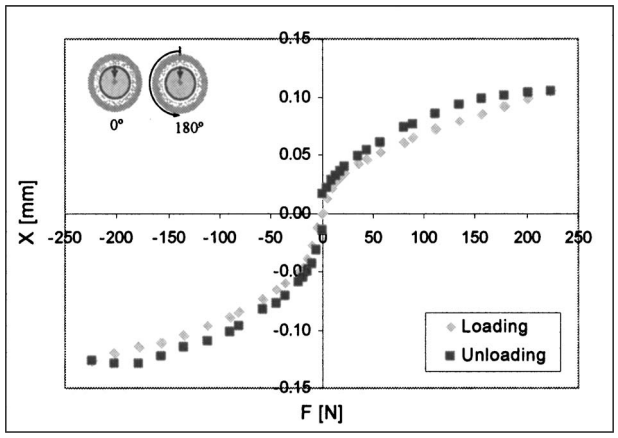

Fig. 8 Hysteretic on test foil bearing. Positions 1–5. D_2 shaft nominal diameter

any magnitude of bearing deflection. Finally, the higher identified structural stiffnesses are obtained when the bearing is preloaded, i.e., by using shaft diameter D_3=38.13 mm (1.501 in.). As explained earlier, the bumps are already compressed (preloaded) when using D_3; therefore the structural stiffness is larger, in particular for low static loads.

In addition to the FB structural stiffness, the hysteresis in a foil bearing is also important to reveal its inherent damping mechanism. To identify such behavior the test foil bearing is loaded and unloaded in the same set of measurements. According to [17], Coulomb-type damping in foil bearings is produced by the sliding between the top foil and the bump foils while in contact, and also by bump foils and the bearing sleeve. The experiments of loading and unloading compliant foil bearing FB1 are shown in Fig. 8, for angular positions 1–5 (0 deg–180 deg). Frictional forces between the foil surfaces restrain the movement of the bump foil and the top foil when the bearing is being unloaded; thus, the unloading path follows a different direction than the loading path.

Predictions of FB Structural Stiffness

The analytical procedure to determine the FB structural stiffness relies on the assembly of reaction forces produced by individual bumps to balance an external load. The bump reaction forces depend of its material properties and geometry; and on its local deflection (ζ) that depends on the rotor displacement (X), nominal clearance (C_{nom}) and assembly preload (r). The model regards the bumps as individual spring-like elements, as shown in Fig. 9, whose stiffnesses are calculated using Iordanoff's formula [6]. This reference details the model including the effects of dry friction effects. Appendix B presents the formula for a prediction of the entire FB structural stiffness. In conducting the predictions, the bump pitch (p) is regarded as constant and the interaction between bumps is neglected.

The FB structural stiffness model is sensitive to the bump dimensions, material parameters, attachment, and disposition. The influence of these parameters was evaluated to assure the reliability of the analytical predictions to the present test results. See [13] for details on the study, including an uncertainty analysis. The best agreement for the largest deflections (predicted versus test) require a bump length 6% larger than its nominal dimension (l_o =2.032 mm). This value is within the uncertainty of the bump manufacturing.

Figure 10 shows the predicted static load versus deflection curve for angular positions 1–5 and the corresponding experimental values for the same angular positions. The predicted loads are determined with the parameters noted in the figure and shaft diameter D_2, i.e., nominal zero preload and selecting C_{nom} =0.0355 mm. Notice in the predictions the flat section at small deflections (no preload), which represents the gap between the shaft and the bearing due to the nominal clearance. On the other hand, the flat region from the experimental load versus the deflection curve is less evident than with the analytical results. The predictions in Fig. 10 are obtained for a dry friction coefficient μ_f=0.1 and for a bump half-length, l_o=2.159 mm. The discrep-

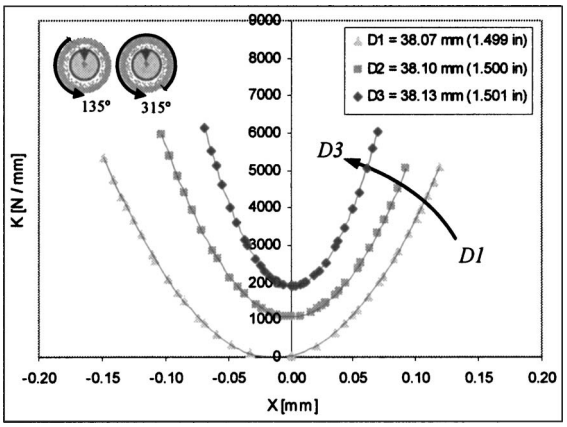

Fig. 7 FB1 structural stiffness versus deflection for three shaft diameters. Positions 4–8 (135 deg–315 deg)

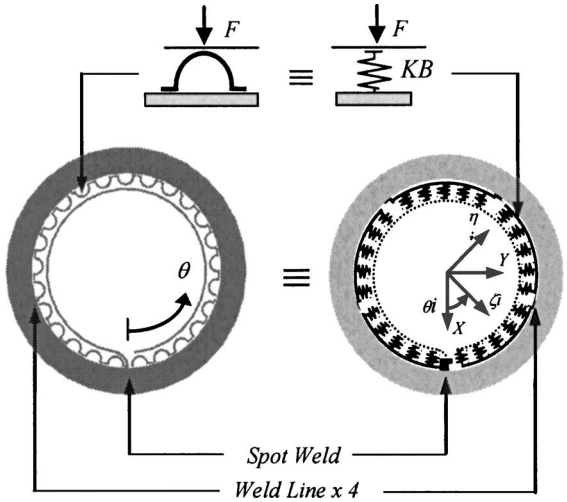

Fig. 9 Equivalent foil structural stiffness model

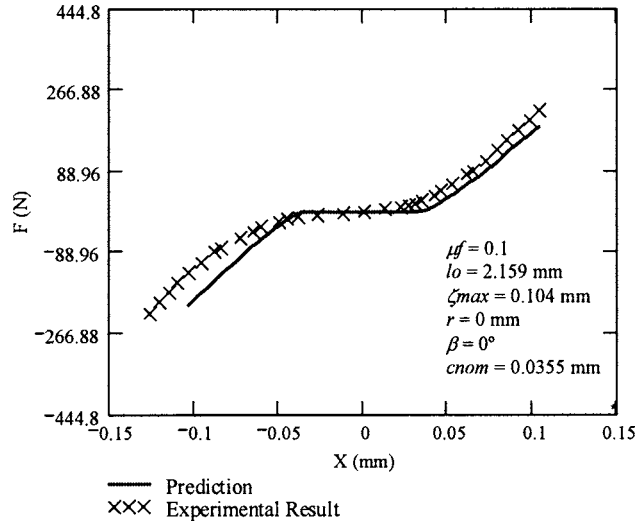

Fig. 10 Predicted and experimental load versus bearing deflection curves for positions 1–5 (0 deg–180 deg) (shaft diameter D_2; μf=0.1; l_o=2.159 mm)

ancies between the predictions and test values attest to the simplicity of the formula used [6], strictly applicable to single bumps with one or both ends constrained.

The foil bearing structural stiffness is also sensitive to the dry friction coefficient. Figure 11 shows that increasing μ_f renders larger reaction forces; thus also increasing the FB stiffness. Ku [12] notes a similar effect. Dry friction coefficients from 0.01 to 0.2 provide the best agreement with the experimental results, as depicted in Fig. 10, implying that low friction coefficients govern the structural characteristics in the test FBs. Salehi et al. [18] obtain a similar dry friction coefficient when exciting a corrugated metal sheet at different frequencies. Results at low frequencies, i.e., approximately 0 Hz, evidence small values of μ_f.

Table 2 shows the effect of radial clearance variations on the prediction of deflection for a large load (±224 N). The table also notes the deviation of predicted displacement relative to the test

Table 2 Prediction of rotor displacements at ±224 N for different values of radial clearances. (Position 1–5 (0 deg–180 deg); μ_f=0.1; r=0 mm; nominal FB1 dimensions)

	Rotor displacement (mm)		
C (μm)	Predictions	Max experimental deflection	Percentage deviation (%)
33.0	0.1061	0.127	+16.6
35.6	0.1089	0.127	+14.8
38.1	0.1122	0.127	+11.6
40.6	0.1153	0.104	−15.4
43.2	0.1270	0.104	−18.0

value. For radial clearances from 33.02 to 38.10 μm; the predictions are lower then the measured values. Conversely, larger clearances of 40.64 and 43.18 μm overpredict the deflections. Thus, radial clearances do not significantly affect the correlation between the predictions and the experimental results, i.e., the maximum error percent difference is 18% when the selected nominal clearance increases by ~20%.

Predicted structural stiffnesses for the FBs follow. The dry friction coefficient and the bump length are selected as μ_f=0.1 and l_o=2.159 mm. Figure 12 shows the predicted structural stiffness with no bearing preload (r=0 mm), and also displays the identified structural stiffness from the experimental results for the D_2 shaft. Figures 13 and 14 show the predicted and experimental foil bearing structural stiffness for the two other shaft diameters, D_1 =38.07 mm (1.499 in.) and D_3=38.13 mm (1.501 in.), respectively. The structural stiffness experimental values in Figs. 12 and 14 are obtained for positions 1–5 (0 deg–180 deg) while Fig. 13 shows results for positions 3–7 (90 deg–270 deg); see Fig. 3 for reference.

Figures 12–14 show similar structural stiffness values for the predicted and experimental results. The predicted stiffness correlates best with the experimental results when the bearing is preloaded. Slightly small differences are noted when the shaft diameter is D_1=38.07 mm (r=−0.0127 mm). Table 3 presents a

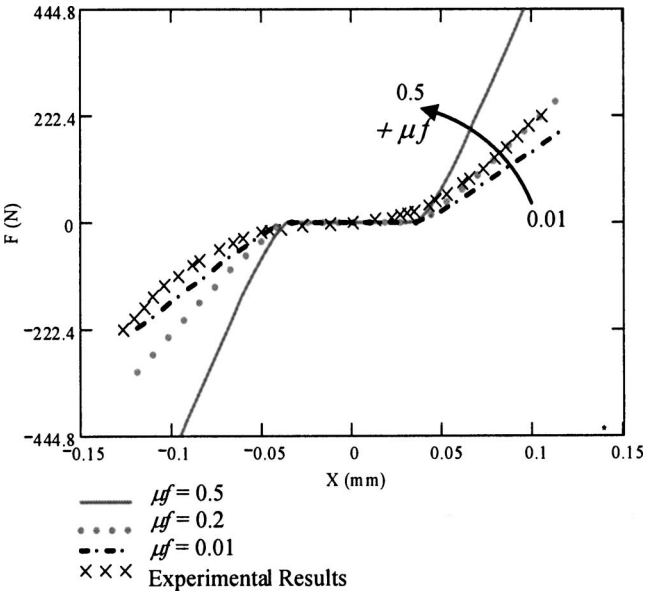

Fig. 11 Predicted load versus bearing deflection curves for increasing dry friction coefficients. (Positions 1–5 (0 deg–180 deg); shaft diameter D_2; l_o=2.159 mm)

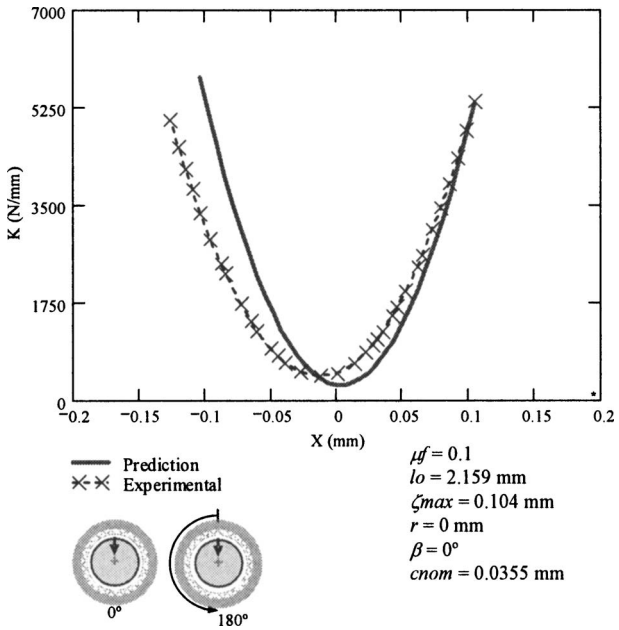

Fig. 12 Predicted and experimental structural stiffness versus shaft displacement (shaft diameter D_2; μf=0.1; l_o=2.159 mm; r=0 mm)

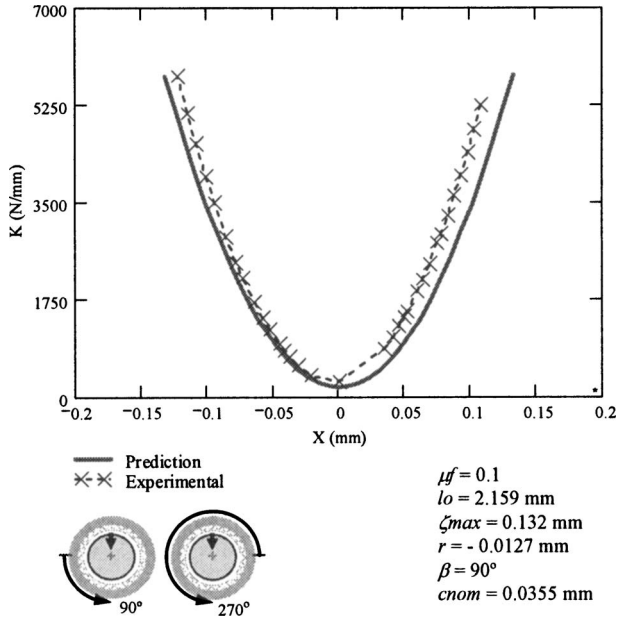

Fig. 13 Predicted and experimental structural stiffness versus shaft displacement (shaft diameter D_1, μf=0.1; l_o=2.159 mm; r =−0.0127 mm)

correlation between the predictions and the measurements of the foil bearing maximum structural stiffness. Table 3 also shows the error percent difference between the predictions and the test results. In general, the maximum predicted stiffness correlates well with the test values. However, some inconsistencies are observed at positions 1–5 (0 deg–180 deg) for a shaft diameter of 38.07 mm, where the error percentage reaches the maximum value of 21%. The rest of the error percentages are within 15%.

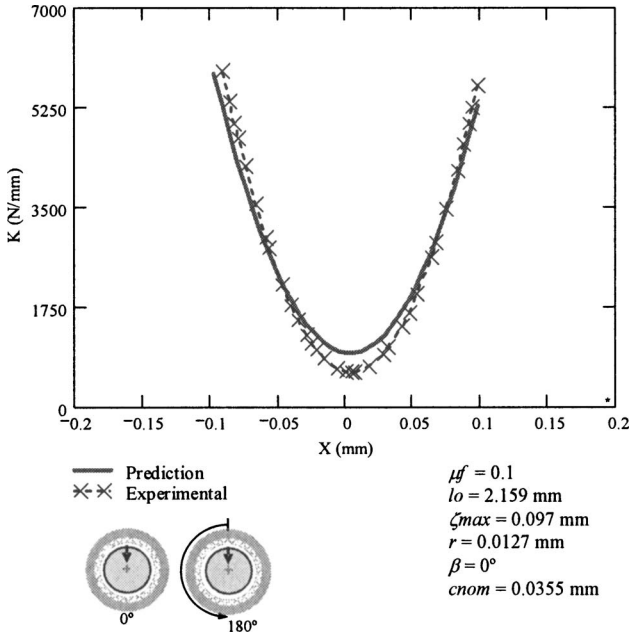

Fig. 14 Predicted and experimental structural stiffness versus shaft displacement (shaft diameter D_3; μ_f=0.1; l_o=2.159 mm; r =0.0127 mm)

Table 3 Experimental and predictions of maximum foil bearing structural stiffness (μ_f=0.1; l_o=2.159 mm; C_{nom} =0.0355 mm)

Journal diameter	Angular position	Predictions	Experimental	Error percent difference
		Maximum K (N/mm)		
D_1 38.07 mm	1–5	5870	4596	+21.7
	2–6	5263	5133	+2.6
	3–7	5695	5734	−0.7
	4–8	5903	5392	+8.9
D_2 38.10 mm	1–5	5921	5371	+10.2
	2–6	5462	5759	−5.1
	3–7	5827	5688	+2.7
	4–8	5872	5969	−1.6
D_3 38.13 mm	1–5	6015	6104	−1.5
	2–6	5910	6958	−15.0
	3–7	5907	6926	−14.7
	4–8	5896	6265	−5.9

Conclusions

Oil-free turbomachinery relies on gas foil bearings for reliable performance. An accurate characterization of foil bearing structural stiffness is important to determine the maximum load support and largest allowable shaft excursions.

Experiments were conducted to determine the structural stiffness of commercially available bump-type foil bearings. The test FBs, of nominal diameter and clearance equal to 38.1 and 0.035 mm, comprise of a single foil supported on 25 bumps around the bearing circumference. The static load versus deflection tests were conducted with three shafts of increasing diameter, inducing a degree of preload into the FB structure. The static measurements show different deflection versus load characteristics depending on the orientation of the applied static load relative to the position of the foil spot weld. The experimental results also demonstrate that the foil bearing structural deflection is nonlinear relative to the applied load. A third degree polynomial describes best the load versus deflection behavior. Static loading and unloading tests evidence a characteristic hysteresis due to the dry friction between the bumps and the bearing housing. The FB structural stiffness derived from the load versus deflection tests increases nonlinearly as the radial deflection increases (hardening effect). The radial preload results in important changes in the FB stiffness, in particular, for small load conditions.

Predictions show that the stiffness of a single bump is most sensitive to the dry-friction coefficient, the bump length, and the bump-ends conditions, i.e., welded or free to move. A simple physical model assembles the individual bump stiffnesses and renders predictions for the FB radial stiffness as a function of the bump geometry and material parameters, dry-friction coefficient, load orientation, radial clearance, and initial preload. The model predicts well the physical behavior, including the apparent nonlinearity, i.e., hardening effect at large loads. In general, the predicted structural stiffnesses correlate well with the experimentally derived coefficients, even for the largest load condition.

The large uncertainty in the actual clearance (if any) upon assembly of the shaft into a FB affects greatly the predictions. The (yet unknown) dry-friction coefficients, between the bumps and foil, and between bumps and bearing housing, are also important. Dynamic force tests are currently being performed to assess the actual dissipation characteristics in the test foil bearings.

Acknowledgment

The authors acknowledge the support of the Turbomachinery Research Consortium (TRC), the Energy Resources Program, and the National Science Foundation (NSF)—Award No. 0322925, Dr. Jorn Larsen-Basse, NSF Program Manager. Thanks to Foster

Table 4 FB1 curve fit equations of load-versus-deflection for the three shaft diameters

Shaft diameter	Angular positions	$F[N]$ vs X(mm) equations	Correlation coefficient
D_1 38.07 mm	1–5	$F=1.19E5x3+4.8E3x2+487.7x$	0.998
	2–6	$F=1.44E5x3-3.8E3x2+379.4x$	0.998
	3–7	$F=1.56E5x3+210.2x2+527.4x$	0.998
	4–8	$F=1.54E5x3+3.8E3x2+379.4x$	0.998
D_2 38.10 mm	1–5	$F=2.45E5x3-7.67E3x2+1666x$	0.998
	2–6	$F=3.15E5x3-1.87E4x2+1723x$	0.993
	3–7	$F=3.11E5x3-1.01E4x2+1961x$	0.995
	4–8	$F=2.90E5x3-853.5x2+1914x$	0.998
D_3 38.13 mm	1–5	$F=2.78E5x3+8.52E3x2-427.3x$	0.996
	2–6	$F=3.80E5x3-1.03E3x2-644.8x$	0.998
	3–7	$F=5.06E5x3+1.01E4x2+491x$	0.989
	4–8	$F=4.29E5x3+1.67E4x2+150x$	0.996

Miller Technologies for providing the test foil bearings.

Nomenclature

C_{nom} = nominal radial clearance (mm)
D = shaft diameter (mm)
E = Young's modulus (Pa)
F = static load (N)
F_X, F_Y = reaction forces, X and Y directions (N)
F_ζ = bump reaction force in the radial direction (N)
H = actual bump height (mm)$=h-\zeta I$
h = bump height (mm)
K = structural foil bearing stiffness (N/mm)
K_F = free bump structural stiffness (N/mm)
K_W = welded bump structural stiffness (N/mm)
L = bearing lengh (mm)
l_o = half of bump length (mm)
N = number of bumps
p = bump pitch (mm)
r = bearing assembly preload (mm)
t = bump foil thickness (mm)
x = foil bearing displacement (mm)
X, Y = shaft displacement along X, Y directions (mm)
α = bump height angle (degrees)
μ_f = dry friction coefficient
θ = foil bearing angular position angle (degrees)
υ = Poisson's ratio
ζ = normal deflection of bump (mm)

Appendix A: Polynomial Coefficients

Table 4 shows the nonlinear (curve fits) polynomials, obtained from the static measurements. Curve fit equations are given for FB1, at all angular positions and shaft diameters. Reference [16] reports the results for FB2.

Appendix B: Prediction of FB Stiffness

Figure 15 depicts a schematic view of a bump and top foil noting the dimensions of importance. The structural stiffness for a one end welded bump (K_W) and a free ends bump (K_F) are given by Iordanoff [6] as:

$$K_W = \frac{F}{\zeta} = \frac{E \cdot t^3 \cdot \sin^3(\alpha/2)}{12 \cdot l_o^3 \cdot p \cdot J(\alpha) \cdot (1-\upsilon_P^2) \cdot p \cdot L} \tag{B1}$$

$$K_F = \frac{F}{\zeta} = \frac{E \cdot t^3 \cdot \sin^3(\alpha/2)}{6 \cdot l_o^3 \cdot p \cdot I(\alpha) \cdot (1-\upsilon_P^2) \cdot p \cdot L} \tag{B2}$$

where F is the applied load on the bump and ζ is the bump deflection. (E, υ) are the material elastic modulus and Poisson ratio, respectively; $(p \times L)$ is the projected area of the top foil, $J(\alpha)$ and $I(\alpha)$ are functions of the bump height (h), angle (α), and the dry friction coefficient (μ_f). $(p, t, 2l_o)$ denote the bump pitch, thickness, and length, respectively.

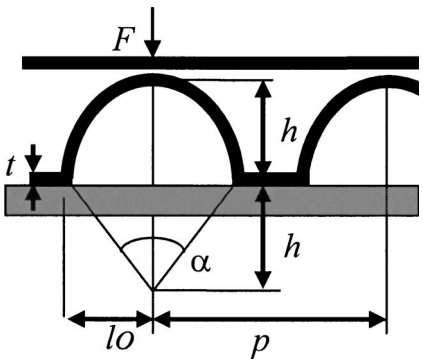

Fig. 15 Bump foil dimensional parameters

The normal deflection of each bump (ζ_i), taking into account the bearing preload and the nominal clearance, is given by

$$\zeta_i = X \cdot \cos(\theta_i) + Y \cdot \sin(\theta_i) + r - c_{\text{nom}}, \tag{B3}$$

where X and Y are the rotor displacements along the (X, Y) axes and θ_i is the angular location of a bump on the bearing circumference. A bump reaction force (F_ζ) follows as

$$F_{\zeta_i} = K_B(H_i) \cdot \zeta_i \quad \text{if } \zeta_i < 0 \tag{B4}$$

where $K_B = K_W$ or K_F, and $H_i = h - i$ is the actual bump height. Importantly enough, a bump does not provide a force if there is no deflection (actual contact). Note that the bump stiffness (K_B) depends on the location of the bump along the foil bearing, i.e., fixed end or free end.

The assembly of the individual bum forces balances the external load with components (F_X, F_Y), i.e.,

$$F_{X_i} = \sum_{i=1}^{N} F_\zeta \cdot \cos(\theta_i) \text{ and, } \quad F_{Y_i} = \sum_{i=1}^{N} F_\zeta \cdot \sin(\theta_i) \tag{B5}$$

The FB structural stiffness follows from small changes in load and displacement, i.e., $K = \partial F / \partial x$.

References

[1] Agrawal, G. L., 1997, "Foil Air/Gas Bearing Technology—An Overview," International Gas Turbine & Aeroengine Congress & Exhibition, Orlando, Florida, ASME Paper No. 97-GT-347.
[2] Heshmat, H., Walomit, J., and Pinkus, O., 1983, "Analysis of Gas-Lubricated Compliant Journal Bearings," ASME J. Lubr. Technol., **105**, pp. 647–655.
[3] Peng, J.-P., and Carpino, M., 1993, "Calculation of Stiffness and Damping Coefficient for Elastically Supported Gas Foil Bearings," ASME J. Tribol., **115**, pp. 20–27.
[4] Ku, C.-P., and Heshmat, H., 1992, "Complaint Foil Bearing Structural Stiffness Analysis Part I: Theoretical Model—Including Strip and Variable Bump Foil Geometry," ASME J. Tribol., **114**, pp. 394–400.
[5] Ku, C.-P., and Heshmat, H., 1993, "Complaint Foil Bearing Structural Stiffness Analysis Part II: Experimental Investigation," ASME J. Tribol., **113**, pp. 364–369.
[6] Iordanoff, I., 1999, "Analysis of an Aerodynamic Complaint Foil Thrust Bearing: Method for a Rapid Design," ASME J. Tribol., **121**, pp. 816–822.
[7] Ku, C.-P., and Heshmat, H., 1994, "Structural Stiffness and Coulomb Damping in Compliant Foil Journal Bearing: Theoretical Considerations," STLE Tribol. Trans., **37**, pp. 525–533.
[8] Ku, C.-P., and Heshmat, H., 1994, "Structural Stiffness and Coulomb Damping in Compliant Foil Journal Bearing: Parametric Studies," STLE Tribol. Trans., **37**, pp. 455–462.
[9] Agrawal, G. L., 1998, "Foil Air Bearings Cleared to Land," Mech. Eng. (Am. Soc. Mech. Eng.), July, pp. 78–80.
[10] DellaCorte, C., Fellenstein, J. A., and Benoy, P., 1999, "Evaluation of Advanced Solid Lubricant Coatings for Foil Air Bearings Operating at 25° and 500°C," STLE Tribol. Trans., **42**, pp. 338–342.
[11] DellaCorte, C., and Valco, M., 2000, "Load Capacity Estimation of Foil Air Journal Bearing for Oil-Free Turbomachinery Applications," STLE Tribol.

Trans., **43**, pp. 795–801.
[12] Ku, C.-P. R., 1993, "An Experimental and Theoretical Study of the Dynamic Structural Stiffness in Compliant Foil Journal Bearings," ASME 14th Biennial Conference on Mechanical Vibration and Noise, Albuquerque, NM, DE-Vol. 63, *Vibration of Mechanical Systems and the History of Mechanical Design*, pp. 83–88.
[13] Ku., C., and Heshmat, H., 1994, "Effect of Static Load on Dynamic Structural Properties in a Flexible Supported Foil Journal Bearing," ASME J. Vibr. Acoust., **116**, pp. 257–262.
[14] Radil, K., Howard, S., and Dykas, B., 2002, "The Role of Radial Clearance on the Performance of Foil Air Bearings," STLE Tribol. Trans., **45**, pp. 485–490.
[15] DellaCorte, C., and Valco, M., 2000, "Load Capacity Estimation of Foil Air Journal Bearings for Oil-Free Turbomachinery Applications," STLE Tribol. Trans., **43**, pp. 795–801.
[16] Rubio, D., "Measurement of Static Structural Stiffness of Bump-Type Foil Gas Bearings," Undergraduate Senior Honor thesis, Texas A&M University, Mechanical Engineering Department, August 2002.
[17] Lu, Y. P., and Sun, C. T., 1995, *Vibration Damping of Structural Elements*, Prentice–Hall, Englewood Cliffs, pp. 6–7.
[18] Salehi, M., Heshmat, H., and Walton, J., 2003, "On the Frictional Damping Characterization of Compliant Bump Foils," ASME J. Tribol., **125**, pp. 804–813.

Unbalance Response of Rotors Supported on Hydrodynamic Bearings Placed Close to Nodal Points of Excited Vibration Modes

Demetrio C. Zachariadis
Department of Mechanical Engineering,
Polytechnic School,
University of São Paulo,
Av. Prof. Mello Moraes 2231,
São Paulo 05508-900, Brazil
e-mail: dczachar@usp.br

The traditional 8-coefficient bearing model, used in linear rotor dynamics, is shown here to be inadequate for the unbalance response calculation of rotor systems supported on hydrodynamic journal bearings placed close to nodal points of excited modes of vibration. In such situations, one cannot neglect the time varying tilt angle between journals and bearings, whose consideration leads to the adoption of a 32-coefficient bearing model. Numerical results indicate that the differences between vibration amplitudes calculated using both bearing models can be greater than 100%, while discrepancies in the predicted stability thresholds are small. The conclusions of the study are coherent with previously published theoretical and experimental results. [DOI: 10.1115/1.2132381]

1 Introduction

For the last four decades, the 8-coefficient hydrodynamic bearing model was established as a trustworthy tool for the linear vibration analysis of rotor systems. Several authors contributed for this, among whom Lund and Orcutt [1], Lund [2,3], and Lund and Thomsen [4] provided landmark works describing methods for the calculation of the dynamic coefficients, examples of their utilization in rotor dynamics and comparisons between numerical and experimental results. Due to these, and many other publications, the 8-coefficient bearing model is presently adopted without restrictions for the calculation of unbalance response and stability threshold of rotating machinery.

Underlying the adoption of the 8-coefficient hydrodynamic journal bearing model is the assumption that only the relative translation displacements and velocities between journals and bearings result in relevant changes on the hydrodynamic static reactions developed in the lubricant film. Hence it is thought that if a bearing is placed close to a nodal point of an excited mode of the rotor, since the amplitudes of those translation displacements and velocities are very small, the resulting elastic and damping forces are insignificant, and do not influence the dynamic response of the system.

Conversely, the relative angular displacements and velocities between journals and bearings attain their maximum values in bearings placed close to nodal points, and, as it will be verified here, the consideration of their influence on the hydrodynamic forces and moments is a determinant factor for the validity of the unbalance response calculation.

The influence of the time varying relative angular misalignment of the journal on rotor vibrations can be considered by introducing additional dynamic coefficients in the 8-coefficient bearing model (here called planar model). When only angular displacement dependent moments are considered relevant, as done by Kikuchi [5], and Mukehrjee and Rao [6], eight extra coefficients must be evaluated, resulting in a 16-coefficient bearing model. The inclusion of the angular displacement dependent forces, and translation displacement dependent moments leads to a set of 32 coefficients, characterizing a complete bearing model. Unlike the coefficients of the planar model, readily available in journal bearing data books, stiffness and damping coefficients of the complete model must be numerically calculated for each particular rotor system, since they are functions of four parameters that define the static equilibrium position of the journal: two coordinates for the journal center and two tilt angles.

Jakeman [7], San Andres [8], and Jang and Kim [9] are among the few authors who evaluated these 32 coefficients for some particular kinds of bearings. Nikolakopoulos and Papadopoulos [10] extended the calculations to include third order terms in the Taylor series expansion of the fluid film reactions, obtaining nonlinear stiffness, damping and hybrid dynamic coefficients.

Except for two previous papers by this author (Zachariadis [11,12]), reports describing the use of the complete bearing model in rotor vibration analyses are almost inexistent. Jakeman [13] studied the dynamic response of a low speed marine propeller shaft supported on a relatively long stern-tube bearing, but did not provide any comments concerning the relevance of the use of the complete bearing model in his analysis. In Lund [2,3], the 32 coefficient model was mentioned but not used. Kikuchi [5] stated that the 16-coefficient model should be used for steady state response calculations of flexible rotors, while Rao [14] considered the effects of those moment coefficients negligible.

The aim of this study is to perform a detailed linear vibration analysis of rotor systems supported on bearings placed close to nodal points of excited vibration modes. It is shown that in such cases the use of the complete bearing model is ineluctable, since the adoption of the planar model leads to wrong results. In the aforementioned works, this author provided qualitative results, based on the short bearing approximation, according to which the differences between the unbalance responses calculated using the 32 and the 8-coefficient bearing models could be greater than 100% in very flexible laboratory rotors. This analysis presents analogous results concerning rotors whose dynamic properties are typical of machinery for industrial applications.

The conclusions are based on the comparison of numerical results obtained using both complete and planar bearing models, now calculated for finite length bearings. Finite Element Method procedures are adopted in order to represent rotating parts and perform linear vibration analysis.

Contributed by the International Gas Turbine Institute (IGTI) of ASME for publication in the JOURNAL OF ENGINEERING FOR GAS TURBINES AND POWER. Manuscript received December 1, 2001; final manuscript received March 1, 2002. Assoc. Editor: E. Benvenuti. Paper presented at the International Gas Turbine and Aeroengine Congress and Exhibition, Amsterdam, The Netherlands, June 3–6, 2002, Paper No. 2002-GT-30318.

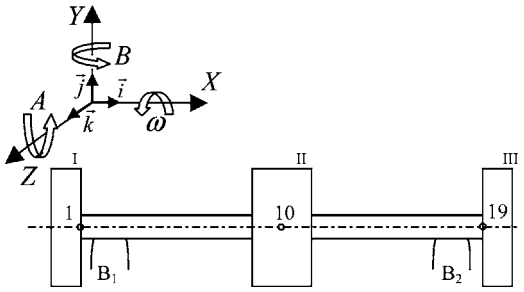

Fig. 1 Rotor system model

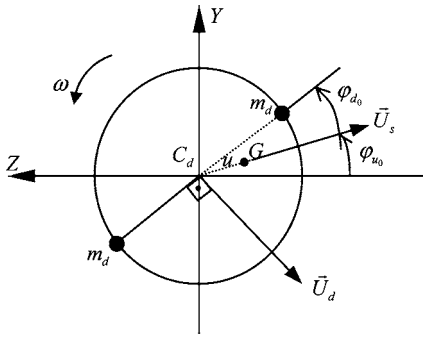

Fig. 2 Unbalance excitations

2 Rotor System

The rotor considered in the analysis, sketched in Fig. 1, is a cylindrical steel shaft with overall length of 1.02 m and a diameter of 0.06 m, with a centrally located integral disk of 0.30 m diameter and 0.15 m length. Two 40 kg disks are clamped to the ends of the shaft, so the total weight of the rotor is 1791.7 N.

Two bearings whose centrelines are symmetrically placed on either side of the shaft centre plan support the rotor. These are two 20 deg opening axial groove bearings, with length to diameter ratio $L/D=1$, diameter $D=0.06$ m, and radial clearance $c_r=70$ μm; a constant average viscosity $\mu=4$ mPa s (ISO 4 lubricant oil) is adopted in the numerical simulations.

Shaft dynamic properties are calculated using the mass and stiffness consistent matrices of the Timoshenko beam element. An 18-element model is adopted in order to represent the shaft and the central disk; overhang disks are assumed to be rigid, and their inertia properties are lumped in nodes 1 and 19. Gyroscopic moments are taken into account, and the bearings are the only source of damping for the system.

Table 1 gives the location of the nodes of the rotor model, together with other relevant properties of the system; the omitted nodes are equally spaced between the given ones. Four different values of length between bearings l_{bb} are considered in order to vary the distance between the bearings and the nodal points, defining rotors *a* to *d*, identified in Table 1.

Table 1 Rotor model properties

Nodal coordinates						
Node	1	3	6	14	17	19
X (m)	0.000	0.120	0.210	0.810	0.900	1.020

Element diameters	
elements	diameters (m)
1 to 8	0.06
9 and 10	0.30
11 to 18	0.06

Lumped inertias			
node	1	10	19
Mass M (kg)	40.0	⋯	40.0
Polar I_p (kg m^2)	0.45	0.90	0.45
Transversal I_t (kg m^2)	0.30	⋯	0.30

Rotor	Bearing location: nodes	l_{bb} (m)
a	6 and 14	0.60
b	5 and 15	0.66
c	4 and 16	0.72
d	3 and 17	0.78

Young's modulus $E=2.1\times10^{11}$ N/m^2; density: 7850 kg/m^3

The harmonic excitations acting on the disks are represented in Fig. 2: $\vec{U}_s$ is the static unbalance vector and the components of the couple unbalance vector $\vec{U}_d$ are given in Eq. (1),

$$\vec{U}_d = \omega(\dot{J}_{XY}\vec{j} + \dot{J}_{XZ}\vec{k}) \tag{1}$$

where $\dot{J}_{XY}$ and $\dot{J}_{XZ}$ are the time derivatives of the products of inertia of the disks and ω is the rotor speed. These products of inertia are computed, irrespective of their origin (skewed disks, for example), assuming that they are caused by two lumped masses m_d positioned 180 deg apart on both faces of the disk (thickness l_d and radius r_d), as exemplified in Fig. 2.

The initial phase angle of the static unbalance is φ_{u_0}, and φ_{d_0} is measured between the longitudinal plane that contains the two masses m_d and the longitudinal plane defined by the shaft centerline and the mass center of the disk. Thus, the resulting expressions for the unbalance vectors are

$$\begin{cases} \vec{U}_s = -Mu\omega^2(\cos\varphi_u\vec{k} - \sin\varphi_u\vec{j}) \\ \vec{U}_d = -m_d r_d l_d \omega^2(\cos\varphi_d\vec{j} + \sin\varphi_d\vec{k}) \end{cases} \tag{2}$$

where M is the mass of the disk, $u=|(G-C_d)|$ is the radial unbalance, $\varphi_u=\varphi_{u_0}+\omega t$ and $\varphi_d=\varphi_{u_0}+\varphi_{d_0}+\omega t$.

3 Hydrodynamic Reactions and Dynamic Coefficients

As shown in Fig. 1, the journal has four degrees of freedom: lateral displacements in Y and Z directions, and angular displacements A and B around axes Z and Y, respectively. Forces and moments are calculated after the pressure field is determined through the integration of the conventional (isothermal, laminar flow) Reynolds equation, as described in Zachariadis [12].

The bearing model chosen for this study allows for the comparison between this author's results with previously published ones related to the theme. Figure 3 displays the nondimensional moments (Qiu and Tieu [15]) around axes Y and Z acting on a journal subject to a static angular misalignment around Y; the magnitude of the angular displacement is 40% of the maximum relative tilt angle between journal and bearing.

In order to calculate the stiffness and damping matrices of the bearings (Eq. (3)), the numerical differentiation procedure described in Jakeman [7] was adopted; some of these coefficients are shown for comparison in Fig. 4.

$$[\mathbf{K}] = \begin{bmatrix} k_{YY} & k_{YB} & k_{YZ} & k_{YA} \\ k_{BY} & k_{BB} & k_{BZ} & k_{BA} \\ k_{ZY} & k_{ZB} & k_{ZZ} & k_{ZA} \\ k_{AY} & k_{AB} & k_{AZ} & k_{AA} \end{bmatrix}; \quad [\mathbf{C}] = \begin{bmatrix} c_{YY} & c_{YB} & c_{YZ} & c_{YA} \\ c_{BY} & c_{BB} & c_{BZ} & c_{BA} \\ c_{ZY} & c_{ZB} & c_{ZZ} & c_{ZA} \\ c_{AY} & c_{AB} & c_{AZ} & c_{AA} \end{bmatrix} \tag{3}$$

These comparative results are merely illustrative, and correspond to a very small portion of the information generated during the calculation process of the dynamic coefficients used in the

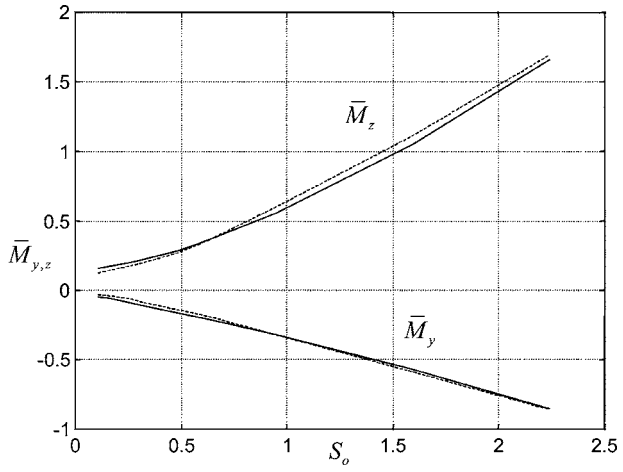

Fig. 3 Moments around axes *Y* and *Z*; —, this work; ---, results taken from Fig. 7(b) in [15]; S_o, Sommerfeld N#

vibration analysis. The slight differences observed in Figs. 3 and 4 can be partly attributed to unavoidable approximations done when reading data from the original graphs and adapting them to the coordinate system here adopted. The results are also susceptive to cumulative discrepancies caused by the probable adoption of different convergence criteria during the determination of the pressure field and static equilibrium position.

4 Vibration Analysis

A nonlinear static analysis must be conducted at selected rotor speeds in order to determine the relative equilibrium position of the journals. This analysis is necessary, even in the case of two-bearing systems, due to the action of hydrodynamic reactive moments that render the rotor statically indeterminate. In this study, the journals are assumed to have zero relative angular misalignment at an intermediary speed, so the bearings must be tilted in order to achieve this configuration. At other speeds, since the system is symmetric and the bearings are equally loaded, the relative angular misalignment remains unchanged. Space limitations do not permit the presentation of results describing the influence of static relative angular misalignment on the dynamic behavior of

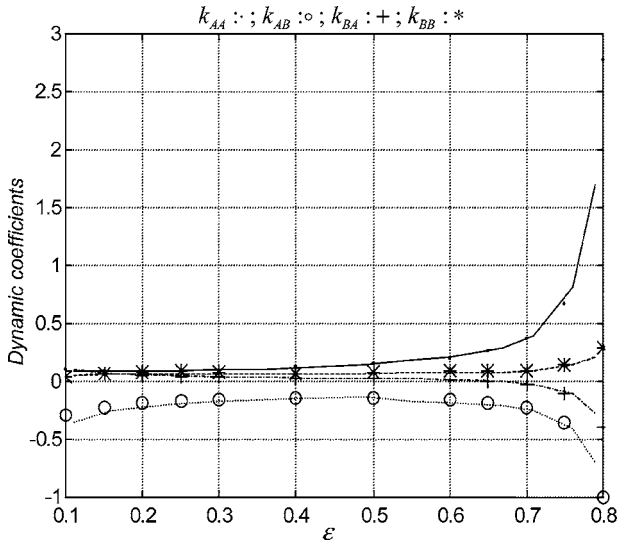

Fig. 4 Nondimensional stiffness coefficients; lines, this work; points, data taken from Fig. 8 in [7]; ε, journal's relative eccentricity

Table 2 Stability thresholds of rotors *a* to *d*

Rotor	*a*	*b*	*c*	*d*
σ_{32} (rps)	108.1	118.6	119.7	114.9
σ_8 (rps)	108.0	118.4	119.7	114.2

the rotor. Once the static equilibrium positions are known, the dynamic coefficients can be calculated and the vibration analysis is done as follows.

First, a free vibration analysis is performed in order to calculate the eigenvalues λ_i together with the corresponding eigenvectors ϕ_i, where $\lambda_i=\rho_i+ip_i$, and ρ_i and p_i are the ith damping exponent and damped natural frequency. Stability thresholds are also determined, and as given in Table 2, the differences between σ_{32} and σ_8, i.e., the stability thresholds calculated using the complete and the planar bearing models, are irrelevant. Similarly, one verifies that the damped natural frequencies, shown in the Campbell diagrams of Figs. 5–8, are little affected by the bearing model adopted for the calculations.

Significant differences between results calculated using both bearing models are found comparing the damping exponents. Since they decisively affect the response amplitudes at the resonance speeds ω_r, their values are shown together in Table 3. The

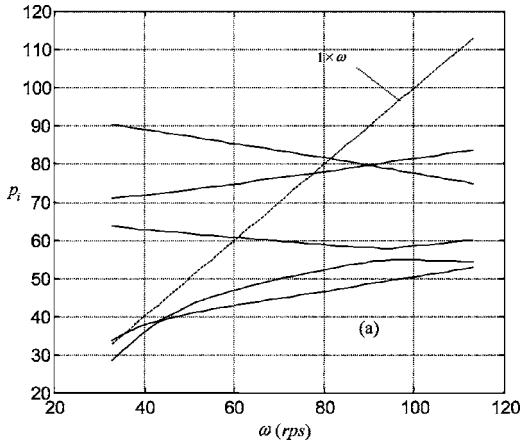

Fig. 5 Campbell diagram, rotor *a*

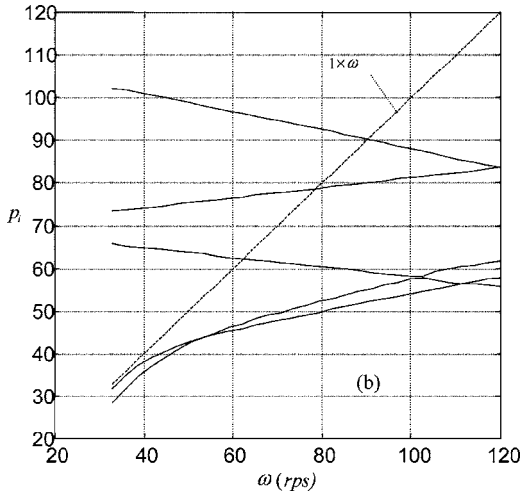

Fig. 6 Campbell diagram, rotor *b*

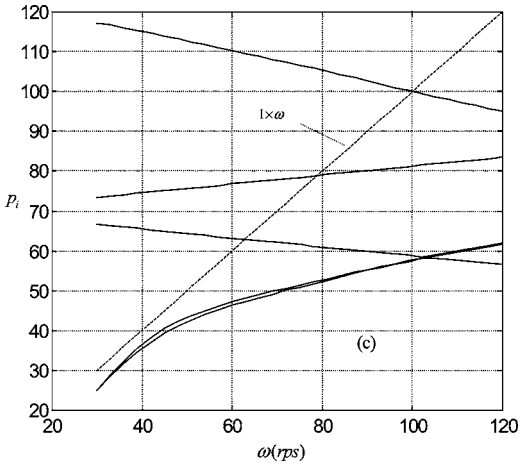

Fig. 7 Campbell diagram, rotor *c*

values of ω_{r_i} are not exactly equal to the corresponding p_i, but they are close enough in order to cause irrelevant changes in the related damping exponents.

Observing the results in Table 3 one notes that at some resonance speeds the values of ρ_{32} and ρ_8 are similar, as in $\omega_r = 35$ rps or $\omega_r = 81$ rps for rotor *a*, whereas at other resonance speeds the differences between ρ_{32} and ρ_8 are pronounced, and become incommensurate for rotor *c* at $\omega_r = 62.8$ rps.

These differences between ρ_{32} and ρ_8 reflect the positions of the bearings respective to the nodal points of the vibration modes of the rotors. In Figs. 9–17 some of the modes of vibration calculated

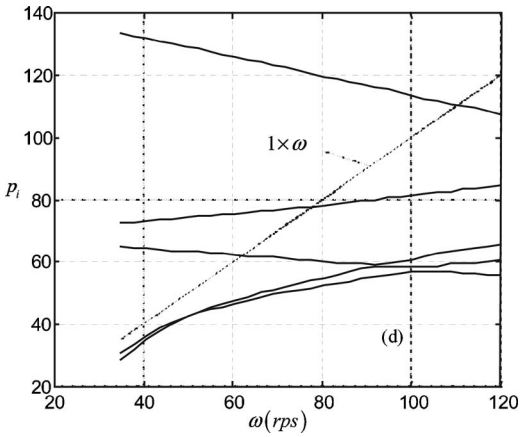

Fig. 8 Campbell diagram, rotor *d*

Table 3 Comparison between damping exponents

Rotor		Damping exponents at the resonance speeds			
a	ω_r (rps)	35.0	61.0	78.0	81.0
	ρ_{32}	−17.081	−1.291	−3.328	−10.578
	ρ_8	−17.029	−0.877	−3.199	−10.360
b	ω_r (rps)	⋯	62.0	79.0	90.0
	ρ_{32}	⋯	−0.747	−0.693	−11.04
	ρ_8	⋯	−0.264	−0.500	−10.74
c	ω_r (rps)	⋯	62.8	78.0	100.0
	ρ_{32}	⋯	−0.558	−0.399	−11.249
	ρ_8	⋯	−0.001	−0.162	−10.871
d	ω_r (rps)	⋯	62.0	78.0	110.0
	ρ_{32}	⋯	−1.003	−2.667	−10.651
	ρ_8	⋯	−0.351	−2.455	−10.138

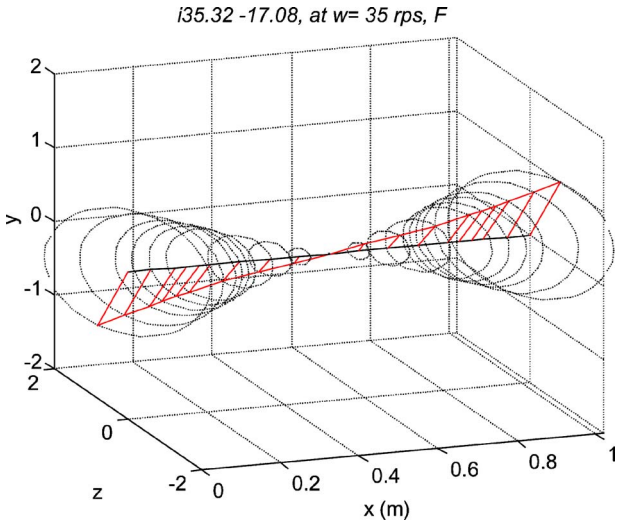

Fig. 9 Vibration mode, rotor *a*, $p \approx \omega_r = 35.0$ rps

at the resonance speeds are described; *F* identifies forward modes, *B* the backward ones, and just like the damped natural frequencies, either planar or complete bearing models lead to equivalent results.

Referring to rotor *a*, Fig. 9 displays a conical rigid mode, and Fig. 12 a conical flexural mode, in which the journals, located distant from the nodal point at the middle plan, execute elliptical orbits of relatively large amplitude, yielding small differences between ρ_{32} and ρ_8. As for Figs. 10 and 11, there are nodal points in the vicinity of the bearings, and the largest difference between ρ_{32} and ρ_8 is verified at $\omega_r = 61$ rps, corresponding to journal orbits of small relative amplitude but large tilt angles.

Analogous results hold true for rotors *b*, *c*, and *d*, and it is evident that the greatest differences between ρ_{32} and ρ_8 are associated with the closest proximity between bearings and nodal points. The extreme situation corresponds to rotor *c* at $\omega_r = 62.8$ rps, in which the bearings are coincident with the nodal points (Fig. 15), and the damping exponent calculated using the planar model is practically null. This means that in an unbalance response calculation the rotor will behave as if it were pinned on rigid bearings, characterizing a modelling mistake, since the corresponding value of ρ_{32} is not negligible.

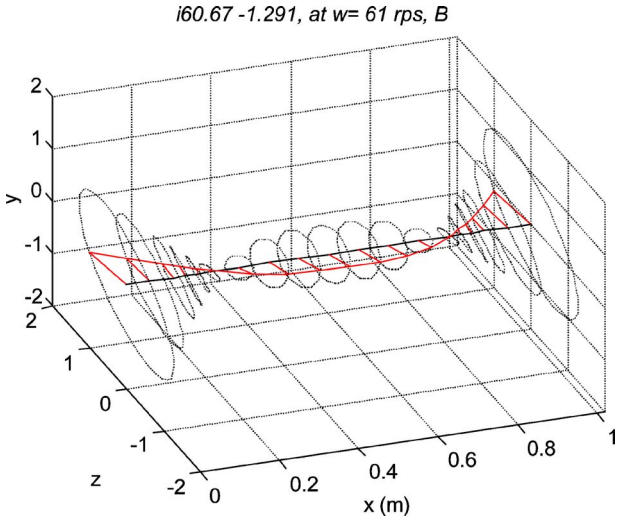

Fig. 10 Vibration mode, rotor *a*, $p \approx \omega_r = 61.0$ rps

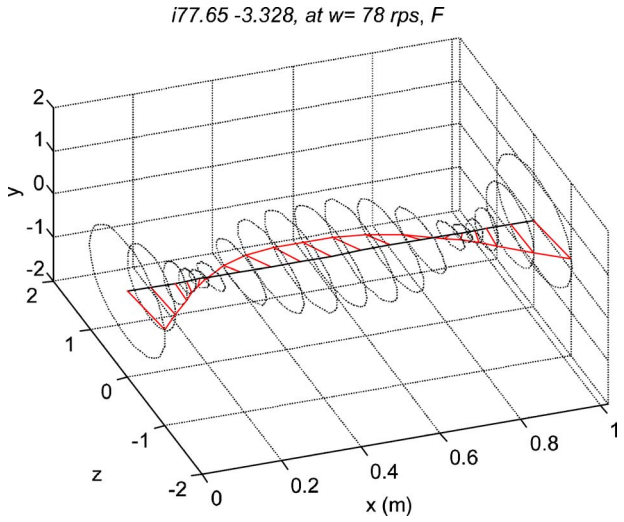

Fig. 11 Vibration mode, rotor *a*, $p \approx \omega_r = 78.0$ rps

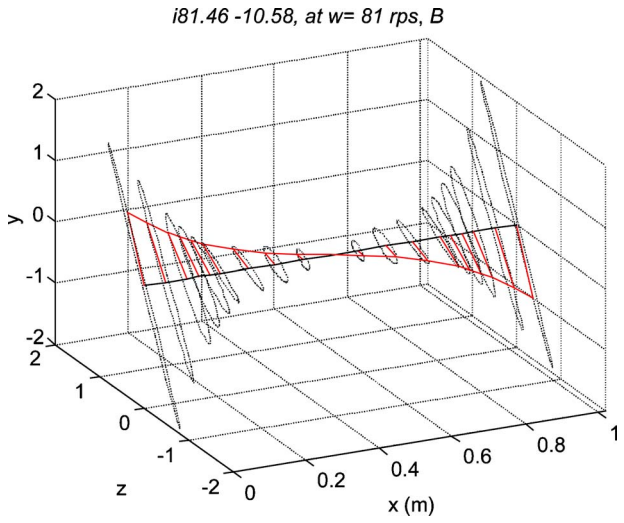

Fig. 12 Vibration mode, rotor *a*, $p \approx \omega_r = 81.0$ rps

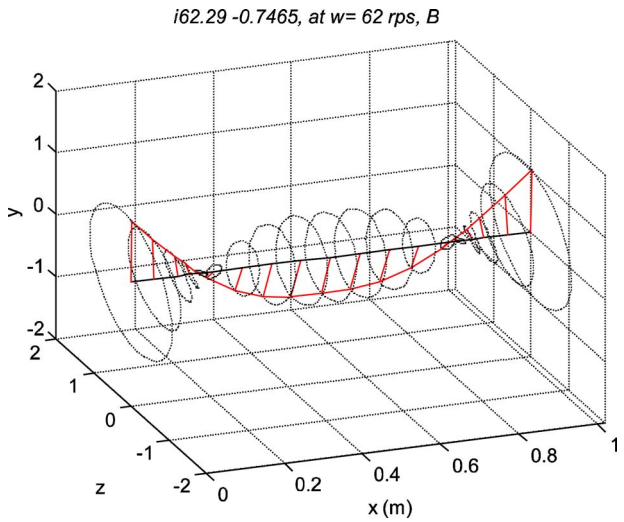

Fig. 13 Vibration mode, rotor *b*, $p \approx \omega_r = 62.0$ rps

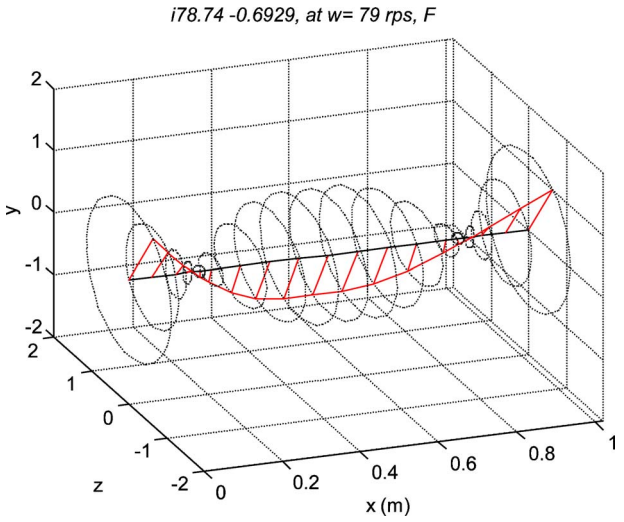

Fig. 14 Vibration mode, rotor *b*, $p \approx \omega_r = 79.0$ rps

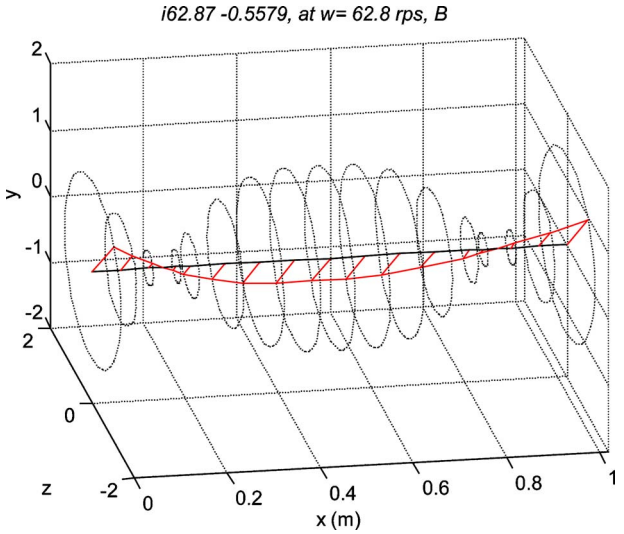

Fig. 15 Vibration mode, rotor *c*, $p \approx \omega_r = 62.8$ rps

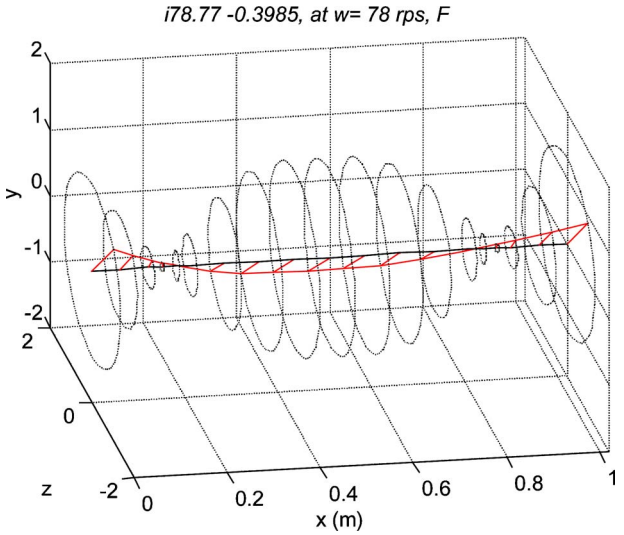

Fig. 16 Vibration mode, rotor *c*, $p \approx \omega_r = 78.0$ rps

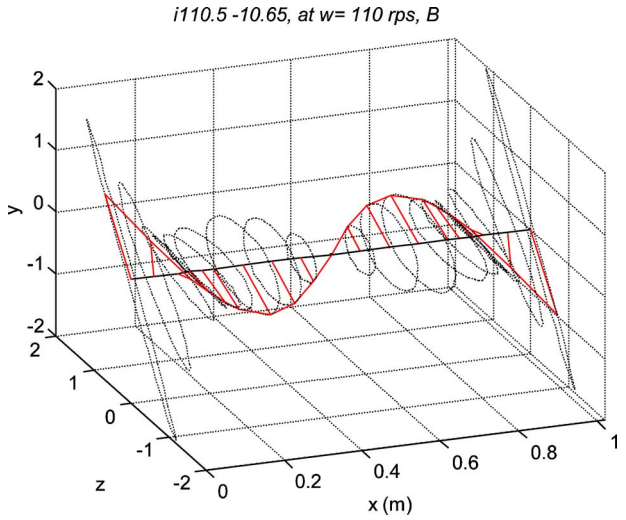

Fig. 17 Vibration mode, rotor *d*, $p \approx \omega_r = 110.0$ rps.

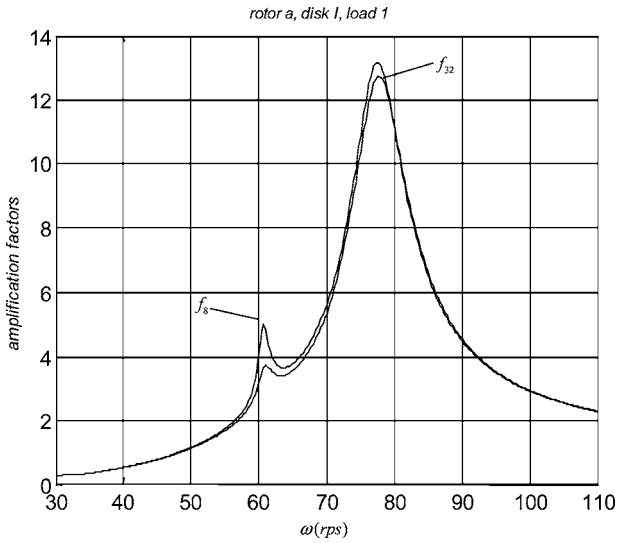

Fig. 18 Amplification factors, rotor *a*, disk I, load 1

On the other hand, the stability thresholds σ_{32} and σ_8, given in Table 2, have similar values because the modes corresponding to the unstable eigenvalues are "rigid" ones, conical in some cases and cylindrical in others. This aspect is very relevant and requires a more extensive discussion, which is beyond the scope of this paper.

Rotor *d* modes corresponding to $\omega_r = 62.0$ rps and $\omega_r = 78.0$ rps are similar to the ones depicted in Figs. 13–16, and their presentation is thus dispensable.

In order to calculate the dynamic response of the rotors, four combinations of static and couple unbalance excitations, described in Table 4, are considered; the "1s" in Table 4 indicate that the corresponding excitations are active. $\varphi^n_{u_0}$ is the initial phase angle of the static unbalance vector acting on the nth disk, and in the four loading conditions $\varphi^I_{u_0} = \varphi^I_{d_0} = 0$; the initial phase angles $\varphi^n_{d_0}$ of the couple unbalance vectors are measured as described in Fig. 2.

Cases 1, 2, and 3 in Table 4 correspond to symmetric unbalance excitations, therefore the amplitudes of vibration in disks I and III are equal. The same radial unbalance $u = 3$ μm is attributed to the three disks, and the magnitudes of the couple unbalance vectors are $|\vec{U}^{\mathrm{I,III}}_d/\omega^2| = 6 \times 10^{-5}$ kg m^2 and $|\vec{U}^{\mathrm{II}}_d/\omega^2| = 12 \times 10^{-5}$ kg m^2. Figures 18–27 show the amplification factors, defined as the ratio between the maximum whirl amplitude of the disks divided by the radial unbalance u; f_{32} and f_8 correspond to the complete and planar bearing models, respectively.

Couple unbalance acting on disks I and III is seen to excite principally the first flexural mode, causing high vibration amplitudes in the range of 60–65 rps. The second peak occurs between 75 and 80 rps, and now the static unbalance is the predominant excitation.

A more general loading condition, with the inclusion of couple unbalance in disk II (case 4 in Table 4) results in three vibration peaks, as shown in Figs. 25 and 27.

Table 4 Unbalance excitations, $\varphi^I_{u_0} = 0, \varphi^I_{d_0} = 0$

Case	$\vec{U}^{\mathrm{I}}_s$	$\vec{U}^{\mathrm{II}}_s$	$\vec{U}^{\mathrm{III}}_s$	$\varphi^{\mathrm{II}}_{u_0}$	$\varphi^{\mathrm{III}}_{u_0}$	$\vec{U}^{\mathrm{I}}_d$	$\vec{U}^{\mathrm{II}}_d$	$\vec{U}^{\mathrm{III}}_d$	$\varphi^{\mathrm{II}}_{d_0}$	$\varphi^{\mathrm{III}}_{d_0}$
1	1	1	1	π	0	⋯	⋯	⋯	⋯	⋯
2	⋯	⋯	⋯	⋯	⋯	1	⋯	1	⋯	π
3	1	1	1	π	0	1	⋯	1	⋯	π
4	1	1	1	π	π	1	1	1	π	π

The differences between f_{32} and f_8 have magnitudes similar to the ones between ρ_{32} and ρ_8 given in Table 3, and are directly related to the vibration modes excited by the unbalance forces and moments.

Taking rotor *a* as an example, Fig. 19 shows that, if static unbalance were the only excitation, it would be nearly indifferent to use the 32 or the 8-coefficient bearing model. On the other hand, the introduction of couple unbalance causes differences of about 50% between f_{32} and f_8.

Referring to rotor *b*, one observes in Figs. 22 and 23 that the differences between the results calculated using both models become more drastic, ranging from about 35% up to 190%.

There is a qualitative similarity between the results of Fig. 24 and the response curves displayed in Figs. 15, 16, and 17 of Lund and Orcutt [1]. In the reference, the authors compared results numerically calculated using the planar bearing model with experimentally measured amplitudes of vibration, and found that the former were incommensurably larger than the latter. The rotor studied was supported on two tilting pad bearings placed very close to nodal points of excited vibration modes, and as stated by the authors, in such situations "*the bearing properties have little*

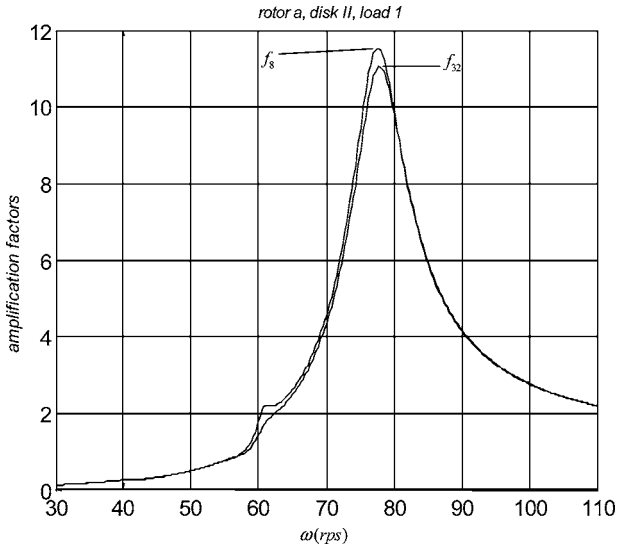

Fig. 19 Amplification factors, rotor *a*, disk II, load 1

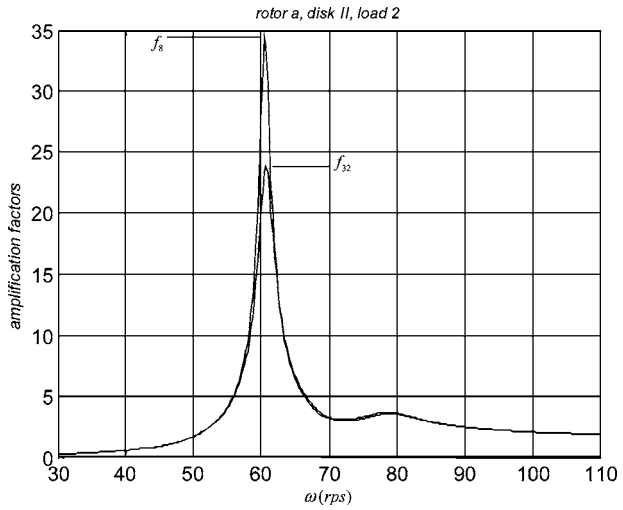

Fig. 20 Amplification factors, rotor *a*, disk II, load 2

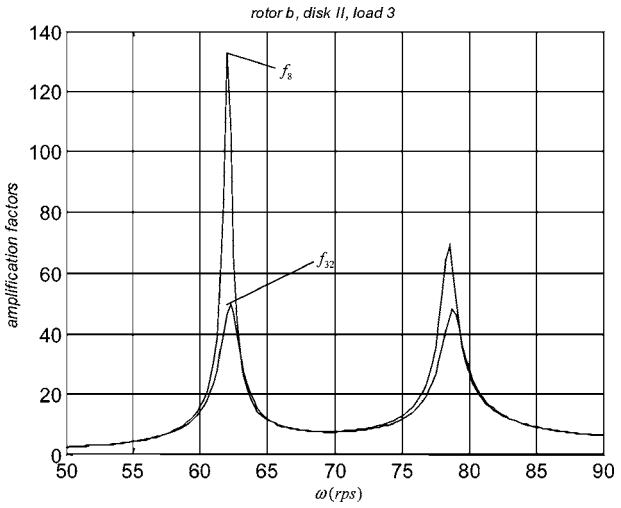

Fig. 23 Amplification factors, rotor *b*, disk II, load 3

effect on the rotor vibration." Although the above statement was coherent with the numerical results only, the way the experiments were conducted did not allow a rigorous quantitative comparison between the measured and the calculated unbalance response, and the authors did not attribute the differences between the results to any kind of inadequacy of the 8-coefficient model. Furthermore, it is not definitely clear whether that assertion concerned that specific kind of tilting pad bearing or had a general validity. None-

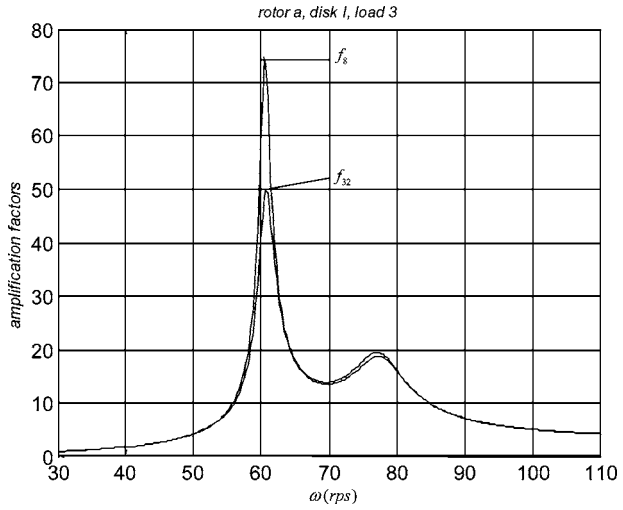

Fig. 21 Amplification factors, rotor *a*, disk I, load 3

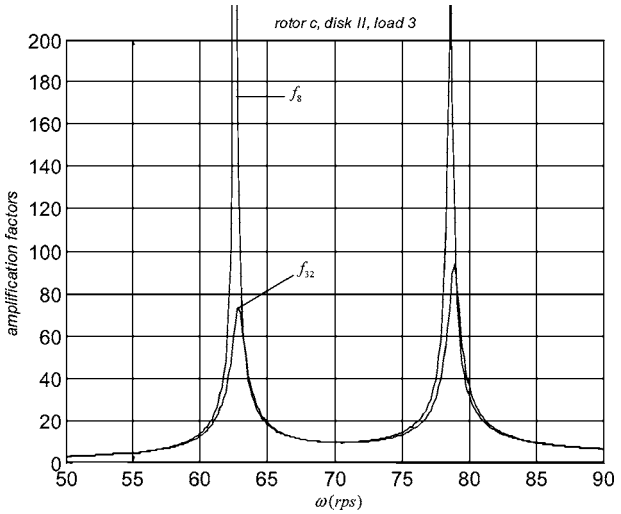

Fig. 24 Amplification factors, rotor *c*, disk II, load 3

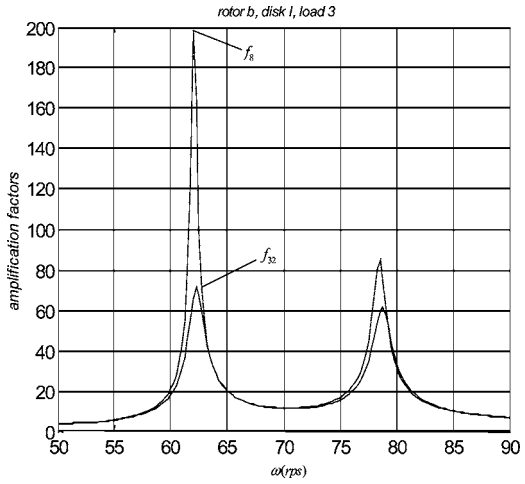

Fig. 22 Amplification factors, rotor *b*, disk I, load 3

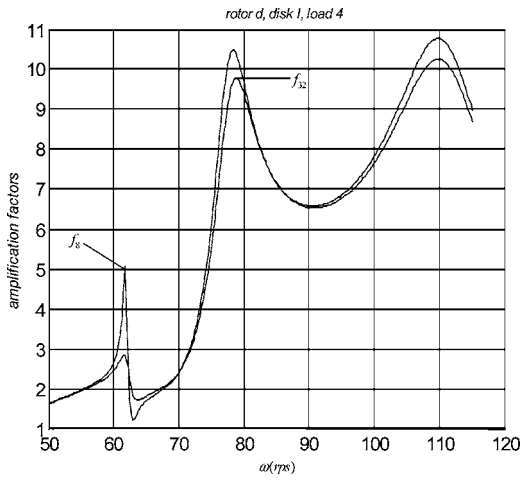

Fig. 25 Amplification factors, rotor *d*, disk I, load 4

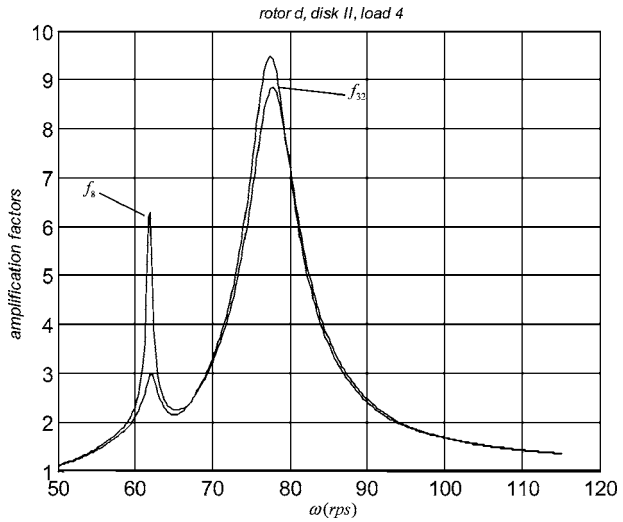

Fig. 26 Amplification factors, rotor *d*, disk II, load 4

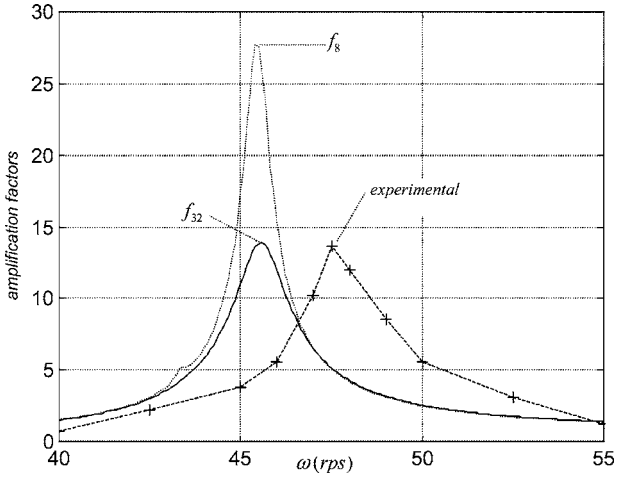

Fig. 28 Comparison between experimental (Kikuchi [5]) and numerical results

theless, the authors' statement is widely accepted by several researches, including Vance [16], Barret et al. [17], and Choudhury et al. [18].

Regarding rotor *d*, the response curves show that great differences between f_{32} and f_8, above 100% in Fig. 26, are not exclusively related to rotors that experience very high vibration levels at the critical speeds. This exemplifies that one might misjudge the viability of a rotor based on an analysis performed with the use of the planar bearing model, without being aware of its limitations.

5 Experimental Validation

As mentioned in the Introduction, linear vibration analyses performed with the use of the planar bearing model are meant to provide reliable predictions of the dynamic behavior of rotor systems. Since the coefficients of the complete bearing model are calculated using the same hypotheses and procedures adopted in the calculation of the planar model, the results worked out with the use of the 32-coefficient model should be regarded as being trustworthy as well. The following experimental validation corroborates the correctness of the preceding vibration analysis, and thus of its conclusions.

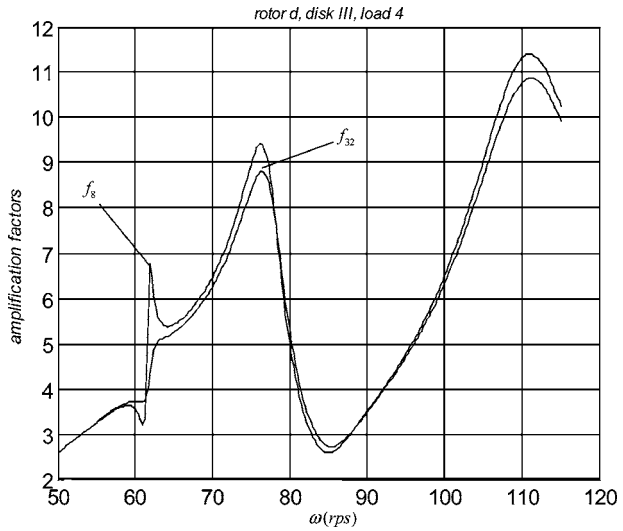

Fig. 27 Amplification factors, rotor *d*, disk III, load 4

First, a comparison between experimental results published by Kikuchi [5] and numerical ones calculated with both bearing models will be presented.

According to the reference, the tested laboratory rotor consists of a single span symmetrical steel shaft with overall length of 1.062 m, length between bearings $l_{bb}=0.800$ m, and a diameter of 0.040 m. It has a centrally mounted 13.44 kg disk and two other nearly identical disks located 0.200 m apart on either side; the moments of inertia are, polar $I_p=0.102$ kg m^2 and transversal $I_t=0.511$ kg m^2. Young's modulus and density were not given, so the values presented in Table 1 are adopted. The bearings are plain cylindrical ones, with length to diameter ratio $L/D=0.60$, diameter $D=0.40$ m, radial clearance $c_r=24$ μm, and due to the symmetry of the system, support equal loads of 254.1 N; the same constant average viscosity $\mu=27$ mPa s is assigned to both bearings in the numerical simulations (the measured viscosities were slightly different: $\mu=28$ mPa s in the left bearing and $\mu=26$ mPa s in the right one). Precise machining of the system resulted in a very slight residual unbalance that caused small vibration amplitudes, no larger than 5 μm within the speed range of the experiments. In order to measure the steady-state response an unbalance mass was added to the central disk, resulting in an equivalent radial unbalance $u=8.93$ μm.

Figure 28 shows the numerically calculated amplification factors (vibration amplitudes divided by $u=8.93$ μm) together with the measured values taken from Fig. 8(a) of the reference; the recorded maximum vibration amplitudes are given explicitly in the reference.

Excepting a less than 5% difference in the critical speeds, the correspondence between experimental amplification factors and f_{32} is very good; the same holds for the stability threshold, $\sigma_{32}=90$ rps. It is noteworthy that Kikuchi's [5] numerical results, calculated with a 16-coefficient model based on the short bearing approach, together with the premise that "*the oil film pressure is distributed in the form of a cubic curve*," also yielded a very similar reproduction of the experimental unbalance response curve.

As for the great difference between the maximum values of f_{32} and f_8, it is due to the closeness of the bearings to the nodal points of the excited vibration mode, shown in Fig. 29.

Although the bearings are almost coincident with the nodal points, the differences between f_{32} and f_8 are not so pronounced as in the case of rotor *c* (see Figs. 15 and 24), because the L/D ratio is smaller in the laboratory rotor. This is a qualitative judgement, since in the context of small oscillations around a static

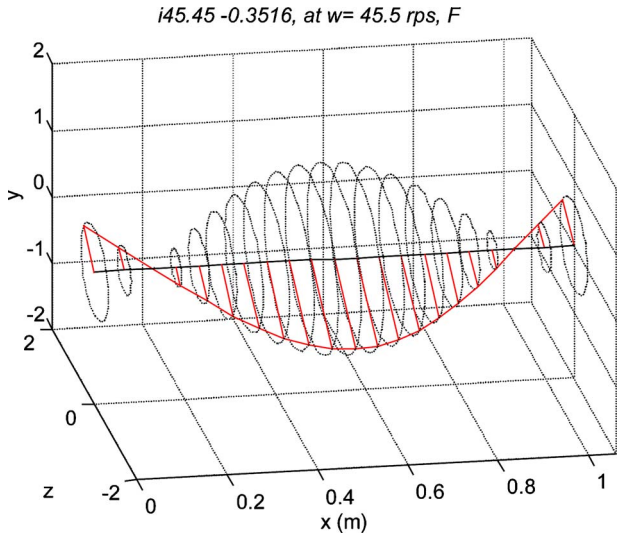

Fig. 29 Vibration mode, tested laboratory rotor

equilibrium position, it is rather intuitive that the shorter the bearing the smaller the influence of the angular displacements on the pressure field.

This influence of the L/D ratio of the bearings on the differences between f_{32} and f_8 is further illustrated by the theoretical and experimental investigation conducted by Choudhury et al. [18]. The results of interest concern the authors' designated "heavy rotor," a seven-stage centrifugal compressor supported on two identical pressure dam bearings having $L/D=0.333$ ratios. Other information necessary for the simulation of the system are omitted, but the dynamic behavior of the rotor is sufficiently characterized by the graphs and figures provided by the authors.

It is shown in Fig. 2 of the reference that the bearings are placed close to the nodal points of the first vibration mode, which is excited by an unbalance mass placed between the bearings. Table 5 gives the maximum amplitudes of vertical vibrations at the inlet and discharge end bearings, taken from Figs. 3, 4 (numerical results calculated with the 8-coefficient model), and 5 (experimental results) of the reference; two experimental response curves are depicted, corresponding to increasing and decreasing rotor speed.

Observing the values given in Table 5 one notes that the numerical results tend to overestimate the amplitudes of vibration, but to a lesser degree when compared to the differences between f_{32} and f_8 found in the preceding analyses.

Besides reinforcing the validity of the theoretical vibration analysis presented in the preceding session, the comparisons between experimental and numerical results show that even in the case of relatively short bearings, with $L/D=0.333$ as in the last example, the differences between f_{32} and f_8 are relevant. A more detailed analysis of the effect of the bearing length on the dynamic behavior of rotors, referring to nearly symmetric single span systems without overhang disks, can be found in Zachariadis [11].

6 Conclusions

A condition was clearly identified in which the use of the 8-coefficient hydrodynamic bearing model leads to invalid predictions of the unbalance response of rotors.

The situation described here deals with rotors supported on bearings placed close to nodal points of excited vibration modes. In such cases, the 32-coefficient bearing model has to be used in the unbalance response calculations, in order to consider the effects of the time varying tilt angle between journals and bearings on the hydrodynamic reactions.

Table 5 Comparison between calculated and measured maximum vibration amplitudes; "heavy rotor," results taken from Figs. 3–5 of [18]

	Vertical vibration amplitudes (mm)	
	Inlet end bearing	Discharge end bearing
Numerical	0.073	0.074
Increasing speed	0.067	0.058
Decreasing speed	0.041	0.038

It was shown that the differences between the vibration amplitudes calculated using the 32 or the 8-coefficient model can be greater than 100%. Conversely, stability thresholds, damped natural frequencies, and vibration modes are little affected by the bearing model adopted for their calculation. Therefore, under the conditions described above, although inadequate for unbalance response analyses, since the 8-coefficient bearing model permits a valid determination of vibration modes, it is suitable for the identification of the situations in which the 32-coefficient has to be adopted

Comparisons with previously published theoretical and experimental results ensure the validity of the formulations and numerical procedures employed in this analysis.

References

[1] Lund, J. W., Orcutt, F. K., 1967, "Calculations and Experiments on the Unbalance Response of a Flexible Rotor," ASME J. Eng. Ind., **89**, pp. 785–796.
[2] Lund, J. W., 1974, "Stability and Damped Critical Speeds of a Flexible Rotor in Fluid-Film Bearings," ASME J. Eng. Ind., **96**, pp. 509–517.
[3] Lund, J. W., 1974, "Modal Response of a Flexible Rotor in Fluid-Film Bearings," ASME J. Eng. Ind., **96**, pp. 525–533.
[4] Lund, J. W., Thomsen, K. K., 1978, "A Calculation Method and Data for the Dynamic Coefficients of Oil-Lubricated Journal Bearings," *Topics in Fluid Film and Rotor Bearing System Design and Optimization*, ASME, New York, pp. 1–28.
[5] Kikuchi, K., 1970, "Analysis of Unbalance Vibration of Rotating Shaft System With Many Bearings and Disks," Bull. JSME, **13**(61), pp. 864–872.
[6] Mukherjee, A., Rao, J. S., 1977, "Stiffness and Damping Coefficients of an Inclined Journal Bearing," Mech. Mach. Theory, **12**, pp. 339–355.
[7] Jakeman, R. W., 1986, "Performance and Oil Film Dynamic Coefficients of a Misaligned Sterntube Bearing," ASLE Trans., **29**, 4, pp. 441–450.
[8] San Andres, L., 1993, "Effect of Shaft Misalignment on the Operation of a Turbulent Flow Hydrostatic Bearing," ASME J. Tribol., **115**, pp. 355–363.
[9] Jang, G. H., Kim, Y. J., 1998, "Calculation of Dynamic Coefficients in a Hydrodynamic Bearing Considering Five Degrees of Freedom for a General Rotor-Bearing System," 98-TRIB-39, ASME/ASLE Tribology Conference, Toronto, Canada.
[10] Nikolakopoulos, P. G., and Papadopoulos, C. A., 1994, "Non-Linearities in Misaligned Journal Bearings," Tribol. Int., **27**, 4, pp. 243–257.
[11] Zachariadis, D. C., 1998, "Short Bearing Model for the Evaluation of Journal's Dynamic Angular Misalignment Effects on Rotor Vibrations," 98-GT-397, ASME International Gas Turbine Technical Congress, Stockholm, Sweden.
[12] Zachariadis, D. C., 1999, "Linear Vibrations of Statically Indeterminate Rotors on Angular Misaligned Hydrodynamic Bearings," 99-GT-333, ASME International Gas Turbine Technical Congress, Indianapolis, USA.
[13] Jakeman, R. W., 1989, "Influence of Sterntube Bearings on Lateral Vibration Amplitudes in Marine Propeller Shafting," Tribol. Int., **22**, 2, pp. 125–136.
[14] Rao, J. S., 1983, *Rotordynamics*, Wiley, Eastern, NY.
[15] Qiu, Z. L., and Tieu, A. K., 1995, "Misalignment Effect on the Static and Dynamic Characteristics of Hydrodynamic Journal Bearings," ASME J. Tribol., **117**, pp. 717–723.
[16] Vance, J. M., 1988, *Rotordynamics of Turbomachinery*, Wiley, New York.
[17] Barret, L. E., Gunter, E. J., Allaire, P. E., 1978, "Optimum Bearing and Support Damping for Unbalance Response and Stability of Rotating Machinery," ASME J. Eng. Power, **100**, pp. 89–94.
[18] Choudhury, P. D., Zsolcsak, S. J., Barth, E. W., 1976, "Effect of Damping on the Lateral Critical Speeds of Rotor-Bearing Systems," ASME J. Eng. Ind., **98**, pp. 505–513.

Identification of Frequency-Dependent Parameters in a Flexible Rotor System

Qingyu Wang[1]
e-mail: qw4k@virginia.edu

Eric H. Maslen
e-mail: ehm7s@virginia.edu

Department of Mechanical and Aerospace Engineering,
University of Virginia,
ROMAC Laboratories, 122 Engineer's Way,
Charlottesville, VA 22904

In a rotor-bearing system, there are usually some under- or unmodeled dynamic components that are considered frequency dependent, such as foundations, bearings, and seals. This paper presents a method to identify the dynamic behavior of these components using an otherwise accurate engineering model of the system in combination with available measurements of system frequency response functions. The approach permits treatment of flexible rotors and allows that the system test excitations and measurement sensors are not collocated. Because all engineering models contain some residual error and all measurements incorporate an element of noise or uncertainty, the quality of the identified parameters must be estimated. This paper introduces application of μ analysis to solve this problem, resulting in acceptable solution time and hard guarantees of solution reliability. Two illustrative examples are provided, showing that the presented approach is an efficient method to identify and bound these parameters. [DOI: 10.1115/1.2135814]

Introduction

Modeling methods for rotating machinery are steadily improving with the result that most elements in such machines can be modeled quite accurately. However, some components, such as shrink fits, foundations, seals, and some types of bearings, still prove problematic to model. Furthermore, these parts or interconnections are very hard to identify because the displacements and forces at points of interaction with the determinant components are not accessible. This means that conventional black-box system identification methods cannot be applied to these components. Furthermore, they are part of the system and typically cannot be separated from the system without altering their dynamic properties. Therefore, such components must be identified, if possible, together with the whole system. Such an identification problem is often referred to as model refinement or model updating.

There are two general approaches to model refinement or updating. The first approach assumes that the structure of the nominal engineering model is correct and seeks to modify specific parameters of the model to make the model input/output (I/O) match the measured I/O. A good overview of this approach is provided by Friswel and Mottershead [1]. These methods assume there are errors in certain model parameters, such as stiffness or mass, and by comparing to the test data, these parameters can be fixed. Usually these methods only improve the existing parameters of the engineering model, and the parameters usually cannot be frequency dependent. Recently, some researchers have begun to focus on frequency-dependent problems, for instance, Sinha et al. [2]. In this work, a model for a machine foundation is extracted from vibration data obtained during a single rundown of a machine. The foundation parameters are assumed to be frequency dependent: the frequency range of the data was divided into a number of bands, and frequency-independent-model updating methods were applied to the data for each band.

A second approach [3] assumes that the engineering model parameters are correct but that the model is completely missing certain dynamic components whose model is completely unknown. All that is known about these missing components is the manner in which they interact with the system described by the engineering model. The goal of model refinement here is to identify the simplest dynamic model of these missing components that will cause the resulting composite model dynamics to reproduce the measured signal I/O behavior.

Either approach usually does not use the test data directly. Instead, some form of black-box identification is performed on the data to extract a parametric model from it which is then used in conjunction with the engineering model to extract a parametric model of the missing dynamics. The process is indicated through the upper analysis path in Fig. 1.

This paper presents another route to identify the unmodeled dynamics from the test data, as the lower process diagrammed in Fig. 1. Here, the engineering model is simulated to produce frequency response data (FRF_2) which are then used in conjunction with the test data (FRF_1) to identify the frequency response function of the unmodeled components (FRF_3). If a parametric model is needed, this result can be passed through a conventional black-box identification process. One advantage of the lower route is that black-box identification of FRF_3 turns out to be easier than the identification problem of the upper route, which includes the entire system dynamics. Another advantage of the lower process is that it is possible and economical to closely bound FRF_3 based on bounds on FRF_1 and FRF_2.

In the upper route of Fig. 1, since the model updating approaches include the engineering model in the identification, the identified dynamic parameters typically depend heavily on the quality of the engineering model. However, very little literature has discussed how to estimate the influence either of the errors of the engineering model, or of noise in the test data: the identified model is simply regarded as true. Without knowing its quality, however, the identified model could be meaningless.

Attention to this problem is increasing, particularly in the controls community. Some system identification methods have been presented, which not only provide models but also provide bounds on the accuracy of those models [4,5], but these methods require an uncertainty bound on the test data from which the model is derived. This paper presents a method to bound FRF_3, so that FRF_3 can be regarded as bounded test data and the existing methods may be applied in deriving a parameterized model and its bounds.

[1]Corresponding author.

Contributed by the International Gas Turbine Institute (IGTI) of ASME for publication in the JOURNAL OF ENGINEERING FOR GAS TURBINES AND POWER. Manuscript received August 25, 2005; final manuscript received September 28, 2005. IGTI Review Chair: K. C. Hall. Paper presented at the ASME Turbo Expo 2005: Land, Sea, and Air, Reno, NV, June 6–9, 2005, Paper No. GT2005-68577.

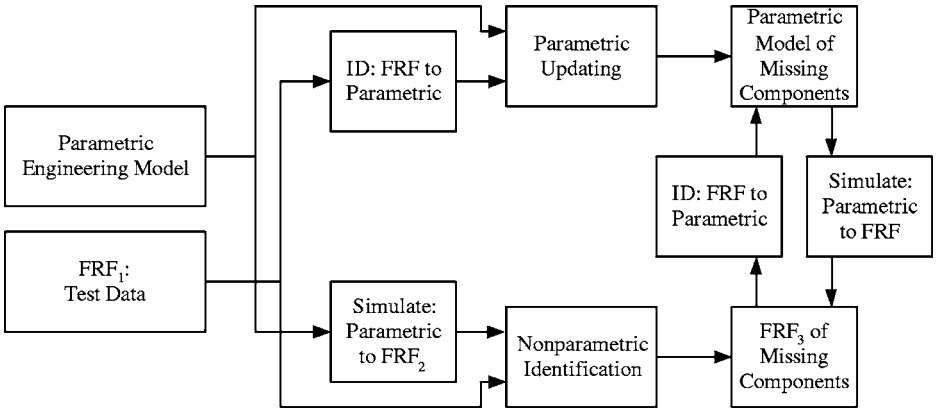

Fig. 1 Identification processes: upper route is parametric updating, lower route is nonparametric updating

Identification of Unmodeled Dynamics

For the analysis of rotating machinery, it is most common to present a model in discrete (finite dimensional) form. The usual form of the model is

$$M_0\ddot{x} + C_0\dot{x} + K_0x = f \tag{1}$$

where M_0, C_0, and K_0 are the mass, damping and stiffness matrices and f represents external loads or other effects, such as mass unbalance. The Laplace transformation of the above equations is

$$Z_0X = F \tag{2}$$

where $Z_0 = s^2M_0 + sC_0 + K_0$ is the dynamic stiffness matrix. The dimension of Z_0 is controlled by the level of discretization in the rotor finite element model. Typically, each element of X corresponds to the displacement or rotation of a certain location along the shaft in either the x-z or y-z plane. The displacements of a collection of specific locations $x_a, x_b, \ldots, x_q$ along the shaft can be extracted by multiplying X by a selector matrix $[T_a]$

$$\begin{Bmatrix} x_a \\ x_b \\ \vdots \\ x_q \end{Bmatrix} = T_a^{\mathsf{T}}X$$

In the same manner, forces applied to locations $x_r, x_s, \ldots, x_v$ along the shaft can be applied using a similar *deselector* matrix $[T_b]$

$$f = T_b\begin{Bmatrix} f_r \\ f_s \\ \vdots \\ f_v \end{Bmatrix}$$

Thus, the transfer function from forces F_b to displacements X_a is

$$X_a = T_a^{\mathsf{T}}Z_0^{-1}T_bF_b$$

In the same manner, if a missing dynamic effect $(D_u(s))$ in the system generates forces F_u in response to displacements X_u with correlation

$$F_u = -D_uX_u$$

then the model (2) is modified by this effect as

$$Z_0X = F - T_uD_uT_u^{\mathsf{T}}X \quad \Rightarrow \quad \left(Z_0 + T_uD_uT_u^{\mathsf{T}}\right)X = F \tag{3}$$

where T_u is the locations of $D_u(s)$. Consider the FRF data of an experiment: only several locations are excited and/or sampled. Let T_e and T_s be the input deselector and output selector matrices so that the I/O relation is

$$Z_0X = T_eF_e \tag{4}$$

$$X_s = T_s^{\mathsf{T}}X \tag{5}$$

or, simply, $X_s = T_s^{\mathsf{T}}Z_0^{-1}T_eF_e$, where F_e are the excitation forces. The true transfer function from F_e to X_s becomes

$$P_1 = T_s^{\mathsf{T}}[Z_0(s) + T_uD_u(s)T_u^{\mathsf{T}}]^{-1}T_e \tag{6}$$

By using the matrix inversion formula [6], Eq. (6) can be written as

$$P_1(s) = G_{11} + G_{12}[I - D_u(s)G_{22}]^{-1}D_u(s)G_{21} \tag{7}$$

in which

$$G_{11}(s) = T_s^{\mathsf{T}}Z_0^{-1}T_e, \quad G_{12}(s) = T_s^{\mathsf{T}}Z_0^{-1}T_u$$

$$G_{21}(s) = T_u^{\mathsf{T}}Z_0^{-1}T_e, \quad G_{22}(s) = T_u^{\mathsf{T}}Z_0^{-1}T_u$$

and $D_u(s)$ can be calculated from (7) as

$$D_u(s) = -[G_{21}(G_{11} - P_1)^{-1}G_{12} - G_{22}]^{-1} \tag{8}$$

If G_{12} and G_{21} are square and full rank, i.e., the number of excitations and sensors matches the I/O dimensions of the unmodeled dynamics, the required inverses will exist. Otherwise, direct inversion will not be possible and a signal norm minimizing pseudoinverse must be used instead.

Notice that the component transfer functions, G_{11} and so forth, do not have to be derived from the model. They are just specific transfer functions of the machine *without* interaction with the unmodeled components, so they could be the same kind of FRF test data as P_1 if the machine can be tested appropriately with the unmodeled component removed. In this special case, the engineering model is not even needed. In general, however, the required testing cannot be performed and these component frequency response functions must be derived from the engineering model.

Calculating the Uncertainty Bound Using μ Analysis

To calculate the uncertainty bound of the identified model, μ analysis is introduced. The basic ideas behind μ analysis are introduced briefly in this section (refer to [6] for a detailed discussion of this powerful tool).

Figure 2 shows the general framework of μ analysis,where

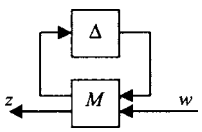

Fig. 2 Analysis Framework

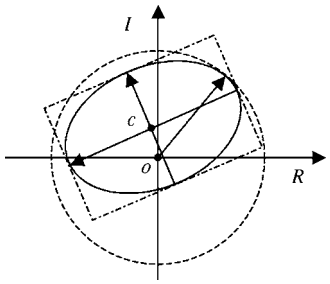

Fig. 3 Uncertainty cloud and bounds

$$z = \mathcal{F}_u(M,\Delta)w \tag{9}$$

w and z are the inputs and outputs of interest, for instance w can be the unbalance forces, and z can be the rotor displacements at bearings. Δ, which represents various kinds of uncertainties, is defined as

$$\Delta = \text{diag}[\delta_1 I_{r1}, \cdots, \delta_s I_{rs}, \Delta_1, \cdots, \Delta_F]$$

in which the I's are identity matrices, and the δ's/Δ's are unknown but bounded complex numbers/matrices. M is a transfer function partitioned as

$$M = \begin{bmatrix} M_{11} & M_{12} \\ M_{21} & M_{22} \end{bmatrix}$$

$\mathcal{F}_u(M,\Delta)$, which describes how Δ is connected to M, is called an upper-link linear fractional transformation (LFT), and defined as

$$\mathcal{F}_u(M,\Delta) = M_{22} + M_{21}\Delta(I - M_{11}\Delta)^{-1}M_{12}$$

LFT is a general connection, and most of the uncertainties, such as additive or multiplicative, can be transferred to an LFT connection to the system (see detailed explanation later).

Consider the simplest situation where $\mathcal{F}_u(M,\Delta) \in \mathfrak{C}^{1\times 1}$ is a scalar and M is a constant complex matrix. Because Δ is uncertain, $\mathcal{F}_u(M,\Delta)$ is a cloud of complex numbers, mapping the domain of Δ (all possible values of Δ) onto the range of the LFT. μ analysis attempts to find a bound for the size of this cloud. Let

$$\gamma_t = \max_{\Delta} |\mathcal{F}_u(M,\Delta)|$$

then γ_t is the true/tightest bound of this cloud measured from the origin. To find γ_t is the same as to find the global minimum of a nonlinear function, which is generally very difficult. μ analysis derives an overbound γ_o, an underbound γ_u, and a worst case Δ_w (a constant complex matrix within the uncertainty range) such that $\gamma_u \geqslant \gamma_t \geqslant \gamma_o$ and $\gamma_u = |\mathcal{F}_u(M,\Delta_w)|$. Note that $\mathcal{F}_u(M,\Delta_w)$ is an actual point on the edge of the cloud, and γ_u is achievable.

This strategy of finding two bounds avoids directly searching for the global minimum, and the search can be finished in polynomial time. Also, fortunately, the two bounds are very close for most systems [6]. Thus, γ_o can be used as the bound, and γ_u can be used to calculate a boundary tightness index (BTI) to show how conservative γ_o is

$$\text{BTI} = \gamma_u/\gamma_o \tag{10}$$

The closer BTI is to 1, the closer γ_o is to γ_t. γ_t can be seen as the furthest distance from the origin to any point in the cloud.

Because of the shape of the cloud, γ_t may not be the best way to describe the cloud, which can be illustrated by Fig. 3. The radius is γ_t, and the solid-line ellipsoid represents the cloud. Another way to describe the cloud is to give the center c and the two principle components of the rectangular box. This can be done by moving the origin several times to get several points on the edge of the cloud. Usually, the rectangular box is smaller than the circle.

Calculation of the Uncertainty Bound. Engineering models and test data have a variety of associated sources of uncertainty. These include approximation, simplification, and parametric errors in the engineering model. Measurement noise and calibration uncertainty contribute to uncertainty in the test data. As a consequence, all of the transfer functions in (8) have uncertainties. Let $\hat{D}_u$ be the unmodeled dynamics with uncertainty, and D_u be the nominal value, so that $\Delta_d = D_u - \hat{D}_u$ is the uncertainty, and it can be calculated as

$$\Delta_d = D_u + [\hat{G}_{21}(\hat{G}_{11} - \hat{P}_1)^{-1}\hat{G}_{12} - \hat{G}_{22}]^{-1} \tag{11}$$

in which the $\hat{G}_{ij}$ and $\hat{P}_1$ are the corresponding transfer functions with uncertainties.

The central step of this section is to transform the right side of (11) into the LFT form introduced in the last section, and then μ analysis can be applied in a relatively straightforward manner to derive the bound. This step can be tedious but can always be accomplished for mechanical systems because

1. $\hat{G}_{11}$ and so forth can be expressed in an LFT form. For instance, for additive uncertainty, $\hat{G}_{11} = G_{11} + \Delta_{g11} = \mathcal{F}(\tilde{G}, \Delta_{g11})$, where $\tilde{G} = \begin{bmatrix} I & G_{11} \\ 0 & I \end{bmatrix}$. For more complicated forms of uncertainty, such as parametric uncertainty in M, C, or K, one can refer to [6] for appropriate formulations. Thus, all transfer functions with uncertainties on the right side of (11) can be transformed into LFT forms individually.
2. For two LFT functions $\mathcal{F}_1$ and $\mathcal{F}_2$, all of the operations on the right side of (11) such as $\mathcal{F}_1\mathcal{F}_2$, $\mathcal{F}_1 + \mathcal{F}_2$, and $\mathcal{F}_1^{-1}$ will result in new LFTs. The required rearrangment can be tedious to realize, but it is straightforward to prove that (11) can be rearranged to a single LFT, relying solely on the definition of the LFT. Therefore, (11) will result an LFT form interconnection of a transfer function matrix and an associated uncertainty block, which subsumes all of the model and measurement uncertainties.

After the final LFT form $\Delta_d = \mathcal{F}(\tilde{M}, \Delta_M)$ is derived, the bounds can be calculated using a software tool like MATLAB's "MU" function (see [7]): $[\gamma_u, \gamma_o] = MU(\tilde{M}, \Delta_M)$.

Other Bounding Methods

For a comparison, two other common bounding methods are considered, nonlinear minimization (NM) and random search (RS), which are widely used in solving nonlinear problems. They are compared to μ analysis (MU) in the following example.

RS: The unmodeled dynamics together with the uncertainty can be expressed as a nonlinear function of the model, the FRF data and their uncertainties

$$\hat{D}_u(s) = f(\Delta, Z_0, P_1) \tag{12}$$

For each frequency point, numerous random exemplars of Δ are chosen and a resulting set of D_u are calculated. The edge of the set can then be identified as the bound. As the size of the random sample increases, the accuracy of the bound improves, although not in a predictable fashion.

NM: The Δ in (12) can be regarded as a set of variables with constraints. This kind of problem can be solved by using a standard nonlinear minimization tool, such as the MATLAB function FMINCON, which includes the interior-reflective Newton method and other nonlinear programing methods. A rectangular box for the uncertainties can be obtained in a manner similar to that used in μ analysis. The initial value of Δ has a big influence on the result, so it is common to seed the initial value randomly and try many starting points.

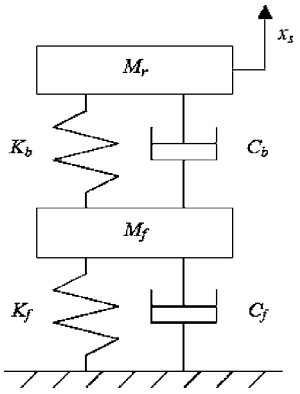

Fig. 4 Simplified rotor-bearing-foundation system

Illustrative Simulation Example

This example shows how the presented method works for a very simple case. To illustrate the efficiency of μ analysis in bounding the parameters, two methods mentioned above are compared.

The Engineering Model and Test Data. Figure 4 shows a simplified rotor-foundation system, where $M_r=20$ kg, $M_f=100$ kg, $C_b=1000$ Ns/m, $C_f=100$ Ns/m, $K_b=10^5$ N/m, and $K_f=10^6$ N/m. For the engineering model, M_f, C_f, and K_f are unknown, so estimated values of $M_g=50$ kg, $C_g=200$ Ns/m, and $K_g=3\times10^6$ N/m are used instead. The engineering model is

$$M_0=\begin{bmatrix} M_g & 0 \\ 0 & M_r \end{bmatrix}, \quad C_0=\begin{bmatrix} C_g+C_b & -C_b \\ -C_b & C_b \end{bmatrix},$$

$$K_0=\begin{bmatrix} K_g+K_b & -K_b \\ -K_b & K_b \end{bmatrix}, \quad T_u=[1\ 0]^{\mathrm{T}} \quad \text{and } T_e=T_s=[0\ 1]^{\mathrm{T}}$$

The eigenfrequencies are 70.11 and 247.02 rad/s. The "true" system is

$$M_1=\begin{bmatrix} M_f & 0 \\ 0 & Mr \end{bmatrix}+\Delta_m, \quad C_1=\begin{bmatrix} C_f+C_b & -C_b \\ -C_b & C_b \end{bmatrix}+\Delta_c$$

and

$$K_1=\begin{bmatrix} K_f+K_b & -K_b \\ -K_b & K_b \end{bmatrix}+\Delta_k$$

where

$$\Delta_m=0.01\begin{bmatrix} m_{11}\delta_{11} & m_{12}\delta_{12} \\ m_{21}\delta_{21} & m_{22}\delta_{22} \end{bmatrix}$$

and $|\delta_{ij}|\leqslant 1$, $i, j=1, 2$ are real uncertainties. Δ_c and Δ_k are defined similarly and also represent 1% uncertainties. The associated eigenfrequencies are 69.61 and 102.13 rad/s. The FRF data are generated using

$$P_1(s)=T_s^{\mathrm{T}}(s^2M_1+sC_0+K_1)^{-1}T_e(1+0.02\delta_p)$$

where $|\delta_p|\leqslant 1$ is a complex uncertainty, and $s=j\omega$, $\omega\in[0.2\pi, 40\pi]$.

The Results. For RS, 10,000 $\hat{D}_u$ were calculated for each frequency point. For NM, the initial value of $\Delta_0=0$ was chosen. Figure 5 shows the calculated $|D_u|$, the true $|D_u|$, $\max|\hat{D}_u|$ and $\min|\hat{D}_u|$. This figure clearly shows that D_u is contained in all of the bounds and the μ bounds contain all other bounds. The bound is rather large for some frequencies, given that only 2% uncertainty was added. For instance, the lower bound at $\omega=5$ rad/s almost reaches 0 and the upper bound is about 2.4×10^6 N/m.

To compare the three methods clearly, normalized upper bounds

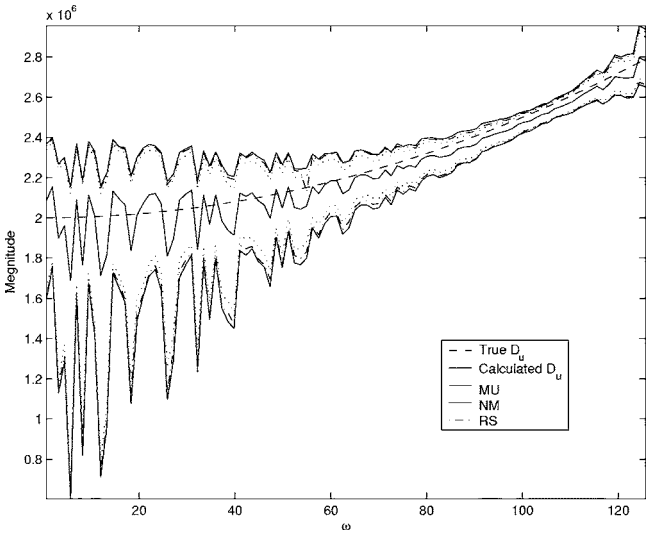

Fig. 5 Uncertainty bound

$(\max_x|\Delta_d|/\max_{\mathrm{MU}}|\Delta_d|$, where x means the method) are plotted in Figure 6, where the MU upper bound is 1. The average value, minimum value and calculation time are summarized in Table 1. The BTI shows that MU is very close to the true bound. NM is closer to MU on average than is RS, but there is a sharp peak at $\omega=55$ rad/s. This problem can be solved by using a number of different Δ_0, but the calculation time will be longer accordingly. For instance, when 20 random Δ_0 were used, the minimum value rose to 0.838, the average value became 0.929, and the calculation time was 385 s. The minimum value is much better, but the average value shows very little improvement.

Figure 7 shows the complex plane at a randomly picked frequency $\omega=37.25$ rad/s, where the rectangular boxes of MU and

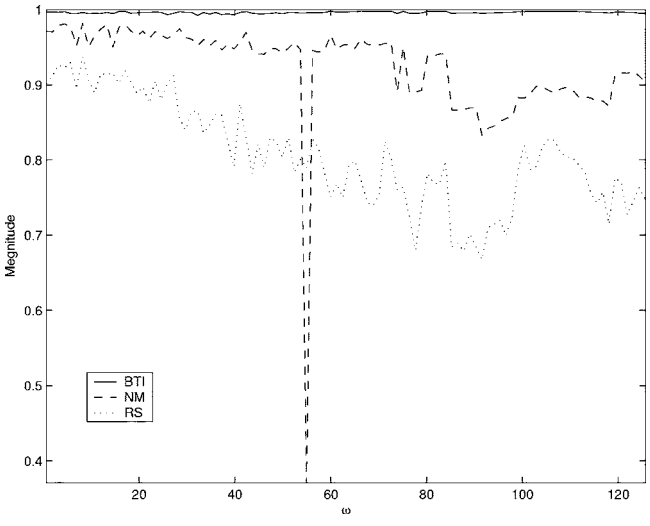

Fig. 6 Normalized uncertainty upper bounds

Table 1 Upper bound comparison

Method	Time (s)	Average value	Min value
MU	218	1	1
BTI	NA	0.996	0.992
NM	18.5	0.924	0.371
RS	434	0.806	0.667

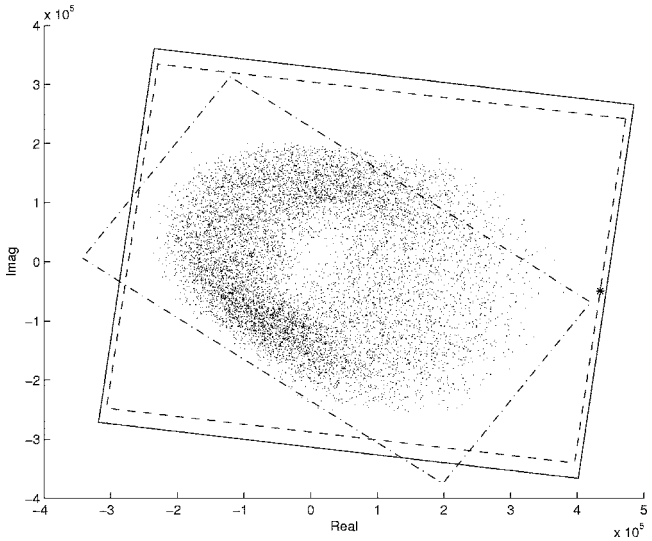

Fig. 7 Uncertainty bounds for ω=37.25 rad/s, where – outer bound of MU, - - inner bound of MU, - · - NM

NM are shown, and the RS set of $\hat{D}_u$ are used directly as the cloud inside the boxes. The star on the right side of the inner MU bound is an achievable point. The MU boxes contain the cloud but not the whole NM box, because the simple shape of a rectangular box brings in non-achievable points, which can also be seen from Fig. 3. This figure shows that, even if 10,000 iterations are used in RS, the edge of the cloud is still far from the achievable point. A more important point is that, without MU, it is not possible to know how far the RS or NM limits are from the true value.

Although the MU bound is very close to the "tightest" bound, there are at least three problems which make even the "tightest" bound conservative:

1. The uncertainties of the engineering model may not be completely independent. For instance, mass density uncertainty would affect all four elements of M_0, but not independently. All three analysis (including μ–) treat uncertainties in the elements of M_0 as independent.
2. The uncertainties for each of the frequency points are assumed to be independent, but actually they may not be. That is, the uncertainty may have some structure in the frequency domain. Again, such structure is ignored by all three analyses.
3. When D_u is not 1 by 1, each element is bounded separately, which can also introduce conservativeness.

These problems are not considered in this paper, but they need to be kept in mind when MU is used.

Detailed Simulation Example

This example applies the presented approach to identify the parameters of 5-pad tilting pad bearings, which are both speed dependent *and* frequency dependent. A tilting pad bearing usually has $2+N_{\text{pads}}$ degrees of freedom. For a 5-pad tilting pad bearing, there could be as many as 59 parameters at any given speed, or these parameters can be reduced to eight frequency dependent parameters [8]: the stiffness

$$\begin{bmatrix} K_{XX}(\omega) & K_{XY}(\omega) \\ K_{YX}(\omega) & K_{YY}(\omega) \end{bmatrix}$$

and the damping

$$\begin{bmatrix} C_{XX}(\omega) & C_{XY}(\omega) \\ C_{YX}(\omega) & C_{YY}(\omega) \end{bmatrix}$$

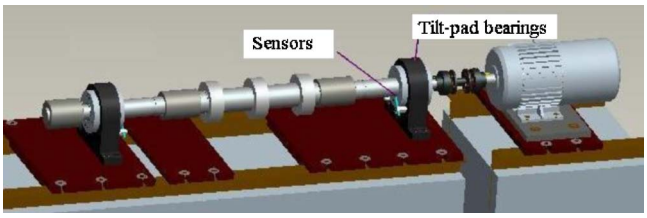

Fig. 8 The test rig

Either the 59 static parameters or the reduced eight coefficients for the given speed and frequency can be calculated by the tilt pad bearing analysis Code THPAD [9], which assumes specific axial pressure profile and a specific cross-film viscosity variation to decrease the dimensionality of the problem to the circumferential direction only. In this example, only one speed, the rated speed 10,000 rpm, is considered, and 59 parameters are calculated based on this speed. The frequency range used in this example is 0–36,000 rpm (0–600 Hz).

Description of the Test Rig. The test rig, as shown in Fig. 8, is built to simulate general multi-stage compressors or pumps. The specifications of the rotor are listed in Table 2, and the relation between excitations and sensors (both x and y directions) are shown in Fig. 9, which is clearly a general noncollocated configuration: the excitation and measurement points do not correspond to the interaction points of the unmodeled components (the bearings.) The first bending mode of this rotor is at 9075.90 rpm, which is within the operating speed range, while the second bending mode is at 21,734.51 rpm.

Simulation Results and Discussion. Because the test rig is not yet fully operational, only simulation results are given in this section. There are four inputs and four outputs (two locations with both x and y directions), so the transfer functions are 4 by 4. The transfer function for each bearing, which needs to be identified, is 2 by 2 as shown in Eq. (13). In this example, only one element of the non-drive-end bearing transfer function $D_{u1,1}=j\omega C_{XX}(\omega)+K_{XX}(\omega)$ is being studied. Other elements of the transfer functions can be studied in a similar manner

$$D_u(j\omega) = j\omega \begin{bmatrix} C_{XX}(\omega) & C_{XY}(\omega) \\ C_{YX}(\omega) & C_{YY}(\omega) \end{bmatrix} + \begin{bmatrix} K_{XX}(\omega) & K_{XY}(\omega) \\ K_{YX}(\omega) & K_{YY}(\omega) \end{bmatrix} \quad (13)$$

The quality of the identified parameters depends on the uncertainties of the model and test data, therefore two uncertainty levels, 1% and 4%, were added to the transfer functions to study this effect, and the identified $D_{u1,1}$ and its bounds are shown in Figs. 10 and 11, respectively. The transfer function of $P_1(1,1)$ and the "true" $D_u(1,1)$ are also plotted as references.

These two figures show that

Table 2 Specification of rotor

Mass	82.1 [kg]
diameter × span	ϕ 57 × 1569[mm]
Rated speed	10,000 [rpm]
Operating range	7000–12,000 [rpm]
Material	4340 steel

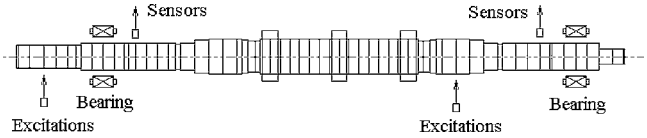

Fig. 9 Excitations and sensors diagram

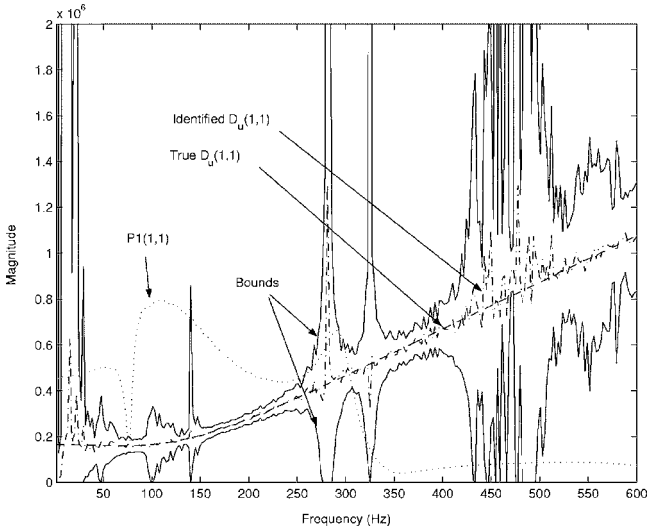

Fig. 10 Identification with bounds for 1% error

1. the "true" $D_u(1,1)$ is frequency dependent, and it increases with increasing frequency. The identified D_u and its bound have a similar behavior.
2. the quality of the identified D_u is directly related to its bound: the tighter the bound is, the better the quality. $P_1(1,1)$ seems not related.
3. the size of the bounds vary for different frequencies, and at some frequencies, the uncertainty is not bounded. The uncertainty level obviously affects the size of the bounds for every frequency point. The bounds also tend to increase with increasing frequency, generally.

Although this example used uniform perturbations (expected value is not a function of frequency), it is quite easy to vary the uncertainties and study the resulting relation to the identified model and its bounds. For real systems, the uncertainty bounds can be derived in various ways. For instance, the mean square error of the test data can be used as the uncertainty bound of (P_1). The autocorrelation function and/or coherence function may also be considered to derive a more reasonable bound. For more complicated noise analysis methods, one can refer to [10]. For model errors, engineers usually can give uncertainty bounds for model parameters based on experience, and parametric uncertainty in the engineering model can be mapped directly into uncertainty in the G_{ij} transfer functions.

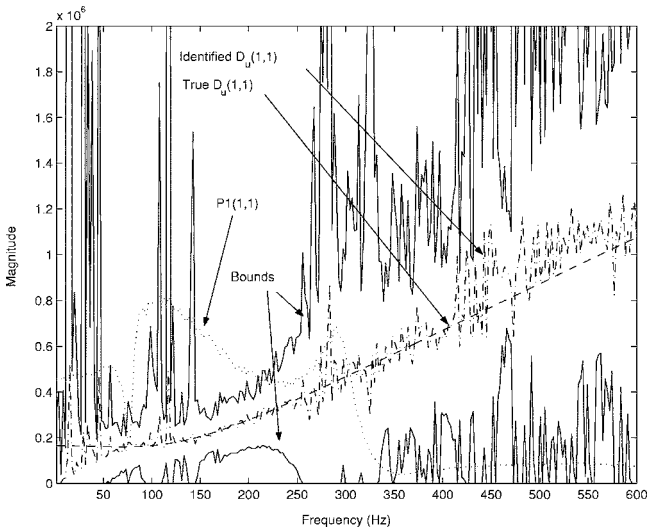

Fig. 11 Identification with bounds for 4% error

The identified $D_u(s)$ in both figures is only a nonparametric FRF, whereas a parametrized model of $D_u(s)$ is usually preferred. If no model for $D_u(s)$ is available or $D_u(s)$ has an arbitrary order (up to the number of data points), then any curve within the bounds could be the true D_u. In this case, the lowest-order model which can fit in the bounds may be the best for further use, but still there could be an infinite number of such models with the same order fit in the bounds, especially when the bounds are big.

If the uncertainties of the rotor model and test data are really random with constant expected value across frequencies (which is usually not true,) then curve fitting (or application of another black-box system identification process), the identified $D_u(s)$ may give the best parametrized model. Instead of trying to pick a best model, some researchers use a *membership set* to include all possible models (see [4,5]).

Quite often, there already exists a model structure for $D_u(s)$, such as for tilting pad bearings. In this situation, the calculated bounds can be used to validate the existing model. If the model does not fit in the bounds, the parameters of the model can be modified until it fits within the bounds. The goal of such a parameter modification would be to find the smallest overall change of the parameters, which brings the model inside the bounds.

Conclusions

This paper presented not only a nonparametric method to identify the frequency response functions of unmodeled machine components, but also a means of estimating the quality of the identified model by using μ analysis. The method is especially suitable for rotordynamics in two ways: First, for a rotor-bearing system, usually there are not many locations with unknown dynamics, which makes it relatively easy to satisfy the rank condition in Eq. (8). Second, the engineering model is often very accurate, i.e., the uncertainties of the model are small, which means that the quality of the identified parameters should not be too bad. Two simulation examples are given in this paper. The first one showed effectiveness of μ analysis and how tight the calculated bound is. The second example applied the method to identifying tilting pad bearing coefficients. The future work will investigate whether or not the given technique can provide bounds on the speed-dependent properties in addition to the frequency-dependent properties.

Nomenclature

C = damping matrix
D_u = missing dynamic effect
F = Laplace transformation of force vector
G = system transfer function
I = identity matrix
K = stiffness matrix
M = mass matrix or a general matrix
$P1$ = measured transfer function
T = selector matrix
X = Laplace transformation of displacement vector
Z = dynamics stiffness matrix
x = displacement vector
γ = Boundary
δ = uncertainty scalar
Δ = uncertainty matrix

References

[1] Friswell, M. I., and Mottershead, J. E., 1995, *Finite Element Model Updating in Structural Dynamics*, Kluwer, Dordrecht.
[2] Sinha, J. K., Friswell, M. I., and Lees, A. W., 2002, "The Identification of the Unbalance and the Foundation Model of A Flexible Rotating Machine From A Single Run-Down," Mech. Syst. Signal Process., **16**(2-3), pp. 255–271.
[3] Maslen, E. H., Vazquez, J. A., and Sortore, C. K., 2002, "Reconciliation of

RotorDynamic Models with Experimental Data," ASME J. Eng. Gas Turbines Power, **124**(2), pp. 351–356.
[4] Milanese, M., and Vicino, A., 1991, "Optimal Estimation Theory for Dynamic Systems with Set Membership Uncertainty: An Overview," Automatica, **27**(6), pp. 997–1009.
[5] Walter, E., and Piet-lahanier, H., 1990, "Estimation of Parameter Bounds from Bounded-Error Data: A Survey," Math. Comput. Simul., **32**, pp. 449–468.
[6] Zhou, K., Doyle, J. C., and Glover, K., 1995, *Robust and Optimal Control*, Prentice-Hall, Englewood Cliffs, NJ.
[7] Doyle, J. C., 1982, "Analysis of Feedback System with Structured Uncertainties," *IEE Proceedings*, Part D, Vol. **133**, pp. 45–56.
[8] Parsell, J. K., Allaire, P. E., and Barrett, L. E., 1982, "Frequency Effects in Tilting-Pad Journal Bearing Dyanmic Coefficients," ASLE Trans., **26**, pp. 222–227.
[9] Branagan, L. A., 1988, "Thermal Analysis of Fixed and Tilting Pad Journal Bearings Including Cross-film Viscosity Variations and Deformations," dissertation, University of Virginia.
[10] Vrudhula, S., Blaauw, D. T., and Sirichotiyakul, S., 2003, "Probabilistic Analysis of Interconnect Coupling Noise," IEEE Trans. Comput.-Aided Des., **22**(9), pp. 1188–1203.

On LMI-Based Optimization of Vibration and Stability in Rotor System Design

Matthew O. T. Cole
e-mail: matt@dome.eng.cmu.ac.th

Theeraphong Wongratanaphisan
e-mail: wong@dome.eng.cmu.ac.th

Department of Mechanical Engineering,
Faculty of Engineering,
Chiang Mai University,
Chiang Mai 50200, Thailand

Patrick S. Keogh
Department of Mechanical Engineering,
Faculty of Engineering and Design,
University of Bath,
Bath, BA2 7AY, UK
e-mail: enspsk@bath.ac.uk

This paper considers optimization of rotor system design using stability and vibration response criteria. The initial premise of the study is that the effect of certain design changes can be parametrized in a rotor dynamic model through their influence on the system matrices obtained by finite element modeling. A suitable vibration response measure is derived by considering an unknown axial distribution of unbalanced components having bounded magnitude. It is shown that the worst-case unbalanced response is given by an absolute row-sum norm of the system frequency response matrix. The minimization of this norm is treated through the formulation of a set of linear matrix inequalities that can also incorporate design parameter constraints and stability criteria. The formulation can also be extended to cover uncertain or time-varying system dynamics arising, for example, due to speed-dependent bearing coefficients or gyroscopic effects. Numerical solution of the matrix inequalities is tackled using an iterative method that involves standard convex optimization routines. The method is applied in a case study that considers the optimal selection of bearing support stiffness and damping levels to minimize the worst-case vibration of a flexible rotor over a finite speed range. The main restriction in the application of the method is found to be the slow convergence of the numerical routines that occurs with high-order models and/or high problem complexity.
[DOI: 10.1115/1.2135818]

Introduction

Structural dynamics are an important consideration in the design of rotating machinery. Dynamic performance will generally be assessed in terms of machine vibration levels and stability. Optimization of a structural design within the constraints imposed by machine functionality and physical feasibility can minimize transmitted noise and vibration, reduce machine wear, and reduce the likelihood of premature failure.

A number of researchers have developed numerical methods for optimizing the structural design of a rotor system subject to dynamic performance constraints, with particular focus on critical speed locations. This work has used finite element methods as the basis for assessing vibration behavior. Early work by Shiau and co-researchers tackled the problem of minimizing the weight of a rotor subject to constraints on critical speed locations and the forces transmitted by the bearings [1,2]. The design variables considered in these studies included the inner radius of hollow rotor sections, the positions of bearings and rigid disk elements, and the bearing stiffnesses. Chen and Wang have tackled similar design optimization problems but used an iterative method to manipulate the eigenvalues of rotor vibration modes [3]. In their study the outer diameter of rotor sections was varied, together with bearing stiffness and damping coefficients. An analysis of the sensitivity of rotor critical speeds to bearing stiffness was also used for optimization by Huang and Lin [4].

More recent work on multiobjective optimization has employed methods based on evolutionary algorithms. Unlike methods based on sensitivity analysis and gradient descent, these methods are particularly effective at finding solutions with global optimality. A study by Choi and Yang considered using immune genetic algorithms to minimize rotor weight and transmitted bearing forces [5]. Further work by Shiau et al. involved a two-stage optimization with a genetic algorithm to find initial values of design variables for further optimization. In their study, various parameter constraints were incorporated in an objective function using a Lagrange multiplier method [6]. Angantyr [7] and Angantyr et al. [8] also considered genetic algorithms as a basis for rotor design optimization and developed alternative methods to handle constraints on design variables.

This paper reports on a different approach to structural design optimization, where objectives for dynamic performance are formulated as a set of linear matrix inequalities (LMIs) that directly incorporate the design variables to be optimized. Linear matrix inequalities are being increasingly used in the analysis and control of dynamic systems as there are fast and efficient numerical algorithms to solve them. Multiple LMIs relating to performance, stability, or parameter constraints can be combined to form a single LMI, which can be solved using the same generic algorithms. This flexibility means that LMIs can be used to solve a wide range of optimization problems [9]. The basic theory of linear and bilinear matrix inequalities and some applications are described in a review paper by VanAntwerp and Braatz [10].

Vibration and Stability Criteria

Frequency and time domain transfer function norms are often used for system analysis and controller design as they provide useful measures of stability margins and response magnitudes. To date, their application in rotor systems has been mainly in the design and synthesis of active vibration control schemes (e.g., Refs. [11,12]). Design criteria used in active control are equally applicable to the optimization of passive rotor system dynamics. However, although many active control optimization problems have known analytical or numerically tractable solutions, passive design optimization problems using the same criteria often do not. This study will consider a class of design optimization problem that has equivalence to the static output feedback control problem. Methods have been developed recently for solving this type of

Contributed by the International Gas Turbine Institute (IGTI) of ASME for publication in the JOURNAL OF ENGINEERING FOR GAS TURBINES AND POWER. Manuscript received October 1, 2003; final manuscript received March 1, 2004. IGTI Review Chair: K. C. Hall. Paper presented at the ASME Turbo Expo 2005; Land, Sea, and, Air, Reno, NV, June 6–9, 2005, Paper No. GT2005-68522.

problem that are based on linear matrix inequalities and involve numerical routines developed for convex optimization [13,14].

The design optimization procedure will be formulated from a discrete parameter model of the linearized dynamics of a rotor system having the form

$$\mathbf{M}\ddot{\mathbf{z}} + \Omega\mathbf{J}\dot{\mathbf{z}} + \mathbf{C}\dot{\mathbf{z}} + \mathbf{K}\mathbf{z} = \mathbf{E}_f\mathbf{f} \tag{1}$$

Here, the mass, gyroscopic, damping, and stiffness matrices ($\mathbf{M}$, $\mathbf{J}$, $\mathbf{C}$, and $\mathbf{K}$, respectively), can be derived from finite element modeling procedures [15]. Ω is the rotational frequency. The vector $\mathbf{z}$ comprises nodal displacement coordinates while the matrix $\mathbf{E}_f$ locates the external disturbance forces $\mathbf{f}$ at the appropriate nodal positions. Such a model can also be represented in state space and transfer function forms as

$$\mathbf{E}\dot{\mathbf{x}} = \mathbf{A}\mathbf{x} + \mathbf{B}_f\mathbf{f} \tag{2}$$

and

$$\mathbf{G}(s,\Omega) = (s\mathbf{E} - \mathbf{A})^{-1}\mathbf{B}_f \tag{3}$$

respectively, where

$$\mathbf{E} = \begin{bmatrix} \mathbf{I} & \mathbf{0} \\ \Omega\mathbf{J} & \mathbf{M} \end{bmatrix}, \quad \mathbf{A} = \begin{bmatrix} \mathbf{0} & \mathbf{I} \\ -\mathbf{K} & -\mathbf{C} \end{bmatrix}, \quad \mathbf{B}_f = \begin{bmatrix} \mathbf{0} \\ \mathbf{E}_f \end{bmatrix} \quad \text{and} \quad \mathbf{x} = \begin{bmatrix} \mathbf{z} \\ \dot{\mathbf{z}} \end{bmatrix} \tag{4}$$

The dynamic performance of a rotor system under linear behavior can be directly assessed from the transfer function $\mathbf{G}(s,\Omega)$. Rotor unbalance vibration response, stability levels, and critical speed locations are commonly used indicators of dynamic performance, and these generally have equivalent transfer function specifications. For example, the requirement that the system has no critical speeds within a range $\underline{\Omega} < \Omega < \bar{\Omega}$ can alternatively be specified as a suitably chosen bound on the frequency response matrix $\mathbf{G}(j\omega,\Omega)$

$$\|\mathbf{G}(j\Omega,\Omega)\| < g(\Omega) \quad \text{for all } \Omega \tag{5}$$

where $\|.\|$ indicates an appropriate matrix norm and $g(\omega) > 0$ is a function chosen to be small in the range $\underline{\Omega} < \omega < \bar{\Omega}$. Other useful transfer function specifications include pole placement (eigenvalue) constraints, which can ensure rotor vibrational modes have adequate damping ratios and/or natural frequencies.

Typically, the exact unbalance condition of an assembled rotor is unknown. However, the maximum unbalance of rotor axial sections or components may be prespecified in manufacture or can be measured or estimated. The unbalance-induced vibration can be modeled by a vector of K external disturbance forces $\mathbf{f} = \mathbf{u}e^{j\Omega t}$, where the complex components $\mathbf{u} = \{u_k\}$, $(k = 1, \ldots, K)$ specify the unbalance force at each rotor section. For the purpose of design optimization, these components are considered to have bounded magnitude but arbitrary unknown phase,

$$u_k = |u_k|e^{j\phi_k}, \quad 0 \leqslant |u_k| < \Omega^2 m_k, \quad 0 \leqslant \phi_k < 2\pi \tag{6}$$

Here m_k are upper limits for the mass unbalance of each rotor section. The vibration magnitude of the nth nodal coordinate is then given by

$$Y_n(\Omega) = |\mathbf{C}_n\mathbf{G}(j\Omega,\Omega)\mathbf{u}| \tag{7}$$

where $\mathbf{C}_n$ selects the appropriate row of $\mathbf{G}(j\Omega,\Omega)$. Consequently,

$$Y_n(\Omega) = \left| \sum_{k=1}^{K} T_k(j\Omega)u_k \right| \leqslant \sum_{k=1}^{K} |T_k(j\Omega)||u_k| \tag{8}$$

where $\mathbf{T}(s) = [T_1(s), T_2(s), \ldots, T_K(s)] = \mathbf{C}_n\mathbf{G}(s,\Omega)$. The worst-case response occurs when all the phases ϕ_k combine constructively so that

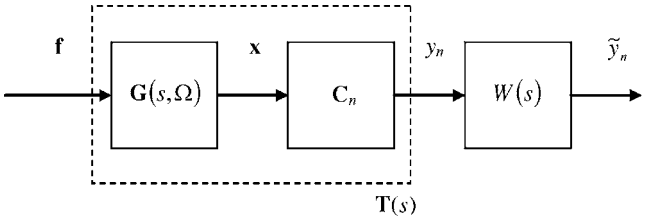

Fig. 1 Block diagram of augmented system with output weighting and overall transfer function $\tilde{\mathbf{T}}(s) = W(s)\mathbf{T}(s)$

$$\bar{Y}(\Omega) = \Omega^2 \sum_k |T_k(j\Omega)|m_k \tag{9}$$

Thus, the worst-case vibration amplitude at a particular machine location is given by the absolute row-sum of the corresponding frequency response matrix $\mathbf{T}(j\Omega)$ with each input scaled by $\Omega^2 m_k$. For the purpose of system design, a constraint can be specified in the form $\bar{Y}(\Omega) \leqslant \gamma f(\Omega)$, giving

$$\sum_k |T_k(j\Omega)|m_k \leqslant \gamma f(\Omega)/\Omega^2 \quad \text{for all } \Omega \tag{10}$$

where the bounding function $f(\Omega)$ may be chosen to reflect any design constraints concerning critical speed locations and running speed ranges. The bound $f(\Omega)/\Omega^2$ can be treated by model augmentation using a stable transfer function $W(s)$ connected at the model output, for which $|W(j\omega)| = \omega^2/f(\omega)$. Considering the augmented system (Fig. 1) with transfer function $\tilde{\mathbf{T}}(s) = W(s)\mathbf{T}(s)$, Eq. (10) is equivalent to

$$\max_{\Omega} \sum_k |\tilde{T}_k(j\Omega)|m_k \leqslant \gamma \tag{11}$$

With a tight bound ($\gamma = \gamma_{\min}$), it follows that there exists some value of $\Omega = \Omega_{wc}$ for which

$$\sum_k |\tilde{T}_k(j\Omega_{wc})|m_k = \gamma_{\min} \tag{12}$$

The objective of the design optimization is, therefore, to minimize $\gamma_{\min}$. The requirement of stable operation of the rotor system can be further specified in terms of quadratic stability of the system $\tilde{\mathbf{T}}(s)$. An additional consideration is the possibility of time-varying or nonlinear dynamics, for example, due to the rotational speed dependency of the system matrices given in Eq. (4). How the methods in this paper may be extended to cover these effects will be discussed in a following section.

To treat the row-sum norm specification of Eq. (11), consider first the more commonly used L_∞ norm-bound on the system $\tilde{\mathbf{T}}(s)$ with inputs scaled by d_k

$$\max_{\Omega} \sum_k \frac{|\tilde{T}_k(j\Omega)|^2}{d_k^2} \leqslant \delta \tag{13}$$

If $d_k = 1/m_k$ and condition (13) is satisfied with minimal $\delta = \delta_{\min}$, it then follows that

$$\sqrt{\delta_{\min}} \leqslant \gamma_{\min} \leqslant \sqrt{\delta_{\min} K} \tag{14}$$

Consequently, the L_∞ norm-bound of Eq. (13) can provide a loose bound on the row-sum norm in Eq. (11). However, it is not an ideal optimization criterion if the number of unbalanced force components K is large.

In an effort to obtain a tighter bound during an optimization procedure, a direct calculation of the worst-case vibration components $t_k = |\tilde{T}_k(j\Omega_{wc})|$ can be used to select $d_k = \sqrt{t_k/m_k}$. The vibration response criteria Eq. (11) can then be tackled with an iterative

design optimization procedure by minimizing the bound δ in Eq. (13) at each design iteration and then updating t_k. If after a number of design iterations

$$\max_{\Omega} \sum_k \frac{|\tilde{T}_k(j\Omega)|^2 m_k}{t_k} \to \sum_k \frac{|\tilde{T}_k(j\Omega_{wc})|^2 m_k}{t_k}$$

it then follows that

$$\sum_k |\tilde{T}_k(j\Omega_{wc})| m_k = \delta_{\min} \tag{15}$$

and thus $\delta_{\min} = \gamma_{\min}$. For some systems, the maxima in Eqs. (11) and (13) may not occur at the same value of Ω. In such cases the input scaled L_∞ norm will not produce the correct value for the row-sum norm and $\gamma_{\min}$ may not reach the optimum value.

LMI Formulation

The time domain equivalent of Eq. (13) is the peak RMS gain bound:

$$\int_0^T y_n^2 dt \leqslant \delta \int_0^T \mathbf{f}^{\mathrm{T}} \mathbf{D}^2 \mathbf{f} dt \tag{16}$$

for all $\mathbf{f}(t)$, where $\mathbf{D} = \mathrm{diag}\{d_1, d_2, \ldots, d_K\}$ is a diagonal scaling matrix. Note that the system considered here and subsequently is the unaugmented system $\mathbf{T}(s)$. However, the formulation would be unchanged by the inclusion of the weighting function $W(s)$, which is omitted from the state-space equations only for the sake of brevity. Quadratic stability of the system can be proved by the existence of a Lyapunov function of the form

$$V(t) = \mathbf{x}^{\mathrm{T}}(t) \mathbf{R} \mathbf{x}(t) \tag{17}$$

where $\mathbf{R}$ is any symmetric positive definite matrix such that $\dot{V} < 0$ for all possible state trajectories with $\mathbf{f} = [\mathbf{0}]$. Defining $\mathbf{P} = (\mathbf{E}^{-1})^{\mathrm{T}} \mathbf{R} \mathbf{E}^{-1} > 0$, it follows that

$$\dot{V} = (\mathbf{A}\mathbf{x} + \mathbf{B}_f \mathbf{f})^{\mathrm{T}} \mathbf{P} \mathbf{E} \mathbf{x} + \mathbf{x}^{\mathrm{T}} \mathbf{E}^{\mathrm{T}} \mathbf{P} (\mathbf{A}\mathbf{x} + \mathbf{B}_f \mathbf{f}) \tag{18}$$

The vibration response condition (16) and stability condition $\dot{V} < 0$ can be combined as

$$\dot{V} + y_n^2 - \delta \mathbf{f}^{\mathrm{T}} \mathbf{D}^2 \mathbf{f} < 0 \quad \text{for all} \quad [\mathbf{x}^{\mathrm{T}} \ \mathbf{f}^{\mathrm{T}}]^{\mathrm{T}} \neq [\mathbf{0}] \tag{19}$$

This is clearly a sufficient condition for $\dot{V} < 0$ when $\mathbf{f} = [\mathbf{0}]$, as y_n^2 is always greater than zero. Moreover, by integrating Eq. (19) over time, with zero initial conditions gives

$$V(T) + \int_0^T (y_n^2 - \delta \mathbf{f}^{\mathrm{T}} \mathbf{D}^2 \mathbf{f}) dt < 0 \tag{20}$$

As $V(t) \geqslant 0$ for all t then it follows that the vibration response condition Eq. (16) will also be satisfied. The necessity of condition Eq. (19) follows from the fact that the matrix $\mathbf{P}$ can be chosen freely [9].

With $y_n = \mathbf{C}_n \mathbf{x}$, Eq. (19) becomes

$$(\mathbf{A}\mathbf{x} + \mathbf{B}_f \mathbf{f})^{\mathrm{T}} \mathbf{P} \mathbf{E} \mathbf{x} + \mathbf{x}^{\mathrm{T}} \mathbf{E}^{\mathrm{T}} \mathbf{P} (\mathbf{A}\mathbf{x} + \mathbf{B}_f \mathbf{f}) + \mathbf{x}^{\mathrm{T}} \mathbf{C}_n^{\mathrm{T}} \mathbf{C}_n \mathbf{x} - \delta \mathbf{f}^{\mathrm{T}} \mathbf{D}^2 \mathbf{f} < 0 \tag{21}$$

Therefore, it is required that

$$\begin{bmatrix} \mathbf{x} \\ \mathbf{f} \end{bmatrix}^{\mathrm{T}} \begin{bmatrix} \mathbf{A}^{\mathrm{T}} \mathbf{P} \mathbf{E} + \mathbf{E}^{\mathrm{T}} \mathbf{P} \mathbf{A} + \mathbf{C}_n^{\mathrm{T}} \mathbf{C}_n & \mathbf{E}^{\mathrm{T}} \mathbf{P} \mathbf{B}_f \\ \mathbf{B}_f^{\mathrm{T}} \mathbf{P} \mathbf{E} & -\delta \mathbf{D}^2 \end{bmatrix} \begin{bmatrix} \mathbf{x} \\ \mathbf{f} \end{bmatrix} < 0 \tag{22}$$

for all $[\mathbf{x}^{\mathrm{T}} \ \mathbf{f}^{\mathrm{T}}]^{\mathrm{T}} \neq [\mathbf{0}]$. Thus, the design criterion is equivalent to the existence of a symmetric matrix $\mathbf{P} > 0$ for which the following symmetric matrix is negative definite:

$$\begin{bmatrix} \mathbf{A}^{\mathrm{T}} \mathbf{P} \mathbf{E} + \mathbf{E}^{\mathrm{T}} \mathbf{P} \mathbf{A} + \mathbf{C}_n^{\mathrm{T}} \mathbf{C}_n & \mathbf{E}^{\mathrm{T}} \mathbf{P} \mathbf{B}_f \\ \mathbf{B}_f^{\mathrm{T}} \mathbf{P} \mathbf{E} & -\delta \mathbf{D}^2 \end{bmatrix} < 0 \tag{23}$$

This is the standard LMI condition [9] for the input scaled system $\mathbf{T}(s)\mathbf{D}^{-1}$ to have an H_∞ norm less than $\sqrt{\delta}$.

Design Optimization

The design optimization procedure considered in this paper can encompass all cases where the state-space matrices have an affine dependence on a design variable matrix $\mathbf{U}(\theta_j)$ according to

$$\mathbf{A} = \mathbf{A}_0 + \mathbf{B}_u \mathbf{U}(\theta_j) \mathbf{C}_u \tag{24}$$

The design variable matrix $\mathbf{U}(\theta_j)$ can have an arbitrary structure and may be a nonlinear function of the physical design variables θ_j. However, the structure of the design variable matrix must be such that feasible solutions for θ_j can be obtained directly from any feasible solution for $\mathbf{U}$. The matrix $\mathbf{U}$ may also be constrained within a suitable ellipsoid, sector bound, or polytope that can be treated within the LMI framework [10].

Cases for which the matrix $\mathbf{E}$ depends on the design variables may also be treated:

$$\mathbf{E} = \mathbf{E}_0 + \mathbf{B}_v \mathbf{V}(\theta_j) \mathbf{C}_v \tag{25}$$

However, simultaneous dependency of the matrices $\mathbf{A}$ and $\mathbf{E}$ on the design variables adds significant complexity to the problem. In such cases the state-space matrices should be transformed, if possible, so that the dependency arises through either $\mathbf{E}$ or $\mathbf{A}$, but not both. The following section will consider some types of problems, together with specific examples, that can be treated through this formulation.

Parametrization of Rotor Design Variables

Lumped Inertias. Components that are modeled by lumped inertia parameters are commonly found in rotor systems. The mass and gyroscopic matrices of an FE model depend linearly on such lumped inertia parameters and so their design optimization can be treated through the formulation of Eq. (25). As an example, consider a rigid disk-like rotor component that may represent a flywheel, hub, impeller, etc. Often the designer will have some freedom over the dimensions of such a component that will consequently determine its inertial properties. In general, the matrices of Eq. (25) would take the form

$$\mathbf{E}_0 = \begin{bmatrix} \mathbf{I} & \mathbf{0} \\ \Omega \mathbf{J}_0 & \mathbf{M}_0 \end{bmatrix}, \quad \mathbf{B}_v = \begin{bmatrix} \mathbf{0} \\ \mathbf{I} \end{bmatrix}, \quad \mathbf{V} = [\Delta \mathbf{J} \ \Delta \mathbf{M}],$$
$$\mathbf{C}_v = \begin{bmatrix} \mathbf{I}\Omega & \mathbf{0} \\ \mathbf{0} & \mathbf{I} \end{bmatrix}$$

where the $\Delta \mathbf{J}$ and $\Delta \mathbf{M}$ are sparse matrices containing the appropriate inertial parameters that must be optimized. For a simple case of optimizing the dimensions of a solid rigid disk, having thickness l and radius r, then these take the form

$$\Delta \mathbf{J}(l,r) = \begin{bmatrix} \ddots & & & & \\ & 0 & 0 & 0 & 0 \\ & 0 & 0 & 0 & 0 \\ & 0 & 0 & 0 & -\pi \rho l r^4/2 \\ & 0 & 0 & \pi \rho l r^4/2 & 0 \\ & & & & \ddots \end{bmatrix}$$

$$\Delta\mathbf{M}(l,r)=\begin{bmatrix} \ddots & & & & \\ & \pi\rho l r^2 & 0 & 0 & 0 \\ & 0 & \pi\rho l r^2 & 0 & 0 \\ & 0 & 0 & \pi\rho l r^4/4 & 0 \\ & 0 & 0 & 0 & \pi\rho l r^4/4 \\ & & & & \ddots \end{bmatrix}$$

A further consideration is that the design variable matrix $\mathbf{V}$ can be constrained appropriately so that feasible values of l and r then follow from the solution $\mathbf{V}$. Other cases with more complex geometries or multiple components would give rise to the same basic problem structure.

Discrete Stiffness or Damping Elements. Discrete stiffness or damping elements arise in a FE or lumped parameter model of a rotor because of compliant components and component interfaces. For example, the mounting of a machine on isolators, the flexible coupling of rotor shafts or the use of squeeze film dampers all give rise to discrete stiffness or damping coefficients. These coefficients can often be influenced through a component's physical design and can therefore be tuned to give the desired dynamic performance of the overall system. In general, a discrete stiffness or damping element will couple two nodes of the system model, such that the matrices in Eq. (24) can be written in the form

$$\mathbf{A}_0=\begin{bmatrix} \mathbf{0} & \mathbf{I} \\ -\mathbf{K}_0 & -\mathbf{C}_0 \end{bmatrix},\quad \mathbf{B}_u=\begin{bmatrix} \mathbf{0} \\ \mathbf{E}_u \end{bmatrix},\quad \mathbf{U}=[\Delta\mathbf{K}\ \Delta\mathbf{C}],$$
$$\mathbf{C}_u=\begin{bmatrix} \mathbf{L} & \mathbf{0} \\ \mathbf{0} & \mathbf{L} \end{bmatrix}$$

The matrices $\Delta\mathbf{K}$ and $\Delta\mathbf{C}$ have diagonal elements that are the stiffness and damping coefficient to be optimized (other elements being 0). The matrices $\mathbf{E}_u$ and $\mathbf{L}$ have elements 1, −1, and 0, chosen to distribute the stiffness/damping forces at the correct nodal location and select corresponding displacement/velocity states, respectively.

Support Stiffness and Damping. The dependency of the system matrix on machine/rotor support stiffness and damping coefficients will generally take the same form as for the previous example. However, rather than coupling together model nodes, the coefficients contribute only to the on-diagonal entries in the overall stiffness and damping matrices, and can thus ensure the positive definiteness of these matrices that is required for system stability.

Shaft Dimensions. Rotor shaft elements are the basis of any flexible rotor FE model. Each rotor element has associated mass, gyroscopic, and stiffness matrices ($\mathbf{M}^e$, $\mathbf{J}^e$, and $\mathbf{K}^e$, respectively) that depend on element dimensions and material properties. For rotor lateral vibration with pure bending these can be derived for an annular beam element (length l, inner radius r_i, outer radius r_o, and density ρ) as given in the Appendix [15].

Without the inclusion of shear effects, the matrix entries of $\mathbf{M}^e$, $\mathbf{J}^e$, and $\mathbf{K}^e$ are proportional to l^n, where n may be −3, −2, …, 2, 3. Therefore, no transformation of the system state-space matrices can produce an affine dependence on the element lengths l. Alternative design variables that could be considered are the dimensions of rotor cross sections. The optimization of a hollow rotor to minimize its weight, subject to critical speed and unbalanced response constraints, has been considered by other authors [2,5]. The usefulness of this type of optimized design is restricted somewhat by the technical difficulties and expense of manufacturing a hollow rotor with varying inner diameter. However, similar optimization problems could be tackled using the LMI methods described in this paper. One method to do so would be to fix the parameter $r_o^4-r_i^4$ (and thus $\mathbf{M}_R^e$, $\mathbf{J}^e$, and $\mathbf{K}^e$) for each rotor section while optimizing the parameter $r_o^2-r_i^2$ that arises in $\mathbf{M}_T^e$. This would lead to an affine parametrization through the system $\mathbf{E}$ matrix (which depends linearly on $\mathbf{M}_T^e$). Optimization schemes based on iterative LMI algorithms may allow other types of rotor design problems to be considered, and this is an area for further research.

Extention to Time-Varying/Uncertain Dynamics. Time varying or uncertain dynamics can be treated within an LMI framework when the variation/uncertainty in the system dynamics gives rise to a convex set of system matrices [9,10]. Typically, the set of state-space matrices is described by a convex hull of matrices (a matrix polytope), for example,

$$\mathbf{E}(t)\in \mathrm{Co}\{\mathbf{E}_1,\cdots,\mathbf{E}_L\}$$

A sufficient condition for the previously considered stability and vibration response criterion can then be written in the form

$$\begin{bmatrix} \mathbf{A}^{\mathrm{T}}\mathbf{P}\mathbf{E}_i+\mathbf{E}_i^{\mathrm{T}}\mathbf{P}\mathbf{A}+\mathbf{C}_n^{\mathrm{T}}\mathbf{C}_n & \mathbf{E}_i^{\mathrm{T}}\mathbf{P}\mathbf{B}_f \\ \mathbf{B}_f^{\mathrm{T}}\mathbf{P}\mathbf{E}_i & -\delta\mathbf{D}^2 \end{bmatrix}<0 \quad \text{for all } i$$

The usefulness of this formulation will depend critically on how the time-varying or uncertain parameters appear within the state-space matrices, together with the free parameters that are to be optimized. However, it can be usefully applied when the state-space matrices depend linearly on rotational speed, as is the case for gyroscopic effects over a finite speed range $\Omega_{\min}<\Omega<\Omega_{\max}$, for which $\mathbf{E}_1=\mathbf{E}(\Omega_{\min})$, $\mathbf{E}_2=\mathbf{E}(\Omega_{\max})$.

Optimization Algorithm

The LMI-based design optimization problem can be solved using an iterative method that was originally applied to system stabilization with static output feedback control. The method adopted here has been modified to accommodate the vibration response bound but uses the same basic algorithm, which will be described only in outline here. Readers are referred to other papers [14] for details and discussions concerning convergence and optimality of the algorithm.

The basic design problem is to find a feasible solution $\mathbf{P}$ and $\mathbf{U}$ for the following matrix inequality:

$$\begin{bmatrix} (\mathbf{A}_0+\mathbf{B}_u\mathbf{U}\mathbf{C}_u)^{\mathrm{T}}\mathbf{P}\mathbf{E}+\mathbf{E}^{\mathrm{T}}\mathbf{P}(\mathbf{A}_0+\mathbf{B}_u\mathbf{U}\mathbf{C}_u)+\mathbf{C}_n^{\mathrm{T}}\mathbf{C}_n & \mathbf{E}^{\mathrm{T}}\mathbf{P}\mathbf{B}_f \\ \mathbf{B}_f^{\mathrm{T}}\mathbf{P}\mathbf{E} & -\delta\mathbf{D}^2 \end{bmatrix}<0 \tag{26}$$

subject to LMI constraints on the design variable matrix $\mathbf{U}$

$$F(\mathbf{U})+F_0<0 \tag{27}$$

The matrix in Eq. (26) is bilinear in $\mathbf{P}$ and $\mathbf{U}$, and so the design problem is not convex. To accommodate the bilinear terms, the following design iteration $\mathrm{U}_i=\mathrm{U}_{i-1}+\Delta\mathrm{U}_i$ can be considered:

Minimize δ, subject to

$$\begin{bmatrix} \mathbf{A}^{\mathrm{T}}\mathbf{P}\mathbf{E}+\mathbf{E}^{\mathrm{T}}\mathbf{P}\mathbf{A}+\mathbf{C}_n^{\mathrm{T}}\mathbf{C}_n-\mathbf{E}^{\mathrm{T}}\mathbf{P}\mathbf{B}_u\mathbf{B}_u^{\mathrm{T}}\mathbf{P}\mathbf{E} & \mathbf{E}^{\mathrm{T}}\mathbf{P}\mathbf{B}_f & \mathbf{E}^{\mathrm{T}}\mathbf{P}\mathbf{B}_u+\Delta\mathbf{U}_i\mathbf{C}_u \\ \mathbf{B}_f^{\mathrm{T}}\mathbf{P}\mathbf{E} & -\delta\mathbf{D}^2 & \mathbf{0} \\ \mathbf{B}_u^{\mathrm{T}}\mathbf{P}\mathbf{E}+\mathbf{C}_u^{\mathrm{T}}\Delta\mathbf{U}_k & \mathbf{0} & -\mathbf{I} \end{bmatrix}<0 \tag{28}$$

$$F(\mathbf{U}_{i-1}) + F(\Delta\mathbf{U}_i) + F_0 < 0 \tag{29}$$

Equation (28) follows directly from the Schur complement of Eq. (26). A dummy matrix $\mathbf{X}$ can now be introduced having the same dimensions as $\mathbf{P}$. Noting that $\mathbf{E}^{\mathrm{T}}(\mathbf{P}-\mathbf{X})\mathbf{B}_u\mathbf{B}_u^{\mathrm{T}}(\mathbf{P}-\mathbf{X})\mathbf{E} \geqslant 0$, it follows that:

$$\mathbf{E}^{\mathrm{T}}\mathbf{P}\mathbf{B}_u\mathbf{B}_u^{\mathrm{T}}\mathbf{P}\mathbf{E} - \mathbf{E}^{\mathrm{T}}\mathbf{X}\mathbf{B}_u\mathbf{B}_u^{\mathrm{T}}\mathbf{P}\mathbf{E} - \mathbf{E}^{\mathrm{T}}\mathbf{P}\mathbf{B}_u\mathbf{B}_u^{\mathrm{T}}\mathbf{X}\mathbf{E} + \mathbf{E}^{\mathrm{T}}\mathbf{P}\mathbf{B}_u\mathbf{B}_u^{\mathrm{T}}\mathbf{P}\mathbf{E} \geqslant 0 \tag{30}$$

and so a sufficient condition for Eq. (28) is

$$\begin{bmatrix} \mathbf{A}^{\mathrm{T}}\mathbf{P}\mathbf{E} + \mathbf{E}^{\mathrm{T}}\mathbf{P}\mathbf{A} + \mathbf{C}_n^{\mathrm{T}}\mathbf{C}_n + \mathbf{E}^{\mathrm{T}}\mathbf{X}\mathbf{B}_u\mathbf{B}_u^{\mathrm{T}}\mathbf{X}\mathbf{E} - \mathbf{E}^{\mathrm{T}}\mathbf{P}\mathbf{B}_u\mathbf{B}_u^{\mathrm{T}}\mathbf{X}\mathbf{E} - \mathbf{E}^{\mathrm{T}}\mathbf{X}\mathbf{B}_u\mathbf{B}_u^{\mathrm{T}}\mathbf{P}\mathbf{E} & \mathbf{E}^{\mathrm{T}}\mathbf{P}\mathbf{B}_f & \mathbf{E}^{\mathrm{T}}\mathbf{P}\mathbf{B}_u + \Delta\mathbf{U}_i\mathbf{C}_u \\ \mathbf{B}_f^{\mathrm{T}}\mathbf{P}\mathbf{E} & -\delta\mathbf{D}^2 & \mathbf{0} \\ \mathbf{B}_u^{\mathrm{T}}\mathbf{P}\mathbf{E} + \mathbf{C}_u^{\mathrm{T}}\Delta\mathbf{U}_i & \mathbf{0} & -\mathbf{I} \end{bmatrix} < 0 \tag{31}$$

This inequality is linear in $\mathbf{P}$ and $\Delta\mathbf{U}_i$ and therefore finding a solution for minimal δ is a generalized eigenvalue problem that can be tackled with standard numerical routines [16]. At each iteration a solution is found to Eqs. (29) and (31) for minimal δ. The dummy matrix is then set as $\mathbf{X}=\mathbf{P}$. The scaling matrix $\mathbf{D}=\mathrm{diag}(t_k/m_k)$ can also be updated if doing so will provide a tighter bound on the row-sum norm; however, this can be done less frequently. The algorithm is halted when either a satisfactory value for the worst-case vibration bound $\delta_{\min}$ is obtained or the algorithm converges. Convergence of the algorithm

$$\Delta\mathbf{U}_i \to 0, \quad \mathbf{X} \to \mathbf{P}, \quad t_k \to |\tilde{T}_k(j\Omega_{wc})|, \quad \delta_{\min} \to \delta_{\mathrm{opt}} = \gamma_{\mathrm{opt}}$$

implies that matrix inequality Eq. (31) will approach direct equivalence to the original design specification Eq. (11).

Numerical Example

The case studies considered in this paper concern the design of a test rig for assessing rolling-element performance during rapid acceleration, as shown in Fig. 2. The system is based on a dry clutch assembly and should be designed to operate safely over a running speed range of 0–10,000 rpm. The design variables are considered to be the bearing support stiffness and damping coefficients. Case studies are examined where the values of these coefficients are constrained within a range considered to be achievable by elastomeric mounting of the bearings units. However, it should be noted that the focus of this study is on the design optimization method rather than the feasibility of the resulting design.

Significant unbalance of the rotor is expected to occur in two axial planes corresponding to the flywheel and clutch locations and the unbalance is assumed to be <0.001 kgm at both locations. The optimization considers the vibration at the test bearing, the amplitude of which will be minimized using a frequency weighted transfer function bound in accordance with Eq. (10). The system foundation is assumed to be completely rigid and immoveable. The system has four bearings with radially isotropic stiffness and damping characteristics that will be parametrized by linear stiffness and damping coefficients (k_n and c_n, respectively, $n=1,\ldots,4$). The speed-dependent bound on the worst-case vibration response ($\gamma f(\Omega)$) is selected as shown in Fig. 3 for $\gamma=1$. The bound is chosen to be approximately constant over the running speed range of 0–1047 rad/s and will thus stipulate an upper limit on the unbalance response magnitude. Above 1047 rad/s, the bound increases slowly and so will also inhibit resonances outside the running speed range. It should be noted that the natural frequencies of the first three free rotor-bending modes derived from the FE model (Fig. 4) are 1405, 3334, and 7301 rad/s, which are all above the maximum rotational frequency. As a consequence, the critical speeds that exist within the running speed range are nominally "rigid-body" modes, but in actuality may be associated with significant rotor flexure.

The subsequent design optimizations will consider selection of the bearing characteristics to minimize the vibration bound γ. In general, the selection of bearing stiffness and damping to optimize system stability and vibration levels is a nontrivial problem. Having insufficient damping at the bearings will result in poor stability margins and large vibration at critical speeds. However, if bearing damping is too high the rotor will tend to be pinned at the bearings and this can reduce damping levels for higher order

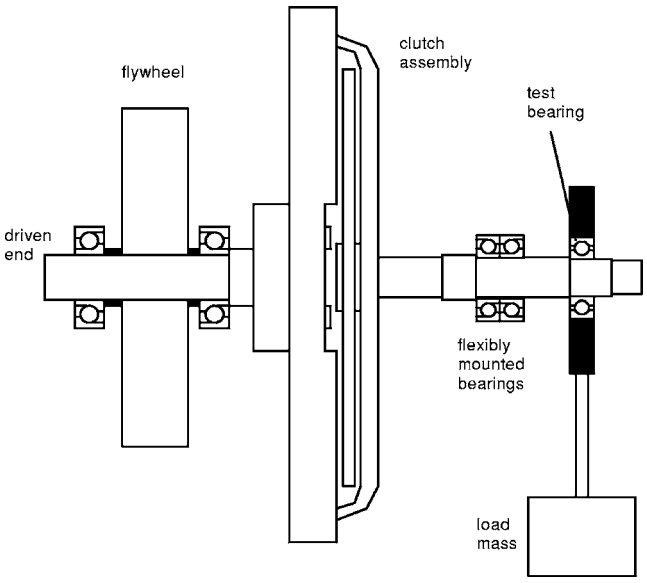

Fig. 2 Schematic of rotor test rig considered in case study

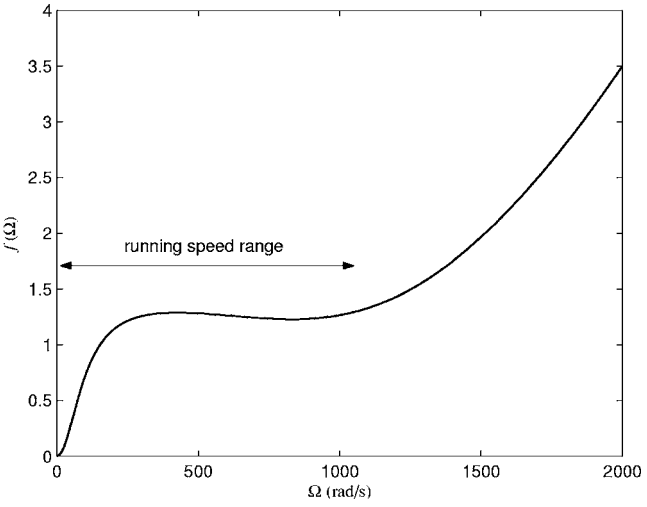

Fig. 3 Vibration response bound $\gamma f(\Omega)$ for $\gamma=1$

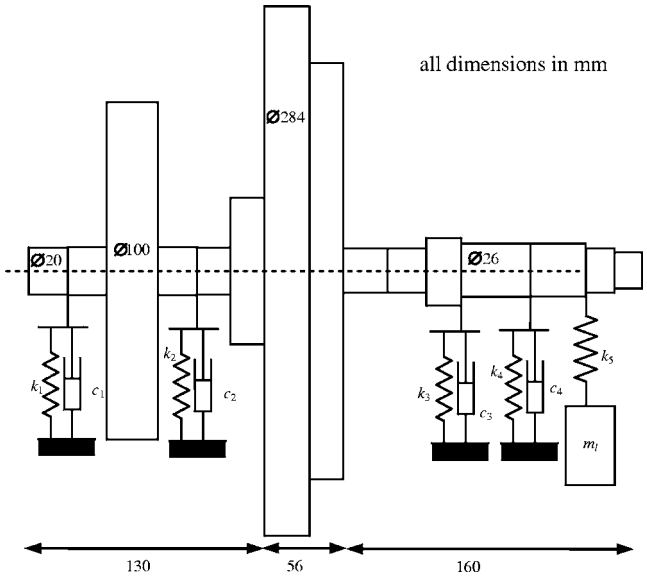

Fig. 4 Rotor-dynamic model, showing selected dimensions

bending modes. Similarly, bearings that are too stiff will tend to pin the rotor and result in low damping of some bending modes, while bearings that are too soft can result in large static deflections.

Case 1 considers global optimization over $k_B=k_1=k_2=k_3=k_4$, $c_B=c_1=c_2=c_3=c_4$. In this case, the bearing coefficients are unconstrained during optimization, but are the same for all four bearings. The minimal value of γ can also be found for this simple case by a numerical search over c_B and k_B. The optimization surface obtained by direct calculation of the minimal γ for a range of values of c_B and k_B is shown in Fig. 5.

The optimization procedure was undertaken with initial values $c_B=0.05$ MNs/m and $k_B=50$ MN/m, which give an initial value of $\gamma_{min}=0.23$. It can be seen from Figs. 5 and 6 that the iterative LMI algorithm converges slowly on the optimal solution, and after ~800 iterations approaches a final value of $\gamma_{min}=0.090$, which is very close to the true optimal value of $\gamma_{min}=0.085$. A jump in the value of γ_{min} occurs every 40 or so iterations when the input scalings t_k are updated.

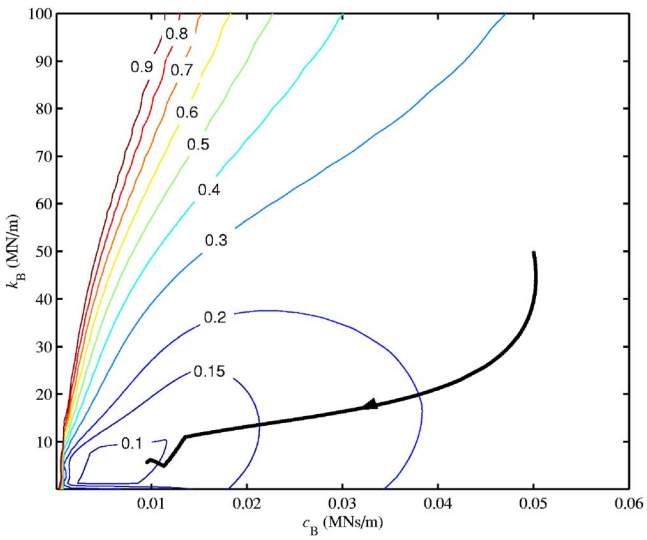

Fig. 5 Optimization surface showing contours of constant γ_{min} and optimization path for case 1

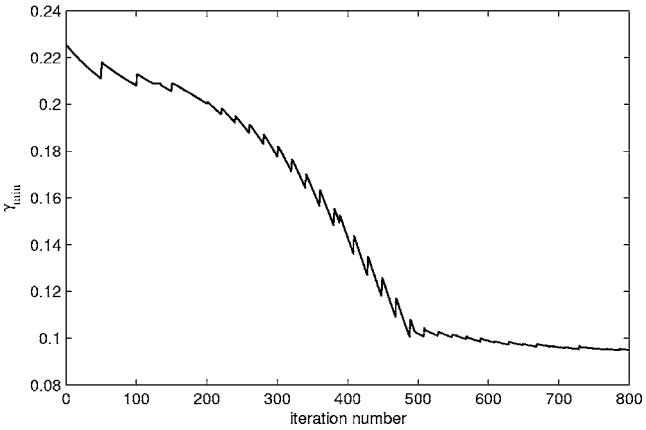

Fig. 6 Optimization of γ_{min} in case 1

Case 2 considers constrained optimization over $k_B=k_1=k_2=k_3=k_4$, $c_B=c_1=c_2=c_3=c_4$. For this case, the bearing coefficients are constrained according to

$$k_B - 10 \times 10^6 < 0, \quad -k_B + 1 \times 10^6 < 0$$

$$c_B - 0.0003k_B < 0, \quad -c_B + 0.0001k_B < 0$$

These constraints are linear and can be included as additional LMIs in the design optimization algorithm. The permissible region for c_B and k_B that results from these constraints is indicated in Fig. 7, together with the results obtained for two optimization runs having different initial values for c_B and k_B. In both cases A and B, the algorithm approaches the optimal values of c_B and k_B, indicated in the figure by ×, for which $\gamma_{min}=0.127$. In these cases the algorithm was stopped when the optimized values of γ_{min} were within 1% of the true optimum. At this time convergence had slowed to give a rate of ~1% decrease in γ_{min} per 100 iterations. The vibration response of the rotor with the initial and optimized bearing characteristics for case 2A is shown in Fig. 8, together with the minimized bound.

Case 3 considers constrained optimization over $k_1,k_2,k_3,k_4,c_1,c_2,c_3,c_4$. For this case, the final optimized values

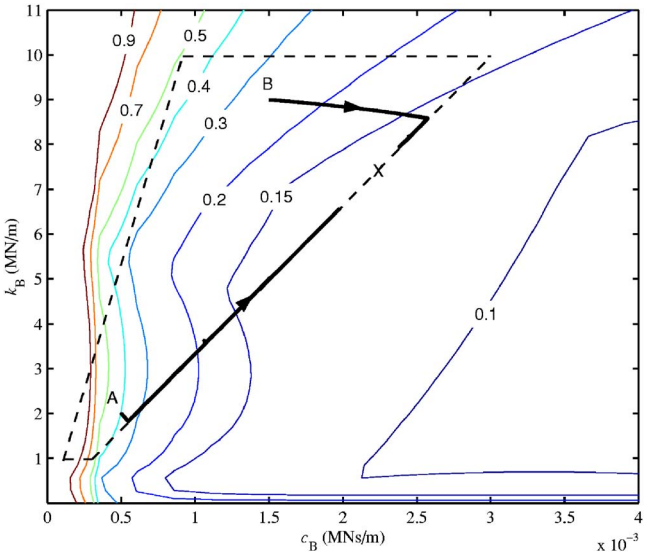

Fig. 7 Optimization surface showing contours of constant γ_{min} and optimization paths for cases 2A and 2B with different initial values of c_B and k_B. The region of permissible values is indicated by - - - boundary.

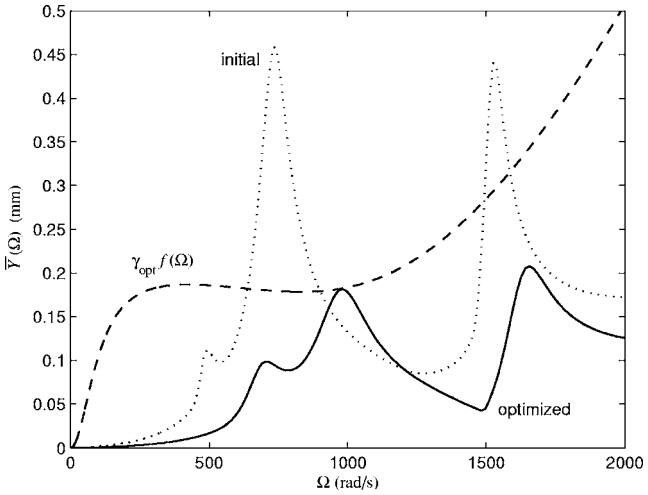

Fig. 8 Worst-case vibration response for optimized and unoptimized bearing coefficients from case 2A. The final bound (scaled by γ_{opt}) is also shown.

of c_B and k_B from case 2A are taken as initial values. The values of the coefficients are constrained within the same region considered in case 2 but are allowed to vary independently. The additional degrees of freedom provided in this case allow significant further optimization of the vibration response, as indicated in Fig. 9.

The results obtained for all three test cases are summarized in Table 1. In closing, it should be remarked that the matrices in Eq. (31) needed to be numerically well conditioned before applying the optimization routine. Moreover, to accelerate convergence of the algorithm, a model reduction procedure was used to reduce the full-order model (122 states) to a reduced-order model with 26 states. This was sufficient to include the first four rotor bending modes.

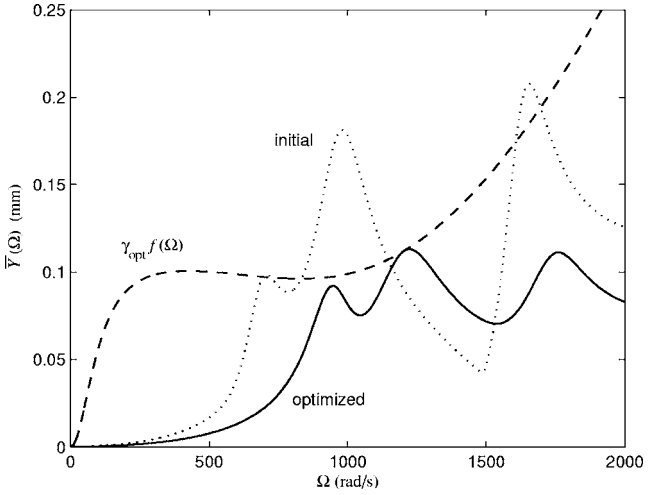

Fig. 9 Worst-case vibration response with optimized bearing coefficients from case 3. The optimized bound (scaled by γ_{opt}) is also shown.

Conclusions

This paper has investigated the use of LMI-based criteria for the optimization of passive rotor system dynamic performance. The proposed method employs a frequency-dependent bounding function that forms an upper limit on the allowable vibration amplitude. An iterative algorithm based on a state-space parametrization of the rotor dynamic model can then be used to minimize the vibration response of the rotor. In test cases on a flexible rotor system, the algorithm was effective in achieving near optimal levels of peak rotor vibration amplitudes through selection of the bearing stiffness and damping coefficients.

The advantage of the proposed method is the flexibility offered by the LMI formulation, which can be used to create design specifications concerning vibration amplitudes, stability, critical speeds, modal damping levels, and parameter constraints. Moreover, multiple criteria can be combined without destroying the underlying mathematical form of the optimization problem or the algorithm required to solve it. Another advantage of the LMI formulation is that it can deal effectively with uncertain or time-varying parameters, particularly those arising from speed-dependent dynamics.

There are currently some drawbacks to the proposed method due to the lack of fast and guaranteed methods to solve bilinear matrix inequalities, which arise through the dependence of the system state-space matrices on the design variables. The importance of developing improved algorithms to solve this problem is widely recognized by researchers in the field of numerical methods. With further development of these numerical tools, LMI-based methods may prove as useful in passive system design as they have in active control system design.

Nomenclature

$\mathbf{A}$, $\mathbf{B}_f$, $\mathbf{E}$ = state-space matrices of rotor dynamic model
$\mathbf{A}_0$, $\mathbf{B}_u$, $\mathbf{C}_u$ = state-space description for design optimization
$\mathbf{C}$ = rotor damping matrix
$\mathbf{C}_n$ = state-space output matrix for nth node
c_B = rotor support damping (Ns/m)
$\mathbf{D}$ = diagonal input scaling matrix
d_k = system input scaling
$\mathbf{E}_0$, $\mathbf{B}_v$, $\mathbf{C}_v$ = state-space description for design optimization
$\mathbf{E}_f$ = disturbance force distribution matrix
F = linear constraint function
$\mathbf{f}$ = disturbance force vector (N)
f = vibration response bound
$\mathbf{G}$ = complete rotor transfer function matrix
g = frequency response bound
$\mathbf{I}$ = identity matrix
$\mathbf{J}$ = rotor gyroscopic matrix
$\mathbf{K}$ = rotor stiffness matrix
k_B = rotor support stiffness (N/m)
l = rotor element length (m)
$\mathbf{M}$ = rotor mass matrix
m_k = mass unbalance upper limit (kgm)

Table 1 Summary of test cases

	Initial values				Optimized values									
Case	k_B (MN/m)	c_B (MNs/m)	γ_{min}	$\bar{Y}(\Omega_{wc})$ (mm)	k_1	k_2	k_3 (MN/m)	k_4	c_1	c_2	c_3 (MNs/m)	c_4	γ_{min}	$\bar{Y}(\Omega_{wc})$ (mm)
1	50.0	0.05	0.23	0.55		5.60				0.0095			0.90	0.11
2A	2.0	0.0005	0.40	0.45		6.44				0.0020			0.13	0.18
2B	9.0	0.0015	0.25	0.45		7.94				0.0024			0.13	0.17
3	6.44	0.0020	0.14	0.18	9.48	10.0	6.52	6.61	0.0028	0.0030	0.0007	0.0009	0.078	0.092

$\mathbf{P}, \mathbf{R}$ = Lyapunov matrices
r = rotor element radius (m)
T_k = elements of rotor transfer function matrix
$\mathbf{T}$ = rotor transfer function matrix
t_k = system input scaling
$\mathbf{U}, \mathbf{V}$ = design variable matrices
u_k = complex amplitude of unbalance force (N)
$\mathbf{u}$ = complex amplitude vector for unbalance forces (N)
V = Lyapunov function
W = weighting transfer function
$\mathbf{X}$ = dummy matrix variable
$\mathbf{x}$ = rotor state vector
Y = complex amplitude of vibration response
$\bar{Y}$ = complex amplitude of worst-case vibration response
y = rotor vibration response in time domain (m)
$\mathbf{z}$ = nodal displacement vector
δ = system norm bound
ϕ = phase of unbalance force component (rad)
γ = vibration response bound scaling
ρ = material density (kg/m^3)
Ω = rotor angular speed (rad/s)
ω = angular frequency (rad/s)

Subscripts

k = unbalance component index
n = nodal coordinate index
wc = worst case value
min = minimum value
opt = optimized value
i, o = inner, outer
R, T = rotational, translational

Superscripts

T = matrix transpose
e = rotor element

Appendix

$\mathbf{M}^e = \mathbf{M}_T^e + \mathbf{M}_R^e$ with

$$\mathbf{M}_T^e = \frac{\rho\pi(r_o^2 - r_i^2)l}{420} \times \begin{bmatrix} 156 & & & & & & & \\ 0 & 156 & & & & & & \\ 0 & -22l & 4l^2 & & & sym & & \\ 22l & 0 & 0 & 4l^2 & & & & \\ 54 & 0 & 0 & 13l & 156 & & & \\ 0 & 54 & -13l & 0 & 0 & 156 & & \\ 0 & 13l & -3l^2 & 0 & 0 & 22l & 4l^2 & \\ -13l & 0 & 0 & -3l^2 & -22l & 0 & 0 & 4l^2 \end{bmatrix}$$

$$\mathbf{M}_R^e = \frac{\rho\pi(r_o^4 - r_i^4)}{120l} \begin{bmatrix} 36 & & & & & & & \\ 0 & 36 & & & & & & \\ 0 & -3l & 4l^2 & & & sym & & \\ 3l & 0 & 0 & 4l^2 & & & & \\ -36 & 0 & 0 & -3l & 36 & & & \\ 0 & -36 & 3l & 0 & 0 & 36 & & \\ 0 & -3l & -l^2 & 0 & 0 & 3l & 4l^2 & \\ 3l & 0 & 0 & -l^2 & -3l & 0 & 0 & 4l^2 \end{bmatrix}$$

$$\mathbf{J}^e = \frac{\rho\pi(r_o^4 - r_i^4)}{60l} \begin{bmatrix} 0 & & & & & & & \\ 36 & 0 & & & & & & \\ -3l & 0 & 0 & & & skewsym & & \\ 0 & -3l & 4l^2 & 0 & & & & \\ 0 & 36 & -3l & 0 & 0 & & & \\ -36 & 0 & 0 & -3l & 36 & 0 & & \\ -3l & 0 & 0 & l^2 & 3l & 0 & 0 & \\ 0 & -3l & -l^2 & 0 & 0 & 3l & 4l^2 & 0 \end{bmatrix}$$

$$\mathbf{K}^e = \frac{E\pi(r_o^4 - r_i^4)}{2l^3} \begin{bmatrix} 12 & & & & & & & \\ 0 & 12 & & & & & & \\ 0 & -6l & 4l^2 & & & sym & & \\ 6l & 0 & 0 & 4l^2 & & & & \\ -12 & 0 & 0 & -6l & 12 & & & \\ 0 & -12 & 6l & 0 & 0 & 12 & & \\ 0 & -6l & 2l^2 & 0 & 0 & 6l & 4l^2 & \\ 6l & 0 & 0 & 2l^2 & -6l & 0 & 0 & 4l^2 \end{bmatrix}$$

References

[1] Shiau, T. N., and Hwang, J. L., 1988, "Minimum Weight Design of a Rotor Bearing System With Multiple Frequency Constraints," ASME J. Eng. Gas Turbines Power, **110**, pp. 592–599.
[2] Shiau, T. N., and Chang, J. R., 1993, "Multi-Objective Optimization of Rotor-Bearing System With Critical Speed Constraints," ASME J. Eng. Gas Turbines Power, **115**, pp. 246–255.
[3] Chen, T. Y., and Wang, B. P., 1993, "Optimal Design of Rotor-Bearing System With Eigenvalue Constraints," ASME J. Eng. Gas Turbines Power, **115**, pp. 256–260.
[4] Huang, S. C., and Lin, C. A., 2002, "Sensitivity Analysis and Optimization of Undamped Rotor Critical Speeds to Supports Stiffness," ASME J. Vibr. Acoust., **124**(1), pp. 296–301.
[5] Choi, B. K., and Yang, B. S., 2001, "Multiobjective Optimum Design of Rotor-Bearing Systems With Dynamic Constraints Using Immune-Genetic Algorithm," ASME J. Eng. Gas Turbines Power, **123**, pp. 78–81.
[6] Shiau, T. N., Kang, C. H., and Liu, D. S., 2004, "Optimization Combines the Genetic Algorithms With Augmented Lagrange Multiplier Method for Rotor-Bearing Systems Under Dynamic Behavior Constraints," *Proceeding of ASME Turbo Expo 2004*, Vienna, ASME, New York, ASME Paper No. GT2004–54058.
[7] Angantyr, A., 2004, "Constrained Optimization of Rotor-Bearing Systems by Evolutionary Algorithms," Licentiate thesis, Lulea University of Technology, Sweden.
[8] Angantyr, A., Andersson, J., and Aidanpää, J.-O., 2003, "Constrained Optimization Based on a Multiobjective Evolutionary Algorithm," *Proceedings of Congress on Evolutionary Computation*, Canberra, IEEE, Piscataway, NJ, pp. 1560–1567.
[9] Boyd, S., El Ghaoui, L., Feron, E., and Balakrishnan, V., 1994, *Linear Matrix Inequalities in System and Control Theory*, SIAM, Philadelphia.
[10] VanAntwerp, J., and Braatz, R. D., 2000, "A Tutorial on Linear and Bilinear Matrix Inequalities," J. Process Control, **10**, pp. 363–385.
[11] Cole, M. O. T., Keogh, P. S., and Burrows, C. R., 1998, "Vibration Control of a Flexible Rotor/Magnetic Bearing System Subject to Direct Forcing and Base Motion Disturbances," Proc. Inst. Mech. Eng., Part C: J. Mech. Eng. Sci., **212**(7), pp. 535–546.
[12] Sivrioglu, S., and Nonami, K., 1996, "LMI Approach to Gain Scheduled Control Beyond PID Control for Gyroscopic Rotor Magnetic Bearing System," *Proceedings of 35th Conference on Decision and Control*, Kobe, IEEE, Piscataway, NJ, pp. 3694–3699.
[13] Fujimori, A., 2004, "Optimization of Static Output Feedback Using Substitutive LMI Formulation," IEEE Trans. Autom. Control, **49**(6), pp. 995–999.
[14] Cao, Y.-Y., Lam, J., and Sun, Y.-X., 1998, "Static Output Feedback Stabilization: An ILMI Approach," Automatica, **34**(12), pp. 1641–1645.
[15] Nelson, H. D., and McVaugh, J. M., 1976, "The Dynamics of Rotor-Bearing Systems Using Finite Elements," ASME J. Eng. Ind., **98**, pp. 593–699.
[16] Gahinet, G., Nemirovski, A., Laub, A. J., and Chilali, M., 1995, *LMI Control Toolbox*, The Mathworks, Inc.

Analysis of Oil Film Thickness and Heat Transfer on a Piston Ring of a Diesel Engine: Effect of Lubricant Viscosity

Yasuo Harigaya
Michiyoshi Suzuki
Fujio Toda

Department of Technology Education,
Utsunomiya University,
Utsunomiya, Japan

Masaaki Takiguchi
Department of Mechanical Engineering,
Musashi Institute of Technology,
Tokyo, Japan

The effect of lubricant viscosity on the temperature and thickness of oil film on a piston ring in a diesel engine was analyzed by using unsteady state thermohydrodynamic lubrication analysis, i.e., Reynolds equation and an unsteady state two-dimensional energy equation with heat generated from viscous dissipation. The oil film viscosity was then estimated by using the mean oil film temperature and the shear rate for multigrade oils. Since the viscosity for multigrade oils is affected by both the oil film temperature and shear rate, the viscosity becomes lower as the shear rate between the ring and liner becomes higher. Under low load conditions, the viscosity decreases due to temperature rise and shear rate, while under higher load conditions, the decrease in viscosity, is attributed only to the shear rate. The oil film thickness between the ring and liner decreases with a decrease of the oil viscosity. The oil film thickness calculated by using the viscosity estimated by both the shear rate and the oil film temperature gave the smallest values. For multigrade oils, the viscosity estimation method using both the mean oil film temperature and shear rate is the most suitable one to predict the oil film thickness. Moreover, the heat transfer at ring and liner surfaces was examined.
[DOI: 10.1115/1.1924403]

Introduction

Most of the mechanical friction power losses in internal combustion engines occur on lubricated surfaces around the piston rings and skirt. The oil film viscosity, which reduces with the increase of temperature, seriously affects the lubrication between ring and liner. Recently, due to the requirement to reduce the friction power losses, the low-viscosity multigrade oils are used. In general, the multigrade oils have a high shear thinning effect, i.e., the viscosity becomes lower by high shear rate. Therefore, effects of the oil temperature and shear rate on oil viscosity must be taken into consideration in analyzing the lubrication characteristics of piston rings.

In most of the analyses of lubrication characteristics for piston ring, the oil film viscosity was estimated by using the liner surface temperature [1–9]. The effect of viscosity on oil film thickness and friction force is very significant. At present, there is little literature on the analysis of viscosity estimated by using oil film temperature on lubricated surfaces between piston ring and cylinder liner [10,11]. Radakovic et al. [10] presented a numerical solution procedure for treating thermohydrodynamic problems involving thin-film flows in the presence of transverse squeeze and shear-thinning effect, and elucidated the influence of both thermal and shear-thinning effects on the performance of ring. In their study, the steady state energy equation was used.

In previous papers [12–14], the authors used an unsteady, two-dimensional energy equation to analyze the oil film temperature on a piston ring. The variations of temperature, viscosity, and oil film thickness between ring and liner for a cycle were predicted. This model was verified with published experimental results for monograde oil [15]. Oil film thickness was calculated by using the viscosity estimated from mean oil film temperature. Satisfactory agreement between calculated and measured values was shown.

Contributed by the Internal Combustion Engine Division of ASME for publication in the JOURNAL OF ENGINEERING FOR GAS TURBINES AND POWER. Manuscript received January 20, 2003; final manuscript received September 24, 2004. Assoc. Editor: D. Assanis.

In the present work, a numerical solution model, i.e., Reynolds equation and the unsteady, two-dimensional energy equation with heat generated from viscous dissipation, was developed to study the effects of temperature and shear rate for multigrade oils on oil film thickness and heat transfer between the ring and the liner in a diesel engine.

Analysis of Temperature, Viscosity, and Thickness in Oil Film on a Piston Ring

The lubrication model on a piston ring analyzed in this paper is shown in Fig. 1. In the oil film flow field, the following assumptions are made.

(1) The space between ring and liner is fully flooded with oil.
(2) The flow is laminar; and the oil is an incompressible liquid.
(3) The specific heat, heat conductivity, and oil density are constant in a cycle; and the oil viscosity is only a function of temperature and shear rate.
(4) The lubrication model is considered as pure hydrodynamic lubrication with fully flooded inlet with Reynolds exit conditions.
(5) The oil starvation is neglected.
(6) The ring motions, the cylinder wall deformation, and the relative deformation of ring and cylinder wall are neglected.

Reynolds Eq. (1) was used to analyze the lubrication characteristics

$$\frac{\partial}{\partial x}\left(\frac{h^3}{\mu}\frac{\partial p}{\partial x}\right) = 6U_{\text{wall}}\frac{\partial h}{\partial x} + 12\frac{dh}{dt}. \tag{1}$$

At the oil inlet side, the inter-ring gas pressure p_2 is equal to the ambient pressure, and the oil film breaks down on the downstream side according to the Reynolds boundary condition such as follows:

$$p = p_2 \quad \text{at inlet side} \quad (x = 0)$$

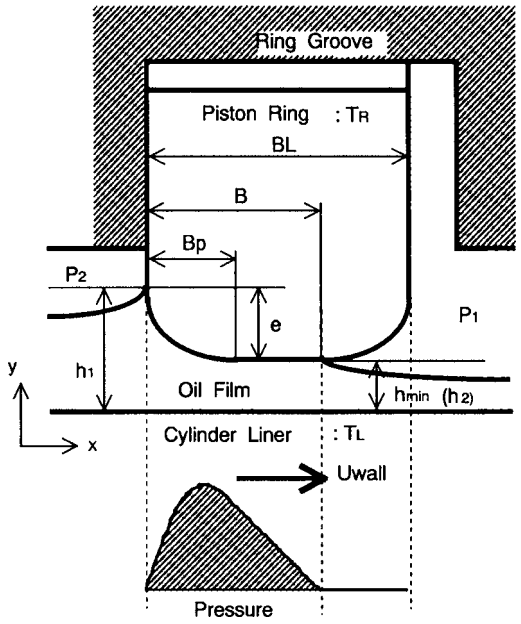

Fig. 1 Lubrication model between ring and liner

$p = p_1$ and $dp/dx = 0$ at the downstream side where the oil film breaks down $(x = B)$

where p_1 is the gas pressure in combustion chamber. The velocity of dh/dt is determined considering the force balance between the lubrication supporting force for the ring from the oil film and the radial force resulted from ring tension and gas pressure behind the ring.

Velocity distributions in the oil film were calculated by using Eqs. (2) and (3).

$$\rho\left(\frac{\partial u}{\partial t} + u\frac{\partial u}{\partial x} + v\frac{\partial u}{\partial y}\right) = -\frac{\partial p}{\partial x} + \mu\left(\frac{\partial^2 u}{\partial x^2} + \frac{\partial^2 u}{\partial y^2}\right), \tag{2}$$

$$\rho\left(\frac{\partial v}{\partial t} + u\frac{\partial v}{\partial x} + v\frac{\partial v}{\partial y}\right) = -\frac{\partial p}{\partial y} + \mu\left(\frac{\partial^2 v}{\partial x^2} + \frac{\partial^2 v}{\partial y^2}\right). \tag{3}$$

In the present model, the oil film viscosity was estimated using the oil film mean temperature and shear rate. Therefore, the analysis of oil film temperature on the piston ring was performed by unsteady, two-dimensional energy equation. Considering the heat generated from viscous dissipation in the oil film, the energy equation for unsteady, two-dimensional flow is expressed [16–18] as follows:

$$\rho C\left(\frac{\partial T}{\partial t} + u\frac{\partial T}{\partial x} + v\frac{\partial T}{\partial y}\right) = \kappa\left(\frac{\partial^2 T}{\partial x^2} + \frac{\partial^2 T}{\partial y^2}\right) + \phi, \tag{4}$$

$$\phi = 2\mu\left[\left(\frac{\partial u}{\partial x}\right)^2 + \left(\frac{\partial v}{\partial y}\right)^2 + \frac{1}{2}\left(\frac{\partial u}{\partial y} + \frac{\partial v}{\partial x}\right)^2\right]. \tag{5}$$

Equation (5) represents the viscous dissipation in the oil film. Thermal boundary conditions are as follows:

$$T = T_L \quad \text{at inflow on inlet side} \quad (x = 0),$$

$$dT/dx = 0 \quad \text{at outflow on inlet side} \quad (x = 0),$$

$$dT/dx = 0 \quad \text{at outlet side} \quad (x = BL),$$

$$T = T_L \quad \text{at liner surface} \quad (y = 0),$$

$$T = T_R \quad \text{at ring surface} \quad (y = h).$$

During the expansion process the oil layer is exposed the combustion gas, and the heat is transferred by the convection. As the oil layer temperature could increase but its temperature rise does not measured. So, in this paper, the oil film temperature at the inlet side is assumed the liner temperature T_L.

Generally, the temperature distribution along the cylinder liner has a higher slope near the top dead center (TDC) and a lower slope near the bottom dead center (BDC). In this work, using the measured temperatures at the TDC, midstroke point and BDC, the following expression is employed to evaluate the liner temperature distribution

$$T_L(s) = m_0 + m_1 \exp(-m_2 s/S), \tag{6}$$

where s is the displacement from the TDC of the top ring, S is the length of engine stroke, and m_0, m_1, and m_2 are correlation parameters.

Moreover, the ring surface temperature T_R can be assumed to be a constant only since the ring surface temperature variation in a cycle is low.

The mean oil film temperature in the effective oil film region T_m is defined as follows:

$$T_m = \frac{1}{hB}\int_0^h \int_0^B T(x,y)dx\, dy, \tag{7}$$

where h is the oil film thickness and B is the effective ring width.

The temperature dependence of the viscosity is estimated by using the relation between the viscosity and temperature. The Vogel equation [19] used in this work is

$$\mu = a_0 \exp\left(\frac{T_1}{T_2 + T_m}\right), \tag{8}$$

where a_0, T_1, and T_2 are correlation parameters.

On the other hand, the viscosity/shear rate is represented by the modified Cross equation [19],

$$\mu = \mu_\infty + \frac{\mu_0 - \mu_\infty}{1 + |\gamma/\gamma_c|} \tag{9}$$

where μ_0 is the oil low-shear viscosity, μ_∞ is the oil high-shear viscosity, and γ_c is critical shear rate.

In this paper, as the main flow in the oil film is assumed to be Couette flow, the shear rate γ is represented by Eq. (10)

$$\gamma = |U_{\text{wall}}|/h_{\min}, \tag{10}$$

where U_{wall} is the wall velocity and $h_{\min}$ is the minimum oil film thickness.

Also, μ_0, μ_∞, and γ_c are expressed as follows:

$$\mu_0 = a_0 \exp\left(\frac{T_1}{T_2 + T_m}\right), \tag{11}$$

$$b = \mu_\infty/\mu_0, \tag{12}$$

$$\gamma_c = 10^{c+dT}. \tag{13}$$

Heat transfer at ring and liner surface, Q_R and Q_L, the viscous heating Q_{vis} and the heat convected by the lubricant Q_{conv} were determined as follows:

$$Q_R = -\kappa\int_0^B \left(\frac{\partial T}{\partial y}\right)_{y=h} dx, \tag{14}$$

$$Q_L = -\kappa\int_0^B \left(\frac{\partial T}{\partial y}\right)_{y=0} dx, \tag{15}$$

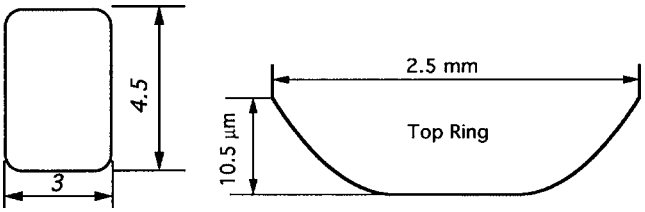

Fig. 2 Configuration of top ring sliding surface (experimental values)

$$Q_{\text{vis}} = \int_0^h \int_0^B \phi \, dx \, dy, \tag{16}$$

$$Q_{\text{conv}} = \rho \, C \left[\int_0^h (u \cdot T)_{x=B} dy - \int_0^h (u \cdot T)_{x=0} dy \right]. \tag{17}$$

Solution Procedure. The numerical procedure is summarized as follows.

(1) The oil film thickness h and the viscosity μ in the oil film at arbitrary crank angles were assumed.
(2) The Reynolds equation was solved numerically by the finite difference method, and the break down point B, pressure, velocity, and temperature distributions were calculated.
(3) The oil film viscosity was estimated by using the mean oil temperature T_m and the shear rate γ; and dh/dt was calculated. Then h at a given crank angle was predicted.
(4) The calculations (h, γ, T_m, and μ) were repeated until the solution converged to a certain condition.

The *semi-implicit method for pressure-linked equations* (simple) method [14,18] was used to solve the energy equation in the oil film temperature analysis. The solution domain representing the oil film on the piston ring was divided into 100 nodes in the direction of ring travel and 40 nodes across the oil film thickness.

Test Engine, Piston Ring and Liner Temperature. The analysis presented was applied to the piston ring of a direct-injection type, naturally aspirated four-stroke, six-cylinder diesel engine. The geometry of the ring sliding surface is the same as that of the top ring used in the oil film thickness measurement [15] as shown in Fig. 2. The ring profile is flat in the middle part and rounded off at both ends. The cylinder liner surface temperatures measured at each engine condition are shown in Fig. 3. Three measurement points, at the top, middle, and bottom of a stroke, were taken. The tested lubrication oils were (SAE) 10W, 30, and 50 for monograde oils, and SAE 10W50a and 10W50b for multigrade oils. Their specifications and the calculation conditions are shown in Tables 1–3.

Table 1 Calculation conditions

Engine	4 stroke NA DI Diesel Engine bore=110 mm stroke=125 mm connecting rod length=198 mm Maximum power=121.3/2800 kW/rpm Maximum torque=451.1/1800 Nm/rpm
Piston ring (Top ring)	BL=3 mm, a_1=4.5 mm h_1-h_2=10.5 μm (measured) Pe=154.4 kPa

Numerical Results and Discussions

Lubricant Properties. Figure 4 shows a plot of the low shear viscosity of the several oils. It can be seen that the oils show different low shear viscosity properties. At 150°C, SAE 10W had the lowest viscosity, and 10W50a and 10W50b had higher viscosities than that of SAE 50.

Figure 5 shows the relation between viscosity and shear rate for the SAE 10W50a multigrade oil. It can be seen that the multigrade

Table 2 Lubricants properties

SAE viscosity grade	Viscosity at 40°C [mPas]	Viscosity at 100°C [mPas]	Viscosity at HTHS [mPas]
10W	31.87	5.175	2.198
30	85.71	9.698	3.544
50	189.09	16.304	5.287
10W50a	105.14	15.800	4.048
10W50b	134.20	15.920	4.800

Note: HTHS: High temperature high shear rate at 150°C and $10^6$1/s.

Table 3 Parameters for equations of Vogel and Cross

SAE viscosity grade	$a0$ [mPas]	$T1$ [°C]	$T2$ [°C]	b	c	d [1/°C]
10W	0.06782	880.29	103.08			
30	0.06735	987.24	96.84			
50	0.06510	1078.25	95.22			
10W50a	0.08360	1184.31	125.94	0.4930	2.430	0.0218
10W50b	0.07399	1134.33	111.18	0.5190	2.280	0.0269

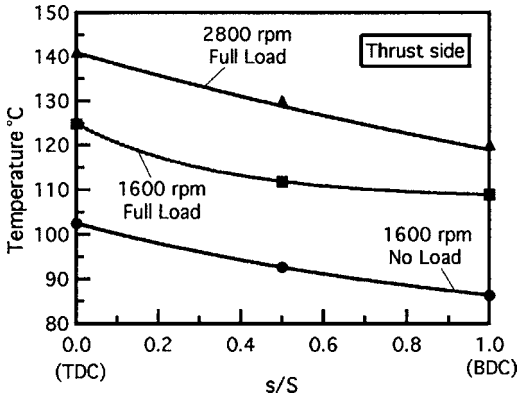

Fig. 3 Cylinder liner surface temperatures (oil: SAE 30, experimental values)

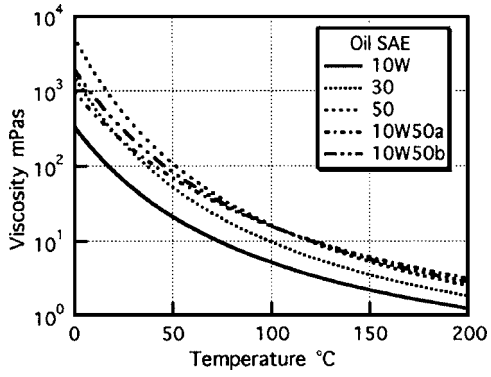

Fig. 4 Relation between viscosity and temperature (low shear rate)

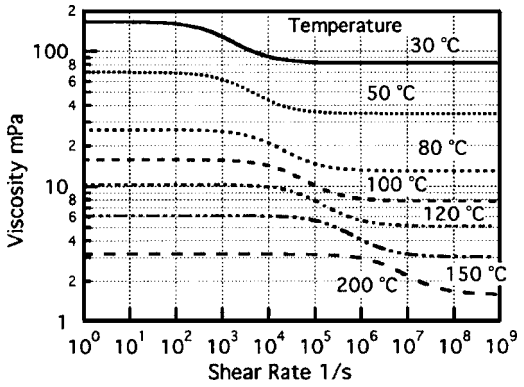

Fig. 5 Relation between viscosity and shear rate for multi grade oil (SAE 10W50a)

oil has high shear thinning effects and its properties are different at each temperature. Moreover, the viscosity decreases with the increase of shear rate.

Oil Film Temperature. The calculated temperature distributions in the oil film are shown in Figs. 6(*a*) and 6(*b*) at an engine speed of 1600 rpm under full load conditions using multi-grade oil 10W50a. These distributions are at a crank angle *CA* of 30 deg (expansion stroke), i.e., near the crank angle for the minimum oil film thickness and at a crank angle of 270 deg (exhaust stroke), i.e., near the crank angle for the maximum oil film thickness in a cycle. In this calculation, the top ring surface temperature T_R was expressed as $T_R=(T_G+T_{L:\mathrm{TOP}})/2$, where T_G was the measured top ring groove temperature and $T_{L:\mathrm{TOP}}$ was the measured liner surface temperature at TDC.

The temperature distribution at a crank angle of 30 deg shows isothermal lines in parallel with the ring surface at the flat region, and the most of heat is transferred from the ring to the liner by heat conduction. While the temperature distribution at a crank angle of 270 deg is influenced by the convection flow at the inlet, so that the oil film temperature at the proximity of the liner surface has a low value from inlet side to the middle part of ring width, and increases along the flow direction.

Oil Film Viscosity and Thickness. Effects of liner temperature, oil film temperature, and shear rate on viscosity of multigrade oil 10W50a were examined. Since the estimation methods for viscosity affect the oil film thickness, the viscosity is estimated by four methods listed below:

(1) The viscosity estimated by using the liner surface temperature distribution along the cylinder surface; $\mu=f(T_L)$.
(2) The viscosity estimated by using the liner surface temperature distribution along the cylinder surface and shear rate; $\mu=f(T_L,\gamma)$.
(3) Viscosity estimated by using the mean oil film temperature; $\mu=f(T_m)$.
(4) Viscosity estimated by using both the mean oil film temperature and shear rate; $\mu=f(T_m,\gamma)$.

To examine the effect of viscous heating, in the case of lower

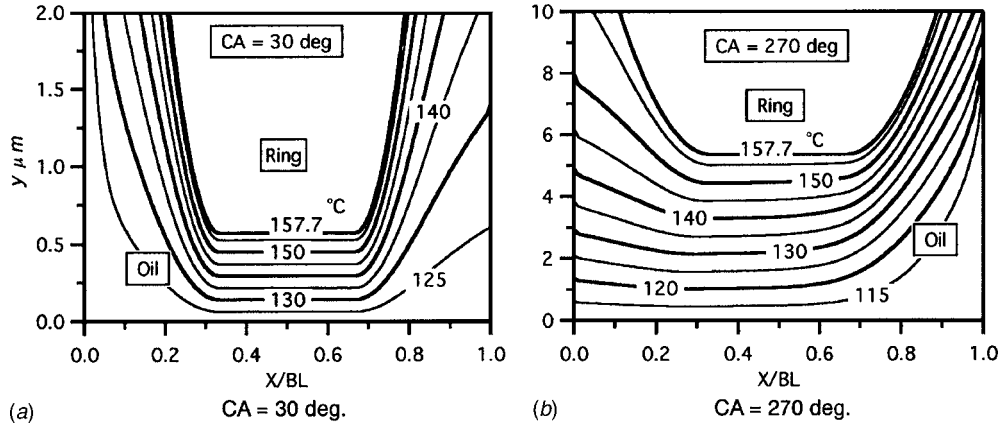

Fig. 6 Temperature distributions in oil film between ring and liner (oil: SAE 10W50a, 1600 rpm, full load). (*a*) CA=30 deg. (*b*) CA=270 deg.

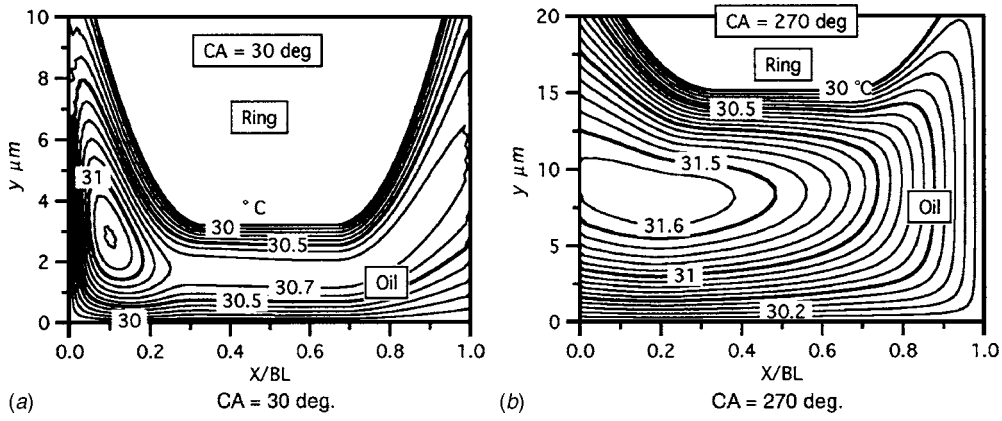

Fig. 7 Temperature distributions ($\mu=f(T_m,\gamma)$, $T_L=T_R=30°\mathrm{C}$, *Oil: SAE 10W50a, 800 rpm, no load*) (*a*) CA=30 deg. (*b*) CA=270 deg.

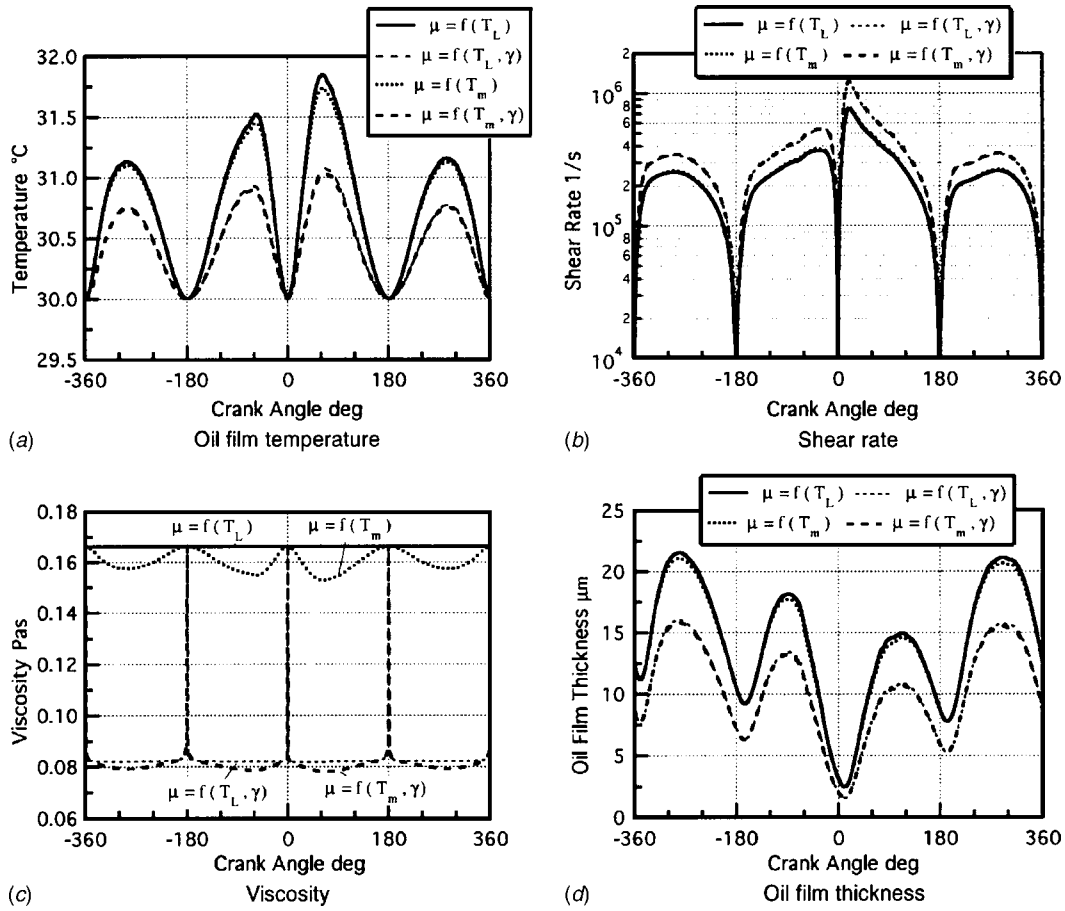

Fig. 8 Oil film temperature, shear rate, viscosity, and thickness under low temperature condition ($T_L = T_R = 30°C$, oil: SAE 10W50a, 800 rpm, no load). (*a*) Oil film temperature. (*b*) Shear rate. (*c*) Viscosity. (*d*) Oil film thickness.

temperature condition such as starting condition, oil film temperature distributions were calculated as shown in Figs. 7(*a*) and 7(*b*). In this calculation condition, the ring temperature is equal to the liner temperature; both are constants in a cycle, $T_R = T_L = 30°C$. The oil film temperature distribution has a peak at the inlet side in the oil film at a crank angle of 30 deg. At a crank angle of 270 deg, the position of maximum temperature in the oil film at the outlet side is near the middle between the ring and liner. Due to the viscous heating, the oil film temperatures are higher than the ring and liner surface temperatures.

Figures 8(*a*)–8(*d*) show the effects of estimation methods of viscosity on oil film temperature, shear rate, oil film viscosity, and the oil film thickness in the case of lower temperature condition.

The variations of mean oil film temperature T_m in a cycle as shown in Fig. 8(*a*) are about one degree in the case of temperature and shear rate effects, and about 1.7 deg in the case of temperature effect only.

The calculated shear rates as shown in Fig. 8(*b*) change from 10^5 to 10^6 s^{-1} in a cycle except around the top and bottom dead centers.

As shown in Fig. 8(*c*), the viscosity estimated from oil temperature is lower than the estimated liner temperature due to viscous heating. In addition, viscosities estimated by both temperature and shear rate decrease about 50% than those estimated by temperature alone due to high shear shinning effect.

As the result, the oil film thicknesses as shown in Fig. 8(*d*) decrease with a decrease in viscosity. The oil film thicknesses using viscosity estimated by both temperature and shear rate become thinner about 6 μm at maximum thickness position and about 1 μm at minimum thickness position than that using constant viscosity.

Figure 9 shows the mean oil film temperature, shear rate, viscosity, and oil film thickness using multi-grade oil 10W50a. Calculation conditions are at a measured ring temperature $T_R = 116.3°C$, liner temperature $T_L = T_L(s)$ under 1600 rpm and no load. The mean oil film temperatures vary widely due to effects of liner temperature, viscous heating, heat conduction, and heat convection between ring and liner as shown in Fig. 9(*a*). As shown in Fig. 9(*b*), shear rates change from 10^5 to 10^7 s^{-1} for most of the cycle. Therefore, it is considered that the estimated viscosity for multi-grade oils is affected by high shear thinning.

As the result, the viscosity estimated from oil film temperature $\mu = f(T_m)$ is about 15% lower at around top dead center and about 31% at around bottom dead center than that from liner temperature $\mu = f(T_L)$ as shown in Fig. 9(*c*). In addition, the viscosities estimated from both temperature and shear rate $\mu = f(T_L, \gamma)$ *and* $\mu = f(T_m, \gamma)$ become about 50% lower than that of $\mu = f(T_L)$. The viscosity estimated by both liner temperature and shear rate $\mu = f(T_L, \gamma)$ is higher than that estimated from oil film temperature and shear rate $\mu = f(T_m, \gamma)$ since the oil film temperature is higher than the liner temperature in a cycle

The oil film thicknesses relate to viscosity in a cycle and the oil film thickness using viscosity $\mu = f(T_m, \gamma)$ estimated by oil film temperature and shear rate is the thinnest as shown in Fig. 9(*d*). With viscosity $\mu = f(T_m, \gamma)$, the minimum value is about 0.47 μm and the maximum value is about 7.3 μm in a cycle and these become about 0.3 and 3.9 μm thinner than that using viscosity $\mu = f(T_L)$, respectively.

Under the higher load conditions, the liner and ring tempera-

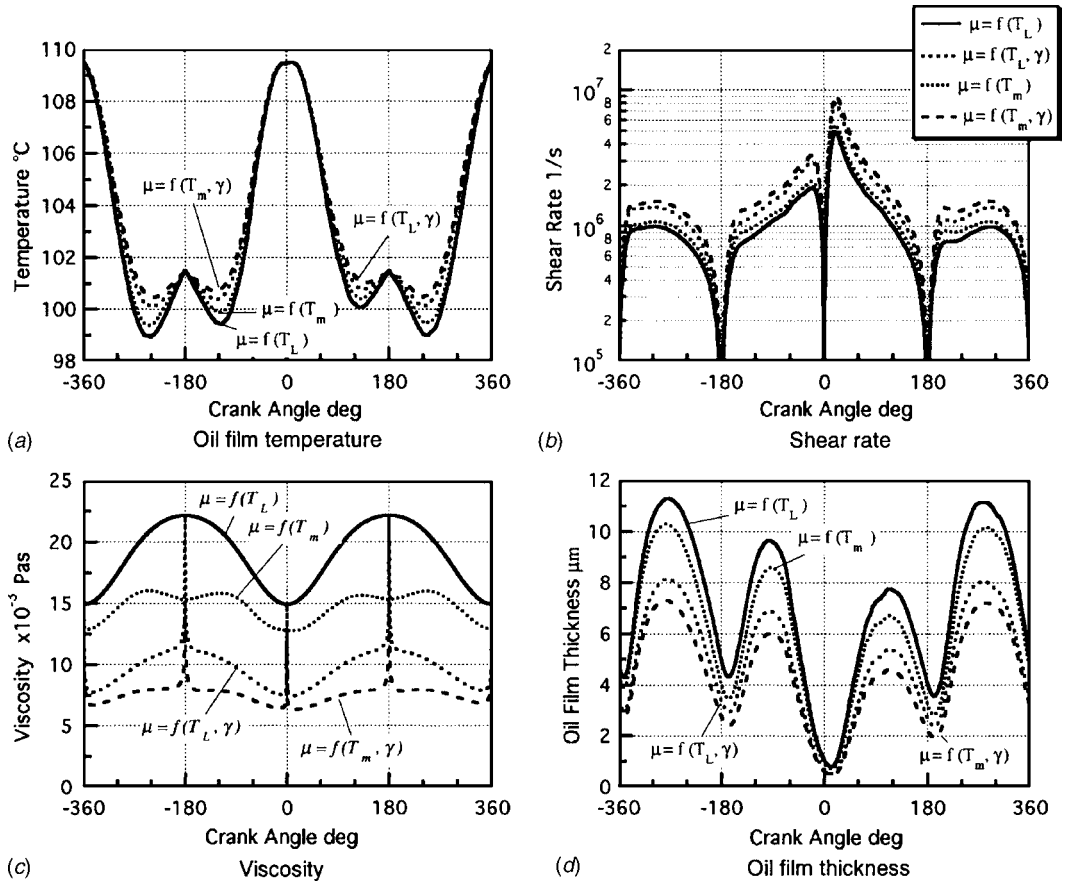

Fig. 9 Oil film temperature, shear rate, viscosity, and thickness (T_L, T_R; *measured values*, oil: SAE 10W50a, 1600 rpm, no load). (*a*) Oil film temperature. (*b*) Shear rate. (*c*) Viscosity. (*d*) Oil film thickness.

tures and shear rate become higher and the viscosity becomes lower. The oil film thickness becomes thinner with higher load as shown in Fig. 10.

Figure 11 shows the oil film thickness under severe condition of 2800 rpm and full load. The oil film temperatures become higher indicating that the temperatures increase due to viscous heating around top dead center at combustion. The range of shear rate is over 10^6 s^{-1} due to increasing sliding speed except around dead centers (refer to Fig. 12(*b*)). The oil film thickness using viscosity $\mu=f(T_m, \gamma)$ is thinner than that using viscosity $\mu=f(T_L, \gamma)$ estimated from liner temperature and shear rate.

As the result, the viscosities of multigrade oils decrease due to the effect of viscous heating and shear rate under low load conditions. On the other hand, under higher load and speed conditions, their viscosities become lower due to the effects of shear rate and increasing oil film temperature. The oil film thickness using viscosity estimated from the liner temperature is the thickest, and that using viscosity estimated by both oil film temperature and shear rate is the thinnest. For multigrade oils, the viscosity estimation method using both the mean oil film temperature and shear rate is the most suitable one to predict the oil film thickness.

Effect of Lubricants. The effects of lubricants on oil film thickness, shown in Fig. 12, were examined. In this calculation

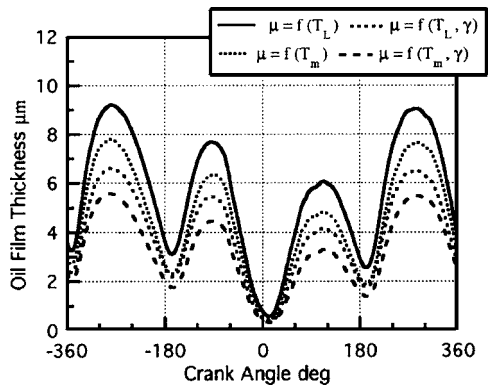

Fig. 10 Oil film thickness (T_L, T_R; measured values, oil: SAE 10W50a, 1600 rpm, full load)

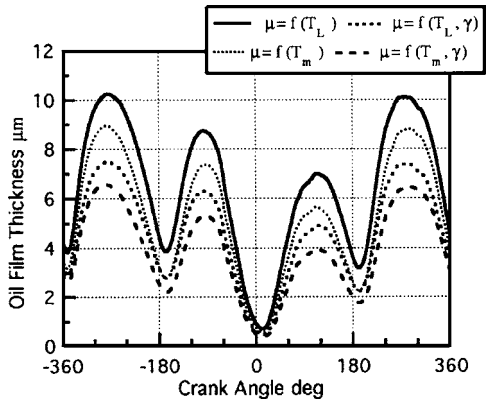

Fig. 11 Oil film thickness (T_L, T_R; *measured values*, oil: SAE 10W50a, 2800 rpm, full load)

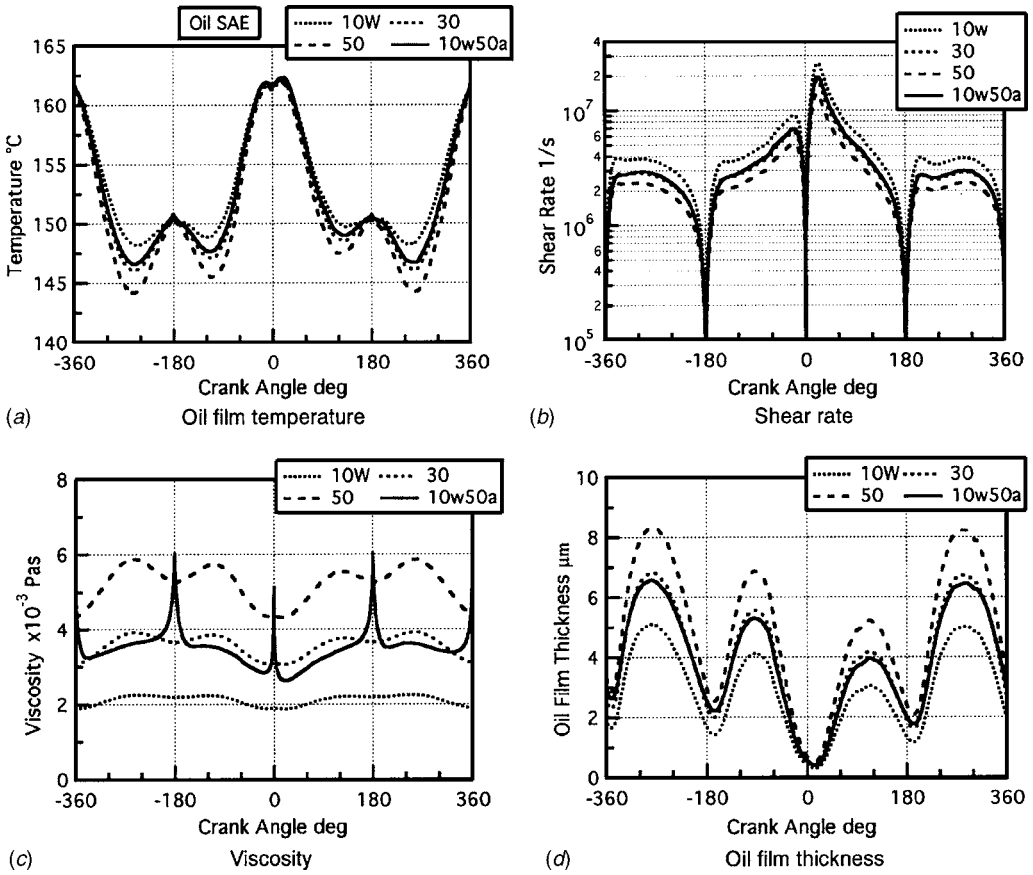

Fig. 12 Oil film temperature, shear rate, viscosity, and thickness (Comparison of various lubricants T_L, T_R; measured values, 2800 rpm, full load). (*a*) Oil film temperature. (*b*) Shear rate. (*c*) Viscosity. (*d*) Oil film thickness.

condition, the measured ring and liner temperatures at 2800 rpm and full load were used. The viscosity was estimated by using the oil film temperature and the shear rate for multigrade oil.

The oil film temperatures of all lubricants at around top dead centers exhibit almost the same values as shown in Fig. 12(*a*). At higher sliding speed range, the oil film temperature decreases with viscosity increase. It is considered that as ring sliding speed increases, oil film thickness becomes thicker and the inflow increases, so that the oil film temperature decreases due to these effects and the lower liner temperature. The shear velocities change from 10^6 to 2×10^7 s^{-1} except around top and bottom dead centers and become higher with decrease in viscosity as shown in Fig. 12(*b*). The variations of viscosity in a cycle for monograde oils become lower with oil viscosity decrease as shown in Fig. 12(*c*).

The oil film thicknesses are thinner with lower viscosity as shown in Fig. 12(*d*). The maximum thicknesses for SAE 50 and 10W are about 8.4 μm and 5.1 μm respectively. The minimum thicknesses for SAE 50 and 10W are 0.51 μm and 0.30 μm, respectively. Variations of oil film thicknesses in a cycle for SAE 30 and 10W50 are the same since these viscosities are almost constant in a cycle.

Effect of Multigrade Oils. For multigrade oils, 10W50a and 10W50b, the effects of oil film viscosity and thickness were examined. By comparing the lubrication properties, it is found that oil film temperature variations are the same in a cycle. As shown in Fig. 13(*a*), both viscosities of multigrade oils affect high shear thinning, and the viscosity of 10W50a oil is about 16% lower than that of 10W50b. As the result, the oil film thickness of 10W50a is thinner by about 10% than that of 10W50b in a cycle, so that the lubrication condition using SAE 10W50a becomes more severe as shown in Fig. 13(*b*).

Heat Transfer. Heat transfer at ring and liner surfaces in a cycle was examined. Figure 14 shows heat transfer and viscous heating in oil film between ring and liner under 2800 rpm and full load condition using multigrade oil 10W50a. Heat transfer at ring and liner surfaces as shown in Fig. 14(*a*) exhibit a peak at near top dead center for combustion. These values become lower at higher ring sliding velocities during half stroke. Heat flow at ring surface Q_R is higher than that at liner surface Q_L. It is considered that the sliding velocity becomes higher increasing the oil film thickness. The inlet flow becomes larger and the oil temperature at the proximity of the liner surface affected by the inlet flow becomes lower. Therefore the temperature gradient in the vertical direction of oil film near the liner surface is lower than that which is near the ring surface as shown in Fig. 6(*b*). The viscous heating is higher than the heat convection from $CA=0$ to $CA=50$ deg as shown in Fig. 14(*b*).

Conclusions

In this paper, the analysis of oil film thickness on a piston top ring of a diesel engine was performed by using thermohydrodynamic lubrication model, i.e., Reynolds equation and unsteady, two-dimensional energy equation with the viscous dissipation, involving effects of oil film temperature and shear rate on oil vis-

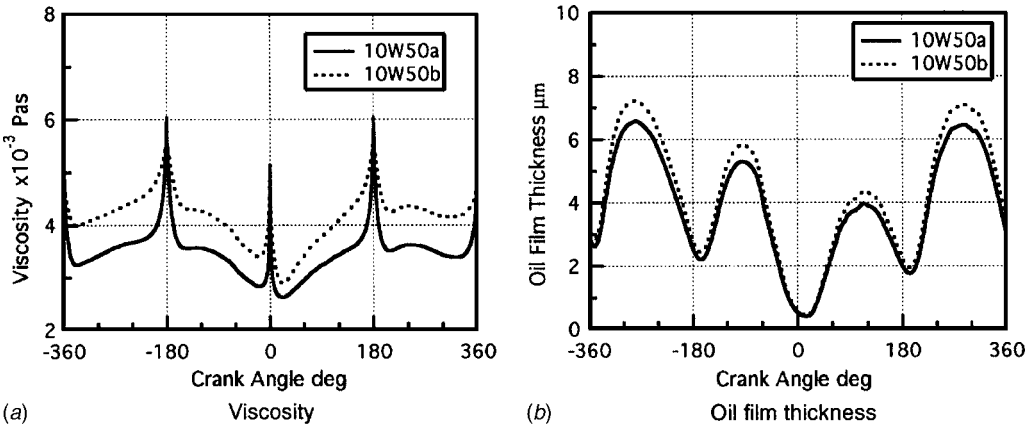

Fig. 13 Oil film viscosity and thickness (comparison of multigrade lubricants T_L, T_R; measured values, 2800 rpm, full load). (*a*) Viscosity. (*b*) Oil film thickness.

cosity for multigrade oils. In addition, the heat transfer between the ring and liner was examined. The results are summarized as follows:

(1) Using the present model for thermohydrodynamic lubrication, the oil film thickness could be calculated for multigrade oil that has high shear thinning effect.
(2) The calculated shear rate γ between the ring and liner is over 10^5 s^{-1} for most of the engine cycle. Therefore the viscosity for multigrade oils should be estimated by using both temperature and shear rate.
(3) Viscosity of multigrade oils affects both viscous heating and shear rate under low load conditions. Under higher load conditions, the viscosity decreases due to temperature increase and high shear thinning effects.
(4) The oil film thickness using viscosity estimated from the liner temperature is the thickest, and that using viscosity estimated by both oil film temperature and shear rate is the thinnest. For multigrade oils, the viscosity estimation method using both the mean oil film temperature and shear rate is the most suitable one to predict the oil film thickness.
(5) Heat transfer between ring and liner could be estimated by using this model.

The oil viscosity and oil film thickness model for multigrade oils has yet to be verified by experiments, and will be the topic of subsequent work. Moreover, the authors plan to develop the present model to include the analysis of oil film thickness involving effects of mixed lubrication condition and heat from friction.

Acknowledgment

This work was supported by the Research Committee 172 of the Japan Society of Mechanical Engineers. Thanks are due to the committee members with whom the authors have discussed this work, in particular Professor Nakahara of Tokyo Institute of Technology, Professor Azetsu of University of Tokyo, and Professor Hamatake of Ohita University.

Nomenclature

a_0 = correlation parameter of the Vogel equation
b = correlation parameter of the Cross equation
B = effective ring width
BL = axial width of ring
Bp = width of parallel region of ring
c = correlation parameter of the Cross equation
C = specific heat
d = correlation parameter of the Cross equation
e = barrel height of ring
h = oil film thickness
$h_{\min}$ = minimum film thickness
m_0, m_1, m_2 = correlation parameter of Eq. (13)
p = hydrodynamic pressure
Pe = surface pressure of ring

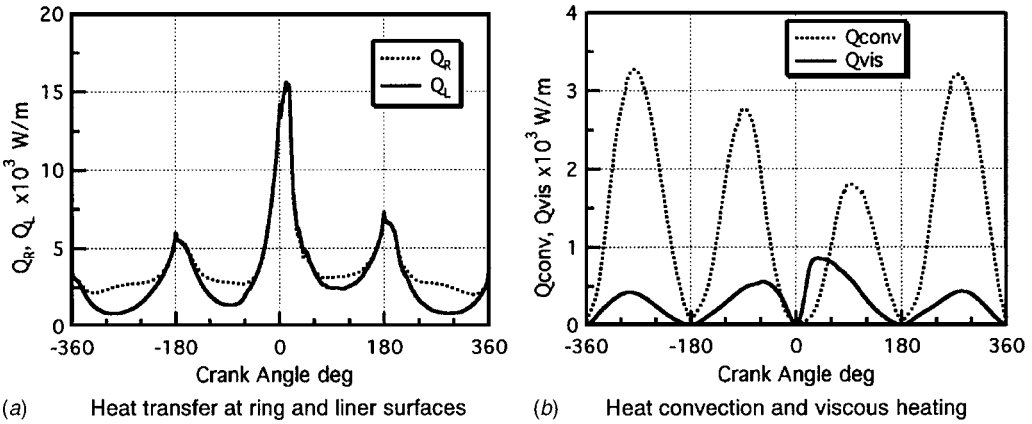

Fig. 14 Heat transfer, heat convection, and viscous heating in oil film 2800 rpm, full load, oil: 10W50a). (*a*) Heat transfer at ring and liner surfaces. (*b*) Heat convection and viscous heating.

p_1 = gas pressure in combustion chamber
p_2 = inter-ring gas pressure
Q_{conv} = Heat flow at convection
Q_{vis} = Heat flow generated from viscous
Q_R = Heat flow at ring surface
Q_L = heat flow at liner surface
s = displacement from position at TDC of top ring
S = length of engine stroke
T = temperature
T_1, T_2 = correlation parameter of the Vogel equation
T_m = mean oil film temperature
T_L = temperature of cylinder liner
T_R = temperature of ring surface
t = time
U_{wall} = sliding velocity of wall
u = x direction velocity
v = y direction velocity
γ = shear rate
κ = oil film thermal conductivity
ρ = density
μ = Viscosity

References

[1] Someya, T., 1999, "Engine Tribology: A Review on the Researches for Friction Reduction," J. Eng. Technol. Manage., **1–2**, p. 24.
[2] Furuhama, S., 1958, "A Dynamic Theory of Piston-Ring Lubrication," Trans. Jpn. Soc. Mech. Eng., Ser. C, **24**(148), p. 1032.
[3] Wakuri, Y., Soejima, M., and Taniguchi, T., 1977, "Oil Film Behavior of Piston Ring," Trans. Jpn. Soc. Mech. Eng., Ser. C, **43**(370), p. 2319.
[4] Sanda, S., and Someya, T., 1989, "The Mechanism of Piston Ring Friction and Lubrication (Improvement in Predicting Friction Force by Reconsidering Boundary Conditions)," Trans. Jpn. Soc. Mech. Eng., Ser. C, **55**(516), p. 2175.
[5] Ting, L. L., and Mayer, J. E. Jr., 1974, "Piston Ring Lubrication and Cylinder Bore Wear Analyses, Part II—Theory Verification," ASME J. Lubr. Technol., **96**, p. 258.
[6] Wakuri, Y., Hamatake, T., Soejima, M., and Kitahara, T., 1993, "Lubrication of Piston Ring Pack," Trans. Jpn. Soc. Mech. Eng., Ser. C, **59**(561), p. 1504.
[7] Tian, T., Wong, V. W., and Heywood, J. B., 1996, "A Piston Ring-Pack Film—Thickness and Friction Model for Multi-grade Oils and Rough Surfaces, SAE Paper No. 962032.
[8] Froelunet, K., Schramm, J., Tian, T., Wong, V. W, and Hochgreb, S., 1996, "Analysis of the Piston Ring/Liner Oil Film Development During Warm-Up for an SI-Engine," ASME ICE, **27**(2), p. 25.
[9] Ma, Ming-Tang, 2000, "Incorporation of Lubricant Shear-Thinning in a Two-Dimensional Lubrication Analysis for Automotive Piston-Ring Packs," CEC & SAE, *Advances in Powertrain Tribology*, SAE, p. 69.
[10] Radakovic, D. J., and Khonsari, M. M., 1997, "Heat Transfer in a Tin-Film Flow in the Presence of Squeeze and Shear Thinning; Application to Piston Rings," ASME J. Heat Transfer, **119**, p. 249.
[11] Nakai, H., Ino, N., and Hashimoto, H., 1998, "Effects of Film Temperature on Piston-Ring Lubrication for Refrigeration Compressors Considering Surface Roughness," ASME J. Tribol., **120**, p. 252.
[12] Harigaya, Y., Tsuji, Y., Kanahashi, H., and Suzuki, M., 1999, "Effect of Oil Film Temperature on Lubrication Characteristics of Piston Ring in Internal Combustion Engines," *Proceedings of the 15th Internal Combustion Engine Symposium (International) in Seoul*, JSAE, p. 179.
[13] Harigaya, Y., Akagi, J., and Suzuki, M., 2000, "Prediction of Temperature, Viscosity and Thickness in Oil Film Between Ring and Liner of Internal Combustion Engine," CEC & SAE, *Advances in Powertrain Tribology*, SAE, p. 109.
[14] Harigaya, Y., Suzuki, M., and Takiguchi, M., 2001, "Analysis of Oil Film Thickness on a Piston Ring of Diesel Engine: Effect of Oil Film Temperature," ASME ICE, **36-3**, ASME, New York, p. 19.
[15] Takiguchi, M., Sasaki, R., Takahashi, I., Ishibashi, F., Furuhama, S., Kai, R., and Sato, M., "Oil Film Measurement and Analysis of a Three Ring Pack in an Operating Diesel Engine, CEC & SAE, *Advances in Powertrain Tribology*, SAE, p. 81.
[16] Pinkus, O., 1990, *Thermal Aspects of Fluid Film Tribology*, ASME, New York.
[17] Namai, T., and Inoue, M., 1992, *Hydrodynamic of Viscous Flow*, Rikogakusha, Tokyo.
[18] Arakawa, C., 1994, *Computational Fluid Dynamics for Engineering*, University of Tokyo Press, Tokyo.
[19] Taylor, R. I., Kitahara, T., Saito, T., and Coy, R. C., 1996, "Piston Assembly Friction and Wear: The Influence of Lubricant Viscometry," *Proceedings of the International Tribology Conference*, Yokohama, Vol. III, p. 1423.

Injection Pressure Fluctuations Model Applied to a Multidimensional Code for Diesel Engines Simulation

Stefano Ubertini
University of Rome "Tor Vergata,"
Via del Politecnico, 1,
00133 Roma, Italy
e-mail: ubertini@mail.mec.uniroma2.it

This paper deals with the pressure supply fluctuations that occur in the fuel rail and in the injector on the immediate upstream side of the atomizer. It has been experimentally demonstrated that this has a considerable effect on the instantaneous mass flow and spray velocity thus affecting the spray hard-core structure and the atomization process. Moreover, considering the oscillatory nature of the phenomenon, the effects on a given spray can change from one injection to the other (in modern multijet systems) and from one engine cycle to the next. The needed computing time and the uncertainty related to a detailed simulation of the injection system fluid dynamics would be unacceptable in a multidimensional computational code. Therefore a simplified model able to predict fuel pressure supply fluctuations on the upstream side of the injector has been developed and is described in this paper. The model is validated and calibrated by comparing numerical results with available experimental data. Some numerical results on a fuel spray injected into a vessel at constant pressure are finally presented, in order to quantify the impact of a given level of pressure fluctuations on fuel spray characteristics.
[DOI: 10.1115/1.2135813]

Introduction

Air quality improvement mechanisms necessarily involve control and reduction of emissions from motor vehicles, which are the single largest contributor to urban air pollution. As a consequence, in the past two decades, controls on these emissions have been progressively tightened and the automotive industries had to invest significantly in making engines cleaner and more efficient.

The main advance in diesel engines technology has been the development of high-pressure fully electronic controlled injection systems. In particular, the computed-controlled common rail technology opens a number of new possibilities to optimize the engine performance; injection timing, injected fuel quantity, and injection pressure can be accurately controlled by an electronic control unit and are independent of engine speed [1,2]. This together with the higher injection pressures (up to 1500 bar) give rise to different characteristics of the fuel spray in the engine, thus allowing improved performances and reduced emissions. However, since stricter emission limits will be introduced in Europe in 2005 and 2008, greater research efforts are required.

It has already been demonstrated that the amount of pollutants in the raw emissions from compressed ignited (CI) engines is directly related to the combustion process and that the in-cylinder mixing between fuel and the surrounding gas is the process that governs the entire combustion event.

Despite the significant amount of research that has been carried out on diesel engines and although the influence of injection parameters has been widely investigated, information on the effects of in-cylinder air-motion and fuel rail pressure on spray and fuel vapor distribution with modern fuel injection systems is far from conclusive. To meet the requirements of a modern exhaust gas legislation, more comprehension of the active combustion chain is necessary and it is inevitable to apply advanced numerical techniques, in order to have direct "insight" into the engine and to allow studying different engine geometries, operating conditions, and injection strategies, thus reducing the number of experimental tests to be performed

The diesel combustion process is complex and difficult to visualize because a variety of factors affect it, including turbulence, spray characteristics, and air-fuel mixing. Our research group has developed a multidimensional fluid dynamics code, which is a KIVA-3V based multiblock structured grid approach, to make accurate predictions of mixture preparation, engine combustion, and emissions of modern diesel engines. The computational prediction of three-dimensional (3D) compressible turbulent and unsteady (both in space and time) flow inside an internal combustion engine represents itself as one of the most challenging fluid mechanics problems. Moreover, the compression ignition combustion process is extremely complex to simulate, since it is greatly influenced by the details of the fuel characteristics, the fuel-air mixing process, the engine geometry, the fuel-injection system, and the engine operating conditions. Great progress has been made on computational fluid dynamics (CFD) tools for diesel engines in recent years with the development of numerical models for spray simulation [3,4], vaporization [5,6], autoignition [7,8], and combustion processes [9]. However, considerable work is still needed in the development and testing of submodels to describe unresolved individual physical processes that, especially for combustion, introduce an excess of empiricism into computation.

For the initiation of the mixture preparation, the fuel-injection system and the fuel injectors themselves are the key elements. Therefore in a three-dimensional diesel engine simulation, in order to better simulate the spray development and the process of mixture preparation, it would be desirable to correctly predict all those parameters involved in fuel injection. Although detailed CFD multidimensional modeling of the injection system can be performed, its computational costs make it not suitable to be coupled with a detailed internal combustion engines multidimensional simulation. Therefore, simplified models are required because of their effectiveness in providing accurate information while maintaining acceptable computational times. Many simpli-

Contributed by the International Gas Turbine Institute (IGTI) of ASME for publication in the JOURNAL OF ENGINEERING FOR GAS TURBINES AND POWER. Manuscript received November 24, 2004; final revision received September 23, 2005. Review conducted by D. N. Assanis.

fied models of the injector or of the injection system (lump models) have been presented in literature, but with the aim of being used in a simulation limited to the sole injector or to the sole injection system [10–13]. Among others, the work of Bianchi et al. [13], which is based on coupling a lump model, involving mechanics, electromagnetism, and fluid dynamics, with CFD two-phase multidimensional computations of the spray, and the paper is worth mentioning. More recently Kolade et al. [14] coupled a one-dimensional (1D) model of the injection system with a 3D CFD code for modeling the in-cylinder combustion process.

It must be considered that the injected mass rate and the spray development depend on the injection pressure, which is usually an input and constant data in multidimensional code. However, as shown in studies found in literature [10,15] and in a previous paper [16], pressure fluctuations phenomena occur between the high-pressure reservoir (rail) and the discharge orifice. In order to control fuel injection in the combustion chamber of a diesel engine, it is necessary to know these pressure variations and the injection system should be designed in order to have an instantaneous pressure at the discharge orifice causing a fuel injection according to the requirements of an efficient combustion.

These injection pressure variations can have a considerable effect on the instantaneous mass flow and spray velocity, thus affecting the spray hard-core structure and the atomization process. Moreover, considering the oscillatory nature of the phenomenon, with modern multi-injection systems, this effect now becomes more important than ever. Therefore, the work presented in this paper is aimed to present a suitable physical model developed in order to predict pressure oscillations at the immediate upstream side of the injector atomizer nozzle. This allows treating injection pressure no more as an input data but as a variable inside the code, thus computing its variation in function of the geometrical characteristics of the common rail (CR) injection system. Supply pressure variation is then taken into account in the overall simulation of spray development and mixture preparation.

The model must satisfy the properties of being fast enough to be used in a multidimensional code and accurate enough to follow real injection pressure fluctuation. Therefore, experimental data have been used to calibrate the constants of the model and to verify that the code is capable of estimating real injection pressure fluctuations. Finally, the code is used to quantify the impact of a given level of pressure fluctuations on fuel spray characteristics.

Injection Pressure Submodel

The common rail diesel injection system (CR system) is designed to supply constant fuel pressure to electronically controlled injectors through a shared fuel reservoir, called common rail. Its main advantage is that, because of the high pressure in the rail and the electromagnetically controlled injectors, it is possible to fix the amount of injected fuel and the injection timing independently of the engine speed.

The CR system can be divided into three different functional groups: the high-pressure circuit, the low-pressure circuit, and the engine control unit (ECU). The latter is the "brain" of the system, which precisely controls injectors flow and timing as well as rail pressure while continuously monitoring the operating conditions of the engine.

A presupply pump drives fuel from the tank through the lines of the low-pressure circuit and through a fuel filter to the high-pressure pump. Uninjected fuel from the rail is led back to the tank through the pressure control valve.

The present model is focused on the high-pressure hydraulic system, from the rail to the injectors. The correct way to calculate injection pressure variation in the immediate upstream of the injector nozzle would be the analysis of the compressible unsteady flow in the ducts that connect the rail to the atomizer. However, since the model should be fast enough to be implemented in the multidimensional code, the real injection system geometry is represented by a simplified geometrical scheme (Fig. 1).

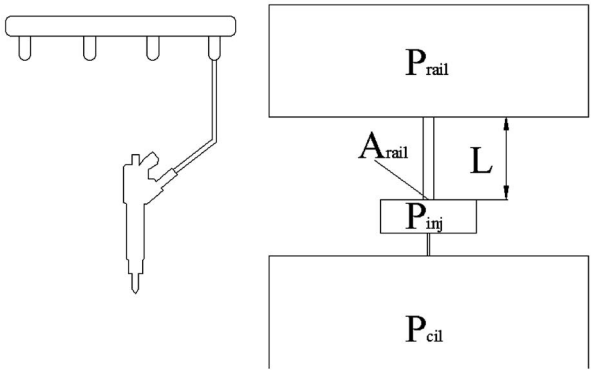

Fig. 1 Simplified geometrical scheme of the high-pressure circuit of the injection system

The high pressure is guaranteed by a high-pressure pump that continuously provides fuel to the pressurized accumulator, the rail (which is common to all the fuel injectors). Since the rail, whose volume is much bigger than the injector volume, is designed in order to damp pressure oscillation and to maintain a stable high-pressure level, rail pressure P_{rail} is considered constant. Every time an injection occurs, in fact, fuel is taken from the rail and a pressure-control valve attempts to keep the pressure at the desired level. Representing the rail as a fuel tank of infinite volume is, therefore, the first assumption of the present model. Then the connection between the rail and the injector is represented through a duct of length L that ends with a nozzle of section A_{rail}. Each cylinder has its own injector that is responsible for injecting fuel into the combustion chamber. Once the ECU sends an "open" signal, after a certain delay, the injector solenoid valve opens and some fuel enters the cylinder. In the present model, the injector is represented by a small volume positioned at the immediate upstream side of the atomizer nozzles. From now onward this volume is called prenozzles volume.

The pressure (density) change in the prenozzles volume results from the one-dimensional continuity equation. The difference between injected mass flow rate $\dot{m}_{\text{inj}}$ and fuel mass flow rate coming from the rail $\dot{m}_{\text{rail}}$, is balanced by density variation

$$\dot{m}_{\text{rail}} - \dot{m}_{\text{inj}} = W\frac{d\rho}{dt} \tag{1}$$

where W is the volume of the prenozzles box and ρ is the fuel density inside the prenozzles volume.

Assuming that compression and expansion of the fluid inside the prenozzles volume are adiabatic, pressure variation can be related to density variation

$$\frac{dP_{\text{inj}}}{a^2} = d\rho \tag{2}$$

where a is the speed of sound and P_{inj} is the pressure at the immediate upstream side of the injector atomizer nozzles, that is to say P_{inj} is the unknown.

Substituting Eq. (2) into Eq. (1), the following relationship is obtained:

$$\dot{m}_{\text{rail}} - \dot{m}_{\text{inj}} = \frac{W}{a^2}\frac{dP_{\text{inj}}}{dt} \tag{3}$$

A relevant integral property of the flow, necessary to calculate the mass flow rate, is the discharge coefficient C_d, which is used to represent the efficiency of a nozzle and thus is a measure of whatever losses occur in the nozzle

$$C_d = \frac{\dot{m}_{\text{inj}}}{n_{\text{noz}} A_{\text{noz}} \sqrt{2\rho(P_{\text{inj}} - P_{\text{cil}})}} \tag{4}$$

where n_{noz} is the number of injector holes.

As it will be described later, the discharge coefficient, the nozzle area and the resulting injected mass flow rate are calculated in the main code by means of other submodels

$$\dot{m}_{\text{inj}} = C_d n_{\text{noz}} A_{\text{noz}} \sqrt{2\rho(P_{\text{inj}} - P_{\text{cil}})} \tag{5}$$

If we consider that the fuel mass flow rate enters the prenozzles volume through the nozzle of section A_{rail} with a velocity v_{rail}, the following relationship is obtained:

$$\dot{m}_{\text{rail}} = \rho A_{\text{rail}} v_{\text{rail}} \tag{6}$$

Therefore, we can write the first differential equation necessary to calculate P_{inj} as follows:

$$\frac{dP_{\text{inj}}}{dt} = \frac{a^2}{W}(\rho A_{\text{rail}} v_{\text{rail}} - C_d n_{\text{noz}} A_{\text{noz}} \sqrt{2\rho(P_{\text{inj}} - P_{\text{cil}})}) \tag{7}$$

where, anyway, v_{rail} is still unknown.

The other equation necessary to solve the problem is the dynamic equilibrium of the system (Newton's 2nd law) with the following assumptions:

- The system mass is constituted only by the fluid column inside the duct of length L that connects the rail to the prenozzles volume; this represents the inertia of the entire system.
- The compressibility of the above mentioned fluid column is neglected.
- The elasticity of the system is given by the fluid contained inside the prenozzles volume.
- As already mentioned, compression and expansion of the fluid inside the prenozzles volume are adiabatic.
- The system is damped with a unique damping constant k_b.

The system equilibrium leads to

$$m_{\text{system}} \frac{dv_{\text{rail}}}{dt} = F_{\text{rail}} - F_{\text{damp}} \tag{8}$$

where F_{rail} is the external force and F_{damp} is the damping force.

With the above hypothesis, referring to Fig. 1, the system mass is given by

$$m_{\text{system}} = \rho L A_{\text{rail}} \tag{9}$$

the external force F_{rail} is given by the differential pressure between the prenozzles volume and the connecting duct

$$F_{\text{rail}} = A_{\text{rail}}(P_{\text{rail}} - P_{\text{inj}}) \tag{10}$$

and the damping force can be expressed by means of k_b

$$F_{\text{damp}} = k_b v_{\text{rail}} \tag{11}$$

The resulting equilibrium equation reads as follows:

$$\rho L A_{\text{rail}} \frac{dv_{\text{rail}}}{dt} - A_{\text{rail}}(P_{\text{rail}} - P_{\text{inj}}) + k_b v_{\text{rail}} = 0 \tag{12}$$

Grouping A_{rail} and v_{rail} into a volume flow rate

$$Q_{\text{rail}} = A_{\text{rail}} v_{\text{rail}} \tag{13}$$

the following differential equations system is obtained:

$$\frac{dQ_{\text{rail}}}{dt} = \frac{k_a}{\rho}\left(P_{\text{rail}} - P_{\text{inj}} - \frac{k_b}{A_{\text{rail}}^2} Q_{\text{rail}}\right) \tag{14a}$$

$$\frac{dP_{\text{inj}}}{dt} = \rho k_w \left(Q_{\text{rail}} - C_d A_{\text{noz}} \sqrt{\frac{2(P_{\text{inj}} - P_{\text{amb}})}{\rho}}\right) \tag{14b}$$

where P_{inj} and Q_{rail} are the independent variables, and k_a and k_w group together the geometrical data of the simplified scheme and the fluid speed of sound

$$k_a = \frac{A_{\text{rail}}}{L} \tag{15}$$

$$k_w = \frac{a^2}{W} \tag{16}$$

The instantaneous injection pressure is calculated in the code as the time marching solution of the differential equations system (14), numerically solved with a finite difference scheme.

A tuning process (model updating) is required because the geometrical parameters of the simplified scheme are obviously different from the actual injection system ones. However, the latter together with the fluid properties are useful to calculate the order of magnitude of the model coefficients:

- The volume W is close to the atomizer volume.
- The length L almost coincides with the length of the connecting pipes between the rail and the injector.
- The area A_{rail} is the effective flow area and is related to the internal flow area of the connecting pipes between the rail and the injector.
- The bulk modulus ρa^2 is commonly used to characterize the compressibility of a fluid; it is sensitive to various environmental factors, such as temperature, pressure, and volumetric ratio of fluid (at 1300 bar the bulk modulus and the density of common diesel fuel are, respectively, about 24×10^8 Pa and 860 kg/m^3).
- Although the damping coefficient is oftentimes (as in this paper) called damping "constant," this coefficient depends on the fluid properties (density, viscosity, and, to a much lesser extent heat conduction), on the system geometry and on the frequency of pressure fluctuations; however, as it will be shown in the next section, k_b influences only the amplitude of the oscillations, thus making its tuning straightforward.

Submodel Results

The first step of the present study is to verify if the proposed submodel is able to simulate actual pressure variation in the immediate upstream side of the atomizer nozzle. Experimental data showing the magnitude and the effects of injection pressure oscillations have been presented by Pontoppidan et al. [16]. The tested CR-injection system has a nominal maximum rail-pressure capacity of 130 MPa. The high-pressure fuel pump is a double-piston boxer-type pump with a maximum rail-pressure capability of 180 MPa and is inserted into a low-pressure supply circuit with a maximum pressure capability of 0.45 MPa.

The fuel rail has a buffer volume of 30 cm^3, and the injector atomizers are of the valve covered orifice (VCO) design. The connecting pipes between the pump and the rail and between the rail and the injector inlets have an internal flow area of 3.15 mm^2. The injector bodies were equipped with a specially manufactured pressure transducer mounting clamp, which provides a direct access to the expansion volume located around the upper part of the atomizer plunger on the downstream side of the calibration bores of the hydraulic amplifying circuit. The center-located atomizer, where the pressure fluctuation measurements were performed, has five nozzle holes with an angular space of 72 deg. The radius of curvature of the smoothed nozzle hole inlet profile is 0.85 times the inlet diameter. The atomizer main data are reported in Table 1.

The submodel presented in the previous section enables calculating pressure variations in function of the design of the fuel injection system and the properties of the fuel.

Table 1 Injector main data

Nozzle type	Static flow rate (mg/ms)	Internal radius (r)	Hole length (L)	D_{in}/D_{out}	D_{out} (mm)
VCO-3.1	8.42	$0.85\times D_{in}$	$3.5\times D_{in}$	1.42	0.14

Figure 2 shows the comparison between numerical results obtained with the present model and the pressure measurements made on the injector test rig with a mean rail pressure of 130 MPa during a single-shot injection. The amount of injected fuel and the time for injections are determined by the ECU and control signals are sent to the injector electromagnet that controls the opening and closing of the valve. Since the valve in the injector is closed, there is an imbalance of pressure between the rail and the injector, and the result is an oscillation, which is damped mainly because of viscous effects.

The instantaneous injected mass flow rate is calculated as a function of time by means of the experimental discharge coefficient and the experimental law of the valve opening and closure. In order to get the right values of the constants k_a, k_b, and k_w, a tuning process has been performed starting from those obtained through the actual geometrical parameters (length and internal flow area of the connecting pipes between the rail and the injector for L and A_{rail} and nozzle volume for W) and the fluid data (speed of sound, density, and viscosity).

The model coefficients that allow reproducing the experimental variation of the injection pressure for the present test (see Fig. 2) are summarized in Table 2. In particular, it is important to underline that the code could capture the experimental measurements in terms of pressure decreasing during the injection phase, which has a great impact on the spray characteristics of the injection itself, and in terms of pressure fluctuations after the injector valve closure, which could have a significant impact on the successive injections.

Once the model has been updated, some tests have been carried out in order to quantify the effect of the CR system characteristics on the injection pressure fluctuations. This has been performed by varying the model constants k_a and k_w, while maintaining unchanged the other parameters.

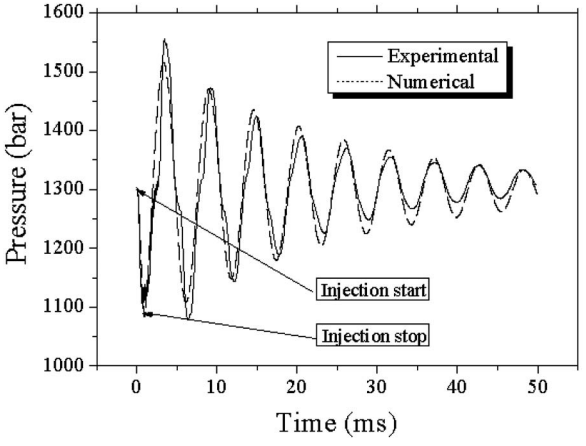

Fig. 2 Comparison between numerical results and injection pressure measurements

Table 2 Model coefficients after the model updating

k_a (m)	k_b/k_{rail}^2 (kg/s m^4)	k_w (1/m s^2)	Injection duration (ms)
0.518×10^{-6}	1.85×10^{11}	2.75×10^{12}	1.0

Figure 3 shows that by increasing k_w, both the amplitude and the frequency of injection pressure oscillations increase. However, since the injector volume W cannot be significantly changed, it is not possible to control injection pressure oscillations through the constant k_w.

On the other hand, k_a can be easily changed by changing L or A_{rail}. However, if L almost coincides with the actual length of the connecting pipes between the rail and the injector, it is hard to find a relationship between the effective discharge flow area of the connecting duct and A_{rail}. As shown in Fig. 4, an increase of k_a produces the following effects:

- reduction of pressure decreasing during injection, that yields a reduction of the oscillations amplitude
- increase of pressure oscillation frequency
- increase of pressure oscillation damping

Furthermore, from the fast Fourier transform of the pressure oscillations at different k_a and k_w, it can be shown that the square

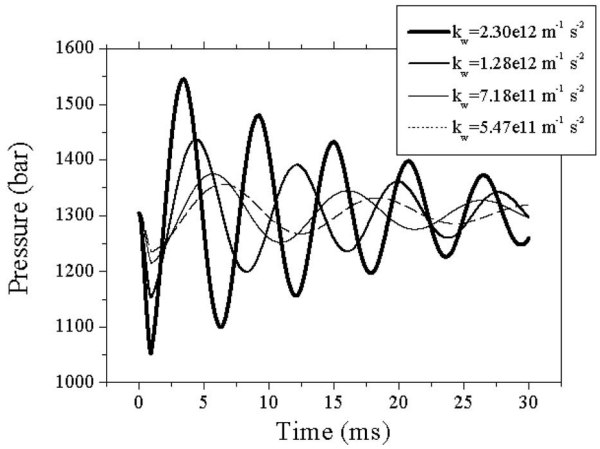

Fig. 3 Injection pressure fluctuations with different values of k_w

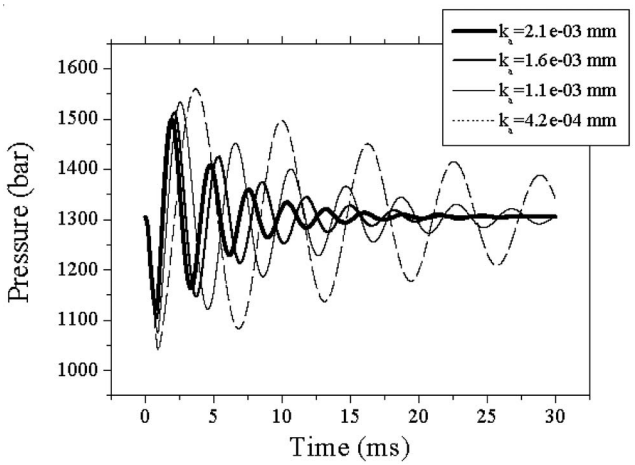

Fig. 4 Injection pressure fluctuations with different values of k_a

of the pressure oscillations frequency varies almost linearly with k_a and k_w. This behavior can be analytically explained with a further simplification of the numerical scheme.

Considering the instant in which the injector nozzle is closed, the mechanical analogous of the system is the damped mass-spring oscillator

$$m\frac{d^2\delta}{dt^2} + K\delta + k_b\frac{d\delta}{dt} = 0 \tag{17}$$

where δ is the displacement of the virtual piston defining the boundary between the orifice and the exterior space.

The equivalent of the oscillator mass is the system mass m_{system}, given by Eq. (8), and the effective stiffness of the system K can be formulated as

$$K = \frac{F_{\text{rail}}}{\delta} \tag{18}$$

where F_{rail} is the virtual force acting on the virtual piston that pushes the fluid through the duct inside the prenozzles volume. The displacement δ can be related to the volume strain of the adiabatically compressed fluid ΔV as follows:

$$\delta = \frac{\Delta V}{A_{\text{rail}}} \tag{19}$$

Considering that compression and expansion of the fluid inside the prenozzles volume are adiabatic, the volume strain ΔV can be related to density and pressure inside the prenozzles volume

$$\Delta V = \frac{\Delta V}{W}W = -\frac{\Delta\rho}{\rho}W = \frac{\Delta P}{\rho a^2}W \tag{20}$$

where ΔP is the pressure variation inside the prenozzles volume.

Therefore, combining Eqs. (10) and (18)–(20), the resulting stiffness of the system is formulated

$$K = \frac{A_{\text{rail}}^2}{W}\frac{(P_{\text{rail}} - P_{\text{inj}})}{\Delta P}\rho a^2 \tag{21}$$

Substituting the preceding results for stiffness and mass, the familiar expression for the natural frequency of an oscillator is

$$f = \frac{1}{2\pi}\sqrt{\frac{K}{m}} = \frac{1}{2\pi}\sqrt{\frac{a^2}{W}\frac{A_{\text{rail}}}{L}\frac{(P_{\text{rail}} - P_{\text{inj}})}{\Delta P}}$$
$$= \frac{1}{2\pi}\sqrt{k_a k_w}\sqrt{\frac{(P_{\text{rail}} - P_{\text{inj}})}{\Delta P}} \tag{22}$$

When the fluid is at rest, the pressure in the nozzle is exactly P_{rail} and then

$$\Delta P = P_{\text{rail}} - P_{\text{inj}} \tag{23}$$

This means that the oscillation frequency is exactly

$$f = \frac{1}{2\pi}\sqrt{k_a k_w} \tag{24}$$

It is important to underline that this is a further simplification of the numerical scheme used to calculate pressure oscillations and cannot be used to predict pressure oscillation. The mechanical analogous of Eq. (1), in fact, supposes that the virtual displacement δ is due only to the flow coming from the rail and cannot predict pressure decreasing during the injection phase, which determines the amplitude of pressure fluctuations. However, this gives a clear indication that the main frequency of the injection pressure fluctuations should scale with $\sqrt{k_a k_w}$.

Figures 5 and 6 show that the damping constant and the injection duration influence only the amplitude of injection pressure oscillation, with no effects on fluctuations frequency.

Finally, it is important to mention that, as can be detected from the experimental data in Fig. 2, actual injection pressure profiles present wiggles also during the injection phase and highlight the presence of other oscillations of smaller amplitude and different frequencies. This model does not take into account these oscillating phenomena, but their effect on the overall spray development and charge formation, which is the main objective of the present submodel, is negligible.

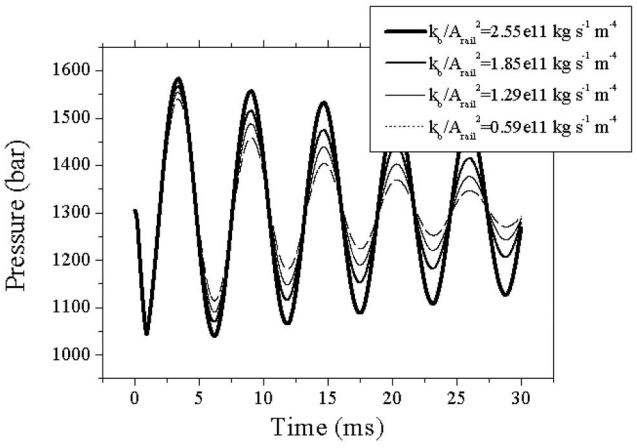

Fig. 5 Injection pressure fluctuations with different values of k_b

Multidimensional Code

The effects of the injection pressure oscillations on the spray development are investigated by means of a multidimensional numerical simulation tool. This code is a modified version of the KIVA-3V code that solves the 3D equations of chemically reactive flows with sprays with a multiblock structured grid approach. A Lagrangian treatment of stochastic particle injection is used for the liquid drops that represent the fuel jet. The fuel that enters the computational domain as a coherent liquid column is artificially divided into a population of simple parcels, and each computational parcel is a statistical representation of a group of identical and noninteracting droplets that exchange mass, momentum, and energy with the surrounding air through source terms in the gas phase equation.

The implemented models enable full 3D computation of both gas and fuel spray dynamics to be made, including atomization, vaporization, autoignition, and combustion.

Although a detailed description of several of the implemented submodels can be found in previous papers [17–19], before de-

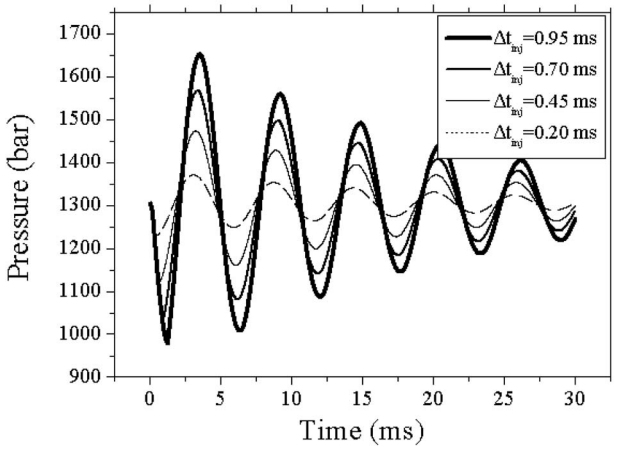

Fig. 6 Injection pressure fluctuations with different injection duration

scribing the data analysis performed with the numerical simulation tool, it is appropriate to describe the main features of the submodels related to the spray formation.

Injection System. First of all, it is important to underline how the common-rail system is treated inside the multidimensional code. In the original KIVA-3V, the input data related to the injection system were geometry in terms of injector position, number of holes and diameter, injected mass or mass flow rate, spray cone angle, and initial spray velocity.

In our modified version, the structure of injection system input data has been completely changed. The injector nozzle geometry, which is not considered in the original KIVA-3V code, is instead very important in diesel engines, since it strongly affects fuel atomization. It being understood that injector position, number of holes, and nozzles diameter are still needed, other geometrical parameters had to be added. As it will be shown later, the implemented nozzle flow model [20] requires as input the length-to-diameter (L/D) ratio and the internal radius-to-diameter (R/D) ratio.

An important feature of modern CR injection systems is that, being the injection timing and pressure unrelated to the engine speed, multiple injections at the same pressure could be performed. Therefore, the KIVA code was modified in order to manage more than one injection in the same run.

The spray initiation within our multidimensional code is based on an initial set of experimental data or on a set of correlations based on literature or on previously acquired experimental data. The input data are organized in order to have the minimum number of input data necessary to identify a single injection.

As it is in a real ECU of a CR diesel engine, in order to unambiguously define each injection, the following two parameters must be fixed:

- SOI (start of injection), which is when the ECU sends the electric signal to the solenoid valve of the injector
- ET (energizing time), which is the duration of the signal.

Then it is the code itself that determines the actual beginning of fuel injection and the actual injection duration directly from experimental data or through correlations. The physical delay in actuating the electrohydraulic system that controls the start of injection is taken into account by considering a delay on the effective start of injection. Moreover, the opening and the closing phases of the nozzle must be considered.

As also shown in Eq. (4), the injected mass flow rate is primarily dependent on the product $C_d A_{\mathrm{noz}}$, where the discharge coefficient C_d represents the efficiency of the nozzle and A_{noz} is the nozzle area. Once the hypothetical discharge coefficient is calculated or read as input by the code, we have to consider that the nozzle area varies during the injector valve opening and closure. Therefore, consider a maximum hypothetical value of $C_d A_{\mathrm{noz}}$, the instantaneous value of $C_d A_{\mathrm{noz}}$ can be calculated by the code once the experimental pintle displacement opening and closure experimental laws are given (to calculate A_{noz}) and once the fuel flow regime is known (to calculate C_d).

Cavitation. The discharge coefficient, in fact, depends on the flow conditions inside the injection holes. Since for CR injection systems the flow inside the injector nozzle is high speed, the orifices are small, the injection duration is very short, and the pressures are very high, experimental investigations on real-size nozzles have shown that the jet surface is already disturbed on exit from the nozzle [21]. Chaves et al. [22] showed that above a certain injection pressure, which depends on the nozzle geometry and on the in-cylinder pressure, cavitation appears at the sharp inlet corner of the nozzle and with increasing injection pressure the cavitation reaches the nozzle exit.

The code presented in this paper uses the phenomenological flow model proposed by Sarre et al. [20] to evaluate the near-nozzle atomization mechanism and to simulate the effects of nozzle geometry on fuel-injection and spray processes. The resulting cavitation predictive submodel provides the initial conditions for the spray model in terms of actual flow area and bubbles injection velocity. The hypothetical discharge coefficient is determined through the L/D ratio. The loss coefficient and the contraction coefficient are calculated by means of the R/D ratio. In order to evaluate whether the flow regime is turbulent or fully cavitating, the mean static pressure of the vena contracta is compared to the fuel vapor pressure. Once the flow regime has been identified, the discharge coefficient can be calculated [20].

Therefore, the mass flow rate is calculated, as shown in Eq. (4), once the injection pressure (input data) and the in-cylinder pressure (given by CFD calculations) are given.

Atomization. The atomization mechanism is simulated through a hybrid approach. It distinguishes between a jet primary breakup and a droplet secondary breakup. A detailed description of the following models can be found in [17,18].

In the primary jet breakup phase a combined approach of turbulence, cavitation, and droplet surface wavelike disturbance is used. In the turbulence-induced atomization model, the interaction between internal jet turbulence, and the surrounding gas inertia are responsible for the breakup. The turbulent fluctuations within the emerging jet produce initial surface instabilities that grow exponentially as a result of interaction with the surrounding gas. A time scale of atomization $\tau_{A,T}$ can be deduced as a function of the turbulence time scale τ_t and the wave growth time scale τ_w dependent on a classical k-ε turbulence model. Alternatively the wave breakup (WB) model can be adopted for liquid core atomization. The WB model is based on a first-order linear stability analysis of a cylindrical liquid jet, which penetrates a steady, incompressible infinite gas medium [23]. In parallel a cavitation-induced model is applied. If the flow is fully cavitating, the occurrence of a high number of cavitating bubbles within the liquid jet core is assumed to induce oscillations on the surface of the jet, which leads to surface disintegration and droplets detachment. A third time scale of atomization $\tau_{A,C}$ can be defined for the bubble collapse. The time scale that produces the fastest setoff of instability is chosen to set off the breakup event.

The secondary droplet breakup modeling is based on droplet deformation by aerodynamic forces, which is a complex flow phenomenon in which the nonhomogeneous pressure distribution on the surface of the bubble leads to shape deformation and then to droplet breakup. Deformation and breakup of a liquid droplet by aerodynamic forces is classified through the Weber dimensionless number We, which defines the ratio between the inertia and the surface tension forces. A critical Weber number We_c, fixed to 12, is the limit over which deformation leads to breakup. Depending on the intensity of the aerodynamic force, five distinct regimes are considered: vibrational, bag, chaotic, stripping, and catastrophic [18]. Each of these regimes is assumed to exist in a certain range of We and for each regime a distinct secondary breakup model is called by the code for estimation of secondary droplets atomization. Secondary breakup criterion in the vibrational regime (slower droplets, usually at the periphery of the spray) is computed with the standard Taylor analogy breakup (TAB) model [24,25]. The droplet deformation and breakup (DDB) approach [26] is used to simulate bag breakup. The stripping regime breakup is modeled through the WB code. In the chaotic regime, in which bag breakup and stripping coexist, a competition between the DDB model and the WB model determines the secondary breakup. Both the TAB and DDB models are based on mechanical droplet oscillation theory described by a second-order one-dimensional differential equation. At higher We the Rayleigh-Taylor (R-T) model [27] is considered. This model simulates the Raleigh-Taylor instabilities that arise on very high-speed droplet surfaces, and as a consequence, it is adopted to model droplet secondary breakup in the catastrophic regime in competition with Kelvin-Helmhotz (K-H) instability based model (wave breakup).

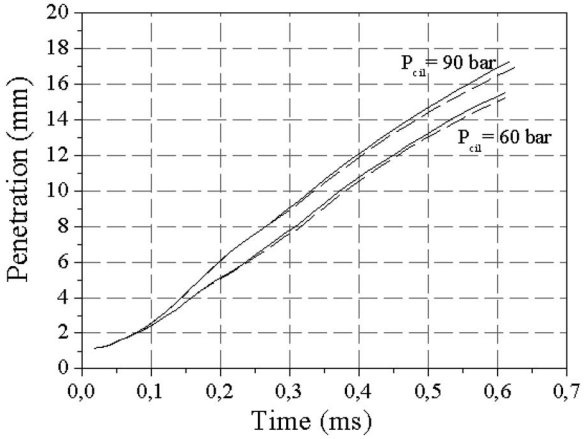

Fig. 7 Supply pressure fluctuations effect on fuel spray penetration

Spray Development

In order to give a quantification of the impact of injection pressure fluctuations on a diesel spray development, the CR injection system with the VCO injector atomizer described in the "Submodel Results" section is considered. As this system behavior is well known through previous works [16,19], it appeared judicious to examine the influence of supply pressure variations on the spray atomization within it. A computational mesh was made, creating a virtual back-pressure vessel, inside which the spray is "virtually" injected.

Among the various consequences due to supply pressure fluctuations, there are two phenomena that produce the greater effects on fuel spray development:

- Considering the single shot injection, supply pressure decreases during the injection phase.
- With multiple injections, the supply pressure variation during the injection phase depends on the previous injections.

As far as the isolated injection is concerned, it can be observed from Fig. 7 that fuel spray penetration is reduced for both 60 bar and 90 bar back pressures when the supply pressure fluctuation model is activated. Moreover, Fig. 8 shows that as the injection pressure decreases, the injection velocity and the injected mass flow rate sensibly decrease (Eq. (5)). Reductions of 9% of fuel flow rate and 5% of total injected mass are observed with variable injection pressure.

Figures 9–11 show supply pressure fluctuation effects for a five-strike multiple injection strategy. A typical injection strategy

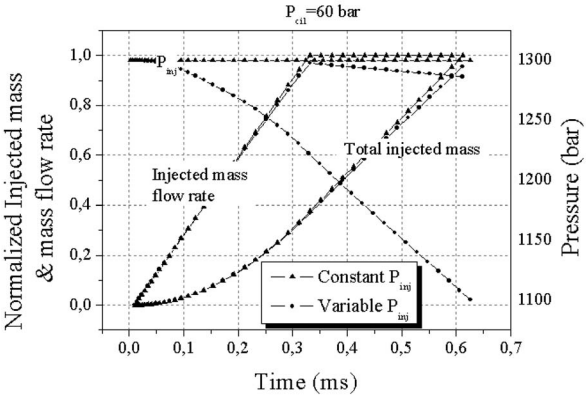

Fig. 8 Supply pressure fluctuations effect on injected mass

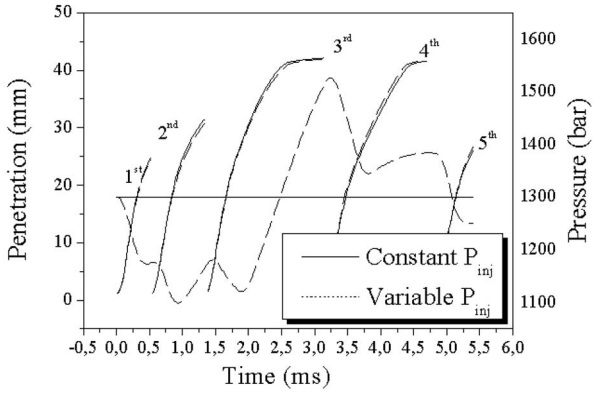

Fig. 9 Supply pressure fluctuations effects on fuel spray penetration with a five-strike strategy

for a direct-injection (DI) diesel engine is chosen [16,19]. As it could be expected, the five-strike strategy is less influenced by the head fluctuation as the injector opening/closure periods represent a higher percentage of the total injection event. Because of the multiple injections, the pressure signal gets an appearance of multiple damped oscillations after each other, as shown in Figs. 9 and 10, and this produces opposite effects from one injection to the other.

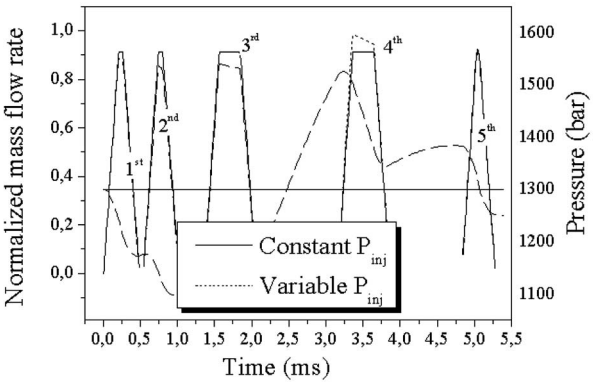

Fig. 10 Supply pressure fluctuations effects on injected mass with a five-strike strategy

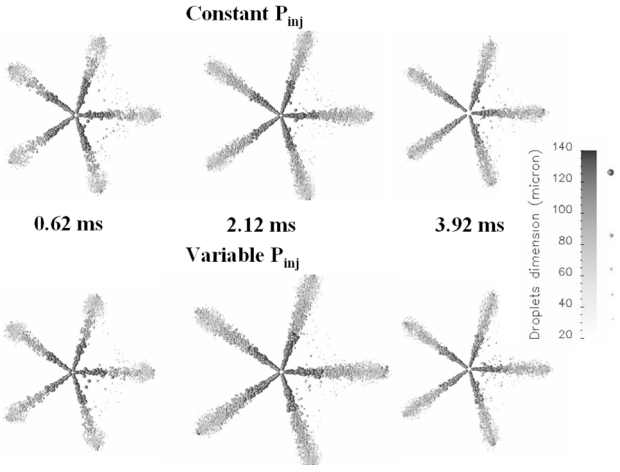

Fig. 11 Supply pressure fluctuations effects on the fuel spray structure with a five-strike strategy

Once supply pressure fluctuations are considered, the following effects are observed from Figs. 9 and 10:

- The injection pressure during the first two shots is always below the nominal value and spray penetration is slightly lower (of the order of 1–2%) than the one calculated with constant pressure; the maximum observed instantaneous mass flow rate difference is around 6%.
- The third injection has a different penetration trend with constant or variable injection pressure and the fuel mass flow rate with variable pressure is significantly lower (about 7% of maximum difference).
- Because of the oscillations produced by the pilot and the main injections, injection pressure is above the nominal value for the two remaining shots that, therefore, present higher fuel spray penetration and fuel mass flow rate; during the fourth shot the fuel mass flow rate calculated with variable injection pressure is up to about 8% greater than that calculated with constant injection pressure.

The above considerations suggest that, moving the spray in a diesel engine, a different power production from the one expected is predictable not only because of a change in the total injected mass (Fig. 10) but also due to an alteration of the spray formation/mixing process (Fig. 11). Moreover, injections timing and duration could be controlled in order to be advantageous, enhancing the mixture formation process.

Observing the details of the spray development shown in Fig. 11, it can be learned that in the case of a variable injector-internal-pressure head, the breakup length, and the secondary breakup conditions do change. In particular, differences up to 10% are observed on the first and the secondary breakup lengths and time scales, thus producing different droplet diameter distributions.

Conclusions

In this paper a physical model to simulate pressure oscillations at the immediate upstream side of the injector atomizer nozzle of a CR injection system is presented. The comparison of numerical results to available experimental data has proven that, after an updating phase, the model can accurately reproduce real injection pressure fluctuations. Obviously, due to the simplicity of the modeling approach, the presence of small amplitude oscillations cannot be predicted.

The model has been implemented in a multidimensional code and numerical results on a 3D virtual spray injected into a constant pressure vessel have shown that the impact of injection pressure fluctuations on injected fuel mass flow rate and fuel spray characteristics is not negligible. Moreover, it is important to note that the shown effects would increase with increasing injection pressures. In the case of multiple injections, the supply pressure fluctuation gets an appearance of multiple damped oscillations that could be controlled to enhance the spray formation/mixing process.

The main advantages of using the presented submodel with respect to conventional 1D/3D coupling are its simplicity, easy numerical implementation, and computational efficiency. In particular, the computational cost of simulating injection pressure fluctuations was found to be negligible with respect to the overall 3D thermofluid dynamics simulation.

Acknowledgment

The author would like to acknowledge Professor Gino Bella for his precious help in the discussion of the results and Dr. Michael Pontoppidan for making available the experimental data.

References

[1] Stumpp, G., and Ricco, M., 1996, "Common Rail—An Attractive Fuel Injection System for Passenger Car DI Diesel Engines," SAE Paper No. 960870.
[2] Boehner, W., and Hummel, K., 1997, "Common Rail System (CR-System) for Commercial Diesel Vehicles," SAE Paper No. 970345.
[3] Arai, M., Hiroyasu, H., Shimizu, M., and Tabata, M., 1984, "Disintegrating Process and Spray Characterization of Fuel Jet Injected by a Diesel Nozzle," SAE Paper No. 840275.
[4] Huh, K., and Gosman, A. D., 1991, "A Phenomenological Model of Diesel Spray Atomization," *Proceedings of the International Conference on Multiphase Flows*, Tsukuba, Japan.
[5] Hiroyasu, H., and Kadota, T., 1976, "Evaporation of a Single Droplet at Elevated Pressures and Temperatures," Bull. JSME, **19**(138), pp. 1515–1521.
[6] Rocco, V., 1993, "Results of Quasi-Steady Evaporation Model Applied to Multi-Dimensional D. I. Diesel Combustion Simulation," SAE Paper No. 930071.
[7] Kong, S.-C., and Reitz, R. D., 1993, "Multidimensional Modeling of Diesel Ignition and Combustion Using a Multistep Kinetic Model," ASME J. Eng. Gas Turbines Power, **101**, pp. 781–789.
[8] Halstead, M. P., Kirsch, L. J., and Quinn, C. P., 1977, "The Autoignition of Hydrocarbon Fuels at High Temperatures and Pressures—Fitting of a Mathematical Model," Combust. Flame, **30**, pp. 45–60.
[9] Kong, S.-C., Han, Z., and Reitz, R. D., 1995, "The Development and Application of a Diesel Ignition and Combustion Model for Multidimensional Engine Simulation," SAE Paper No. 950278.
[10] Ahlin, K., 2000, "Modelling of Pressure Waves in the Common Rail Diesel Injection System," Masters thesis, LiTH-ISY-EX-3081, Linköping Universitet, Linköping.
[11] Digesu, P., Ficarella, A., La Forgia, D., Bruni, G., and Ricco, M., 1994, "Diesel Electro-Injector: A Numerical Simulation Code," SAE Paper No. 940193.
[12] Bianchi, G. M., Pelloni, P., Filicori, F., and Tannini, G., 2000, "Optimization of the Solenoid Valve Behaviour in Common-Rail Injection Systems," J. Fuels Lubr., vol. **109**.
[13] Bianchi, G. M., Falfari, S., Parlotto, M., and Osbat, G., 2003, "Advanced Modeling of Common Rail Injector Dynamics and Comparison With Experiments," SAE Paper No. 2003-01-0006.
[14] Kolade, O. B., Morel, T., and Kong, S. C., 2004, "Coupled 1-D/3-D Analysis of Fuel Injection and Diesel Engine Combustion," SAE Paper No. 2004-01-0928.
[15] Rothrock, A. M., 1931, "Pressure Fluctuations in a Common-Rail Fuel Injection System," NACA Report No. 363, pp. 669–678.
[16] Pontoppidan, M., Ausiello, F., Ubertini, S., and Bella, G., 2004, "Study of the Impact of the Spray Shape Stability and the Combustion Process of Supply Pressure Fluctuations in CR-Diesel Injectors," SAE Paper No. 2004-01-0023.
[17] Ubertini, S., Mariani, F., and Postrioti, L., 2004, "Experimental Validation of a Spray Breakup Model in High Pressure Ambient Conditions," *Selected Papers From the THIESEL 2002*, Springer-Verlag, Berlin, pp. 61–86.
[18] Bella, G., Rocco, V., and Ubertini, S., 2003, "Combustion and Spray Simulation of a DI Turbocharged Diesel Engine," J. Engines, **2002**, pp. 2549–2565.
[19] Pontoppidan, M., Ausiello, F., Bella, G., and Ubertini, S., 2003, "Study of the Impact of the Combustion Process of Injector Nozzle Layout Creating Enhancing Spray Secondary Break-up," SAE Paper No. 2003-01-0706.
[20] Sarre, C. von K., Kong, S. C., and Reitz, R. D., 1999, "Modeling the Effects of Injector Nozzle Geometry on Diesel Sprays," SAE Paper No. 1999-01-0912.
[21] Arcoumanis, C., Flora, H., Gaivaises, M., Kampanis, M., and Horrocks, R., 1999, "Investigations of Cavitation in a Vertical Multi-Hole Injector," SAE Paper No. 1999-01-0524.
[22] Chaves, H., Knapp, M., Kubitzek, A., Obermeier, F., and Schneider, T., 1995, "Experimental Study of Cavitation in the Nozzle Hole of Diesel Injectors Using Transparent Nozzles," SAE Paper No. 950290.
[23] Reitz, R. D., and Diwakar, R., 1987, "Structure of High Pressure Fuel Sprays," SAE Paper No. 870598.
[24] Tanner, F. X., 1997, "Liquid Jet Atomization and Droplet Breakup Modelling of Non-Evaporating Diesel Fuel Sprays," SAE Paper No. 970050.
[25] O'Rourke, P. J., and Amsden, A. A., 1987, "The Tab Method for Numerical Calculation of Spray Droplet Breakup," SAE Paper No. 872089.
[26] Ibrahim, E. A., Yang, H. Q., and Przekwas, A. J., 1993, "Modeling of Spray Droplets Deformation and Breakup," J. Propul. Power, **9**, pp. 651–654.
[27] Patterson, M. A., and Reitz, R., 1998, "Modeling the Effects of Fuel Spray Characteristics on Diesel Engine Combustion and Emission," SAE Paper No. 980131.

H.-J. Kretzschmar[1]
Department of Technical Thermodynamics, University of Applied Sciences of Zittau and Gorlitz, P. O. Box 1455, D-02754 Zittau, Germany
e-mail: hj.kretzschmar@hs-zigr.de

J. R. Cooper
Department of Engineering, Queen Mary University of London, London, UK

A. Dittmann
Department of Technical Thermodynamics, Technical University of Dresden, Dresden, Germany

D. G. Friend
Physical and Chemical Properties Division, National Institute of Standards and Technology, Boulder, CO

J. S. Gallagher
Physical and Chemical Properties Division, National Institute of Standards and Technology, Gaithersburg, MD

K. Knobloch
Department of Technical Thermodynamics, University of Applied Sciences of Zittau and Gorlitz, P.O. Box 1455, D-02754 Zittau, Germany

R. Mareš
Department of Thermodynamics, University of West Bohemia, Plzeň, Czech Republic

K. Miyagawa
Tokyo, Japan

I. Stöcker
Department of Technical Thermodynamics, University of Applied Sciences of Zittau and Gorlitz, P.O. Box 1455, D-02754 Zittau, Germany

J. Trübenbach
Department of Technical Thermodynamics, Technical University of Dresden, Dresden, Germany

W. Wagner
Lehrstuhl für Thermodynamik, Ruhr-Universität Bochum, Bochum, Germany

Th. Willkommen
Department of Technical Thermodynamics, Technical University of Dresden, Dresden, Germany

Supplementary Backward Equations for Pressure as a Function of Enthalpy and Entropy $p(h,s)$ to the Industrial Formulation IAPWS-IF97 for Water and Steam

In modeling steam power cycles, thermodynamic properties as functions of the variables enthalpy and entropy are required in the liquid and the vapor regions. It is difficult to perform these calculations with IAPWS-IF97, because they require two-dimensional iterations calculated from the IAPWS-IF97 fundamental equations. While these calculations are not frequently required, the relatively large computing time required for two-dimensional iteration can be significant in process modeling. Therefore, the International Association for the Properties of Water and Steam (IAPWS) adopted backward equations for pressure as a function of enthalpy and entropy $p(h,s)$ as a supplement to the IAPWS Industrial Formulation 1997 for the Thermodynamic Properties of Water and Steam (IAPWS-IF97) in 2001. These $p(h,s)$ equations are valid in the liquid region 1 and the vapor region 2. With pressure p, temperature $T(h,s)$ can be calculated from the IAPWS-IF97 backward equations $T(p,h)$. By using the $p(h,s)$ equations, the two dimensional iterations of the IAPWS-IF97 basic equations can be avoided. The numerical consistency of pressure and temperature obtained in this way is sufficient for most heat cycle calculations. This paper summarizes the need and the requirements for the $p(h,s)$ equations and gives complete numerical information about the equations. Moreover, the achieved quality of the equations and their use in the calculation of the backward function $T(h,s)$ is presented. The three aspects, numerical consistency with the IAPWS-IF97 basic equations, consistency along subregion boundaries, and computational speed important for industrial use are discussed. [DOI: 10.1115/1.1915392]

1 Introduction

In 1997 the International Association for the Properties of Water and Steam (IAPWS) adopted the IAPWS Industrial Formulation 1997 for the Thermodynamic Properties of Water and Steam (IAPWS-IF97) [1,2]. This set of equations contains fundamental equations, saturation equations, and equations for the most often used backward functions $T(p,h)$ and $T(p,s)$ valid in liquid region 1 and vapor region 2; see Fig. 1.

In modeling power cycles and steam turbines, the backward functions $p(h,s)$ and $T(h,s)$ are also required, though not as often as $T(p,h)$ and $T(p,s)$. Table 1 contains the relative frequency of

[1]To whom correspondence should be addressed.

Submitted to ASME for publication in the JOURNAL OF ENGINEERING FOR GAS TURBINES AND POWER. Manuscript received October 20, 2003; final manuscript received June 22, 2004. Editor: L. S. Langston.

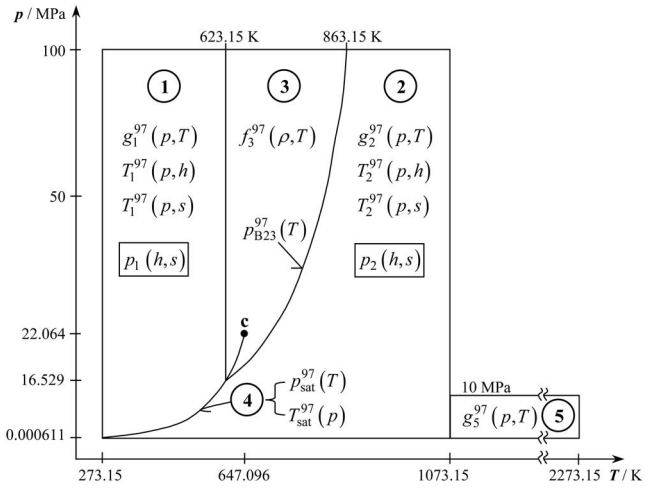

Fig. 1 Range of validity and equations of IAPWS-IF97, and presented backward equations $p(h,s)$

use of the backward functions $p(h,s)$ and $T(h,s)$ in comparison with $T(p,h)$ and $T(p,s)$ determined as a result of an international survey [3].

Although the functions $p(h,s)$ and $T(h,s)$ are seldom used in modeling power cycles, the computing time to calculate them from the IAPWS-IF97 basic equations is very high [4]. The reason is that two-dimensional iterations from $h^{97}(p,T)$ and $s^{97}(p,T)$ are necessary to calculate $p(h,s)$ and $T(h,s)$, where $h^{97}(p,T)$ and $s^{97}(p,T)$ are derivatives of the IAPWS-IF97 fundamental equations $g^{97}(p,T)$.

Therefore, IAPWS decided to develop backward equations $p(h,s)$ for the IAPWS-IF97 regions 1 and 2 (see Fig. 1). With pressure p, temperature T can be calculated from the IAPWS-IF97 backward equations $T^{97}(p,h)$ or $T^{97}(p,s)$.

The $p(h,s)$ equations were adopted by IAPWS at its meeting in Gaithersburg (USA), September 2001, under the name "Supplementary Release on Backward Equations for Pressure as a Function of Enthalpy and Entropy $p(h,s)$ to the IAPWS Industrial Formulation 1997 for the Thermodynamic Properties of Water and Steam [5]." This article provides the technical documentation for the equations.

2 Numerical Consistency Requirements

The backward equations $p(h,s)$ that should be developed have to be numerically consistent with the IAPWS-IF97 equations $h^{97}(p,T)$ and $s^{97}(p,T)$ derived from the Gibbs equation $g^{97}(p,T)$, as shown in Fig. 2.

The permissible value of Δp_{tol} can be determined based on the numerical consistency of the IAPWS-IF97 backward equations $T^{97}(p,h)$ and $T^{97}(p,s)$ using the total differential:

$$\Delta p_{tol} = \left(\frac{\partial p}{\partial h}\right)_s \Delta h_{tol} + \left(\frac{\partial p}{\partial s}\right)_h \Delta s_{tol}, \tag{1}$$

where $(\partial p/\partial h)_s$ and $(\partial p/\partial s)_h$ are derivatives calculated from the IAPWS-IF97 basic equations [6] and Δh_{tol} and Δs_{tol} values set up by IAPWS when developing the IAPWS-IF97 [7].

Table 1 Relative frequency of use of important backward functions in process modeling

	$p(h,s)$ and $T(h,s)$	$T(p,h)$	$T(p,s)$
Liquid region	0.5%	3.2%	1.1%
Vapor region	1.0%	12.4%	6.1%

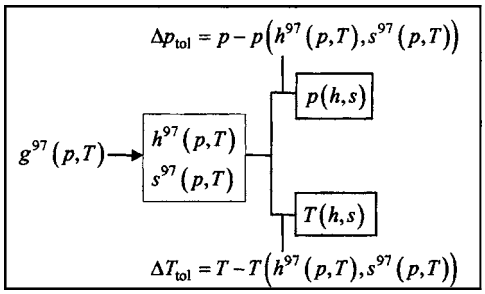

Fig. 2 Numerical consistency relations of the backward functions $p(h,s)$ and $T(h,s)$ with the IAPWS-IF97 equations $h^{97}(p,T)$ and $s^{97}(p,T)$

These Δh_{tol} and Δs_{tol} values are results of an international survey made among power plant companies and related industries. In order to be on the safe side, only the smaller of both summands of Eq. (1) was taken for determining Δp_{tol} in each region.

Table 2 shows the resulting numerical consistencies Δp_{tol} for the liquid region 1 and the vapor region 2. In region 2, the numerical consistency requirement is higher for entropies greater than $s=5.85$ kJ kg^{-1} K^{-1}. The values of Δp_{tol} had to be kept by the developed equations $p(h,s)$.

For the numerical consistency ΔT_{tol} of the backward function $T(h,s)$, Table 2 contains the same values IAPWS set up for the backward equations $T^{97}(p,h)$ and $T^{97}(p,s)$ when developing IAPWS-IF97 [8].

3 Development of the $p(h,s)$ Equations

A short computing time was one of the most important criteria for developing IAPWS-IF97 and also for the supplementary $p(h,s)$ backward equations. Investigations during the development of IAPWS-IF97 showed that polynomials in the form of a series of additions and multiplications are favorable as basic terms [9]. Therefore the following general functional expression was used:

$$\frac{p(h,s)}{p^*} = \sum_i n_i \left(\frac{h}{h^*} + b\right)^{I_i} \left(\frac{s}{s^*} + d\right)^{J_i}. \tag{2}$$

Based on test calculations with Eq. (2), banks of terms with

$$I_i, J_i = 0 \cdots (1) \cdots 7, 8 \cdots (2) \cdots 22, 24 \cdots (4) \cdots 36$$

were generated. The structures of the final equations were found from Eq. (2) by using the approximation algorithm [10–13]. The algorithm combines a special modification of the structure-optimization method of Wagner [14] and Setzmann and Wagner [15] with elements for optimizing nonlinear parameters, automatic data weighting, and data-grid condensation. The modification takes into account the computing time needed to run the equation while it is being developed.

Table 2 Required numerical consistency values Δp_{tol} for $p(h,s)$ and ΔT_{tol} for $T(h,s)$

Region		$\lvert\Delta p\rvert_{tol}$	$\lvert\Delta T\rvert_{tol}$
1	$p \leq 2.5$ MPa	0.6%	25 mK
	$p > 2.5$ MPa	15 kPa	
2	$s < 5.85$ kJ kg^{-1} K^{-1}	0.0088%	25 mK
	$s \geq 5.85$ kJ kg^{-1} K^{-1}	0.0035%	10 mK

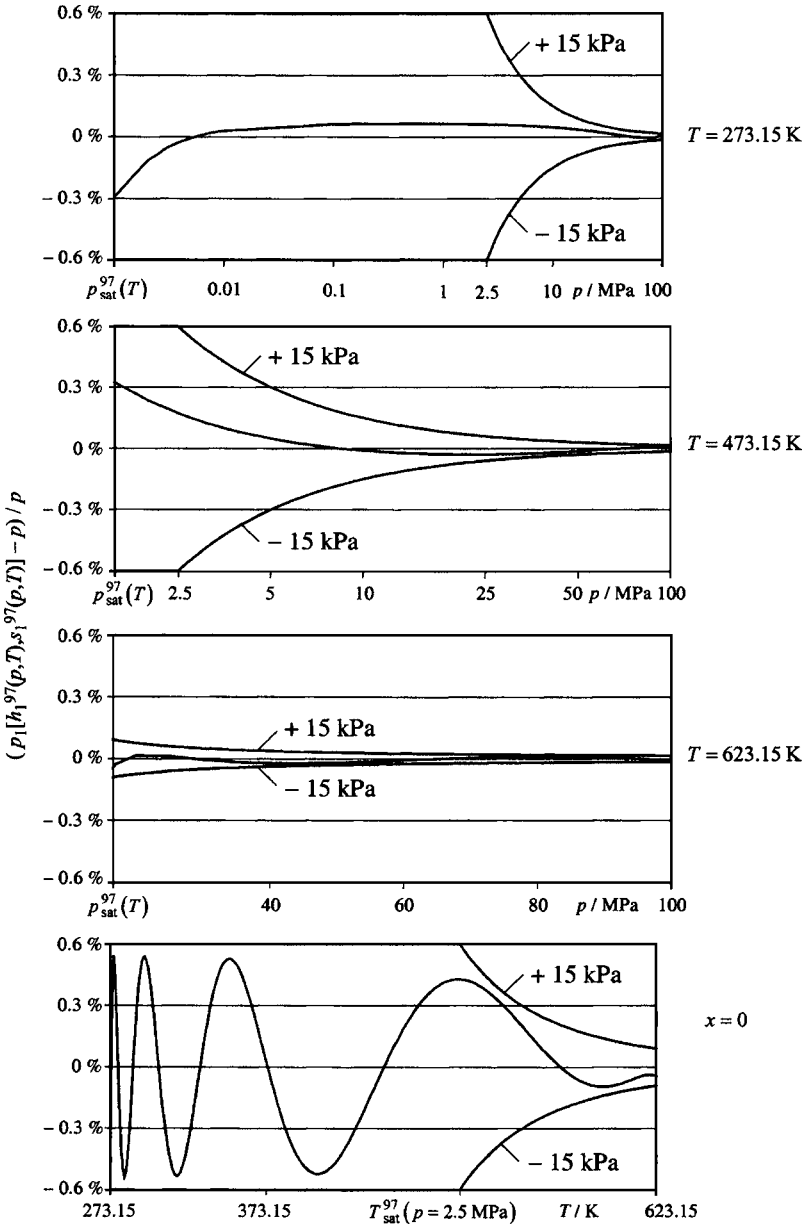

Fig. 3 Numerical consistency of equation $p(h,s)$, Eq. (3), with IAPWS-IF97 equation $g_1^{97}(p,T)$ for selected temperatures and along the saturated liquid line $x=0$

4 The Backward Equation $p(h,s)$ for Region 1

4.1 The Equation. The backward equation $p_1(h,s)$ for region 1 has the following dimensionless form:

$$\frac{p_1(h,s)}{p^*} = \pi(\eta,\sigma) = \sum_{i=1}^{19} n_i(\eta+0.05)^{I_i}(\sigma+0.05)^{J_i}, \qquad (3)$$

where $\pi=p/p^*$, $\eta=h/h^*$, and $\sigma=s/s^*$, with $p^*=100$ MPa, $h^*=3400$ kJ kg^{-1}, and $s^*=7.6$ kJ kg^{-1} K^{-1}. The coefficients n_i and exponents I_i and J_i of Eq. (3) are listed in Table 6 of the Appendix.

4.1.1 Test values. To assist the user in computer-program verification of Eq. (3), Table 7 contains test values for calculated pressures.

4.1.2 Development of Eq. (3). Equation (3) has been developed based on Eq. (2). The reducing parameters p^*, h^*, and s^* are the maximum values of the range of validity of the equation. The shifting parameters b and d were determined by optimization. The exponents I_i, J_i, and the coefficients n_i are results of the structure optimization. In the optimization process, Eq. (3) was fitted to p-h-s values, where h and s had been calculated from the IAPWS-IF97 equation $g_1^{97}(p,T)$, for given values of p and T distributed as selected grid points over region 1. Details of the fitting processes are given in [10].

Table 3 Maximum differences and root-mean-square differences between pressures calculated from Eq. (3) and from IAPWS-IF97 equation $g_1^{97}(p,T)$ in comparison with the permissible differences

	$\lvert\Delta p\rvert_{tol}$	$\lvert\Delta p\rvert_{max}$	$(\Delta p)_{RMS}$
$p \leq 2.5$ MPa	0.60%	0.55%	0.11%
$p > 2.5$ MPa	15 kPa	14 kPa	6 kPa

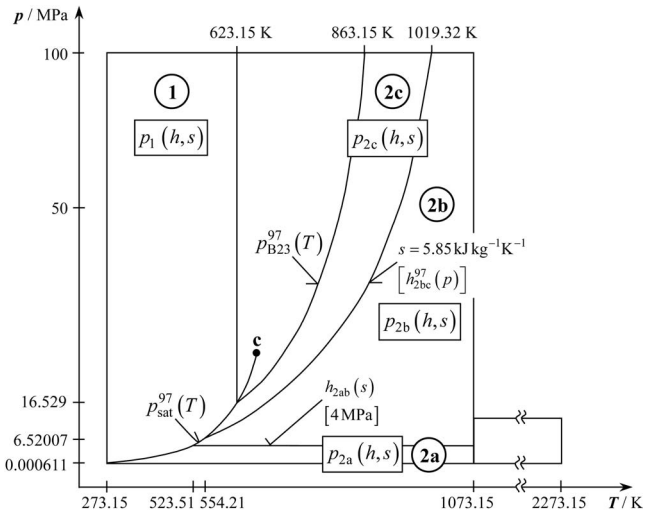

Fig. 4 Division of the IAPWS-IF97 region 2 into three subregions 2a, 2b, 2c for the backward equations $p(h,s)$

4.2 Numerical Consistency. The maximum pressure differences and related root-mean-square differences between $p_1(h,s)$, Eq. (3), and the IAPWS-IF97 fundamental equation $g_1^{97}(p,T)$ are listed in Table 3. For the calculation of the root-mean-square (RMS) values, 100 million points were generated for both pressure regions.

Thus, Eq. (3) meets the numerical consistency requirements of 0.6% for pressures less than or equal to 2.5 MPa and 15 kPa for pressures greater than 2.5 MPa. Figure 3 shows diagrams including relative pressure differences for selected temperatures and along the saturated liquid line $x=0$.

5 The Backward Equations $p(h,s)$ for Region 2

5.1 Subregions. Investigations in the process of developing the backward equations $p(h,s)$ for IAPWS-IF97 region 2 have shown that it was not possible to meet the numerical consistency values Δp_{tol} of Table 2 with a simple $p(h,s)$ equation. The problem was solved by dividing region 2 into three subregions 2a, 2b, and 2c (see Fig. 4). The division corresponds to that used for the IAPWS-IF97 backward equations $T(p,h)$ and $T(p,s)$.

The boundary between the subregions 2b and 2c is the entropy line $s=5.85$ kJ kg^{-1} K^{-1}. It can be tested directly because the specific entropy is a given parameter in the calculation of $p(h,s)$. If the given specific entropy s is greater than or equal to 5.85 kJ kg^{-1} K^{-1}, then the point of state to be calculated is situated in subregion 2b; otherwise it is in subregion 2c, see Fig. 4.

The boundary between subregions 2a and 2b corresponds to the isobar $p=4$ MPa. In order to decide which $p(h,s)$ equation, 2a or 2b, must be used for given values of h and s, the boundary equation $h_{2ab}(s)$, Eq. (4), has to be calculated. It is a polynomial of the third degree and reads

$$\frac{h_{2ab}(s)}{h^*} = \eta(\sigma) = n_1 + n_2\sigma + n_3\sigma^2 + n_4\sigma^3, \tag{4}$$

where $\eta=h/h^*$ and $\sigma=s/s^*$, with $h^*=1$ kJ kg^{-1} and $s^*=1$ kJ kg^{-1} K^{-1}. The coefficients n_1 to n_4 of Eq. (4) are listed in Table 8.

The range of equation $h_{2ab}(s)$ is from $s''(p=4$ MPa) on the saturated vapor line to $s_2^{97}(p=4$ MPa, $T=1073.15$ K); see Fig. 4. Based on its simple form, Eq. (4) does not exactly describe the isobaric line $p=4$ MPa. The maximum deviation in pressure was determined as

$$|\Delta p_{2ab}|_{max} = |p_2^{97}[h_{2ab}(s_2^{97}), s_2^{97}] - 4\ \mathrm{MPa}| = 22\ \mathrm{kPa},$$

where p_2^{97} was obtained by iteration, and $s_2^{97}(p=4$ MPa, $T)$.

If the given specific enthalpy h is greater than $h_{2ab}(s)$ calculated from the given specific entropy s, then the point of state to be calculated is situated in subregion 2b, otherwise it is in subregion 2a (see Fig. 4).

5.1.1 Test Values. For computer-program verification, Eq. (4) gives the following s-h point: $s=7$ kJ kg^{-1} K^{-1}, $h_{2ab}=3376.437\,884$ kJ kg^{-1}.

5.2 The Equations

5.2.1 Subregion 2a. The backward equation $p_{2a}(h,s)$ for subregion 2a in its dimensionless form reads as follows:

$$\frac{p_{2a}(h,s)}{p^*} = \pi(\eta,\sigma) = \left[\sum_{i=1}^{29} n_i(\eta-0.5)^{I_i}(\sigma-1.2)^{J_i}\right]^4, \tag{5}$$

where $\pi=p/p^*$, $\eta=h/h^*$, and $\sigma=s/s^*$, with $p^*=4$ MPa, $h^*=4200$ kJ kg^{-1}, and $s^*=12$ kJ kg^{-1} K^{-1}. The coefficients n_i and exponents I_i and J_i of Eq. (5) are listed in Table 9.

5.2.2 Subregion 2b. The backward equation $p_{2b}(h,s)$ for subregion 2b in its dimensionless form reads as follows:

$$\frac{p_{2b}(h,s)}{p^*} = \pi(\eta,\sigma) = \left[\sum_{i=1}^{33} n_i(\eta-0.6)^{I_i}(\sigma-1.01)^{J_i}\right]^4, \tag{6}$$

where $\pi=p/p^*$, $\eta=h/h^*$, and $\sigma=s/s^*$, with $p^*=100$ MPa, $h^*=4100$ kJ kg^{-1}, and $s^*=7.9$ kJ kg^{-1} K^{-1}. The coefficients n_i and exponents I_i and J_i of Eq. (6) are listed in Table 10.

5.2.3 Subregion 2c. The backward equation $p_{2c}(h,s)$ for subregion 2c in its dimensionless form reads as follows:

$$\frac{p_{2c}(h,s)}{p^*} = \pi(\eta,\sigma) = \left[\sum_{i=1}^{31} n_i(\eta-0.7)^{I_i}(\sigma-1.1)^{J_i}\right]^4, \tag{7}$$

where $\pi=p/p^*$, $\eta=h/h^*$, and $\sigma=s/s^*$, with $p^*=100$ MPa, $h^*=3500$ kJ kg^{-1}, and $s^*=5.9$ kJ kg^{-1} K^{-1}. The coefficients n_i and exponents I_i and J_i of Eq. (7) are listed in Table 11.

Equations (5)–(7) are valid in the respective subregion 2a, 2b, and 2c. The boundaries between these subregions are defined in Sec. 5.1.

Table 4 Maximum differences and root-mean-square differences between pressures calculated from Eqs. (5)–(7) and from the IAPWS-IF97 equation $g_2^{97}(p,T)$ in comparison with the permissible differences

Subregion	Equation	$\lvert\Delta p/p\rvert_{tol}$	$\lvert\Delta p/p\rvert_{max}$	$(\Delta p/p)_{RMS}$
2a	(5)	0.0035%	0.0029%	0.0013%
2b	(6)	0.0035%	0.0034%	0.0005%
2c	(7)	0.0088%	0.0063%	0.0010%

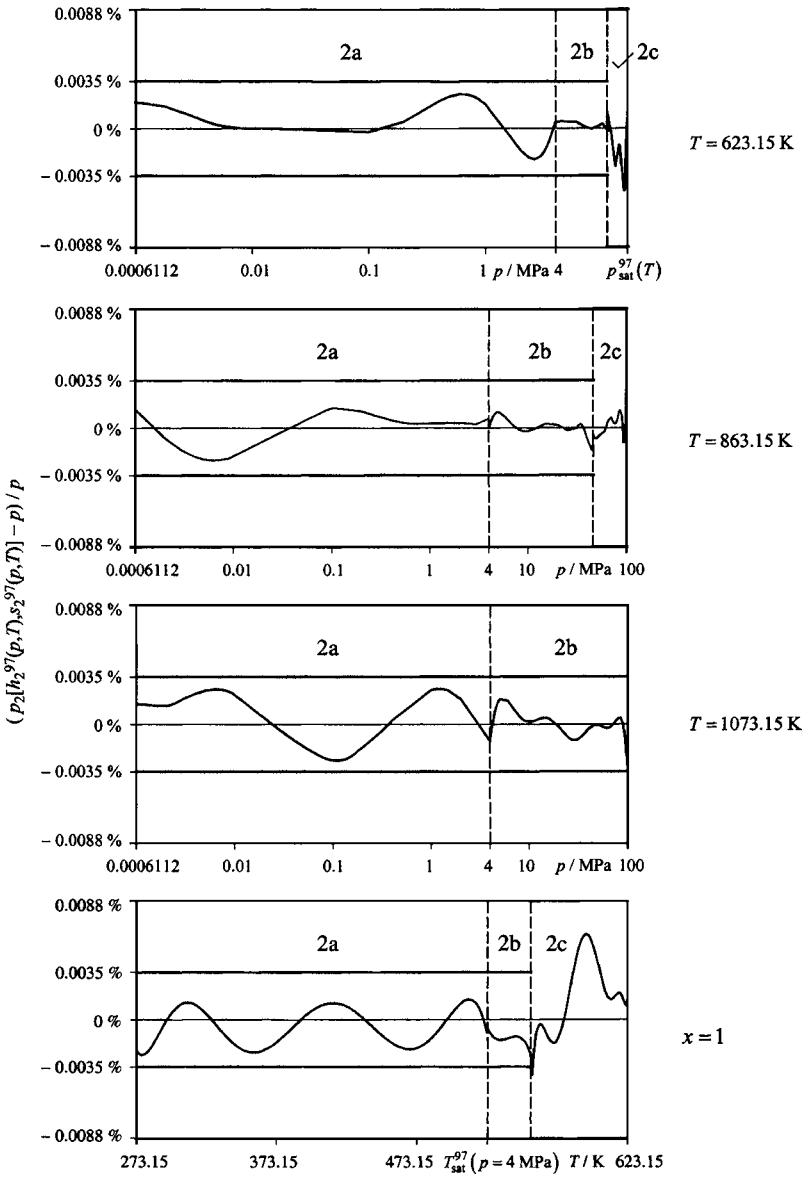

Fig. 5 Numerical consistency of equations $p(h,s)$, Eqs. (5)–(7), with the IAPWS-IF97 equation $g_2^{97}(p,T)$ for selected temperatures and along the saturated vapor line $x=1$

5.2.4 Test Values. To assist the user in computer-program verification of Eqs. (5)–(7), Table 12 contains the test values for calculated pressures.

5.2.5 Development of Eqs. (5)–(7). Equations (5)–(7) have been developed based on Eq. (2). The reducing parameters p^*, h^*, and s^* are the maximum values of the range of validity of the equations. The shifting parameters b and d were determined by optimization. The exponents I_i, J_i, and the coefficients n_i are results of the structure optimization. In the optimization process Eqs. (5)–(7) were fitted to p-h-s values, where h and s had been calculated from the IAPWS-IF97 equation $g_2^{97}(p,T)$, for given values of p and T distributed as selected grid points over subregions 2a, 2b, and 2c. Details of the fitting processes are given in [10].

5.3 Numerical Consistency. The maximum percentage deviations for pressure and related root-mean-square values of the Eqs. (5)–(7) from the IAPWS-IF97 fundamental equation $g_2^{97}(p,T)$ in comparison with the permissible differences are listed in Table 4. The RMS values were calculated from 100 million points for each subregion.

The maximum percentage deviations are less than the permissible differences of 0.0035% for subregions 2a and 2b and 0.0088% for subregion 2c; see Table 2.

Figure 5 illustrates the numerical consistency for selected isotherms and the saturated vapor line $x=1$, where $p(h,s)$ is calculated from Eq. (5) for subregion 2a, from Eq. (6) for subregion 2b, and from Eq. (7) for subregion 2c.

Comparatively, the maximum pressure difference of older equations for $p(h,s)$ for superheated steam of Schwindt [16], and Dohrendorf and Schwindt [17] with the previous industrial standard, the IFC-67 [18], was 1%.

5.4 Consistency at Subregion Boundaries. The relative pressure differences between the two backward equations of the adjacent subregions are smaller than the required numerical con-

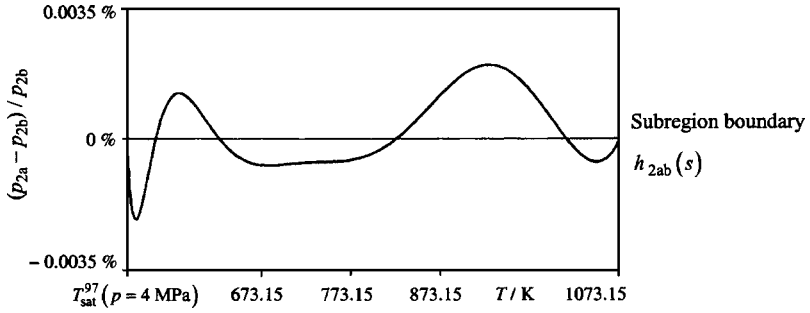

Fig. 6 Numerical consistency between $p_{2a}(h,s)$ and $p_{2b}(h,s)$ equations at the subregion boundary $h_{2ab}(s)$

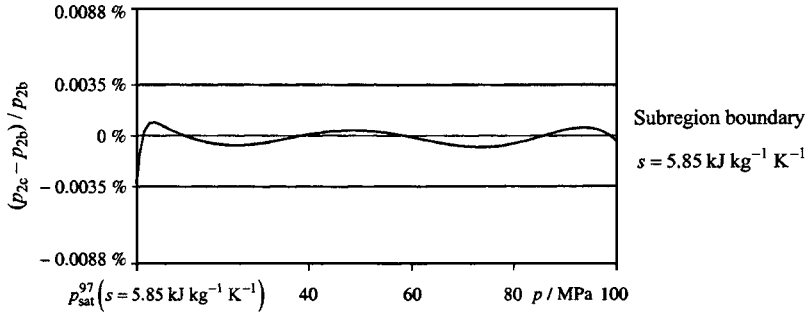

Fig. 7 Numerical consistency between $p_{2b}(h,s)$ and $p_{2c}(h,s)$ equations at the subregion boundary $s=5.85\ \text{kJ kg}^{-1}\ \text{K}^{-1}$

sistencies with the IAPWS-IF97 equation.

At the boundary equation $h_{2ab}(s)$, Eq. (4), between subregions 2a and 2b (see Fig. 4), the maximum difference between the corresponding equations was determined as:

$$|\Delta p/p|_{\max} = |p_{2a}(h,s) - p_{2b}(h,s)|/p_{2b}(h,s) = 0.0022\ \%\ .$$

Figure 6 illustrates the numerical consistency.

At the boundary line $s=5.85\ \text{kJ kg}^{-1}\ \text{K}^{-1}$ between subregions 2c and 2b, the maximum difference is

$$|\Delta p/p|_{\max} = |p_{2c}(h,s) - p_{2b}(h,s)|/p_{2b}(h,s) = 0.0033\ \%\ .$$

Figure 7 illustrates the numerical consistency.

6 The Backward Function $T(h,s)$

6.1 Calculation of the Backward Function $T(h,s)$. The $p(h,s)$ equations described in Secs. 4 and 5 together with the backward equations $T^{97}(p,h)$ [the alternative use of the IAPWS-IF97 backward equations $T^{97}(p,s)$ leads to lower numerical consistency] of IAPWS-IF97 allow the determination of the temperature T from the enthalpy h and entropy s without iteration.

6.1.1 Liquid Region 1. For calculating T from a given h and s in region 1, the following steps should be made:

Table 5 Maximum differences and root-mean-square differences between calculated temperatures and IAPWS-IF97 equations $g_1^{97}(p,T)$ and $g_2^{97}(p,T)$ in comparison with the permissible differences

Region/subregion	$\lvert\Delta T\rvert_{\text{tol}}$	$\lvert\Delta T\rvert_{\max}$	$(\Delta T)_{\text{RMS}}$
1	25 mK	24.0 mK	13.4 mK
2a	10 mK	9.7 mK	3.0 mK
2b	10 mK	9.8 mK	4.0 mK
2c	25 mK	24.9 mK	10.3 mK

(1) Calculate pressure p using the equation $p_1(h,s)$, Eq. (3).
(2) Calculate temperature T using the IAPWS-IF97 equation $T_1^{97}(p,h)$ (see Fig. 1), where p was previously calculated.

6.1.2 Vapor Region 2. For calculating T from given h and s in region 2, the following steps should be made:

(1) Use the equation $h_{2ab}(s)$, Eq. (4), and the entropy line $s=5.85\ \text{kJ kg}^{-1}\ \text{K}^{-1}$ (see Fig. 4) to identify the subregion (2a, 2b, or 2c) for the given values of h and s. Then, calculate the pressure p for the subregion using the equations $p_{2a}(h,s)$, Eq. (5), or $p_{2b}(h,s)$, Eq. (6), or $p_{2c}(h,s)$, Eq. (7).
(2) Use the IAPWS-IF97 equation $h_{2bc}^{97}(p)$ and pressure line $p=4$ MPa to identify the IAPWS-IF97 subregion (2a, 2b, or 2c) for the given value of h and the calculated value of p. Then, calculate temperature T for the subregion using the IAPWS-IF97 backward equations $T_{2a}^{97}(p,h)$, $T_{2b}^{97}(p,h)$, or $T_{2c}^{97}(p,h)$.

6.2 Numerical Consistency. The maximum temperature differences and related root-mean-square differences between the calculated temperature and the IAPWS-IF97 fundamental equations $g_1^{97}(p,T)$ and $g_2^{97}(p,T)$ of regions 1 and 2 are listed in Table 5 together with the permissible differences. The temperature differences were calculated as:

$$\Delta T = (T_1^{97}(p_1(h_1^{97},s_1^{97}),h_1^{97}) - T) \text{ for region 1; and as}$$

$$\Delta T = (T_2^{97}(p_2(h_2^{97},s_2^{97}),h_2^{97}) - T) \text{ for subregions 2a,2b, and 2c.}$$

The function T_2^{97} represents the calculation of $T(p,h)$ using the IAPWS-IF97 backward equations of region 2 including the determination in which subregion (2a, 2b, or 2c) the point is located. The RMS values were calculated from 100 million points for region 1 and subregions 2a, 2b, and 2c.

Figure 8 illustrates the numerical consistency for selected isotherms and along the saturated liquid line $x=0$ for region 1. Figure 9 shows the numerical consistency for selected isotherms and

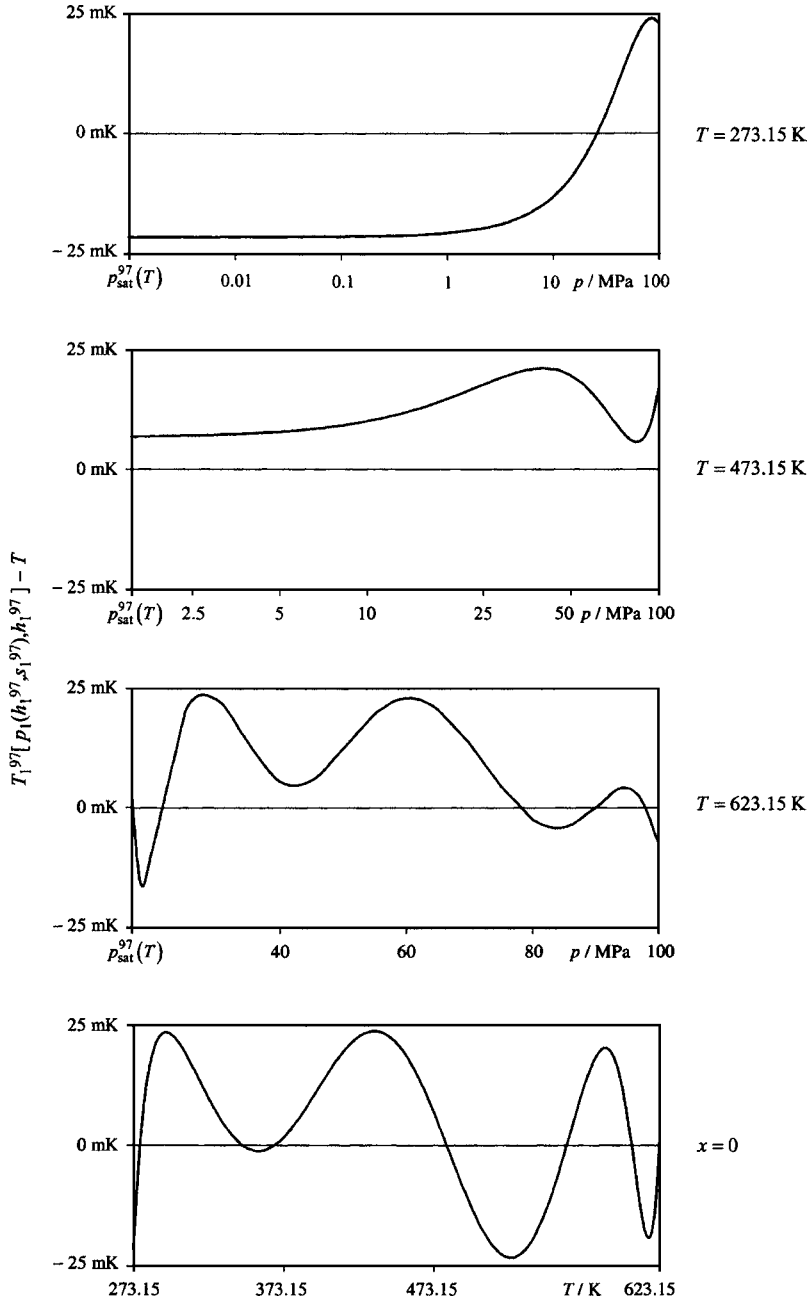

Fig. 8 Numerical consistency of the temperature calculated by $T_1^{97}[p_1(h^{97},s^{97}),h^{97}]$ with the IAPWS-IF97 equation $g_1^{97}(p,T)$ for selected temperatures and along the saturated liquid line $x=0$

along the saturated vapor line $x=1$ for region 2.

The deviations are less than the permissible differences of 10 mK for subregions 2a and 2b, and 25 mK for region 1 and subregion 2c; see Table 2. This means that the accuracy of the pressure calculated by the equations $p(h,s)$ is sufficient for calculating temperature from the IAPWS-IF97 backward equations $T^{97}(p,h)$.

Comparatively, the maximum temperature difference of the older equations $T(h,s)$ for superheated steam of Schwindt [16], and Dohrendorf and Schwindt [17] from the former industrial standard, the IFC-67 [18], was 2 K.

6.3 Consistency at Subregion Boundaries. The temperature differences between the two backward equations of the adjacent subregions have the following values.

6.3.1 Boundary between Subregions 2a and 2b. Along the boundary equation $h_{2ab}(s)$, Eq. (4), the maximum temperature difference was determined to be:

$$|\Delta T|_{max} = |T_2^{97}[p_{2a}(h_{2ab},s),h_{2ab}] - T_2^{97}[p_{2b}(h_{2ab},s),h_{2ab}]| = 6.7 \text{ mK},$$

where the function T_2^{97} represents the calculation of $T(p,h)$ from the IAPWS-IF97 backward equations of region 2 including the determination of the subregion (2a, 2b, or 2c). Figure 10 illustrates the numerical consistency. The peaks result from the fact that the boundary equation $h_{2ab}(s)$, Eq. (4), does not exactly de-

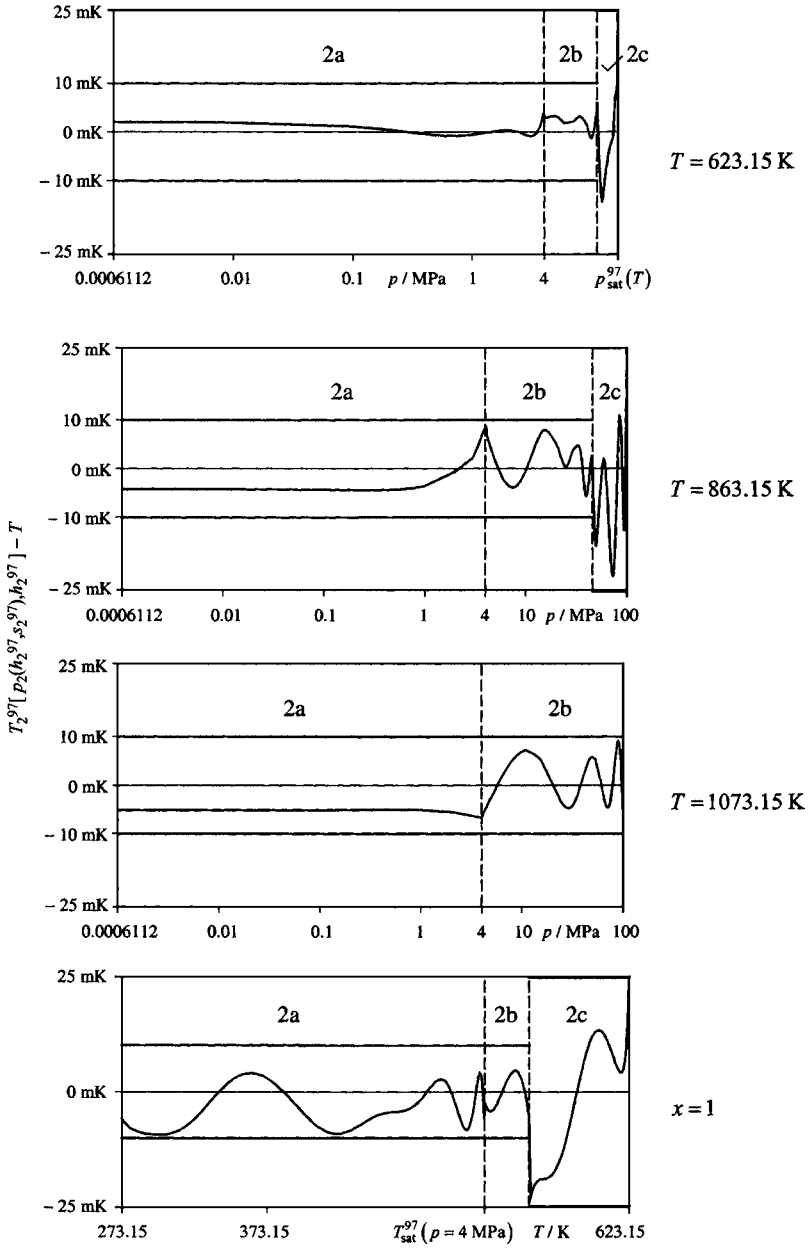

Fig. 9 Numerical consistency of the temperature calculated by $T_2^{97}[p_2(h^{97},s^{97}),h^{97}]$ with IAPWS-IF97 equation $g_2^{97}(p,T)$ for selected temperatures and along the saturated vapor line $x=1$

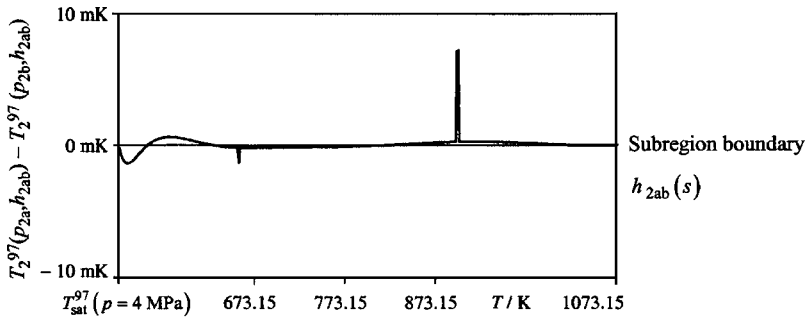

Fig. 10 Numerical consistency of $T_2(h,s)$ at the subregion boundary $h_{2ab}(s)$, Eq. (4)

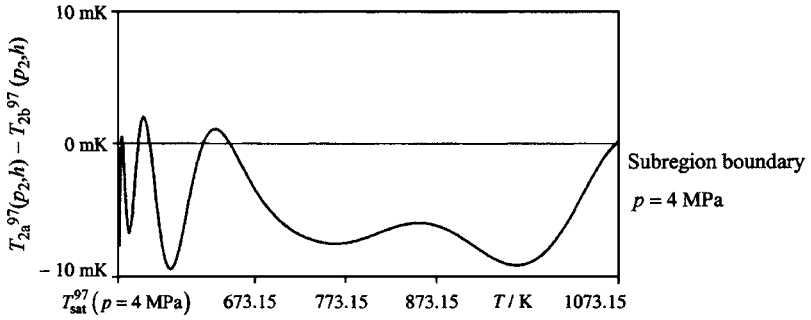

Fig. 11 Numerical consistency of $T_2(h,s)$ at the IAPWS-IF97 subregion boundary line p=4 MPa

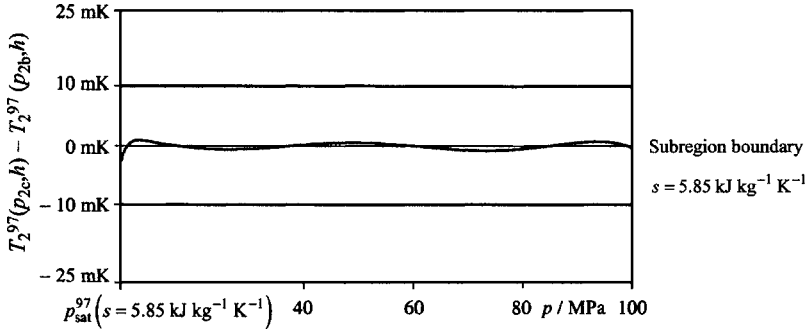

Fig. 12 Numerical consistency of $T_2(h,s)$ at the IAPWS-IF97 subregion boundary s=5.85 kJ kg^{-1} K^{-1}

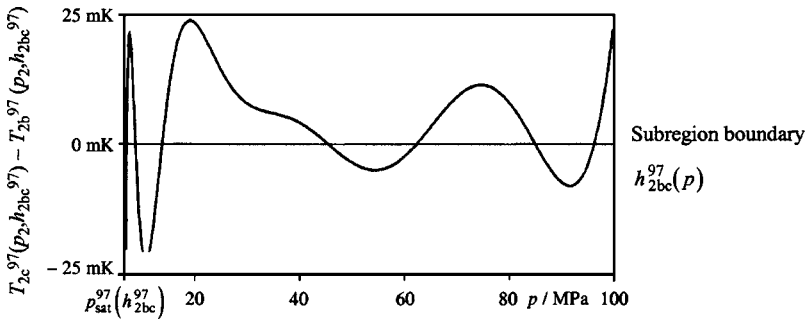

Fig. 13 Numerical consistency of $T_2(h,s)$ at the IAPWS-IF97 subregion boundary $h_{2bc}^{97}(p)$

scribe the isobaric line p=4 MPa.

Along the IAPWS-IF97 boundary line p=4 MPa, the following maximum difference was determined:

$$|\Delta T|_{max} = |T_{2a}^{97}(p_2(h_2^{97},s_2^{97}),h_2^{97}) - T_{2b}^{97}(p_2(h_2^{97},s_2^{97}),h_2^{97})| = 8.7\ \text{mK},$$

where $h_2^{97}(p=4\ \text{MPa},T)$ and $s_2^{97}(p=4\ \text{MPa},T)$. The function p_2 represents the calculation of $p(h,s)$ from the backward equations of region 2, Eqs. (5)–(7), and includes the determination of the subregion (2a, 2b, or 2c). Figure 11 illustrates the numerical consistency.

6.3.2 Boundary between Subregions 2b and 2c. Along the boundary line s=5.85 kJ kg^{-1} K^{-1}, the maximum temperature difference was determined to be:

$$|\Delta T|_{max} = |T_2^{97}[p_{2c}(h,s),h] - T_2^{97}[p_{2b}(h,s),h]| = 2.7\ \text{mK}.$$

Figure 12 illustrates the numerical consistency.

Along the IAPWS-IF97 boundary equation $h_{2bc}^{97}(p)$, the maximum temperature difference was determined to be

$$|\Delta T|_{max} = |T_{2c}^{97}(p_2(h_{2bc}^{97},s_2^{97}),h_{2bc}^{97}) - T_{2b}^{97}(p_2(h_{2bc}^{97},s_2^{97}),h_{2bc}^{97})| = 21.8\ \text{mK}.$$

Figure 13 illustrates the numerical consistency.

7 Computing Time in Relation to IAPWS-IF97

A very important motivation for the development of the backward equations $p(h,s)$ was reducing the computing time to obtain the values of p and T from given values of h and s. In IAPWS-IF97, time-consuming iterative processes, e.g., the two-dimensional Newton method, are required. Using the $p(h,s)$ equations combined with the IAPWS-IF97 backward equations $T^{97}(p,h)$, the calculation speed is between 20 and 30 times faster than two-dimensional iteration of IAPWS-IF97 basic equations.

8 Application of the $p(h,s)$ Equations

The numerical consistency of p and T obtained in the described way is sufficient for most heat-cycle calculations. For users not

satisfied with the numerical consistency of the backward equations, the equations are still recommended for generating good starting points for an iterative process. It will significantly reduce the time to meet the convergence criteria of the iteration.

The backward equations $p(h,s)$ can be used only in their ranges of validity described in Secs. 4 and 5. They should not be used for determining any thermodynamic derivatives. Thermodynamic derivatives can be determined from the IAPWS-IF97 fundamental equations $g_1^{97}(p,T)$ and $g_2^{97}(p,T)$ as described in [6].

In any case, depending on the application, a conscious decision should be made whether to use the backward equations $p(h,s)$ or to calculate the corresponding values by iteration from the basic equations of IAPWS-IF97.

9 Summary

This paper has presented backward equations $p(h,s)$ for water and steam within the IAPWS-IF97 regions 1 and 2. With the determined pressure $p(h,s)$, the temperature $T(h,s)$ can be calculated from the IAPWS-IF97 backward equations $T^{97}(p,h)$. The numerical consistencies of calculated p and T values with those obtained from the IAPWS-IF97 basic equations $g^{97}(p,T)$ are sufficient for most applications in heat-cycle and steam-turbine calculations. For applications where the demands on numerical consistency are extremely high, iterations using the IAPWS-IF97 equations may still be necessary. In these cases, the equations $p(h,s)$ can be used for calculating very accurate starting values.

The calculations of $p(h,s)$ and $T(h,s)$ using the new equations are between 20 and 30 times faster than iteration from IAPWS-IF97.

Users who are interested in these equations can receive the source code upon request; see web site http://thermodynamics.hs-zigr.de.

Acknowledgments

The authors are indebted to other members of the following IAPWS groups: Working Group "Industrial Requirements and Solutions," and Working Group "Thermophysical Properties of Water and Steam." We are grateful to all IAPWS colleagues who contributed to the project of the development of the supplementary equations for the IAPWS Industrial Formulation 1997 for the Thermodynamic Properties of Water and Steam. Special thanks are due to A.H. Harvey for his very effective help. Two of us (H.-J.K. and K.K.) are particularly grateful to the Deutscher Akademischer Austausch Dienst (German Academic Exchange Service) for its financial support and to the National Institute of Standards and Technology, Physical and Chemical Properties Division, for arranging the working period of six months in Boulder, CO, USA.

Nomenclature

f = specific Helmholtz free energy
g = specific Gibbs free energy
h = specific enthalpy
p = pressure
s = specific entropy
T = absolute temperature [1]
x = vapor fraction
Δ = difference in any quantity
η = reduced enthalpy, $\eta=h/h^*$
π = reduced pressure, $\pi=p/p^*$
σ = reduced entropy, $\sigma=s/s^*$
n = coefficient
I = exponent
i = serial number

Superscripts

97 = quantity or equation of IAPWS-IF97
* = reducing quantity
$''$ = saturated vapor state

Subscripts

1 = region 1
2 = region 2
2a = subregion 2a
2b = subregion 2b
2c = subregion 2c
2ab = boundary between subregions 2a and 2b
2bc = boundary between subregions 2b and 2c
3 = region 3
4 = region 4
5 = region 5
B23 = boundary between regions 2 and 3
max = maximum value of a quantity
RMS = root-mean-square value of a quantity
sat = saturation state
tol = tolerance of a quantity

Root-mean-square value:

$$\Delta z_{\mathrm{RMS}} = \sqrt{\frac{1}{m}\sum_{i=1}^{m}(\Delta z_i)^2}$$

where Δz_i can be either the absolute or relative difference between the corresponding quantities z; m is the number of Δz_i values (100 million points well distributed over the range of validity).

Appendix

This appendix contains Tables 6–12, in which the coefficients, exponents, and test values for computer-program verification are listed.

[1]Note: T denotes absolute temperature on the International Temperature Scale of 1990 (ITS-90).

Table 6 Coefficients and exponents of Eq. (3)

i	I_i	J_i	n_i	i	I_i	J_i	n_i
1	0	0	−0.691 997 014 660 582	11	1	4	$-0.319\,947\,848\,334\,300\times10^{3}$
2	0	1	$-0.183\,612\,548\,787\,560\times10^{2}$	12	1	6	$-0.928\,354\,307\,043\,320\times10^{3}$
3	0	2	$-0.928\,332\,409\,297\,335\times10^{1}$	13	2	0	$0.303\,634\,537\,455\,249\times10^{2}$
4	0	4	$0.659\,639\,569\,909\,906\times10^{2}$	14	2	1	$-0.650\,540\,422\,444\,146\times10^{2}$
5	0	5	$-0.162\,060\,388\,912\,024\times10^{2}$	15	2	10	$-0.430\,991\,316\,516\,130\times10^{4}$
6	0	6	$0.450\,620\,017\,338\,667\times10^{3}$	16	3	4	$-0.747\,512\,324\,096\,068\times10^{3}$
7	0	8	$0.854\,680\,678\,224\,170\times10^{3}$	17	4	1	$0.730\,000\,345\,529\,245\times10^{3}$
8	0	14	$0.607\,523\,214\,001\,162\times10^{4}$	18	4	4	$0.114\,284\,032\,569\,021\times10^{4}$
9	1	0	$0.326\,487\,682\,621\,856\times10^{2}$	19	5	0	$-0.436\,407\,041\,874\,559\times10^{3}$
10	1	1	$-0.269\,408\,844\,582\,931\times10^{2}$				

Table 7 Selected pressure values calculated from Eq. (3) for selected enthalpies and entropies

h, kJ kg^{-1}	s, kJ kg^{-1} K^{-1}	$p_1(h,s)$, MPa
0.001	0	$9.800\,980\,612 \times 10^{-4}$
90	0	$9.192\,954\,727 \times 10^{1}$
1500	3.4	$5.868\,294\,423 \times 10^{1}$

Table 8 Coefficients of Eq. (4)

i	n_i	i	n_i
1	$-0.349\,898\,083\,432\,139 \times 10^{4}$	3	$-0.421\,073\,558\,227\,969 \times 10^{3}$
2	$0.257\,560\,716\,905\,876 \times 10^{4}$	4	$0.276\,349\,063\,799\,944 \times 10^{2}$

Table 9 Coefficients and exponents of Eq. (5)

i	I_i	J_i	n_i	i	I_i	J_i	n_i
1	0	1	$-0.182\,575\,361\,923\,032 \times 10^{-1}$	16	1	22	$0.431\,757\,846\,408\,006 \times 10^{4}$
2	0	3	$-0.125\,229\,548\,799\,536$	17	2	3	$0.112\,894\,040\,802\,650 \times 10^{1}$
3	0	6	$0.592\,290\,437\,320\,145$	18	2	16	$0.197\,409\,186\,206\,319 \times 10^{4}$
4	0	16	$0.604\,769\,706\,185\,122 \times 10^{1}$	19	2	20	$0.151\,612\,444\,706\,087 \times 10^{4}$
5	0	20	$0.238\,624\,965\,444\,474 \times 10^{3}$	20	3	0	$0.141\,324\,451\,421\,235 \times 10^{-1}$
6	0	22	$-0.298\,639\,090\,222\,922 \times 10^{3}$	21	3	2	$0.585\,501\,282\,219\,601$
7	1	0	$0.512\,250\,813\,040\,750 \times 10^{-1}$	22	3	3	$-0.297\,258\,075\,863\,012 \times 10^{1}$
8	1	1	$-0.437\,266\,515\,606\,486$	23	3	6	$0.594\,567\,314\,847\,319 \times 10^{1}$
9	1	2	$0.413\,336\,902\,999\,504$	24	3	16	$-0.623\,656\,565\,798\,905 \times 10^{4}$
10	1	3	$-0.516\,468\,254\,574\,773 \times 10^{1}$	25	4	16	$0.965\,986\,235\,133\,332 \times 10^{4}$
11	1	5	$-0.557\,014\,838\,445\,711 \times 10^{1}$	26	5	3	$0.681\,500\,934\,948\,134 \times 10^{1}$
12	1	6	$0.128\,555\,037\,824\,478 \times 10^{2}$	27	5	16	$-0.633\,207\,286\,824\,489 \times 10^{4}$
13	1	10	$0.114\,144\,108\,953\,290 \times 10^{2}$	28	6	3	$-0.558\,919\,224\,465\,760 \times 10^{1}$
14	1	16	$-0.119\,504\,225\,652\,714 \times 10^{3}$	29	7	1	$0.400\,645\,798\,472\,063 \times 10^{-1}$
15	1	20	$-0.284\,777\,985\,961\,560 \times 10^{4}$				

Table 10 Coefficients and exponents of Eq. (6)

i	I_i	J_i	n_i	i	I_i	J_i	n_i
1	0	0	$0.801\,496\,989\,929\,495 \times 10^{-1}$	18	3	12	$0.336\,972\,380\,095\,287 \times 10^{8}$
2	0	1	$-0.543\,862\,807\,146\,111$	19	4	1	$-0.586\,634\,196\,762\,720 \times 10^{3}$
3	0	2	$0.337\,455\,597\,421\,283$	20	4	16	$-0.221\,403\,224\,769\,889 \times 10^{11}$
4	0	4	$0.890\,555\,451\,157\,450 \times 10^{1}$	21	5	1	$0.171\,606\,668\,708\,389 \times 10^{4}$
5	0	8	$0.313\,840\,736\,431\,485 \times 10^{3}$	22	5	12	$-0.570\,817\,595\,806\,302 \times 10^{9}$
6	1	0	$0.797\,367\,065\,977\,789$	23	6	1	$-0.312\,109\,693\,178\,482 \times 10^{4}$
7	1	1	$-0.121\,616\,973\,556\,240 \times 10^{1}$	24	6	8	$-0.207\,841\,384\,633\,010 \times 10^{7}$
8	1	2	$0.872\,803\,386\,937\,477 \times 10^{1}$	25	6	18	$0.305\,605\,946\,157\,786 \times 10^{13}$
9	1	3	$-0.169\,769\,781\,757\,602 \times 10^{2}$	26	7	1	$0.322\,157\,004\,314\,333 \times 10^{4}$
10	1	5	$-0.186\,552\,827\,328\,416 \times 10^{3}$	27	7	16	$0.326\,810\,259\,797\,295 \times 10^{12}$
11	1	12	$0.951\,159\,274\,344\,237 \times 10^{5}$	28	8	1	$-0.144\,104\,158\,934\,487 \times 10^{4}$
12	2	1	$-0.189\,168\,510\,120\,494 \times 10^{2}$	29	8	3	$0.410\,694\,867\,802\,691 \times 10^{3}$
13	2	6	$-0.433\,407\,037\,194\,840 \times 10^{4}$	30	8	14	$0.109\,077\,066\,873\,024 \times 10^{12}$
14	2	18	$0.543\,212\,633\,012\,715 \times 10^{9}$	31	8	18	$-0.247\,964\,654\,258\,893 \times 10^{14}$
15	3	0	$0.144\,793\,408\,386\,013$	32	12	10	$0.188\,801\,906\,865\,134 \times 10^{10}$
16	3	1	$0.128\,024\,559\,637\,516 \times 10^{3}$	33	14	16	$-0.123\,651\,009\,018\,773 \times 10^{15}$
17	3	7	$-0.672\,309\,534\,071\,268 \times 10^{5}$				

Table 11 Coefficients and exponents of Eq. (7)

i	I_i	J_i	n_i	i	I_i	J_i	n_i
1	0	0	0.112 225 607 199 012	17	3	0	0.772 465 073 604 171
2	0	1	$-0.339\,005\,953\,606\,712\times10^{1}$	18	3	5	$0.463\,929\,973\,837\,746\times10^{5}$
3	0	2	$-0.320\,503\,911\,730\,094\times10^{2}$	19	3	8	$-0.137\,317\,885\,134\,128\times10^{8}$
4	0	3	$-0.197\,597\,305\,104\,900\times10^{3}$	20	3	16	$0.170\,470\,392\,630\,512\times10^{13}$
5	0	4	$-0.407\,693\,861\,553\,446\times10^{3}$	21	3	18	$-0.251\,104\,628\,187\,308\times10^{14}$
6	0	8	$0.132\,943\,775\,222\,331\times10^{5}$	22	4	18	$0.317\,748\,830\,835\,520\times10^{14}$
7	1	0	$0.170\,846\,839\,774\,007\times10^{1}$	23	5	1	$0.538\,685\,623\,675\,312\times10^{2}$
8	1	2	$0.373\,694\,198\,142\,245\times10^{2}$	24	5	4	$-0.553\,089\,094\,625\,169\times10^{5}$
9	1	5	$0.358\,144\,365\,815\,434\times10^{4}$	25	5	6	$-0.102\,861\,522\,421\,405\times10^{7}$
10	1	8	$0.423\,014\,446\,424\,664\times10^{6}$	26	5	14	$0.204\,249\,418\,756\,234\times10^{13}$
11	1	14	$-0.751\,071\,025\,760\,063\times10^{9}$	27	6	8	$0.273\,918\,446\,626\,977\times10^{9}$
12	2	2	$0.523\,446\,127\,607\,898\times10^{2}$	28	6	18	$-0.263\,963\,146\,312\,685\times10^{16}$
13	2	3	$-0.228\,351\,290\,812\,417\times10^{3}$	29	10	7	$-0.107\,890\,854\,108\,088\times10^{10}$
14	2	7	$-0.960\,652\,417\,056\,937\times10^{6}$	30	12	7	$-0.296\,492\,620\,980\,124\times10^{11}$
15	2	10	$-0.807\,059\,292\,526\,074\times10^{8}$	31	16	10	$-0.111\,754\,907\,323\,424\times10^{16}$
16	2	18	$0.162\,698\,017\,225\,669\times10^{13}$				

Table 12 Selected pressure values calculated from Eqs. (5)–(7) for selected enthalpies and entropies

Equation	h, kJ kg^{-1}	s, kJ kg^{-1} K^{-1}	p, MPa
$p_{2a}(h,s)$, Eq (5)	2800	6.5	1.371 012 767
	2800	9.5	$1.879\,743\,844\times10^{-3}$
	4100	9.5	$1.024\,788\,997\times10^{-1}$
$p_{2b}(h,s)$, Eq (6)	2800	6.0	4.793 911 442
	3600	6.0	$8.395\,519\,209\times10^{1}$
	3600	7.0	7.527 161 441
$p_{2c}(h,s)$, Eq (7)	2800	5.1	$9.439\,202\,060\times10^{1}$
	2800	5.8	8.414 574 124
	3400	5.8	$8.376\,903\,879\times10^{1}$

References

[1] International Association for the Properties of Water and Steam, 1997, "Release on the IAPWS Industrial Formulation 1997 for the Thermodynamic Properties of Water and Steam," IAPWS Release, IAPWS Secretariat, available at www.iapws.org.

[2] Wagner, W., Cooper, J. R., Dittmann, A., Kijima, J., Kretzschmar, H.-J., Kruse, A., Mareš, R., Oguchi, K., Sato, H., Stöcker, I., Šifner, O., Tanishita, I., Trübenbach, J., and Willkommen, Th., 2000, "The IAPWS Industrial Formulation 1997 for the Thermodynamic Properties of Water and Steam," J. Eng. Gas Turbines Power, **122**, pp. 150–182.

[3] Rukes, B., 1991, "Relative frequencies of use of property functions in process modeling," Report to the Subcommittee Industrial Calculations of IAPWS, Siemens KWU, Erlangen.

[4] Weber, I., 1997, "Test der neuen industriellen Formulierung für Routinen der Wasser-/Dampf-Zustandsgrößen (Test of the new industrial formulation for water and steam)," Report, Siemens Power Generation, Erlangen.

[5] International Association for the Properties of Water and Steam, 2001, "Supplementary Release on Backward Equations for Pressure as a Function of Enthalpy and Entropy $p(h,s)$ to the IAPWS Industrial Formulation 1997 for the Thermodynamic Properties of Water and Steam," IAPWS Release, IAPWS Secretariat, available at www.iapws.org.

[6] Kretzschmar, H.-J., Stöcker, I., Klinger, J., and Dittmann, A., 2000, "Calculation of Thermodynamic Derivatives for Water and Steam Using the New Industrial Formulation IAPWS-IF97," in Tremaine, P. R. et al., eds., "Steam, Water and Hydrothermal Systems: Physics and Chemistry Meeting the Needs of Industry," in Proceedings of the 13th International Conference on the Properties of Water and Steam, NRC Press, Ottawa, pp. 238–247.

[7] Rukes, B., and Wagner, W., 1991, "Final Set of Specifications for the New Industrial Formulation," in Dooley, B., ed., Minutes of the Meetings of the Executive Committee of the International Association for the Properties of Water and Steam, Tokyo 1991, IAPWS Secretariat, pp. 78–82.

[8] Rukes, B., 1994, "Specifications for Numerical Consistency," in Dooley, B., ed., Minutes of the Meetings of the Executive Committee of the International Association for the Properties of Water and Steam, Orlando 1994, IAPWS Secretariat, pp. 31–33.

[9] Kruse, A., and Wagner, W., 1998, "Neue Zustandsgleichungen für industrielle Anwendungen im technisch relevanten Zustandsgebiet von Wasser (New equations of state for water for industrial use)," *Fortschr.-Ber. VDI, Reihe 6*, Nr. 393, VDI-Verlag, Düsseldorf.

[10] Trübenbach, J., 1999, "Ein Algorithmus zur Aufstellung rechenzeitoptimierter Gleichungen für thermodynamische Zustandsgrößen (An algorithm for developing equations of state optimized regarding their computing time consumption)," *Fortschr.-Ber. VDI, Reihe 6*, Nr. 417, VDI-Verlag, Düsseldorf.

[11] Willkommen, Th., Kretzschmar, H.-J., and Dittmann, A., 1995, "An Algorithm for Setting up Numerically Consistent Forward and Backward Equations for Process Modeling," in White et al., eds., Physical Chemistry of Aqueous Systems, in Proceedings of the 12th International Conference on the Properties of Water and Steam, Begell House, New York, pp. 194–201.

[12] Willkommen, Th., 1995, "Ein Algorithmus zur Aufstellung numerisch konsistenter Gleichungen für die in Prozessmodellierungen benötigten thermodynamischen Umkehrfunktionen (An algorithm for developing numerically consistent backward equations for use in process modeling)," Dissertation Faculty of Mechanical Engineering, Technical University of Dresden, Dresden.

[13] Kretzschmar, H.-J., 1990, "Zur Aufbereitung und Darbietung thermophysikalischer Stoffdaten für die Energietechnik (The preparation and processing of thermophysical properties for power engineering)," Habilitation, Faculty of Mechanical Engineering, Technical University of Dresden, Dresden.

[14] Wagner, W., 1974, "Eine mathematisch statistische Methode zum Aufstellen thermodynamischer Gleichungen-gezeigt am Beispiel der Dampfdruckkurve reiner fluider Stoffe (A mathematical statistical method for developing equations of state-demonstration with the vapor pressure curves of pure fluids)," *Fortschr.-Ber. VDI, Reihe 3*, Nr. 39, VDI-Verlag, Düsseldorf.

[15] Setzmann, W., Wagner, W., 1989, "A New Method for Optimizing the Structure of Thermodynamic Correlation Equations," Int. J. Thermophys., **10**, pp. 1103–1126.

[16] Schwindt, H., 1978, "Neue Näherungsformeln für die Zustandsgrößen der Wasserdampfes in Abhängigkeit von Enthalpie und Entropie (New approximations for the properties of steam as a function of enthalpy and entropy)," Brennst.-Waerme-Kraft, **30**, pp. 30–32.

[17] Dohrendorf, E., and Schwindt, H., 1970, "Näherungsformeln für die Zustandsgrößen des Wasserdampfes in Abhängigkeit von Enthalpie und Entropie (Approximations for the properties of steam as a function of enthalpy and entropy)," Brennst.-Waerme-Kraft, **22**, pp. 578–583.

[18] International Formulation Committee of the 6th International Conference on the Properties of Steam, 1967, "The 1967 IFC Formulation for Industrial Use," Verein Deutscher Ingenieure, Düsseldorf.